

**Nanostructured Materials for
Photovoltaics and Microwave
Electronics: methods and
applications.**



Simone Quaranta

April 2017

Contents

List of Figures	1
I Nanomaterials for Photovoltaics and Microwave electronics: background	10
1 Introduction	11
1.1 Thesis's motivation and scope	11
1.1.1 Publications	17
1.2 Nanostructured materials overview	19
1.3 Nanomaterials classification	26
1.4 Techniques for synthesis of nanomaterials	30
1.4.1 Gas phase methods	31
1.4.2 Liquid Phase synthesis	34
1.4.3 Solid state phase synthesis	38
2 Photovoltaics cutting edge	44
2.1 Photovoltaics: definitions	44
2.1.1 Renewable energy	44
2.1.2 "Conventional" PV technologies	49
2.1.3 Additional photovoltaic parameters	56
2.1.4 "New generation" PV technologies	60
3 DSSCs	67
3.1 Introduction	67
3.2 DSSC mechanism: energetics	69
3.3 DSSCs' mechanism: kinetics	75
4 Morphology, doping and heterojunctions	83
4.1 Introduction	83

<i>CONTENTS</i>	3
4.2 Morphology control	84
4.3 Doping: electronic properties control	90
4.4 Heterojunctions: transport properties control	96
5 Colorimetric sensors	112
5.1 "Terpy-based" complexes	112
6 Nanomaterials for microwave sensing devices	119
7 Carbon based microwave devices	134
7.1 Carbon Materials for RF and microwave sapplication	134
II Experimental	145
8 Materials and Methods	146
8.1 Materials	146
8.2 Materials' synthesis and preparation methods	148
8.2.1 Titanium dioxide synthesis	148
8.2.2 TiO ₂ synthesis by soft-polymeric templating method	152
8.2.3 Anatase beads	153
8.2.4 SWCNTs Chirality separation procedures	154
8.3 Materials Characterization	157
8.3.1 Scanning Electron microscopy	157
8.3.2 X-ray diffraction	157
8.3.3 Thermal Analysis	158
8.3.4 UV-Vis. spectroscopy	159
8.3.5 Raman spectroscopy	160
8.3.6 Photoluminescence Excitation (PLE) Spectroscopy	161
8.3.7 Specific surface area determination and porosimetry	162
8.3.8 Chemisorption studies	163
8.3.9 Scanning Tunnel Microscopy	164
8.3.10 Profilometry	164
8.3.11 X-ray Photoelectron Spectroscopy	164
8.4 Devices Fabrication	165
8.4.1 Screen Printing pastes preparation	165
8.4.2 DSSCs' assembly	168

8.4.3	Iron colorimetric sensors	170
8.4.4	Electrochromic devices	172
8.4.5	Microstrip devices (Microwaves resonators)	173
8.5	Devices characterization	176
8.5.1	DSSCs	176
8.5.2	Iron Colorimetric sensors and electrochromic devices	183
8.5.3	Microstrip devices (microwaves resonators)	183
III Results and Discussion		185
9	Materials for DSSCs	186
9.1	TiO ₂ morphology optimization	186
9.1.1	Materials characterization	186
9.1.2	DSSCs characterization	195
9.2	Lanthanides doped TiO ₂ beads	200
9.2.1	Structural, morphological and optical characterization	200
9.2.2	DSSCs with RE doped photoanodes characterization	207
9.3	TiO ₂ /chirality selected SWCNTs heterojunctions	216
9.3.1	SWCNTs characterization	216
9.3.2	Performances of DSSCs with single chiralities CNTs (photoanode)	224
9.3.3	Performances of DSSCs with single chiralities CNTs (cathode)	230
9.4	Conclusions	234
10	Iron Colorimetric sensors and electrochromic devices	238
10.1	Iron Colorimetric sensors	238
10.2	Electrochromic devices	246
10.3	Conclusions	247
11	Microstrip devices (Microwaves resonators)	251
11.1	Iron sensitive antenna	251
11.2	Graphene and MWCNTs loaded antennas	252
11.2.1	Materials characterization	252
11.2.2	Raman analysis	254
11.2.3	MWCNTs samples	262
11.3	Conclusions	263

<i>CONTENTS</i>	5
IV Final conclusions and future work	266
12 Final conclusions and future work	267

List of Figures

1	Thesis's map	5
1.1	Key physical factors that determine DSSC's I-V characteristics. . .	13
1.2	Metallic (gold and silver) nanoparticles of different size.	20
1.3	Different applications of nanomaterials in everyday life.	23
1.4	Moore's law graph	24
1.5	Schematics of an RFID tag.	25
1.6	Classification of dispersed systems according to W. Ostwald.	27
1.7	example of material composed of crystallites	30
1.8	PVD process flow diagram	32
1.9	Van Arkel-deBoer VPT method for group IV metals purification . .	33
1.10	Schematic diagram of a flame pyrolysis	34
1.11	Sol-gel synthesis and its final products	36
1.12	Schematic diagram of hydrothermal-solvothermal synthesis setup . .	38
2.1	Crude oil price (1947-2011)	45
2.2	Energy density graph of energy materials and devices.	47
2.3	Percentage distribution of energy sources (2010).	48
2.4	Solar thermal energy applications.	49
2.5	Best Research-Cell Efficiencies	50
2.6	Schematic representation of p-n junction.	51
2.7	Complete structure of a standard screen printed silicon solar cell. .	54
2.8	I-V (and power) characteristic of a solar cell.	55
2.9	Equivalent circuit for a silicon solar cell.	57
2.10	Effect of R_s and R_{sh} on a solar cell polarization curve.	58
2.11	"Standard" solar spectrum.	59
2.12	Quantum efficiency curve for silicon solar cells.	60
2.13	Crystal structure of $\text{CH}_3\text{NH}_3\text{PbX}_3$ perovskites (X=I, Br and/or Cl). .	61
2.14	Schematic of a sensitized perovskite solar cell.	63

2.15	Structures of an organic solar cell	65
3.1	N-aromatic moieties of DSSCs metal complexes	68
3.2	Common Ru-based dyes for DSSCs	71
3.3	Structure an operative principle of a DSSC.	72
3.4	DSSC materials energy level	73
3.5	Example of a D- π -A sensitizer	74
3.6	Kinetics of charge transfer and electron transport in a DSSC.	76
3.7	Example of bulky substituent for DSSC's dyes	79
4.1	Ordered and disordered porosity of TiO ₂	87
4.2	Schematic representing the various stages of an EISA process	89
4.3	Effect of dopants on TiO ₂ CB and E _F	92
4.4	Schottky junction formation for an n-type semiconductor/metal contact	97
4.5	Schottky Junction at the ZnO-Au interface in a DSSC	98
4.6	Origin of CNTs chirality from a graphene sheet	102
4.7	Experimental (from our lab) absorption spectrum of N-719	104
4.8	Example of <i>type I</i> heterojunction.	106
4.9	<i>Type II</i> (staggered) heterojunction.	107
5.1	Pictorial representation (from our lab) of the iron-(L) complex	117
6.1	Inductive and back-scattered antenna coupling.	122
6.2	schematics of a microstrip device.	123
6.3	Schematics representation of a microstrip patch antenna.	125
6.4	Example of microwave resonant circuit used for chipless RFID sensing	128
6.5	Gas-chromic sensor developed at the Fraunhofer Institute	132
7.1	Example of 3-D gain radiation pattern for a microstrip patch antenna.	140
7.2	Bidimensional section of an antenna's radiation pattern	142
7.3	Example of an RF anechoic chamber for antenna testing	143
8.1	TEOS hydrolysis and condensation mechanism.	150
8.2	SiO ₂ seeding procedure	151
8.3	Schematics of SWCNTs chirality separation by SEGC	155
8.4	Apparatus for single pass SWCNTs chromatographic separation.	156
8.5	Example of Tauc's plot (our lab) for the TiO ₂ mesoporous beads.	161
8.6	TiO ₂ screen printing paste for DSSCs preparation's steps	166
8.7	DSSCs assembled with photoanodes comprising of SWCNTs films	169

8.8	ITO loaded microstrip patch antenna	173
8.9	Microstrip line with graphene thick film deposition in the gap. . . .	175
8.10	DSC thermogram of ethyl cellulose screen printing binder and FR-4 substrate	175
8.11	Extrapolation of R_s and R_{sh} from DSSCs (our lab) I-V under illumination.	177
8.12	Extrapolation of I_0 from a DSSC (our lab) dark polarization curve.	178
8.13	Impedance (Nyquist) plots for typical DSSCs	179
8.14	Profilometry of titania screen printed photoanodes after particles' sintering	182
9.1	X-ray diffraction pattern for the TiO_2 -MSC1 and MSC-2 samples .	187
9.2	XRD pattern (complete and low angles scans for the TiO_2 samples obtained by the soft polymeric templating agent synthetic route . .	188
9.3	XRD spectrum of titania beads from the HDA synthetic approach .	189
9.4	FE-SEM micrographs of TiO_2 MSC-1 sample its silica template . .	190
9.5	SEM micrographs of TiO_2 MSC-2 compared to its silica template .	191
9.6	FE-SEM micrographs of soft-templated TiO_2 samples	192
9.7	FE-SEM micrographs of TiO_2 mesoporous beads obtained with the aid of HDA template	192
9.8	Complete surface characterization (N_2 adsorption isotherm, BET fit and pore size distribution) for TiO_2 mesoporous beads.	194
9.9	TGA-DTA graphs of polymer-templated TiO_2 samples	195
9.10	J-V curves under illumination and dark for cells assembled by using hard, soft-polymeric templated, and and TiO_2 beads materials . . .	197
9.11	IPCE curves of DSSCs assembled by using hard and soft-polymeric templated TiO_2 as photoanode materials	199
9.12	IPCE curves of DSSCs assembled by using TiO_2 mesoporous beads as photoanode materials	200
9.13	XRD spectrum of $TiO_2:Er^{2+}$ beads sample	201
9.14	Mean crystallites size of RE doped titania beads as a function of the lanthanide ions size	202
9.15	SEM micrographs of synthesized bead particles with 0.2 at% of dopant in anatase	203
9.16	High magnification SEM micrographs of synthesized bead particles with 0.2 at% of dopant in anatase	204

9.17 Dye loading vs "film's volume" and vs ionic radius ratios of lanthanides doped DSSC photoanodes	206
9.18 -V polarization curves of DSSCs assembled with titania mesoporous beads doped with the six lanthanides under investigation.	209
9.19 J_{sc} trend vs radius ratio of the RE dopants with respect to the Ti^{4+} ion.	210
9.20 Asymptotic fit of the efficiency values of cells assembled with photoanodes with 0.2 RE % cations solid solutions versus the RE^{3+}/Ti^{4+} radius ratio	210
9.21 Electron diffusion length and energy conversion efficiency vs RE ionic radius	212
9.22 Bode plot for DSSCs assembled with pure and RE doped titania beads 0.2 % at.	214
9.23 Nyquist plots (for 0.2% RE cations solid solutions and pure TiO_2 DSSC photoanodes	215
9.24 Lanthanides doped DSSCs normalized quantum efficiency spectra.	216
9.25 Thermogravimetric analysis of HiPCO prepared raw carbon nanotubes	217
9.26 Raman spectrum of carbon nanotubes prepared by high-pressure carbon monoxide	217
9.27 UV-vis-NIR spectroscopy of dispersed HiPCO carbon nanotubes in 2 wt% SDS	219
9.28 (7,3) chirality SWCNTs obtained by a single pass separation procedure	220
9.29 UV-vis-NIR spectrum of single-pass separation of (7,3)/(6,4) chiralities.	221
9.30 Uv-vis. spectrum and photoluminescence map for a single pass separation of (6,5)/(6,4) tubes	222
9.31 Uv-vis. spectrum for a single pass separation of (6,5) tubes	223
9.32 Transmittance measurements of chirality-specific films on FTO-coated glass	224
9.33 I-V curves of DSSCs taken under an irradiance of 1 sun for chirality specific solar cells.	225
9.34 Dark polarization curves on linear and semi-logarithmic scale for chirality specific DSSC photoanodes	227
9.35 Quantum Efficiency performance of the DSSCs with mixed and single chirality films in the photoanode	228

9.36 I-V Curves of DSSCs taken under an irradiance of 1 sun for DSSCs employing mixed chirality SWCNTs, (6,5) chirality and Pt as a counter electrode.	231
9.37 Quantum efficiency performance of the DSSCs with platinum, mixed chirality films, and (6,5) CNT films	232
9.38 I-V Curves of DSSCs in a dark environment for cells employing Pt, mixed and (6,5) films as cathodes	233
10.1 Representative STM images for (L) -functionalized flat substrates .	240
10.2 Representative TEM images of commercial TiO ₂ anatase nanopowder functionalized with (L)	241
10.3 TEM micrograph of the P-90 TiO ₂ powder (by Evonik, Germany) for iron colorimetric detection	242
10.4 P-90 "cells" for iron (II) colorimetric detection	243
10.5 Profilometry curves of the mesoporous titania beads films deposited and sintered on RCA treated (basic piranha) substrates	243
10.6 Diffusone reflectance spectra of (L) -functionalized screen printed mesoporous titania beads before and after iron adsorption	244
10.7 Color wheel showing the color change of detecting films after applying varying volumes of aqueous Fe ²⁺ solutions	245
10.8 Comparative X-ray photoelectron spectra of (L) anchored to mesoporous TiO ₂ screen-printed films before and after iron adsorption .	246
10.9 Uv-vis spectroscopy analysis reflecting the decrease of (L) concentration in the solution when treated with ITO NPs	247
10.10 BET linear fit of ITO nanoparticles before (a) and after annealing.	248
10.11 Thermal gravimetric analysis in air of L -grafted ITO NPs	249
10.12 Example of "time driven" absorbance spectrum (at 560 nm) for an electrochromic device relying on the ITO-Fe ^{2+/3+} (L) ₂ system. . . .	250
11.1 Return loss (S ₁₁ scattering parameter) for a microstrip patch antenna comprised of etched copper traces and ITO screen printed film loaded either with (L) or with Fe(III)(L) ₂ . The latter obtained by adsorption of Fe ³⁺ on the ITO film sensitized with (L)	252
11.2 Thermal analysis of FR-4 substrate (a) and ITO paste performed in air	253
11.3 Graphene powder FESEM micrographs collected at different magnifications.	254

11.4 FESEM images (at different magnifications) of a MWCNTs thick film deposited on FR4 substrate from a paste containing ethyl cellulose and castor oil dispersed in 80/20 wt% α -terpineol/NMP mixture.	255
11.5 Raman spectrum of the Nanoinnova graphene used for microstrip patch antenna resonator	256
11.6 Raman spectrum of the MWCNTs under investigation for microwaves devices applications.	256
11.7 Nyquist plot for the 12.5 wt % and 25 wt % graphene films	258
11.8 S_{21} (transmission coefficient) for various graphene loadings on a copper etched microstrip line	259
11.9 Microwaves equivalent circuit model of the 25 wt% graphene printed film	260
11.10 Return loss for microstrip patch resonator loaded with different amounts of graphene	261
11.11 Return loss of the reference antenna and of the same devices loaded with a three layers thick MWCNTs film.	263
11.12 E-plane and H-cut radiation patterns of reference antenna and 3-layers loaded MWCNTs antenna	264

List of Tables

9.1	Rietveld refinement parameters for TiO ₂ synthesized by means of different templating agents.	189
9.2	Specific surface area values of the different mesoporous titania samples.	191
9.3	Band gap values of different morphology TiO ₂ samples	196
9.4	Salient photovoltaic parameters of DSSCs assembled with different photoanodes morphology.	196
9.5	Saturation dark current and diode's ideality factors of DSSCs containing morphology specific photoanodes	196
9.6	Rietveld refinement unit cell constants for TiO ₂ beads doped with different amounts of lanthanide ions	202
9.7	Specific surface area and average pores size for the 0.2 % metal atoms RE doped titania beads.	204
9.8	Film thickness and dye loading for all the RE doped TiO ₂ samples.	205
9.9	Band gap values for all lanthanides doped TiO ₂ samples	207
9.10	Experimental photovoltaic parameters of DSSCs as a function of the RE doping (concentration and cation) of the anatase photoanodes under illumination.	208
9.11	DSSCs' with lanthanides doped photoanodes dark parameters (J_0 and m)	208
9.12	Electron diffusion length (L_n) and charge collection efficiency η_{coll} values for lanthanides doped photoanodes.	212
9.13	Estimated electron recombination lifetimes for RE doped and undoped titania photoanodes (0.2 % at).	214
9.14	Sheet Resistance measurements of chirality-specific films.	224
9.15	Significant Photovoltaics parameters for chirality specific photoanodes under 1 kW/m ² irradiance AM 1.5 G and in dark (I_0 and m).	224

9.16 “Schottky-like” barrier height at the TiO ₂ /SWCNTs interface for chirality-specific films into DSSCs	226
9.17 IPCE values at 530 nm measured from curves reported in Figure 9.35	229
9.18 Significant photovoltaics parameters for chirality specific cathodes derived from I-V curves under illumination	230
9.19 IPCE values at 530 nm measured from curves reported in Figure 9.37	232
11.1 Raman peaks’ ratio for the graphene employed in the microstrip patch antenna fabrication.	256
11.2 Sheet resistance (Ω/\square) of different thickness graphene films	257

Acknowledgments

First of all i would like to thank my supervisor Dr. Franco Gaspari and Dr. Alessandro Latini from the Reactivity of inorganic Materials Lab (RIMLab) at Rome "La Sapienza" that have instilled in me most of the science knowledge i have. Furthermore, my gratitude goes to the all RIMLab (Dr. Carmen Cavallo, Riccardo Panetta, Dr. Francesco Di Pascasio, Daniele Gozzi and Alessandro Latini of course)and POLITO (polytechnic of Turin) Carbon group (Alberto Tagliaferro, Mauro Giorcelli, Pravin Jagdale, Aameer Khan, Tanveer Ahmed) members with whom we have established proficuous and steady collaborations devoted to the development and characterization of nanostructured inorganic (with the RIMLab) and carbon materials for different applications (spanning from DSSCs to electromagnetic interference shielding materials). These collaborations have been instrumental to the accomplishment of the present thesis and to publish papers related to the research we have carried out. Without all these people this thesis would have never been accomplished.

A special thank goes also to Dr. Olena Zenkina, Dr. Iraklii Ebralidze, their group and to life's fortunate coincidences. In fact, a advantageous collaboration and true friendship started over the reciprocal necessity to find practical application for terpyridine metal complexes and nanostructured titanium dioxide.

In addition i must thank the people who have introduced me to the high frequency electronic research and that designed the microwave circuit that have been used for the thesis work. In particular, Dr. Khrisna Naishdam from Georgia Tech. and Dr. Patrizia Savi from POLITO's department of electronics and telecommunications that also performed the antenna propagation measurements.

Other people have been of fundamental importance to realize the present thesis. For instance my lab co-worker Victoria Davis that carried out with me a work as massive as separating enough chirality selected carbon nanotubes to fabricate DSSCs photoelectrodes. Finally, i'd like to thank Dr. Jesse Allan (and Dr. Brad Easton) for instructing me about four probes electrical measurements and Genevieve Barnes

for providing me with free access to the rotavapor facilities that have been crucial for screen printing pastes preparation.

Abstract

Nanoscale particles and thin layers are today used for a variety of applications to make industrial products lighter, stronger or more conductive.

This study investigates synthesis, characterization and application of nanostructured materials for “low-cost” photovoltaics and high frequency (microwaves) analog electronics. Indeed, the two areas investigated demonstrate the enormous potential for diverse applications of nanostructured materials.

The initial research stage focused on the optimization of titanium dioxide morphology for Dye Sensitized Solar Cells (DSSCs) applications. Four different combined sol-gel/solvothermal synthetic approaches were adopted and six different anatase phase mesoporous titania were prepared and tested as photoanodes in DSSCs. Superior light scattering properties, stemming from their sub-micrometric mesoporous structure, were proved for TiO_2 beads synthesized by using the hexadecylamine method. An energy conversion efficiency $\eta = 7.0 \%$ was achieved.

The second stage of the research aimed at further DSSC performances' improvements by introducing trivalent rare earth dopants (Pr, Nd, Sm, Gd, Er and Yb) into the “standard” TiO_2 beads. Rare earth ions' dimension was found to affect TiO_2 average crystallites size through nucleation control and ultimately electron recombination lifetime through TiO_2 natural oxygen defectivity and electron-impurity scattering control. While the largest (i.e. the lightest) ions of the lanthanide series (Pr^{3+} and Nd^{3+}) suppress DSSCs performances, cations heavier than Sm^{3+} produce an energy conversion increase compared to pure anatase. The best performances were obtained for a rare earth dopants concentration of 0.2 % erbium atoms ($\eta = 8.7 \%$, 20% efficiency improvement compared to un-doped TiO_2).

The third research step investigated materials capable of modulating TiO_2 optoelectronic and interfacial properties at once, e.g. chirality separated Single Walled Carbon Nanotubes (SWCNTs). Chirality selection allowed for tuning the energy barrier at the TiO_2 /SWCNTs/FTO interface, electronic conductivity enhancement and reduced SWCNTs-Ruthenium dye competition for light absorption resulting in

a 81 % η improvement compared to mixed chirality cells. Besides, certain SWCNTs chiralities were ruled out as useful materials for DSSCs applications.

By taking advantages of high porosity TiO_2 beads, titania affinity for phosphate based moieties and group 8 metals coordination behavior toward pyridyl ligands (like Ruthenium in the N-719 dye used for DSSCs), a high sensitivity (0.3 ppm by naked eye), reusable, Fe^{2+} colorimetric sensor was developed. A terpyridine based ligand, **L** (2,2':6',2''-terpyridin-4'-phosphonic acid), was used as iron sensitive molecule, whereas screen printed TiO_2 beads as scaffold material. Furthermore, **L**-functionalized Indium Tin Oxide (ITO) thick films were proved to be reliable electrochromic materials and possible candidates for trivalent iron detection predicated on microwaves antennas' resonant frequency shift.

Finally, Multiwalled Carbon Nanotubes (MWCNTs) and Graphene films for resonant frequency tuning of copper etched printed circuit boards antennas were produced and electrically characterized over a large range of operating frequencies. The evolution of the thesis' path is illustrated in figure 1

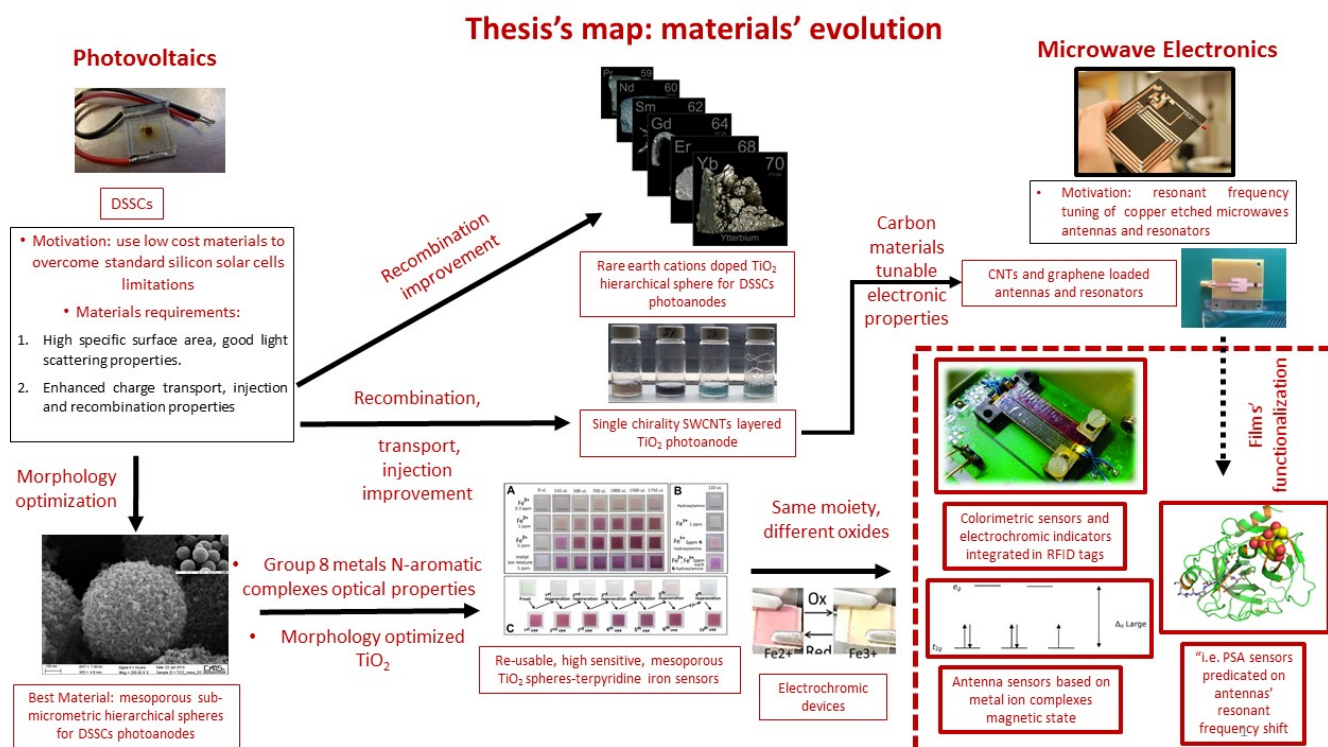


Figure 1: Schematics of present research's evolution, dashed lines represent areas under current investigation.

List of abbreviations

AC – Alternating current

AZO – Aluminum doped Zinc Oxide

BET – Brunauer-Emmett-Teller

BHJ – Bulk Heterojunction

BJH – Barret-Joyner-Halenda

°C– Celsius

C_{μ} – Chemical Capacitance

CB – Conduction Band

CNT – Carbon Nanotubes

DC – Direct current

DOE- Department of energy

DSC – Differential Scanning Calorimetry

DSSC – Dye Sensitized Solar Cell

DTA – Differential Thermal analysis

EC – Electrochromic material

E_F – Fermi Energy

EG– Energy (Band) Gap

EIS– Electrochemical Impedance Spectroscopy

EISA – Evaporation Induced Self Assembly

η – Energy conversion efficiency

FTO – Fluorine doped Tin Oxide

HiPCO – HiPressure Carbon monoxide

HDA – Hexadecylamine

HOMO – Highest Occupied Molecular Orbital

IPCE – Incident Photon to Current Efficiency

I_{sc} – Short circuit current

I₀ – Saturation dark current

I_{0B} – Schottky barrier saturation dark current

j – imaginary unit ($\sqrt{-1}$)

J₀ – Saturation dark current density

J_{sc} – Short circuit current density

(**L**)– 2,2':6',2''terpyridin-4'-ylphosphonic acid

L_n– Electron diffusion length

LUMO – Lowest Unoccupied Molecular Orbital

MWCNT – Multivalled Carbon Nanotubes

NMP – N-methyl-pyrrolidone

n_{cb} – Number of electron in conduction band

PLE– Photoluminescence emission

PMMA-Polymethylmetaacrylate

PVA-Polyvinyl Alcohol

PVB–Polyvinyl Butyral

PVP–Polyvinyl Pyrrolidone

RCT – Charge transfer resistance

R_s – Series resistance

R_{sh} – Shunt resistance

R_{sheet} – Sheet resistance

TiO₂Brij58 – Titanium dioxide synthesized by the soft polymeric templating route employing surfactant Brij-58 as a templating agent

TiO₂MSC1 – Titanium dioxide synthesized by the hard templating route employing 50 nm SiO₂ nanoparticles as a templating agent

TiO₂MSC2 – Titanium dioxide synthesized by the hard templating route employing 20 nm SiO₂ nanoparticles as a templating agent

TiO₂P123 – Titanium dioxide synthesized by the soft polymeric templating route employing surfactant Pluronic 123 as templating agent

TGA – Thermogravimetric analysis

τ_{rec} – Electron recombination lifetime

τ_{rec} - Electron transport time

UPS – Ultraviolet photoelectron spectroscopy

V_j – Junction Built-in potential

V_{FB} – Flat band potential

V_{oc} – Open Circuit Voltage

ω – Angular frequency

XRD – X-ray diffraction

XPS – X-ray photoelectron spectroscopy

Z' – Real impedance

Z'' – Imaginary impedance

φ – Phase angle

Φ_B – Schottky barrier height

Part I

Nanomaterials for Photovoltaics and Microwave electronics: background

Chapter 1

Introduction

1.1 Thesis's motivation and scope

Nanosized materials are involved in countless industrial processes dedicated to the development of lighter, stronger or more conductive commercial products. Everyday usage nanomaterials (and nanotechnology) based items includes: computer hard drivers, bumpers on cars, solid state compasses, protective and glare reducing coatings for eyeglasses and windows, automobile catalytic converters, metal cutting tools, dental bonding agents, longer lasting tennis balls, inks, etc.

Among the innumerable nanotechnology-related research topics, renewable energies, photovoltaics in particular, electronics, environmental and bio-science applications have been assuming a prominent role in the academic and industrial investigations concerning nanostructured materials.

Current photovoltaics research and market aim at developing low-cost and efficient devices capable of working even in low light conditions [1], [2]. Dye Sensitized Solar Cells (DSSCs) represent a valuable alternative to traditional silicon and thin film solar cells in terms production costs and energy conversion efficiency under low and diffuse light irradiance. Unfortunately, DSSCs's efficiency has been improved of only 5% in the last 25 years (from 7 to 13%) [3], and it is still far away from commercial silicon solar cells performances ($\eta= 25\%$ for monocrystalline Silicon and $\eta= 20.4\%$ for polysilicon devices). Nevertheless, DSSCs continue to draw interest from scientists and technologists. In fact, raw materials availability, relatively simple production process, moderate cost compared to traditional photovoltaic, easy fabrication on flexible substrates and different colors layout make DSSCs attractive for portable electronics and building integrated photovoltaics applications. Photoanode semiconductor plays a crucial role among

DSSCs' different components by acting as scaffold material for dye chemisorption and an electron diffusion medium. Anatase TiO_2 allotropic phase remains the best candidate as photoanode material because of its chemical and optoelectronic properties:

- Low toxicity and thermodynamic stability.
- Wide band gap (3.2 eV for the anatase phase) that prevents photoelectrochemical degradation processes.
- Favorable conduction band edge position for electron injection from the ruthenium based dye.
- Possibility to exploit inexpensive synthetic routes (i.e. sol-gel, hydrothermal, solvothermal, titanium anodization, etc.) to obtain nanostructures with enhanced dye adsorption, light scattering and electron transport properties.

However, DSSCs' efficiency improvement remains a complicated task predicated on the delicate balance of beneficial and detrimental effects brought about by any photoanode, electrolyte or counter electrode materials optimization procedure.

During the last ten years the world largest DSSCs manufacturer, Dyesol (Australia) has releasing a series of industrial reports (see references [4], [5], [6]) defining materials and manufacturing guidelines for DSSCs' energy conversion efficiency improvement. Figure 1.1 provides an example of such a Dyesol's recommendations devoted to maximize the DSSCs' output. By limiting the discussion to the photoanode's requirements, Dyesol's reports emphasize the role of TiO_2 morphology in determining the dye's light harvesting efficiency through light scattering. In addition, photoanode doping with hetero-atoms is regarded as an effective technique for charge injection properties and open circuit voltage enhancement. In this work, we focus on maximizing DSSC power output by synthesizing different TiO_2 morphologies capable of improving light absorption by the dye, while retaining long range structural order for fast electron transport and long recombination lifetime. Because of the multiple effects involved (e.g. morphology and dye loading modification, bands energy level shifts, traps compensation, electron-impurity scattering, etc.) DSSCs' energy conversion efficiency enhancement through TiO_2 doping present numerous challenges both in terms of theoretical prediction and in terms of interpretation of the experimental results [7]. Consequently, nature (alkali metal, alkaline earth metals, transition metals, semi-metal or non metals, p-type, n-type, etc.) and concentration of the dopants are decided on empirical basis [7].

Parameter	Target values <i>Comments</i> Underperformance for ...	Influence on			
		ff	V _{oc}	I _{sc}	Eff
Diode ideality factor	Ideally n = 1 For 2 > n >> 1	↘	↘	-	↘
Temperature	Ideally 20-50°C	↘	↗	↘	↘
	< 0°C	↘	↘	↘	↘
	> 50°C	↘	↘	↘	↘
Electrolyte conductivity	Ideally not much lower than 0.01 S/cm, mainly to maintain high enough D(I ₃ ⁻), see sections 7-9				
TCO conductivity	Needs compromising for performance and cost				
	< 10 Ohm/□	↗	↘	↘	↗
	> 15 Ohm/□, low light levels	↘	↗	↘	↘
	> 15 Ohm/□, at higher light levels	↘	↗	↘	↘
Cell width	Needs optimisation for the application >> 10 mm, at higher light levels	↘	-	↘	↘
Cell contacts	Bus bars with sufficient cross section and conductivity. Soldered leads Otherwise:	↘	-	-	↘
Counter electrode	R _{ct} < 3 Ohm cm ²	↘	↘	-	↘
	R _{ct} >> 3 Ohm cm ² , at higher light levels	↘	↘	-	↘
	Too much electrocatalyst	↘	↘	↘	↘
Iodine concentration	To be optimised depending on the application, design and the solvent used				
	>> 0.1 M	↗	↘	↘	↘
	<<0.02 M, at higher light levels	↘	↗	(↘) ⁿ	↘
Mass transport	D(I ₃ ⁻)×[I ₃ ⁻] / d ≥ 7.5×10 ⁻⁸ mol/(cm ² s) = 7.5×10 ⁻⁴ mol/(m ² s)				
	[I ₃ ⁻] too low	↘	↗	(↘) ⁿ	↘
	D(I ₃ ⁻) too low (electrolyte too viscous)	↘	-	(↘) ⁿ	↘
	d too thick	↘	↘	(↘) ⁿ	↘
TiO ₂ layer thickness	To be optimised for each dye				
	Too thin	↘	↗	↘	↘
	Too thick	↘	↘	↘	↘
Optical engineering	Light scattering particles, back reflectors or diffusers, antireflection layer If inadequate:	↘	↘	↘	↘

Figure 1.1: Key physical factors that determine DSSC's I-V characteristics. Adapted with permission from [4].

Thus, we decided to undertake a systematic TiO₂ doping using hetero-atoms within the lanthanides series. This investigation was driven by two motivations:

- Provide a relatively low-cost and industrially scalable approach for dye sensitized solar cells efficiency improvement predicated on titania deep traps compensation.
- Clarify the impact of dopants' chemical and physical characteristics on TiO₂ optoelectronic properties and consequently on DSSCs photovoltaic parameters. Needless to say, a methodical investigation on dopant size and concentration on DSSCs performances grants the possibility to shed light on the behavior of hetero-atoms into the TiO₂ crystalline structure for further DSSC's efficiency increase [8].

Indeed, rare earths' chemical properties regularity (i.e. charge density, acidity, covalent character, etc.) and their dependence on the ionic radius along the series of the fourteen lanthanides elements, permit to establish detailed correlations between macroscopic (e.g. J_{sc} , R_s), microscopic (e.g. τ_{rec} , L_n) photovoltaic parameters and the nature of the dopant.

Besides being a valuable low-cost alternative to crystalline silicon and thin films (i.e. CdTe and CIGS) solar cells, DSSCs constitute also an exceptional "stepping stone" to investigate applicability of opto-electronically engineered materials to high efficiency solar cells such as perovskite devices [9], [10] (see Chapter 2). In fact, DSSCs' photoelectrochemical working principle allows to study the effect of semiconducting materials' work function, band gap, and electrical conductivity on charge injection and recombination, electron transport, light absorption and overall photovoltaic efficiency (see Chapter 3).

SWCNTs chirality separation is a relatively easy approach to select carbon nanotubes opto-electronic properties. Hence, we carried out HiPCO SWCNTs chirality enrichment aiming at:

- The fabrication of TiO₂/chirality selected SWCNTs hetero-structures for switching electron transport media in DSSC photoanodes: from a highly disordered (TiO₂) to an ordered one (CNTs). Therefore, specific chiralities possessing better electron diffusion and capable of increasing the charge injection driving force at the TiO₂/SWCNTs [11] were targeted to boost DSSCs' η compared to cells employing chirality mixed tubes.

- Identifying beneficial effects stemming from chirality separation (e.g. enhanced conductivity of bundles of single chirality CNTs, reduced competition with photovoltaic light absorbing materials, creation of energy barriers to suppress charge electron recombination, etc.) to be used in future researches concerning perovskite solar cells.

As mentioned previously, the characteristics of nanomaterials allow for applications in a variety of fields other than PV, in particular electronics and sensing. In this work, we have tested the properties of the nanostructures developed for DSSC in another applications area (sensing). In particular, optimization of the porosity characteristics (i.e. titania mesoporous beads) has proven to lead to particularly efficient substrate material for metal ion detection [12], as described below.

Inexpensive and rapid detection and quantification of metal cations in aqueous solutions is in high demand for a variety of environmental, industrial (e.g. waste water and plating solutions for the PCBs industry), forensic, biological, and health applications. Especially interesting are systems that allow colorimetric detection to be performed by untrained personnel in field conditions by the naked eye [13]. Ions colorimetric sensors must fulfill plenty of requirements such as stability in aqueous solution (also in harsh pH conditions), reversibility, visible contrast between the colored and colorless states, fast color change, low detection limit and high sensitivity [14], [13]. Because of their intense metal-to-ligand charge transfer (MLCT) optical transitions [15], modified terpyridine ligands-iron(II) complexes have been already used for Fe^{2+} ions fluorimetric and colorimetric detection [16], [17], [18]. However, terpyridines' low solubility in water, chemical and photo-instability, and low specific surface area of the polymer matrix used as ligands' scaffold limits the large scale applicability of such a systems [19], [20]. On the other hand, iron colorimetric in aqueous solution detection through terpyridine complexes can benefit from the use of large surface area and extended porosity inorganic materials like the oxides (TiO_2 , ZnO , Nb_2O_5 , NiO , etc.) employed in DSSCs. In fact, thermodynamic and photochemical stability of nanostructured oxides coupled to suitable mesoporosity for ligand adsorption, make them ideal materials for the colorimetric detection of ions. Furthermore, "tailor made" like scattering properties stemming from sub-micrometric particles morphology improves the terpyridine-Fe(II) complex light harvesting (similarly to the Ru dyes in DSSCs) bringing down both the naked eye and spectrophotometric lower detection limit to the tens of ppm levels [14]. Thus, we investigated TiO_2 hierarchical submicrometric beads previously used as scattering layer for DSSC photoanodes as scaffold materials for phosphonic group modified

iron sensitive terpyridine. The phosphonate group bond to the terpyridine moiety performs two functions: increases the solubility in water of the metal complex and provides a stable chemical link to the titanium dioxide surface [21], [22].

“Smart” materials are able to reversibly change their properties in a controlled fashion by applying an external stimulus. Electrochromic (EC) materials are a class of “smart” materials that are designed to change their optical properties under an applied voltage. The ability of these materials to switch between two colors, usually to bleach and to revive the color, has resulted in their widespread applications in smart windows/mirrors, reflective-type displays, battery charge sensors, and electro-optic modulators [23]. EC materials are represented mostly by the products that incorporate EC redox molecules or transition metal oxides that have a mixed redox state at the metallic center, in conductive polymers. The properties of these composites drastically depend on the overall composition and fine distribution of the EC species in the polymer [24].

In contrast to well-developed polymer chemistry, organo-metallic molecular assemblies with EC properties have only caught the attention of researchers in the past decade, with published reports being rare [25]. Most of these assemblies are based on metal complexes of bipyridine and its derivatives, due to their excellent stability and straight dependence of the light absorption properties of these complexes on the metal oxidation state. While EC molecular assemblies are much more atom efficient than EC polymers, their fabrication process on a flat surface requires precise layer-by-layer deposition sequences that can be time-consuming [26], [27]. When designing materials based on EC molecular assemblies, two limitations should be taken into account: the amount of EC molecular layers should be large enough so that it is visible by the naked eye; and the nature of the involved molecules, the positioning of layers, and overall thickness should permit bidirectional electron-transfer [28].

Phosphonate modified terpyridyne ligands like the ones suitable for iron colorimetric detection possess an extended charge delocalization that might favor the electronic communication between the variable oxidation state metal cation responsible for the electrochromic effect and the semiconductor scaffold. Taking this into account, we hypothesize that the implementation of a conductive nanostructured substrate for metalorganic EC molecules could result in controllable light-reflective devices where high coloration efficiency (CE) and enhanced contrast ratio (significant change of optical density) can be achieved even on a single EC molecular layer [29]. This could have the advantage of minimizing manufacturing time and improving atom efficiency

of the metalorganic moiety required for the EC device. Hence, we investigated new EC material prepared on an indium tin oxide (ITO) screen-printed support by the dip-coating deposition of phosphonate functionalized terpyridyne followed by corresponding metal (Fe, Ru) complex formation.

Another class of smart materials is constituted by “microwave sensitive” nanostructures. These materials are capable of changing their radio-frequency (and microwaves) electrical properties under an external stimulus. Thus, if such as materials are inserted into a microwave resonator or antenna positioned on a RFID (radio frequency identification) tag, a reader’s signal frequency shift and attenuation related to their electrical impedance change can be produced. In fact, microscopic level variation of chemical and physical properties such as electronic and dipole polarizability (i.e. dielectric constant and loss tangent), number of unpaired electrons (i.e. paramagnetism and diamagnetism) electron mobility (i.e. resistivity) generate resonator’s (or antenna’s) capacitance, or inductance or resistance changes [30], [31], [32]. Although this detection principle has been already used for pH, humidity, temperature and light remote sensing [33], it has never be applied to the identification and quantification of neither bio-molecules nor metal ions. Therefore, our approach for remote ions (i.e. Fe^{2+} and Fe^{3+}) relies on phosphonate modified terpyridine ligands chemisorbed on ITO thick films. Indeed, the d^5 configuration of Fe(II) complex with strong field ligands (i.e. N-aromatic ligands) may result into a resonator’s inductance change brought about by the unpaired electron of the coordination compound. On the other hand, graphene and CNTs are renowned for their tunable resistivity and capacitance in presence of surface modifying agents [34]. Thereby, we used MWCNTs and graphene screen printed films to load copper etched resonators to be functionalized with prostate specific antigen antibodies.

1.1.1 Publications

This thesis work has produced the following publications:

- A Comparison of the Performances of Different Mesoporous Titanias in Dye-Sensitized Solar Cells; A. Latini, R. Panetta, C. Cavallo, D. Gozzi, S. Quaranta. *Journal of Nanomaterials* (2015).

S.Q. contribution: I was responsible for synthesis and characterization of different morphology materials (with C.C. and R.P), DSSCs assembly and devices characterization.

- Solid solutions of rare earth cations in mesoporous anatase beads and their

performances in dye-sensitized solar cells; C. Cavallo, A. Salleo, D. Gozzi, F. Di Pascasio, S. Quaranta, R. Panetta, and Alessandro Latini; *Scientific Reports*, 16785(5):1-15, 2015.

S.Q. contribution: I was responsible for synthesis and characterization of lanthanides doped anatase, DSSCs assembly and devices characterization (with C.C. and R.P).

- Effect of Single-Chirality Single-Walled Carbon Nanotubes in Dye Sensitized Solar Cells photoanode; V.L. Davis, S. Quaranta, C. Cavallo, A. Latini, Franco Gaspari. Accepted on *Solar Energy Materials and Solar Cells*.

S.Q. contribution: I was responsible for SWCNTs chirality separation and characterization (with V.L.D.), DSSCs assembly and devices characterization.

- Rational design of a material for rapid colorimetric Fe^{2+} detection N.O. Laschuk, I. I. Ebralidze, S. Quaranta, S. T. W. Kerr, J. G. Egan, Scott Gillis, F. Gaspari, A. Latini, O. V. Zenkina *Materials and Design* 107: 18-25 (2015).

S.Q. contribution: I was responsible for titania synthesis and films deposition, colorimetric sensors production and characterization (with J.G.E. and O.V.Z.).

- Monolayer Electrochromic Materials J .T. A Allan, S. Quaranta, I. I. Ebralidze, J. G. Egan, B. Easton, F. Gaspari, O. V. Zenkina submitted to *Chemistry of Materials*.

S.Q. contribution: I was responsible for bare and ligand-functionalized materials characterization, ITO films deposition, electrochromic devices assembly and spectro-electrochemical characterization (with J.T.A)

- Multi-Walled Carbon Nanotube Thin Film Loading for Tuning Microstrip Patch Antennas P. Savi, K. Naishadam, A. Bayat, Mauro Giorcelli, S. Quaranta *Eucap Proceedings* (2016).

S.Q. contribution: I was responsible carbon materials characterization (with M.G.), films deposition, antenna fabrication and characterization (with P.S.).

- Microwave Characterization of Graphene Films for Sensor Applications P. Savi, K. Naishadam, A. Bayat, Mauro Giorcelli, S. Quaranta *I2MCT Proceedings* (2017).

S.Q. contribution: I was responsible for graphene characterization (with

M.G.), films deposition and their electrical characterization, resonator fabrication and characterization (with P.S.).

1.2 Nanostructured materials overview

Nanoscale materials can be defined as those whose characteristic length scale lies within the nanometric range, i.e in the range between one and several hundreds of nanometers (preferably between 0-100 nanometers) [35]. A nanometer (nm) is one billionth of a meter, or 10^{-9} m. One nanometer is approximately the length equivalent to 10 hydrogen or 5 silicon atoms aligned in a line. On the nanoscale, some physical and chemical material properties can differ significantly from those of the bulk structured materials of the same composition. In fact, crystals in the nanometer scale surface atoms or ions becomes a significant fraction of the total number of atoms or ions and the surface energy plays a significant role in the thermal stability, reactivity and physical-chemical properties ¹. Therefore, many material properties must be revisited in light of the fact that a considerable increase in surface-to-volume ratio is associated with the reduction in material size to the nanoscale, often having prominent effect on material performance. A few examples of chemical and physical materials properties affected by materials size and surface/volume ratio are provided below [36]:

Structural properties . Nanocrystals have a lower melting point (the difference can be as large as 1000 °C) and reduced lattice constant compared to bulk phase materials.

Magnetic properties . The large surface area to volume ratio results in a substantial proportion of atoms having different magnetic coupling with neighboring atoms leading to differing magnetic properties (ferromagnetism, antiferromagnetism, diamagnetism, superparamagnetism, etc.). Bulk gold and platinum are non magnetic but at the nano size they act as magnetic particles, however Au nanoparticles become ferromagnetic when they are capped with the appropriate molecules such as thiols. Giant magnetoresistance (GMR) is a phenomenon observed in nanoscale multilayers consisting of strong ferromagnet (Fe, Co, Ni) and a weaker magnetic or non magnetic buffer(Cr, Cu). It is

¹ i.e. Kelvin (nucleation kinetics) and Young-Laplace (stability of bubbles) equations represent two well-known, everyday, examples of materials reactivity depending on the size. Furthermore, most of the modern heterogeneous catalysis research and applications are predicated on the enhanced reactivity of nanosized metals or oxides.

usually employed in data storage and sensing.

Optical properties . In small nano clusters the effect of reduced dimensionality on electronic structure has the most profound effect on the energies of highest occupied molecular orbital (HOMO) which is valence band and the lowest unoccupied molecular orbital(LUMO), which is essentially the conduction band. Thus, optical absorption and emission transition energies, which determine nanomaterials color, depend on particles' size and shape (see Fig.1.2) Semiconducting quantum dots devices (LED, solar cells, photodetectors, etc.)

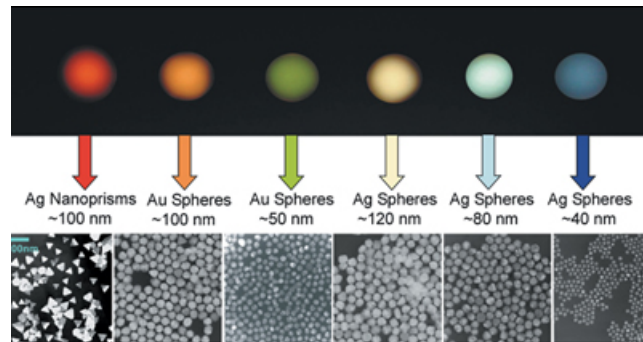


Figure 1.2: Metallic (Gold and Silver) nanoparticles of different size. Particles' color is related to both size and shape. From <http://sciencegeist.net/the-shape-of-things/>

constitute an example of optical properties (i.e. high extinction coefficient and plasmonic resonance) tuning based on nanoscale materials' manipulation. Finally, nanostructured materials can be exploited to control light scattering properties to reduce reflection from surfaces (i.e. nanoporous silica used as antireflective coating in solar panels).

Electronic properties The changes which occur in electronic properties as the system length scale is reduced are related mainly to two parameters: the increasing influence of the electrons wave-like properties (quantum mechanical effects) and presence of a large amount of structural defects (i.e. ions interstitials and vacancies, grain boundaries, etc.) due to the high surface-to-volume ratio. For example, intrinsic electrons wave-like nature can be exploited to achieve quantum mechanical tunnel effects between two closely adjacent nanostructures. On the other hand, high defective surfaces can be easily functionalized to modulate charge generation and transport properties. These phenomena can be used to produce radically different types of components for electronic, optoelectronic and information processing applications,

such as resonant tunneling transistors and single-electron transistors, bulk heterojunction solar cells, etc..

The size effects just described may be divided into two types, the internal and external [37]. Internal or intrinsic size effects are determined as a change of the properties particular to particles (i.e. lattice parameters, melting temperature, hardness, band gap, luminescence, diffusion coefficients, chemical activity, etc.) irrespective of external disturbances. External size effects arise inevitably and always in the processes of interaction between different physical fields and matter under decreasing of its building units (particles, grains, domains) down to a crucial value, when this size becomes to be comparable with a length of physical phenomena (electron diffusion length, phonons, coherent length, Debye screening length, radiative wave length, etc.). Hence, studying the size effects in novel nanostructured materials activated by different external fields one can hope for the discovery of novel effects and phenomena for the development of novel nanotechnology on this base.

Although nanotechnology is a new area of research, the history of nanomaterials began immediately after the big bang when nanostructures were formed in the early meteorites [38]. Nature later evolved many other nanostructures like seashells, skeletons etc. Nanoscaled smoke particles were formed during the use of fire by early humans. Plenty of nanomaterials uses (most of them unaware) can be found the in Ancient World. For instance, the Chinese used gold nanoparticles as an inorganic dye to introduce red color into their ceramic porcelains more than thousand years ago. Roman glass artifacts contained metal nanoparticles, which provided beautiful colors. Recently it has been found that the Maya blue paint is a nanostructured hybrid material. The origin of its color and its resistance to acids and bio-corrosion are still not understood but studies of authentic samples from Jaina Island show that the material is made of needle-shaped palygorskite (a clay) crystals that form a superlattice with a period of 1.4 nm, with intercalates of amorphous silicate substrate containing inclusions of metal (Mg) nanoparticles. The beautiful tone of the blue color is obtained only when both these nanoparticles and the superlattice are present, as has been shown by the fabrication of synthetic samples. Although studies on materials in the nanometer scale can be traced back for centuries, the first scientific report is the colloidal gold particles synthesized by Michael Faraday as early as 1857. Nanostructured catalysts have also been investigated for over 70 years. By the early 1940's, precipitated and fumed silica nanoparticles were being manufactured and sold in USA and Germany as substitutes for ultra-fine

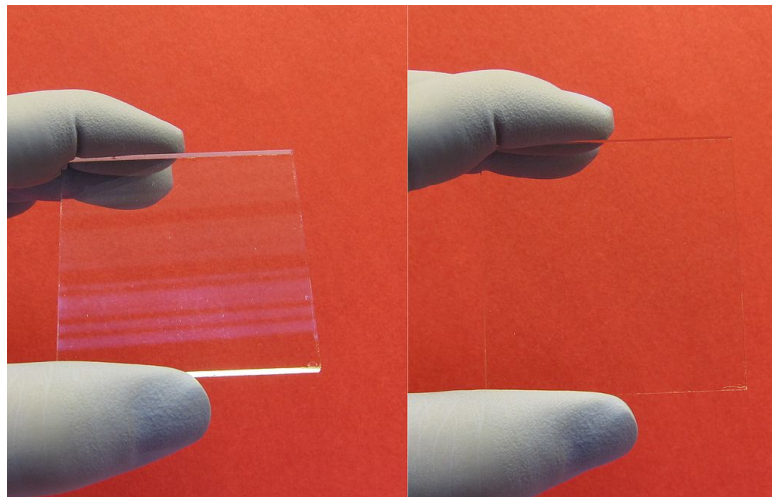
carbon black for rubber reinforcements. Nanosized amorphous silica particles have found large-scale applications in many every-day consumer products, ranging from non-diary coffee creamer to automobile tires, optical fibers and catalyst supports. In the 1960s and 1970s metallic nanopowders for magnetic recording tapes were developed. In 1976, for the first time, nanocrystals produced by the now popular inert gas evaporation technique was published by Granqvist and Buhrman. Probably the most celebrated historical comment on the advancement of nanomaterials was the public speculation by physicist Richard Feynman in 1959 at a meeting of the American Physical Society about the effects of manipulating minuscule bits of condensed matter in his famous talk "*There's plenty of room at the bottom*" [39]. Today nanosized materials are used in numerous industries, e.g., carbon nanofibers are used for insulation and reinforcement of composites; nano zinc oxides and titania are used as sunblocks for UV rays, etc.. Nanoscale particles and nano thin layers of materials are being used to make products lighter, stronger or more conductive. Some of the products on the market using nanotechnology are (see figure 1.3): computer hard drivers, bumpers on cars, solid state compasses, protective and glare reducing coatings for eyeglasses and windows, automobile catalytic converters, metal cutting tools, dental bonding agents, longer lasting tennis balls, inks, etc. Promising applications of nanotechnology in medicine and/or biology have attracted a lot of attention and have become a fast growing field. One of the attractive applications in nanomedicine is the creation of nanoscale devices for improved therapy and diagnostics [40]. Although nowadays nanomaterials are involved in every and each aspect of materials technology, the current research of nanotechnology is still largely driven by miniaturization of devices for the semiconductor industry. The continued decrease in device dimensions has followed the well-known Moore's law predicted in 1965 [41]. The trend line illustrates the fact that the number of transistor transistor size has decreased by a factor of 2 every 18 months since 1950 (see Figure 1.4). Examples of nanomaterials applications introduced with the (2012) 22 nm node technology for CMOS (Complementary Metal-Oxide-Semiconductor) fabrication are thin films (1-10 nm) [42] of high-k dielectrics² and polymers for nano-imprint lithography³.

²High-k materials are insulators materials meant to overcome SiO₂ limitations as MOSFET (Metal-Oxide-Semiconductor Field Effect Transistor) dielectric. In fact, a relative dielectric constant value higher than 3.9 (the corresponding value for thermally grown SiO₂) allows for higher drain saturation current with smaller devices and less leakage current. Most of High-k dielectrics are Hf and Zr based oxides and silicates

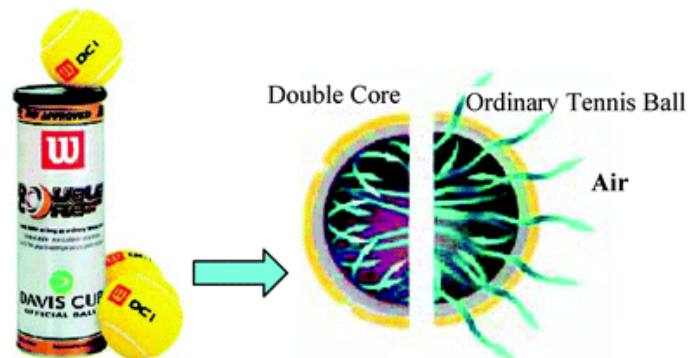
³Unlike traditionally optical lithographic approaches, which create pattern through the use of photons or electrons to modify the chemical and physical properties of the resist, Nanoimprint



(a) Uv Sun screen. From <http://www.vivawoman.net/2007/11/best-sunblock-review-keys-solar-rx/>



(b) Antireflective Coating. From https://en.wikipedia.org/wiki/Anti-reflective_coating#/media/File:Antireflection_coating_split_pic.jpg



(c) Long life tennis Wilson tennis balls. From https://www.researchgate.net/figure/220020746_fig26

Figure 1.3: Different applications of nanomaterials in everyday life. (a) Zinc Oxide (wide band gap semiconductor) nanoparticles are used in sun screen formulations as UV filters. (b) Magnesium Fluoride (MgF_2) thin films (refracion index 1.38) are routinely employed as antireflective coating on crown glass. Thin film interference (based on the refraction index matching principle) is visible when the glass is tilted. (c) Wilson Double Core tennis balls optimized to avoid air leaking. A thin coating of mortmollite (a clay) nanoparticles act as a sealant, making it very difficult for air to escape the ball.

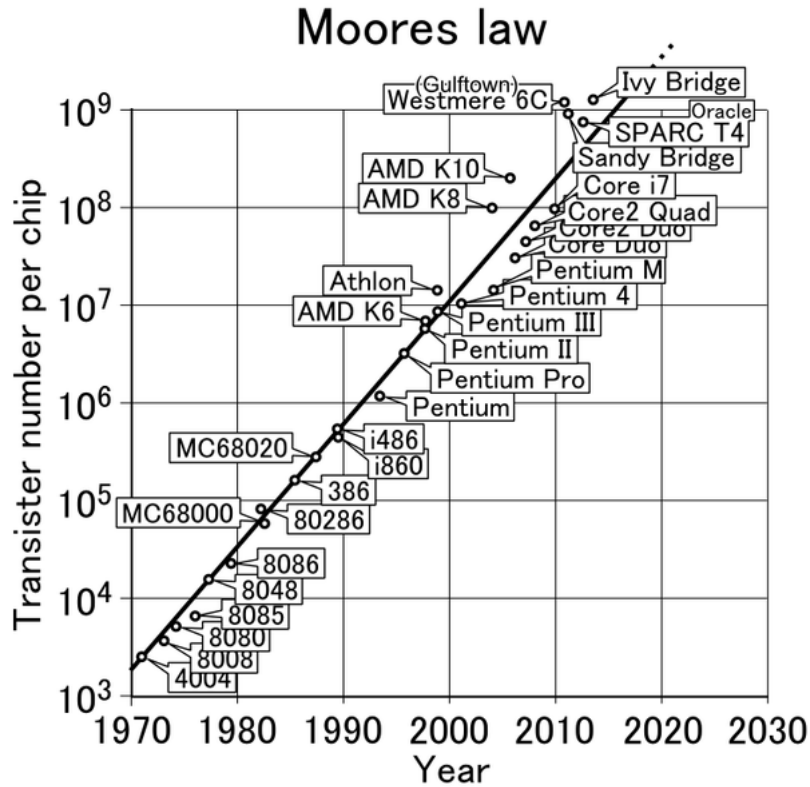


Figure 1.4: Moore's law graph. The actual ITRS (International Technology Roadmap for Semiconductors, <http://www.itrs2.net/>) technology node is 14 nm (the smallest feature size realizable on a chip). That corresponds to the 1.9 billions of transistors per chip. From <http://www.cringely.com/2013/10/15/breaking-moores-law/>

Aside from conventional crystalline silicon based electronics, scientific research has been focusing on nanostructures for flexible electronics (preferably roll-to-roll processable) and low-cost photovoltaics. Amorphous silicon (a-Si) and nanocrystalline silicon (nc-Si) have been extensively investigated and applied as channel materials for thin film transistors (TFTs) to be integrated on flexible, low temperature substrates such as polyethylene terephthalate (PET), polyethylene naphthalene (PEN), polyimide (e.g Kapton) and polycarbonate (e.g. Lexan). New transparent conductive oxide materials based on ZnO and SnO₂ and mixed ternary and quaternary oxides have been developed and deposited as thin film (with deposition techniques spanning from spray pyrolysis to ink-jet printing) for ITO replacement in touch screen displays.

(soft) lithography relies on direct mechanical deformation of the resist and can therefore achieve resolutions beyond the limitations set by light diffraction or beam scattering that are encountered in conventional lithographic techniques. A thin resist film is mechanically modified using a template (mold, stamp) containing the micro/nanopattern, in a thermo-mechanical or UV curing process. Various polymeric materials, including polydimethylsiloxane (PDMS), polyurethane acrylate (PUA), polyvinyl alcohol (PVA) and polyvinyl chloride (PVC), are used as templating materials.

Also Carbon nanotubes and graphene have been used for the same purpose and as gate electrode and channel materials for TFTs. Conductive inks made of dispersed metallic, carbon or conductive polymers nanoparticles have been formulated and deposited on low cost substrate (i.e. paper) for radio frequency identification (RFID) capacitive coupled antennas (see figure 1.5. Furthermore, many organo-metallic syn-

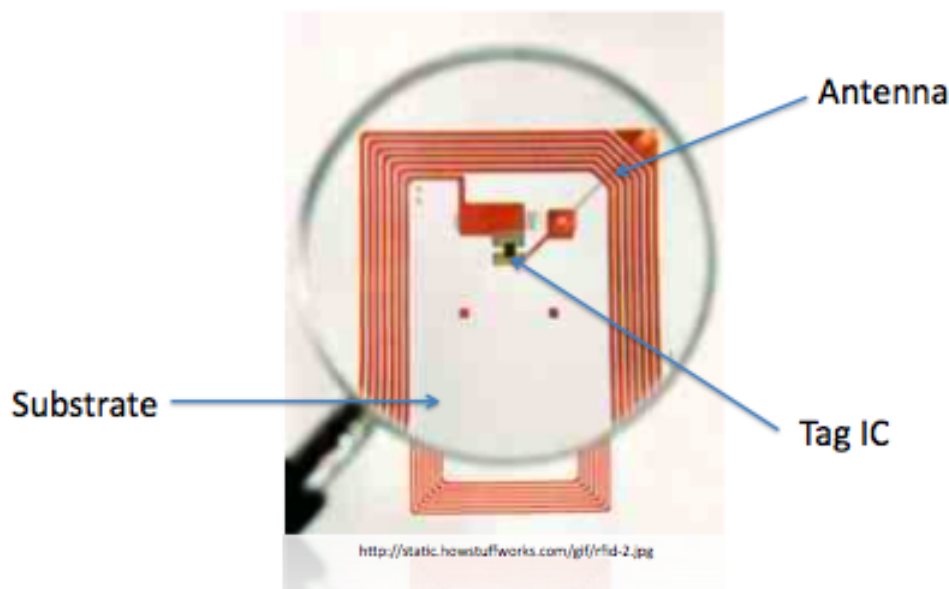


Figure 1.5: Schematics of an RFID tag. The copper spiral (etched and/or printed) serves as the antenna of the device. The "chip" at the center of the tag is used to power the device (passive RFID) by exploiting the RF signal from the reader and also to generate a clock for the tag's digital logic. From <http://rob.sh/post/8/>

thesis methodologies (Grignard reaction, organoboron cross-coupling polymerization, Stille reaction, etc.) have been optimized to produce and dope polythiophene based polymers, "low-frequency" (13.56 MHz) to employ in organic thin film transistors (O-TFT) for RFID applications [43]. Besides, O-TFT can be used to fabricate back-plane electronics for a large variety of optoelectronic flexible devices such as active matrix liquid crystals displays (AMLCD), electrophoretic displays, conformal "skin" sensors for Hydrogen, sheet type Braille sensors, actuators, etc. Finally, copper and zinc phthalocyanine, pentacene, fullerenes, 3,4,9, 10-perylenetetracarboxylic bis-benzimidazole, poly(2-methoxy-5-(3', 7'dimethyloctyloxy)-1,4-phenylene-vinylene) (MDMO-PPV), regioregular poly(3-hexylthiophene) (RR-P3HT), etc. have been investigated together with nanostructured inorganic materials (ZnO, TiO₂, CuO, etc.) to realize organic or hybrid organic-inorganic inexpensive bulk heterojunction (BHJ) solar cells.

This thesis deals with nanomaterials for two particular kinds of RFID and

hybrid organic-inorganic solar cells: antennas for chipless RFID systems to use in ions detection and Dye Sensitized Solar Cells (DSSCs).

1.3 Nanomaterials classification

Numerous nanomaterials classifications have been proposed along the years. However, the two most renowned classifications are either based on the aggregation state of the nanomaterial or on their dimensionality. Usually, aggregation state classification distinguishes between hard materials (in the nanoscale) and colloids (soft) [44]. Hard materials can be further divided into three categories. The first category is comprised of materials and/or devices with reduced dimensions and/or dimensionality in the form of isolated, substrate-supported or embedded nanometer-sized particles, thin wires or thin films. The techniques that are most frequently used to produce this type of microstructure are chemical vapor deposition (CVD), physical vapor deposition (PVD), various aerosol techniques, and precipitation from the vapor, supersaturated liquids or solids [45]. Well-known examples of technological applications of materials the properties of which depend on this type of microstructure are catalysts and semiconductor devices using single or multilayer quantum well structures. The second category is comprised of materials and/or devices in which the nanometer-sized microstructure is limited to a thin surface region of a bulk material. PVD, CVD, ion implantation and laser beam treatments are the most widely applied procedures to modify the chemical composition and/or atomic structure of solid surfaces on a nanometer scale. Surfaces with enhanced corrosion resistance, hardness, wear resistance or protective coatings are examples taken from today's technology in which the properties of a thin surface layer are improved creating a nanometer-sized microstructure. Another example of such as materials are patterns in the form of an array of nanometer-sized islands (e.g. quantum dots) connected by thin(nanometer-scale) wires. Patterns of this type may be synthesized by lithography, by means of local probes (e.g. the tip of a tunneling microscope, near-field methods, focused electron or ion beams) and/or surface precipitation processes. Such kind of processes and/or devices are expected to play a key role in the production of the next generation of electronic devices such as highly integrated circuits, terabyte memories, single electron transistors, quantum computers, etc. The third category is comprised of bulk solids with a nanometer-scale microstructure [40]. These are solids in which the chemical composition, the atomic arrangement and/or the size of the building blocks (e.g.

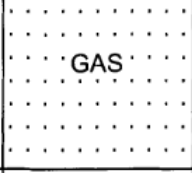
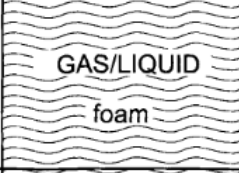
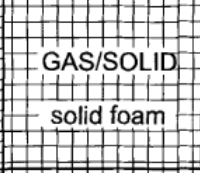
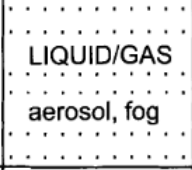
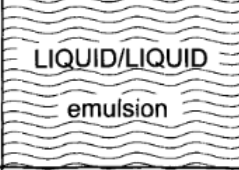
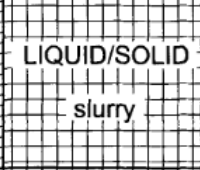
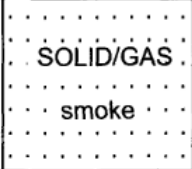
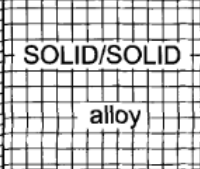
disperse phase	gaseous	GAS 	GAS/LIQUID foam 	GAS/SOLID solid foam 
	liquid	LIQUID/GAS aerosol, fog 	LIQUID/LIQUID emulsion 	LIQUID/SOLID slurry 
	solid	SOLID/GAS smoke 	SOLID/LIQUID suspension 	SOLID/SOLID alloy 
		gaseous	liquid	solid
continuous phase				

Figure 1.6: Classification of dispersed systems according to W. Ostwald [49]. The central column includes foams, emulsions and suspensions the are particularly interesting for materials science synthetic applications. Adapted with permission from [47].

crystallites or atomic/molecular groups) varies on a length scale of a few nanometers throughout the bulk. Needless to say, those kind of materials are the most employed in materials science research and in particular in the present thesis.

Colloidal dispersions (the second group of nanomaterials according to the aggregation state classification) are two-phase systems consisting of a disperse phase (for example a powder) finely distributed in a dispersion medium (see Figure 1.6 [46]). Sols and emulsions are the most important types of colloidal dispersions from the industrial point of view [47]. The fine distributions of solids in a liquid formerly known as sols (the expression sol was used to distinguish colloidal from macroscopic suspensions) are now called suspensions or simply dispersions. Unlike these, emulsions consist of liquid droplets distributed in an immiscible liquid dispersion medium. In the first place colloids are classified according to the nature of the dispersed phase and the dispersing medium (i.e. emulsion = dispersion of two immiscible liquids, foam = gas dispersed into a solid or liquid phase, etc.) rather than by the size of the dispersed phase [48]. Figure 1.6 illustrates the original classification of dispersed systems by Ostwald [44].⁴ Colloids size discrimination

⁴Some typical "colloidal" systems, not necessarily nanostructured, that can be encountered in everyday life are mud, clay, and toothpaste (slurries, dispersion of solids in liquids); milk, butter, mayonnaise, asphalt, cosmetic creams (emulsions); fog, spray, vapor, tobacco smoke, aerosol

distinguishes between particle sizes of the colloidal dispersion state on the one hand and those of smaller molecules and of coarse heterogeneous systems on the other. These size ranges are only guidelines; in some special cases, such as suspensions and emulsions, particles of diameter greater than $1\ \mu\text{m}$ are generally present. The threshold at which colloidal behavior becomes the behavior of a molecular solution lies at about $1\ \text{nm}$.

Special kind of colloids, not included in the original Ostwald classification are microemulsions, association colloids and gels. IUPAC defines microemulsion as *Dispersions made of water, oil, and surfactant(s) that is an isotropic and thermodynamically stable system with dispersed domain diameter varying approximately from 1 to 100 nm, usually 10 to 50 nm* [35]. However, the principal distinction between a microemulsion and an ordinary emulsion is neither the size of the droplets nor the degree of cloudiness, but the facts that microemulsions form spontaneously, that their properties are independent of the manner in which they were produced, and that they are thermodynamically stable. Ordinary emulsions, in contrast, require mechanical or chemical work for their production, so that at best they are kinetically stable, that is, the droplets are protected from coalescence. The concept of thermodynamic stability extends to association colloids also. In fact, certain substances can form colloidal associations spontaneously, owing to their particular molecular structure. These association colloids (e.g. spherical micelles) are distinct from other substances in that they are in a state of unrestricted thermodynamic equilibrium. Solutions of surface-active substances have unusual characteristics. At a certain concentration, some of their physical properties change abruptly, for example osmotic pressure, electrical conductivity, and surface tension. The abnormal behavior of the solution can be explained in terms of the formation of organized aggregates, or micelles. The concentration at which micelle formation becomes observable is known as the critical micelle concentration, CMC [50]. Above the CMC, the micelle is the thermodynamically stable form, although it is in equilibrium with single molecules and oligomers. As a result of micelle formation, the thermal behavior of tensides differs from that of other low molecular weight compounds. At low temperatures, the solubility changes little initially, but as the temperature rises to a point characteristic for that substance, the Kraft point, the solubility increases sharply as a result of micelle formation. As an example, sodium dodecyl sulphate 2 and 5 wt% aqueous solution used as mobile phase for chirality separation of CNTs

sprays, flue aerosols gases (liquid or solid aerosols); opals, pearls, colored glass, solid dispersions pigmented plastics (solid dispersions); blood (bio-colloids), ect.

represent a tenside system above its CMC.

A liquid phase dispersed in a solid medium is known as a gel, but this formal definition does not always convey the full sense of the nature of the "solid". The latter may start out as a powdery or granulated material such as natural gelatin or a hydrophilic polymer, but once the gel has formed, the "solid" part is less a "phase" than a cross-linked network that extends throughout the volume of the liquid, whose quantity largely defines the volume of the entire gel. Usually, thickeners (i.e. hydrocolloids such as gelatin, casein, pectin, gum arabic, alginic acids and synthetic polymers suitable for stabilizing aqueous suspensions such as poly-vinyl alcohol, polyvinylpyrrolidone, polyacrylamide, poly-styreneoxyethylene, poly-vinyl alcohol-vinyl acetate), are added to dispersions for increasing the viscosity of the suspension medium, and to form three-dimensional gel structures [51]. Many gels display thixotropy, they become fluid when agitated, but re-solidify when resting. By replacing the liquid with gas it is possible to prepare aerogels, materials with exceptional properties including very low density, high specific surface areas, and excellent thermal insulation properties. Unlike the thermodynamically stable association colloids, microemulsions (and solvated macromolecules), other colloids are thermodynamically unstable. For instance, all the screen printing pastes formulated and used in this thesis are ultimately thermodynamically unstable dispersions (suspensions), kinetically stabilized by dispersants and polymers (binders). The other classification of nanostructured materials and systems essentially depends on the number of dimensions which lie within the nanometer range:

- 3D-systems confined in three dimensions, e.g. structures typically composed of consolidated equiaxed crystallites.
- 2D-systems confined in two dimensions (e.g. filamentary structures where the length is substantially greater than the cross-sectional dimension)

Three-dimensional structures or bulk materials with a nanometer-sized microstructure are assemblies of nanometer-sized building blocks or grains that are mostly crystallites [52]. These building blocks may differ in their atomic structure, their crystallographic orientation and/or their chemical composition. If the building blocks are crystallites, incoherent or coherent interfaces may be formed between them, depending on the atomic structure, the crystallographic orientation and/or the chemical composition of adjacent crystallites. In other words, materials assembled of nanometer-sized building blocks are microstructurally heterogeneous consisting of the building blocks (e.g. crystallites) and the regions between adjacent

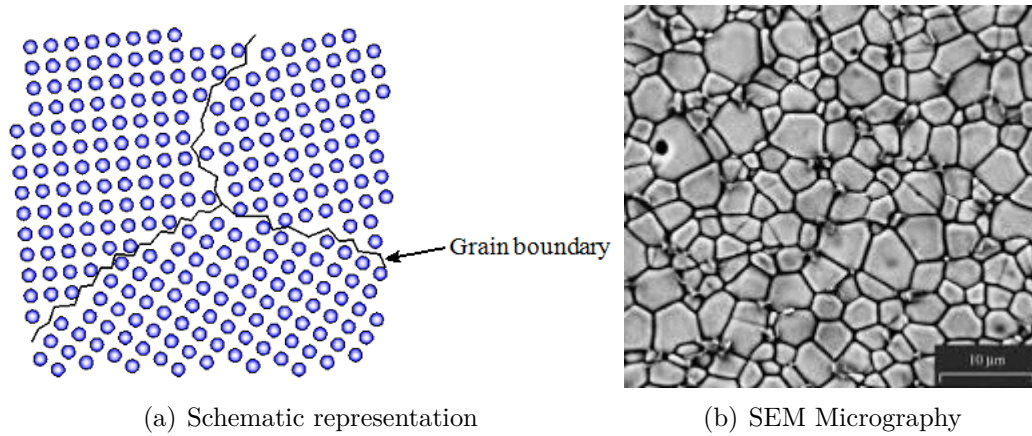


Figure 1.7: **(a)** Schematic representation of a 3-D nanostructured material composed of crystallites separated by grain boundaries. **(b)** Micrograph of $\text{SnO}_2\text{-MnO}$ polycrystalline ceramic. Presence of Mn_2SnO_4 precipitates are evident at the grain boundaries triple point. Phase separation may occur on oxide systems (or in alloys in general) and is related to the of ionic radius and the atomic percentage of the foreign atom introduced into the host matrix structure. From <https://en.wikipedia.org/>

building blocks are called grain boundaries. The schematic model and a SEM micrograph of a nanostructured 3-D material is shown in figure 1.7. Grain boundaries are 2D defects in the crystal structure, and tend to decrease the electrical and thermal conductivity of the material (by electron or phonon scattering). Furthermore, most grain boundaries are preferred sites for the onset of corrosion and for the precipitation of new phases from the solid. They are also important to many of the mechanisms of creep. However, the presence of grain boundaries, which means small average crystallites size, increases the surface area available for nucleation and chemisorption. Besides, grain boundaries, along with other crystallographic defects (i.e. vacancies and dislocations) constitute a preferred site for catalytic activity [52], [53].

Most of the research concerning third generation solar cells and nanostructures for opto-electronics in general is dedicated (included the present thesis) to develop materials possessing a high specific surface area for light absorption and retaining good charge transport properties at the same time.

1.4 Techniques for synthesis of nanomaterials

here are two general approaches to the synthesis of nanomaterials and the fabrication of nanostructures: the bottom-up approach and the top down approach. The former includes the miniaturization of materials components (up to atomic

level) with further self-assembly process leading to the formation of nanoparticles [40]. Typical examples are quantum dot formation during epitaxial growth and formation of nanoparticles from colloidal dispersion. Top-down approaches use larger (macroscopic) initial structures, which can be externally-controlled in the processing of nanostructures. For instance, milling is a typical top-down method for making colloidal dispersions of nanoparticles. Usually bottom up approaches belong to the materials science field, while top-down approaches are widely employed in formulation chemistry⁵. Sometimes, the two synthetic approaches can be used in conjunction and it is hard to distinguish between the two methodologies. Lithography in semiconductor industry, for example, may be considered a hybrid approach, since the growth of thin films is bottom-up whereas etching is top-down. Nanostructures, in particular nanoparticles, can be synthesized in many different ways that can be grouped in three categories:

- Gas phase processes including vapor deposition (physical and chemical), flame pyrolysis, high temperature evaporation and plasma synthesis.
- Liquid phase methods in which chemical reactions in solvents lead to the formation of colloids or aerosols. Electrodeposition, sol-gel and hydrothermal methods belong to this class.
- Solid phase processing: solid state reactions, grinding, milling and alloying.

1.4.1 Gas phase methods

Vapor phase methods

Vapor phase deposition can be used to fabricate thin films, multilayers, nanotubes, nanofilaments or nanometer-sized particles. The general techniques can be classified broadly as either physical vapor deposition (PVD) or chemical vapor deposition (CVD). PVD involves the conversion of solid material into a gaseous phase by physical processes by different physical processes (cathodic arc deposition, electron beam beam physical vapor deposition, pulsed laser deposition, thermal evaporative deposition); the material is then cooled and re-deposited on a substrate with perhaps some modification, such as reaction with a gas [45]. A schematics of the steps involved in the PVD are illustrated in figure 1.8 Sputtering is a physical

⁵Formulation chemistry is the branch of manufacturing that addresses substances that do not react with each other, but have desirable properties as a mixture. Paints, varnishes, cosmetics, petroleum products, inks, adhesives, detergents, pesticides, pharmaceutical drugs are just a few example of formulations obtained by top-down methods.

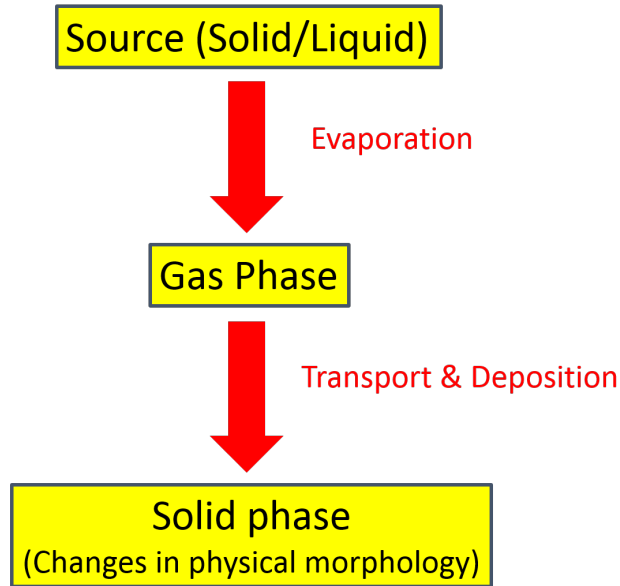


Figure 1.8: PVD process flow diagram. The specific deposition technique (electron beam, laser ablation, thermal evaporation, etc.) is chosen on the basis of the particular application and volatility of the target. For example, low melting point (high-volatile) metals such as aluminum are evaporated with resistive heating under vacuum, whereas refractory materials group V and VI carbides are laser ablated.

vapor deposition method where materials are vaporized from a solid surface by bombardment with ions of inert gas from sputter sources like an ion gun or hollow cathode plasma sputter. Plasma is created by the application of a large DC or RF potential between two parallel plates. In CVD processes, vapor is formed in a reaction chamber by pyrolysis, reduction, oxidation or nitridation, disproportionation, hydrolysis and chemical transport and then deposited on the surface. Countless variations have been introduced to the original Vapor-Phase Transport (VPT) concept that constitute the base for all the CVD. VPT, sometimes called chemical transport reaction, relies on the conversion of non-volatile solids into volatile compounds by setting the proper thermodynamic condition to favor gas species formation and solid re-deposition. For example, in an exothermic reaction, like the formation of refractory metal halides, the solid is converted into a volatile compound (an iodide for instance) in the "cool" zone of the reactor; then the reaction is "reversed" leading to solid re-deposition in the "hot" zone of the reactor. The Van Arkel-deBoer process (dated 1925) for purification of group IV metals (Ti, Zr, and Hf) is one of the oldest and well-known examples of VPT. A schematic description of the Van Arkel-deBoer method is provided in figure 1.9 Catalytic CVD and High pressure carbon monoxide disproportionation (the Boudouard reaction) for synthesizing

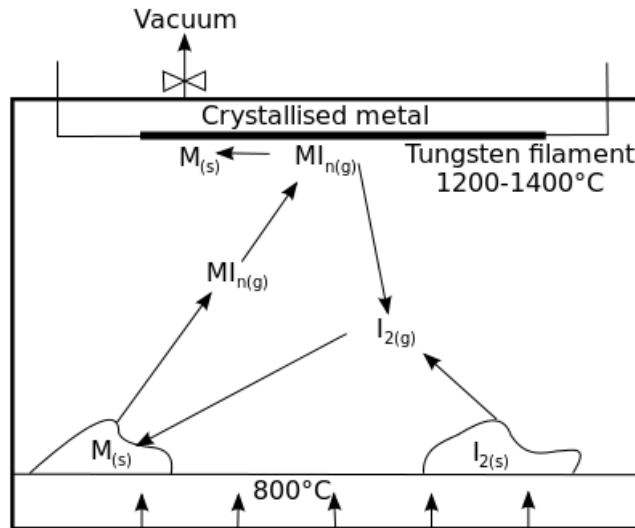


Figure 1.9: Van Arkel-deBoer VPT method for group IV metals purification. Ti, Zr, or Hf are heated up under vacuum in presence of iodine: TiI_4 , ZrI_4 or HfI_4 are formed and vaporized, whereas the impurities remain in the solid phase. The reduced pressure is necessary to decrease the boiling points of the MI_4 compounds. The gaseous metal tetraiodide is decomposed on a white hot tungsten filament. From https://en.wikipedia.org/wiki/Crystal_bar_process#/media/File:Van-Arkel-de-Boer-Verfahren.svg

carbon nanotubes are predicated on the same concept of unbalancing a chemical equilibrium towards either the reactants or the products.

Nowadays, vapor phase epitaxy (VPE), plasma enhanced chemical vapor deposition (PECVD), and metal-organic chemical vapor deposition (MOCVD), have assumed a great deal of technological importance in the fabrication of a number of optoelectronic and high speed electronic devices. MOCVD is particularly interesting for his versatility and the similarities (i.e. the chemical nature of the precursors) with solution methods such as Sol-gel. Much of the appeal of MOCVD lies in the fact that readily transportable, high purity organometallic compounds can be made for most of the elements that are of interest in the epitaxial deposition of doped and undoped compound semiconductors, mostly III-V and II-VI semiconductors. In fact, The growth of Al-bearing alloys (difficult by chloride vapor phase epitaxy due to thermodynamic constraints) and P-bearing compounds (difficult in conventional solid source molecular beam epitaxy, MBE, due to the high vapor pressure of P) can be easily carried out by MOCVD. The III-V and II-VI compounds and alloys are usually grown using low molecular weight metal alkyls such as dimethyl cadmium, or trimethyl gallium] as the metal (Group II or Group III) source. The non-metal (Group V or Group VI) source is either a hydride an organometallic such as trimethyl

antimony or dimethyl tellurium. The precursors are introduced as vapor phase constituents into a reaction chamber at approximately room temperature and are thermally decomposed at elevated temperatures by a hot susceptor and substrate to form the desired film in the reaction chamber. Furthermore, MOCVD permits to use complex organic precursors such alkoxides and β -diketonate allowing for the formation of oxides possessing different electrical properties.⁶ Flame pyrolysis is widely used in the production of carbon black, fumed silica, titanium dioxide and many other materials [54]. In this process flame heat is used to initiate the chemical reactions. The disadvantage of this method is that it usually yields agglomerated particles. However, the crystallites size can be easily controlled by adjusting the precursor flow rate. Furnace flow reactors (see figure 1.10) are the simplest systems used to produce saturated vapor for substances having a large vapor pressure (i.e. TiCl_4) at intermediate temperatures. In these systems a crucible containing the source material is placed in a heated flow of inert carrier gas. Materials with low vapor pressure can be fed in as suitable precursors.

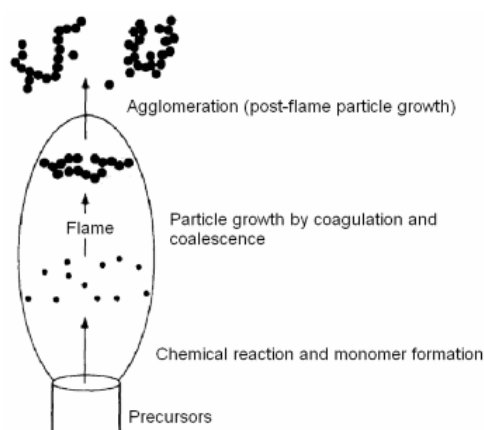


Figure 1.10: Schematic diagram of a flame pyrolysis.

1.4.2 Liquid Phase synthesis

Precipitating nanoparticles from a solution of chemical compounds can be classified into six major categories:

1. colloidal methods.

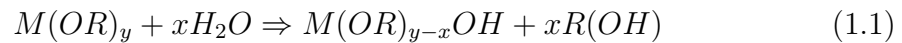
⁶A classical example of the MOCVD versatility for oxides systems is the praeosodimium oxide employed as dielectric for semiconductor devices. Pr_6O_{11} is the most thermodynamically stable oxide but is characterized by a low value of dielectric constant. On the other hand, PrO_2 and Pr_2O_3 possess improved dielectric properties but can be deposited only by using alkoxides and β -diketones.

2. sol-gel processing.
3. water-oil microemulsions method.
4. hydrothermal (or solvothermal) synthesis.
5. polyol method.
6. electrodeposition

Sol-gel and hydrothermal (and solvothermal) synthesis are described in further details in the following sections because were used for TiO₂ synthesis in this thesis.

Sol-gel synthesis

Sol-gel technology is a well-established colloidal chemistry technology, which offers the possibility to produce various materials with novel, predefined properties in a simple process and at relatively low production cost [55]. As explained in section 1.3 "sol" is a name of a colloidal dispersions made of solid particles few hundred nm in diameter, suspended in a liquid phase. The gel can be considered as a solid macromolecule immersed in a solvent. Thus, in general terms, the sol-gel process consists in the chemical transformation of a liquid (the sol) into a gel-state and with subsequent post-treatment and transition into solid oxide material. Figure 1.11 shows the fundamental steps involved in a sol-gel synthesis and all the possible routes bringing to materials of different consistence. First stage of the sol-gel process is the preparation of the precursor solution. Precursors play a key role in sol-gel technology directly affecting the porosity, refractive index, hardness and other performance characteristics of the resultant material. The precursor can be inorganic, but more often metal organic precursors are used. Common metal organic precursors are metal alkoxides: $M(OR)_y$, where R stands for an alkyl group. In a typical sol-gel process, the precursor is subjected to a series of hydrolysis and polymerization reactions to form a colloidal suspension (the sol). For example, in the case of metal alkoxides, it is dissolved in alcohol and then the water is added under acidic, neutral or basic conditions. The addition of the water leads to a hydrolysis in which the alkoxide ligand is replaced with a hydroxyl (a nucleophilic reaction) liquid:



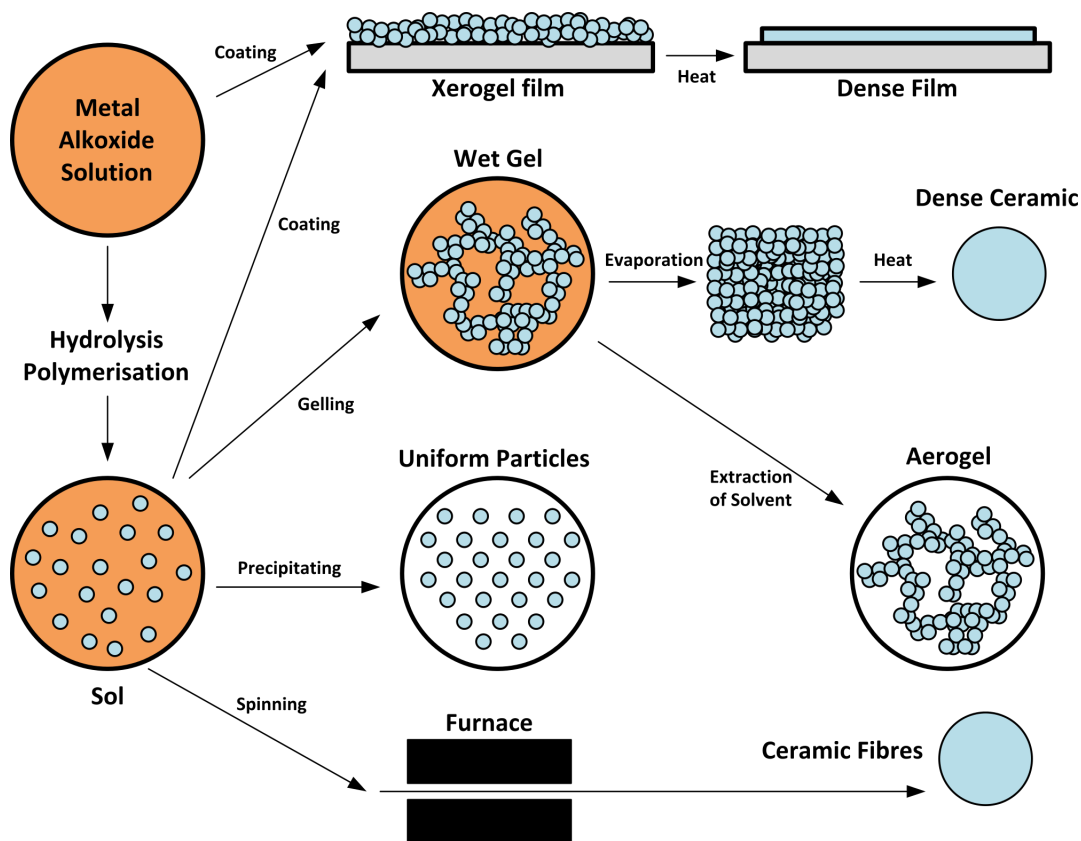


Figure 1.11: Sol-gel synthesis and its final products. From https://en.wikipedia.org/wiki/Sol-gel#/media/File:Sol-Gel_Scheme.svg

The chemical reactivity of metal alkoxides is related to the R: the larger the R, the slower the hydrolysis of metal alkoxides. Metal alkoxides are very moisture-sensitive (except silicon alkoxides) and require special handling environments. There are also more stable precursors developed like e.g. metal carboxylate, metal dialkylamides, amorphous and crystalline colloidal sol solutions, and organic/inorganic hybrids. They are not moisture-sensitive, easy to use, and produce good coatings. Next stage of the sol-gel process after the preparation of the precursor solution is a condensation reaction in which particles condense in the gel phase. For metal alkoxides, condensation occurs when either hydrolyzed species react with each other and release a water molecule, or a hydrolyzed species react with an unhydrolyzed species and release an alcohol molecule. In both cases polymers composed of M-O-M bonds are produced. Subsequent processes following gel formation involve its aging (increasing of gel reticulation degree) and drying to remove the solvent. Gels can be cast and molded to form a microporous pre-form and dried to produce a monolithic bulk material (e.g. a xerogel or an aerogel) that can be used to form filters and membranes. The interconnected nanoscale porosity in the dried gel can be filled

via incorporation of a second material using techniques such as liquid infiltration or chemical reaction in order to obtain nanocomposites. Sols can also be spin coated or dipped to produce thin (typically 50-500 nm) films on substrates. Next stage is a gelation (densification) of the layer by solvent evaporation and finally annealing to obtain the oxide coating. Alternately, fibers can be drawn from the gel (e.g., silica fibers for light transmission).

Hydrothermal-solvothermal synthesis

The hydrothermal technique has been most popular, garnering interest from scientists and technologists of different disciplines, particularly in the last thirty years. The term hydrothermal is purely of geological origin. It was first used by the British Geologist, Sir Roderick Murchison (1792-1871), to describe the action of water at elevated temperature and pressure in bringing about changes in the earth's crust leading to the formation of various rocks and minerals. From the materials science stand point hydrothermal syntheses are defined as reactions occurring under the conditions of high-temperature-high-pressure ($>100^{\circ}\text{C}$, >1 atm) in aqueous solutions in a closed system. More generally, solvothermal reaction means any chemical in the presence of a solvent in supercritical or near supercritical conditions. The purpose behind using any solvent other than water in the chemical reactions is essentially to bring down the pressure-temperature conditions. Hydrothermal (and solvothermal) synthesis are performed in autoclaves which are pressure chambers used to carry out processes requiring elevated temperature and pressure different from ambient air pressure (see Figure 1.12 [56]). Under hydrothermal conditions, the reactants which are otherwise difficult to dissolve go into solution as complexes under the action of mineralizers or solvents. Hence, one can expect the conditions of chemical transport reactions to the aforementioned Van Arkel-deBoer process. Therefore, some workers even define hydrothermal reactions as special cases of chemical transport reactions. Owing to the specific physical properties, particularly the high solvation power, high compressibility, and mass transport of these solvents, one can also expect the occurrence of different types of reactions like:

- Synthesis of new phases or stabilization of new complexes.
- Crystal growth of several inorganic compounds.
- Leaching of ores in metal extraction.
- Decomposition, alteration, corrosion, etching.

- Preparation of finely divided materials and microcrystallites with well-defined size and morphology for specific applications.

Needless to say, the last case is particularly important for the synthesis of nanostructured particles. Nanopowders are normally produced by means of either high

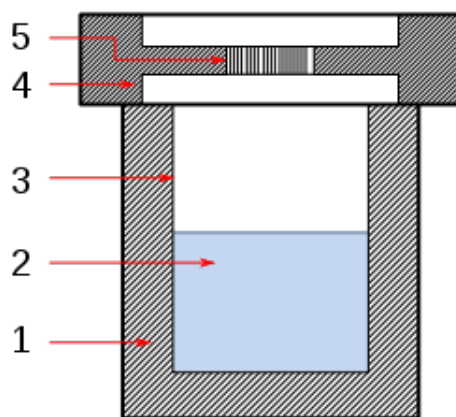


Figure 1.12: Schematic diagram of hydrothermal-solvothermal synthesis setup: (1) stainless steel autoclave (2) precursor solution (3) Teflon liner (4) stainless steel lid (5)

temperature hydrolysis reactions of various compounds directly in the autoclave or hydrothermal treatment of reaction products at room temperature; the latter case is based on the sharp increase in the rate of crystallization of many amorphous phases in hydrothermal conditions. In the first case the autoclave is loaded with aqueous solution of precursor salts, in the second case, with suspension of products derived from solution reactions flowing under normal conditions. Substantial enhancement of the hydrothermal method facilitates the use of additional external factors to control the reaction medium during the synthesis process. As of now, this approach is implemented in the hydrothermal-microwave, hydrothermal-ultrasonic, hydrothermal-electrochemical and hydrothermal-mechanochemical synthesis methods.

1.4.3 Solid state phase synthesis

Milling

One of the nanofabrication processes of major industrial importance is the high-energy ball milling, also known as mechanical attrition or mechanical alloying. In contrast to previous two groups (gas phase and liquid phase synthesis), where particles were produced in bottom-up processes, mechanical methods are based

on top-down (size reduction) processes like attrition and disintegration of larger particles. When particle size lies in nanometer range, terms ultra-fine grinding or nanosizing are often used for the process. Mechanical attrition methods give very high production rates (up to tons per hour) and are widely used for industrial production of clay, coal and metal powders. The production process often involves wet milling in milling chamber with rotating perforated plates. Wet milling results in suspensions that need to be stabilized either electrostatically (by adjusting the PH for example) or sterically (by adding protective colloids for example) or both (by adding polyelectrolytes) to prevent particle recombination due to increasing particle-particle interactions. Although over 99% of the energy used in grinding is lost to friction, nearly all industrial production of nanosized colloidal dispersions and suspensions relies on comminution, usually wet grinding. The procedure of dispersion can be split into three steps:

- wetting of the powder
- comminution and distribution of the particles (deagglomeration)
- stabilization of the particles

For optimal dispersion, the powder from which the dispersion is to be manufactured must be completely wet. Good wetting agents must cause complete wetting (contact angle between solid and liquid phase close to zero) with rapid equilibrium and in low concentrations, without depressing excessively the liquid surface tension. The concentrations in which wetting agents are used lie in the range of the CMC, for example 0.2% for sodium dodecil sulfate. Furthermore, some wetting agent (mostly polyelectrolytes when water is used as dispersion and grinding medium) can act also as deflocculants. In fact, when a substance is ground, an equilibrium is achieved: the fine particles produced gather together into agglomerates or flocs because of their increased surface energy. Thus, deflocculants must be added to prevent particles from re-agglomerating. A distinction must be made between crystalline and agglomerated materials: crystalline materials are usually harder to pulverize and require grinding aids, such as polyacrylates, acrylamides, polystyrenesulfonates, or abietic acid derivatives . Agglomerated powders are easier to pulverize; the process is usually not really one of grinding but one of separation of the agglomerated particles. The primary particles or fragments thus formed must be prevented from reagglomerating or flocculating; this is the purpose of deflocculants. Most deflocculants are charged tensides that adsorb onto the particles and cause

repulsion between them. Their charge must be of the same sign as the charge on the particles. When the charges have opposite signs, flocculation occurs. On adsorption, the hydrophobic tails of the tensides are located in the area known as the Stern layer (double layer theory). Both anionic (i.e. dodecylbenzenesulfonate, isopropyl naphthalenesulfonate, diamylsulfosuccinate) or cationic (Dodecyltrimethylammonium bromide, cetyltrimethylammonium bromide) deflocculants are routinely used. Polyelectrolytes such as the condensation product of naphthalenesulfonic acid and formaldehyde, sodium dinaphthylmethanedisulfonate and lignin can act as wetting agents, deflocculants and dispersants. Then, after grinding, the dispersion has to be stabilized. A "stable dispersion" is one in which the total number and size of the particles in the dispersion does not change over time. Dispersants are used to stabilize dispersions. Usually a dispersant is meant for electrostatic stabilization, steric stabilization or both. Briefly, electrostatic repulsion can be effectively exploited in aqueous solution where the high dielectric constant of the continuous phase allows for a great extension of the diffuse double layer; conversely dispersion stabilization in organic media mainly relies on steric repulsion. A large number of dispersants are available for stabilization of aqueous dispersions⁷. Most of them possess multiple charges (polyelectrolytes) and a long hydrophobic chain that preferentially adsorbs at the solid surface in aqueous suspensions. Hence, the general rules for the design of a dispersant in water borne systems predict the necessity of several ionic groups (multiple charges), which are distributed over the entire molecule, and hydrophobic groups with polarizable structures such as aromatic rings and ether groups instead of hydrocarbon chains. This is the reason why small molecular weight tensides (alkali metals, ammonium, or chloride salts of stearate, palmitate and oleate, morpholinium salt of fatty acids, succinate esters, etc.) are effective as wetting agents and deflocculants but ineffective as dispersants. Furthermore, the usual tensides are not suitable for stabilization of electrically charged particles. If the particles and the tenside have opposing charges, flocculation occurs [57]. On the surface, now neutralized, a second layer can be adsorbed. However, this results in ineffective stabilization, since the second layer is easily removed. If the particles and the tenside have the same charge sign, adsorption of the polar head of the tenside onto the particle surface is hindered by

⁷Besides the classification based the electrical charge (anionic, cationic or non-ionic) dispersants are also classified according to their synthetic route: Natural (polysaccharides such as gum arabic and alginic acid), semi-synthetic (cellulose ethers, esters and lignine sulfonates), and synthetic (polyethyle glycols, polyvinyl alcohols, polyvinyl pyrrolidones, polystyrene sulfonates, polyacrilates, polymetacrylates, etc.).

electrostatic repulsion, and the non-polar groups of the tenside are oriented towards the water. Stabilization is possible only at high tenside concentrations (like the aforementioned 5% SDS solution used for carbon nanotubes chirality separation). In non-aqueous dispersions with low dielectric constant coulombic repulsion is usually ineffective (because of the small Debye screening length) for stabilization and a layer of steric protection is needed. Furthermore, in organic media dispersions, particle size has an interesting influence on stability, in contrast to the case of aqueous systems, in which particle size is of only secondary importance. In water, near the flocculation point the range of electrical forces is generally small in comparison with the particle size, so the decisive forces and energies can come into play in the region of the closest approach of the two particles [58]. The average particle size is therefore only of secondary importance. In non-polar media, we can expect electrostatic repulsion to extend over a large volume and steric repulsion to rise sharply at small distances between particles. The electrostatic repulsion is approximately proportional to the square of the charge on the particle. For a constant surface potential, it decreases with particle size, and for small particles may not be able to overcome the van der Waals force (attractive forces between particles). Steric repulsion, on the other hand, is only sufficient to keep the particles a certain distance apart from one another. The van der Waals force increases with the size of the particle. It follows that, for the stabilization of coarse particles (micron-sized), electrostatic repulsion is more effective than steric, whereas for very small particles (submicron range) the relationship is reversed. Most dispersants for non-polar media are specific to a particular system. There are no generally effective dispersants suitable for stabilization of a wide variety of solids in organic media like, say, lignin sulfonates or dinaphthylmethanedisulfonates in aqueous systems. Effective dispersants for non-aqueous dispersions must meet the following criteria: they must interact strongly with both the particles and the dispersion medium, that is, adsorb strongly onto the particle surfaces and be readily soluble in the solvent. Therefore, they must have anchor groups that adsorb onto the solid and solvated groups that, in the form of loops and trailing tails, create a sufficiently thick layer to prevent attraction between the particles. There should also be a mechanism for charge transfer between the dispersant and the particle surface so that, on top of the steric repulsion, electrostatic repulsion is active. A wide variety of tensides and polymers are suitable for use as dispersants for dispersions in organic media, depending on the solid (polycaprolactones, polyureas, block copolymers such as polystyrene-polybutylstyrene, polystyrene-polyacrylonitrile, etc.).

When it is necessary to prepare colloidal dispersions of metal oxides or sulfides alkyl modified polyvinyl pyrrolidones, block copolymers of propylene oxide and ethylene oxide (Pluronic) and a class of "hyperdispersants" going under the name of Disperbyks (from Byk corporation) come into consideration. Disperbyks (but also Solsperse by Avecia) are called hyperdispersants because they provide multiple anchor groups to bind on particles surface. Disperbyk family includes ammonium salts of acrylate co-polymers, solutions of hydroxyfunctional carboxylic acid esters, block co-polymer polyesters of phosphoric acid, etc. In our case, for example, we used a Pluronic dispersant for directing the structure formation and stabilizing TiO₂ nanoparticles in ethanol; whereas a Disperbyk dispersant was used to stabilize ITO and aluminum doped zinc oxide in an ethanol/terpineol screen printing paste. Finally, a thickener is usually added to the stable colloidal dispersion either to avoid sedimentation (caking) or to confer special rheological properties to a dispersion (i.e. make a dispersion printable with a specific printing technique). Thickeners increase dispersions' viscosity (compensating for the density difference between the particles and the dispersing media) thus preventing particle settling. A countless number of thickeners have been developed over the years and they span from cellulose and starches derivatives to ethoxylated castor oil to gums (locust bean gums, xanthan gum, guar gum etc.), to clays (mortmollite and betonite derivatives) to polyvinyl alkyl aldehyde resins (like the polyvinyl butyral used for the ITO dispersions in the present thesis.)

Solid state reaction route

Reactions between or within solid reactants to yield a solid product are prototypical of solvent free reactions. They all rely on the synthesis of polycrystalline (because of the high temperatures involved, from 800 to 1500 °C) from a mixture of solid reactants [53]. The main difference with liquid phase syntheses is that diffusion of the precursors is hindered in the solid state. Thus diffusion rate is improved by:

- increasing the temperature
- introducing defect by starting with reagents that decompose prior or during the synthetic reaction such as carbonates and nitrates.

Furthermore, intimate contact between crystallite (usually achieved by pelletizing the reaction mixture) is required. Although of great importance for the industrial

synthesis of ceramics, solid state synthesis will not be discussed in further details because it is not directly related to this thesis.

Chapter 2

Photovoltaics cutting edge

2.1 Photovoltaics: definitions

2.1.1 Renewable energy

Among the many energy production and interconversion systems, renewable energy has been gathering interest since the 1970s energy crisis. Renewable energy is defined as energy collected from resources that are naturally replenished on human timescale. The interest in renewable energy has been sparked by the following reasons:

- Most of the G7 (world's most advanced economies) countries and many developing nations have reached and surpassed the peak oil. This term identify (according to the Hubbert's theory) the maximum extraction rate of petroleum (and fossil fuels in general) after which it is expected to decline.
- Fossil fuels price is profoundly affected by political and military events in "unstable" areas of the planet (Middle East, Central Asia, South America, see figure 2.1). The 1973 oil embargo by the OAPEC (Organization of Arab Petroleum Exporting Countries) ¹ following the Yom-Kippur war is credited for being the beginning of large scale scientific research and commercialization of renewable energy systems.
- Environmental issues connected to fossil fuel extraction, delivery and consumption. For instance, the explosion of the BP Deepwater Horizon drilling

¹The OPEC (Organization of Petroleum Exporting Countries) is an international organization founded in 1960 in Baghdad and group 14 of the major oil producers (i.e. Saudi Arabia, Venezuela, Iraq, Iran, etc.). The OAPEC is comprised of the Arab countries belonging to the OPEC together with Egypt and Syria.

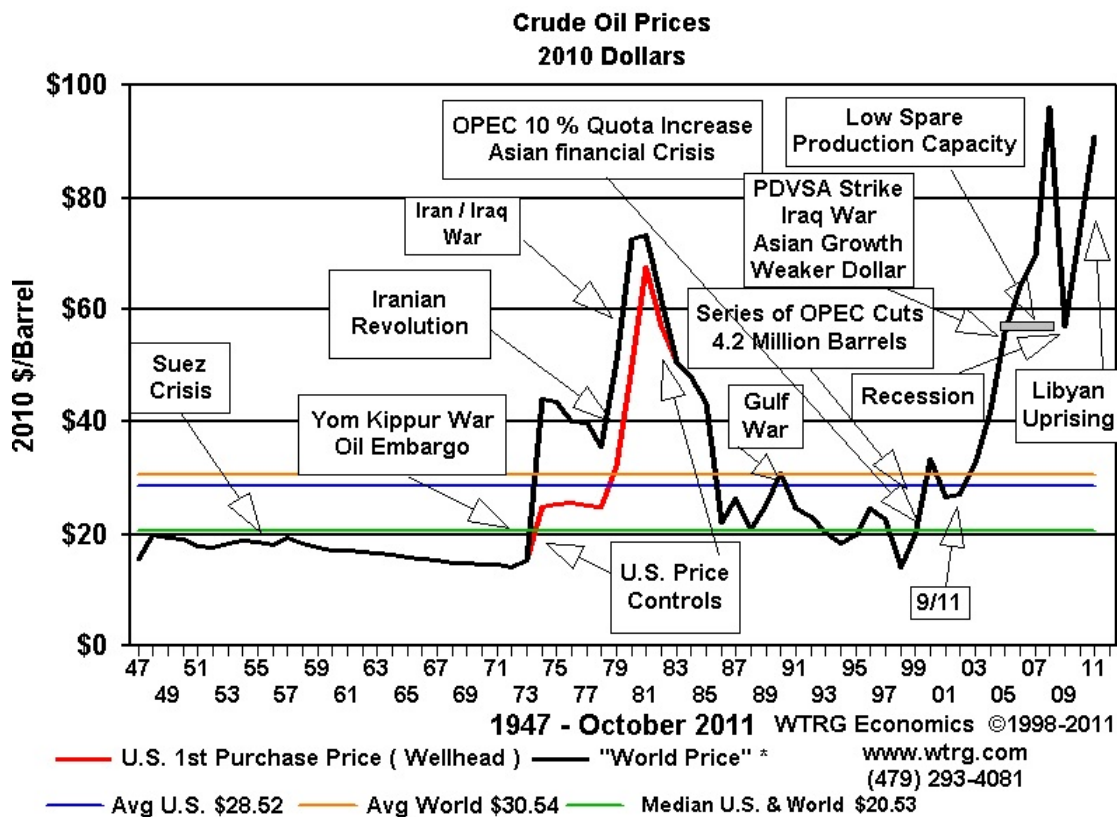


Figure 2.1: Crude oil price (1947-2011). Barrel's price peaks overlap with political-military crises (i.e. Yom-Kippur war, Iran Revolution, first Persian Gulf War, etc.) in the Middle East. The price per barrel is normalized for the 2010 U.S. dollar stock exchange value. Brent crude's cost (oil extracted in the North Sea) serves as main benchmark price for international oil purchase. From <http://www.wtrg.com/prices.htm>

rig, in 2010, is estimated to have spilled 4.9 million of crude oil barrels into the Mexican Gulf. Furthermore, combustion of fossil fuels produces large amounts of gaseous pollutants. A typical coal power plant produces every year:

3.5 million tons of CO₂, which is the principal greenhouse gas largely responsible for the global warming effect.

720 tons of CO (short-lived greenhouse gas) aggravating general health conditions of people suffering from cardiovascular diseases.

14,100 ton of sulfur oxides (SO_x) or 7,000 tons if flue gas desulfurization is performed. Sulfurous anhydride (SO₂) in particular, is one of the main causes of acid rains.

500 tons of particulate matter causing respiratory system's pathologies.

10,300 tons of nitrogen oxides (NO_x) stemming from both atmospheric nitrogen oxidation during high temperature combustion processes and nitrogen containing residues (mainly heterocyclic compounds) in the coal. NO_x undergoes to photochemical degradation increasing the ozone ground levels with harmful effects on human respiratory system (i.e. alveoli inflammation) and certain materials (synthetic and natural rubbers).

220 tons of uncombusted hydrocarbons that are released as volatile organic compounds (VOCs) and promote NO_x photodegradation.

150 Kg of heavy metals (As, Cd, Pb, etc) stemming from ashes.

- Finally, energy interconversion through fossil fuel belongs to the thermoelectric power generation systems. It implies that electrical power is produced through the following steps:

chemical energy \Rightarrow heat \Rightarrow mechanical energy \Rightarrow electrical power

The first two steps constitute the "bottleneck" of the all process. In fact, limitations on the calorific value of the fuels and the Carnot limit for the heat conversion into mechanical energy restrain fossil fuel power plants efficiency to 20-30 %.

However, power generation from fossil fuels has some advantages compared to renewable energy:

1. Technologies and infrastructures for fossil fuels based electrical power generation are largely available all over the world and are accessible even to the developing countries.
2. Fossil fuels energy density is larger than renewable energy sources and storage devices (i.e. batteries, capacitors, supercapacitors, ect. see Figure 2.2).
3. The actual cost of one watt/peak (W_{peak}) of electrical power produced from fossil fuels is immensely lower than any renewable energy. This point is one of the advantages of Graetzel cells compared to traditional photovoltaics devices.

The main renewable energy sources are (see Figure 2.3):

- Wind power

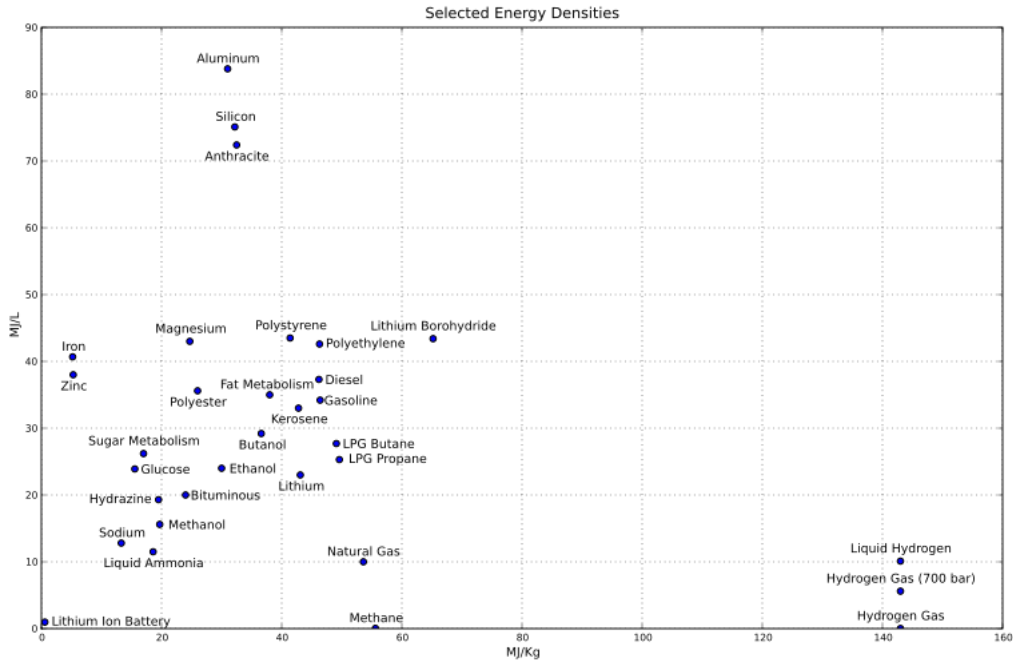


Figure 2.2: Energy density graph for some strategic energy materials and energy storage devices. Energy density is defined as the amount of energy stored per volume (MJ/L) or mass unit (MJ/Kg). It is worth to notice that silicon and hydrogen (the fundamental materials for solar and fuel cells respectively) own a relatively high energy density. From https://en.wikipedia.org/wiki/Energy_density#/media/File:Energy_density.svg

- Hydropower
- Biomass (Biofuel)
- Geothermal energy
- Solar energy ²

the last item of the list deserves some further clarification. Indeed, there are two different kind of "solar" energy technology use: solar thermal energy (STE) and photovoltaics (PV). The former collects (through simple mirrors, Fresnel lenses, solar towers, etc.) the thermal energy released by sun irradiation to increase the enthalpy content of fluids possessing special heat capacity and thermal conductivity characteristics (see figure 2.4). The latter involves the direct conversion of solar

²Although nuclear energy is considered clean energy its inclusion in the renewable energy list is a subject of major debate. In fact, the low carbon emission aspect of nuclear energy as its major characteristic could bring it to be defined as renewable energy. However, being uranium availability limited nuclear power shouldn't be considered a renewable energy unless thorium (largely more abundant than uranium) based energy production systems are used. Also the clean aspect of nuclear power is questionable since radioactive waste is produced.

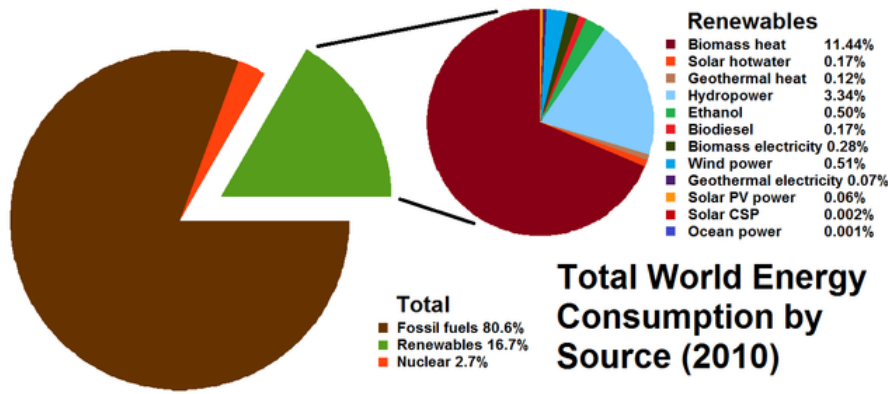
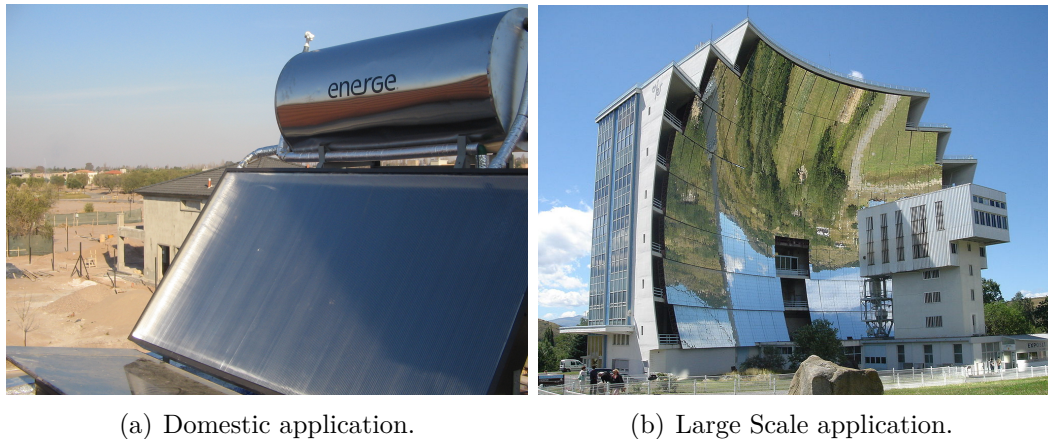


Figure 2.3: Percentage distribution of energy sources (2010). Although fossil fuels remain the principal energy source, alternative energies have been growing in interested because of their low environmental impact and their perpetual availability. From https://en.wikipedia.org/wiki/Energy_development#/media/File:Total_World_Energy_Consumption_by_Source_2010.png

radiating energy into electrical power. Since photovoltaic energy conversion does not involve any transformation of heat into mechanical energy, it does not abide by the Carnot theorem (that stands for fossil fuels based power plants, nuclear plants, internal combustion engines, Diesel engines, etc.)³. The following discussion will deal only with PV devices (solar cells) because DSSCs (or Graetzel cells) belong to a particular kind of PV devices: hybrid-bulk heterojunction solar cells. DSSCs relies on both physical phenomena concerning conventional solar cells (carrier diffusion, Fermi levels splitting and rectifying junctions) and photoelectrochemical processes. Usually solar cells are classified according to the kind of manufacturing technology and materials used (see figure 2.5). Thus, first generation (monocrystalline and polycrystalline silicon, GaAs, multijunction solar cells), second generation (thin film solar cells: CdTe, copper indium gallium selenide, amorphous silicon) and third generation (DSSCs, organic solar cells, quantum dots solar cells, perovskite solar cells) are the currently used definition to classify solar cell technologies. Regardless of the particular technology used for their manufacture, electrical power generation from light in solar cells involves the three following steps:

1. Electron-hole pairs generation (see next chapter for complete explanation about the term).
2. Electron-hole pairs separation. Strongly bound electron-hole pairs are known as excitons. Electron-hole pairs right after their generation, when they are

³Solar cells energy conversion efficiency limitations are described by the Shockley-Queisser limit



(a) Domestic application.

(b) Large Scale application.

Figure 2.4: Two different applications STE applications (solar thermal energy). **(a)** Water heating system for a building not connect to the a power supply grid (from https://en.wikipedia.org/wiki/Odeillo_solar_furnace). **(b)** Solar furnace in Odeillo (eastern Pyrenees, France; from https://en.wikipedia.org/wiki/Odeillo_solar_furnace). Such a solar energy collector is capable of producing temperatures up to 3800 °C.

still coulombically bound, are known as geminate pairs.

3. Charge transport toward the metallic contacts and the external load.

What really distinguishes third generation solar cells from the "conventional" devices are step 2 and 3. In conventional solar cells (first and second generation) the charge separation and collection is at least partially assisted by an electric field and part of the carriers transport occurs by drift. On the other hand, most of the third generation solar cells are composed of nanostructured materials (TiO₂ nanoparticles, quantum dots, fullerenes, etc.) that make the accommodation of an electrical field [59] unfeasible. Hence, charge separation relies on interfacial kinetics, energy steps at the interfaces (heterojunctions) and the charge transport is completely diffusion driven. The two following sections illustrate the operative principles of these two different types of solar cells and prelude to the detailed explanation of the DSSCs working principle in the next chapter.

2.1.2 "Conventional" PV technologies

The three main PV technologies currently available on the PV market (monocrystalline Si, polycrystalline Si and thin film CdTe) are all devices based on minority charge carriers that result into a photogenerated current given by:

$$I_{op} = eg_{op}A(L_p + L_n + W) \quad (2.1)$$

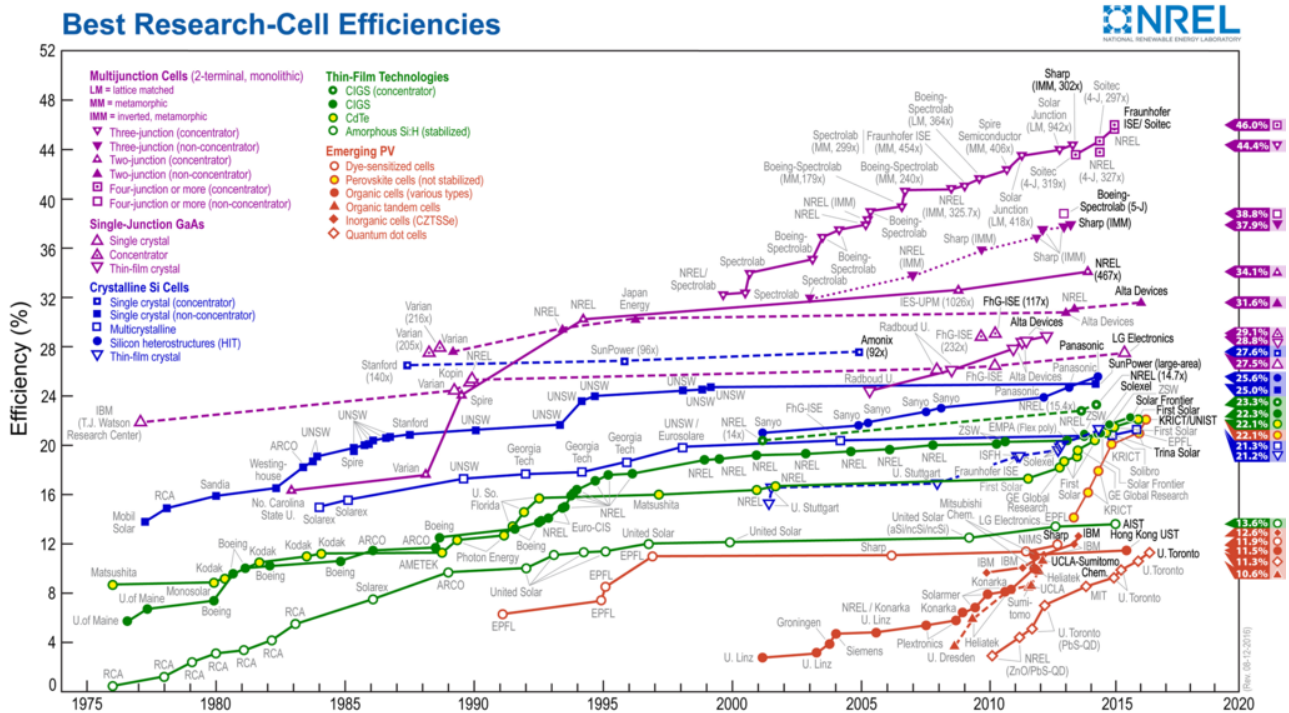


Figure 2.5: NREL (National National Renewable Energy Laboratory (a research structure affiliated to the U.S. Department of Energy <https://www.nrel.gov/pv/>) graph relating different solar cells "generations" to their efficiency. First generation cells are characterized by high efficiency achieved either by using low defectivity materials (monocrystalline silicon) or by overcoming the Shockley-Queisser limit through multilayer structures (epitaxial multijunctions solar cells, i.e. GaAs/InP/Ge structures). Second generation devices are comprised of thin film solar cells. Instead of p-n junction obtained by different crystal growth methods (Czocharalski, zone floating, etc.) and doping (diffusion, ion implantation, etc.) this technology relies on thin (1-5 μm) films of semiconductors (p-type CdTe, n-type CdS, n-type CIGS, etc.) deposited on a transparent conductive substrate (i.e. ITO). The p-n junction can be formed between two different compounds (i.e. p-type CdTe and n-type CdS) and the cost is much lower than first generation solar cells, although the efficiency is less. Third generation solar cells (or new generation solar cells) are characterized by low manufacturing cost and by charge separation mechanisms that do not involve a depletion layer formation. In fact, the traditional of p-n junction is replaced by different kind of interfaces (i.e. semiconductor-electrolyte, electron donor-electron acceptor, etc.. From https://en.wikipedia.org/wiki/Photovoltaics#/media/File:Best_Research-Cell_Efficiencies.png

Where A is there area of the p-n junction; e is the elementary charge, g_{op} is the optical generation rate of the electron-hole pairs; L_n and L_p are the electron and holes diffusion length respectively, W is the depletion layer thickness (see below). To completely understand equation 2.1 is necessary to analyze figure 2.6 shows the energy diagram for a p-n junction. The equalization of the Fermi Level on

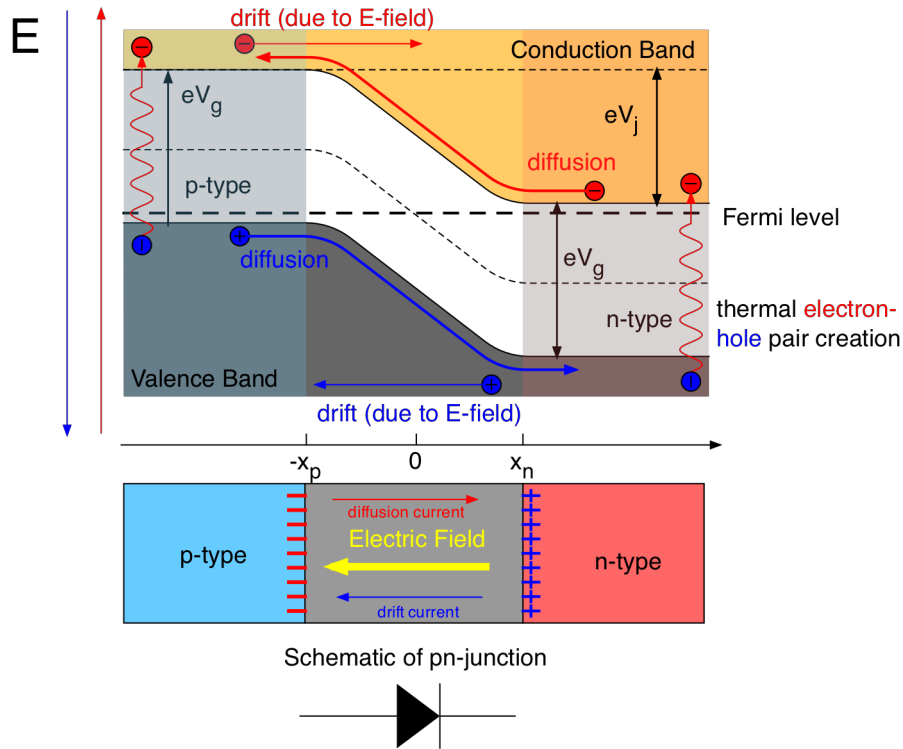


Figure 2.6: Schematic representation of p-n junction energy levels (conventional solar cells). From http://wanda.fiu.edu/teaching/courses/Modern_lab_manual/pn_junction.html

both sides of the junction (that can be a homojunction like for Si solar cells or an heterojunction like for CdTe based devices) brings about the formation of a depletion layer (or space charge layer) across the junction. No free charge (electron or holes) is present inside the depletion layer. The only charge within the depletion layer at the thermodynamic equilibrium are the the ionized acceptor dopants (negative charge) on the p-side of the junction and the ionized donor dopants (positive charge) on the n-side. N_{A-} and N_{D+} are the concentration of the acceptors and donor dopants respectively. This electrical double layer ⁴ prevents further electron and holes diffusion once the electrochemical potentials of the two different charge carriers are equalized. V_j is the contact potential stemming from

⁴By solving the Poisson equation in conjunction with the electrical neutrality conditions for the p-doped and the n-doped regions the following formula for the depletion layer width is obtained: $W = \sqrt{\frac{2\epsilon_r V_j}{e} \left(\frac{1}{N_D} + \frac{1}{N_A} \right)}$. Thus, the depletion layer width is inversely proportional to the dopants concentration. A similar behavior (and the Debye screening length is a parameter valid for both semiconductors and electrolyte solutions) occurs at the electrode/electrolyte interface in batteries, DSSCs and colloids.

the Fermi levels equilibration and is given by the formula:

$$V_j = \frac{KT}{e} \ln \frac{N_A N_D}{n_i^2} = \frac{KT}{e} \ln \frac{p_p}{p_n} \quad (2.2)$$

where K is the Boltzmann constant and T the thermodynamic temperature; n_i is the concentration of intrinsic carriers (thermally generated); p_p and p_n are the concentration of holes (majority carriers) and electrons (minority carriers) in the p-doped material, respectively. Hence, when a photon with an energy higher than the semiconductor band gap ($eV_g = E_g$) strikes on the neutral region of the semiconductor or the material is provided with a thermal energy (KT) larger than the band gap energy value, an electron is promoted to the conduction band and a hole is left into the valence band. Light or thermal excitation leave the majority carriers concentration unchanged but increase the minority carrier concentration and moves the Fermi levels from the equilibrium position. This is the essence of the photovoltaic effect: an electric potential difference appears across the p-n junction following the generation of minority carriers in the bulk of the material. This electrical potential diminishes the contact potential of the junction (equation 2.2) and it is equivalent to applying a forward bias to the junction itself. The relatively high dielectric constant of inorganic semiconductors (11.6 for Si and 10.2 for CdTe) is enough to separate the geminate pairs (electron and holes right after their generation). The total current crossing the junction is comprised of two terms: the diffusion current of majority carriers (i.e. electrons on the n-doped side surmounting the potential energy barrier stemming from the contact potential) and a minority carrier drift current (i.e. electrons on the p-doped side which wander into the depletion layer and are swept to the n-doped side by the junction electrical field). Under forward electrical bias the drift current is negligible because thermal energy is insufficient (except for low band gap semiconductors like Ge) to generate minority carriers. On the other hand, photons with an energy $h\nu$ higher than the semiconductor band gap can produce minority carriers and results into a generation current given by equation 2.1. However, outside the depletion layer carriers motion is diffused controlled. Therefore, most of the recombination in first and second generation solar cells occurs after the initial separation of the geminate pairs during carriers' diffusion path. Carriers recombination occurs either by direct the electron-hole annihilation (radiative recombination) or by trap and defects mediated recombination. (Shockley-Reed-Hall non-radiative recombination). This has an impact on first and second generation manufacture, in particular on silicon

solar cells ⁵.

1. Silicon solar cells realize the narrow base condition.
2. A silicon solar is assembled using the p-doped material as base and the n-doped as emitter (see Figure 2.7).

Photovoltaics parlance defines the base of a solar cell like the material dedicated to light absorption carriers photogeneration. It is usually made of a direct band gap semiconductor and is thick up to 200 μm for silicon solar cells. The top semiconductor constitute the other side of the p-n junction, it has to be thin ($1 \mu <$) to allow light to pass and it is known as emitter. A narrow base device satisfies the following condition:

$$L_n \gg W_p - x_p \quad (2.3)$$

where W_p is the depletion layer width on the p-doped side and x_p is the total base width. Hence, if for example an electron-hole pair is photogenerated within a diffusion length L_n from the into the p-doped side, the electron can diffuse to the junction without recombining with a hole and can be swept down the energy barrier to n-side by the depletion layer electric field. Equation 2.3 is a general principle. In fact, even in a DSSCs, where the particles size is too small for a depletion layer to exist [60] the electron diffusion length has to be greater than the TiO_2 film thickness for charge collection to be effective [61]. That sets the optimum TiO_2 mesoporous film thickness to 10-15 μm .

Figure 2.7 shows the complete schematics of an assembled commercial Si solar cell. The base is made of p-type monocrystalline or polycrystalline Si wafer⁶. This configuration ascribes the longest diffusion travel toward the depletion region to the minority electrons into the p-type material. Consequently, the larger electrons diffusion coefficient, related to the lower effective mass of the electrons compared to the holes brings about a higher charge collection efficiency. A similar principle is involved also involved in DSSCs fabrication. One of the reason why anatase is the

⁵For CdTe based solar cell the lower effective mass of electrons, see below, in p-type CdTe is just one of the reasons for having a p-doped base. Indeed, p-type CdTe is used as excitons generating material because of his favorable band gap ($\approx 1.4 \text{ eV}$) and because n-doped CdTe is hard to obtain.

⁶Recently, academic and industrial research has been focusing on development and commercialization of n-type Si solar cells. The aim of those efforts is to eliminate the LID (light induced degradation) that consists of a reduction of electrons life time after the first hours of operation. Boron-oxygen complexes formed during the Czochralski crystal growth are responsible for this detrimental effect. N-type phosphorus doped bases cut down the LID [62]. To compensate for the lower holes mobility compared to electrons a lighter doping of the base is used.

preferred TiO_2 polymorph for DSSCs photoanodes is the lower electron effective mass (higher diffusion coefficient) of the metastable phase (anatase) compared to the thermodynamically stable one (rutile) [63], [64] Fundamental photovoltaic

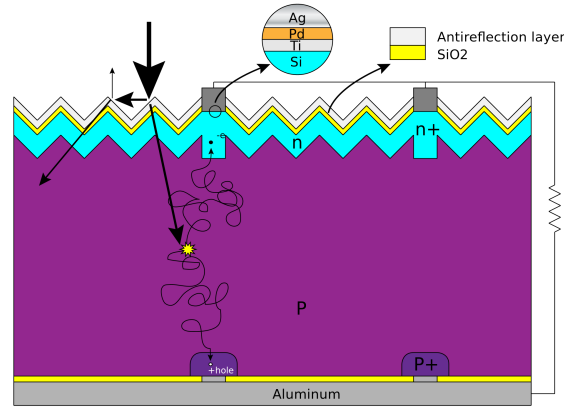


Figure 2.7: Complete structure of a standard screen printed silicon solar cell (with back surface field, SiO_x passivation layer, Si_3N_4 anti-reflective coating and contacts). Ti and Ag are used as fillers for the front contacts screen printing paste because they create ohmic contacts on Si through the formation of silicides. Pd is added to the front contact screen printing paste formulation to prevent silver electromigration. The p^+ areas on the bottom of the cell constitute the back surface field (BSF), that are heavily p-type doped regions obtained by diffusing Al dopants at high temperature after the back contact has been screen printed. The BSF keeps the holes from recombining with the electrons at the back contact. The top surface of the cell is chemically textured to increase the amount of light coupled to the cell (a similar effect is shown in this thesis through the synthesis of light scattering structures for DSSC photoanodes. From https://commons.wikimedia.org/wiki/File:Silicon_Solar_cell_structure_and_mechanism.svg

parameters are used to characterize photovoltaic devices regardless of the typology of solar cell, and their cell-specific meaning (i.e. although the dark current takes into account all the solar cell recombinative processes, it comes from different sources: HOMO-LUMO quenching in organic bulk heterojunction solar cells, Shockley-Reed-Hall recombination in silicon solar cells, electron transfer to the electrolyte in DSSCs, etc.). Therefore, some "universal" relation that allow to understand solar cells I-V curves (see Figure 2.8) can be stated. The first of these relations is the Shockley equation for solar cells current output:

$$I = I_{sc} - I_0 \left(\exp \frac{q(V - V_j)}{KT} - 1 \right) \quad (2.4)$$

Equation 2.4 establishes two crucial concepts:

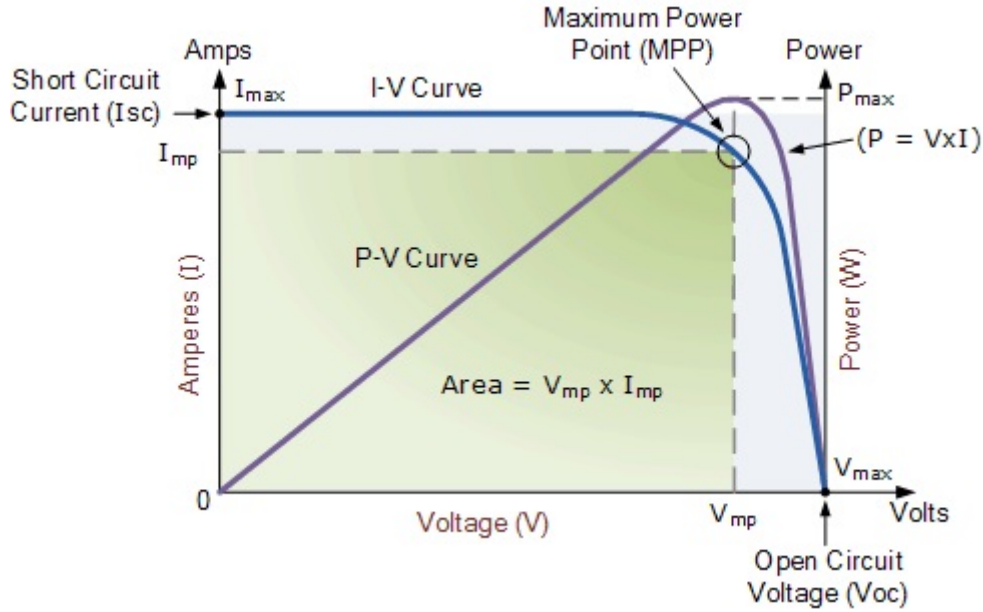


Figure 2.8: I-V (and power) characteristic of a solar cell.

- A photovoltaic device represent a current photogenerator that produces short circuit current I_{sc} (see Figures 2.8 and 2.9). In the specific case of a p-n junction is given by equation 2.1.
- Recombination phenomena in a solar cells are due to the rectifying behavior of the interface between two different carriers conductive media (p-n junction, electron-donor, semiconductor-electrolyte, perovskite-holes conductive polymer, etc.). I_0 is the saturation dark current of the "diode", that is the rectifying interface. I_0 is the current that passes through the cell in absence of light and with no electrical bias applied and that is due to thermal generation of carriers.

Furthermore, Schockley equation allows a qualitative understanding of efficiency vs temperature behavior of photovoltaic devices. In fact, the higher the temperature, the higher the thermal generation of minority carriers, the higher the recombination current, the lower the current output ⁷.

⁷Actually, different thermal effect have to be taken into account for a complete description of solar cell performances with respect to temperature changes. A temperature increase brings about semiconductor band gap narrowing and an increase of the carriers diffusion coefficient. However the dominant effect in first and second generation solar cells is the increased recombination that diminishes the open circuit voltage and the fill factor of the device. Conversely, for DSSCs an optimum operative temperature (around 40 °C) exists. In fact, below the optimum temperature the effect of increased ions mobility due to a temperature increase reduce the losses due to the electrolyte resistance. Above the optimum temperature the effect of the increased recombination rate becomes dominant.

Recombination processes affects also the open circuit voltage of the cell, V_{OC} , which is the intersection of current with the voltage axis in figure 2.8 and is the electromotive force of the cell. The relationship between V_{OC} and the recombination current is given by:

$$V_{OC} = \frac{KT}{q} \ln \left(\frac{I_{SC}}{I_0} + 1 \right) \quad (2.5)$$

The power delivered by the solar cell to the external load is the area underneath the I-V curve, and the maximum power output of the device corresponds to the "knee" of the polarization curve (MPP, maximum power point). Another parameter connected to the power (and energy conversion efficiency) of the cell is the fill factor (FF) that is a measurement of the "squareness" of the I-V:

$$FF = \frac{MPPV_{OC}I_{SC}}{P_{in}A} 100 \quad (2.6)$$

where A is the area of the device and P_{in} is the incident sun irradiance. The fill factor is related to the energy conversion efficiency, η through the formula:

$$\eta = \frac{FFV_{OC}I_{SC}}{P_{in}A} \quad (2.7)$$

The parasitic resistances of the (that are equivalent to the overpotentials for an electrochemical device like DSSCs, see appendix A) make the power output deviate from the ideal value given by the product of the I_{sc} and V_{OC} and depresses the fill factor. Parasitic resistances are explained in the next section.

2.1.3 Additional photovoltaic parameters

Besides the aforementioned parameters (open circuit voltage, short circuit current, dark current, etc.) the overall energy conversion efficiency of a solar cell is affected even by other optoelectronic characteristics. Since quantum efficiency, series and shunt resistance are fundamental parameters concerning DSSCs' recombination, charge injection and transport processes, a brief explanation of their meaning is provided here.

Parasitic resistances

As already mentioned, parasitic resistances affect solar cells efficiency in terms of fill factor. Two kind of parasitic resistance exists: series R_s and shunt R_{sh} resistance. Series resistance, R_s , losses are caused by the same factors regardless of the solar

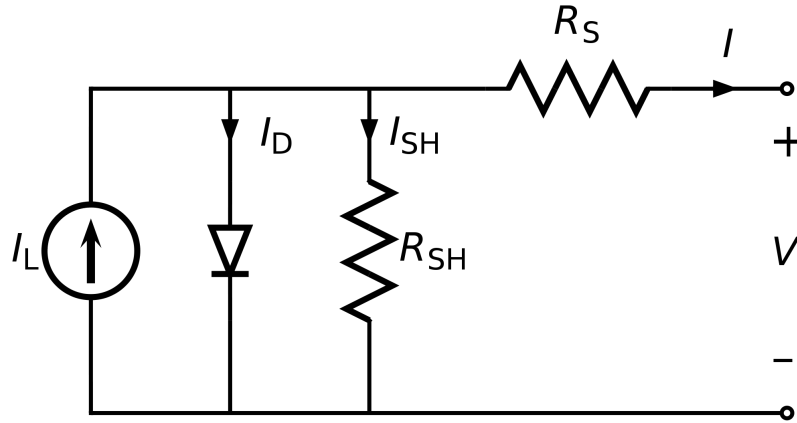


Figure 2.9: Equivalent circuit for a silicon solar cell (one diode model) predicated on equation 2.4. The model does not take into account generation of carriers inside the depletion layer. Although quite simple, the same equivalent circuit can be applied (with some modification concerning the diode ideality factor) to DSSCs. On the other hand, bulk heterojunction solar cells require a two-diodes model. R_{sh} is placed in parallel to the current photogenerator, hence a high value of the shunt resistance is necessary to prevent power losses.

cell design: the contacts, screen printed grid, or transparent conducting oxide ohmic losses, and semiconductor resistivity. DSSCs have an additional non-ohmic series resistance contribution from the electron transfer at the platinum counter electrode. R_s manifests its effect by decreasing cell's FF and, for very high values, the V_{OC} also (see figure 2.10. R_{sh} brings about a local increase of the dark forward current of the cell. A “shunt” can be thought as a short circuit between the emitter and base contacts. Plenty of reasons can prompt low shunt resistance values and they depend on the particular solar cell under consideration: insufficient junction insulation, silicon nitride inclusions in the base in silicon solar cells, recombination at the scaffold material-perovskite interface in perovskite solar cells [65], electron transfer from the the photoanode FTO to the electrolyte in DSSCs, etc. Regardless of the source shunt resistance reduces the fill factor first and, for low values, the I_{SC} also. Two examples of how the parasitic resistances can drastically affect solar cell performances will be presented in the present thesis: the high series resistance (due to the high contact resistance between the FTO the the porous TiO_2 film) of DSSCs prepared with anatase obtained by "hard" templating agents that limits the energy conversion efficiency; the very low shunt resistance of DSSCs with single chirality CNTs, that affected both the fill factor and the open circuit voltage.

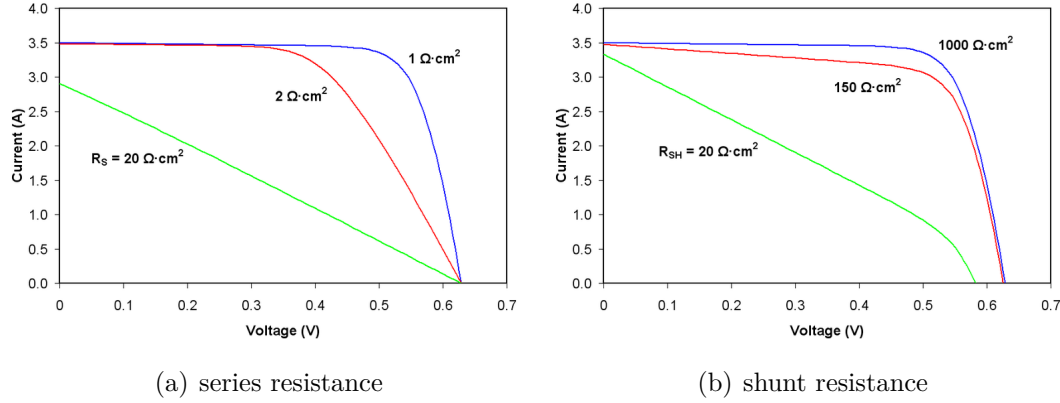


Figure 2.10: Effect of R_s and R_{sh} on a solar cell polarization curve. They both affect the fill factor. When the series resistance dominates the I_{SC} decreases, whereas if R_{sh} is the most important effect the V_{OC} drops.

Quantum efficiency

Quantum efficiency or IPCE (incident photon to current efficiency) gives the number of electrons collected under short circuit conditions per a given number of incident photons. The IPCE is measured for each wavelength of the solar spectrum (see figure 2.11). Thus, the short circuit current of the cell is the integrated IPCE over all the wavelengths:

$$I_{SC} = \int_{\lambda} IPCE(\lambda, V) \phi(\lambda) d\lambda \quad (2.8)$$

Where $\phi(\lambda)$ is the incident photon flux. IPCE's voltage dependence stems from the following formula:

$$IPCE = \eta_{abs} \eta_{harv} \eta_{gs} \eta_{cc} \quad (2.9)$$

where η_{abs} , η_{harv} , η_{gs} , η_{cc} are the light absorption, electron-holes harvesting, geminate pairs separation, and charge collection efficiency, respectively. Being the last two terms of equation 2.9 affected by charge injection level the whole IPCE becomes a function of the voltage. For DSSCs, where there is no electron-holes pair generation (at least when an electrolyte is used for dye's regeneration) the second and third term are replaced by the electron injection efficiency (η_{inj}) from the dye LUMO to the TiO_2 conduction band. η_{cc} depends on the balance between carrier transport and recombination processes. Ideally, the quantum efficiency graph against the wavelength should resemble of a rectangle delimited by the semiconductor absorption edge (see figure 2.12). However, recombination decreases the IPCE that then deviates from the ideal shape. For example, carriers generated by blue light (where

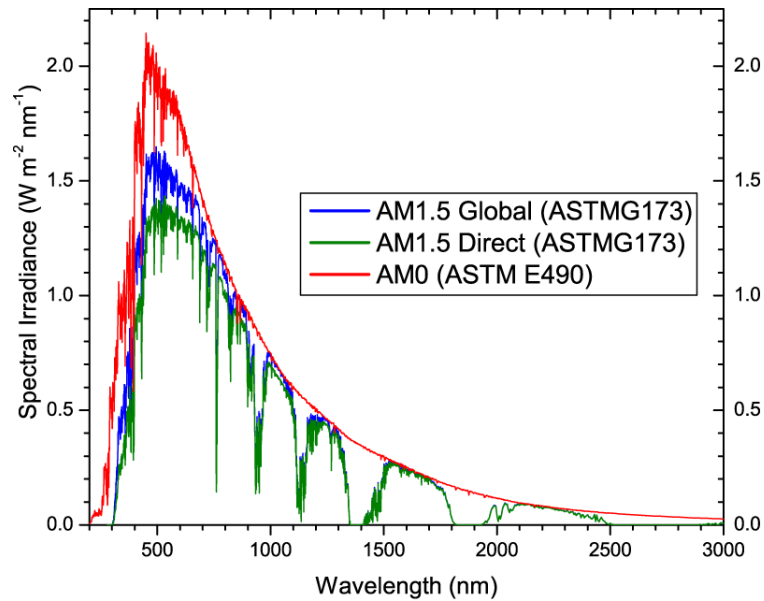


Figure 2.11: "Standard" (American Society for Testing and Materials, ASTM) solar spectrum employed to determine the performances of photovoltaic devices. Since the solar spectrum (in terms of wavelength and irradiance) changes according to the location and time of the day three standards are defined. AM 0, AM 1.5 D and AM 1.5 G. The first one refers to the solar spectrum in the space where there is no light absorption by the atmosphere and is characterized by an irradiance of 1366.1 W/m². AM 0 is the most used standard to characterize high efficiency/high cost multijunction solar cells for aerospace applications. AM 1.5 D and AM 1.5 G are the solar spectra, with an integrated irradiance of 1000 W/m² scaled by attenuation factor given by light absorption due to molecules in the atmosphere, the air mass AM factor. Absorption bands in the AM 1.5 D and AM 1.5 G belong to oxygen, water, carbon dioxide and ozone present in the atmosphere. The AM factor depends on the sun incidence angle with respect to the azimuth. Thus, AM =1 at the earth's poles and AM = 1.5 in North America and Europe. D and G stands for direct and global, respectively. The former indicates the light reaching the sea level without being scattered (direct light). The latter take into account also the diffuse light (included the soil albedo) and this is the reason why the maximum emission of the AM1.5 G is slightly blue shifted compared to the AM 1.5 D. Being silicon almost unresponsive to diffuse light, most of the silicon solar cells I-V curves are collected under AM 1.5 conditions. On the other hand DSSCs and perovskite solar cells are capable of charge generation and transport even under diffuse light conditions. From <http://pveducation.org/pvcdrom/appendices/standard-solar-spectra>

the radiation penetration depth is limited to the top surface of the cell) are subjected to surface recombination. Whereas, green light generates carriers in the bulk of the material where the main recombination mechanism is the electron-hole pair annihilation through the defects (impurities, vacancies, grain boundaries, etc.). Similarly, the IPCE under green light for a DSSC corresponds to the maximum light ruthenium dye light absorption (i.e. 530 nm for the N-719) and maximum

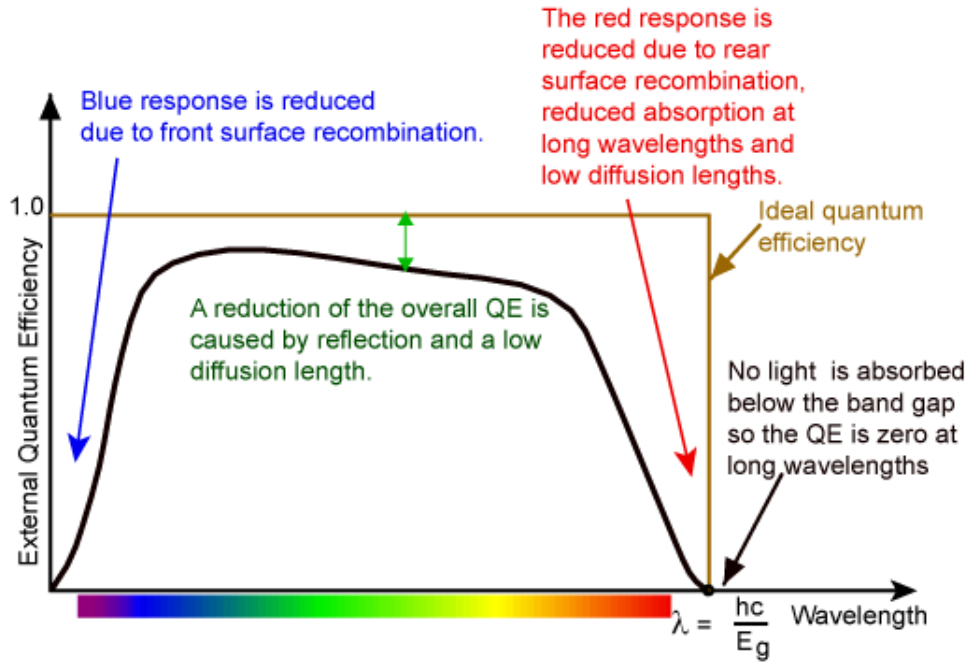


Figure 2.12: Quantum efficiency curve for silicon solar cells. From <http://pveducation.org/pvcdrom/quantum-efficiency>

electron injection rate to the TiO_2 conduction band. Thereby, η_{abs} and η_{inj} can be considered close to 1. Consequently, IPCE in the green range of the solar spectrum constitutes an estimation of TiO_2 conduction band electrons diffusion length (which is diminished by trapping and electron-electrolyte recombination).

2.1.4 "New generation" PV technologies

Third generation solar cells encompasses multiple PV technologies: DSSCs, perovskites, and organic (polymer) cells. DSSCs will be treated in details in the next chapter, perovskite solar cells represent the natural evolution of DSSCs [10], whereas organic solar cells share some characteristics with DSSCs because the charge is generated by organic molecules or polymers and because of the high interpenetration level of the hole and electron conducting media (in a DSSC the "holes" are carried either by an electrolyte or by a holes conducting polymer, see next chapter.).

Perovskites solar cells

Perovskite solar cells are photovoltaic devices based on organometal halides of general formula $\text{CH}_3\text{MNH}_3\text{X}_3$ ($\text{X} = \text{Br}, \text{I}, \text{Cl}$; $\text{M} = \text{Pb}, \text{Sn}, \text{Ge}$) possessing the crystal structure of the perovskite materials (ABX_3 where X is either a halogen or

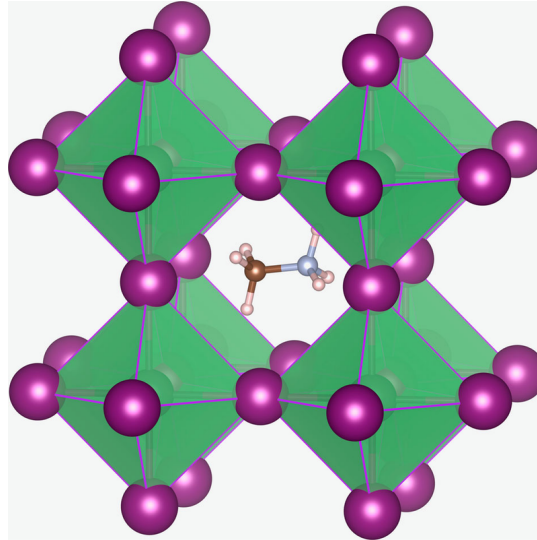


Figure 2.13: Crystal structure of $\text{CH}_3\text{NH}_3\text{PbX}_3$ perovskites ($\text{X}=\text{I}$, Br and/or Cl). The methylammonium cation (CH_3NH_3^+) is surrounded by PbX_6 octahedra. From https://en.wikipedia.org/wiki/Perovskite_solar_cell#/media/File:CH3NH3PbI3_structure.png

oxygen, A the larger cation occupying the cubo-octahedral sites and B the smaller cation occupying the octahedral sites, see figure 2.13). Methylammonium lead halides perovskite have been used instead of ruthenium based sensitizers to enhance TiO_2 light absorption properties in a conventional electrolyte-based DSSC structure [66]. However efficiency comparable to standard DSSCs (9.7 %, in 2012) have been achieved only by replacing the electrolyte with a solid state hole spiro-OMeTAD conductor [9] ⁸. Hence, the base technology for perovskite solar cells is solid-state sensitized solar cells that are based on dye-sensitized Graetzel solar cells. Then, perovskite solar cells (PSC) evolved from the original "sensitized" architecture (see figure 2.14). PSCs configuration evolution has also helped to understand the fundamental principles of their charge generation and separation mechanisms. In fact, the high performances achieved ([67] 10.9 % energy conversion efficiency in 2012) by using Al_2O_3 instead of TiO_2 as scaffold material for $\text{CH}_3\text{PbNH}_3\text{I}_2\text{Cl}$ have demonstrated that organo-metal halides do not require any nanostructured n-type

⁸Being the Methylammonium lead halides very polar structures, electrolytes tend to solubilize and degrade the light absorbing material. Thus, although perovskite own tunable band gaps suitable for photovoltaic energy conversion (ranging from 1.5 to 2.3 eV depending on the halide counter-ion.) these materials do not match the stability and band edges requirements for electrolyte based DSSCs. HTM (hole transporting materials) solved the stability problem. Spiro-OMETAD is the preferred hole transporting material for perovskite solar cells assembled in the "sensitized" configuration because completely infiltrate the mesoporous TiO_2 to induce a heterojunction for charge separation. Conventional p-type CuI and CuSCN are also used as HTM but with lower performances

semiconductor to accept electrons injected from the perovskite conduction band ⁹. Since there is no need for a nanostructured semiconductor, PSC could be fabricated without involving typical high temperature sintering stages (that are required for the mesoporous oxides used in DSSCs). PSCs seem to rely on a classical p-i-n junction heterojunction for charge separation (like an amorphous silicon thin film solar cell for example). The ambipolar nature of perovskites absorbers [68] has brought to high efficiency (17-18 %) planar p-i-n structures (see figure 2.14) that can be produced with standard evaporation methods [69]. The physico-chemical process involved in a p-i-n perovskite-based solar cell can be summarized as follow. Electron-holes pair are created by the light driven promotion of a electron into the perovskite conduction band (the instrinsic layer with a thickness of 200-300 nm). Perovskite high permittivity and the low binding energy are sufficient to separate the geminate pairs at least at room temperature. Then electrons diffuse within the perovskite to n-type contact (a compact, planar layer of TiO₂, 30-50 nm thick, that acts as a blocking layer to keep the spiro-OMETAD from touching the FTO) and holes diffuse towards the spiro-OMETAD. The two n-type an p-type contact materials (compact TiO₂ and spiro-OMETAD respectively) possess conduction and valence band positions favoring electrons and holes injection at the two heterojunctions (CH₃NH₃PbX₃/compact TiO₂ and CH₃NH₃PbX₃/spiro-OMETAD, respectively). Finally, electron are collected at the FTO contact and holes at an evaporated (Au or Ag) contact.

The highest energy conversion efficiency to date (March 2016) is 22.1% (NREL certified). However two major challenges remain for commercialization of perovskites based solar cells: materials stability and devices' performance hysteresis. Organo-metal halides perovskites present thermodynamyc stability issues. Besides the obvious problem of the decomposition a highly polar structure like the perovskites when exposed to moisture, ethylammonium-lead halide perovskites start decomposing to the corresponding solid lead (II) halide and gaseous methylamine and hydrogen halide at moderate temperatures (60°C) [70] precluding any long term operation under solar light. Finally, the I-V response of the perovskite solar cells demonstrate anomalous dependence on the voltage scan direction/rate/range, voltage conditioning history, and device configuration [71]. The hysteresis behavior is not fully understood and accumulation of ions at the perovskite/HTM interface,

⁹The alumina scaffold "forces" electron transport to occur into a ordered matarial, the perovskite rather than into the disordered TiO₂A similar concept has been used even in the present thesis: the CNTs/TiO₂ heterojunction employed in our DSSC photoanodes forces the electron diffusion into an ordered medium: a thin film of CNTs.

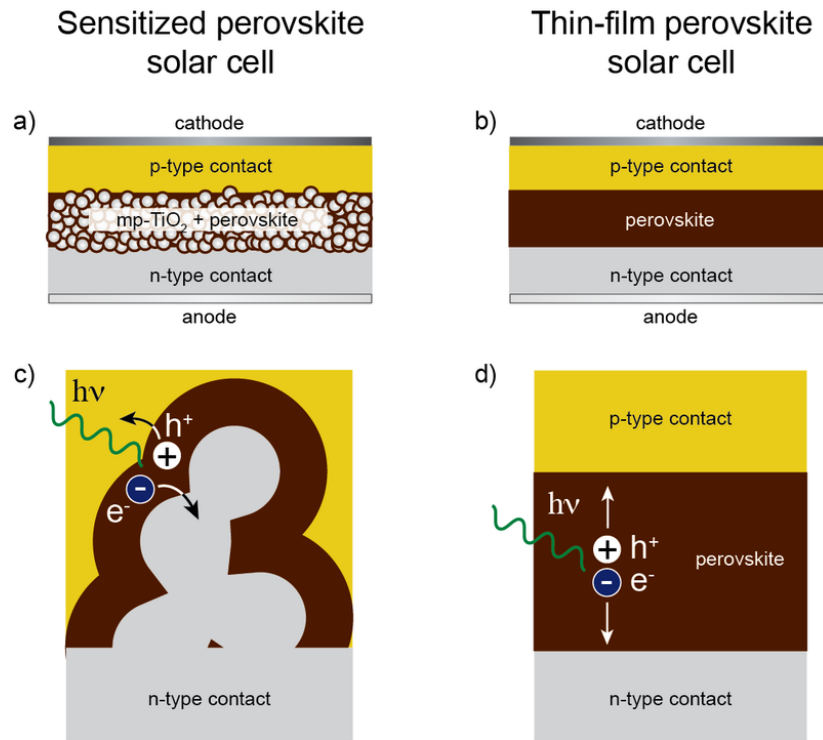


Figure 2.14: Schematic of a sensitized perovskite solar cell and its architecture from the "sensitized" (a) to the thin film structure (b). Sensitized: the active layer consist of a mesoporous TiO_2 film coated with the perovskite absorber. The active layer is contacted with an n-type material for electron extraction (usually a compact thin layer of TiO_2 deposited by spray pyrolysis) and a p-type material for hole extraction (spiro-OMETAD). Thin film: a flat layer of perovskite is sandwiched between to selective contacts and function as both light absorber and carrier transport material. (c) charge generation and extraction in the sensitized architecture. After light absorption in the perovskite absorber the photogenerated electron is injected into the mesoporous TiO_2 through which it is extracted. The concomitantly generated hole is transferred to the HTM. (d) Charge generation and extraction in the thin-film architecture. After light absorption both charge generation as well as charge extraction occurs in the perovskite layer. From https://en.wikipedia.org/wiki/Perovskite_solar_cell#/media/File:Perovskite_solar_cell_architectures_1.png

ferroelectric effects and light induced electronic accumulation confined within the Debye length in the vicinity of contacts are usually invoked as explanations.

Organic solar cells

Organic photovoltaics is a general definition that sometimes includes also perovskites solar cells and DSSCs because of the HTM, methylammonium salts, or light absorbing dyes used for their fabrication. Nevertheless, organic solar cells are primarily intended for low-cost devices on flexible substrates and that limits

the discussion to polymer solar cells¹⁰. Deposition of organics by techniques such as screen, sputtering, doctor blade, inkjet printing, spin coating, dip coating, spray deposition lends itself to incorporation in high-throughput low-cost roll-to-roll coating systems. These are low temperature deposition techniques that allow the organics to be deposited on plastic substrates such that flexible devices can easily be made. However the power conversion efficiency of organic solar cells is currently limited to 10 % because of the huge impact of recombination processes on charge collection.

The efficient conversion of a photon absorbed by an organic chromophore to an electron-hole pair extracted and driven through an external circuit involves many steps. Upon photon absorption a strongly bound electron hole pair (exciton) is formed. At this point the main difference between organic solar cells and all the other photovoltaic has to come into consideration. In fact, electrical permittivity of polymers and organic molecules is not sufficient to separate the exciton. Thus, excitons have to migrate to an interface where there is a sufficient electrochemical potential drop to drive exciton dissociation into an electron-hole pair that spans the interface across (material with low electron affinity) and the acceptor (material with high electron affinity) [72]. This geminate pair is still coulombically bound [73] and must be separated. After exciton dissociation and geminate pair separation each charge must be transported through the device, avoiding trapping or bimolecular recombination to the contacts. Hence, organic solar cells suffer from low energy conversion efficiency because of low η_{harv} , η_{gs} , and η_{cc} . In a planar (see figure 2.15) heterojunction polymer cell, less than half of the incident photons over the absorption spectrum are absorbed and ultimately converted to free electrons and holes. The primary reason for this is low exciton harvesting. In fact, excitons typically migrate distances of only 3-8 nm[74] before decaying. Consequently, most excitons created in the organic films do not arrive at the heterojunction before decaying [75]. Excitons short lifetime is the main peculiarity of organic solar cells; even in DSSCs, that still possess a relatively low charge collection efficiency because of trap mediated recombination, "exciton" (the electron in the TiO_2 and the oxidized Ru^{3+} in the dye) is a very efficient process (see chapter 3) Exciton harvesting can be increased by using a bulk heterojunction, which is an intimately mixed blend of two materials (acceptor and donor) that has a high internal junction interfacial area. This random blend can be composed of small domains such that an exciton can

¹⁰Although plenty of research has been dedicated for the last 20 years to the development of flexible DSSCs and perovskite cells they are mostly meant for application on TCO coated glasses.

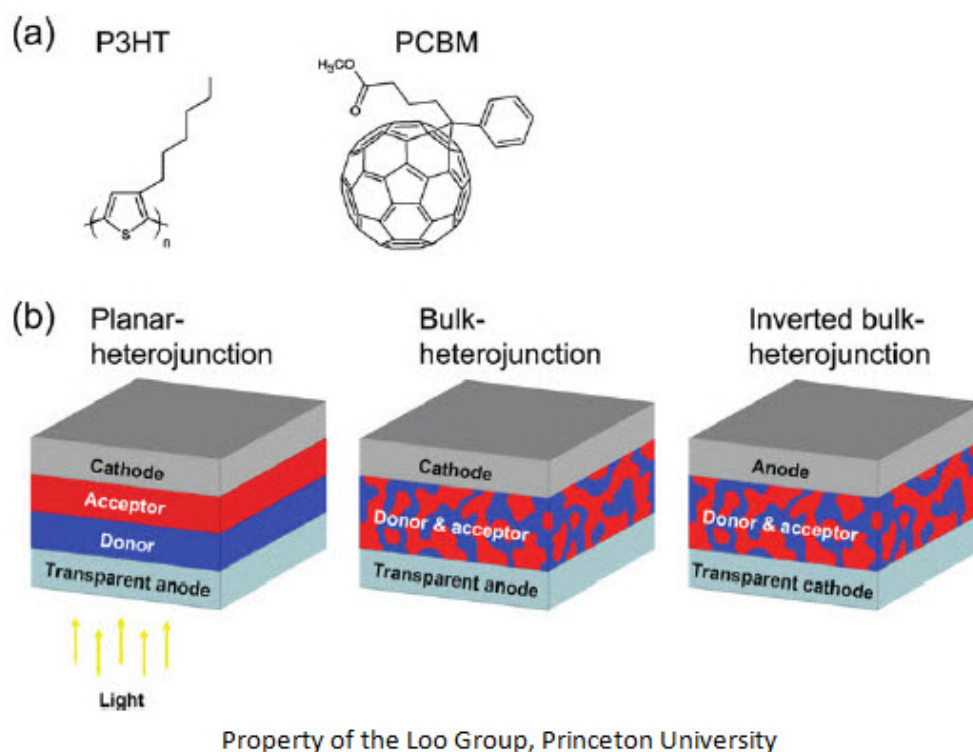


Figure 2.15: Structures of an organic solar cell: planar thin film and bulk heterojunction. (a) electron donor-acceptor pair: P3HT (poly-3-hexyl thiophene-2,5-diyl)-PCBM (Phenyl-C61-butyric acid methyl ester). Regioregular (RR) P3HT and non-functionalized C-60 can be used as electron donor-acceptor pair also. (b) the electron-donor pair can be arranged in a thin film or in bulk heterojunction configuration. The transparent contact is usually ITO, for glass encapsulated cells, or PEDOT:PSS (poly(3,4-ethylenedioxythiophene) polystyrene sulfonate) for plastic encapsulated devices. From <http://www.ngsf.org/multimedia-archive/loo-group-princeton-university/>

easily migrate to a heterojunction before decaying. In many bulk heterojunction, improved exciton harvesting comes at expenses of poor charge collection (like for example in a DSSCs increased surface area, which means increased light absorption comes at expenses of electron collection efficiency). Therefore new organic cells's designs are looking at the synthesis and optimization of ordered bulk heterojunction [76].

The materials employed as electron acceptor and donors for organic solar cells have been already mentioned in section 1.2. Although a large availability of materials exist, fullerene derivatives and P3HT (poly-3-hexyl thiophene-2,5-diyl) derivatives are the most employed electron acceptor and donor, respectively (see figure 2.15).

After this general view on solar cells, the next chapter will focus on DSSCs' structure, components and operative principles. As an anticipation of the topics,

it can be said that DSSCs represent a unique device compared to the other kinds of solar cells. Indeed, no geminate pairs are generated and charge separation and transport is driven by energy band position at the different heterojunctions (Dye/TiO₂, TiO₂/electrolyte, Dye/Electrolyte, FTO/TiO₂) and by the different kinetics of the process involved.

Chapter 3

DSSCs

3.1 Introduction

Dye sensitized solar cells (DSSCs) are unusual photovoltaic devices because they exploit a metallo-organic molecule for light absorption and carriers generation (i.e. a bipyridine Ru dye), a nanostructured wide band gap semiconductor for the electron transport, and a semiconductor-electrolyte interface for charge separation [77] (see figure 3.3). Although concept of using an illuminated semiconductor-electrolyte junction to generate a photopotential can be back-tracked to the 19th century ¹, stable and efficient photoelectrochemical cells (PEC²) have not been developed until materials technology has permitted to synthesize nanostructured wide band gap semiconductors at the beginning of the 1990s [2]. In fact, traditional "low" band gap semiconductors (n-type and p-type Si, n-type GaAs, p-type Inp, n-type CdS, etc.) are subjected to photocorrosion when in contact with an electrolyte. On the other hand, using wide band gap semiconductor oxides (ZnO, TiO₂, Nb₂O₅, WO₃) can result in a "catch-22" situation: the large band gap produces a sufficient band bending at the semiconductor-electrolyte interface preventing charge accumulation and then photocorrosion; but it incapacitate carriers photo-generation by the semiconductor. Thereby, an oxide needs to be "sensitized" by light absorbing materials like organic chromophores or quantum dots. The sensitizer absorbs photons in the visible range, promotes an electron to its LUMO (lowest unoccupied molecular orbital) and injects the e⁻ (if a favorable bands' alignment exists) into the oxide conduction band (CB).

¹The first ever photovoltaic device by Bequerel was a photoelectrochemical device. It was comprised of an AgCl electrode immersed into an electrolyte solution and Pt counter-electrode

²PEC is a general definition that includes both DSSCs and photogeneration cells. The latter is basically an electrolyzer activated by light. The photocurrent generated by the light absorbed by the semiconductor is used to split water in a electrolysis cell

However, the first sensitized electrochemical devices (fabricated in the 1970s) used mono or polycrystalline materials limiting the amount of sensitizer adsorbable on the photoelectrode surface. Furthermore, the original dyes used to sensitize wide band gap semiconductors (i.e. Rhodamine B, fluorescein or chlorophyll) covered only a small portion of the solar spectrum. Thus, two main breakthroughs in the field of sensitized PEC have been:

- The synthesis of photoactive metal-polypyridine (based on 2,2'-bipyridine, 2,2';6',2"-terpyridine and 1,10-phenanthroline, see figure 3.1 moieties) capable of intense (high molar extinction coefficient, $\epsilon \approx 10000 \text{ M}^{-1} \text{ cm}^{-1}$) metal-to-ligand charge transfer (MLCT) optical transitions.
- high specific surface area oxides capable of linking dyes through carboxylic or phosphonic bonds.

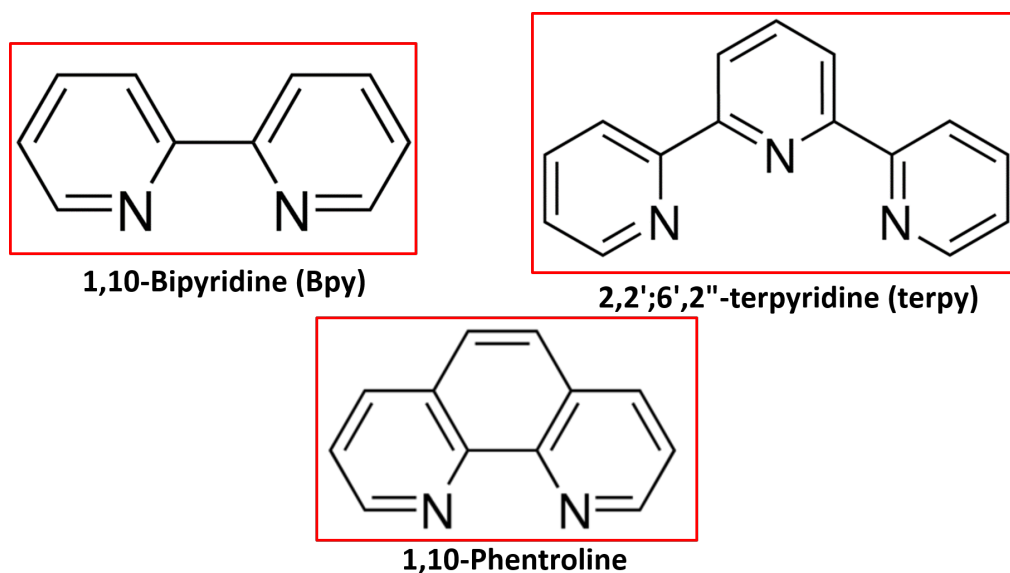


Figure 3.1: N-containing aromatic rings moieties of metal complexes capable of light absorption in the visible spectra. Metal ions (especially Ru) are coordinated by bis- and tris-bipyridine, bis-terpyridine and tris-phenanthroline ligands in an octahedral coordination. Usually three types of chemical modification are introduced to the basic bipyridine, terpyridine or phenanthroline structures. Alkyl, aryl, heterocyclic substituents on the N-aromatic ring to improve, by the enhanced electronic delocalization, the charge injection into the TiO_2 CB (better overlapping between the π^* ligands orbitals and the 3d Ti^{4+} orbitals); thiocyanate (SCN) metal coordinating groups to reduce the HOMO-LUMO gap extending the dye absorption spectrum into the red region; carboxylate or phosphonate groups on the N-aromatic rings to anchor oxide surfaces

Those improvements have brought to the fabrication of the first (7% efficient) DSSC

[2] by Graetzel and O'Regan in 1991. The use of ruthenium based bis-bipyridine complexes and nanostructured TiO_2 (see the following section for the reason of this particular combination of materials) has increased the quantum efficiency to values comparable to conventional solar cells (the IPCE for the most efficient DSSCs is around 80-85 %). Thus, the innovation introduced by Graetzel and O'Regan and additional efficiency improvements achieved in the last 25 years have made DSSCs competitive with standard silicon solar cells from the cost/efficiency standpoint. In fact, although DSSCs are less efficient than polycrystalline and monocrystalline silicon solar cells (14.7 % [78] vs 18% of poly- and 25 % of mono- crystalline Si), their manufacture cost is immensely lower. Indeed, DSSCs do not require any high-vacuum or materials purification steps (like zone refining for example). Furthermore, material properties tunability (TiO_2 morphology, dye light absorption properties, etc.) makes DSSCs more versatile than Si devices (where most of the optoelectronic properties are controlled only by doping). Moreover, DSSCs are capable to operate under low-irradiance and diffuse light exposure (like cloudy days conditions). On the other hand energy conversion efficiency of silicon solar cells is strongly reduced in those conditions. Finally, DSSCs' transparency make them ideal for building integrated applications.

3.2 DSSC mechanism: energetics

Sometimes DSSCs are defined either as an artificial equivalent of natural photosynthesis or as light activated electrochemical batteries. The reasons for these comparison is the fact that light absorption and charge generation occur in the dye (equivalent to photosystem I and photosystem II for plants photosynthesis), whereas charge transport occurs in a different media. The nanostructured semiconductor functions like the cytochrome b6f complex in the photosynthetic electron transfer chain, it carries electrons. In addition, the presence of redox mediators to achieve high levels of charge separation resemble the working principle (and the structure, see Figure 3.3) of an electrochemical battery

Although plenty of modification have been implemented to the original DSSCs configuration (i.e. metal-free dyes, different oxide semiconductors, solid state electrolytes and hole transport materials), we limit our discussion to the initial technology form of Graetzel cells: **a ruthenium(II)-based dyes (see figure 3.2) adsorbed on a high surface nanostructured TiO_2 film and an iodide-iodine based liquid electrolyte as redox mediator.** This is also the cell

configuration used in the present thesis.

Changes to the primary DSSCs structure will be mentioned when instrumental to a better understanding of DSSCs internal mechanisms (i.e. the modification related to the introduction of D- π -A dyes [79]). Figure 3.3 shows the structure of a "classical" DSSC and its operative principle. From left to right, the cell is comprised of a transparent conducting oxide coated glass, usually fluorine doped tin oxide (F:SnO₂, FTO). Although other TCOs such as ITO, AZO (aluminum doped zinc oxide), ATO (antimony doped tin oxide) possesses a lower sheet resistance (R_{sheet}) and transparency than FTO, fluoride doped tin oxide is the preferred transparent contact for DSSCs because its (R_{sheet}) remains relatively low even at the high temperatures needed for the photoanode's particles sintering step [81]. In addition, the FTO/TiO₂ interface owns a low energy barrier for the electron transfer from the nanostructured semiconductor to the transparent contact [82]. A porous nanostructured TiO₂ layer thick 10-15 μ m is deposited on the TCO providing the electrode with high specific surface area for the sensitization. Ru-based dye, for example N-719 which is the most used for DSSCs, is chemisorbed (through an ester bond due to dye's the COO⁻ groups) onto the TiO₂ surface forming a monolayer. The photoanode is joined to a Pt-coated FTO glass that serves as counter electrode. A liquid electrolyte composed of an organic solvent (acetonitrile [83], methoxypropionitrile [84], valeronitrile [85] or benzonitrile [86]), Iodine (I₂), lithium iodide (LiI) and a series of additives like alkyl-imidazolium iodide salts (i.e. 1-ethyl-1-methylpyrrolidinium iodide, 1,2-dimethyl-3-propylimidazolium iodide, 1-methyl-3-propylimidazolium iodide, etc.) and tert-butylpyridine. The I₃⁻/I⁻ pair is the redox mediator of the electrolyte. The role of the additives will be clarified later in the discussion.

When light strikes on the cell from the photoanode side, photons are absorbed by the Ru-based dye and a Laporte permitted MLCT transition occurs. The MLCT consists in a charge transfer from the metal center to the ligands and corresponds to the promotion of one electron from the dye HOMO (the Ru d-orbitals) to the LUMO (the NCS group π^* orbitals). Then, the e⁻ is injected from the dye LUMO into the the TiO₂ CB. This step relies on the electronic interaction of the N-aromatic bipyridine rings (having a large degree of electronic delocalization) with the TiO₂ acceptor states through the carboxylate bi-chelating groups anchored on the semiconductor surface. Afterwards, the electron diffuses through the disordered TiO₂ network, is collected at the FTO contact and is routed to external circuit. This initial stage has generate a photocurrent but has also produced a Ru³⁺ ion

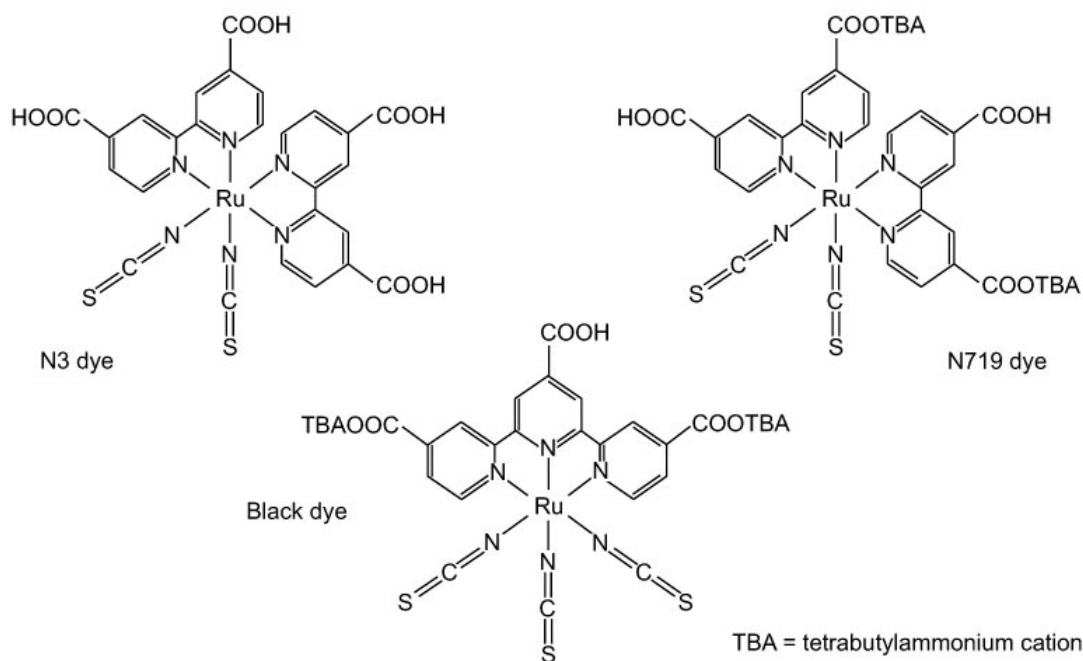


Figure 3.2: Ru containing dyes based on the moieties illustrated in figure 3.1. N-3, N-719, N-749 (black dye) and Z-907 (a para position alkylated bis-pyridine not reported in the figure) are the most common metal based dyes employed in DSSCs. Since DSSCs' function mechanism is predicated on the relative energy difference between the dye LUMO, the semiconductor CB, and the potential of the redox mediator (RE), the composition of the electrolyte solution and the semiconductor band structure have to be optimized accordingly to the particular dye used[80]. For example, N-719 dye possesses the same structure of the N-3 dye but the former has two TBA⁺ ions instead of H⁺ at two carboxyl groups over four. N-3 can provide at most four protons per dye molecule, the protons can adsorb on the TiO₂ surface basic sites and can shift the semiconductor conduction band (and Fermi level) energy to more positive values (closer to the redox couple potential) decreasing the V_{OC} of the cell (see text). Usually, ruthenium-bipyridine and terpyridine complexes produce high electron injection efficiency and high regeneration rate when used in conjunction with TiO₂ and an electrolyte containing the I⁻/I₃⁻ redox pair.

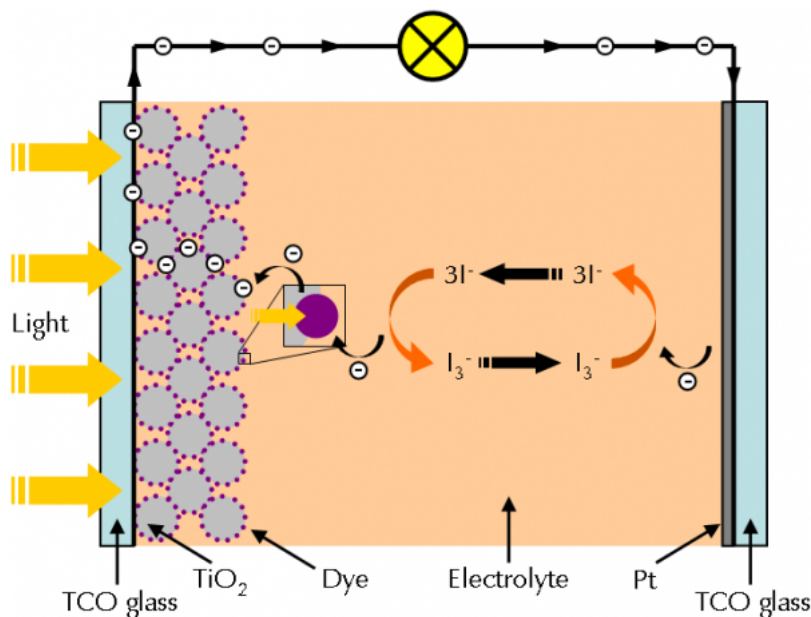


Figure 3.3: Structure and operative principle of a DSSC.

center in the dye that has to be reduced back to Ru^{2+} to avoid the degradation of the sensitizer. At the Pt counter electrode the e^- is transferred to the electrolyte where the redox mediator is reduced according to the reaction:



Then, the electron is transferred back to the dye HOMO and the oxidation state of the sensitizer is replenished. The diffusion of the oxidized redox shuttle (I_3^-) to the Pt counter electrode either by Stokes diffusion or by Grotthus jumping assisted by the imidazolium salt [87], [88] completes the cycle and closes the circuit. The driving force of the whole process is **the favorable position of the energy states involved in the charge generation, injection and transport**, see **Figure 3.4**. In fact, no electron injection can be carried out from the dye to the semiconductor unless the dye LUMO is positioned at more negative potentials (higher energy level) than the TiO_2 CB. Similarly, no dye regeneration can occur unless the redox shuttle potential (RE) is situated at more negative potentials than the dye's HOMO. This simple explanation helps to understand why high efficiency cells can be obtained with the following combination: anatase, Ru-based dyes (with proper ligands) and I_3^-/I^- redox shuttle (with proper electrolyte additives). Indeed, anatase is the only TiO_2 polymorph with a CB edge position suitable for electron injection from Ru dyes. For example, iron [90] and osmium [91] polypyridine complexes show low quantum efficiency when absorbed on TiO_2 surfaces because

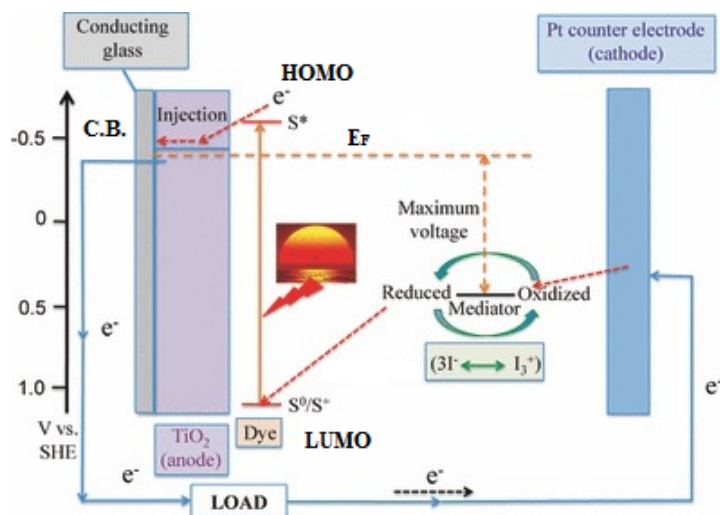
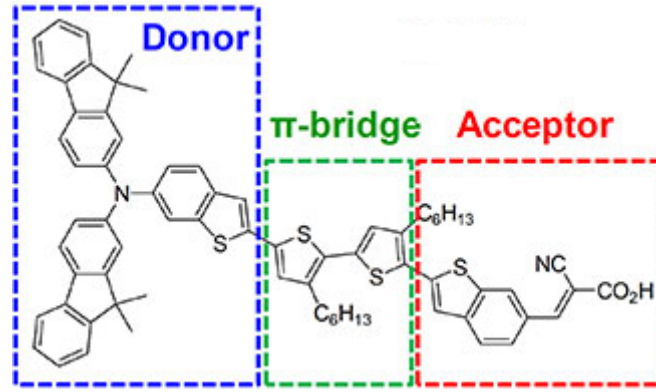


Figure 3.4: Energy Diagram and charge transfer processes in a DSSC. The figure reports only the forward processes. Recombination mechanisms and kinetics are discussed in the next section (3.3). The potential scale is referred to the standard hydrogen electrode (SHE). Adapted with permission from [89].

their LUMO is located close to the anatase CB edge generating an insufficient energy difference to drive the e^- injection. The small "push" for the electron toward the TiO₂ causes the dye excited state to decay (see 3.3)³.

Most of the research on DSSCs is dedicated to shift in a proper direction the dye's HOMO and LUMO, TiO₂ CB and redox mediator RE to increase cells J_{SC} and V_{OC} . The short circuit current depends on the dye's ability to absorb light, consequently, the HOMO-LUMO energy gap reduction is a suitable strategy to exploit the part of the spectrum above 700 nm (red and infrared). High quantum efficiency for injection is achieved when the dye LUMO is both energetically matched and reasonably strongly coupled with the underlying semiconductor. Since the dye's excited state cannot be shifted to more positive potentials (lower energies) without impairing the electron injection efficiency into the TiO₂ CB, the dye's ground state can be shifted up (to more negative potentials) by adjusting the orientation of the thiocyanate ligands [93] and by changing the bipyridyl ligands [94]. However, those modifications move Ru dyes HOMO closer to the I₃⁻/I⁻ pair redox potential slowing down the dye regeneration by the redox shuttle and lowering the driving force for the reaction [95], [96]. Furthermore, to compensate for the relatively low molar extinction coefficient of Ru-polypyridine complexes [97], co-adsorbants [98], [99] may be used to improve the e^- injection into the TiO₂ CB.

³Recently (November 2015) good IPCE for modified N-heterocyclic carbene-Fe(II) complex adsorbed on anatase has been proved [92].

Figure 3.5: Example of a D- π -A sensitizer

An alternative approach to increase J_{SC} is to use prototype dipolar architectures **donor- π bridge linker-acceptor (D- π -A)** (see figure and 3.5) as sensitizers instead of ruthenium dyes. D- π -A dyes possess molar extinction coefficients (ϵ) higher than $50000 \text{ M}^{-1} \text{ cm}^{-1}$ that allow for maximization of light absorption at longer wavelengths [100]. Moreover, larger ϵ permits to work with thinner TiO_2 reducing, see next section (3.3) the electron transport-recombination competition. D- π -A dyes for DSSCs applications are metal-free organic dyes [101], [100] where electrons are excited through an intramolecular charge transfer (ICT). Metal-free sensitizers are classified on the basis of their chemical structure: porphyrines [80] [79], phenothiazine based [102], quinoxaline (π linker)-indoline (donor) [103], triarylamine (donor)-cyanoacrylic acid (both electron acceptor and anchoring group) [104], etc. Besides the high molar extinction coefficient, another advantage of metal-free organic dyes is the possibility modify the donor and the acceptor moieties to match their HOMO position to the RE of high V_{OC} redox shuttles like cobalt polypyridine complexes [105]. As stated before, for the dye regeneration to occur the dye HOMO has to be at more positive potentials than RE [106]. However, see figure 3.4 the cell V_{OC} is set by the energy difference between the titanium oxide Fermi level E_F and the electrolyte RE that depends on the redox standard potential and concentration of the redox species. Co(II)/Co(III) polypyridine complexes allow for good energy bands matching with most of the D- π -A sensitizer, while keeping a sufficient energy offset with respect to the TiO_2 Fermi level. [107], [108], [109]. On the other hand for the I^-/I_3^- there are two way to increase the shift the RE to more positive values and consequently increase the V_{OC} . The first one exploits the Nernst equation:

$$RE = E'_0 + \frac{RT}{2F} \ln \frac{C_{I^-}}{C_{I_3^-}} \quad (3.2)$$

Where E'_0 is the formal potential of the redox couple and C_{I^-} and $C_{I_3^-}$ are the concentration of iodine and triiodide respectively. Although might be reasonable to decrease the triiodide concentration to shift down (positive potentials with respect to the SHE) RE, that causes mass transport issues being I_3^- the main charge carrier in the electrolyte. Therefore, low triiodide concentration hinders also the dye's regeneration process [110].

The second approach relies on large cations released in the process of dye anchoring on the TiO_2 surface, the TBA^+ for the N-719, and on the imidazolium salt ions, for example the DMP^+ , present as additives into the electrolyte. Bulky positive ions [111] modulate the TiO_2 flat-band potential. In particular large cations like TBA^+ and DMP^+ shift the TiO_2 Fermi level to more negative potentials (toward the vacuum level) [110], [112]. Furthermore, ion adsorption at the TiO_2 /dye/electrolyte interface brings about different "kinetic" effect that will be treated in the next section (3.3), and next chapter.

3.3 DSSCs'mechanism: kinetics

The previous discussion has considered only the energy states diagrams and the driving forces leading to the charge injection. However, the kinetics of forward (generating photocurrent) and reverse (recombination) processes has not been dealt with yet. Charge transfer reaction rates affect the electron collection efficiency η_{coll} , which means the IPCE (see Chapter 2.1.2) and through the dark current also the V_{OC} (see equation 2.5). The competition between forward and reverse processes can be expressed in terms of characteristic time constants [113]:

$$\eta_{coll} = 1 - \left(\frac{L}{L_n} \right)^2 \quad (3.3)$$

where L is the TiO_2 film thickness and L_n the the electron diffusion lenght given by the equation:

$$L_n = L \sqrt{\frac{\tau_r}{\tau_{tr}}} \quad (3.4)$$

where τ_r and τ_{tr} are the electron recombination life time and the electron diffusion time into the photoanode, respectively. Hence, improving DSSC implies **prolonging electron lifetime by reducing the recombination, lowering the electron diffusion time, that means increasing electron diffusion length**. In addition, equation 2.5 establishes that to increase the V_{OC} the electron injection (the

direct process that generates J_{SC}) has to be more favorable than the recombination process occurring in dark conditions.

Figure 3.6 shows *whole* sequence of electron injection and charge transfer processes that result in photovoltaic device function. Forward electron transfer and charge

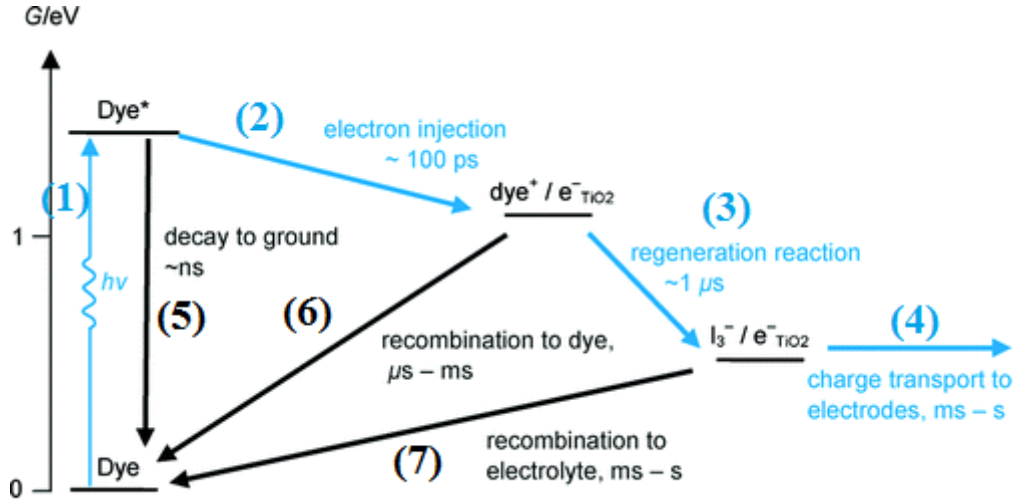


Figure 3.6: Kinetics of charge transfer and electron transport in a DSSC. Sky-blue arrows indicates the forward electron injection steps necessary for cell's operation. Black arrows refer to the reverse charge transfer: recombination processes. Adapted with permission from [114]

transport (process 1-4) are in competition with three loss pathways: decay of the dye excited state to the ground state (5), electron recapture by the oxidized dye from the TiO₂ CB (6) and recombination of electron into the TiO₂ (not necessarily in the CB, see next chapter section) with the I₃⁻ ions (7). The first loss pathway is negligible because the electron injection from the dye LUMO to the TiO₂ (CB) occurs immediately after (pico to femto seconds) the photoexcitation [94]. The reason for such a fast e⁻ transfer can be found in the Fermi golden rule equation that gives the kinetic constant for electron injection reactions, K_{inj} , in quantum mechanical terms:

$$K_{inj} = \frac{4\pi}{h} |V|^2 \rho(E) \quad (3.5)$$

where h is the Plank constant, $\rho(E)$ is the conduction band density of state and $|V|(E)$ is a parameter used to describe the degree of overlapping between the dye excited state and the acceptor states in the TiO₂. The high values of $|V|$ stem from the large overlapping between the unoccupied 3d orbitals of the Ti⁴⁺ ions and the π^* orbitals of the dye's ligands. On the other hand, ZnO electron accepting level are composed of the empty 4s orbitals of the Zn²⁺ that overlap only partially

with the dye's π^* orbitals. This is the main reason of TiO_2 outstanding performance in DSSC with Ru-based dye compared to other oxides (CdO , SnO_2 , Nb_2O_5 . etc.) [115], [116], [117]. Furthermore, ruthenium dyes are prone to intersystem crossing from a singlet state to a triplet state. Lifetime of the latter is longer than the former one (from nano to millisecon for the triplet; from tents of picoseconds to nanoseconds for the singlet, [114]). Hence the decay of dye's excited state to his ground state is highly improbable because comparatively slower than electron injection into the TiO_2 CB.

Process (6) is in direct competition with dye's regeneration (electron transfer (3)). Being the the concentration of oxidized dye molecules sparked by light (compared to their thermal generation) electron recombination through the sensitizer becomes important under high illumination or when the electron transport through the nanostructured TiO_2 is extremely slow.⁴ The high dielectric constant of TiO_2 , coupled with the high ionic strength of the electrolyte, is generally thought to result in negligible coulombic interactions between the sensitizer dye cation and the injected electron. Thereby, no significant geminate decay (recombination between the electron immediately after the injection into the TiO_2 CB and the oxidized dye) occurs in DSSCs [118], [119]. This is the main difference between DSSCs and other hybrid cells (i.e. bulk heterojunction polymer solar cells where high surface nanostructured oxides are employed either as electron acceptors or scaffold materials). Moreover, process (6) can be controlled by selecting a particular dye (i.e. N-3 instead of N-719) and by the electrolyte additives. In fact, Li^+ and H^+ . or small cations in general (i.e. guanidinium) adsorbed at the TiO_2 /dye/electrolyte interface screen the electrons into the TiO_2 CB from the positive charged oxidized dye because of their high charge density. Furthermore, high charge density cations adsorb at the TiO_2 /electrolyte interface forming an electrical double layer that increases the local concentration of I^- ions speeding up the dye regeneration [120] and consequently reducing the electron recombination route through the dye. However, the Fermi level shift to positive potential caused by small cations adsorption has to be compensated by tert-butylpyridine addition to keep the V_{OC} at high levels [121], [122]. The regeneration reaction rate depends also on the iodide concentration, electrolyte charge transport ability, and counter electrode capacity to re-convert the redox shuttle oxidized form into the reduced one. For the N-719 sensitizer dye, coupled with a Pt cathode, and employing either a low-viscosity solvent electrolyte

⁴Notwithstanding the fact the the recombination through the dye requires light, this thesis will present a case where recapture of electrons by the oxidized dye may become important even in absence of light and becomes the main source of saturation dark current I_0 .

or higher viscosity electrolyte (i.e. benzonitrile) characterized by a fast Grotthus mechanism [86] the regeneration reaction take approximately $0.4 \mu\text{s}$ [123]. This is sufficiently fast to compete effectively with the competing recombination reaction and ensuring that the regeneration reaction can be achieved with unity quantum efficiency. Therefore, the recapture of electrons by the oxidized dye molecules does not usually constitute an issue in DSSCs [121], [110], [124].

Efficient charge collection to the external circuit requires the electron transport (τ_{tr}) through the nanostructured TiO_2 toward the FTO contact to be faster than charge recombination of injected electrons with the triiodide ion. In other words, process (4) in figure 3.6 has to be faster than process (7). The latter reaction is known as interception and represent the main source of dark current in DSSCs, but contributes to cells recombinative loss also under illumination. In fact the saturation dark current (no electrical potential applied) is given by the formula:

$$I_0 = K_{int}[I_3^-]n_{CB0} \quad (3.6)$$

where K_{int} is the kinetic constant for the interception reaction, $[I_3^-]$ the concentration of triiodide ions and n_{CB0} the conduction band electron concentration in dark and at the thermal equilibrium. When the TiO_2 Fermi level is shifted to more positive potentials (E_F get closer to E_{CB} , the energy of the conduction band edge) either by applying a forward bias to the cell or by providing the photoanode with radiation the e^- concentration in BC is perturbed from its equilibrium value according to the equation

$$n_{CB} = \rho(E) \exp - \frac{E_{CB} - E_F}{KT} \quad (3.7)$$

Consequently, more electrons populate the TiO_2 CB and recombination increases⁵. Thus, the interception mechanism is active not only with no illumination but even during the cell's photovoltaic operation and adds up to the the recombination through the dye. Equation 3.6 is a first order kinetics reaction which is favored by large concentrations of triiodide ions. Even if $[I_3^-]$ is not high (a standard electrolyte formulation contains 0.05 M of I_2) the great interpenetration level between the nanostructured semiconductor and the electrolyte favors the availability of triiodide ions close to the TiO_2 conduction band. Presence of large-sized cations (like TBA^+ and DMP^+) or bulky molecules (like the *tert*-pyridine) impedes the the access

⁵The macroscopical result of a polarization, either optical or forward electrical, applied to the DSSC in terms of recombination current is its exponential dependence on the voltage as given by the Shockley equation 2.4 for conventional solar cell.

of triiodide ions to the TiO_2 e^- (but due to the smaller I^- can still penetrate the TiO_2 /dye interface to regenerate the sensitizer). When D- π -A dyes are used, π spacer steric hindrance can be raised by adding alkyl or alkoxy substituents and the dark current is suppressed (see figure 3.7 as an example [125]). This

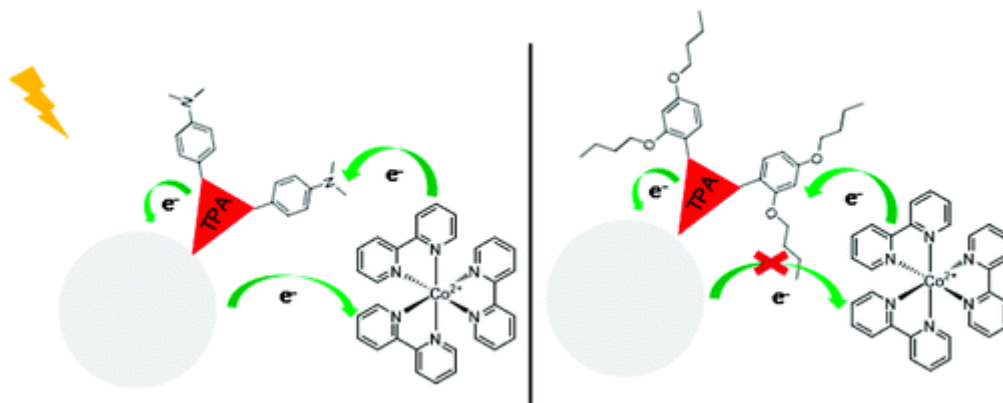
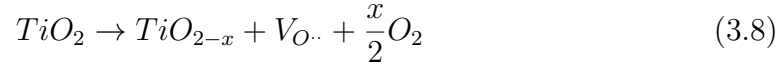


Figure 3.7: Example of bulky substituent (Triphenylamine, TPA) bond on a D- π -A structure. Adapted with permission from [125]

method has been proved to be effective for D- π -A dyes coupled with Co(II)/Co(III) based electrolytes where the interception reaction of the e^- in the TiO_2 CB by the redox shuttle is favored by the single-electron charge transfer mechanism that does not involve any molecular bond breaking [125], [103], [126], [109]. On the other hand, the reduction of I_3^- to I^- is a two electron, multistep process that requires breaking the triiodide molecule [122], [127]. Thus, K_{int} should be low because of the high activation energy of the process [124], [127] and the interception reaction should occur on a longer time scale than the electron diffusion through the TiO_2 . Nevertheless, **TiO_2 nanostructured nature, which is indispensable for dye adsorption, accelerate the interception reaction and slows down electron diffusion.** In fact, large specific surface area is associated with high degree of morphological, structural and electronic disorder. The first one is identified with random distribution of irregular shaped particles arranged in a 3-D network. Structural disorder is brought about by two dimensional crystallographic defects: dislocation and grain boundaries [128]. Finally, electronic disorder is caused by intra-gap electronic states known as traps. The effect of morphological disorder is simple to understand: the lack of long range orientation for the charge transport hinders the electron diffusion through the photoanode compared to ordered structures [129]. Grain boundaries and dislocations are electron scattering locations that decrease the electron diffusion current. Indeed, scattering raises the τ_{tr} rendering the e^- - I_3^- more probable.

Mesoporous TiO_2 and nanostructured titanium dioxide in general are full of lattice point defects that arise during synthesis or from the DSSC assembly, resulting in a multitude of electronic sub-band gap states that are able to trap charges. Defects arising from TiO_2 synthesis are positively charged oxygen vacancies generated by the thermodynamically favored reaction:



Interstitial Ti^{3+} [7] are created to compensate for the oxygen vacancies. Being the trivalent titanium atoms donor defects, TiO_2 is a natural n-type semiconductor. Thus, oxygen vacancies are the cause of TiO_2 n-type conductivity, but not the primary source of donors defects. In fact, since the TiO_2 valence band is made up of O^{2-} 2p orbitals, oxygen vacancies are located near the valence band (VB) edge. A similar effect is instigated by the addition of lithium salts in the electrolyte: since Li is a strong reducing agent Ti^{3+} ions *on the TiO_2 surface* are generated. Other ions adsorbed on the TiO_2 surface and dangling bonds can also act as traps [130]. Under cell's working conditions more than 90% of electrons in TiO_2 are trapped and <10% in the conduction band [131], [132]. Trap states can be distinguished into shallow, which are located near the TiO_2 CB and deep, which are positioned in the middle of the TiO_2 energy gap or close to the VB. The two natural (intrinsic) shallow and deep traps in the TiO_2 are Ti^{3+} ions and oxygen vacancies, respectively [133], [134]. Different effects are induced by shallow and deep traps formation. In this section we limit the discussion to the two natural shallow and deep traps postponing the discussion on doping induced traps to section 4.3. The first effect influences the TiO_2 energy levels. (E_F) is shifted upward (more negative potentials) by shallow traps. As a consequence V_{OC} increases. However, TiO_2 conduction band edge is shifted close to the dye's LUMO, hence the driving force for electron injection is lowered and J_{sc} decreases. On the other hand deep traps provoke the opposite effect (higher short circuit current and lower open circuit voltage) because E_F shifts downwards. The second effect concerns the electron transport and recombination. Semiconductors' conductivity is given by the formula:

$$\sigma = n_{CB}\mu e \quad (3.9)$$

where μ is the electron mobility. As stated before (see equation 3.7) the closer E_F to E_{CB} , the higher the electron population in CB. Since deep traps shift the E_F downwards TiO_2 film conductivity is low. Nevertheless, this does not represent a

major liability because under cell's operation conditions TiO_2 CB is "flooded" with electrons injected by the dye [135]. A more crucial problem is that electrons falling into deep traps cannot be thermally re-emitted into the CB. Oxygen vacancies, are located at the TiO_2 /electrolyte interface like suggested by the strong pH dependence of traps density [131], [128], [136]. Therefore, once an electron is permanently trapped in a deep defect on the surface it recombines with the triiodide ion. Furthermore, it is well known from catalysis technology that surface point defects are preferred sites for dissociative chemisorption of small molecules [137], [138], [139]. Thus, the enhanced catalytic activity of the oxygen vacancies increases K_{int} by facilitating the I_3^- splitting. In such a manner the interception reaction rate is accelerated.

Shallow traps are directly responsible for the slow, i.e., ms, electron diffusion in the TiO_2 . Indeed, e^- diffusion in the photoanode is controlled by trapping and detrapping events between the CB and the shallow traps [140], [141], [142], although a small electron tunneling contribution between shallow traps cannot be completely excluded [143]. Since the electron diffusion is trap mediated unless high level of irradiance or electrical bias shift E_F into the TiO_2 saturating all the traps [144], the charge transport through the photoanode is extremely slow (trap-diffusion limited mechanism) [145]. Consequently, electrons have plenty of time to recombine with the electrolyte causing L_n to shorten.

To be able to effectively modify trapping states it is important to know their *exact* energy and spatial distribution. Open circuit photovoltage decay, intensity modulated photocurrent spectroscopy, intensity modulated photovoltage spectroscopy, time resolved charge extraction and above all measurements of chemical capacitance (C_μ) vs voltage through impedance spectroscopy, have been used to determine of intragap states over certain ranges of V_{OCs} [146]. C_μ , for example, increases exponentially in certain photopotential ranges indicating an exponential energy distribution of traps. Unfortunately, the correlation of energy (shallow or deep) with spatial location (bulk or surface) of the intra-gap trap state remains hard to be established precisely. First of all because most the measurement techniques are limited to narrow ranges of photopotentials that do not overlap with the potential range in which certain defect (i.e. dangling bonds) are involved in the electron transport or recombination process [146]. Secondly, because the TiO_2 synthesis method heavily affects defect locations and type [7]. This makes it difficult to modify the TiO_2 keeping intact the electronic properties.

Our approach to maximize the forward DSSCs' power generation processes

and minimize the recombination consists in decreasing the morphological disorder by different TiO_2 morphologies obtained with different synthetic methods. Once identified the best performing morphology, the electronic disorder is modified through doping to prevent recombination and injection properties by shifting TiO_2 CB edge and compensating for deep traps. Finally, heterostructures are used to switch electron transport media: from a highly disordered (TiO_2) to an ordered one (CNTs).

Chapter 4

Morphology, doping and heterojunctions

4.1 Introduction

The current chapter presents the general effects introduced by the three (morphology optimization, doping, heterojunction formation) approaches we used to improve DSSCs performances. The description of beneficial effects and issues connected to each methodology should help to understand the reasons of the particular kind of morphology (TiO_2 mesoporous hierarchical beads), dopants (lanthanide cations) and heterojunctions (TiO_2 /chirality selected SWCNTs) we used to achieve three general goals:

- A.** Developing ordered mesoporous structures able to maximize light collection efficiency and charge generation without penalizing excessively the electron transport properties.
- B.** Doping anatase with ions capable of controlling the charge injection properties by tuning TiO_2 energy bands' positions and reducing the electron-electrolyte recombination by suppressing the electronic defectivity (disorder).
- C.** Improving charge injection, electron transport and recombination by using a high surface, high light scattering capability medium for light absorption and charge generation while exploiting a high electron mobility medium for charge collection.

Since modifying even a single property of the photoanode material (i.e. the specific surface area) affects multiple DSSC photovoltaic parameters, a detailed

description of the consequences of morphology change, titanium dioxide doping and heterojunction fabrication are described in details in each section.

4.2 Morphology control

The ultimate goal of any TiO₂ morphology optimization procedure is to couple high specific surface areas to allow for the adsorption of large amounts of dye without jeopardizing the electron transport properties. Besides, extended porosity and suitable band gap are desirable for intimate contact between the dye and the electrolyte and to control charge injection processes, respectively.

Ideally, an anatase mesoporous single crystal would match all the requirements. Such a structure can be obtained by growing an anatase single crystal and by inducing porosity on its surface by a focused ion beam source (FIB). However, two complications arise when this approach is used. First, the most reactive anatase crystallographic facet for N3 and N-719 adsorption is the $\langle 001 \rangle$ [147], [148], [149], [150] but the most thermodynamically stable is the $\langle 101 \rangle$ because of surface energy minimization [151], [152]. Therefore, it is difficult to grow a $\langle 001 \rangle$ oriented single crystals in order to maximize the dye adsorption. Secondly, DSSCs are meant for low cost applications and employing FIB techniques would prohibitively raise the production costs.

The "benchmark" TiO₂ for DSSCs are commercially available P25 and P90 Degussa-Evonik nanoparticles. These materials, obtained by TiCl₄ flame pyrolysis, are comprised of non-agglomerated nanoparticles with size ranging from 10 to 30 nm and characterized by a specific surface area of approximately 100 m²/g for the P90 and 60 m²/g for the P25 [153]. Therefore, P25 and P90 represent a textbook case of 0-D nanostructures (see chapter 1.2). Needless to say, their high surface area and the fact that particles are well-separated are beneficial for dye adsorption. Furthermore, the low degree of particles agglomeration leads to high performances screen printing pastes by using small amounts of low molecular weight dispersants easily removed at relatively low temperatures [154]. Finally, the small particle size brings about high reactivity that is fundamental for particles' sintering during the photoanode thermal treatment. However, they suffer from several drawbacks:

- Both P25 and P90 contain approximately 20% (by mass) of rutile. Although, this TiO₂ allotrope is desirable for *photocatalytic* applications [155], [156], [157] it is detrimental for DSSCs photoanode structures (see section 3.2).

- The small particles (and crystallites) size, that is responsible for the high reactivity during the sintering stage also contribute to increase the amount of rutile in the final annealed photoanode.
- P25 and P90 printed films are transparent[154]. Hence, a layer of larger particles (400-500 nm) has to be subsequently deposited in order to scatter photons back into the transparent film (increasing the optical path) and enhance red and near-IR light harvesting [154],
- P25 and P90 nanoparticles are not porous.

The limited porosity is an issue shared with other nanoparticles structures [158], [159], [160]. Furthermore, because of their zero dimensional morphology P25, P90 and TiO₂ nanoparticles in general are subjected to the limitations stemming from the high degree of morphological disorder. In fact, a titanium dioxide nanoparticles photoelectrode is a random network of crystallographically misaligned crystallites, and lattice mismatches at the grain boundaries that favor enormously electron scattering, trapping and ultimately recombination [161], [162], [163]. One-dimensional TiO₂ structures such as wires [164], tubes [165] and rods have a relatively small amount of grain boundaries and can act as single crystals, which are able to reduce the grain boundary effect and provide fast electron transport [166], [167], citeorder3. For example, the electron recombination rate in TiO₂ nanotubes has been found to be 10 times slower than in nanoparticles because of the directional electron transport that efficiently subtract charge from the recombinative routes[168], [94]. The more the mono dimensional structure is spatially oriented, the faster the electron transport (i.e. L_n is larger for vertically aligned nanotubes compared to randomly oriented nanorods). In addition, it is more difficult for the liquid electrolyte to penetrate into one dimensional titania than into nanoparticles network, because the one-dimensional titanias have usually relatively low surface areas. This leads to a large interfacial charge-transfer resistance that further impedes the interception reaction by the I_3^- ion. However, the lack of intimate contact between the dye and the electrolyte causes slow sensitizer regeneration's rates consequently increasing the recombination process through the oxidized dye. Furthermore, the absence of morphological (i.e. pores) and structural (i.e. exposed Ti⁴⁺ ions) defects in conjunction with the low surface area brings about lower dye loadings for 1-D structures compared to nanoparticles [164], [165]. Charge generation improved quantum efficiency combined with decent electron transport properties has been proved for "hybrid" hierarchical structured 1-D materials comprised of tubes and

particles [169].

Previous discussion suggests that a morphology optimized TiO₂ photoanode should be made out of a material capable of combining: a) the high specific surface area of nanometric particles, b) the light scattering properties of submicrometric particles, c) the electron transport directionality provided by monodimensional structures. For the three properties to co-exist it is necessary to further increase the dimensionality of TiO₂ nanostructures and introduce mesoporosity to achieve *3-D ordered mesoporous titania*. The fundamental component to synthesize powders characterized by an ordered porosity with pore sizes between 2 and 50 nm (that is the IUPAC definition of mesopore) is the templating agent that acts as a scaffold to spatially direct the TiO₂ growth during the synthesis. Template-free methods can also produce mesoporous TiO₂ (see figure 4.1 but generally with disordered mesostructures, which derive from the irregular packing of building blocks. The templated material is a (see figure 4.1) a 1:1 (but inverted) copy of the structure directing agent and no change in order or length scale of the template structure occurs. Templating can therefore be an effective approach to form mesoporous materials, as size and shape of the resulting pores can be tuned by choosing the appropriate template structure. Templating agents can be either soft or hard. The former are typically soft materials such as micelles, gels, nature-derived scaffolds (i.e chitin), affording the formation of globular or spherical systems that serves as template for the final 3-D, typically spherical, templated material. On the contrary, in the case of hard structure directing agents, hard inorganic materials (pre-formed) such as alumina or silica are employed as negative replica of the targeted material. In both cases, the removal of the templating agent allows for the formation of a material displaying a morphology which is the replica of the templating scaffold. Hard structure directing agents have to be removed by treating the obtained material either with HF or concentrated NaOH. Thus, TiO₂ has to grow *within* the template to easy remove the structure directing agent. On the other hand, the critical issue for preparing mesoporous TiO₂ under the guidance of surfactant templates is controlling the hydrolysis and condensation rates of titanium dioxide precursors to effectively match the cooperative assembly with the templates. In addition, the recovery of mesoporous TiO₂ without framework collapse should be paid much attention to during the soft template removal and crystallization. While hard templates simply act as a "cast" for the TiO₂ growth, soft templating exploits the cooperative assembly between titanium dioxide intermediates and surfactants. The sol-gel process of titanium precursors is characterized by their

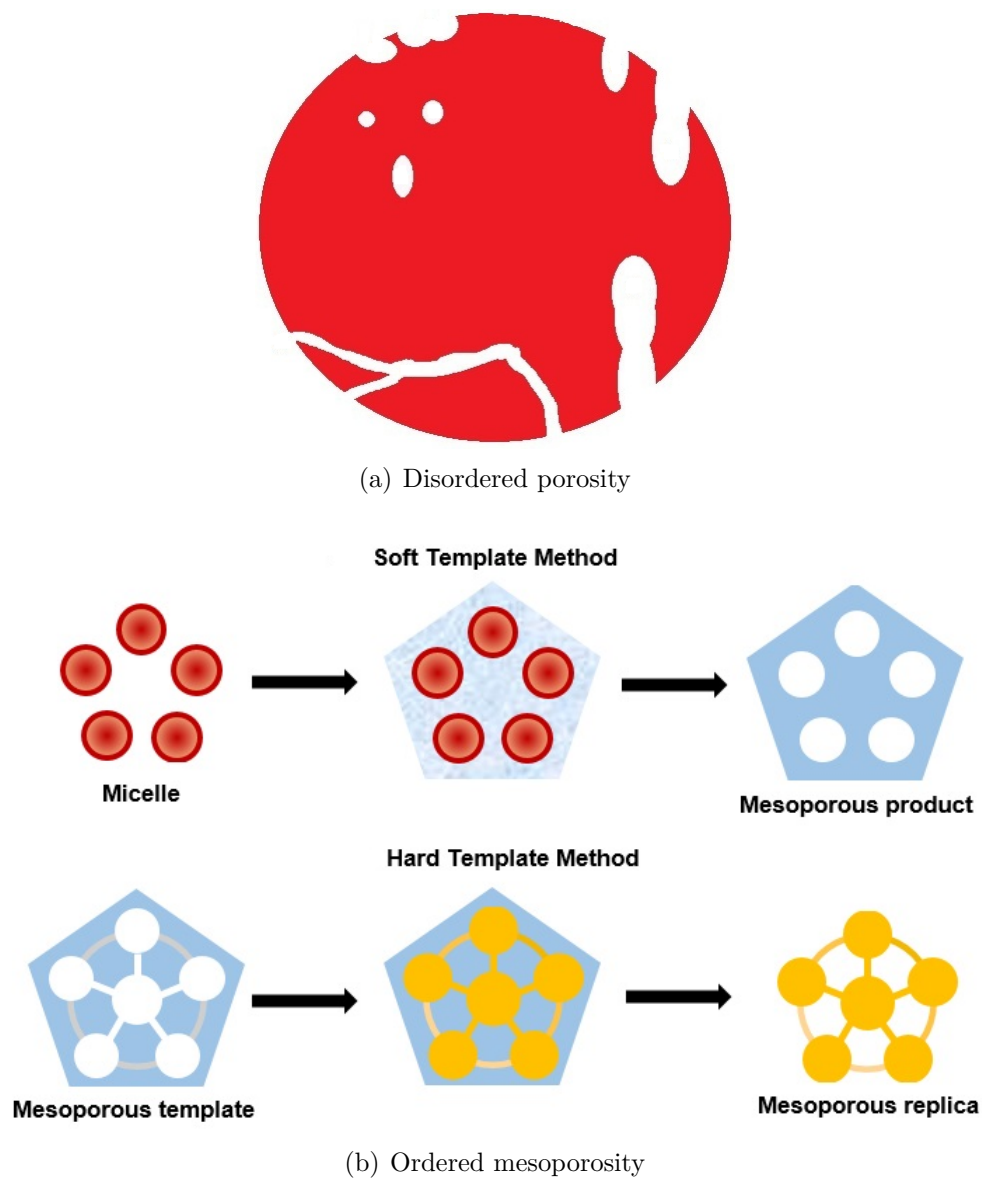


Figure 4.1: Pictorial representation of disordered (a) and ordered porosity (b). The latter can be achieved only by using either soft or hard templating agents. The figure shows a particular case of soft templating agent: micelles formed by surfactants. Adapted with permission from [170].

high chemical reactivity resulting from the low electronegativity of titanium and its ability to exhibit several coordination states so that coordination expansion occurs spontaneously upon reaction with water or even moisture. Thus, titanium dioxide precursors tend to fast hydrolyze and form dense precipitates, which overwhelm the cooperative assembly with surfactants, leading to undesired phase separation. For example, the hydrolysis rate of titanium alkoxides is about five orders of magnitude faster than that of silicate ones [171].

The chemical composition of the surfactant used as templating agent is also one of the crucial parameters. For example, in aqueous solutions, surfactants containing phosphate head groups are very effective in co-assembly with small sized oligomers owing to their strong interactions with titanium¹. Small dimensions oligomers can be obtained by performing titanium's precursors hydrolysis in presence of a ligand (i.e acetylacetonate) that regulate the rate of condensation of titanium containing precursors (i.e. titanium isopropoxide, TIPO) [172]. However, the phosphorus from the template cannot be fully removed by either calcination or solvent extraction. Therefore, these materials are better designated as titanium oxo-phosphates rather than titania and their energy bands' position do not match with the dye and the electrolyte. Furthermore, because of the high reactivity of titanium precursors, it is difficult to control their hydrolysis and condensation rates and enable the cooperative assembly with templates in an aqueous solution. Thus, the resultant mesoporous TiO₂ generally exhibit wormhole-like mesostructures rather than ordered regularity over large domains. High quality TiO₂ films with a long range ordering can be successfully synthesized via sol-gel process in *non-aqueous solvents* coupled with the EISA (evaporation induced self assembly) method [173], [174], [175]. In this case, an acid regulated sol-gel chemistry of titanium containing precursors in a non-aqueous solution (i.e. in ethanol) first proceeds, which leads to the formation of titanium hydroxides or oligomers. Subsequent deposition of the sol solution on a substrate (commonly a Petri dish) induces the evaporation of the solvent. Then, with the increase of concentrations of both titanium species and templating agents (usually block co-polymers), the cooperative assembly is enabled. Furthermore, when TiCl₄ is used either as a precursor or as PH adjuster (and TIPO as precursor for example) the HCl generated from its hydrolysis inside the mesoporous structure is simultaneously removed under evaporation. This prevents the HCl from disrupting the cross-linkage of TiO₂ frameworks and allows to form

¹Actually, the affinity of oxides, in particular TiO₂ for phosphate groups has been exploited for colorimetric sensors in the present thesis

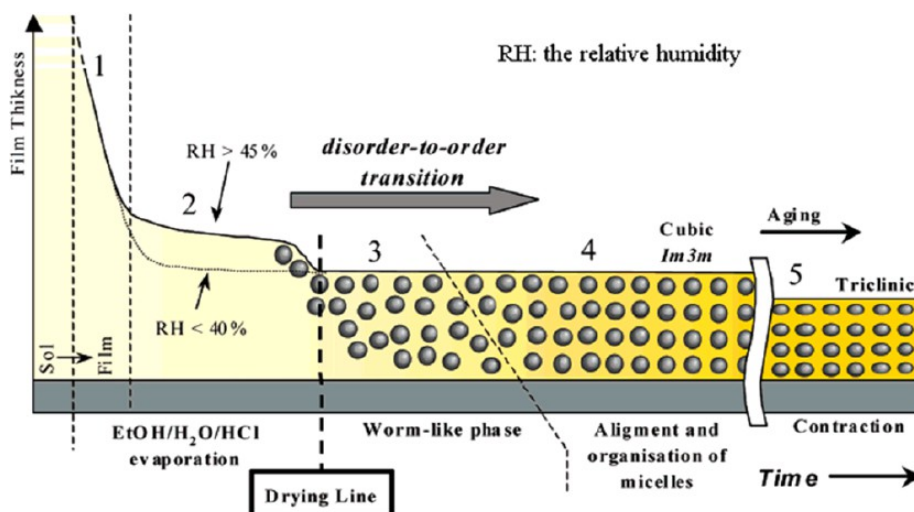


Figure 4.2: Schematic representing the various stages for the synthesis of ordered mesoporous TiO_2 via an EISA process. Adapted with permission from [176].

highly ordered mesostructures [177], [176]. Needless to say, the long range ordering of mesoporous TiO_2 structures synthesized by the templating approach favors the electron diffusion and increases the charge collection efficiency compared to a disordered network of nanoparticles. In addition, vast specific surface area and consequently adsorption of large concentration of dyes and penetration of I_3^- into the photoanode are then ensured by the, possibly monodispersed, mesoporosity. Being the size of N-719 and I_3^-/I^- redox couple 1.8 and 4 nm respectively, it is possible to accommodate many dye molecules into the mesopores and avoid mass transfer limitations due to the electrolyte diffusion [178]. This is the reason why mesoporosity is preferred over microporosity (pore size below 2 nm) for DSSCs' applications.

Light scattering properties in ordered mesoporous materials can stem from two sources: light trapping effect caused by the pores of the mesoporous nanoparticles and size dependent Mie Scattering [179]. The former is characteristic of all mesoporous materials and is widely exploited in silica antireflective coatings for photovoltaic glasses [180]. The latter occurs only if the mesoporous nanoparticles are arranged into a submicrometric (i.e. 800 nm) or micrometric structure [181]. In other words, a hierarchical structure of mesoporous particles is needed to benefit from the Mie scattering. Hence, improved dye loading and light scattering can be achieved by synthesizing nanosized crystallites assembled into mesoporous nanoparticles in turn assembled into a micrometric structure. Alternatively, nanometric crystallites can be packed into non-mesoporous particles allowing for multiple contacts between neighboring crystallites with the next level of structural organization

made out of those particles arranged into a mesoporous micrometric structure.

Our morphology optimization procedure consists of identifying the best photo-voltaic performing photoanode TiO_2 synthesized by using four different templating agents:

Hard templating agent: monodisperse silica nanosphere differing by diameter (20 and 50 nm) [182].

Soft Polymeric (block co-polymers) templating agents: Brij58 and Pluronic 123. The former is employed in a "classical" sol-gel synthesis in which the crystallization and organization of TiO_2 nanoparticles into three-dimensional assembled mesostructures occur together [183]. The latter is exploited for a combined sol-gel/EISA synthesis [184], [185].

Soft non-polymeric templating agent: hexadecylamine. This approach leads to the formation of monodispersed mesoporous titania beads with tunable crystallite and pore size [186], [181] by combining sol-gel synthesis and solvothermal treatments.

For all the samples the photovoltaic parameters have been correlated to morphological and structural properties through FE-SEM analysis, XRD, UV-vis diffuse reflectance spectroscopy (DRS) and surface area/porosity analysis (BET/BJH). The most suitable material for DSSCs application (TiO_2 mesoporous beads) has been used for further studies predicated on the electronic and charge transport properties optimization.

4.3 Doping: electronic properties control

An approach to moderate electron trapping and control electronic properties is doping the TiO_2 with heteroatoms. Doping is routinely exploited to control electronic properties (mainly conductivity) in silicon solar cells where the principal effect is an increase of free charges by the donation of electrons from dopants with a valency higher than that of the native material (n-type doping), or holes for dopants with a lower valency (p-type doping). In the case of TiO_2 the mechanism is much more complicated. In fact, doping acts on both trap states and TiO_2 band edges position and DSSCs efficiency improvements can be achieved even by doping with of equal valency as the host TiO_2 ions [187]. A further complication stems from the fact that, as mentioned before, is hard to determine the traps distribution within

the TiO_2 energy gap. Therefore, when a specific kind of dopant is introduced in the TiO_2 structure at a certain concentration is not trivial to understand if deep or a shallow trap [188], [7] are produced. In addition, there are effects going beyond the electronic properties modification to be taken into account when doped titanium dioxide is used for DSSCs. Usually, five different effects have to be considered:

1. Energy position trapping states generated by the dopant (deep or shallow).
2. Valency of the doping ions with respect to the ion to be replaced in the host structure (Ti^{4+} or O^{2-}). In both cases a p-type or n-type can be performed.
3. Crystal ionic radius and concentration of the the dopant with respect to the size of the ion to be substituted.
4. The effect of the dopant on the TiO_2 structures growth rate. In fact, different dopants can produce different crystallite size [189] (usually it is reduced). Because the dopant is inserted into the TiO_2 during the synthesis the nature of the dopant precursor also influences the crystallites size [190]. Charge transport is affected by electron scattering from the grain boundaries and the dye loading on the TiO_2 film by the different surface area stemming from the different crystallites size. Besides, since the dye linking on the TiO_2 surface occurs by forming an ester bond between the carboxylate group of the sensitizer and the titanium, the replacement of Ti with another cation also affects dye adsorption due to different binding strengths between the dye and the dopant [191], or because the dopant induces oxygen vacancies [192].
5. Dopants can favor or inhibit the anatase-rutile phase transition [193].

The final beneficial or detrimental outcome on the DSSCs efficiency is the combination of the five effects.

Doping of titanium dioxide can be achieved by either replacing the Ti^{4+} cation or the O^{2-} anion. Since the lower edge of the TiO_2 CB is made up of Ti^{4+} 3d orbitals (see previous section), replacing Ti by a different cation is thus expected to heavily affect the CB structure. The upper edge of the VB consists of O^{2-} 2p bands and replacing O^{2-} by a different anion affects the VB energy. Anionic dopants are non-metals such as sulfur, nitrogen and carbon. Cationic dopants are typically metal ions (alkaline and alkaline earth metals, transition metals, p-block metals such as aluminum, indium, gallium, tin, etc.) or metalloids (boron, silicon, germanium, antimony). Because our goal is to investigate the effect of lanthanide

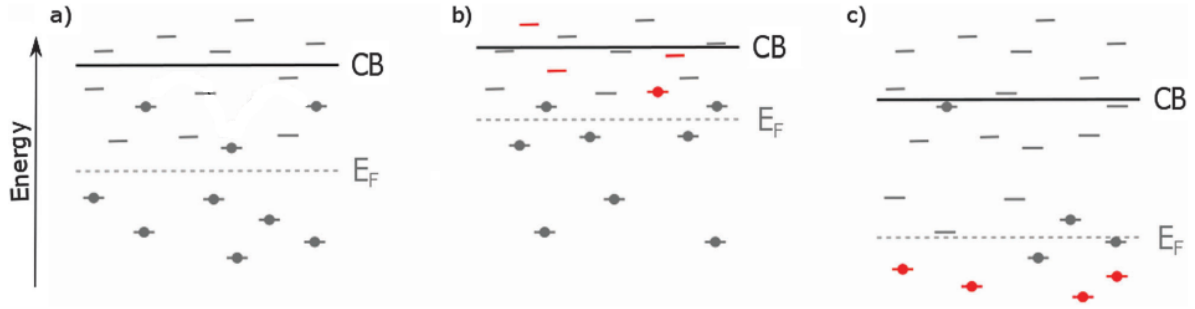


Figure 4.3: Effect of dopants on TiO_2 CB and E_F . The doping induced states are shown in red. Adapted with permission from [7]

dopants on the photovoltaics characteristics of TiO_2 photoanodes the following discussion will be limited to the effect of transition metals (the d-block metals and the f-block lanthanides).

A general view of the effect of transition metals doping on TiO_2 energy levels is the illustrated in figure 4.3. As mentioned before, a dopant can induce shallow or deep trap levels, both of them, or none of them [188], [194], [195]. Pristine (undoped) TiO_2 (see figure 4.3 (a)) possesses a band gap of approximately 3.2 eV and a bulk resistivity of $10^{15} \Omega \text{ cm}$. Ti^{3+} interstitials are located roughly 0.5 eV below the TiO_2 CB edge and act as n-type defects by being oxidized to Ti^{4+} ions and excting electrons to the CB. Otherwise, charge transport can occur through e^- from one Ti^{3+} ion to the other with a mechanism that resembles the Grotthus transport for protons in electrolyte solutions. However, when a TiO_2 electrode is part of a DSSC charge injection from the ruthenium dye to the CB occurs and the Ti^{3+} contribution to the free carriers concentration and transport becomes negligible. Besides, now trivalent titanium ions can act as trapping sites increasing the electron transport time through the photoanode and the probability of recombination with the oxidized dye or the I_3^- ion. On the other hand, $V_{O\cdot}$ states associated with Ti^{3+} ions can act as deep traps (see section 3.3) and surface sites for the electron interception reaction by the triiodide. In both cases the effect is a less efficient charge collection that causes J_{SC} and V_{OC} to drop. One method to control the oxygen defectivity and passivate surface traps in pristine TiO_2 is by thermal treatment and material exposure to oxygen or inert atmospheres, [196], [197], [198].

When dopants induce shallow states that are sufficiently close to the CB (4.3 (b)) trapping and subsequent electron re-excitation into the CB is fast enough to avoid a substantial increase of τ_{tr} . Furthermore, shallow traps *can* decrease the deep trap density resulting in a upward (higher energy) E_F shift that increases the V_{OC} . The elimination of deep traps retards recombination and boosts the V_{OC} even further.

Thus, the overall effect is a V_{OC} increase (stemming from the Fermi level shift to higher energies and from the recombination depression/suppression) and a longer electron diffusion length (i. e. better charge collection efficiency). Nevertheless, the TiO_2 CB is shifted towards the dye LUMO and J_{SC} is expected to be lowered.

When doping contributes to the formation of deep traps (see figure 4.3 (c)), the conduction band edge and E_F are shifted downwards. In combination with the increased recombination through the deep trap states V_{OC} decreases. Because of the larger offset between the CB and the sensitizer LUMO, electron injection is then improved and the J_{SC} increases. Ideally, DSSCs efficiency improvement can be achieved by introducing dopants that eliminate deep traps and introduce new states close to the TiO_2 CB to ensure a *fast* trapping-detrapping transport mechanism. In addition to the energy position of the traps inside the TiO_2 forbidden gap, also the effect of the dopant valency has to be considered. The change in the concentration of trivalent titanium ions and oxygen vacancies (and the consequent CB and E_F shift) induced by the introduced impurities depends on the nature of the dopant: p-type or n-type. Being the titanium ions into the anatase (or rutile) structure tetravalent any transition metal ion with a valence lower than 4^+ constitute a p-type dopant. A p-type dopant shifts the E_F closer to the VB (i.e. to more positive potentials, lower energies) causing V_{OC} to decrease and the J_{SC} to increase because of the enhanced driving force for the electron injection from the dye. Notwithstanding the E_F downwards shift, the open circuit voltage of the cell can be still improved by the reduced dark current brought about by the p-type doping. Indeed, the lower valency of the ion substituting the Ti^{4+} creates hole into the TiO_2 valence band. To preserve the electroneutrality, V_{OC} concentration is decreased. Being oxygen vacancies the main responsible for electron deep trapping and recombination with the I_3^- ion, the dark current of the cell is partially suppressed and the V_{OC} loss due to the E_F shift is compensated. This approach has been proved to be effective for many low valency transition metal ions such as Fe^{3+} [199], Cr^{3+} [200], Zn^{2+} [201], [202] Ni^{2+} [203] [204], Mn^{2+} [205], Sm^{3+} [206], Y^{3+} [194], and Sc^{3+} [188]. Transition metal ions with a valency greater than 4^+ acts as n-type dopants. Nb^{5+} and W^{6+} are the most studied (and efficient) n-type dopants. Their insertion into the TiO_2 photoanode benefits from both electronic and structural effects. Niobium has been initially employed as pulsed laser deposited compact film sandwiched between the FTO glass and the porous TiO_2 network because of the difficulty to evenly distribute the Nb^{5+} ions into the anatase structure [207]. The result was the formation of an heterojunction (see section 4.4) improving the J_{SC} and slightly

decreasing the V_{OC} because of the E_F downwards shift and the improved catalytic activity of Nb_2O_5 for the interception reaction [208]. Then, the direct inclusion of Nb^{5+} ions into the anatase lattice, allowed by the implementation of niobium containing water soluble precursors [209], boosted the performances of $Nb:TiO_2$ through different effects. First, the crystallite sizes can be enlarged compared to the pure anatase [210]. Consequently, the electron transport showed an improvement due to reduced e^- -grain boundaries scattering. Nevertheless, the dye loading is not affected. No satisfactory explanation regarding this effect exists. However, the reason can be speculated on the basis of Bronstead acid sites on the doped TiO_2 surface. One of the interactions between the dye and the oxide surface take place through the Bronsted acid sites (i.e OH groups bound to the Ti that bind the dye's carboxylate group through a dehydration reaction). Hence, differences in dye loading might stem from the different number of acid Bronsted sites on the surface of the doped and undoped TiO_2 (that is synthetic route dependent also). Niobium doping have been proven to increase the number of Bronsted acid sites on the TiO_2 surface [211]. The main drawback of niobium doping is that Nb^{5+} is prone to introduce traps within the TiO_2 energy gap decreasing the V_{OC} by shifting down E_F . Thus, the amount of dopants has to be "tailor made" accordingly to the TiO_2 level of electronic disorder. In fact in low-defectivity titania, a small amount of niobium dopant produces a beneficial effect on the V_{OC} by passivating the surface oxygen vacancies traps and thereby decreasing the dark current and improving τ_r . This implies that only a few Nb^{5+} sub-band gap states are formed and that the TiO_2 CB shift to lower energies caused by these states on is compensated by a reduction in recombination, while they increase J_{SC} by enhancing electron injection. For lower quality TiO_2 much higher doping concentrations are needed to passivate the oxygen traps, resulting in more sub-band gap states, which lower V_{OC} more than can be compensated through recombination suppression [212], [213], [195]. A similar effect has been observed for tungsten doping [214]. However, W^{6+} shows the opposite behavior of Nb^{5+} in terms of crystallites and particles size. Tungsten doping produces smaller crystallites and smaller particles. Surprisingly, no dye loading improvement manifests [215], [216], [217]. In addition to the acid Bronsted sites the TiO_2 surface possesses also hard Lewis acid sites that are constituted by the exposed Ti^{4+} ions. Being the dye's carboxylate groups a hard Lewis base, the formation of an ester bond is favored. When hexavalent tungsten ions are introduced in TiO_2 the excess positive charge is compensated by the generation of Ti^{3+} ions with the consequence that a hard Lewis acid site is removed from the

TiO₂ surface. This is a possible explanation of why an increase of the specific surface area for W doped TiO₂ does not correspond to a higher dye uptake.

Besides the electronic properties modification, there are different effects related to the ionic radius of the dopant that affect TiO₂ photoanodes photovoltaic behavior. In fact, the dopants' ionic radius should not differ much from the Ti⁴⁺ to form a solid solution and prevent phase separation or excessive lattice distortion that creates crystallographic defects hampering the electron transport. For example the good performances shown by Nb and W doped titania photoelectrodes are partially due to the proximity of their crystal ionic radii to the Ti⁴⁺ one (ionic radii: Ti⁴⁺ = 0.745 Å and Nb⁵⁺ = 0.780 Å W⁶⁺ = 0.740 Å). In this manner crystal structure distortions are avoided. The difference in the crystal ionic radius also limits the amount of dopant that can be introduced, usually from 0.1 to 3 at%. Furthermore, the level of lattice distortion depends on the kind of solid solution formed: substitutional or interstitial. The former occurs when the dopants occupy the original lattice sites of the ion to be replaced (Ti⁴⁺). The latter occurs if the dopant enters one of the holes or interstitial sites between the original ions. It is predicted that substitutional doping causes less distortion of the TiO₂ lattice resulting in higher charge collection efficiency than interstitial doping. This has been verified not only for transition metals [188], but also for p-group cations like B³⁺ [218] and for alkaline earth metals like Mg²⁺[219]. Finally, any impurity introduced into the TiO₂ crystal lattice constitute a scattering center that can delay the electron transport. The intensity of electron-impurity scattering strongly depends on the ionic radius of the dopant[188], [220], [194].

Among all the transition metal ions suitable for TiO₂ doping we have picked out lanthanides (in particular six of them whose isopropoxide precursors are commercially available: Pr³⁺, Nd³⁺, Sm³⁺, Gd³⁺, Er³⁺ and Yb³⁺) for two reasons:

- They possess only one stable oxidation state: 3⁺. Thus, they are all supposed to induce a p-type doping in the TiO₂. The only exceptions are cerium (that can be tetravalent) and europium (that can be bivalent) which are not investigated in the present study.
- Their ionic radius decreases from the lighter (Ce³⁺) to the heavier (Lu³⁺) ion with a trend dictated by the lanthanide's contraction: an increase of the ion nuclear charge not compensated by the electron shielding of the 4f orbitals. Since chemical reactivity of transition metal ions depends on their charge

density, in the case of lanthanides this is determined by the atomic radius that follows a well defined trend through the series of fourteen elements from cerium to lutetium. As mentioned before, chemical reactivity of the dopants affects both the TiO₂ growth during the synthetic stage (i.e. the number of grain boundaries) and the amount of dye adsorbed on the photoelectrode surface.

The main drawback stemming from the use of lanthanides as dopants is that small amounts can be employed because of the ionic radii difference with respect to the Ti⁴⁺ ion [221].

Numerous techniques can be used to investigate the effect of doping on TiO₂ structural and electronic properties. We employed FESEM to detect any morphological change. XRD to determine the crystallite size of lanthanides doped sample together with the elementary cells parameters too see the degree of lattice distortion induced by the trivalent ions. Dye loading measurements together with BJH and BET surface characterization to identify the amount of sensitizers adsorbed on the doped mesoporous TiO₂ beads' surface. DRS to investigate samples band gap changes that are associated to the band edges positions shift and valence band holes formation induced by the dopants. Then, the photovoltaic characterization has been carried out in conjunction with I-V curves in dark. Finally, the recombination/transport properties have been investigated through impedance spectroscopy by using the electron diffusion length as charge collection efficiency significant parameter.

4.4 Heterojunctions: transport properties control

Besides doping another way to control TiO₂ electronic properties and in particular charge injection is to fabricate heterojunctions. The simplest kind of heterojunction that can be exploited for DSSCs photoanodes is a TiO₂/ Noble metal (Pd, Pt, Ag, Au, etc.) or CNTs Schottky junction [153], [222], [223]. Figure 4.4 shows the energy levels of a metal/n-type Schottky junction. Basically, for a Schottky barrier contact to exist the metal work function Φ_m has to be larger than the n-type semiconductor one Φ_s . This is the reason why either CNTs or noble metals are used to create Schottky junctions with TiO₂). The work function is defined as the potential required to remove an e⁻ at the Fermi level to the vacuum

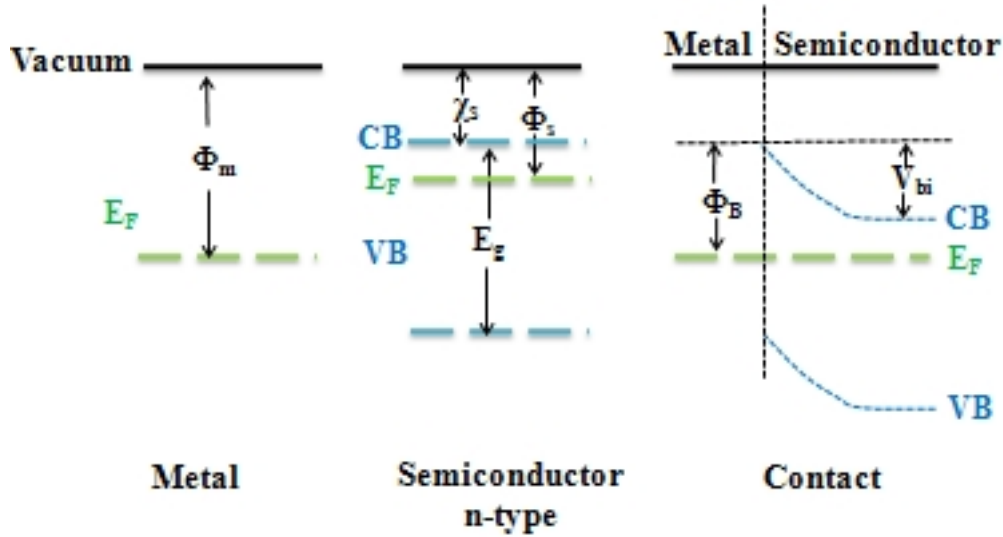


Figure 4.4: Schottky junction formation for an n-type semiconductor/metal contact.

outside the metal or semiconductor. When the metal and the semiconductor are brought in contact charge transfer occurs until the Fermi levels align at the equilibrium. For this to happen, the potential of the semiconductor has to be raised (i.e. electron energy must be lowered). Hence, an electron transfer from the n-type semiconductor to the metal takes place. At the two materials' interface the positive charge due to uncompensated donor ions on the semiconductor side matches the negative charge on the metal. The equilibrium contact potential V_{bi} which prevents net electron diffusion from the semiconductor conduction band into the metal is the difference in work function potentials $\Phi_m - \Phi_s$. The potential barrier height Φ_B for electron injection from the metal into the semiconductor CB is $\Phi_m - \chi_s$, where χ_s is the semiconductor's electron affinity that corresponds to the potential necessary to remove one electron from the CB bottom to the vacuum level.

If a Schottky barrier composed of anatase and metal nanoparticles is employed in a DSSC photoanode V_{OC} , J_{SC} and η_{coll} are affected. In fact, since TiO_2 E_F is shifted down with respect to the vacuum level the open circuit voltage of the cell decreases and J_{SC} increases because of the higher driving force for the electron injection from the dye into the anatase CB. Besides, charge injection from the dye when the cell is illuminated decreases the barrier for the electron transfer from the TiO_2 to the metal. Consequently, e^- diffusion occurs into a medium where electron transport is highly favored. Furthermore, Φ_B keep the electrons from returning into the TiO_2 where they can be trapped and ultimately recombine with the oxidized dye or the electrolyte.

Three different Schottky barrier configurations are usually employed into TiO_2 photoanodes :

1. Composite comprised of metal nanoparticles or CNTs dispersed into the TiO_2 photoanode [224], [225]. For concentrations above the the percolation threshold a continuous conductive path from the top to the bottom of the photoelectrode is generated. Metals nanoparticles are more conductive than CNTs that are comprised of a mixture of metallic and semiconducting structures (see further below). However, the large aspect ratio of CNTs allows for lower percolation thresholds compared to metal nanoparticles. In addition, the 0-dimensional nanoparticles are hard to sinter unless high temperatures are used with the consequence of reducing the TiO_2 specific surface area.
2. Films of CNTs, possibly vertically aligned, pre-deposited on the FTO substrate before being coated with the nanostructured TiO_2 . Again, electrons are transferred into the nanotubes and diffuse toward the FTO contact without encountering grain boundaries. [222], [223].
3. TiO_2 (or ZnO) tubes *coated* with noble metal nanoparticles (i.e. Au, Ag, etc) capable of plasmonic excitation [226], [227], [228].

Case (3) is not straightforward to understand because τ_r improvements rely on V_{bi} rather than Φ_B . Figure 4.5 helps to clarify what happens for configuration (3) by using gold nanoparticles and ZnO nanotubes. The electrons generated from the

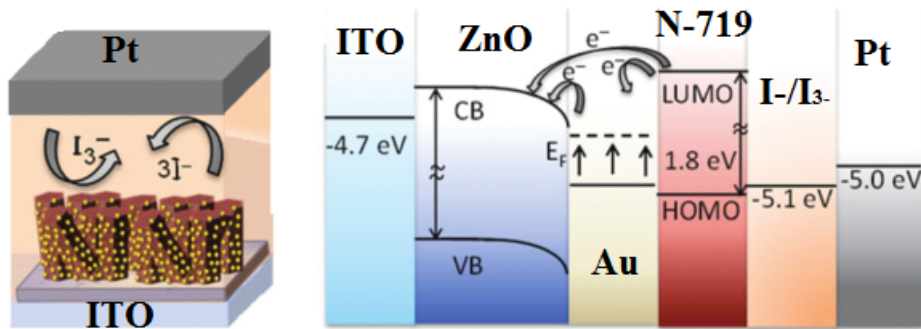


Figure 4.5: Schematics (configuration (3)). Adapted with permission from [226].

photoexcited dye molecules could be transported directly to the ZnO conduction band. Alternatively, the generated electrons could also be transferred indirectly to the deposited Au Nanoparticle first and then onto the ZnO nanotubes surface. The charge transfer from the metal to the semiconductor cannot occur by classical

thermionic emission because as stated before a Schottky barrier for the electron injection into the ZnO nanotubes exists. Thus, electrons can be transferred to the semiconductor by tunneling rather than by surmounting the Schottky barrier. The tunneling mechanism takes advantage of a resonant interaction of photons with the collective motion of free charge carriers in a metallic nanoparticle, referred to as localized surface plasmon resonance (LSPR). A "surroundings induced" LSPR relaxation channel is the mechanism that allows the forbidden electron transfer from the metal nanoparticle to the semiconductor [229]. In fact, if the nanoparticles are *chemically* linked to the semiconductor electrons generated by plasmonic excitation can tunnel through the chemical bond. Electron back transfer to the gold nanoparticles and then to the oxidized species into the dye or the electrolyte is prevented by V_{bi} and fast charge transport ensured by monodimensional structures such as the ZnO nanotubes.

Since our goal is to investigate the effect of chirality separated SWCNTs on injection, recombination and transport properties of DSSCs photoanode further discussion will be limited to the "Schottky" junctions created by CNTs in contact with nanostructured TiO_2 .

Carbon nanotubes (CNTs) are considered remarkable materials owing to their unique structural and mechanical properties such as high electrochemical stability, low resistivity, and high surface-to-volume ratio [230], [231], [232]. In general, carbon nanotubes can be divided into two categories: single-wall carbon nanotubes (SWCNTs) and multi-wall carbon nanotubes (MWCNTs). SWCNTs generally have fewer defects and a higher degree of crystallinity than MWNTs, giving rise to superior performance in most applications. Depending on the folding angle and the diameter, SWCNTs may be metallic, insulating or semiconducting, [233], [234]. MWCNTs are constituted from a random alternation of semiconducting and metallic layer and are conductive on the average. The kind of CNTs (single or multiwalled) and their band gap structure (metallic or semiconducting) determine the most suitable photoelectrode configuration (case **(1)** or **(3)**) to use, the kind of barrier at the TiO_2/CNTs interface, the light absorption properties with respect to the ruthenium based dye, the kinetics of electron-electrolyte recombination reaction, and the rate of electron diffusion through the photoanode. In composite electrodes CNTs have to be: (i) non-agglomerated; (ii) evenly distributed inside the the photoanode and (iii) uniformly coated by TiO_2 particles. Conditions (i) and (ii) are needed to ensure reasonable films conductivities in conjunction with low percolation thresholds (see below). Requirement (iii) is necessary to avoid the presence of

"naked" tubes into the electrode. In fact, CNTs show catalytic activity toward the reduction of the triiodide ion to iodide [235], [236], [237]. Indeed, tubes directly exposed to the electrolyte increase the interception reaction rate. Furthermore, naked CNTs are not able to adsorb dye molecules causing the photoanode dye loading to drop compared to pristine TiO₂ electrode. In addition, exposed tubes can compete with the dye for light harvesting [238]. CNTs homogenous coating can be achieved only by CNT's functionalization with with carboxylic groups [238], [239], [240], [241]. However, the acid treatment necessary to functionalize the CNTs damages their walls and shortens them resulting in decreased electron diffusion coefficients. When SWCNTs are employed in a composite electrode acid functionalization could even destroy some of the tubes rendering the amount of CNTs introduced into the photoanode uncontrollable and then unreproducible. For the beneficial effects (improved electron injection from the dye to the TiO₂, grain boundaries-free electron transport, reduced trapping and recombination because of the effect of the Schottky barrier) to prevail on the detrimental effects (competition with the the dye for light absorption and catalytic effect on the interception reaction) CNTs concentration has to be accurately controlled. Usually less than 0.5 wt % with respect to TiO₂ is employed in composite electrodes [242], [243], [244]. For CNTs thin film thickness between 50 and 100 nm are used [223], [?].

One method to favor beneficial effects over the detrimental ones is to control, during the growth, the CNTs aspect ratio. In fact, the conductance (G) of a percolating network (like pure thin films of CNTs or a TiO₂/CNTs photoelectrode) is given by:

$$G \approx (N - N_c)^\alpha \quad (4.1)$$

where N is the density of CNTs per unit area and N_c is the critical density known as percolation threshold and is given by:

$$N_c = \frac{5.7}{L_T^2} \quad (4.2)$$

where L_T is the tubes length. α is an exponent depending solely on the dimension of the percolating space (1.33 for two dimensions and 1.99 for three dimensions [245]). Hence longer tubes allow for higher conductivities at lower concentration reducing the competition with the dye for light harvesting for both thin film and composite electrodes. However, high aspect ratios are not determining in suppressing the interception reaction and "tuning" the height of the barrier at the CNTs/TiO₂ to maximize the charge injection by the dye and minimize the the back transfer

to the nanostructured titanium dioxide where the probability of trapping and recombination with the dye and the electrolyte are higher than in the CNTs.

An alternative way to control photoanode electronic properties at once by CNTs introduction is the use of *chirality selected SWCNTs*.

The starting point to understand the electrical and electronic properties of CNTs is the graphite structure. Quantization present in nanoscale graphitic fragments results in electronic properties which cannot be duplicated by nanowires composed of normal metals or semiconductors. Graphite has a layered structure composed of parallel planes of sp^2 bonded carbon called graphene layers. These layers are 0.34 nm apart and only interact via weak Van der Waals forces. A single electron is assumed to travel through a perfectly periodic lattice, like the graphite one. Because of the wave nature of electrons the electron wave function is assumed to be in the form of a plane wave moving, for example, in the x direction with propagation constant \mathbf{k} , also called wave vector. The valence and conduction bands of all materials are drawn as continuous but are actually composed of closely spaced, discrete states. These states have a regular separation Δk inversely proportional to L , the macroscopic length of the sample, and for large L (compared to the atomic lattice spacing) the states are effectively continuous. For nanometer-scale materials, Δk can increase to the point where very few \mathbf{k} values are allowed and the bands of states become quite scarce. Under these conditions, electrons no longer freely hop from one state to another, the change in either momentum (wave vector) or energy becomes too great for the available thermal fluctuations, and the material is considered to be strongly quantized. Of course, a sample can be quantized in one of its dimensions and not another. A suitably thin film will retain a continuum of allowed states \mathbf{k}_x and \mathbf{k}_y in the plane of the film, even if only a few, well-separated wave-vectors \mathbf{k}_z remain accessible perpendicular to the plane. On the other hand, 3D graphite possesses allowed states in the direction perpendicular to the graphene sheets and this is the reason why it is categorized as a semi-metal, exhibiting a relatively high conductivity perpendicular to the basal plane and a non-linear current-voltage dependence. In a nanowire, one of the wavevectors remains quasi-continuous while the two wave-vectors perpendicular to the wires longitudinal axis become strongly quantized. To visualize the available electronic states for a nanoscale 2D film or 1D wire, it often suffices to extract a plane or a line, respectively, out of the materials 3D band structure. For a typical metal or semiconductor, this extra quantization rarely results in dramatic electronic effects: bulk metals tend to produce metallic nanowires, and bulk semiconductors produce

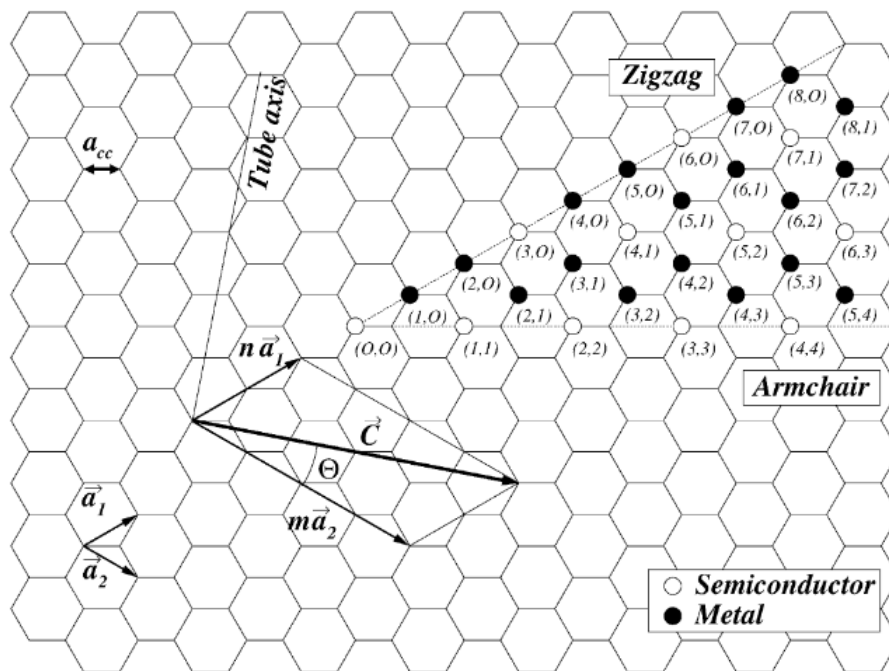


Figure 4.6: graphene sheet showing indexed lattice points (\mathbf{n}, \mathbf{m}) . \vec{a}_1 and \vec{a}_2 are the unit cell vectors of the two-dimensional lattice and Θ the chiral angle. Θ is defined as the angle between the chiral vector and zig-zag axis. Adapted with permission from [246].

semiconducting nanowires, though with possibly modified band gaps. This does not happen for graphitic materials.

Graphene begins as a 2D material, but it may be further quantized by slicing a narrow strip from the sheet. In this case, the allowed electronic states constitute a line of points, or band, sliced from the graphene 2D band structure. A slice in a direction \mathbf{K} , where \mathbf{K} is the edge of the first Brillouin zone is metallic, whereas a slice in a different direction may not. Accurately describing a 1D graphene strip therefore requires two independent parameters: both the width of the strip as well as the angle of the strip with respect to the atomic lattice. Only with both parameters the electronic properties of the strip can be completely specified. Being SWCNTs isoelectronic with graphene similar considerations can be applied to single walled carbon nanotubes if we think of them like a single folded graphene sheet. It is convenient to specify the circumference of a SWNT as a vector composed of the two primitive lattice vectors (see figure 4.6):

$$\vec{C} = n\vec{a}_1 + m\vec{a}_2 \quad (4.3)$$

where \vec{C} is the chiral vector or simply *chirality*. The two parameters specifying

the SWCNT are the chiral vector indices (\mathbf{n}, \mathbf{m}) instead of the magnitude of the circumference and an angular orientation. The use of chiral vector and its "roll-up" indices \mathbf{n}, \mathbf{m} permits to define the concept of chirality and its implications for the specific case of SWCNTs. According to IUPAC nomenclature chirality is defined as "*the geometric property of a rigid object of being non-superposable on its mirror image*". Thus, SWCNTs can be classified on the basis of their chirality into: **armchair**, **zig-zag** and **chiral** tubes. All the SWCNTs with $\mathbf{n} = \mathbf{m}$ (armchair SWCNTs) are non-chiral. Armchair tubes are metallic because one of the allowed subbands of states runs directly from $\mathbf{k} = 0$ to $\mathbf{k} = \mathbf{K}$. Zig-Zag tubes possess $\mathbf{n} =$ integer number and $\mathbf{m} = 0$ and are non-chiral. Chiral tubes are characterized by the following roll-up indices: $\mathbf{n} \neq \mathbf{m} \neq 0$. A geometric construction proves that when the difference between \mathbf{n} and \mathbf{m} of *zig-zag or chiral* tubes is divisible by 3 one of the various allowed sub-bands intersects the \mathbf{K} causing the SWCNT to be metallic. This leads to the result that 1/3 of all possible carbon SWCNTs are metallic and 2/3 are semiconducting. It is believed that the effects of curvature may introduce very small gaps in the metallic SWCNTs with $n \neq m$, but these gaps have energies well below room temperature. The SWCNTs which are not metallic have direct semiconducting E_g the magnitude of which follows a straightforward rule. Because graphene's energy dispersion near E_F is linear in \mathbf{k} , the energy gap between states is directly proportional to the separation $\Delta\mathbf{k}$ between sub-bands. $\Delta\mathbf{k}$ is itself solely determined by the width of the graphene strip (or of an unrolled SWCNT) and the lattice constant a . Thus, all SWCNTs of a given diameter D will have the same semiconducting band gap E_g , regardless of the precise value of n and m and will be $E_g = (0.85 \text{ eV} \cdot \sqrt{\mathbf{n} \cdot \mathbf{m}}) / D$. Typical experimental SWCNT diameters of 0.7, 1.0, 1.4, and 2.0 nm give optical bandgaps of approximately 1.02, 0.85 eV, 0.60 eV, and 0.43 eV, respectively.

Since chiral tubes are comprised of equal amount of the both enantiomers (namely \mathbf{P} and \mathbf{M}) if in addition to the \mathbf{n}, \mathbf{m} chirality separation also an enantiomeric selection is performed circular dichroism and optical activity can be observed. However, since the polarization state of light does not affect the performances of DSSCs, the phenomena stemming from chiral tubes enantiomers separation are not further discussed here. On the other hand, separation of semiconducting from metallic tubes and the selection of specific semiconducting chiralities is of crucial importance for DSSCs opto-electronic properties optimization. Although *in theory* [11] metallic tubes facilitate electron transport through the photoanode, they carry plenty of drawbacks. Since metallic tubes are characterized by continuous absorption

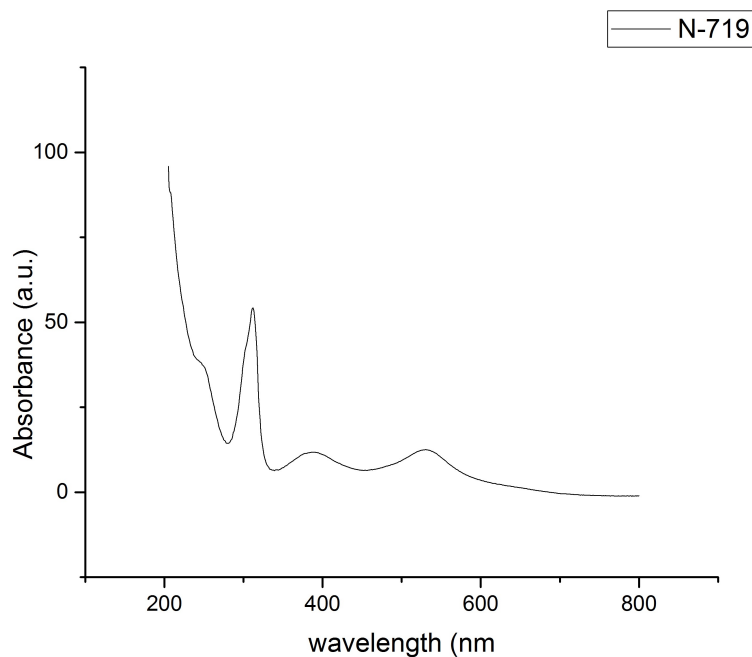


Figure 4.7: Experimental (from our lab) absorption spectrum of N-719 in anhydrous ethanol.

spectra in the Uv-visible region, eliminating or at least minimize their amount in DSSCs photoanodes limits the competition with the dye for light absorption [?]. Furthermore, the greatest level of optimization in terms of light harvesting can be achieved if among semiconducting SWCNTs only those whose absorption bands do not overlap with the N-719 absorption spectrum are used. Hence, selecting chiralities possessing optical transitions away from 540 and 390 nm (the two MLCT transitions) and 313 nm the intraligand (π - π^* internal charge transfer) transition) helps improving charge generation by the dye.

Another effect related to the presence of metallic tubes is the fastest rate of the interception reaction. Indeed, it is reasonable to assume that metallic tubes have more catalytic activity toward the breaking of the triiodide ion than semiconducting tubes [247], [248], [11], [249], [250], [251]. Thereby, reduced amounts of metallic tubes into the photoanode are supposed to slow up the electron-electrolyte recombination. To compensate for the conductivity loss due to the exclusion of metallic tubes pure single chirality semiconducting tubes have to be used. In fact, bundles of same chirality semiconducting tubes are expected to show less intertube resistance than mixed-chirality SWCNTs networks [43], [252], [253]. Furthermore, cutting down the quantity of metallic tubes diminishes the probability of creating metallic-to-semiconducting tube junctions possessing a high energy barrier for the

electron diffusion. Finally, chirality influences the nature and the height of the energy barrier at the TiO₂/SWCNTs interface through nanotubes work function. As stated before when SWCNTs and TiO₂ are brought into contact a Schottky barrier is built, which means that the SWCNTs will act as an electron sink resulting in the TiO₂ behaving similar to a p-type semiconductor as the holes in its valence band travel to the surface [222], [223], [254]. Hence, DSSC's V_{OC} becomes the result of a balance between the detrimental effect caused by the TiO₂ E_F shift and the improved recombination both stemming from the Schottky barrier creation [254], [223], [255]. Most likely the Schottky barrier formation occurs because 1/3 of SWCNTs are metallic. Once metallic tubes are almost completely removed and only semiconducting tubes or chirality specific semiconducting tubes are in contact with the TiO₂ an heterojunction between two semiconductors is formed. When semiconductors of different band gaps, work functions, and electron affinities are brought together to form a junction, we expect discontinuities in the energy bands as the Fermi levels line up at equilibrium. In "conventional" semiconductor physics the energy levels alignment for heterojunctions produced by the contact of two different semiconductors is determined by the Anderson's affinity rule [256]. Anderson's rule is applicable to both anyotype and isotype heterojunctions. The former refers to junctions comprised of two different semiconductors with different doping type; the latter indicates a junction between two different semiconductor possessing the same doping type. Figure 4.8 depicts the application of the Anderson's affinity rule to a p-n heterojunction of two *similar* semiconductors: n-type Al_{0.3}Ga_{0.7}As and p-type GaAs. In this case the heterojunction is called p-N (small p for the small band gap and large N for the large band gap). The band diagrams of Al_{0.3}Ga_{0.7}As and GaAs by themselves (figure 4.8 a) and after the junction formation (figure 4.8 b) are shown. For this material pair, the conduction and valence bands of the smaller bandgap semiconductor lie completely within the band gap of the wider band gap semiconductor. Heterojunction pairs which line up as illustrated in figure 4.8 are known as *type I* heterojunctions. The discontinuities in the conduction band ΔE_c and the valence band ΔE_v accommodate the difference in band gap between the two semiconductors ΔE_g . In an ideal case, ΔE_c would be the difference in electron affinities $q(\chi_2 - \chi_1)$, and ΔE_v would be found from $\Delta E_g - \Delta E_c$. This is the Anderson's affinity rule. In terms of charge transfer a *type I* heterojunction requires that both types of carriers, electrons and holes, possess energy (ΔE_c and ΔE_v respectively) to change from the material with the smaller band gap to the one with the larger gap. Hence, electrons will transfer and accumulate on the smaller band

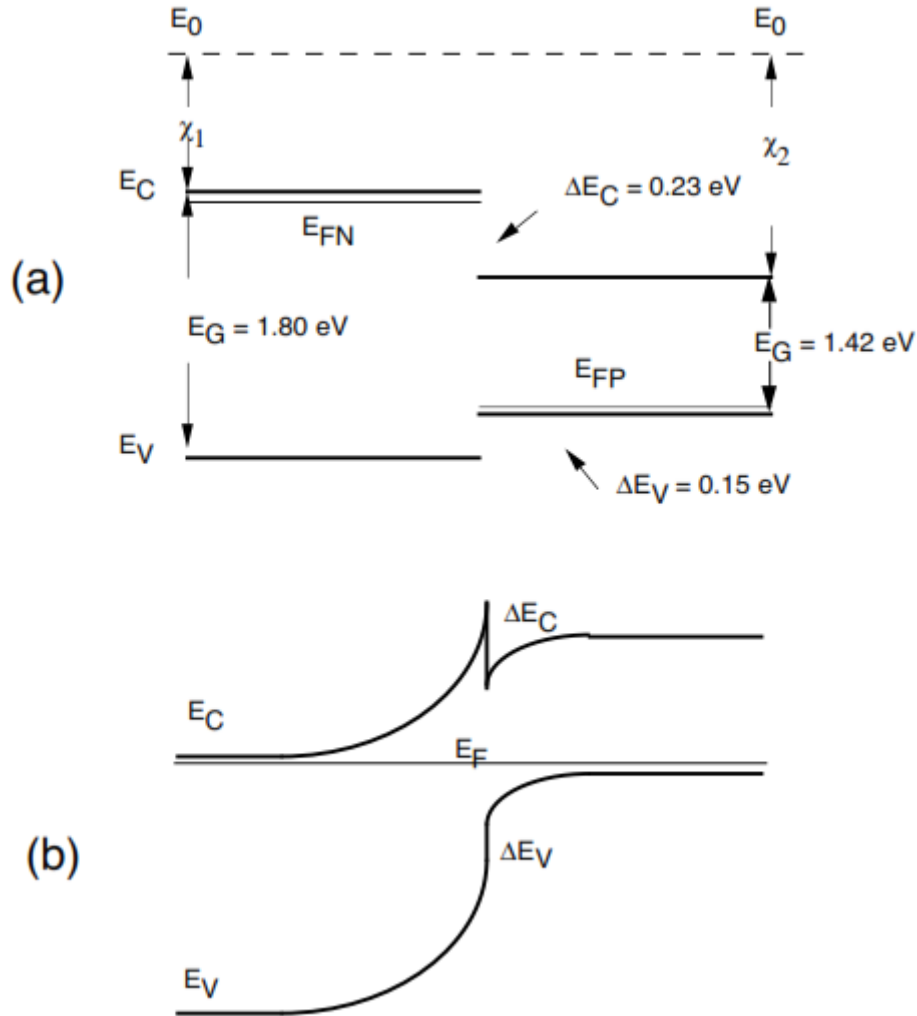


Figure 4.8: $\text{Al}_{0.3}\text{Ga}_{0.7}\text{As}$ -GaAs/N-p heterojunction. (a) before contact. (b) after contact. *Type I* heterojunction.

gap semiconductor by thermionic emission over the junction barrier if the junction is abrupt, by drift-diffusion mechanism if the junction is graded or by tunneling if the junction is heavy doped [256]. Therefore, once electrons are injected from the wide band gap semiconductor into the smaller gap semiconductor a *barrier of ideal height* ΔE_c prevents them from returning into the large band gap material.

The energy levels discontinuity at the TiO_2 -semiconducting SWCNTs interface should be treated as an heterojunction between a wide band gap n-type semiconductor (the TiO_2) and a narrower band gap p-type semiconductor (the semiconducting SWCNTs). SWCNTs are naturally p-type semiconductors because of their exposure to O_2 species [257]. Thus, the case illustrated in figure ?? should fit the semiconducting SWCNTs- TiO_2 interface that then behaves as a *type I* heterojunction favoring the electron injection from the dye to the TiO_2 and from the TiO_2 to

the carbon nanotubes. In reality, plenty of complications arises from the fact that the work function and electron affinity of chirality specific semiconducting tubes are not known. In fact, the experimental determination of the carbon nanotubes conduction band edge (i.e. electron affinity) and Fermi level (i.e work function) with respect to the vacuum level (vacuum or absolute scale) is hard to perform. Also the band edges position of the nanostructured TiO_2 are difficult to locate. For example, by considering the valence band edge located at -5.1 eV, the conduction band edge at -3.9 eV on the vacuum scale [258] for the **(6,5)** chirality and a conduction band edge at -4.21 eV with a 3.2 eV [188] band gap for the anatase we obtain a staggered or *type II* heterojunction see figure 4.9. In a staggered junction either the conduction band edge of the smaller gapped material might lie above that of the larger gapped material or its valence band might lie below the wider band gap semiconductor valence band. The case reported in figure 4.9 for the **(6,5)**/ TiO_2 interface corresponds to *type II* heterojunction where the p-type small gap semiconductor conduction band lies above the wide gap semiconductor one. Thus, according to data reported in literature electrons should remain into the

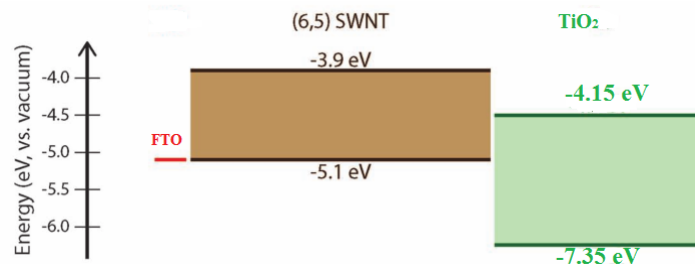


Figure 4.9: *Type II* (staggered) heterojunction structure for the **(6,5)**/anatase interface inferred from data reported in [258], [188]

TiO_2 without being transferred to the **(6,5)**. However, the work function reported in reference [258] is derived from DFT calculations and does not take into account some experimental parameters. In fact separation of SWCNTs by any technique (see further below) never produces 100% single chirality pure tubes. Thereby, contamination by other semiconducting and metallic chiralities may lead to changes in the work function, especially in tubes smaller than 1 nm where the work function strongly depends on the diameter [259]. Besides, SWCNTs work function depends on the treatment to which SWCNTs have been subjected during their dispersion and junction fabrication. For instance, dispersion with anionic surfactants can cause intercalation of the tensioactive counter-ion into the tubes (especially alkali metals) leading to dramatic modifications of the tubes work function [260]. In addition,

SWCNTs work function depends on the concentration of defects on the tube walls. Finally, for the specific case of DSSCs electrode fabrication the sintering step of TiO_2 has to be performed either in an inert gas or under vacuum to keep the smaller diameter tubes from being completely destroyed by the thermal treatment. Vacuum behaves as a slightly reducing atmosphere that can change the "doping" level of the SWCNTs and consequently modify the work function. As stated before, also experimental determination of single chirality tubes work functions is problematic. First because it requires to have a sufficient amount of single chirality material to perform ultraviolet or X-ray photoelectron spectroscopy. Besides the CoMoCAT growth method that produces **(6,5)** [261] chirality enriched tubes other SWCNTs synthesis techniques result in a mixture of different chiralities each of them in very small amounts. Thereby, the determination of semiconducting chiralities' work function other than **(6,5)** is almost precluded. Second, work function measurements by photoelectron spectroscopy or scanning tunnel microscopy require almost epitaxial, uniform and smooth SWCNTs film deposited on noble metals which is an unrealistic situation for the real life application of SWCNTs to devices. Finally, the other main method to measure SWCNTs work function, the thermionic emission current, is very difficult to apply to chirality separated tubes [262].

Besides the SWCNTs work function also the band edges position of TiO_2 determination is challenging. Indeed, most of the methods used to obtain E_{CB} in TiO_2 are based on photoelectrochemical measurement (like in reference [188]) such as Mott-Schottky curves, photocurrent onset, open circuit photovoltage, etc. rely on a semiconductor-electrolyte contacts and on the flat-band potential (V_{FB}) formalism. When a semiconductor is brought into contact with an electrolyte, its E_F is adjusted to the Fermi Level of the electrolyte. This equilibration happens through electron transfer across the interface which results in the formation of a depletion layer (analogous to the Schottky or p-n junction case) since the surface region of the semiconductor is depleted of its majority carriers. In an n-type semiconductor, this interfacial charge transfer process produces an excess of positive charges in the semiconductor (immobile charges of ionized donors) and an excess of negative charges in the electrolyte. As a consequence, the semiconductor bands are bent upwards, which can be understood in terms of a continuously growing barrier for interfacial electron transfer when moving from the bulk of the semiconductor to the interface due to the continuously less efficient screening of the negative charges in the solution by the positive charges in the depletion layer. The height of the barrier is the energy difference between the conduction band edge in the bulk (E_{CB}

and the conduction band edge at the surface E_{CB_s} and corresponds to the potential drop in the depletion layer V_s . The potential at which $V_s = 0$ and the bands in the semiconductor are flat is V_{FB} . Hence, V_{FB} gives a direct information on the position of the conduction band edge. In other words, the determination of the conduction band edge of a thin compact TiO_2 film often translates into the measurement of the flat band potential. However, it should be emphasized that, in the context of nanomaterials, the above described formalism applies only to thin compact highly doped TiO_2 films that behave in a manner similar to compact crystalline semiconductors. In contrast, in small TiO_2 particles and in highly porous nanocrystalline electrodes, the formation of the space charge layer is improbable due to the very small crystallite size (see chapter 2 [263]) and the potential drop occurs mainly in the electrolyte Helmholtz layer. Finally, in a nanostructured semiconductor E_F can be "pinned" to the energy level of its surface defects and the contact with another material (metal, electrolyte or another semiconductor) may not produce the expected band shift.

All these factors make difficult to predict the kind of heterojunction created at the chirality selected tubes-anatase interface and to choose the semiconducting chirality with a suitable energy gap that would facilitate electron injection from mesoscopic TiO_2 and impede the reverse process.

Being the growth of single chirality SWCNTs (besides the (6,5)) hard to achieve, different techniques have been developed over the years to separate by chirality batches of synthesized tubes [264]. They span from density gradient ultracentrifugation (DGU) [265], to electrophoresis [266]. All these methods rely on non-covalent functionalization of SWCNTs with synthetic [267] or bio-polymers (i.e. DNA) [268], or low-molecular weight surfactants [269] for both tubes dispersion and chirality selection. Indeed, different chirality tubes possess different electronic density that results into different Van der Waals interactions with the same polymer for instance. Then, electronic specific SWCNTs batches can be obtained by exploiting particular physical properties stemming from the polymeric or surfactant functionalization. For instance, sedimentation coefficient into a density gradient medium (i.e. Iodixanol) in DGU [270], charge density deriving from deprotonated backbone phosphate groups on the DNA wrapped around the tubes in ion-exchange chromatography [271], [272] or electrophoretic mobility [273], [274] coming from cationic or anionic surfactants functionalization.

Size exclusion gel chromatography (SEGC) is an effective chirality separation technique that can be used to separate metallic from semiconducting tubes, single

chiralities of semiconducting tubes, and enantiomers of single chirality metallic tubes [275]. It takes advantage of two principles involved into the formation of SWCNTs/surfactant micelles: size exclusion and chemical affinity for a bio-polymer based gel. The most used gel for SEGEC is Sephacryl, which is composed of allyl dextran chains cross-linked by N,N'-methylene bis-(acrylamide), with dextran being a biopolymer and chiral compound (it is α -D-glucan, that is a D-glucose polysaccharide with the glycosidic bond in the α form). When SWCNTs are dispersed into an aqueous solution of a surfactant such as SDS or sodium cholate (SC) above the CMC at a temperature higher than the surfactant Kraft point (see chapter 1.2), micelles of surfactant forms around the tubes. The size of the micelles depends on the SWCNTs diameter. Hence, smaller tubes [276], [277], [278] have a smaller coverage of SDS (or SC) molecule than larger tubes and are more prone to penetrate into the gel pores. It means that smaller tubes have more chances of interacting with the gel because they spend more time inside the stationary medium pores while traveling down the chromatographic column. Besides the level of SWCNTs penetration into the gel, a further diameter/chirality dependent discrimination occurs because of the different SWCNTs charge density. In fact, different chiralities means different (\mathbf{n},\mathbf{m}) chiral indices, that means different diameter and chiral angles, that means different radii of curvature. Those chirality peculiar geometric parameters in conjunction with the different distribution of π electrons (i.e. semiconducting or metallic, different band gaps) causes the charge density on the SWCNTs to be different for each chirality with the consequence of diverse interaction strength between the gel and the tubes. One of the proofs that a real interaction between SWCNTs and the gels exists and that the chirality selection is not merely based on the size exclusion principle is provided by the separation of enantiomers within the same chirality that is possible only because of the interaction with the chiral dextran moieties of the gel.

The general SEGC chirality selection procedure reported in ref. [279] is a two-pass process that results in the chirality separation of SWCNTs [278]. The main drawback of such a two-steps chromatographic process is the decrease in CNT concentration after each pass. Obtaining as much as possible of the enriched-chirality CNTs in one pass is mandatory for PV devices fabrication. Thus, we modified the original procedure to achieve chirality pure SWCNTs in a single pass by exploiting the concept of gel "overloading" (see chapter ??). That allows to collect a sufficient amount of chirality separated tubes to be used in DSSCs' photoanodes.

Five different samples have been investigated: a mixed chiralities (30 chiralities)

sample, two samples containing mixtures of two different semiconducting chiralities ((**6,4**)/(**6,5**) and (**6,4**)/(**7,3**)), and two single semiconducting chirality samples ((**7,3**) and (**6,5**)). Samples have been investigated by absorbance Uv-Vis. spectroscopy and visible photoluminescence spectroscopy for chirality purity. SWCNTs thin films have been characterized by sheet resistance and optical transmittance measurements to identify the effect of chirality separation on electron transport and competition with the dye for light harvesting. Photoanodes containing single chirality (or dual chirality or mixed chirality) tubes have been used in a three layered (CNTs/P90/Mesoporous anatase beads) structure. These photoelectrodes have been employed in DSSCs and tested for photovoltaic parameters.

Chapter 5

Colorimetric sensors

This chapter goes into the “state of art” of metal ions colorimetric sensors based on terpyridine derivatives. The intent of the chapter is to provide a general knowledge concerning iron ions colorimetric sense and reaffirm the extensibility of particular materials used for DSSCs (i.e. TiO_2 mesoporous beads to other fundamental and applied research field. In fact, the close similarity between DSSC’s Ru-based dyes and iron-terpyridine coordination complexes [21], [22], [280] make TiO_2 thermodynamical, morphological, and optical properties desirable for Fe colorimetric detection. Similar colorimetric systems relying on mesoporous titania have been already used in literature for Bi(III) detection [12]

5.1 "Terpy-based" complexes

Bi-, Ter-pyridine and poly-N-aromatic compounds in general (i.e. 1, 10 phenanthroline) constitute a class of polydentate *chelating* agents capable of forming coordination complexes with almost all metals of the periodic table. Poly-N-aromatic moieties belong to the group of strong-field ligands in the spectrochemical series. Hence, their metal complexes benefit from high CFSE (crystal field stabilization energy) coming from the large (especially for octahedral coordination compounds) crystal field d-orbitals splitting parameter (Δ). Polypyridine-metal complexes own their stability (high CFSE, large Δ) to two effects:

1. The presence of multiple nitrogen electron lone pairs able to coordinate the central metal ion (chelating effect).
2. π -backbonding, that is the electron donation from the occupied t_{2g} metal

orbitals¹ to the ligands π^* anti-bonding molecular orbitals.

Since π -backbonding is the main contributor to Δ , polypyridine ligands tend to stabilize electron-rich, transition metals low oxidation states.

From the photophysical properties standpoint, the most studied polypyridine complexes are: the d^6 ions (Re^{1+} [281], Fe^{2+} [282] [283], Ru^{2+} [284], [285] Os^{2+} [286] [287], Rh^{3+} , Ir^{3+} [288]) octahedral, d^{10} (Cu^{+1} [289], [290]) octahedral, and the d^8 (Pt^{2+} [291], Pd^{2+} [292], Au^{3+} [293]) square-planar coordination compounds. In fact, long-lived and intense luminescence, high molar extinction coefficient for the MLCT transitions, synthetically tunable absorbance and emission wavelengths, have triggered plenty of research over polypyridine-metal complexes for DSSCs, photocatalysis, OLEDs, phosphorescent gas sensors and bioimaging applications [294], [295], [296].

Among the countless polypyridines ligands, "terpy" (2,2':6',2"-terpyridine) moieties and their derivatives have found a specific application as colorimetric and fluorimetric sensors for anions and metal cations. Fluorimetric detection of cations relies on photons absorption by the metal-terpy complex and radiation re-emission to a longer wavelength with respect to the energy of the absorbed photon (i.e. the principle is similar to the collection of PL maps for single chirality SWCNTs). The fluorescence emission stems from the radiative relaxation of the metal-terpy complex excited state. The shift between the absorption and the emission frequency is called Stokes shift. Modified terpy-metal coordination compounds have been extensively used for fluorimetric detection of Fe^{3+} [16], Fe^{2+} [17], [18] Zn^{2+} [297], Cd^{2+} , Hg^{2+} [298]. Although terpy-metal dyes luminescence based sensors are selective and sensitive and allow to detect and quantify even spectroscopically (or magnetically, see ??) silent ions (i.e. d^{10} metal cations like Zn^{2+}), they require expensive and dedicated equipment (the spectrofluorimeter).

A terpy-metal coordination compound has to fulfill the following requirements to be employed as a colorimetric sensor.

- The terpy-metal ion complex must possess an *intense* optical transition visible to the naked eye.
- The metal complex has to be incorporated into a polymer or an inorganic matrix that permits the fabrication of a solid state device. Moreover, the terpy

¹Since polypyridine moieties are strong-field ligands, tetrahedral complexes where the electron-filled (low-energy) states is comprised of the e_g orbitals do not form. Indeed, tetrahedral coordination compounds usually exist for weak-field ligands (i.e. halogens), where the CFSE loss ($\delta_t \approx 4/9 \delta_o$) is not crucial.

moiety that acts as linker (probe) for the metal cation has to be water-soluble to avoid absorption peak shifts caused by the nature of the organic solvent.

- The color change should be selective, reversible, and sensitive to different concentrations of a specific metal ion.

Intuitively, deep colored sensing responses can be achieved by exploiting electronic transitions not restricted by spin and Laporte selection rules. Hence, charge transfer transitions are the most indicated for metal ions colorimetric detection. Thus, visible metal-to-ligand charge transfers characteristic of group 8 d^6 cations (in their low oxidation state (II)) are suitable for colorimetric detection. In fact, terpyridine (or ferriin-like indicators) chelating agents have been used as colorimetric reagents for homogeneous (i.e. not involving adsorption on solid surfaces) sensing of Fe^{2+} in solution since the 40s [15]. Since Fe(II)-terpyridine moieties complexes absorb in the green range of the visible spectrum, their formation is detected by a color change from colorless or pale colored (ligand only) to reddish-purple solutions. One inconvenience related to total iron determination by using terpyridine complexes is that if Fe^{3+} is present in the solution it has to be converted into iron(II) by using reducing agents (i.e. hydroxylamine, stannous chloride, formaldehyde, sodium hypophosphite, etc.). Nevertheless, simultaneous *spectrophotometric* detection of Fe(II) and Fe(III) can be accomplished by exploiting the LARVA (light absorption variation approach) technique [299]. Such a methodology is predicated on the analysis of ligand-to-metal charge transfer transition (LMCT) rather than MLCTs. In general, intensity of LMCT bands depends on the central metal ion ability to polarize the ligands and induce electron transfer from π (or σ) orbitals of the ligand to the partially filled d orbital of the metal (conversely an MLCT transfers electron from the metal d orbitals to the empty anti-bonding orbitals of the ligand). Thereby, Fe^{3+} ions coordinated to terpy moieties favor the electron transfer from the ligands compared to Fe^{2+} . The reason is the higher charge density of the trivalent ion and the larger accessibility of empty d orbitals (Fe^{3+} allows for charge transfer to both the e_g and the t_{2g} orbitals). For instance, Liang et. al [299] have used the absorbance ratio between two LMCT transitions in the UV range (318 and 366 nm) to spectrophotometrically titrate the amount of Fe(III) and Fe(II) in aqueous solutions. In fact, the intensity ratio of the two LMCT bands doesn't change by adding Fe^{2+} while varies as Fe^{3+} concentration is increased. The "standard" MLCT at 560 nm is then used to colorimetrically discriminate between the two iron ions and the other cations. Unfortunately for an LMCT transition to lie in the visible,

the ligand has to be extremely polarizable (i.e. large radius alogens like I^- and Br^-) [300]. Otherwise, like in the case of terpy-iron complexes, the charge transfer bands from the ligands to the metal lie in the UV region that is not profitable for colorimetric detection. LMCT transitions are exploited also for Hg^{2+} colorimetric detection based on $Hg(II)$ binding to terpyridine derivatives [301]. Furthermore, Hg^{2+} "indirect" colorimetric detection can be performed by a LARVA-like detection system relying on square-planar $Pt(II)$ -terpy complexes such as $[Pt(terpy)(Cl)][Cl]$ or $[Pt(terpy)(Cl)][ClO_4]$ (where (Cl) occupies the fourth binding site of the square-planar complex, while $[Cl]$ is the counter-ion). Typically, these metal complexes possess multiple optical transitions such as MLCT and ligand-to-ligand (ICT, internal charge transfer) in the visible region [302]. The binding of protons or cations perturbs the charge density in the binding unit and subsequently induces optical signal switching between different energy states to achieve the desired optical responses. Chung et. all [303] tuned the optical properties of $Pt(II)$ -terpy complexes by modifying the $[Pt(terpy)(Cl)][Cl]$ coordination compound with the insertion of a dithiaazacrown-functionalized stilbene unit on the para position of the central pyridine ring. Such a complex possesses two charge transfer absorption bands in the visible: an ICT at about 500 nm given by $\pi \rightarrow \pi^*$ transition within the molecular orbitals with ligands character and a MLCT at about 420 nm stemming from the $d \rightarrow \pi^*$ transition. The ICT to MLCT intensity ratio decreases (causing the color of the solution containing the Pt -terpy complex to switch from pale pink to pale yellow) by addition of $Hg(II)$ perchlorate. Intuitively, the encapsulation of Hg^{2+} into the to the dithiaazacrown moiety suppresses the ICT process but enhances the MLCT transition. Finally, also d-d transitions for tetragonally distorted Cu^{2+} (d^9 external shell electronic configuration) have been used for colorimetric detection through terpy derivatives ligands [304], [19]. In fact, Jahn-Teller distorsion due to unevenly occupied e_g orbitals and most importantly ligands' vibrations reduce the complex symmetry causing the Laporte selection rule to relax and the d-d transitions to be relatively intense (in the red region).

Most of the research concerning terpy-metal complexes has been performed in DMF, DMSO, methanol, acetonitrile, because of terpyridine poor solubility in water. Thus, for instance, Fe^{2+} visual detection systems rely on color change reactions occurring upon the formation of the $Fe(II)$ -terpyridine complex in solutions made out of *organic solvents or their mixtures with water* [16], [305], [306], [307]. A main issue stems from this approach: limited applicability to waterborne systems (i.e. bio-fluids, irrigation, waste water, etc.). Besides, solvatochromic effects have to be

taken into account [308]. Therefore, a widespread technique to use terpy based molecules for colorimetric detection of Fe^{2+} (or Cu^{2+} and Co^{2+} [19]) [17] in aqueous environment, is to substitute one of the terpyridyl ring positions with with polar functional groups to improve terpy solubility in water and possibly create anchoring sites for adsorption on solid surfaces. For instance, Sis et. all [17] prepared aqueous dispersions of graphene oxide flakes functionalized with 2-4-[(2,2':6',2"-terpyridin)-4'-yl] phenoxy ethyl-3-[(2-hydroxyethyl)amino]propanoate and employed them for iron(II) colorimetric detection. In fact, water dispersions of graphene oxide flakes functionalized with the modified terpy motif become purple colored upon addition of 200 ppm of Fe^{2+} (and yellowish if Co^{2+} is added). On the other hand, Trigo-Lopez et. all [19] implemented a full-solid state colorimetric sensor by modifying the terpy structure with with a polymerizable methacrylamide group. Then, the terpy-monomer compound is radically co-polymerized with 1-vinyl-2-pyrrolidone and methyl metacrylate monomers to obtain solid membranes with surface exposed terpy ligands. The membranes have been successfully used for Sn(II), Fe(II), Cu(II) and Fe(III) colorimetric detection.

Our approach aims at terpy-functionalizing inorganic surfaces and use them as solid state colorimetric sensor for the Fe^{2+} ion [12]. The strong affinity of phosphonate groups ($\text{C-PO}(\text{OR})_2$, where R can be an H atom, an alkyl or an aryl group) for metal oxides [309], [310], [310] in general and for TiO_2 [311] [12] in particular, makes titania sub-micrometric beads an ideal supporting material for 2,2':6',2"-terpyridin-4'-ylphosphonic acid (ligand (**L**)) and its hexacoordinated Fe(II) complex ((bis)2,2':6',2"-terpyridin-4'-ylphosphonic acid-Fe(II) or (bis)L-Fe(II) or $\text{Fe}(\text{L})_2$). In fact, material's high specific surface area and mesoporosity allow for chemisorption of large amounts of (**L**) creating a monolayer of coordination sites for the Fe^{2+} ions. Furthermore, the phosphonic group renders the terpy motif water soluble (up to 66mM) permitting the pre-forming of the Fe(II) complex both in aqueous solutions and on the TiO_2 surface. Moreover, the non-hydrolysable nature of the Ti-O-P bond, the high light harvesting provided by submicrometric titania beads (see Chapter 9) and the intense MLCT transition of the $\text{Fe}(\text{II})(\text{L})_2$ complex, makes our methodology ideal for low-detection limit and reusable iron colorimetric sensors. In addition, if screen printing (or any other *thick* film deposition technique) is used for the deposition of the TiO_2 (or any other oxide) scaffold the sensitivity of the colorimetric detection system can be adjusted and improved (see Figure 5.1). Indeed, by controlling the thickness of the printed film (i.e. by changing the screen mesh size, the paste composition, the substrate's surface treatment procedures and

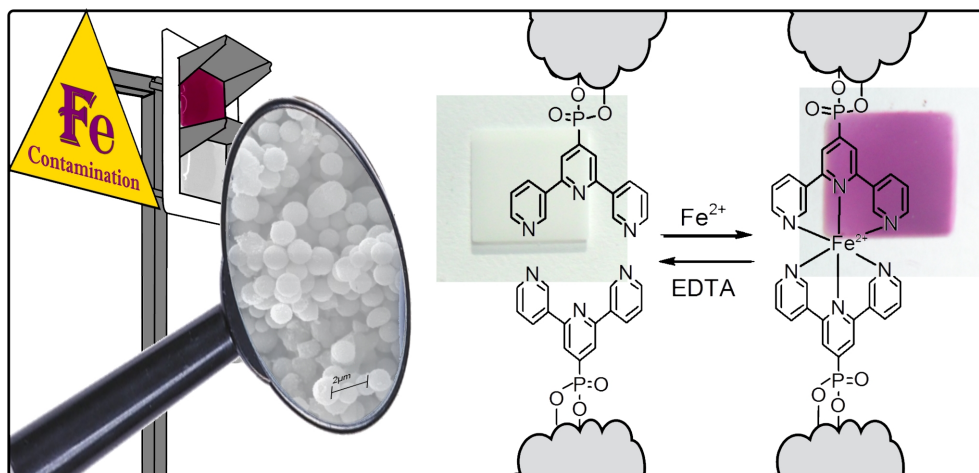


Figure 5.1: Pictorial representation of the iron-(L) complex colorimetric sensor operative principle. The phosphonate groups on the N-aromatic terpyridine structure assure molecule water solubility and a stable chemisorption onto oxides surfaces. Like in the N-719, the group 8 trivalent cation is hexacoordinated with two nitrogen atoms from the terpyridine replacing the two thiocyanate ligands (see also figure 3.1). The sensor can be used to detect iron contamination in different water environments (irrigation, drinking, waste water, etc.). Before come into contact with trivalent iron the 2,2':6',2"-terpyridin-4'-ylphosphonic acid is chemisorbed on the TiO₂ surface and is colorless. When Fe²⁺ is coordinated by the the two terpyridine ligands the TiO₂ screen printed film color changes from white to purple because of the MLCT optical transition (at about 560 nm). Ethylenediaminetetraacetic acid (EDTA) can be used to regenerate the sensor.

the number of printed layers) it is possible to adsorb more or less terpy linker, that is different Fe(II) surface concentrations, that is different color intensities. In essence, thickness control corresponds to a device sensitivity modulation. Finally, the colorimetric detection should be as much selective as possible. Usually, chelating π acceptors ligands tend to form complexes with any metal ion creating interfering effects for the colorimetric detection of the targeted ion(s). Colorimetric sensors response selectivity is predicated on two principles:

1. The larger the thermodynamic stability (or formation) constant of a specific metal-ligand complexes, in a specific geometry, the higher is the driving force leading to its formation.
2. The higher the molar extinction coefficient of an optical transition, the more vivid is the color of the metal-ligand complex.

Hence, when various ions compete for binding (L) (either in solution or adsorbed on the titania surface) *preferential coordination of the metal cation giving the most stable complex occurs*. Generally many parameters affect the thermodynamic

stability of a metal ion-terpy complex. First, high charge density ions possessing empty orbitals of suitable energy are prone to form complexes. Second, complex's stability benefits from an effective atomic number (EAN) matching the electronic configuration of a noble gas. In other words, the metal atom tends to surround itself with sufficient ligands that the resulting effective atomic number is numerically equal to the atomic number of the noble gas element found in the same period in which the metal is situated. When applied only to the valence shell electrons the EAN rule is often named "18 electrons" rules: the stability of a metal complex improves if the number of valence electrons reaches 18. Finally, high values of CFSE stabilize the metal-ligand coordination compound. Needless to say, Fe(II)-(L)₂ satisfies all the three conditions. In fact, Fe²⁺ is a relatively small ion (it belongs to the first series of the transition metals), is a d⁶ (when it is coordinated by the six (bis) terpy nitrogen atoms it completes the 18 electrons valence shell) and the complex benefits from a high CFSE (-2.4 Δ_{terpy}) due to the six electrons paired in the t_{2g} orbitals. Thus, Fe(II)-(L)₂ is supposed to be (and it is) a very stable coordination compound. Unfortunately, it is difficult to theoretically predict if a metal cation interferes with the colorimetric detection of Fe(II) because the d-orbitals splitting parameter depends on the ion charge and on its periodic table position (i.e it increases as the metal charge increases and by descending the group). Nonetheless, large ions such as alkali metals, alkaline earth metals and lanthanides can be usually ruled out as interfering ions because their complexes are immensely less stable than transition metal complexes [312], [313]. Moreover, even though many different transition metal ions can be chelated by the terpy motif, only cations capable of changing the sensor color intensity can be considered actual interfering species. For instance, metal ion-terpy complexes possessing low molar extinction coefficient optical transitions (i.e. d-d) or intense bands in the UV region are unlikely to interfere with the detection of ions owning charge transfer transitions in the visible (like Fe(II)).

Chapter 6

Nanomaterials for microwave sensing devices

Radio frequency identification (RFID) tags have been proposed as a low cost item-level tracking system supplementing or replacing printed bar codes [314], [315], [316]. Usually a standard RFID system is comprised of a reader (or interrogator), and the tag itself that is usually referred as the transponder. RFID tags can be either active or passive. Active tags contain a battery, while passive tags draw their power from the RF signal broadcast by the tag reader. Regardless of the power source, an RFID tag is composed of an "antenna" (see below for the specific meaning of this term) and an integrated circuit chip containing the digital logic necessary for data processing (see figure 1.5). The kind of IC employed to implement the digital data acquisition, storage and transmission depends on the tag's operation frequency. Five carrier frequency bands are currently used for RFID tags:

Low Frequency < 135 kHz band . The near field of an electromagnetic wave occurs at distances less than $\lambda/2\pi$. The far field occurs at larger distances. Therefore, the antenna for an RFID tag operating in this band does not function as a conventional radio antenna, communicating with the reader via a propagating electromagnetic wave. Instead the antenna is a coil that provides magnetic coupling to a coil in the reader, like the coupling between primary and secondary windings of a transformer. Wound wire coils with many turns are typically used to achieve high inductance with low resistance (high Q-factor). These coils are expensive and this type of tag is not considered for low-cost, item-level tags. Nevertheless, low-frequency, low-cost RFID tags can be produced by using OTFT-based (organic thin film transistor) digital logic in conjunction with capacitive rather than inductive coupling. In

fact a capacitive coupling antenna can be printed¹ at low cost and it is easy to integrate with flexible, organic-based electronics. Carbon or conductive polymer inks can be used to fabricate such a device exploiting low-cost printing techniques (i.e. flexography, screen printing, ink-jet printing, etc.) to produce the capacitive antenna, the conductive traces and the OTFTs. However, there are significant disadvantages to capacitive coupling. Nearby conductive objects disrupt the electric field. Furthermore, RFID tags typically use an inductor and a capacitor in parallel at the input to form an LC tank circuit with resonance at or near the carrier frequency, in order to boost the voltage generated by the carrier to a level that can drive the tag electronics. But since the goal of the capacitive coupling approach is to eliminate the expensive coil, an on-tag resonant circuit is not practical, and the tag's read range is limited by low induced voltages.

High frequency: 13.56 MHz band . Tags operating in this band also operate in the near field of the reader, since the near field is found at distances closer than $\lambda/2\pi$ or 3.5 m. The higher operating frequency permits a planar inductor rather than a wound wire coil to be used for magnetic coupling to the reader, significantly reducing the cost. The planar inductor is typically fabricated by copper or aluminum etching, copper plating, or silver ink printing and possesses a reduced number of coils. Although attractive because of their low costs and applicability to flexible substrates 13.56 MHz RFID tags challenge the reliability of electronics components fabricated using the OTFT technology

¹Usually in electronic engineering the term "printed" is prone to misleading. Often, the definitions of "printed electronics" refers to devices assembled by using Printed Circuit Boards (PCB)s manufacturing techniques. However, PCB technology relies on conductive copper traces obtained by *etching* (i.e with FeCl_3 , CuCl_2 , or an alkaline ammonia solution) copper sheets laminated onto an insulating substrate. Hence, the process is intrinsically subtractive. The copper traces interconnect different devices (capacitors, inductors, resistors, silicon integrated circuits, etc.) that are surface mounted on the board. The metal pattern to be etched is defined by using *photolithography*. Hence, printing is not instrumental to PCB fabrication. Nevertheless, in the early days of modern electronics (at the end of the 50s) the copper traces would be etched by using a negative screen printed pattern made out of an etchant-resistant ink. This is the origin of the adjective printed in the acronym PCB. Since screen printing is still used today (together with ink-jet, spray and curtain coating) to deposit the *photo-imageable* etch-resist and the photo-imageable solder mask, the expression printed circuit boards remains in the electronic engineering parlance to indicate the interconnection of electronic components by exploiting copper etched tracks on the insulating board. However, nowadays printed electronics means also the technology involving dielectrics, conductive and semiconductive *inks* to create electronics components on different substrates (usually flexible) *without* employing neither photolithography nor etching. Thus, the process is completely additive. To avoid confusion we will use the word printed referring *only* to the deposition of electronic components (i.e. conductive traces or transistors) by using an ink and a suitable printing technique (ink-jet, flexo, screen, etc).

because of the relatively high operation frequency.

Ultra high frequency (UHF): 860-960 MHz . Within this range only certain frequencies are assigned for RFID applications. The operative RFID tags frequencies in the UHF range vary from one country to another (i.e. 865-868 MHz in Europe, 917-922 MHz in China, 902-928 in North America). Microwaves RFID tags operating in the 2.45-5.8 GHz and 3.10-10.00 GHz bands are usually grouped together with UHF tags. In fact, transponders operating in the UHF and microwaves bands share common features differentiating them from low and high frequency tags:

- The tag's antenna is coupled to the reader neither inductively nor capacitively but *radiatively* (back-scattered, see figure 6.1). *The back-scattered coupling is instrumental to the RFID tag operation in the far field of the reader.* Typically an etched or printed (by ink-jet or screen printing) dipole or microstrip antenna [317] is used to receive the signal transmitted by the reader and to reflect back a modulated wave.
- A silicon ASIC (Application Specific Integrated Circuit) is required for data storage and processing.
- The reading performance of UHF and microwave tags is severely dependent on the working environment. At these frequencies electromagnetic signals are incapable of penetrating materials such metals and liquids.

In some applications, RFID tags need to be mounted on the surface of metallic objects such as steel plates or steel containers. However, when an etched or printed dipole-like antenna is placed on a metallic surface it suffers severe performances degradations due to shift in operating frequencies, distorted radiation pattern and impedance mismatch that quickly reduce its reading range or even cannot be read [319], [320], [321]. In order to mitigate this problem, microstrip transmission line geometry can be used [322], [323]. A microstrip is a type of electrical transmission line which can be fabricated using printed circuit board technology, and is used to convey microwave-frequency signals (see figure 6.2). The core of any microstrip device is a "strip" feeding line fabricated by etching one side of an FR-4 board coated with copper on both sides. The intact copper plate provides a ground plane shielding the device from electromagnetic interference. Besides the feeding microstrip, such a device can be comprised of different copper etched patterns arranged as RF filters, antennas, resonators, couplers, etc.. A main drawback of

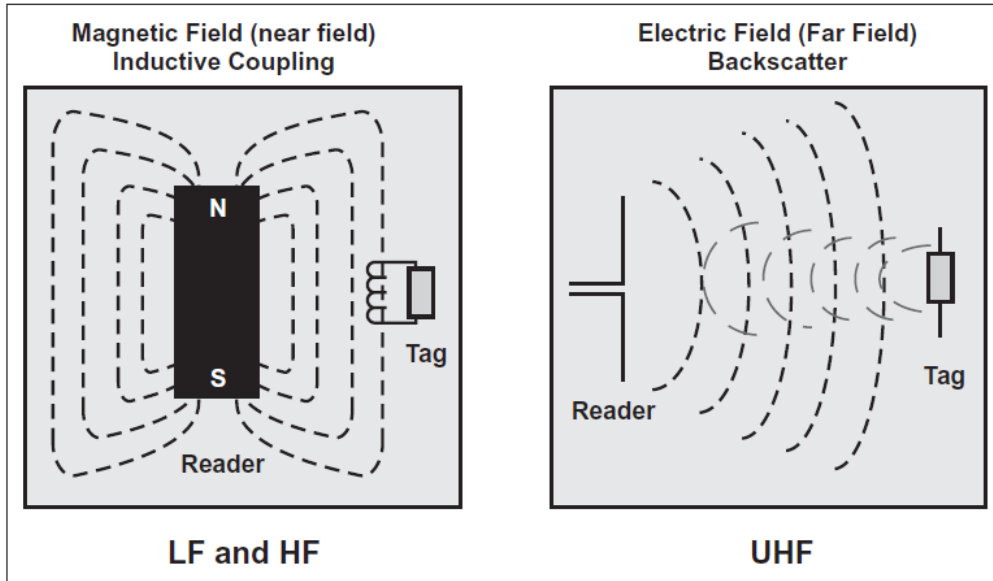


Figure 6.1: Inductive (left) and back-scattered (right) antenna coupling between an RFID tag and its reader. Inductive (and capacitive) coupling can be used in the reader's near field. Back-scattered coupling is meant for far field communication between the transponder and the interrogator (reader). Adapted with permission from [318]

microstrips structures is their high power dissipation (signal attenuation). This is the reason, for example, why for high frequency applications (i.e the 3GHz-10 GHz RFIDs band), PTFE-based laminated are preferred to FR-4 based printed circuit boards. FR-4 is a composite made out of fiber glass-reinforced (usually E-glass with a low percentage of alkaline metals oxides) epoxy resin. The FR-4 polymer (the epoxy resin) possesses a dielectric dissipation factor ² at least one order of magnitude higher than high frequency optimized materials such as Teflon-ceramic composites, hydrocarbon thermoset resins-aramyde fibers, cyanate esthers-woven fiber glass, etc. (i.e. $D_{fFR-4} \approx 0.0180$; $D_{fPTFE-ceramic} \approx 0.0013$). Residues of cross-linking catalyst, bromine based flame retardants, high polarizability of the epoxy

²Dielectric dissipation factor, D_f is usually expressed as *loss tangent*, $\tan \delta$, which is defined as: $D_f = \tan \delta = \frac{\epsilon''}{\epsilon'}$; where ϵ' and ϵ'' are the real and imaginary component of the dielectric constant (permittivity), respectively. Being $\tan \delta$ the ratio between the dielectric capability to dissipate (ϵ'') and store energy ϵ' , it is deeply connected to the equivalent (lumped) circuit model used to represent dielectric materials. In fact, any dielectric material can be visualized, in terms of equivalent circuit, as a capacitor connected in series to a resistor. Thus, the equivalent capacitance gives an estimation of the ability of the system to store energy through different dielectric polarization mechanisms (electronic, molecular dipoles, atomic, ionic), whereas the equivalent series resistance (ESR) represents the energy losses comprised of both conductivity and dielectric relaxation losses. The latter occurs when an AC electric field oscillates at a frequency too high for the particular polarization mechanism to contribute to the dielectric constant and it "relaxes" by generating heat.

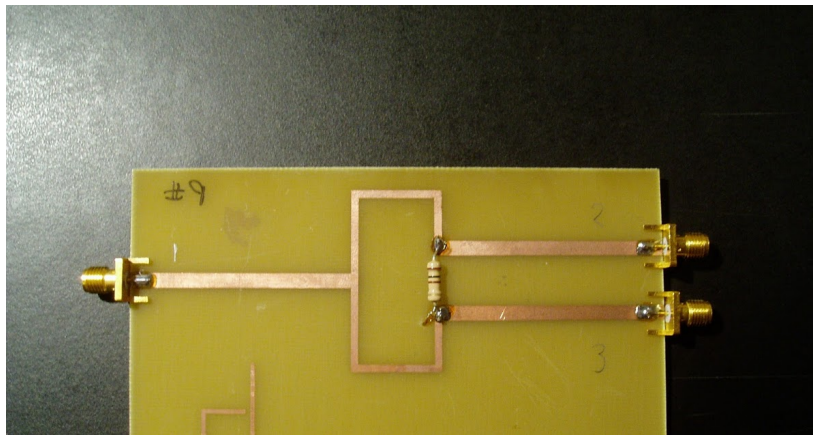
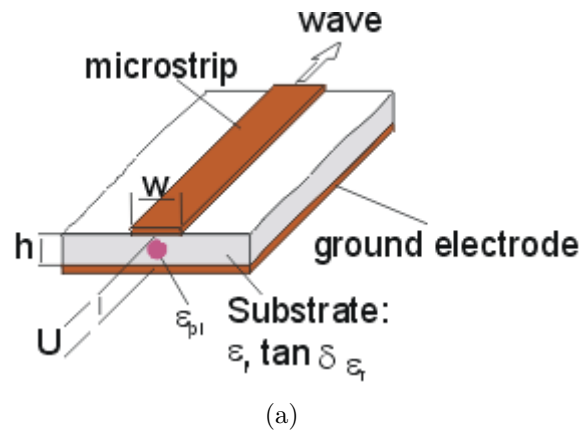


Figure 6.2: **(a)**, schematics of a microstrip device. The top side of the device is constituted by a copper etched feeding line of width w . The dielectric constant (ϵ_r) and the loss tangent ($\tan \delta$) of the insulating substrate determine the speed (in digital applications) and the attenuation (in analog applications) of the electromagnetic signal used to feed the microstrip. **(b)**, a complex microstrip device used as a filter. The copper etched conductive traces define a pattern that can be used to filter RF (or microwave) signals.

bond capable of relaxing at the microwave frequencies, coupling agents to promote adhesion between the epoxy resin and the fiber glass, and moisture adsorption contribute to the high D_f of FR-4 . High dielectric losses produces strong signal attenuation. As the microstrip circuit operates, the dielectric medium absorbs energy from the input signal. Attenuation of the signal by the dielectric is directly proportional to the square root of the real part of the dielectric constant and directly proportional to the loss tangent. Moreover, substrate dielectric constant is one of the parameters determining the speed of high frequency digital circuits. In addition, dielectric losses increase as the frequency increases consequently decreasing the bandwidth (see below for the meaning of the term) of the propagating microwave

signal. Furthermore, additional signal attenuation stems from conductors resistive losses [317].

An RFID tag's antenna operating in the UHF or microwave bands should be capable of functioning at a particular resonant frequency and have a large bandwidth. This last statement requires some further clarification. When dealing with "high frequency" transmission lines is useful to refer to electrical signals as propagating waves instead of using lumped parameters (voltage, current, etc.). The term "high frequency" means that the AC voltage frequency feeding the transmission line corresponds to a wavelength comparable to the physical dimensions of the circuit. Thereby, the return loss (RL) of an UHF or microwave device is defined as:

$$RL(dB) = 10 \log \frac{P_r}{P_i} \quad (6.1)$$

Where P_i and P_r are the power of the wave impinging on the device and reflected by the device, respectively. Hence, *the more negative is the return loss at the resonant frequency, the more power is available to an antenna for being radiated through the space*. RL is related to the concept of impedance mismatching. Any kind of power generator, also in the microwaves, is characterized by an internal impedance Z_G . Any device (or load) is characterized by an impedance Z_L . If the microwaves power source is connected to an antenna (or any other device operating in the microwaves) the maximum power transfer from the generator to the radiating device occurs when $Z_G = Z_L^*$, where the second term is the complex conjugated of Z_L . Thus, RL can be rewritten as:

$$RL = 20 \log |\Gamma| \quad (6.2)$$

where Γ is the reflection coefficient and is defined as:

$$\Gamma = \frac{Z_L - Z_G}{Z_L + Z_G} = \frac{V_R}{V_I} \quad (6.3)$$

V_R and V_I are the amplitude of the reflected and incident wave, respectively. Alternatively, the impedance mismatch can be described in terms of mismatch loss coefficient (M_L) defined as:

$$M_L = 1 - (\Gamma)^2 \quad (6.4)$$

Thereby unless the antenna impedance is matched to the one of the generator, *part of the power delivered to the transmitting device is reflected back*. Electrical impedance is given by:

$$Z = R + jX \quad (6.5)$$

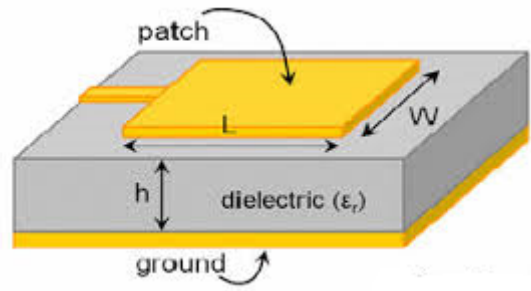


Figure 6.3: Schematics representation of a microstrip patch antenna. The patch width W (or its length) define (along with substrate's dielectric constant) the resonant frequency.

where the real part is the resistance (\mathbf{R}) and the imaginary part (\mathbf{X}) is the reactance than can be either capacitive ($X_C = \frac{1}{\omega C}$) or inductive ($X_L = \omega L$). Since impedance's reactance term depends on the angular frequency ω , it will exist a particular *resonant frequency*, f_{res} corresponding to a minimum in the return loss, that virtually goes to $-\infty$, or to $M_L = 1$, when Z_L is matched with Z_G . RF and microwaves sources and coaxial cables possess a 50Ω impedance. Thereby antennas' materials and geometry are designed to match a 50Ω input impedance allowing for the maximum power transmission to the radiating device. Therefore, antenna maximum power radiation occurs at the resonant frequency, which *constitute the antenna operative frequency* Antennas' f_{res} is expressed in mathematical terms as:

$$f_{res} = \sqrt{\frac{1}{2\pi L_T C_T}} \quad (6.6)$$

where L_T and C_T are the inductance and the capacitance of the *whole* antenna , respectively. The simplest microstrip antenna configuration is the *patch antenna* (see figure 6.3). Considering that standard PCB substrates are non-magnetic, the patch antenna resonant frequency expression reduces to:

$$f_{res} = \frac{1}{2W \sqrt{\frac{\epsilon_r + 1}{2} \epsilon_0 \mu_0}} \quad (6.7)$$

where as illustrates in figure 6.3 W is the patch width and ϵ_r , ϵ_0 , μ_0 are the substrate relative dielectric constant, the free space dielectric permittivity (8.85×10^{-12} F/m), and the free space magnetic permittivity (1.256×10^{-6} H/m), respectively.

The bandwidth of an antenna is defined as the range of frequencies where the RL is more negative (higher) than -10 dB. Unfortunately, conventional microstrip antennas are narrow bandwidth systems especially when they become small with

respect to the wavelength. Furthermore, since the operative frequency is set by the metal pattern defined on the PCB, a limited number of accessible frequencies available to the reader for communicating with the transponder. Nevertheless, microstrip antennas frequency tuning by inserting dielectric, magnetic materials [324] or liquids [325] on a small area of the PCB has already been proved. Hence, one of the aims of the present thesis is to demonstrate that *carbon materials printed films can be used in conjunction with standard copper etched microstrip devices to achieve a resonant frequency shift and bandwidth improvements*. Indeed, loading an etched microstrip structure with a printed film of carbon materials should produce a variation in the surface impedance of the device leading to a frequency shift of the resonance and a bandwidth enhancement. This shift is dependent on film composition (i.e. kind of carbon material and film's binder).

One of the advantages of adding printed layers to etched microstrip structures, or using fully printed antennas is that the printed layer can be used to produce either *chipless chemical RFID transponders* or *sensor-enabled RFID tags*. Chemical RFID transponders are meant to eliminate the most expensive part of an RFID tag: the ASIC. The major reason why RFID tags haven't replaced barcodes yet is the higher cost including the expenditure of chips, batteries, antennas, and assembly processes [326], [327]. By eliminating the use of silicon IC chips, chipless RFID tags can offer more competitive price than normal silicon IC based tags [328], [329]. Besides, chipless tags possess longer communication range since they do not necessitate the use of transistors as silicon based tags that require a threshold voltage to power up IC circuits [330]. Furthermore, developing *printable* chipless RFID tags seems a very attractive topic given the fact that printing techniques are high throughput processes. Additionally, printing technologies are fully additive processes, solely depositing material on the demanded positions of substrates, offering a potential pathway to save a large amount of expensive electronic materials during the fabrication. Also, printing techniques are compatible with cheap flexible substrates including plastic and paper sheets, holding high possibility to further drive down the tag costs.

Among the countless types of chipless RFID tags a prominent role is occupied by chemical transponders. Their operation principle is based on the use of printing inks comprised of nanomaterials exhibiting different degree of magnetism [331], and when electromagnetic waves impinge on them they resonate with distinct frequencies, which are picked up by the reader. Hence, the different frequency features stemming from the magnetic materials can be used for data encoding: each

particular resonant frequency represents a bit.

Sensor-enabled RFID tags allow for two options:

Chipless sensing . This approach aims at integrating printed sensing nanomaterials capable of changing their conduction, dielectric or magnetic properties according to specific chemical or physical conditions (i.e temperature, strain, light irradiance, humidity, pH, presence of gasses) directly *into a microwave resonators*. The change of sensor electrical impedance as a consequence of the environmental stimulation produces a change in the scattering properties of the antenna. The change in the scattering properties of the antenna appears as a modulation in the back scattered signal amplitude. The reader uses a continuous signal for the interrogation of the tag and detects the change in the back scattered signal amplitude.

Chipped sensing . In this case, sensing does not necessarily require a variation of sensor's electrical impedance in the RF and microwaves range as long as the measured physical parameter involved in the detection mechanism can be converted into an electrical current. Then, the IC on the tag processes the signal which is finally transmitted to the reader through the antenna.

Although conceptually simple, chipless sensor enabled RFID tag is a quite complicated multicomponent system. In fact, at least five components are required: one printed or etched receiving antenna and one printed or etched transmitting antenna; an etched (or printed) microstrip line connecting the two antennas; a microwave resonator circuit (printed or etched) and a printed film of a "smart" material. The purpose of the antennas and microstrip line is quite straightforward to understand: the antennas allow for communication with the reader and the microstrip line permits the communication between the receiving and the transmitting ends of the tag. Numerous geometries have been developed for the microwave resonator to be integrated onto the RFID tag. They span from slot ring resonators, to spiral shaped, to stepped impedance resonators to ELC (electric field inductor couple capacitor) resonators, CPW (co-planar waveguide resonator), etc. (see figure 6.4). Regardless of their particular shape microwave resonant circuits are always comprised of gaps between the etched (or printed) copper traces and resonate at a frequency determined by their inductance (**L**) and capacitance (**C**) equivalents components. One of the most diffused to integrate the resonators onto the RFID tag is to built a cascade of etched resonator coupled through a gap to the microstrip line connecting the receiving and the transmitting tag's antennas 6.4 (**b**). The

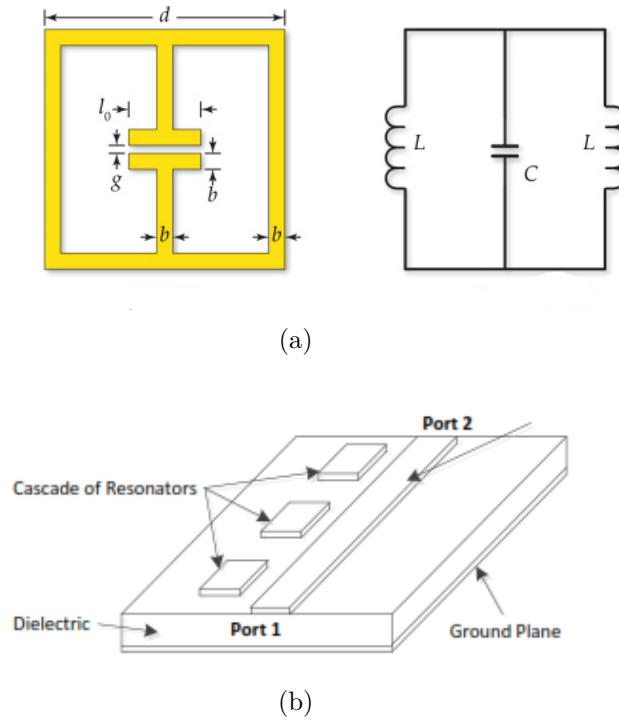


Figure 6.4: Example of microwave resonant circuit used for chipless RFID sensing. **(a)** ELC resonator and its equivalent circuit. The geometrical parameters of the copper etched traces (i.e. g , b , d) determine the capacitance of the middle planar capacitor and the inductance of the two parallel loops. **(b)** Cascade of resonators. The single resonator can be an ELC or another structure. Resonators are "gap coupled" to the microstrip line that connects the RFID tag receiving and the transmitting antennas. Adapted with permission from [331]

multiresonator circuit is designed to resonate at specific frequencies given by the inductive and capacitive components of the single resonator (i.e. ELC, SIR, split ring, U-shaped, etc.). At these frequencies, the stop band effect is created on the interrogation signal. The stop band effect is predicated on different current distribution at different frequencies. Current distribution is greatest in the resonator at its resonant frequency [331]. At resonance, the resonator creates a low impedance path to ground which absorbs the majority of the current propagating from port 1 to port 2 of figure 6.4 **(b)**. When not at resonance, the resonator couples almost none of the surface current propagating between port 1 to port 2. Therefore, at the output of port 2, the interrogation signal becomes modified by magnitude attenuations at different frequencies determined by the resonances of the resonators. Hence, if the transmitting antenna is connected to port 2 (and the receiving antenna to port 1) the tag's response signal to the reader will contain **magnitude attenuations at fixed frequencies** due to the multi-resonator circuit on the tag, which creates a

unique spectral signature. However, when a "smart" material is incorporated in the resonator (i.e. a sensing dielectric material in the capacitive gap of figure 6.4 **(b)** or a resistive material at the end one of a SIR structure) the response signal will have a amplitude attenuation which can shift in frequency and is not fixed. A smart or functional nanostructured material is capable of *changing its electrical properties upon a chemical or physical environmental change in the RFID tag's surroundings* [33]. Example of such a materials are CdS (because of its photoconductivity), phenanthrene (because of its dielectric constant discontinuity at the sublimation temperature), PEDOT (pH sensitive electrical conductivity), Nitinol alloys (because of their shape memory effect) CNTs and transition metal oxides (because of their gas-sensitive resistivity), just to mention a few. For instance, if a film of CdS nanoparticles is placed into a stepped impedance resonator an attenuation of the signal sent back to the reader is observed at different light intensity. In fact, CdS nanoparticles act as a photoresistor in the RF range (although their light sensitivity is lower compared to DC operation mode). Hence, the CdS nanoparticles resistivity change produces an impedance variation in the SIR that reflects into a reader signal attenuation [332]. Another example of smart materials applied to chipless sensor-enabled RFID tags is the phenanthrene: a sublimation substance from the polycyclic aromatic hydrocarbons group. Phenanthrene sublimates at 72 °C generating a drastic increase in the dielectric constant (from 2.7 to approximately 80) that becomes permanent if the vapor is not de-sublimated [333]. When phenanthrene is used as superstrate for a microwave resonators, a temperature change produces a *resonance frequency shift*, of the signal transmitted back to the reader. In fact, a variation of the *real* part of the dielectric permittivity (i.e. the relative dielectric constant) of the smart material is associated with a change in the reactive component of resonator impedance. Thus, a change in resonator's capacitance change produces a corresponding resonant frequency shift. Needless to say, this effect (that result into a frequency shift of the signal sent back to the reader) can be exploited in temperature threshold sensors for sensor-enabled chipless RFID tags [33]. Other smart materials used for chipless RFID sensing respond by varying multiple electrical properties upon a single environmental stimulus. For instance, PVA (polyvinyl alcohol) shows both a resonant frequency shift and magnitude attenuation in presence of moisture. In fact, PVA dielectric constant and loss tangent shows opposite trends [32] between 2 and 20 GHz (ϵ_r' increases and ϵ_r'' peaks above 5 GHz) with increasing water content caused by the breaking and reforming of hydrogen bonds of water molecules with -OH groups present in PVA

chain. Hence, a change in ϵ_r' causes a resonant frequency shift, whereas a variation of ϵ_r'' results in a resonance power drift at a particular frequency. Furthermore, PVA composite films conductivity show a linear dependence on relative humidity [334]. Thus the reader will receive back a magnitude attenuated and frequency shifted signal.

Although attractive because of their low manufacture cost, chipless sensor-enabled RFID tags present numerous technological challenges on both the fabrication and testing sides. Practically all smart materials are semiconductors or dielectrics, or conductors (i.e. CNTs or graphene) exhibiting a resistivity higher than pure conductors. Hence, they are deposited on a small area of the resonator rather than being used as the main component of the circuit. Furthermore, fully printed (smart material, resonators, conductive traces, receiving and transmitted antenna) is impractical especially for what concerns the two antennas. In fact, silver or copper conductive inks, regardless of the printing technology employed, never match the conductivity values of etched metals traces preventing suitable antennas resonance (i.e. return loss close to zero throughout the frequency spectrum) and bringing about low radiation efficiency (see Chapter 7) ³. The problem is aggravated in (polymer thick film) antennas where the conductive metal is deposited by screen printing [335]. Indeed, after the deposition the thermoset or thermoplastic binder remains as a matrix for the Cu or Ag nanoparticles. Thus, particles interconnection relies only on solvent evaporation, for the thermoplastic binders, or on thermal (or UV) curing for the thermoset PTFs. The second issue related to chipless sensor-enabled RFID tags regards discrepancies between field application and lab tests. Indeed, the "real life" complete system requires the *reader* and the tag equipped with the aforementioned five components. Readers architectures are quite complicated to implement because they require: a digital section (microprocessor, analog-to-digital converters, memory block, etc.) an RF section (local oscillators, directional couplers, demodulator, modulator, demodulator, etc.) and the antenna. Therefore, lab test methodologies for sensor-enabled chipless RFID *do not involve* the direct testing of the whole wireless system. In fact, usually *only* the microwave resonator functionalized with the smart material or the antenna connected to the smart material are tested with a network analyzer. Basically, the return loss or the insertion loss ⁴ of the resonator

³The radiation efficiency of an antenna is defined as the ratio of the radiated power to the total power delivered to the antenna. The radiation efficiency is an indication of how much incident power is dissipated as heat in the antenna. Thereby, high ohmic losses stemming from excessive resistance of the antenna's conductors result in low radiation efficiency, see chapter 7

⁴Similarly to the return loss that is a measure of the power reflected in a single port system, the insertion loss is a measure of the power transmitted in a two port system

are measured by connecting it to one port (or two ports for the insertion loss) of a network analyzer. Then, return (or insertion) loss attenuation or frequency shift upon the change of the smart material electrical impedance in response to the environmental stimulus is monitored through the network analyzer. The same principle is exploited when the smart material is connected to an antenna.

When a chemical (or physical) sensor is not incorporated into the microwave resonator (or directly into the antenna), electrical (and high frequency) characteristics of the sensing printed film do not play a key-role in transmitting the signal back to the reader. Thus, chipped sensor-enabled RFID tags allow to exploit any kind of environmental-dependent physical property of the material used as a sensor. The electronic circuitry of the film sensor on the tag controls the measurements and the communication to the reader by transmitting data through the antenna. Among suitable detection systems, color change (i.e. light absorption measurements) represents a low cost, simply implementable (i.e through colorimetric pH indicators) sensing tool for a wide range of chemical analytes. Furthermore, colorimetric sensors are relatively easy to be integrated on a RFID tag. "Gas-chromic" sensors have been developed and integrated on RFID tags fabricated on FR-4 PCBs (see figure 6.5) at the Fraunhofer Institute for Physical Measurement Techniques (IPM) (Germany) by Pannek et al [336]. The principle of the sensor is based on a color change of the gas sensitive layer when it comes into contact with the target gas. The IPM group has developed different color dyes for CO, NO₂ and NH₃. Granulated dyes (a di-nuclear aromatic rhodium complex for CO, a quinone derivative for NO₂ and bromophenol blue pH indicator for NH₃) have been mixed with suitable polymer matrixes (PVC, EC, PMMA) and deposited on a half of a microscope glass slide by spin coating or by other low cost techniques. The authors suggest that screen printing represent the most suitable deposition technique for the "lab on a chip"-like production of RFID tags. In that case, a single glass substrate (i.e a thin flexible glass sheet) acts as support for the sensing material, for the conductive traces, for the printed organic digital logic and as planar waveguide (see below). The color change material coated glass slide has been placed on the surface of a planar waveguide [337], [338]. Light from a LED, coupled into the front of the waveguide, passes by total internal reflection and is focused on a photodetector at the opposite side. A change in color of the gas sensitive material corresponds directly to the change in absorption of the light. The particular color change is associated to the specific reaction between the gas and the analyte sensitive dye. For instance, the oxidation of the quinone derivative by NO₂ produces the Wurster's blue compound

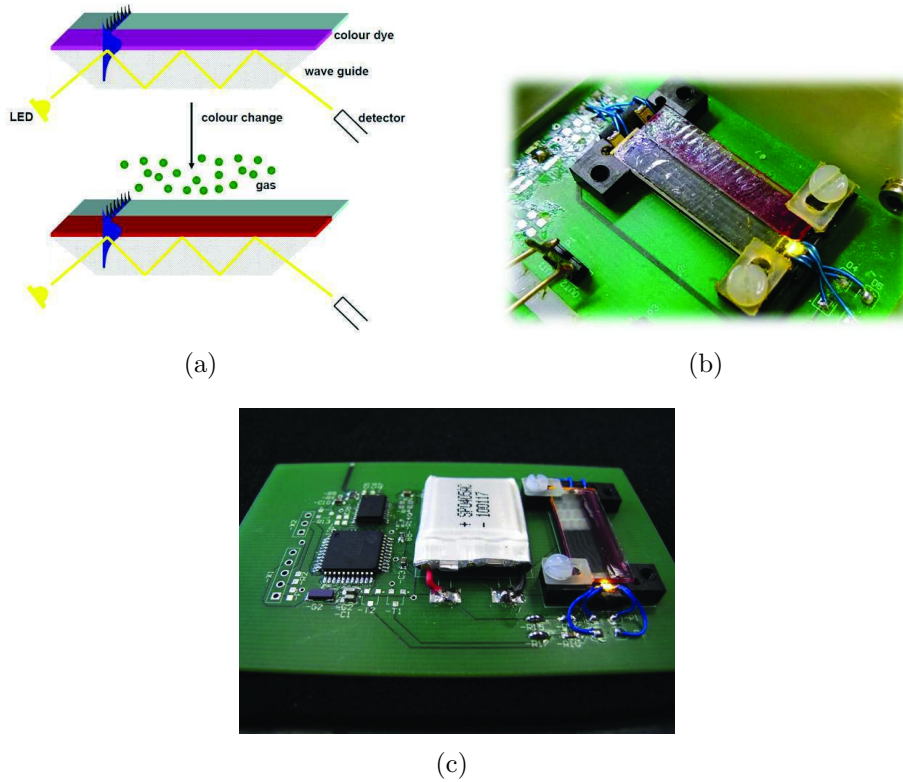


Figure 6.5: Gas-chromic sensor developed at the IPM-Fraunhofer Institute in Freiburg, Germany. **(a)** Sketch of the gas-chromic sensor consisting of a microscope slide with the lower half covered with the color changing material film. The light of an LED is coupled into one end of the waveguide and travels through it by total internal reflection before being focused onto a photodetector. Depending on the specific gas adsorbed of the sensor different colors (that is different light absorption levels) are generated **(b)** The actual gas-chromic device. **(c)** the sensor integrated on a 13.56 MHz RFID transponder. The tag is an active one (the battery is clearly visible in the center of the transponder). The device's electronics is comprised of different surface mounted IC on a standard FR-4 PCB (the green color of the substrate is due to the solder mask). The inductively coupled antenna for to communicate with the reader is placed on the rear side of the tag and is not visible. Adapted with permission from [336].

generating a sensor's color change from brown to blue. The color change detected by the photodetector is processed by the RFID microcontroller (by also using an EEPROM). Finally an output electromagnetic signal is forwarded to the reader by using a printed inductively coupled antenna placed on the RFID tag's back and meant for the 13.56 MHz band operation.

The operating principle proved at the Fraunhofer institute allows to extend remote sensing also to different systems. In fact, a colorimetric sensor based on the $\text{TiO}_2/\text{L}/\text{Fe}^{2+}$ configuration (see figure 5.1) is now being integrated by our

Polytechnic of Turin research partners on a 2.45 GHz RFID transponder. In addition, the great flexibility of **L**-functionalized oxides surface opened up two new RFID-related investigations in our lab: (i) electrochromic devices; (ii) iron sensing through microwave resonators. The former application relies on an electrical current driven color change on **L**-functionalized ITO thick films capable of coordinating Ru(II/III) and Fe (II/III) ions. An electrochromic device is also suitable for RFID transponders integration and can act as a visual indicator of the operative state of the RFID tag. Such a visual indicator may be human readable and/or machine readable, and may provide visual indication that is dependent on a change in an operative state of the device. The operative state that triggers the visual indication may include a state in which the chip has temporarily or permanently been rendered inoperative or disabled, that is, in which the chip no longer responds to, or otherwise interacts with, ordinary incoming RF signals such as from a device reader [339]. Furthermore, for active RFID tags (like the one shown in figure 6.5 (c)) an electrochromic device can act as battery charge sensor.

Fe³⁺ colorimetric detection cannot be accomplished by using (**L**) because the resulting complex doesn't show any MLCT transition in the visible. Nonetheless, iron(III) identification through microwaves resonant frequency shift is under investigation because is predicated on the magnetic properties of **L**-iron(II/III) complexes rather than on their optical properties. In fact, If Fe(III)-terpy complexes chemisorbed on ITO thick films are inserted into a microwaves resonator structure a shift in the antenna resonant frequency due to the d⁵ electronic configuration of the Fe³⁺ ion may occur. Indeed, even low-spin complexes like the Fe(III)(**L**)₂ possess one unpaired electron occupying the t_{2g} orbitals. Hence, the paramagnetic nature of the complex should affect the magnetic permeability (see Chapter 7 of the film producing a change in the inductive component of the antenna impedance. Consequently, the device's resonant frequency should shift with respect to the case without Fe(III) ⁵. Electrochromic devices and microwave resonator for iron detection are still under investigation by our group, hence they will only briefly discussed in the III part.

⁵This concept shouldn't be confused with the principle employed in the electron spin resonance (ESR) spectroscopy of paramagnetic metal coordination compounds. In that case a *static magnetic field* is used to remove the unpaired electrons spin degeneracy by Zeeman's energy levels splitting and a microwave radiation is exploited to promote an electronic transition between the two spin states. In the experimental practice a monochromatic microwave radiation is used and the magnetic field is swept until the resonance condition for the low level to high level energy spin transition is reached provoking the absorption of the radiation.

Chapter 7

Carbon based microwave devices

7.1 Carbon Materials for RF and microwave application

Although carbon materials (i.e. CNTs, graphene, graphite, carbon black, carbon fibers, etc.) lend themselves to execute numerous functions in fully printed electronic circuits (see chapter 6 for the specific meaning of the term) their use for high frequency (RF and microwaves) electronics is limited to a small handful of applications. In fact, carbon materials inks and pastes deposited with flexible electronic, roll-to-roll compatible printing techniques (flexography, ink-jet, gravure, rotatory screen printing) are mostly used for *low frequency* (from DC to tens of MHz) applications such as membrane switches, PTCs (positive temperature coefficient) polymer resistors, supercapacitors, solar cells, electrochemical sensors, TFTs, emitters for field emission displays, HF or LF inductively coupled antennas, LF or HF electromagnetic shielding, etc. [231], [340], [341], [342], [43], [343], [?], [344], [345], [346], [347]. The conductive component of the deposited films can be either the carbon material or its mixture with silver. In the latter case two inks are blended together and the carbon component is used as low-cost alternative to palladium to prevent silver electromigration [335].

Carbon materials, and conductive inks in general, applicability to electronic devices becomes rare and rarer as the operative frequency is increased unless high thermal budget, non-flexible LTCC (low temperature co-fired ceramics) or HTCC (high temperature co-fired ceramic) ¹ technologies are used. However, in UHF or

¹LTCC technology is predicated on stacks ceramic tapes (usually Al_2O_3) amalgamated with organic adhesive, glass frits (based on $\text{SiO}_2\text{-B}_2\text{O}_3\text{-CaO}$ systems) and screen printable pastes of dielectrics, resistive and conductive materials for printing of resistors capacitors and inductors.

microwave LTCC (or HTCC) circuits dielectric (i.e. BaTiO₃, ZnO, etc.), conductive (Ag, Ag-Pd, W, Ta, etc.), resistive (i.e. RuO₂) or sacrificial (i.e. graphite) inks are employed for the printing of capacitors, resistors, and conductive traces, but *usually are not used for the antenna fabrication* that is generally a copper structure etched on PCB substrates (i.e. FR-4 or high frequency substrates, see chapter 6) and integrated by surface mounting either on the LTCC/HTCC substrate or on a standard PCB guesting the co-fired ceramic circuit. Hence, in the last 30 years there has been a large commercial availability of carbon, silver, and copper inks for LF and HF fully printed antennas, a large expansion of the silver inks market for antennas operating in the UHF region [348], [349], and practically no alternatives to copper etched antennas for the microwaves frequencies. To understand the reasons of such a market (and research) trend it is necessary to explore two topics:

- Conductive inks parameters affecting the electrical resistance of a printed film in the UHF and microwaves. For the sake of simplicity, only screen printing pastes (which are the most employed for deposition of conductors) will be discussed. Nevertheless, most of the considerations standing for screen printing pastes are applicable to other inks. In fact, the main screen printing pastes distinguishing feature concerns the presence of higher relative amounts of binders and rheological modifiers compared to flexographic, ink-jet or gravure inks. The reason for such a special kind of formulation is the higher viscosity, η , required for paste transfer on the substrate through the screen mesh (i.e. $\eta = 500-5000$ cP for screen printing; $\eta = 50-500$ cP for flexography; $\eta = 10-20$ cP).
- Antenna's materials properties affecting two parameter: the return loss RL and the gain. Every back-scattered (radiative) antenna, that is used for transmitting signals through propagating electromagnetic waves, is characterized by a parameter named gain (G) combining antenna's electrical efficiency and directivity (see below).

When the circuit pattern and components have been defined by printing, the tape is fired at 800-900 °C, producing sinterization of both ceramic tape and circuit components embedding into the ceramic substrate. HTCC is a similar technology but meant for higher processing temperatures (from 1600 to 1800 °C). The main difference between HTCC and LTCC technologies lies in the passive components and metal traces to be integrated on the ceramic substrate. Indeed, materials with relative dielectric constant higher than 100 require such as perovskites (i.e. BaTiO₃) sintering temperature above 1200 °C for their densification and can be applied only to HTCCs. On the other hand LTCCs circuit's capacitors rely on HfO₂, TiO₂, ZnO, etc. that are compatible with "low-temperature" sintering. Similar considerations stand for the conductive traces: Ag, Pd, and Au are employed in LTCCs whereas W, Mo, or Ta are used for HTCCs

Conductive inks' industry uses the DC volume resistivity (ρ_{vdc}) of inks in $\Omega/\square/\text{mil}^2$ to link the printed film conduction properties to the ink's formulation and the sheet resistance (i.e. thickness dependent) to determine if a printed conductor is meeting a performance spec. ρ_{vdc} depends on multiple factors. The intrinsic bulk resistivity ρ of the conductive powders and their wt% used for inks formulation are the first parameters to be taken into account. In fact ρ varies from $1\text{-}2 \times 10^{-8} \Omega\text{m}$ for Ag, Cu and graphene (i.e. $\rho_{Ag}=1.58 \times 10^{-8} \Omega\text{m}$, $\rho_{graphene}=1.17 \times 10^{-8} \Omega\text{m}$ [?]), [350] to $3\text{-}60 \times 10^{-5} \Omega\text{m}$ for graphite, to the $1.6 \times 10^{-5} \Omega\text{m}$ ballistic limit for a single CNT [43]. Needless to say, the higher the wt% of conductive filler in the screen printing paste the lower ρ_{vdc} . However, filler's content limits are set by the dispersants, binders, and inks manufacturing techniques capability of dispersing uniformly, prevent re-agglomeration and avoid settling of filler's particles or low dimensional structures. Usually the conductive filler wt% are: 60-90 for silver and copper particles (50% for flakes), 0.1-40 for graphene flakes and CNTs, 30-40 for graphite and carbon black. The percentages are predicated on the dispersions stability for three roll mill-processed pastes, the printing rheology [335] and on the application-dependent required sheet resistance and adherence to the substrate [351].

A prominent role in determining inks volume resistivity is played by film's post-deposition thermal treatment. In fact different processes occur during the film curing³. Provided that printing on FR-4, high frequency and flexible (i.e. PEN, PET, PI, etc.) substrates precludes binder's removal, heat treatment in the 70-300 °C temperature range is responsible for solvent evaporation and particles sintering assisted by either oligomers cross-linking (for thermoset binders such as epoxy, phenolic, thermoset alkyds resins etc.) or polymer chains reorganization in proximity of the thermoplastic binder T_g (i.e PVC, polyester, cellulose ethers and esters, acrylates, thermoplastic polyurethanes, etc). Solvent evaporation is generally required for thermoplastic binders that are dissolved into the paste's solvent or pre-solubilized into a low boiling point solvent. On the other hand, thermoset pre-polymer ingredients (monomers, oligomers, and polymerization initiators) are usually liquid and don't require their dissolution in a solvent. Besides conventional diffusion based particles sintering, a new family of metallorganic reactive (MOR) pastes based on Ag (I) and Cu (II) organic precursors instead of metal nanoparticles

²Mil is a thickness unit commonly employed in the electronics industry to specify films thickness, etched copper profile and dielectric substrate height. 1 mil is 1/1000 of a inch and corresponds to $25.4 \mu\text{m}$.

³Solvent-free UV curable inks excluded from the actual discussion

has been developed [352], [353] [354]. However, copper based MORs pastes are far away from their commercial application because an N_2 or 3% H_2 atmosphere heat treatment treatment is needed for precursor's conversion and to avoid copper particles oxidation.

Commercial "standards" volume resistivity of silver inks for UHF printed antennas is 0.006-0.05 $\Omega/\square/\text{mil}$ (which corresponds to a 6-50 $\text{m}\Omega/\square$ sheet resistance for a 25 μm thick film). Sheet resistance of 1.4 mil thick (36 μm , corresponding to a standard 1 oz. copper clad laminate) etched copper traces is 0.5 $\text{m}\Omega/\square$. Furthermore, copper etching doesn't involve any thermal treatment and the resulting metal pattern can be easily protected from oxidation by immersion silver or ENIG (electroless nickel immersion gold) finishes. Although graphene, CNTs, graphite, and carbon black high conductivity pastes for DC applications would be attractive for UHF antennas because they don't suffer from oxidation problems, their minimum achievable ρ_{vdc} is 10 (graphene), 30 (CNTs), 25 (graphite) ,20 (carbon black) $\Omega/\square/\text{mil}$. Even though is possible to decrease the printed film sheet resistance by increasing the number of depositions , carbon materials pastes *won't never match the conductivity neither of silver pastes nor etched copper traces*. In addition, increasing the number of prints without raising the heat treatment period doesn't result into significant sheet resistance drops. Moreover, DC sheet resistance, or ρ_{vdc} does not take into account the effect of the film's skin depth that further increases the effective resistance. Hence, copper etched antennas remain the only practical option for frequencies higher than the UHF's (300 MHz-1GHz) such as the microwaves S (2-4 GHz) or C (4-8 GHz) bands. In fact, the low sheet resistance provided by copper traces allows for

1. High return losses at the resonant frequency.
2. High gains.

The first condition defines the suitable resonance (and thus the antenna's operative wavelength) frequency to be used for signal transmission or reception. An accepted rule of thumb sets the "benchmark" minimum $|\text{RL}|$ to 10 dB for a resonant frequency to be useful. Furthermore, theoretical and experimental studies carried out on carbon materials thin and thick films antennas have proved that 40 Ω/\square is the sheet resistance limit value to appreciate a resonance [355]. When the film's sheet resistance exceeds 40 Ω/\square no power is absorbed by the antenna because of the impedance mismatch ($M_L \approx 0$, $\text{RL} \approx 0$ at the resonant frequency, all power delivered to the antenna is reflected back). On the other hand, when film's sheet resistance

is $< 3 \Omega/\square$, the dielectric constant mismatch between the substrate and the air becomes the main source of impedance mismatch (low M_L values).

Thus, the higher sheet resistance (at least one order of magnitude) of printed films compared to copper etched antennas leads to impedance mismatch and consequently decreases the absolute value of the return loss for antennas operating in the S or C bands.

The gain (G_A) is defined as the antenna's capability to convert input power into radio waves headed in a *specified direction*. G_A 's expression is comprised of two terms: the antenna's electrical efficiency, or simply the efficiency ϵ_A , and the directivity $D_A(\theta, \phi)$ expressed in spherical coordinates. In other words, ϵ_A is the ratio of the power irradiated by the antenna with respect to the power *delivered* (available) to the antenna ($\frac{P_{rad}}{P_{in}}$) by the feeding source whereas D_A is the antenna's ability to direct the power radiated toward the RF receiver. In mathematical terms:

$$G = \epsilon_A D_A(\theta, \phi) \quad (7.1)$$

Usually the gain is normalized for a lossless isotropic antenna and is given in dB_i where i stands for isotropic. For instance, $G = 3$ dBi means that the power accepted by an RF receiver placed in the antenna's far field will be 3 dB higher (twice as much) than what would be received from a lossless isotropic antenna with the same input power. Similarly, a -3 dBi antenna gain means that the power received in the far field of the antenna is 3 dB shy of the power received from a lossless isotropic antenna. Because of electromagnetic reciprocity, the the gain of any antenna when receiving is equal to its gain when transmitting and the distinction between the two cases becomes immaterial.

ϵ_A in equation 7.2 contains in turn two terms:

$$\epsilon_A = M_L \epsilon_{rad} \quad (7.2)$$

where ϵ_{rad} is the antenna radiation efficiency, that is the power radiated by the antenna relative to the feeding line power *accepted* by the antenna ($\epsilon_{rad} = \frac{P_{rad}}{P_{acc}}$). The return loss and consequently M_L are the ties between the power delivered to and accepted by the antenna. Thus, all the power accepted by the antenna (not reflected because of impedance mismatch) which is not radiated is dissipated into heat. Hence, dielectric and resistive losses result into $\epsilon_{rad} < 1$. To simplify the discussion a radiation efficiency $\epsilon_{rad\alpha}$ taking into account only the resistive losses is

often used:

$$\epsilon_{rad\alpha} = \frac{R_{rad}}{R_{ohm} + R_{ohm}} \quad (7.3)$$

where R_{ohm} is the ohmic resistance (i.e. the sheet resistance) of the antenna conductors and R_{rad} is the self-induced resistance created by the antenna's own dynamic electric field [356], [355], [357]. When an AC electric field is impressed on the antenna electrons will radiate electromagnetic waves. These waves carry energy that is taken away from the electrons. Therefore, the electrons' loss of energy appears as an effective resistance their movement. This is the meaning of R_{rad} . Thereby, $\epsilon_{rad\alpha}$ evaluates how much power is "dissipated" as radiated power (useful to transmit signals) and how much is dissipated as heat. The relatively high ρ_{vdc} of carbon materials based conductive inks is the main responsible for low $\epsilon_{rad\alpha}$ values of fully printed antennas. In addition, equation 7.3 doesn't take into account dielectric losses. For thick films printed antennas power heat dissipation is aggravated by the binder component of the film. Indeed, common polymer resins employed as binders are characterized by dielectric losses (in terms of loss tangent) comparable to FR-4 substrates (i.e. $\tan \delta$ is 0.008-0.01 at 3 GHz for an ordinary FR-4 substrate, 0.01-0.05 for phenolic-formaldehyde resins, and 0.02-0.09 for cellulose derivatives depending on the polarity of groups substituting one of the OH positions in the glucose units [358]). Thus, even if their contribution to power dissipation through heating is smaller compared to the one brought about by the substrate, dielectric losses caused film's binder still generate ϵ_{rad} drops. Finally, large amounts carbon materials embedded [359], [360], [361], [362] in polymeric matrices causes the loss tangent of the composite material to raise conspicuously in the 1-30 GHz range further reducing the radiation efficiency.

The second term of equation 7.2, the antenna directivity, is defined in spherical coordinates as:

$$D_A(\theta, \phi) = 4\pi \frac{P_{\theta, \phi}}{P_{rad}} \quad (7.4)$$

where $P_{\theta, \phi}$ is the power radiated per unit solid angle in a specific direction and P_{rad} total power radiated by antenna. $D_A(\theta, \phi)$ depends on antenna's geometry and for *dipole* antennas may depend on particular orientation of mono-dimensional structures such as CNTs [363], [364]. However, CNTs embedded in a thick film binder matrix are intrinsically disoriented and any effect on the directivity vanishes. Because of the $D_A(\theta, \phi)$ component G_A is directly connected to the antenna radiation pattern measurements. The radiation pattern is defined as a mathematical function or graphical representation of radiation properties of the antenna as a function of

the space coordinates. Radiation properties include power, radiation intensity, field strength, directivity phase or polarization, and gain. The radiation pattern may be displayed in variety of 3-D or 2-D formats. Figure 7.1 illustrates an example of 3-D (gain) radiation pattern for a simple microstrip patch antenna. Each two-dimensional radiation pattern taken at an increment of ϕ is called "pattern cut". If the radiation pattern is collected along the $\phi = 0^\circ$ or $\phi = 90^\circ$ planes it is named "principal cut" [356], [357]. For antennas radiating a linearly polarized field (like microstrip patch antennas), the principal planes are those chosen to be parallel and perpendicular to the electric field vector of the antenna. A E-plane or electric-plane radiation pattern records the electric field magnitude or power at $\phi = 0^\circ$, whereas the magnetic plane or H-plane pattern is recorded at $\phi = 90^\circ$. By referring to the antenna's orientation of figure 7.1 (fed along the y axis) the E-plane is the YZ plane and the H-plane is the XY plane. Being the electrical current direction the Y axis, the electric field oscillates in the YZ plane and the antenna is vertically polarized. Experimentally antennas' radiation pattern are collected as follows. First

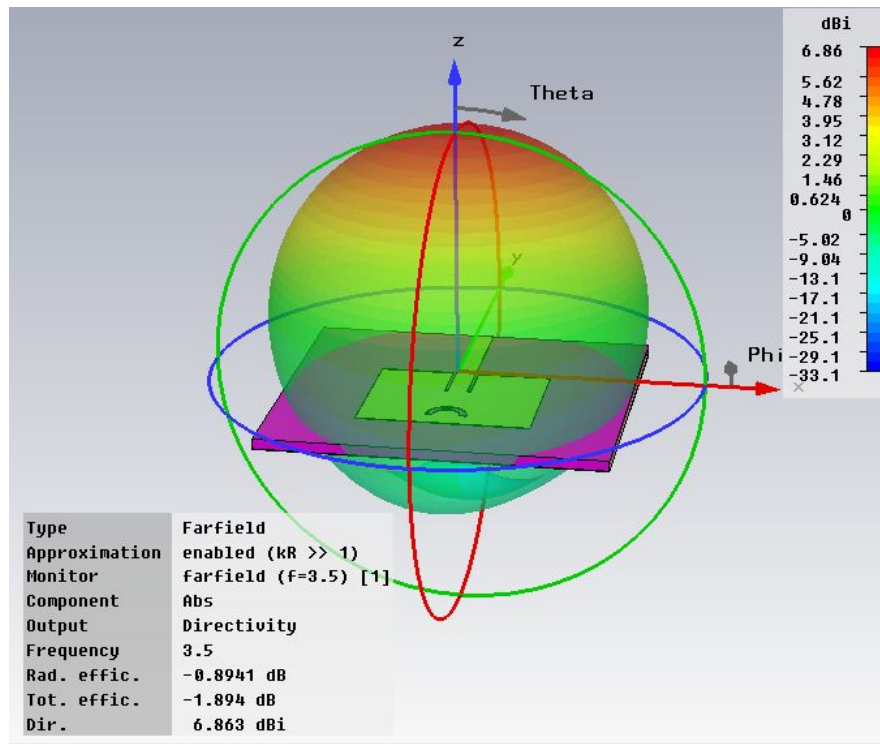


Figure 7.1: Example of 3-D gain radiation pattern for a microstrip patch antenna. θ is the vertical or elevation angle and ϕ the azimuthal or horizontal angle. For linearly polarized antennas (like microstrips patch antennas) the elevation or azimuthal planes coincides either with the the H or E-plane depending on the antenna polarization state (see main text).

the measurement frequency (usually corresponding to antenna's resonant frequency)

is set. Then, a value of angle ϕ can be chosen and the electric field magnitude or power received or transmitted by the antenna under test (AUT) are measured for increments of θ . The angle ϕ is then increased and the process is repeated. The required equipment for antennas' radiation pattern measurements includes a transmitter coupled to a source antenna (usually a horn antenna), a bolometer connected to the AUT to measure, a positioning system that controls the orientation of the AUT and produces the angular displacement with respect to the source. Although conceptually simple, radiation pattern collection is complicated by two experimental difficulties:

- The power received or transmitted by the AUT depends on its relative orientation with respect to the source antenna.
- The pattern has to be acquired in the AUT's far field.

Assuming that the AUT is tested in the receiving mode (same consideration apply to the transmitting mode because of electromagnetic reciprocity) the source antenna can possess either the same (i.e. vertical if we refer to figure 7.1) or the opposite polarization state of the AUT. The former case (same polarization) leads to the *co-pol* radiation pattern, while the latter case generates a *cross-pol* radiation pattern. Needless to say the power measured in the co-pol mode is larger than the one measured in the cross-pol mode. A distinction concerning the AUT's far field definition exist for "electromagnetic short" and "electromagnetic long" antenna. The former class is constituted by antennas shorter than half of the wavelength of the radiation they emit and the far field is characterized by a distance $r \gg 2\lambda$. Electromagnetic long antennas are physically longer than a half-wavelength of the radiation they emit and two conditions define the far field: $d_f \gg D$; $d_f \gg \lambda$. D is the largest physical linear dimension of the antenna and d_f is the far-field distance. An anechoic chamber (see figure 7.3) is the only facility allowing for *indoor* radiation pattern measurements in the microwaves S and C-bands. Besides, a 3-5 m distance between the source and the receiving antenna ensures that the microwaves impinging on the AUT are plane waves. Anechoic chambers comprised of walls, ceiling and floor lined with special electromagnetic wave absorbing material such as a carbon black loaded polyurethane foam. The material is often jagged in shape (see figure 7.3). The jagged triangle shapes are designed that electromagnetic waves reflected from them tend to spread in random directions and to add incoherently. Even though it is possible to calculate G_A by integrating the radiation pattern, the gain is usually measured by the *substitution (or comparison) method* [356]. Unless

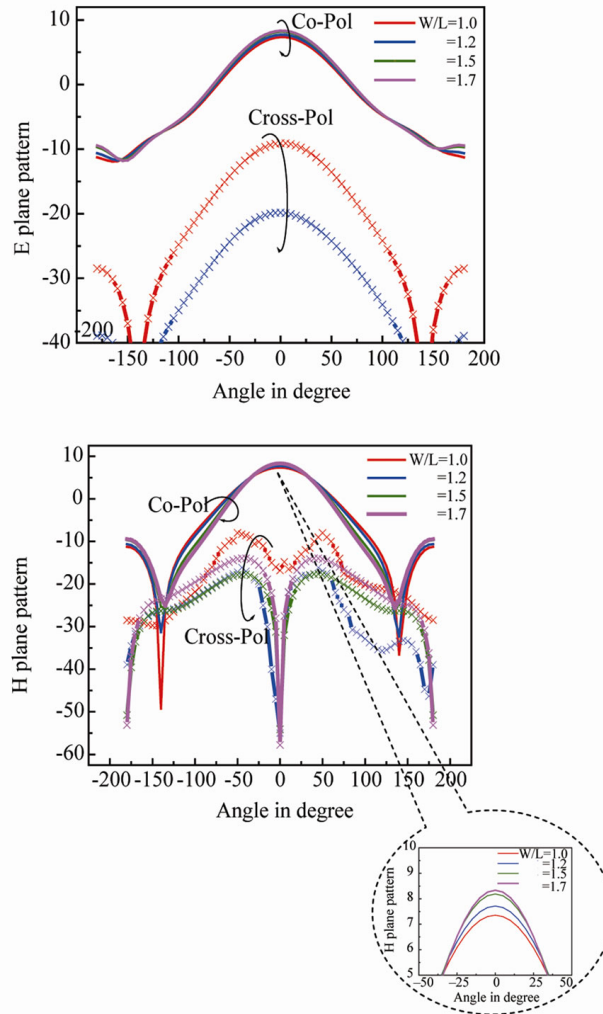


Figure 7.2: "Non-normalized" radiation pattern reported on a rectangular Cartesian plot. Very often the radiation pattern is normalized for the power corresponding to the direction of maximum emission of the antenna. Hence, a normalized radiation pattern shows (-dB) on the Y axis (with 0 dB) corresponding to the antenna's main lobe. Principal planes' received power (or electric field strength) can be reported either in the co-polarization or cross-polarization mode. The graph shows the radiation pattern dependence on the patch width/length ratio. Adapted with permission from [365].

otherwise specified, G_A is usually taken to be the power gain in the direction of its maximum value. The comparison method exploits a standard antenna with gain exactly known. the same source antenna is used for measuring the power received by both the standard and the AUT.

Nanostructured carbon materials such as CNTs and graphene are potentially attractive for microwave devices application because of their tunable electrical properties (adjustable by doping, by controlling the aspect ratio, printing vehicle composition, etc.) mechanical strength and chemical stability. However, the

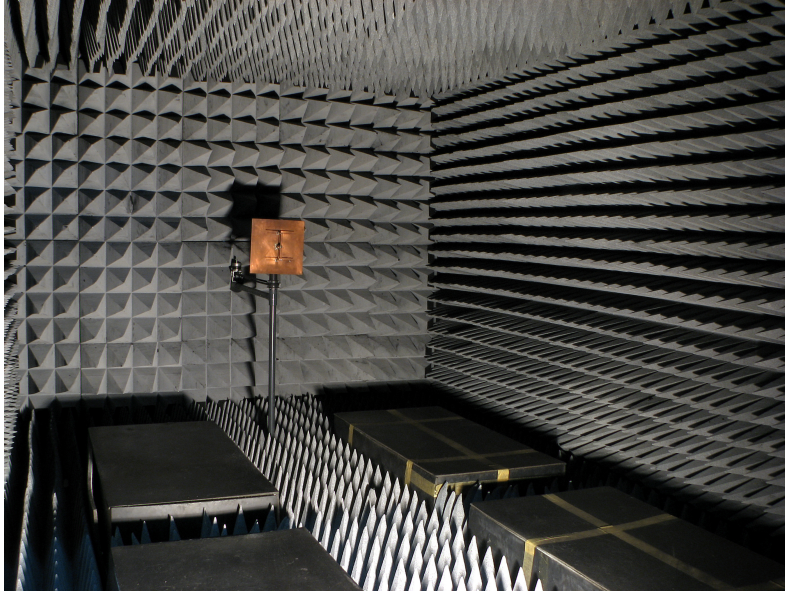


Figure 7.3: Example of an RF anechoic chamber for antenna testing. The AUT far-field can be expressed as: $(r_{source-AUT} \gg \lambda)$. Where $r_{source-AUT}$ is the distance between the source's antenna and the AUT. In the microwaves S and C-bands the condition is satisfied for chamber's sizes larger than 3m.

aforementioned restrictions dictated by the resistive and dielectric losses (affecting the impedance mismatch factor and the radiation efficiency) make full printed (thick film) or thin film graphene or CNTs antennas unsuitable for microwaves applications [366], [?], [?], [367], [355]. Hence, nanostructured carbon materials films are usually deposited on a limited area of a resonant microwave structure for two kind of applications:

- Shifting the copper etched microstrip antennas' operative frequency and increase the antenna bandwidth *without excessively penalizing the gain*. Furthermore, the "rheostat-like" nature of graphene (voltage dependent conductivity) is under investigation for microwaves passive components (i.e. filters and attenuators) [368], [368]. Besides, the plasmonic nature of their conductivity in *the THz range*, allows to use graphene films "varactor-like" materials to reconfigure antennas [369], [370].
- Sensors for chipless RFID tags as mentioned in chapter 6. In fact, CO₂ [31], NH₃ [371], humidity [372], and NO_x detection by exploiting microwaves resonators' (microstrip antennas, dual split ring resonators, etc.) signal attenuation due to CNTs resistivity change upon gas adsorption or frequency shift stemming from sensor's dielectric properties variation [373], [374], [375], [30]. On the other hand, graphene and reduced graphene oxide have been used

for more "exotic" wireless sensors such as deposition on biosorbable silk to stick to teeth for detection of bacteria [331] or wearable Uv semi-regenerable NH_3 and CO sensors [376].

On the basis of the topics and issues discussed above the following sections will present the experimental procedures and the characterization of two types of microwaves devices predicated on copper etched microstrips loaded with screen printed nanostructured carbon materials films:

- A graphene microstrip patch resonator (provided with the same copper stub shown in figure 8.8 loaded with two different amounts of graphene (12.5 and 25 wt% before thermal treatment). Return loss and "low-frequency" (0.1 Hz-32 MHz) impedance measurements were performed to try to relate the resonant frequency shift brought about by the graphene thick film to the microscopic materials' properties. In addition, in order to understand graphene films' microwave properties, scattering parameters of a microstrip feed line loaded with different graphene concentrations were measured.
- A microstrip copper stub-modified patch antenna containing a 12.5 wt% (before thermal treatment) MWCNTs film. Radiation properties (i.e. gain and radiation pattern) were collected to verify the device's feasibility as C-band transmitting (or receiving) antenna.

Furthermore, functionalization and responsivity to prostate specific antigen (PSA) of both graphene and MWCNTs loaded devices are currently under investigation at the Lausanne Lausanne EPFL.

Part II
Experimental

Chapter 8

Materials and Methods

The present chapter describes *all* the experimental procedures used for the synthesis of the nanostructured materials employed in this thesis and their morphological (FE-SEM, SSA measurements, porosimetry), chemical (TGA/DTA/DSC and XPS), structural (XRD, Raman Spectroscopy), optical (UV-vis. spectroscopy, photoluminescence spectroscopy), electrical (R_{sheet} measurements, EIS, microwaves scattering parameters determination). The chapter is organized in sections and subsections specific for each kind of material, characterization technique and application. Furthermore, a detailed description of fabrication and characterization of the optoelectronic devices assembled with the produced nanostructured materials (DSSCs, colorimetric sensors, electrochromic devices, microwaves resonators and antennas) is provided.

8.1 Materials

- Titanium (IV) isopropoxide (TIIP) (Vertec, 97+%), lithium iodide (ultradry, 99.999%), potassium chloride (ACS, 99.0-100.5%) erbium isopropoxide, ytterbium isopropoxide, tetrafluoroboric acid (48% in water) and ethylenediaminetetraacetic acid disodium salt dihydrate were purchased from *Alfa Aesar*.
- Praseodymium, neodymium, samarium and gadolinium isopropoxides were purchased from *Strem Chemicals*.
- titanium (IV) chloride (99.9%), titanium (IV) n-propoxide (98%), iodine (99.999%), 4-tertbutylpyridine (TBP) (96%), acetonitrile (absolute, 99.5%, over molecular sieves), ditetrabutylammonium cis-bis(isothiocyanate) bis(2,2'-

bipyridyl4,4'-dicarboxylate) ruthenium (II) (N719 dye, 95%), tetrabutylammonium hydroxide 30-hydrate (TBAH), ethanol (absolute, 99.8%), hydrogen peroxide solution (34.5-36.5%), acetic acid(99-100%), ammonium hydroxide solution (30-33%), hydrochloric acid (37% wt), anhydrous terpeneol, 5-15 mPa·s ethyl cellulose (48.0-49.5% w/w ethoxyl basis), 30-70 mPa·s ethyl cellulose (48.0-49.5% w/w ethoxyl basis), 1-hexadecylamine (HDA) (technical, 90%), tetraethyl orthosilicate (99.0%), Pluronic P123, Brij 58, guanidinium thiocyanate (GuSCN) (99%), benzonitrile (99.9%), sodium dodecyl sulphate (SDS, 99%), indium tin oxide nanopowder (ITO NPs, particles size < 50 nm), polyvinyl butyral (Butvar-88 PVB, molecular weight 40000-70000 g/mol determined by GPC), hexane anhydrous, 95%), propylene carbonate (PC, 99.7%), poly(methyl methacrylate) (PMMA, MW \approx 120000 by GPC), trifluoromethylsulfonamide lithium salt (99.95%), 2-(2-Butoxyethoxy)ethyl acetate (\geq 99.2), castor oil (meets testing specifications per USP), ferric chloride (FeCl_3 , 95%), Fe(II)perchlorate hydrate ($\text{Fe}(\text{ClO}_4)\cdot x\text{H}_2\text{O}$), cobalt nitrate hexahydrate ($\text{Co}(\text{NO}_3)_2 \cdot 6\text{H}_2\text{O}$) and isopropanol were purchased from *Sigma-Aldrich*.

- Hydrogen hexachloroplatinate (IV) hydrate (40% Pt by weight) was purchased from *Chempur*.
- 3mm thick FTO glass slides with sheet resistances of 10 Ω/\square and 15 Ω/\square were purchased from *XOP Fisica* (Spain).
- ITO-coated glass slides 15x25x1.1 mm, $R_{sheet} = 5-15 \Omega/\square$ were purchased from Delta Technologies (Canada)
- Aeroxide VP P90 fumed titanium dioxide was kindly given as a free sample by Evonik.
- Cerasolzer CS186-150 soldering alloy was purchased from *MBR Electronics* (Switzerland).
- Kynar PVDF 502-CUH-HC film was used as antireflective and UV blocking layer (<400 nm) and was kindly given as a free sample by *Arkema Inc.*
- HiPCO SWCNTs were purchased from *NanoIntegriss*.
- MWCNTs (diameter 25-45 nm, length > 10 μm) were purchased from *Nanothinx* (Greece).

- Sephacryl size exclusion gel (200HR) was purchased from *GE-Healthcare*.
- Graphene nanoplatelets were kindly provided by *Nanoinnova* (Spain).
- 2-[2-(2-methoxyethoxy)-ethoxy] acetic acid (pH 1.8 100 g/L in H₂O) and 2-butoxyethanol were purchased from *EMD Milli-pore (U.S.)*.
- N-methyl pyrrolidone (≥ 99.5) and linoleic acid (99%) were purchased from *Acros Organic (U.S.)*.
- Cellulose Nitrate membranes (pores size 0.2 μm , diameter 20 mm) were kindly provided by *Whatman (U.S.)*.
- Disperbyk-111 (a polyester co-polymer functionalized with acid groups kindly provided by *BYK Additives and Instruments, Germany*)
- Double sided copper clad FR-4 laminates ($\epsilon_r = 4.35$, $\tan\delta = 0.018$, copper thickness 34 μm , insulator thickness 1/16th “) were purchased from *MG Chemicals (U.S.)*
- All chemicals were used as received with the exception of 4-tert-butylpyridine, which was vacuum distilled before use. Benzonitrile and acetonitrile, were used after prolonged drying (>72 h) over activated 3 Å molecular sieves.

8.2 Materials' synthesis and preparation methods

8.2.1 Titanium dioxide synthesis

The present section describes the experimental procedures used to obtain different titania morphologies. Each sample preparation methodology is classified according to the kind of structure directing agent employed: SiO₂ (MSC-1 and MSC-2), soft-polymeric(Pluronic P-123, Brij-58) and hexadecylamine. Because of its particular morphology, this last sample is referred as *titania (anatase) beads* (consistently with the definition reported in [188], [220], [280], [181], [186]). Three different synthetic approaches were used: hydrothermal (for the silica templated samples), sol-gel (for the soft-polymeric materials), and hybrid sol-gel/solvothermal (for the titania beads).

The ultimate goal of the current investigation stage was to identify the most suitable

(in terms of DSSCs' energy conversion efficiency) TiO₂ morphology to be used for lanthanides doped and chirality selected SWCNTs photoelectrodes.

TiO₂ synthesis by hard templating methods

As mentioned in Chapter 4, TiO₂ mesoporous single crystal (MSC) are particularly attractive as DSSCs' photoanode materials because are capable of coupling large surface area with long-range electron connectivity. Such a structure is achieved by using hard template materials, usually Al₂O₃, SiO₂ or zeolites and the synthetic approach employed is known as "hard nanocasting". Regardless of the kind of templating agent, titania MSCs synthesis is always accomplished by infiltrating of the TiO₂ precursor *into* the template mesopores where the hydrolysis occurs. Hard nanocasting procedures leading to MSCs titania structures requires two fundamental conditions:

- The reaction environment leading to single crystalline structures has to be comprised of a *dilute* non-aqueous solution containing a stabilized TiO₂ precursor to ensure slow nucleation rates [377], [378], [379].
- The growth of TiO₂ has to be confined to the guiding template to achieve an ordered mesoporosity.

Unfortunately, these requirements struggle against each other. In fact, low titania's precursor concentrations favor homogenous (in the bulk solution) over heterogeneous nucleation (within the scaffold material) [380], [379]. Crossland et. al [182] solved this issue by "seeding" mesostructured silica with microscopic nucleation sites for crystal growth. Their approach relies on the following four steps:

1. Synthesis of a closed packed, particles size tunable, array of silica beads by controlled TEOS hydrolysis.
2. Pre-treatment of the silica template with a TiCl₄ solution (seeding).
3. Hydrolysis of the TiF₄ precursor performed under hydrothermal conditions in presence of the SiO₂ scaffold and a stabilizing agent (1-methylimidazolium tetrafluoroborate, imi-H-BF₄).
4. Template's removal by selective etching in aqueous NaOH.

Since this methodology has been proved to be effective to produce TiO₂ thick films with improved electronic mobility compared to nanoparticles [182], [381], we

followed through the procedure reported in [182] and synthesized two MSC titanias to use as DSSCs photoanode materials. Experimental details concerning each step are reported in the next paragraphs.

SiO₂ templating agents synthesis Silica templates were produced by an ammonia catalyzed TEOS hydrolysis-condensation synthetic procedure (see Figure 8.1) in ethanol. Two different SiO₂ (particles size 20 and 50 nm) were targeted by hydrolyzing the TEOS at different NH₃/H₂O ratios. In fact, an empirical equation originally formulated by Bugosh [382] and later perfected by Razink [383], allows to predict silica particles size under different reaction condition:

$$d = A[H_2O]^2 \exp\left(-B[H_2O]^{\frac{1}{2}}\right) \quad (8.1)$$

where the particles size (the diameter d) is given in nm. A and B are to be calculated by using the equations:

$$A = [TEOS]^{\frac{1}{2}}(82 + 151[NH_3] + 1200[NH_3]^2 - 366[NH_3]^3) \quad (8.2)$$

and

$$B = 1.05 + 0.523[NH_3] - 0.128[NH_3]^2 \quad (8.3)$$

Hence, 333 mL of absolute ethanol, 14.2 mL of milli-Q water, 8 mL of NH₄OH (total ammonia concentration 0.3M), 44 mL of TEOS (0.5 M concentration in the

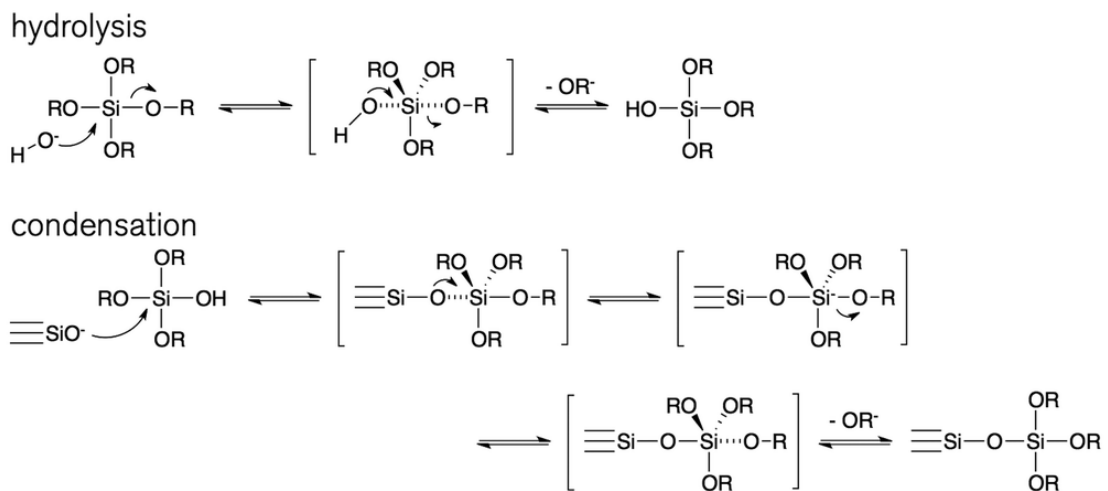


Figure 8.1: General reaction mechanism for a base catalyzed TEOS hydrolysis and condensation. R represent the ethyl (CH₃CH₂-) group.

[385]. It is theoretically predicted that the different surface coverage fractions can greatly affect the surface energy and thus the percentage of $\langle 001 \rangle$ facets during the growth of crystals. Although the fluorine may be released from different sources such as hydrofluoric acid, ammonium fluoride, ammonium bifluoride and the TiF_4 precursor itself, imi- H-BF_4 produces a higher fluorine surface coverage on the TiO_2 nuclei assisting the growth of the $\langle 011 \rangle$ facets [386].

11.8 mL of tetrafluoroboric acid (48% water solution) were added drop-wise to 7.5 g of 1-methylimidazolium under vigorous stirring and ice bath cooling. The reaction mixture was kept under stirring for 2h. After vacuum evaporating the residual water (at 80 °C) a colorless oil (the imi- H-BF_4) was obtained.

For the the MSCs titania hydrothermal synthesis a 40 mM titanium tetrafluoride aqueous solution was prepared by dissolving 1.098 g of TiF_4 in 220 mL of Milli-Q water. The solution pH was adjusted to 2.1 by adding 0.176 mL of 37% HCl. 50 mL of solution were added in a 125-mL-volume Teflon-lined autoclave together with 1.67 mL of imi- H-BF_4 and 0.650 g of silica template. The sealed vessel was kept in a oven for 12 h at 170 °C. The reaction product (a white powder) was collected at the bottom of the autoclave, rinsed with milli-Q water and vacuum filtrated on a 1.2 μm mesh size paper filter (by Whatman). The silica template was removed by selective etching with a 2 M NaOH aqueous solution at 80°C for one hour in a polypropylene becker. The remaining TiO_2 was collected by ultracentrifugation . The whole synthetic procedure was performed for both the 50 nm SiO_2 beads (sample TiO_2 MSC-1) and the 20 nm template sample (TiO_2 MSC-2).

8.2.2 TiO_2 synthesis by soft-polymeric templating method

Polymeric templates

Two different kind of block, non-ionic, co-polymers with tensioactive properties were used to synthesize ordered mesoporous TiO_2 by the sol-gel method: Pluronic P-123 and Brij-58. The former is a tri-blocks co-polymer made out of polyethylene glycol and polypropylene glycol (PEG-PPG-PEG, MW = 5,800 g/mol) chains; the latter is a two-blocks co-polymer comprised of ethoxylated (20 $-\text{CH}_2-\text{CH}_2-\text{O}$ units) cetyl (C-16) group (MW = 1124 g/mol).

TiO_2 -Pluronic P-123

1g of Pluronic P-123 was pre-dissolved by stirring in 25 mL of ethanol. 0.350 mL of TiCl_4 and 2.7 mL of TIIP were added to the solution which was stirred

for 2h in a capped round-bottom flask. TIP constitutes the main Ti source while TiCl_4 was employed as PH adjuster ¹. The reaction mixture possessed a pH of approximately 1.2. The effect of gelation time on the final TiO_2 morphology was investigated by producing two samples: namely TiO_2 -P123A and TiO_2 -P123B. In the former case the sol was kept at 40 °C for 24 h in a Petri dish. In the latter case, the sol was left in the uncapped reaction flask for one week at 40 °C by an oil bath. Both samples were calcinated at 350 °C (ramp rate 5°C/min) for 5 hours.

TiO_2 -Brij-58

A single sample was prepared through this classical surfactant (supramolecular) assisted sol-gel methodology by reproducing the procedure reported in [183]. Briefly, 1 g of Brij-58 was dissolved in 11 mL of absolute ethanol along with 0.175 mL of TiCl_4 and 0.450 mL of titanium n-propoxide under vigorous stirring. The aging of the yellow colored solution was carried out 40 °C over a period of 7 days at . After a multistep thermal treatment (12 hours at 100 °C, 6 hours 260 °C) the resulting gel was calcined in air for 4h at 350 °C to remove the polymeric templating agent and to induce particles crystallization and interconnection.

8.2.3 Anatase beads

Hexadecylamine (HDA) was used as soft, non-polymeric, templating agent in a combined sol-gel/solvothermal synthesis. This preparation method is a well established procedure of TIP controlled hydrolysis in a hydroethanolic solution of HDA (structure directing agent) and KCl (ionic strength regulator) for the production of mesoporous anatase beads [181], [188], [186]. The whole synthetic procedure can be divided in two parts: (i) the preparation of the amorphous precursor beads through the sol-gel method and (ii) the solvothermal process leading to mesoporous, crystalline and monodispersed, anatase submicrometric hierarchical structures. During the first stage of the synthesis 3.98 grams of HDA were dissolved in 400 mL of absolute ethanol along with 1.60 mL of 0.1 M KCl aqueous solution. 9.05 mL of TIP were added to this solution under vigorous stirring. The white milky sol was let settling for 18 h before being filtrated. The amorphous beads precursor were washed three times with ethanol and dried at room temperature. The conversion of the amorphous product into a highly crystalline framework was

¹Although the amount of TiCl_4 is negligible compared to the TIP one, a mixed condensation mechanism between Ti-O-R and Ti-Cl groups leading to the formation of Ti-O-Ti bridges has been reported [387] by other groups.

performed by dispersing it into a solution comprised of ethanol and Milli-Q water in a 2 to 1 v/v ratio in presence of ammonia (0.22 M concentration in the dispersing solution). The resulting mixture was thermally treated in a sealed Teflon-lined autoclave for 18 h at 160 °C. After filtration, ethanol washing and air drying the product was calcined at 500 °C for 2h in air to remove organic residues and produce the mesoporous anatase beads.

A similar procedure was applied to the synthesis of lanthanides doped TiO₂ mesoporous beads. The six lanthanides trivalent ions (Pr³⁺, Nd³⁺, Sm³⁺, Gd³⁺, Er³⁺, and Yb³⁺) were inserted into the anatase structure by replacing the proper amount of TIP with the corresponding lanthanide's alkoxide. Dopant concentrations equal to 0.1, 0.2 and 0.3 at% (the percentage of lanthanide relative to the total number of metallic atoms) were used. Since lanthanide isopropoxides are solid at room temperature, a pre-dispersion step (by sonication in mL of absolute ethanol) before mixing with the TIP in the hydroalcoholic solution containing KCl and HDA was required.

8.2.4 SWCNTs Chirality separation procedures

SWCNTs purification

Raw HiPCO (High Pressure Carbon Monoxide) CNTs were purified using the organic-aqueous phase separation procedure outlined in [277]. Briefly, one gram of HiPCO tubes was sonicated for 5 min in 20 mL of Milli-Q water and transferred into a separation funnel. Hexane was added to the SWCNTs/H₂O mixture to purify the carbon material by phase separation. The procedure was completed when the aqueous phase did not contain any carbon flakes and turned yellow because of the presence of impurities (amorphous carbon, catalyst residues, etc.). Hexane was removed from the organic phase (a mixture of hexane and SWCNTs) by rotatory evaporation. Then, a SWCNTs coarse suspension was created at 1 mg/mL in an aqueous solution of 2% wt. sodium dodecyl sulphate. The mixture was put first in an ultrasonic bath for 5 min to break up the large CNTs agglomerates before being placed under a tip sonicator (Sonifire 450D, Branson, U.S.) with a 0.5 inch flat tip at 20 W/cm² for 20 hours. Before sonication, the tip was set 1 cm away from the bottom of the beaker and placed in a temperature-controlled bath held at 10 °C. Immediately following tip ultra-sonication the sample was ultra-centrifuged at 197,000 G for 15 minutes at 10 °C. The top 90% of the supernatant was removed from each ultracentrifuge tube and directly poured into the gel column described

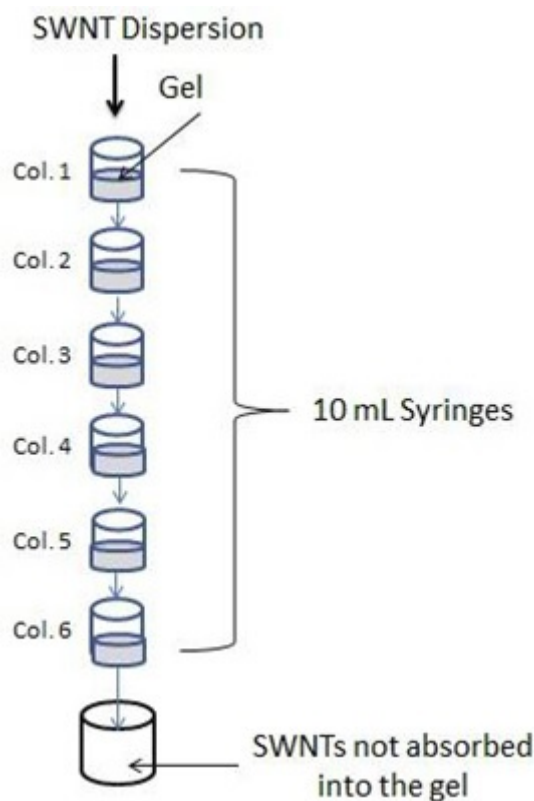


Figure 8.3: Schematics of the original procedure for SWCNTs chirality selection by SEGC.

in the following section.

Chirality separation by SEGC

The general procedure, introduced and outlined by Liu et al. [279], is a two-pass process where chirality separation was performed using the size exclusion gel chromatography (SEGC) method. In this method a number of 10 mL syringes were connected vertically in series and filled with 1.4 mL of allyl dextran-based size-exclusion gel beads (Sephacryl S-200 HR or S-300 HR, GE Healthcare). An illustration of the separation process is presented in Figure 8.3. After the columns were equilibrated with a 2 wt% SDS solution, 5-10 mL of SWNTs, held in an aqueous suspension and ultracentrifuged, were added to the top column. After the SWNT solution had gone through the column, the column was then taken apart and 6 mL of a 2 wt% SDS aqueous solution was added to each syringe to elute the unbound nanotubes. The semiconducting tubes that were trapped inside the gel were eluted with 4 mL of a 5 wt% SDS solution. In order to separate the majority of the semiconducting tubes from the metallic ones, the column was equilibrated

with 2 wt% SDS solution. After the column was equilibrated, the procedure was repeated by loading the unbound tubes into the column until there were no more semiconducting tubes trapped in the gel leaving only highly enriched metallic tubes. In order to get an enriched single chirality, a second pass of the previously filtered tubes was required. Prior to secondary separation, each of the samples were diluted to a 2 wt% SDS solution. Again, a number of 10 mL syringes were arranged vertically in a series and equilibrated. The diluted semiconducting fractions were then added to the top column and allowed to flow through the syringes. The column was then disassembled and the unbound tubes eluted with a 2 wt% SDS solution. The semiconducting tubes that were absorbed into the gel were eluted by inserting 4 mL of 5 wt% SDS solution. The result was a solution with an enriched single chirality.

One disadvantage of requiring two passes through the column is a reduction in CNTs concentration following each pass. As the separated CNTs are to be used in a DSSC, it was necessary to obtain as much of the enriched-chirality CNTs in one pass as possible. In our study, we modified the original procedure to maximize the collection of enriched single-chirality in a single pass. Similar to the original procedure, a number of syringes were vertically arranged in series and plugged with glass wool (see Figure 8.4). The number of syringes arranged depended on the chirality we were targeting to separate from the rest. 1-2 mL of gel was injected into each syringe and equilibrated with 10 mL of 2 wt% of SDS solution. Unbound



Figure 8.4: Apparatus for single pass SWCNTs chromatographic separation

tubes were eluted with 1.8 wt% SDS solution. The number of syringes arranged depends on the specific chirality to be isolated. 1-2 mL of gel have been injected into each syringe and equilibrated with 10 mLs of 2 wt% of SDS solution. Unbound tubes have been eluted with a 1.8 wt% [388] SDS solution. The chiralities targeted in this study are **(6,5)** and **(7,3)**. It was found that in order to separate only those chiralities in a single pass, different ratios of gel/SWNTs were to be used according to the different affinity of specific chiralities for the allyl-dextran gel. In fact, smaller diameter tubes (**(7,3)** diameter = 0.696 nm [270]) strongly interact with the gel requiring a lower degree of gel "overloading" [389]. Thus, to separate enriched **(7,3)** 11 mLs of SWNT/SDS solution have been injected into the top column with 1.4 mL of gel in each syringe. The (7,3) chirality came out in the first three columns; however the most pure sample has turned out to be in the first. On the other hand, by injecting 17 mLs of SWCNTs-SDS solution into 1.4 mL of gel into the top column of a 4 columns stack has resulted in the separation of highly enriched (6,5) (diameter = 0.747 nm [270]) in the fourth column.

8.3 Materials Characterization

8.3.1 Scanning Electron microscopy

Scanning electron microscopy images of the TiO₂, graphene and MWCNTs samples were collected by using a Zeiss Auriga FE-SEM microscope.

8.3.2 X-ray diffraction

Powder X-ray diffraction analysis was used to investigate phase composition, crystallite size, lattice parameters and ordered porosity (i.e. low angle scans) of the produced titanium dioxide solids (different morphology TiO₂ and lanthanides doped titania beads samples). XRD pattern were collected with a Bragg-Brentano reflection geometry by using a Panalytical X'Pert PRO MPD diffractometer employing a Cu K α source ($\lambda = 0.154184$ nm) and a X'Celerator ultrafast RTMS detector. The angular resolution (in 2θ) was 0.001° . A 0.04 rad Soller slit, a 1° divergence slit, and a 20 mm mask were used on the incident beam path, while a 6.6 mm antiscatter slit and a 0.04 rad collimator were used on the diffracted beam path. Low angle scans (0.5 - 10°) were performed on TiO₂-P123-A, samples by using a beam knife, 20 mm mask, a $1/8^\circ$ divergent slit, and a 5 mm antiscatter slit. The soller slit and the collimator were the same as above.

Structural parameters (unit cell's lattice constants) and crystallite size were obtained by the Rietveld refinement procedure performed with the MAUD [390], [391] software. The Rietveld method uses a least squares approach to refine a theoretical line profile until it matches the measured profile [392]. Rietveld refinement is predicated on the following equation:

$$y_{ic} = y_{ib} + \sum_{\phi} S_{\phi} \sum_k G_{\phi}(2\theta_i - 2\theta_k) I_k \quad (8.4)$$

where y_{ic} is the calculated diffraction intensity at point i of the diffraction pattern, G is the normalized profile shape function, I_k is the intensity of the k^{th} reflection, θ_i and θ_k are the angles at point i and of the k^{th} reflection, respectively; S is the scale factor of phase ϕ and the summation is performed over all phases ϕ and over all the k reflections. The intensity of the Bragg reflections I_k is given by the equation:

$$I_k = m_k L_k |F|^2 P_k A_k \quad (8.5)$$

where m_k is the k^{th} reflection multiplicity (the number of symmetry-equivalent reflections contributing to the single observed peak); L_k is the Lorentz polarization factor; $|F|^2$ is the structure factor; P_k is the preferential orientation factor; A_k is the absorption factor. Each parameter in equations 8.4 and 8.5 is affected by both material's and instrumental parameters. For instance, L_k depends on the sample volume, x-ray beam size, sample angular positioning, whereas $|F|^2$ depends on the unit cell volume and on the Debye-Waller temperature factor that quantify atoms displacement from their equilibrium position due to thermal motion. The Rietveld refinement is an iterative procedure to minimize the residual the XRD intensities residual function:

$$y_{res} = \sum_i w_i (y_i^{obs} - y_i^{calc})^2 \quad (8.6)$$

where $w_i = 1/y_i^{obs}$, y_i^{obs} is the observed intensity at the i^{th} point of the diffraction pattern and y_i^{calc} is the calculated one.

8.3.3 Thermal Analysis

Thermal analysis for multiple purposes:

- Verify the removal of the structure directing agents in the TiO₂ samples prepared through the organic polymeric templating route (TiO₂-P123-A, TiO₂-P123-B, and TiO₂-Brij). Simultaneous TG-DTA analyses were performed

on the samples before calcination. The measurements were performed in air between room temperature and 800 °C with a scan rate of 5 °C/min. A Thermal Analysis Apparatus by Netzsch (Germany), model Model STA 409 PC Luxx, was used for the measurements.

- Investigate HipCO SWCNTs thermal stability. In fact, the thermal treatments necessary for DSSCs photoanode sintering may lead to smaller CNTs combustion. Consequently, TGA on the HipCO tubes was instrumental in determining the maximum annealing temperature and atmosphere for the photoanodes containing chirality separated SWCNTs. Thermal analysis was accomplished by using a Q Series SDT Q600 Model (TA Instruments) by burning the samples in air, with a flow rate of 50 mL/min. SWCNTs samples of approximately 3 mg were gradually heated in air from 30 °C to 1000 °C at a rate of 5 °C/min.
- Verify the formation of an (L) monolayer on the screen printed ITO films employed for the electrochromic devices. In this case, 40 mg of annealed (see Section 8.4) ITO nanopowder scratched off the screen printed electrodes was used. Measurements were made in the 30-800 °C temperature range (heating ramp of 5 °C/min) by using a Q Series SDT Q600 Model (TA Instruments). A flowing of air stream was used as atmosphere.
- Screen printing pastes (ITO, graphene, MWCNTs) and FR-4 substrates were characterized for thermal stability by using the same equipment. DSC and thermogravimetric analysis was performed in air in the 30°-800°C temperature range with a scan rate of 5 °C/min. The purpose of this characterization was to determine the maximum heat treatment temperatures for the carbon materials screen printing pastes compatible with the FR-4 substrate decomposition temperature.

8.3.4 UV-Vis. spectroscopy

UV-vis. spectroscopy, both in transmittance and in reflectance mode, was involved in the:

- TiO₂ powder samples (i.e. different morphologies and doped TiO₂ beads) optical characterization. The band gap of the powder materials was calculated by using the UV-Vis diffuse reflectance spectra of the samples. The spectra were collected in the 250-800nm (5.64-1.55eV) range, by using a double-beam

spectrophotometer (Shimadzu, Japan, model UV2600) equipped with a diffuse reflectance integrating sphere accessory. Baseline spectra (100% reflectance) were collected using pressed BaSO₄ powder compacts that were positioned in the sample and reference beams. Data were collected at a scan rate set in slow mode and a slit width of 0.5 nm. Band gap values were determined through the Kubelka-Munk (K-M) function:

$$F(R') = \frac{(1 - R')^2}{2R'} = \frac{\kappa}{\alpha} \quad (8.7)$$

Where R' is the reflectance corrected for the background, κ and α are sample's scattering and absorption coefficient, respectively. When sample's particles size is monodispersed, the K-M function is directly proportional to the absorbing species concentration. Hence, K-M function reported against the incident photons energy can be used to extrapolate the band gap energy from a Tauc's plot. Being TiO₂ an indirect semiconductor [393] 1/2 is used as exponent for the $[F(R')h\nu]$ function. An example of such a procedure is reported in Figure 8.5) for the mesoporous titania beads obtained by the HDA templated synthetic route.

- Chirality separated SWCNTs purity analysis. CNT solutions, before and after the chromatographic chirality separation were analyzed using a Perkin Elmer Lambda 750S UV-vis Spectrometer with a 60 mm Integrating Sphere with wavelengths ranging from 200 nm to 1350 nm. Data were collected in transmittance mode. The UV- Vis resolution of the instrument was from 0.17 to 5.00 nm and the resolution of the NIR ranged from 0.20 to 20.0 nm. Furthermore, The UV-vis-NIR transmittance spectra of CNTs film deposited on FTO glasses were collected in the 1350-250 nm to evaluate the competition between SWCNTs and N-719 dye for light absorption.

8.3.5 Raman spectroscopy

Structural characteristics (i.e graphitization degree) of the carbon materials used for devices fabrication (HipCO SWCNTs, MWCNTs, graphene) were investigated by Raman spectroscopy Raman spectra were acquired with a Renishaw Raman microscope equipped with a 514 nm wavelength argon laser.

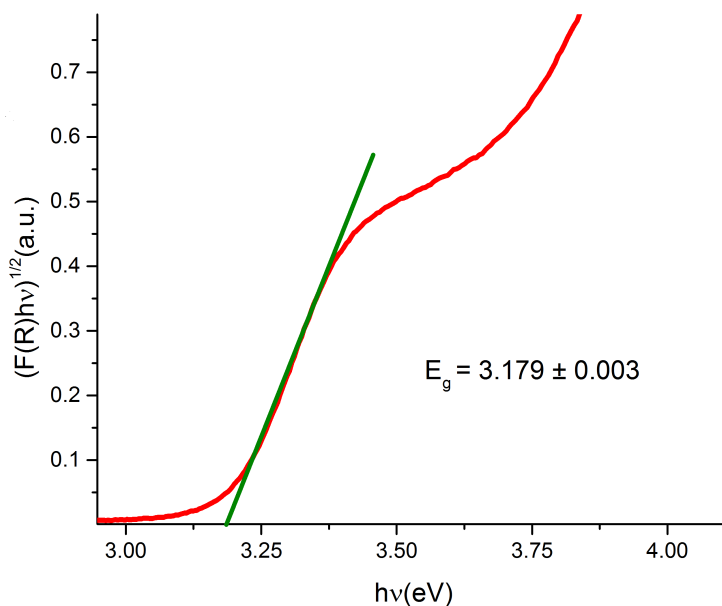


Figure 8.5: Example of Tauc's plot for the anatase beads synthesized through the HDA soft templating approach. "Shoulder peaks" are usually found in proximity of the semiconductor absorption edge because of the large amount of surface defects of nanostructured materials. When the concentration of point defects (i.e. oxygen vacancies) is high enough to shift E_F inside the conduction band an *apparent* shift to higher energies of the measured E_g (i.e. absorption edge) occurs because of the semiconductor's degeneration (Moss-Burnestein shift).

8.3.6 Photoluminescence Excitation (PLE) Spectroscopy

Photoluminescence Excitation (PLE) Spectroscopy provides a useful tool for confirming the chirality separated SWCNTs' purity. In fact, samples containing more than a single chirality, the peaks in the UV-vis-NIR spectra can be very broad. This is aggravated if two species in the same sample have similar band gaps (i.e. close wavelength of the absorption band). To detect and specify the semiconducting species in the sample, UV-vis. absorption spectra can be corroborated by a photoluminescence map (see figure 9.31). To excite the nanotube for PL characterization, transitions involving the second van Hove singularity are generally used. Photoluminescence excitation spectroscopy (PLE) is used to determine all of the semiconducting chiralities in the sample. This technique records the photoluminescence emission spectra while scanning the wavelength of the exciting radiation. From this one can create a 3D map of the PL intensity vs. the emission

and excitation wavelength. Each spot in the map represents a single (\mathbf{n} , \mathbf{m}) species. Since metallic tubes do not luminesce, having a large amount of metallic species in the sample will dilute the semiconducting species causing them to be less intense in the map. Therefore, to produce the desired results, it is important to limit the amount of metallic tubes in the sample.

PLE spectra on chirality selected tubes solutions were obtained with a Jobin-Yvon SPEX Fluorolog 3.22, equipped with 450 W Xe lamp and an InGaAs detector using a 10 mm quartz cuvette. Slit widths for both excitation and emission were set to a 10 nm band-pass, and correction factor files were applied to account for instrument variations. Photoluminescence maps were obtained at 25 °C, with 5 nm intervals in both excitation and emission.

8.3.7 Specific surface area determination and porosimetry

The surface area of hard and polymeric-templated titania samples was determined by using a Quantachrome Monosorb single point BET (Braunaur-Emmet-Teller) system. Specific surface area (SSA) and pore size distribution of the mesoporous anatase beads (and lanthanide doped samples) were further investigated by acquiring the complete N₂ adsorption-desorption isotherm with a with Quantachrome Nova 1200e surface analyzer. The additional surface characterization for the titania beads was required because it is the reference materials for lanthanides doped photoanodes and the scaffold used for phosphonate modified terpyridine metal complexes used employed in colorimetric sensors. SSA and pore size distribution were determined by the BET method (in the 0.05-0.3 relative pressure range) and from the N₂ adsorption isotherm hysteresis loop by the BJH method [394], respectively.

As mentioned in section 4 doping can bring about specific surface area and morphology modifications (because of the dopant effect on the TiO₂ nuclei generation and growth) and can affect the dye loading on the the photoelectrode surface (by changing the number and "strength" of Bronsted or Lewis acid sites on the titania surface). Thereby, complete N₂ adsorption isotherm, porosimetry and dye loading measurements (see section 8.3.8) were performed on the lanthanides doped titania mesoporous beads.

The specific surface area of ITO nanopowders' used for the electrochromic devices was also determined by acquiring the complete N₂ adsorption-desorption isotherm with a with Quantachrome Nova 1200e surface analyzer. Measurements were carried

out before and after the ITO screen printed films annealing. The purpose of such a investigation is to find out the level SSA shrinkage (or increase) due to the paste's processing (see Section 8.4.1) and film's thermal sintering (see section 8.4.4). ITO annealed powders SSA is needed to calculate **L** packing density on the screen printed film and prove the formation of a ligand monolayer on the nanostructured material surface.

8.3.8 Chemisorption studies

Dye loading determination for DSSCs' photoanodes

The amount of dye absorbed by the TiO₂ mesoporous beads films was measured photometrically after chemical desorption of the dye with a 0.02M NaOH solution in a ethanol/water (ratio 1:1) solvent. A Shimadzu UV2600 double-beam spectrophotometer was used for the absorbance determination of the 530 nm peak of the N-719 dye. Similar measurements were carried out on the lanthanides doped films to investigate the effect of doping on the chemisorption equilibrium of the N-719 on the TiO₂ surface.

L packing density determination on ITO powders

Because of the high stability of the Ti-O-P bond, the amount of ligand (i.e. concentration) chemisorbed on the ITO powders cannot be determined by the standard desorption technique described in the previous section and routinely employed for DSSCs photoanodes. Hence, a kinetic chemisorption study by means of Uv-vis. transmittance spectroscopy was carried out.

To estimate the packing density of **L** on ITO nanopwders, 5.0 mg of **L** were dissolved in 140 mL of DI water and the Uv-vis spectrum of the starting solution was recorded. To a 100 mL of this solution, containing 1.14×10^{-5} mol of **L**, 400 mg of ITO NPs were added and the suspension was stirred. After one hour, 2.5 mL aliquot of the suspension was taken, sonicated for 5 min to remove potentially physisorbed molecules from the NPS, and centrifuged. The Uv-vis spectrum of the clear solution was recorded. The aliquots were taken and processed every hour for 5 h. There is no changes in Uv-vis after 2 h of **L** deposition. According to the Beer-Lambert law, the concentration of **L** in the solution is proportional to the absorbance of the solution:

$$C_1 = \frac{A_1}{\epsilon x d}; C_2 = \frac{A_2}{\epsilon x d} \rightarrow C_2 = \frac{C_1 x A_2}{C_1} \quad (8.8)$$

Where C_1 and A_1 are the initial concentration of **L** in the solution, and the absorbance of the initial solution, respectively. C_2 and A_2 are the concentration and absorbance of the solution after deposition. Since the concentration, C (mol/L) is proportional to the amount of substance, n (mol), the equation can be re-written as follows:

$$n_2 = \frac{n_1 x A_2}{A_1} \quad (8.9)$$

Hence, the number of moles of **L** chemisorbed on the ITO nanopowder can be found from the amount of **L** remaining in solution. Then, the packing density (molecules/m²) of **L** on the nanostructured conductor by knowing the ITO powder's SSA.

8.3.9 Scanning Tunnel Microscopy

STM images of bare and (**L**)-functionalized hydrophilic quartz and FTO glasses were recorded with a Nanosurf NaioSTM using Nanosurf Naio 3.4.0 software. All STM images were obtained in the constant current mode by applying a tunneling current, I_t from 70 to 250 pA and a sample bias, V_t , from 200 to 800 mV. The STM tips were mechanically cut from Pt/Ir wire (80/20, diameter 0.25 mm, Nanoscience). The calibration of the piezoelectric positioners was verified by atomic resolution imaging of graphite.

8.3.10 Profilometry

The thickness of DSSCs' photoanodes was measured by using a stylus profilometer (model MAP3D-25, A.P.E. Research, Italy) with a nominal resolution of 10 nm. Photoanodes thickness was instrumental to the dye loading (see section 8.3.8) and electron diffusion length determination through impedance spectroscopy (see section 8.5.1).

A Tencor Alpha-Step-200 profilometer equipped with a standard stylus of 12.5 μm radius was used for the colorimetric sensor films' thickness measurements. Sample leveling was automatically computed after each scan and digitized using GetData Graph Digitizer 2.24 software. Typical scan lengths were 10,000 μm .

8.3.11 X-ray Photoelectron Spectroscopy

XPS measurements on the phosphonic acid-modified terpyridine ligand (**L**) and FeL₂ functionalized hydrophilic quartz and mesoporous TiO₂ beads were

performed using a Thermo Scientific K-Alpha surface analysis system equipped with a monochromated Al K α X-ray source (1486.7 eV). Ultrahigh vacuum (UHV) conditions (10^{-9} to 10^{-10} Torr) were maintained during the experiment. The instrument is fitted with an electron flood source for an effective charge compensation. The Ti $^{4+}$ 2p $_{3/2}$ peak of TiO $_2$ at 458.6 eV was used as an internal reference peak for calibrating the binding energy. A Shirley algorithm was used for background subtraction and a Powell peak-fitting algorithm for data analysis [22], [395], [396]. The elemental ratio was determined using Wagner atomic sensitivity factors [22]. In fact, conversion factors are needed for XPS quantitative analysis because peaks' area depends on both the number of atoms in the detected volume and on the degeneracy of each spin state due to spin-orbit coupling. For instance, the area ratio for the two spin orbit peaks (2p $_{1/2}$:2p $_{3/2}$) will be 1:2 (corresponding to 2 electrons in the 2p $_{1/2}$ level and 4 electrons in the 2p $_{3/2}$ level). These ratios must be taken into account when analyzing spectra of the p, d and f core levels. When quantifying XPS spectra, Relative Sensitivity Factors (RSF) are used to scale the measured peak areas so that variations in the peak areas are representative of the amount of material in the sample surface. Wagner atomic sensitivity factors (S_i) are special RSF tabled for a wide range of experimental conditions. Indeed, (S_i) take into account the RSFs and instrumental parameters to relate the XPS peaks' area (I_i) to the number of atoms per cm 3 (n_i):

$$n_i = \frac{I_i}{S_i} \quad (8.10)$$

where S_i is given by the equation:

$$S_i = f\sigma\phi yAT \quad (8.11)$$

where f is the X-ray flux density, σ is the photoelectric cross-section, ϕ is an angular correction factor, y is a photoelectric ground state factor, A is the area from which photoelectrons are detected, and T is the efficiency of detection of emitted photoelectrons of that energy by the analyzer.

8.4 Devices Fabrication

8.4.1 Screen Printing pastes preparation

Screen printing pastes were formulated and used for six different kind of devices:

- DSSCs and iron colorimetric sensors (TiO_2 pastes).
- Electrochromic devices and iron sensitive microwaves resonators (ITO pastes).
- Microwave patch resonators and antennas (graphene and MWCNTs pastes).

TiO_2 pastes

TiO_2 screen printing pastes preparation was based on the procedure described by Ito et al. [154] concerning the formulation of glass-frit free inks for DSSCs electrodes (see figure 8.6 for all the steps involved). α -terpineol was employed as paste non-

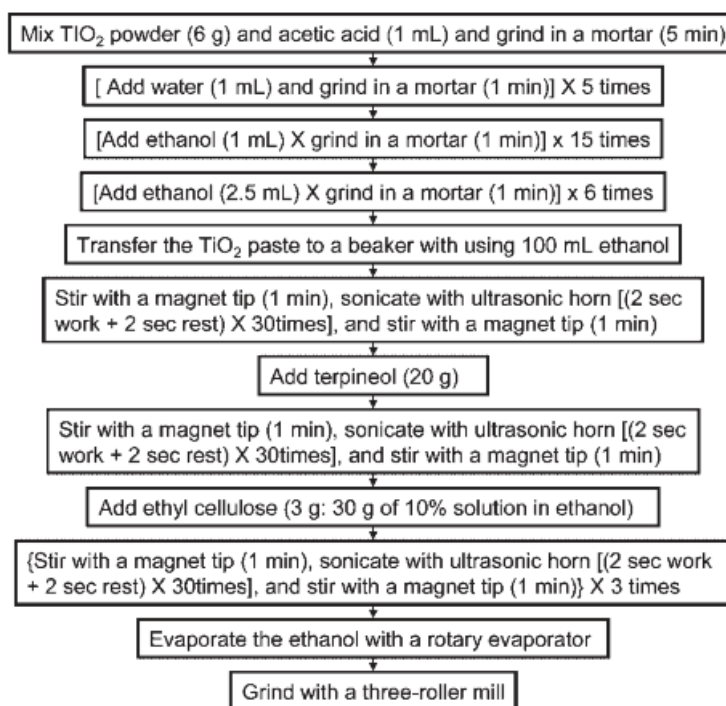


Figure 8.6: Fabrication scheme of screen printing paste from a TiO_2 nanocrystalline powder. Adapted with permission from [154].

volatile solvent. Absolute ethanol was used as vacuum heating removable solvent for the TiO_2 powders and binder (ethyl cellulose) dispersion. A combination of acetic acid and Milli-Q water were used as dispersing agent (with a $\text{CH}_3\text{COOH}/\text{H}_2\text{O}$ volume ratio of 1:5). A modification was introduced to the original procedure: a 80 °C thermal treatment (4h) to improve long term storage stability [194]. Furthermore, titania powders synthesized by the hard templating route were mixed with a small amount of P90 titania (10 wt % based upon TiO_2 -MSC-1 and TiO_2 -MSC-2 amount). The reason for such a modification stems from the low SSA of the silica templated samples (see section 9.1.1). Indeed, a small percentage of P90 favors the

high temperature particles sintering ensuring the formation of an interconnected framework throughout the photoanode.

ITO paste

ITO based screen printing paste was prepared as follows. ITO NPs were dispersed in anhydrous ethanol by using a PQ-N04 planetary ball milling (by Across International, U.S.) system equipped with 75 mL agate jars and 6mm agate beads. The milling time and speed were 24 h and 200 rpm, respectively. A mixture of 2-[2-(2-methoxyethoxy)-ethoxy] acetic acid surface treating agent and in a ratio 4.7:1 was used as dispersing agent during the milling. The dispersing agent had been previously diluted with anhydrous ethanol. The mass ratio of dispersing agent to ITO NPs has been set to 1:3.5 (5.0 wt% Dispebyk 111 and 23.3 wt% of 2-[2-(2-methoxyethoxy)-ethoxy] acetic acid based upon ITO solid). Disperbyk 111 amount was kept relatively low to avoid an excessive viscosity reduction during the printing step. Besides, further steric stabilization of the dispersion was achieved by adding a mixture of high boiling point solvents (α -terpineol, 2-butoxyethanol, 2-(2-Butoxyethoxy)ethyl acetate) along with a proper amount of Butvar 98 Polyvinyl butyral (PVB, molecular weight 40000-70000 g/mol determined by Size Exclusion Chromatography, Sigma Aldrich) . PVB had been pre-solubilized in anhydrous ethanol (48 h at 50°C) to obtain a 15 wt% binder solution. The stabilized ITO dispersion showed negligible settling after ball milling. and was evaporated under reduced pressure for 2 h at 40°C to remove the excess of ethanol and obtain a printable paste.

Graphene and MWCNTs pastes

Graphene and MWCNTs screen printing pastes were prepared through a high energy homogenization procedure. Briefly, ethyl cellulose (9.4 wt %), which acts as a binder and dispersion steric stabilizer, a 80:20 wt% α -terpineol/NMP mixture, castor oil (5.2 wt%), linoleic acid (3.3 wt%), $\text{Co}(\text{NO}_3)_2 \cdot 6\text{H}_2\text{O}$ (0.05 wt%) and graphene (or MWCNTs), were dispersed in 80 mL of ethanol by stirring (2 hours) and sonication (15 hours by using a Ti horn). Ethanol was evaporated under reduced pressure in order to produce a printable paste. Two formulation differing for the graphene amount (25 and 12.5 wt%) were prepared, whereas a single 12.5 wt% paste was used for MWCNTs deposition.

8.4.2 DSSCs' assembly

Photoanodes' active area (about $3.5 \times 3.5 \text{ mm}^2$) was patterned on the FTO glass by screen printing the ethyl cellulose-based pastes in α -terpineol with a manual screen printing table (model 60-90, Mismatic, Italy) equipped with a 34 T polyester mesh screen. The printing process was repeated in order to achieve a TiO_2 electrode thickness after thermal treatment of 10-15 μm (corresponding to 2-3 layers depending on the screen printing paste composition). Titania films annealing in air was performed through different stages to avoid film cracking caused by the thermal expansion coefficient difference between FTO and TiO_2 : 325 °C for 5 minutes, 350 °C for 5 minutes, 450 °C for 15 minutes, and then finally 500 °C for 15 minutes. The furnace temperature was ramped up at a rate of 5 °C/min. The main goal of this first thermal treatment was to burn off the organic components of the screen printed film. Following the first heat treatment, the glasses were soaked again in a TiCl_4 solution at 70 °C for 30 minutes and then rinsed with deionized water and ethanol. The second TiCl_4 treatment aims at the hydroxylation of the TiO_2 electrode surface which is instrumental to promote particles sintering during the second thermal annealing carried out a 500 °C in air for 30 minutes.

The photoanodes were sensitized for 15 min by using a 20 mM solution of N719 with 25 mM tetrabutylammonium hydroxide 30-hydrate (TAAH) in acetonitrile, according to the procedure of Nazeruddin et. all [397]. TAAH serves as dye's solubilizer in acetonitrile.

Pt (as 50 mM hydrogen hexachloroplatinate (IV) solution in absolute ethanol) was "painted" on a drilled (1 mm diameter hole) FTO glass to serve as DSSCs cathode. Pt-coated FTO glass slide was thermally treated at 450 °C for 30 minutes. The two electrodes were sandwiched together by means of a 25 thick Surlyn gasket cured for 30 min at 120 °C. The electrolyte was injected into the cell's structure with a vacuum syringe. The electrolyte composition used was 0.6 MEMII, 0.5 M TBP, 0.1 M GuSCN, 0.1 M LiI, and 0.03 M I in benzonitrile [86]. The hole in the counter electrode was sealed with a 60 μm thick Surlyn gaskets covered with a thin microscope glass slide by melting the gasket with a hot solder tip. Copper wires were fixed on both electrodes by using a MBR Electronics USS.9210 Ultrasonic Soldering System with Cerasolzer CS246-150 as soldering alloy. Kynar antireflection and UV-blocking film was applied over the cell on the photoanode side by fixing it using 3M bi-adhesive tape.

The original procedure was modified for the cells employing chirality selected DSSCs photoanodes. In fact, the photoanodes' structure was comprised of a thin layer (50-

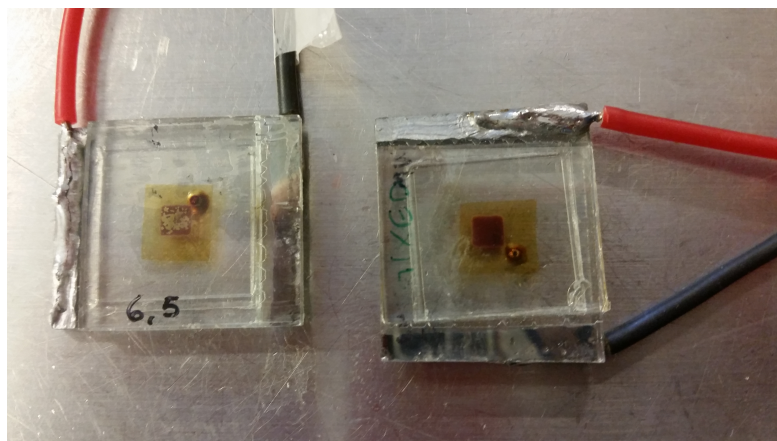


Figure 8.7: DSSCs assembled with photoanodes comprising of SWCNTs films. Left: a cell assembled by printing the anatase beads directly on the SWCNTs film, lack of adherence of TiO_2 on the CNTs is evident. Right, DSSCs with a three layered photoanode: SWCNTs/P90/titania beads. The TiO_2 adherence on the CNTs film was considerably improved.

100 nm) of SWCNTs deposited on the FTO substrate. Mixed and single chirality SWCNTs films were prepared by vacuum filtrating of SDS-SWCNTs solutions obtained from the chromatographic process on $0.2 \mu\text{m}$ pore size cellulose nitrate membranes. Isopropanol has been used as wetting agent to prevent films' cracking. The CNTs accumulated on the cellulose nitrate filter were washed many times to remove any SDS residue. SWCNTs films were transferred to the FTO coated glass by decomposing the cellulose nitrate filter in a acetone vapors bath [398]. The FTO/SWCNTs substrate was then coated with a thick layer of P90 TiO_2 and a scattering layer composed of anatase mesoporous beads. Although, as mentioned in Chapter 4, ordered mesoporous titanias possess desirable properties for DSSCs applications (high specific surface area, light harvesting due to radiation scattering, long range order for electron transport, etc. see also Sections 9 and 9.1.2) their direct printing on SWCNTs presents adherence issue coming from the porous nature of the material. Hence a $10 \mu\text{m}$ layer of P90 nanoparticles was printed on top of the CNTs as buffer layer. Finally, a $4\text{-}5 \mu\text{m}$ thick layer of titania beads was screen printed to complete the photoelectrode structure. Furthermore, photoanodes annealing was also modified: $325 \text{ }^\circ\text{C}$ for 5 minutes in air, $350 \text{ }^\circ\text{C}$ for 5 minutes in air, $350 \text{ }^\circ\text{C}$ for 5 minutes in vacuum, $450 \text{ }^\circ\text{C}$ for 15 minutes in vacuum, and then finally $500 \text{ }^\circ\text{C}$ for 15 minutes also in vacuum. TiO_2 sintering steps ($450\text{-}500 \text{ }^\circ\text{C}$) were carried out in vacuum to prevent the SWCNT films from combusting.

8.4.3 Iron colorimetric sensors

2,2':6',2"-terpyridin-4'-ylphosphonic acid, (**L**), was synthesized according to the procedure reported in [21] and [22]. A detailed compositional (NMR) and structural characterization (single crystal XRD) is provided in reference's [21] supporting information. (**L**) and its Fe(II) complex were anchored on three morphologically different supports:

- (1) **"Flat", non-nanostructured surfaces** : FTO coated soda-lime glasses and hydrophilic quartz slides. These two systems represent the prototypes of thin films substrates. Quartz slides had been functionalized with -OH groups by the RCA treatment as described in [280].
- (2) **Nanostructured oxide** : anatase nanopowder.
- (3) **TiO₂ thick films** : P-90 and TiO₂ mesoporous beads screen printed films. These structures constitute the actual colorimetric sensor.

(**L**) and Fe(**L**)₂ self assembled monolayers (SAMs) anchored on hydrophilic quartz or FTO surfaces were characterized by scanning tunnel microscopy (STM) and UV-Vis. spectroscopy. (**L**)-SAMs were formed on the FTO (or OH functionalized quartz) by immersing the substrates into a 1.3 mM (**L**) aqueous solution for 8 hours. To test the formation of the Fe(**L**)₂ complex from the ligand chemisorbed on FTO or hydrophilic quartz, the substrates were immersed in a 0.1 mM Fe(ClO₄)₂ solution. Furthermore, Fe(**L**)₂ coordination compound was pre-formed in solution by combining 4.5 10⁻⁵ M (**L**) aqueous solutions with a 4.5 10⁻⁵ M Fe(ClO₄)₂ solutions to verify the formation of complex SAM on flat surfaces.² UV-vis spectroscopy was used to determine the molecular density of monolayer films deposited on 1 mm thick quartz substrates as previously reported [399]. The instrument used for these experiments was a dualbeam Varian Cary 50 UV-vis spectrophotometer, with a modified sample holder for thin film measurements. Assuming uniform distribution of Fe(**L**)₂ complex molecules on the surface and also that the extinction coefficient in solution and in a monolayer is the same, we can relate the absorbance spectra

²Although this approach is easy to implement other complexes besides [Fe(**L**)₂](ClO₄)₂ can be created. For instance hydration water or perchlorate counter ions can penetrate the metal ion coordination sphere and replace one of the two terpyridine ligands. A similar effect can occur when the ligand is chemisorbed on a solid surface and is sensitized with a solution containing the metal ion. This is the reason why, for example, the whole metal-polypyridine complexes have to be obtained as pure powders by organic chemistry synthetic approaches when they are employed as dyes in DSSCs.

with a calculated surface concentration, rewriting the Beer-Lambert law as follows:

$$\Gamma_{monolayer}[\text{molecules} \cdot \text{cm}^{-2}] = \frac{A10^{-3}[\text{cm}^{-3}]N_{av}[\text{molecules} \cdot \text{mol}^{-1}]}{2\epsilon[M^{-1}\text{cm}^{-1}]} \quad (8.12)$$

where $\Gamma_{monolayer}$ is the complex surface concentration, A is the monolayer absorbance N_{av} is the Avogadro number and ϵ is the molar extinction coefficient for the 560 nm MLCT band ($11970 \text{ M}^{-1} \text{ cm}^{-1}$ for the complex in solution). The factor 2 in the denominator was employed because the quartz slides were functionalized on both sides. The monolayer absorbance for $\text{Fe}(\mathbf{L})_2$ was 0.0029. $\Gamma_{monolayer}$ turned out to be approximately $0.7 \text{ molecules/nm}^2$, which corresponds to a molecular cross section (area) for the $\text{Fe}(\mathbf{L})_2$ complex of 1.43 nm^2 . The value is close to the 1.21 nm^2 per molecule determined by X-ray crystallography [21]. The peak at 313 nm (the ligand ICT transition) was chosen to estimate the surface coverage of (\mathbf{L}) . Peak's extinction coefficient is $4910 \text{ M}^{-1} \text{ cm}^{-1}$ (in solution). (\mathbf{L}) monolayer absorbance was 0.002. (\mathbf{L}) area was found out to be 0.81 nm^2 per molecule.

Pristine and (\mathbf{L}) -functionalized anatase nanopowders (and P-90 powders as well) were morphologically characterized by transmission electron microscopy (with an Hitachi H7000 TEM). (\mathbf{L}) was immobilized on the anatase nanopowder by creating a suspension of anatase (200 mg) in a 0.127 mM ligand solution in DI water (40 mg of (\mathbf{L}) in 40 mL of water. The mixture was kept under stirring for 24 hours before being centrifuged and the liquid supernatant removed. The solid residue (the (\mathbf{L}) -functionalized anatase nanopowder) was thoroughly washed with DI water (50 mL for three times), centrifuged, decanted, washed with ethanol (50 mL for three times) and vacuum dried for 24 h.

\mathbf{L} -nanoanatase compound was once again used to create a suspension in 40 mL of DI water containing 45 ppm of Fe^{2+} ions (from $\text{Fe}(\text{II})(\text{ClO}_4)_2 \cdot 2\text{H}_2\text{O}$). The mixture was stirred for 24 hours. However, the color change (from white to deep pink) of the nanoanatase powder occurs within 30 s and longer stirring times have no influence on the light absorption. The suspension was separated by centrifugation. The resulting deep magenta solid was washed six times with 50 mL of DI water, and three times with 50 mL of ethanol, centrifuged and decanted. The solid precipitate was then dried in vacuum for 24 hours.

P-90 and TiO_2 mesoporous beads were screen printed on RCA treated soda-lime microscope glass slides. Paste composition was based on the α -terpineol ethyl cellulose solvent binder combination. Since film uniformity is instrumental to the color change appreciation and there is no specific film thickness to be targeted

(like the 10-15 μm needed for the DSSCs photoanode), a 90T (230 mesh) mesh count screen was used for printing the titanium dioxide films (instead of the 34 T, 86 mesh, employed for the DSSCs). Higher mesh count leads to lower thickness per printed layer but less surface indentation. Consequently, films' color appears more uniform. Films geometrical area was 1 cm^2 . Different number of layers were deposited on the glass substrate to enhance sensors sensitivity. The screen printed TiO_2 films were "activated" for colorimetric detection by immersing them into a 0.065 mmolar (**L**) aqueous solution for 30 minutes. Then, the films were washed with DI water and isopropanol and finally dried by a stream of air or N_2 . The same procedure was used for films regeneration.

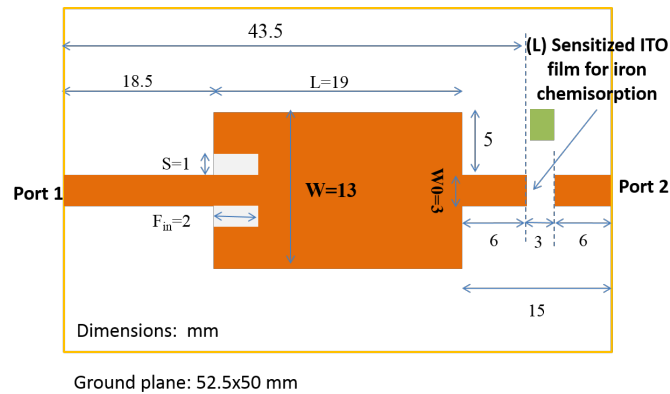
8.4.4 Electrochromic devices

Screen printing of the ITO based paste on ITO glass was performed with a 90 T polyester mesh screen (by Mismatic, Italy). The printing procedure was repeated 3 times to achieve a suitable thickness of the porous ITO support. A drying step of 5 min at 120 $^\circ\text{C}$ was performed between each layer print-ing. To anneal the screen-printed film, it was placed into the Fisher Scientific Programmable Muffle Furnace and the temperature was increased (5 $^\circ\text{C}/\text{min}$) to 500 $^\circ\text{C}$ and held at that temperature for 1 h, after which the temperature was (5 $^\circ\text{C}/\text{min}$) to 600 $^\circ\text{C}$, and held at 600 $^\circ\text{C}$ for 1 h. Screen printed and annealed ITO films were functionalized by immersing the plate in an aqueous solution of **L** (1 mM). The plates were left in the solution for 2 hours then removed, washed with isopropanol, and dried by an N_2 stream. The **FeL**/ITO complexes were formed by adding known volumes of 10 ppm FeCl_2 solution onto the **L**/ITO plates. The electrolyte used for the electrochromic devices was synthesized following a procedure by Shankar et al. [400] Polymethylmethacrylate (700 mg), trifluoromethylsulfon-amide lithium salt (300 mg), dry acetonitrile (8.9 mL), and dry propylene carbonate (1.7 mL) were added to an oven-dried glass vessel under a nitrogen atmosphere. The weight percent of each component was maintained at 70:20:7:3 wt% respectively. The electrolyte was stirred vigorously overnight, at which point it was viscous liquid. Approximately 0.2 mL of this electrolyte was drop cast onto a modified ITO plate to ensure full coverage of the modified section of the ITO. The plate was placed into an oven at 60 $^\circ\text{C}$ for 10 minutes before a second unmodified ITO plate was placed onto the electrolyte to create an electrochromic device.

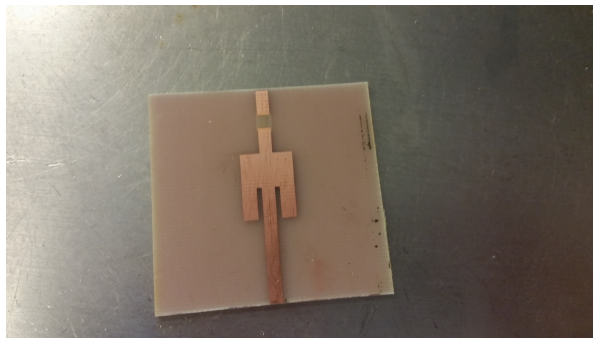
8.4.5 Microstrip devices (Microwaves resonators)

Iron sensitive antenna

Standard double sided FR-4 ($\epsilon_r = 3.8$, copper thickness 1 oz., i.e. $34 \mu\text{m}$, dielectric thickness 1.57 mm) was used as substrate for the device fabrication. Copper antenna's pattern was defined by the toner transfer method. Antenna's pattern (see figure 8.8 a)) was printed on Konica Minolta Photo Quailty Matte paper (Konica Minolta Inc., Japan) by using a high resolution laser printer. Then, the "mask" was transferred on one side of the copper laminate by a clothes iron. Metal etching was performed into a 40 wt% FeCl_3 aqueous solution. Finally, the antenna structure was washed with a mixture of water, sodium carbonate, and 2-buthoxyethanol [317] to remove the printer toner from the intact copper traces. The device was "loaded" with a 3x3 mm screen printed ITO nanoparticles film inserted into a gap on a stub opposite to the feeding line (opposite to the patch wings, see Figure 8.8 b)). Screen printed paste's curing (i.e. solvents evaporation)



(a)



(b)

Figure 8.8: (a) schematics of microstrip (etched) patch antenna loaded with an ITO film across the gap in the copper etched traces. The ITO film is comprised of indium tin oxide nanoparticles (with dispersing agent functional groups adsorbed on the surface) and a thermoplastic binder: PVB. (b) picture of the actual device.

was performed in a muffle furnace at a temperature of 160 °C for 3 hours. The ITO film was sensitized with a 0.064 mM aqueous solution of (**L**). Fe³⁺ uptake was performed with 25 μL of a 10 ppm ferric chloride solution.

Graphene and MWCNTs loaded antennas

Microstrip patch antennas (i.e resonators) were fabricated as described in the previous section. However, the bare (not loaded with carbon materials films) microstrip patch rectangular resonator (and antenna) was designed to operate at 4.9 GHz, which is within the microwaves C-band. Since the antenna shown in Figure 8.8 resonates at around 7.9 GHz, the patch W/L ratio needed to be changed for the resonance to occur in the low frequency part of the C-band. Hence, the patch dimension was set to 15x12 mm² and the feed line width to 3 mm (to match a 50 Ω impedance input RF cable). On the other hand, the length of the stub opposite to the feeding line, where 3 mm gap for the carbon materials films insertion is located, was kept to a 15 mm like in figure 8.8. Furthermore, a 1 mm hole was drilled into the PCB to short circuit the antenna with the copper ground plane. Three different carbon materials loadings were used: (i) 25 wt and 12.5 wt % for the graphene loaded antenna; (ii) 12.5 wt % MWCNTs (for the microstrip patch antenna). The amount of carbon materials refers to the the total mass of ink formulation. In each case the ethyl cellulose binder concentration was kept at 9.5 wt% with respect to the total ink's mass. Additionally, 2x1 cm graphene films were deposited deposited on bare FR-4 substrate, after previous copper etching on both sides, for sheet resistance measurements and low frequency impedance characterization. Moreover, 3x3 mm graphene films were deposited also into a 2.6 mm gap photo-etched out of a 3mm wide microstrip feed line fabricated on 1.57 mm thick FR-4 substrate (see figure 8.9). All films were cured at 180 °C for 3h. Such a temperature is insufficient to promote complete particles diffusion and sintering. On the other hand, the bi-dimensional nature of graphene sheets (and monodimensional shape of MWCNTs) ensures electrical connectivity throughout the film (how verified by the sheet resistance measurements). In addition, as shown in Figure 8.10, a 180 °C curing temperature is about 35 °C higher than the ethyl cellulose binder glass transition temperature and largely above the FR-4 glass transition mid-point. Thus, polymer chains' reorganization occurring at T_g should favor conductive filler units contact and embedding into the substrate.

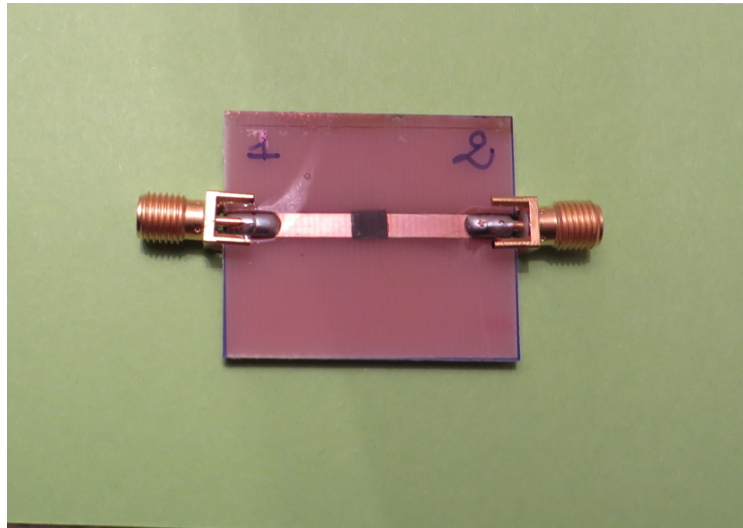


Figure 8.9: Microstrip line with graphene thick film deposition in the gap. An identical but graphene-unloaded transmission line was used as reference. The ground plane is located on the rear part of the device and is not visible.

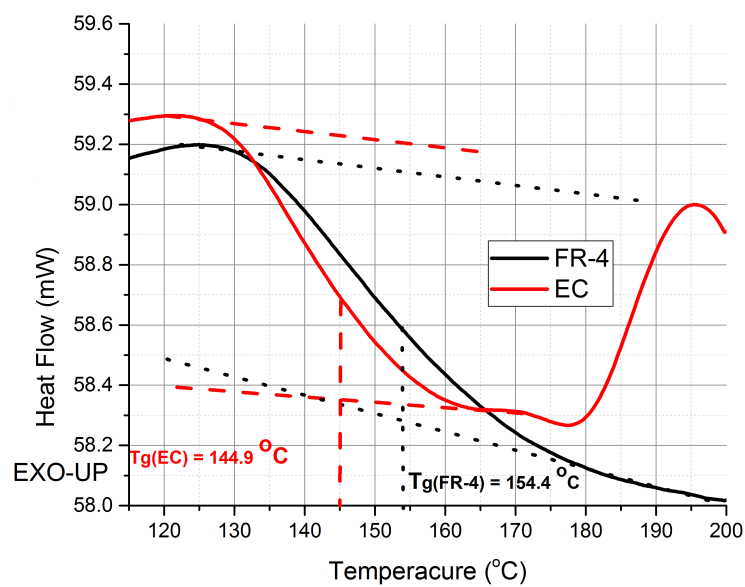


Figure 8.10: DSC thermogram of ethyl cellulose binder (EC) and FR-4 substrate. Glass transition mid-point temperatures are reported.

8.5 Devices characterization

8.5.1 DSSCs

I-V curves

Current-Voltage characteristics (under dark and illumination) were acquired by a 1286 electrochemical Interface from Solartron Analytical, U.K., using full combo Zplot/corrware software by Scribner Associated Inc., U.S.A. During irradiation measurements, the cell was placed underneath an Asahi Spectra HAL-320 Sun Simulator measuring 1 sun at AM 1.5 G. Prior to experiments, calibration was performed with an Asahi Spectra sun checker to verify the intensity of the irradiance to be within $\pm 1\%$. DSSCs V_{OC} , I_{SC} , FF, R_s and R_{sh} were obtained from the cells polarization curves under illumination. R_s and R_{sh} were obtained through the graphical procedure depicted in Figure 8.11. In fact, It is possible to approximate the series and shunt resistances from the slopes of the I-V curve at V_{OC} and I_{SC} , respectively [256]. The resistance at V_{OC} , however, is *proportional* to the series resistance but it is larger than the series resistance. Nevertheless, the method is an effective technique to estimate R_s without collecting I-V curves at different irradiances [256]. On the other hand, dark polarization curves allow for the determination of cell's saturation dark current I_o by using the following procedure predicated on the single-diode model for solar cells (see Figure 8.12):

$$I_{dark} \approx I_0 \exp \frac{qV}{mKT} \quad (8.13)$$

where the approximation stands at intermediate voltages (high enough to neglect the -1 term in the Shockley equation but not too large to be affected by the series resistance effects). Furthermore, since the cell V_{OC} is used as voltage reference the term V_j (the built-in potential of the junction) is already taken into account. The "diode" junction, in the specific case of DSSCs corresponds to the $\text{TiO}_2/\text{dye}/\text{electrolyte}$ interface. Hence, plotting $\ln |I_{dark}|$ vs voltage permits to extrapolate I_0 from the intercept and m from the slope. Figure 8.12 reports the special case of a DSSC (from our lab) containing **(6,5)** chirality SWCNTs in the photoanode. For this cell two junctions are present: the one corresponding to the $\text{TiO}_2/\text{dye}/\text{electrolyte}$ interface, located between 0.3 and 0.5 V, and the one belonging to the $\text{TiO}_2/\text{chirality separated SWCNTs}$ interface located between 0.1 and 0.2 V [153]. As explained in Chapter 4 the thermionic emission model for

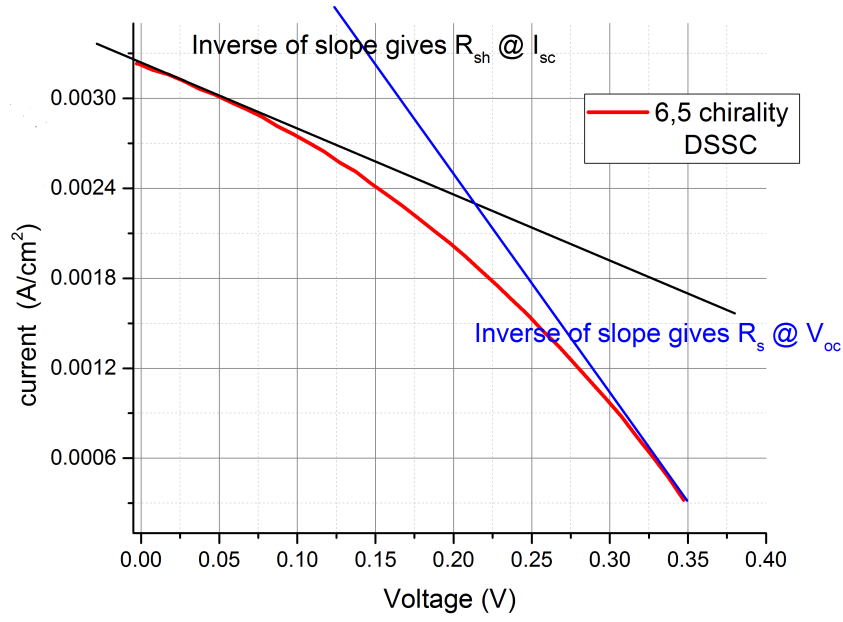


Figure 8.11: Extrapolation of R_s and R_{sh} from DSSCs I-V under illumination. DSSC containing (6,5) chirality SWCNTs is reported in figure as an example. The low R_{sh} effect due to the contact between CNTs and the electrolyte results into high values of the slope at the I_{SC} point.

the charge transfer between the TiO_2 and the CNTs can be applied. Hence, the “Schottky-like” barrier height Φ_B is then obtained through the thermionic emission current equation:

$$\Phi_B = \frac{k_B T}{e} \ln \frac{a A T^2}{I_o} \quad (8.14)$$

where k_B is the Boltzmann constant, T the temperature, e the elementary charge, A the Richardson constant for TiO_2 ($6.71 \times 10^6 \text{ AK}^{-1} \text{ m}^{-2}$) and a the area of the junction. Quantum Efficiency (IPCE) IPCE was measured in DC mode by a custom made apparatus between wavelengths of 400-800 nm and a scan interval of 5 nm. The instrument was assembled with a 250 W halogen lamp 84 (Newport-Oriel), a Spectral Products CM110 1/8 m monochromator with variable resolution slits, a Newport broadband beam splitter, a calibrated poly-Si detector, and all of the necessary lenses to focus the beam of light. Data were collected with a National Instruments NI 9219 24-bit universal analog input, and the control software was written by LabView.

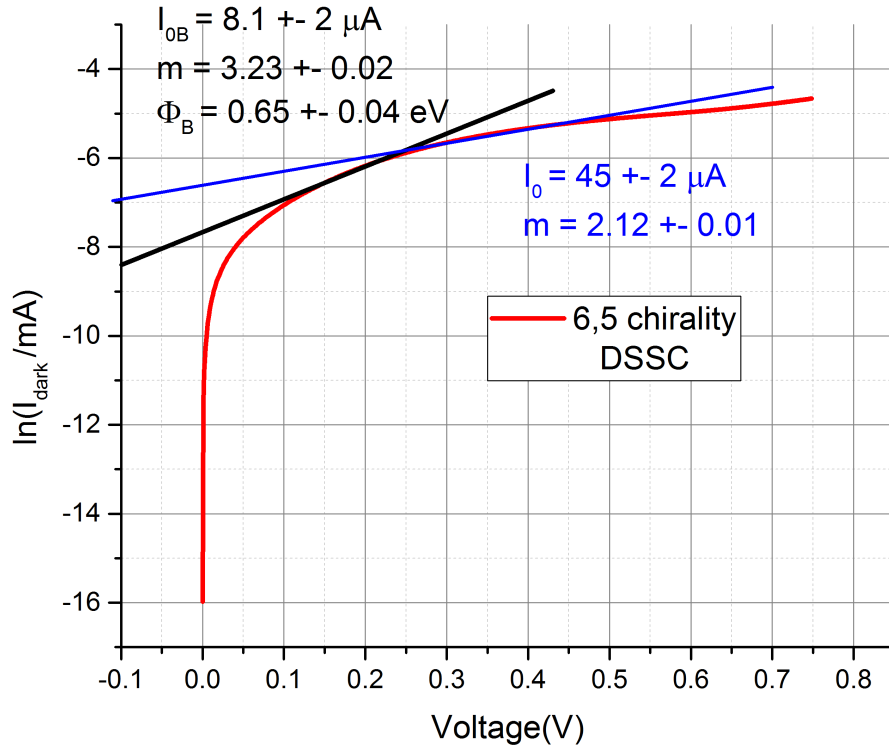


Figure 8.12: Example of the extrapolation procedure to calculate of I_0 from a DSSC. DSSC containing (6,5) chirality SWCNTs is reported in figure as an example. Two junction, and consequently two saturation dark currents and two ideality factors are present. I_0 belongs to the TiO₂/dye/electrolyte interface, whereas I_{0B} refers to the SWCNTs/TiO₂ interface. I_{0B} allows to estimate the Schottky-like barrier at the anatase/CNTs junction (see text).

Electrochemical impedance spectroscopy

Electrochemical impedance spectroscopy characterization (by means of a Solartron 1260 analyzer) was carried out with the specific aim of determining the electron diffusion length as parameter indicative of transport to recombination competition for lanthanides doped TiO₂ mesoporous beads photoanodes (see Chapter 4. The EIS spectra were acquired under 1 sun illumination provided by a white light led with a DC bias of ≈ 0.5 V. Measurement frequency range was 0.1-10⁵ Hz. The spectra were fitted by using the ZView software and adopting the transmission line model [401]. A schematics of the equivalent circuit employed for the fitting of the data and typical DSSCs' impedance spectra are provided in figure 8.13. Each cells'

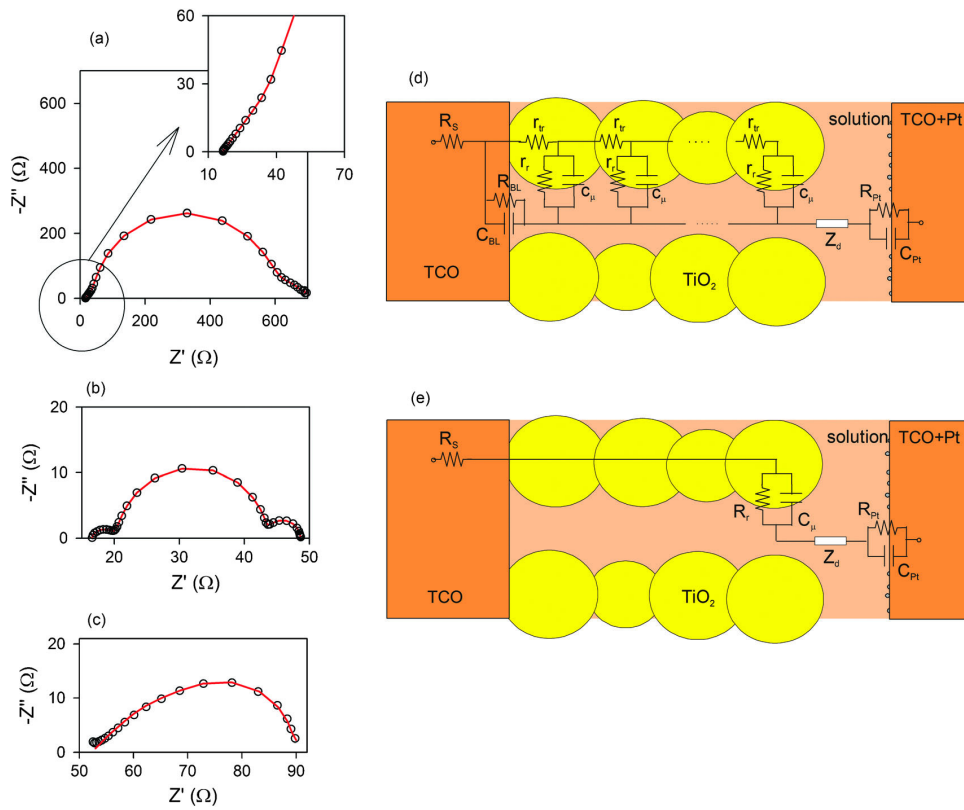


Figure 8.13: Impedance (Nyquist) plots for typical DSSCs, adapted with permission from [401]. Experimental impedance spectra of a DSSC with an ionic liquid based electrolyte under 50 mW/cm² illumination at (a) 0.40 V and at (b) open circuit conditions, 0.65 V. (c) The Gerischer impedance spectra appearing in a "defective" cell, which presents lower values of recombination resistance than transport resistance. Data are taken at 0.45 V under 100 mW/cm² illumination. (d) The complete equivalent circuit model to fit experimental data of (a) and (c). (e) Simplified equivalent circuit model that is valid for the spectra measured at high voltage as in (b). In (a) to (c) experimental data are represented by dots and fits to models (c) and (d) are represented by lines. Adapted with permission from [402]

component can be modeled by a proper combination of resistance and capacitance elements connected either in series or in parallel:

Pt-cathode/electrolyte interface . A parallel RC circuit represents the combination of the electron transfer from the Pt to the electrolyte (R_{Pt}) and the Helmholtz capacitance (C_{Pt}) at the electrode/electrolyte interface. Cathode impedance is usually seen at high frequencies (in the order of the KHz). R_{Pt} , in the limit of low over-potentials is given by the linear approximation of the Butler-Volmer equation:

$$R_{Pt} = \frac{RT}{nFi_0} \quad (8.15)$$

where n is the number of electrons exchanged during the charge transfer reaction (i.e. 2 for the reduction of the iodide to triiodide) and i_0 is the exchange current. ³.

Electrolyte . Usually, for "standard" electrolyte formulations, in which $[I^-] \gg I_{3-}$, the impedance can be expressed by the equation:

$$Z_N = \frac{Z_0}{(j\omega)^\alpha} \tanh(j\tau_d\omega)^\alpha \quad (8.16)$$

The N subscript indicates that the I_{3-} concentration gradient is limited to the Nernst layer (where the mass transport is impeded) that usually corresponds to TiO_2 pores depth. j is the imaginary unit, τ_d the triiodide diffusion time (related to their diffusion length and coefficient), ω the AC electric field angular frequency and α is an exponent related to the type of ion diffusion (infinite, semi-infinite, finite). When $\alpha = 0.5$ (infinite diffusion) equation 8.16 reduces to the the Warburg formula

$$Z_0 = Z_W = \frac{RT}{n^2F^2c_0\sqrt{D_{I_{3-}}}}A \quad (8.17)$$

where A is the photoanode area, c_0 is the triiodide concentration in the bulk of the electrolyte solution, and $D_{I_{3-}}$ is the triiodide diffusion coefficient. Electrolyte impedance can be appreciated at low frequencies ($< 1\text{Hz}$).

TCO (Transparent conducting oxide) glass. FTO glass is represented by the charge transfer resistance (to the interception reaction) of the thin TiO_2

³The exchange current reflects intrinsic rates of electron transfer between the electrode and the electrolyte. Indeed, it is the current at zero overpotentials, when the cathodic current is balanced by the anodic one

blocking layer (R_{BL}), its Helmholtz double layer capacitance (C_{BL}), and the series (sheet) resistance of the FTO coating (R_S).

TiO₂ photoanode . The mesoscopic network of titania particles is modeled as a transmission line. This means that every single photoanode TiO₂ particle is schematized as a transport resistance (r_{tr}) stemming from the diffusion of electrons through the titania film, connected in series to a parallel RC circuit comprised of a charge transfer resistance (r_r the resistance to the electron-triiodide recombination) and a chemical capacitance (c_μ , describing the TiO₂ density of states and the occupancy of the intra-gap electron traps). These microscopic quantities are related to the macroscopic photoanode transport and recombination parameters through the formulas: $R_{tr} = r_{tr} L$, $R_r = r_r/L$, $C_\mu = c_\mu/L$. Where L is the TiO₂ nanostructured film thickness (see figure 8.14 for height profile of the titania beads screen printed electrodes.)

Thus, the electron diffusion length can be calculated by equation 8.18

$$L_n = L \sqrt{\frac{\tau_r}{\tau_{tr}}} = L \sqrt{\frac{R_r}{R_{tr}}} \quad (8.18)$$

Where, as explained in section 3.3 τ_r and τ_{tr} are the electron recombination lifetime and transport (diffusion) time, respectively. Hence, equation 8.18 states that *the higher the resistance to the recombination with the electrolyte and the smaller the diffusion resistance through the photoanode, the longer the electron diffusion length, that is higher charge collection efficiency*. The (see figure 8.13) R_r to R_{tr} ratio also determine the DSSCs' Nyquist plot shape. High efficiency cells (i.e. $R_r \gg R_{tr}$) present an impedance spectra ($Z_{imm.}$ vs Z_{real}) as shown in figure 8.13 **(a)** and **(b)**. The difference between the two graphs lies on the experimental data acquisition condition. In fact, **(a)** has been collected by applying a DC voltage close to the maximum power point of the DSSC (≈ 0.4 V), while **(b)** has been collected with $V_{DC} = V_{OC}$. The former case requires a complete transmission line model to fit the experimental data, whereas under open circuit voltage conditions (high voltage) the equivalent circuit is simplified. In fact, at high voltages the Fermi level of electrons approaches the conduction band of TiO₂ and a very high concentration of electrons is present in the semiconductor. As a consequence, the TiO₂ resistance becomes negligible, $R_{tr} \approx 0$, which reduces the complexity of the impedance spectrum. The equivalent circuit of figure 8.13**(d)** can then be simplified as shown in 8.13**(e)**, with the transmission line reduced to a simple RC parallel combination, which is the

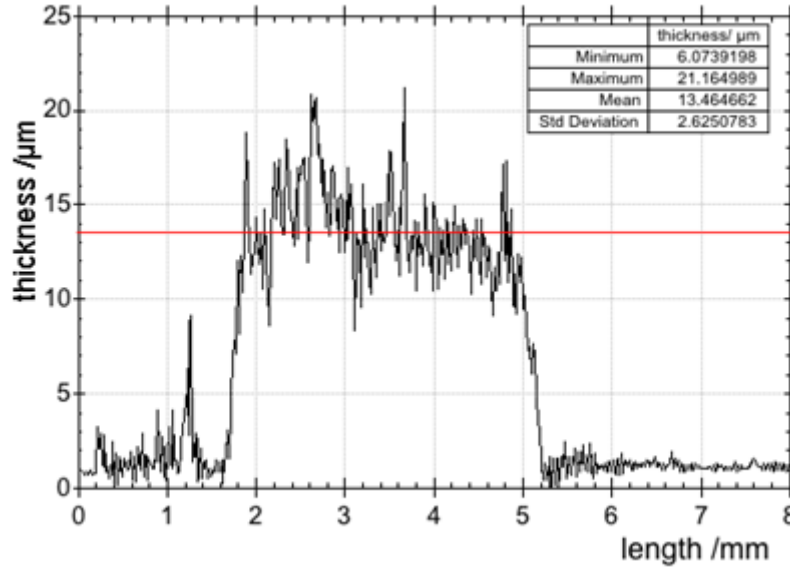


Figure 8.14: Profilometry of titania screen printed photoanodes after particles' sintering. The thickness of the TiO_2 depends on the screen-mesh size (34T for the DSSCs study) substrate chemical composition and treatments, screen printing paste viscosity and thermal treatment procedures. For DSSCs the optimum thickness for the beneficial effects (high dye chemisorption) to prevail on the detrimental effects (charge recombination) is 10-15 μm . TiO_2 is necessary to calculate L_n .

model shown in fig. 8.13(e). Regardless of the experimental conditions the central arch of the Nyquist plot always corresponds, for high efficiency DSSCs, to the TiO_2 contribute.

Low efficiency cells ($\eta < 2\%$) are characterized by Nyquist plots like the one in figure 8.13 (c). This case corresponds to $R_{tr} \gg R_r$ (or equivalently $L \gg L_n$) and the equivalent circuit for the TiO_2 film is predicated on the Gerischer impedance equation:

$$Z = \sqrt{\frac{R_{tr}R_r}{1 + j\omega/\omega_r}} \quad (8.19)$$

The main issue related to the Gerischer impedance is that it is complicated to distinguish between the recombination and the transport components [403]. Indeed, it is not possible to appreciate the maximum of the Nyquist arch belonging to the titanium dioxide electrode.

8.5.2 Iron Colorimetric sensors and electrochromic devices

Iron colorimetric sensors

Iron lower detection limit concentration of **L**-functionalized titanium dioxide mesoporous beads thick films was carried out by Uv-vis. diffuse reflectance spectroscopy. measurements have been performed on the bare, N-aromatic ligand sensitized and iron adsorbed films. The latter sample was obtained by treating the screen printed device with 150 μL of aqueous Fe^{2+} solution with different iron concentrations (0.2, 2, and 45 ppm). The diffuse reflectance spectra were collected in 280-1200 nm the range using a double-beam Lambda 750S spectrophotometer (Perkin-Elmer, U.S.) equipped with a 60 mm Spectralon integrating sphere.

Electrochromic devices

ITO/ $\text{Fe}^{2+/3+}$ **L**₂ based devices assembled as described in section 8.4.4 were tested for electrochromic effect. A Perkin Elmer Lambda 750S Uv-vis with the integrating sphere 60 mm was used as the UV-instrument. Spectralone was used as a 100% reflectance standard. The sample was placed into the solid state clamp in such a way the modified surface would interact with the UV-light first. A Pine Wavedriver 10 potentiostat was used to change the potential from -1V to 3V during the cycling experiment. First, a scan of a modified sample was performed between 320 nm to 800 nm holding the potential at -1V. Afterwards, the potential was held at 3 V, with the scan repeated. Afterwards, the wavelength was held at the wavelength at which the MLCT was strongest (561 nm). The cycling time was held at 60 s and 1500 cycles were performed

8.5.3 Microstrip devices (microwaves resonators)

Iron sensitive antenna

The microstrip patch antenna modified with the screen printed ITO film was characterized for microwaves scattering parameters. Reflection coefficient (return loss) was determined at the device feed port by measuring the S_{11} scattering parameter with a Network Analyzer (Agilent E8361A). Data were collected for the device containing only the ITO film functionalized with the terpyridine ligand (ITO +**(L)**) and for the Fe(III) exposed device (ITO +**(L)** + Fe^{3+}).

Graphene and MWCNTs loaded antennas

Both the microstrip patch resonator loaded with the two different graphene wt% (25 and 12.5) and the microstrip patch antenna loaded with the 12.5 wt% MWCNTs film were tested for return loss in the 1-10 GHz by using a vector network analyzer (Agilent E8361A). Devices' resonant frequency behavior was simulated by using ANSYS HFSS software. Furthermore, sheet resistance and impedance measurements were performed on graphene thick films (see Section 8.4.5) with a Solatron 1286 electrochemical interface and a Solartron 1260 Frequency response Analyzer, respectively. Impedance data were collected in the range 0.1 Hz-32 MHz frequency range ($V_{rms} = 10$ mV, $V_{dc} = 0$ V). Impedance data were fitted by using Z-view software by Scribner. Graphene loaded microstrip lines (see Figure 8.9) were also characterized for microwaves transmission coefficient (i.e. insertion loss, S_{21} ; see Chapter 6) in order to develop a material (graphene + binder) microwaves frequencies equivalent circuit model. Data fit and equivalent circuit modeling were performed by means of ADS software by Keysight Technologies.

MWCNTs microstrip patch antenna radiation pattern and gain measurements were performed in an anechoic chamber with a double ridge horn antenna. The AUT was the receiving antenna and the ridge horn the transmitting one. The distance between the ridge horn antenna and the AUT was 2.7 and 5 m for the unloaded and loaded antenna, respectively. A Pasternak WR-284 Standard Gain Horn Antenna Pasternak Enterprise in, US; nominal gain 10 dBi) was used as a G_A standard.

Part III

Results and Discussion

Chapter 9

Materials for DSSCs

9.1 TiO₂ morphology optimization

9.1.1 Materials characterization

Figures 9.1, 9.2, and 9.3 show the XRD patterns of the samples synthesized through the three different templating approaches. Samples' spectra refers to the materials collected after calcination and are compared with the reference diffraction pattern of tetragonal anatase from the JCPDS database. Both materials obtained by means of silica nano-spheres are comprised of a single phase: anatase. Similar considerations stand for the TiO₂-P123(A), TiO₂-P123(B), TiO₂-Brij-58 and TiO₂ beads. They all are monophasic being anatase the only titanium dioxide allotrope detected from the XRD patterns. Hence, the calcination procedure did not convert the TiO₂ synthesis products into the thermodynamically stable rutile phase and the metastable anatase, which is the desired TiO₂ allotrope for DSSCs applications, was obtained.

Among the titania synthesized by the soft polymeric approach, ordered mesoporosity was identified by low-angle XRD scans (0.5-10° in 2θ) *only* on the TiO₂-P123(A) sample *before* calcination (see figure 9.2 (b)). Two large peaks were detected. These peaks are centered at 0.711° and 4.353°, respectively, corresponding to two distributions of mesopores centered at 124 Å and 20 Å, respectively. In the inset of Figure 9.2 (b), a magnification of the sample before calcination in the lowest angle region (up to 1.6°) is given to better appreciate the peak centered at 0.711°. The peaks disappear after the calcination step, most likely due to a structural reorganization of the sample stemming from thermally induced crystallization. Indeed, during the thermal treatment, the tetrahedral coordination of Ti⁴⁺ in titanium isopropoxide

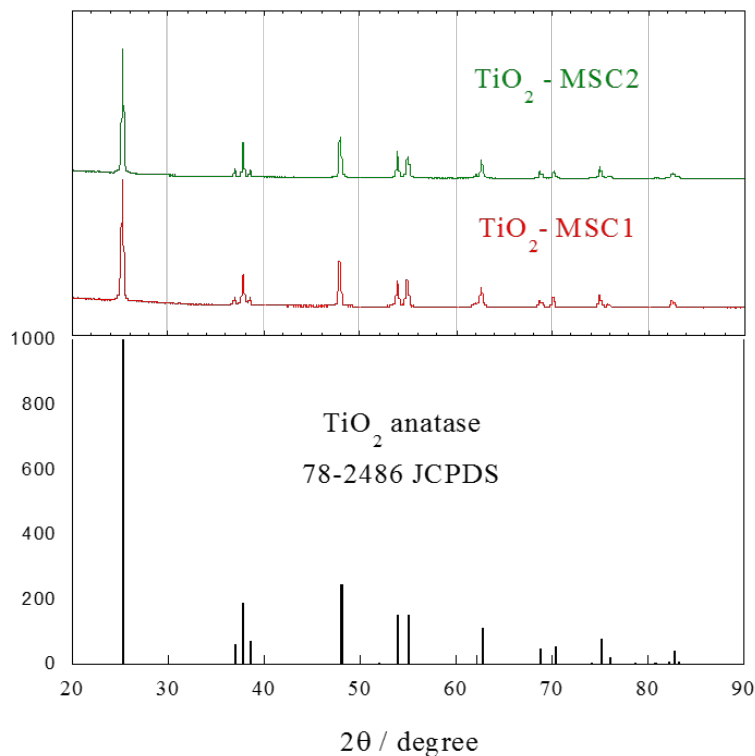
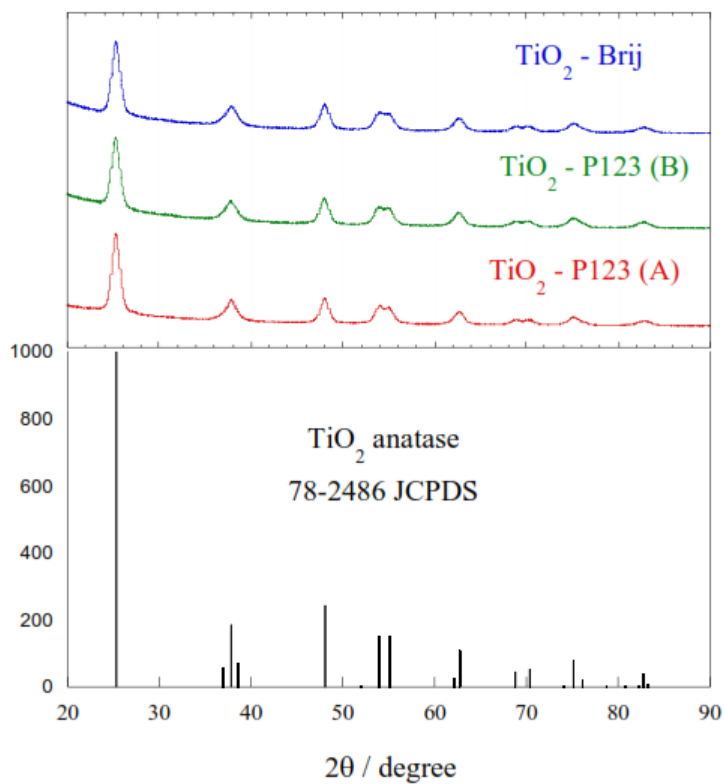
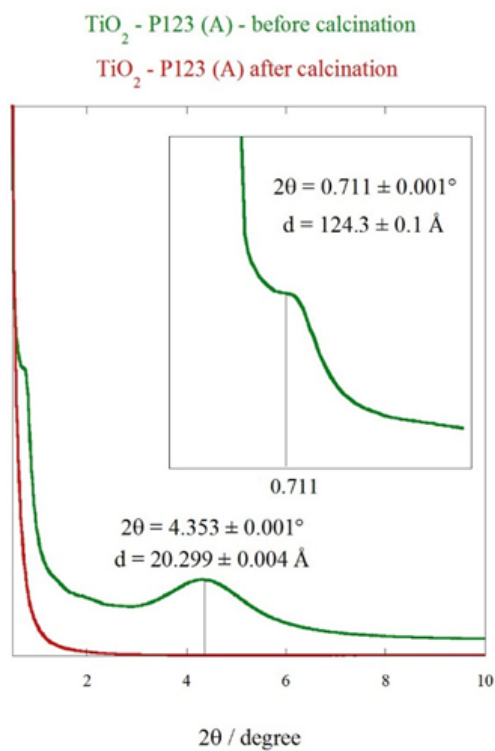


Figure 9.1: X-ray diffraction pattern for the TiO_2 -MSC1 and MSC-2 samples. The bottom panel illustrates the diffraction pattern of pure (tetragonal) anatase (JCPDS database, <http://www.icdd.com/>).

evolves in the typical octahedral coordination in the structure of anatase.

Structural differences among samples can be detected by analyzing the lattice fundamental parameters and average crystallites size calculated from the Rietveld refinement algorithm (see table 9.1. Although no significant differences concerning the a and c axis unit cell parameters, the mean crystallites size substantially varies between the hard-templated TiO_2 samples and the soft-templated ones. In fact, TiO_2 -MSC1 and MSC-2 are comprised of large crystallites typical of a closed-packed morphology resembling a single crystalline structure (see FE-SEM images, Figures 9.4, 9.5, 9.6). On the other hand, TiO_2 -P123(A), TiO_2 -P123(B) and TiO_2 -Brij-58 crystallites are considerably smaller than the MSCs' ones. An explanation to this can be found in the different size of the structure orienting agents used as templates. Pluronic-123 and Brij-58 act as scaffolds for the growing TiO_2 by forming micelles. Their micelles' size in polar solvents (i.e. the ethanol used for the synthesis) is 10-15 nm for Pluronic 123 [404] and 4-10 nm for the Brij-58 [405]. Conversely, SiO_2 spheres possess 20 and 50 nm diameters (see also figures 9.4 and 9.5). Hence, it is reasonable to infer that the soft-polymeric templates produced a smaller crystallite

(a) X-Ray diffraction pattern for soft-polymeric TiO_2 samples(b) Low angle XRD scan for TiO_2 -P-123(A) before and after calcinationFigure 9.2: XRD characterization (complete scans (a) and low angle diffraction for the TiO_2 -P123(A) (b)) of the polymeric-templated titanias.

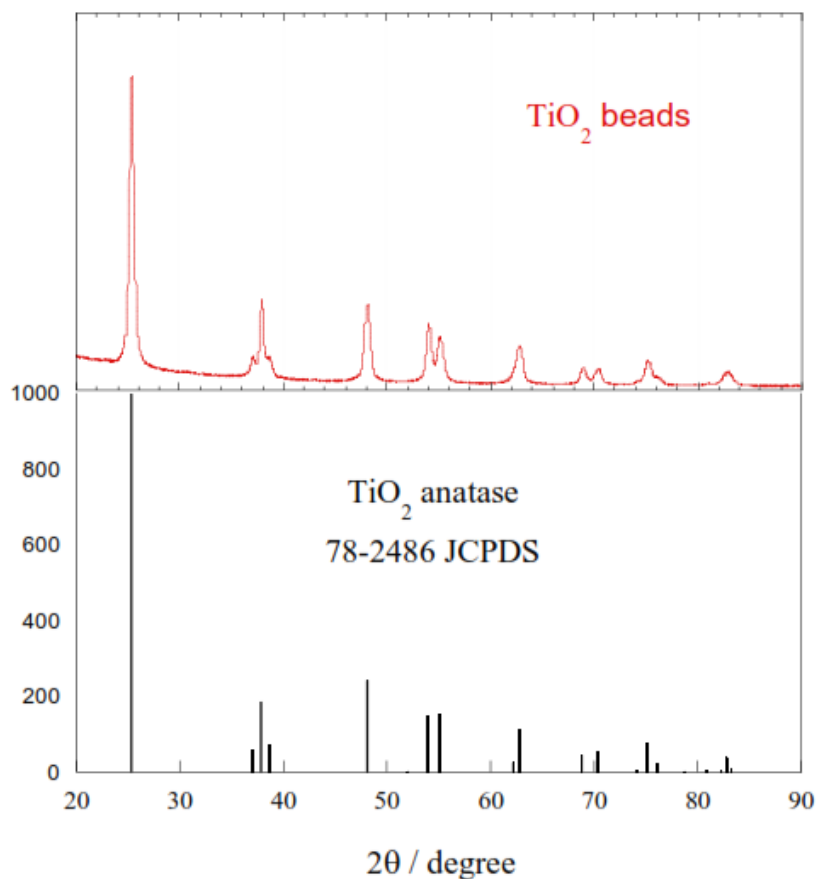


Figure 9.3: XRD spectrum of titania beads from the HDA synthetic approach. The diffraction pattern does not show presence of either rutile or brookite.

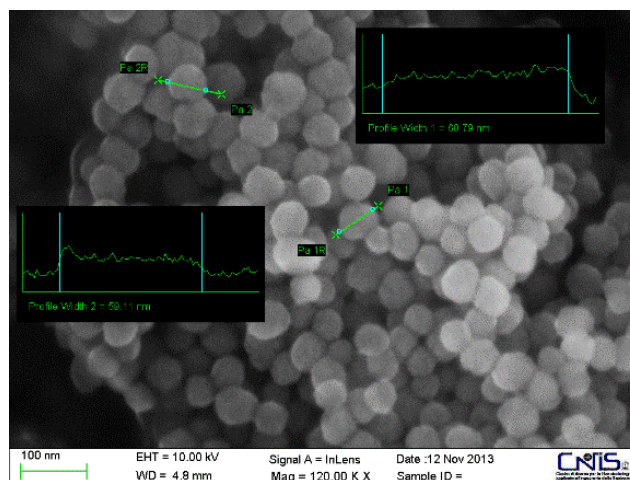
size because of the low micelles "hydrodynamic diameter" during the synthesis stage. Also the lower crystallite sizes of the TiO_2 -Brij-58 compared to the Pluronic based samples seems to confirm this hypothesis. The smaller crystallites dimension for the TiO_2 -Brij-58 sample is also due to its more compact morphology (see figure 9.6) Figures 9.4 and 9.5 show the FE-SEM micrographs of titanias obtained from the

Sample	a/Å	c/Å	d/nm
TiO_2 -MSC-1	3.794 ± 0.002	9.502 ± 0.008	≈ 66
TiO_2 -MSC-2	3.790 ± 0.001	9.505 ± 0.002	≈ 90
TiO_2 -P123-A	3.788 ± 0.002	9.506 ± 0.008	≈ 13
TiO_2 -P123-B	3.791 ± 0.002	9.513 ± 0.008	≈ 13
TiO_2 -Brij-58	3.778 ± 0.002	9.51 ± 0.01	≈ 10
TiO_2 -beads	3.782 ± 0.001	9.492 ± 0.003	≈ 25

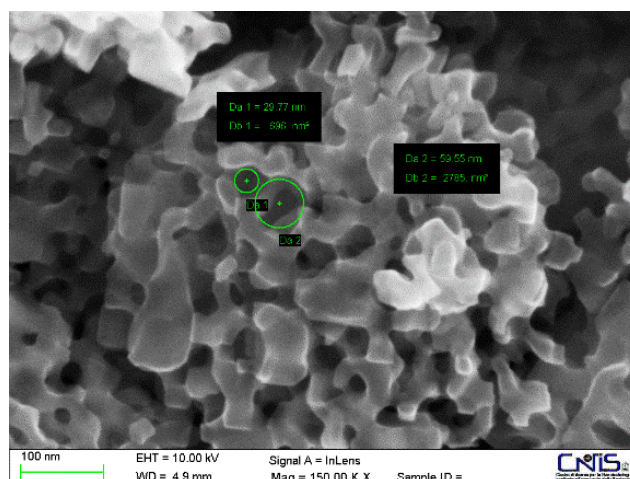
Table 9.1: Rietveld refinement parameters for TiO_2 synthesized by means of different templating agents.

two silica hard templates. The presence of a well-defined (anisotropic) mesoporous

crystal structure is evident especially for the TiO₂-MSC-1 sample (fig. 9.4 (a)). In both cases the TiO₂ final products are the negative replica of their silica templates. Figure 9.6 presents the SEM images of the three samples synthesized through the



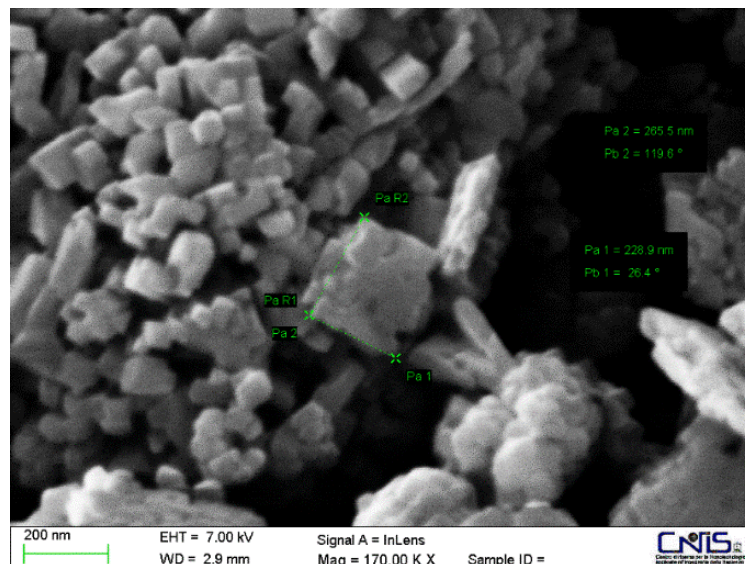
(a)



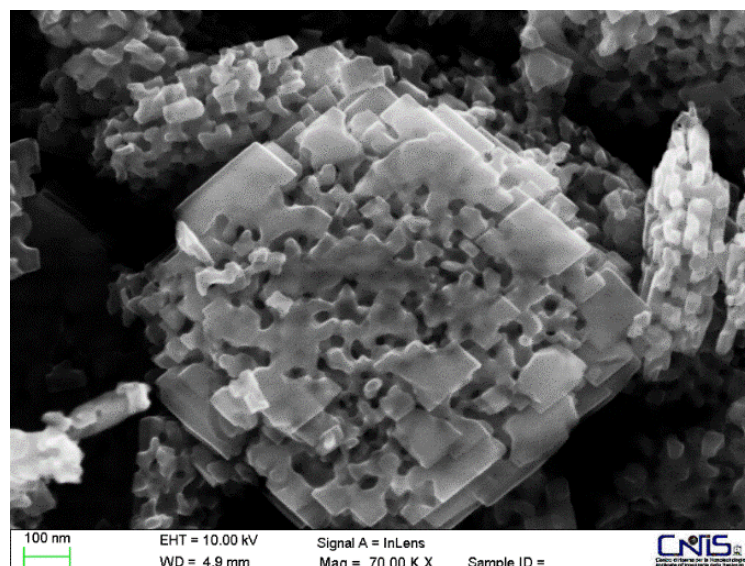
(b)

Figure 9.4: FE-SEM micrographs of TiO₂ MSC-1 sample (b) and its silica template (a).

soft-polymeric approach. All the samples show a nanocrystalline texture. However, TiO₂-Brij-58 presents a more compact structure compatible with its lower SSA compared to the Pluronic derived samples (see below). TiO₂ beads appear as hierarchically structured spherical particles, with an average diameter around 600 nm, made of randomly oriented nanocrystals (see figure 9.7). Table 9.2 reports the SSA values for all samples. Specific surface area data are in good agreement with the observations derived from the Rietveld analysis and from electron microscopy. In fact, TiO₂-P123(A) and (B) open structure and their small crystallites size



(a)



(b)

Figure 9.5: SEM micrographs of TiO_2 MSC-2 (a) compared to its silica template (b).

Sample	SSA/m ² /g
TiO ₂ -MSC-1	13 ± 2
TiO ₂ -MSC-2	16 ± 2
TiO ₂ -P123-A	120 ± 5
TiO ₂ -P123-B	120 ± 4
TiO ₂ -Brij-58	75 ± 3
TiO ₂ -beads	79 ± 3

Table 9.2: Specific surface area values of the different mesoporous titania samples.

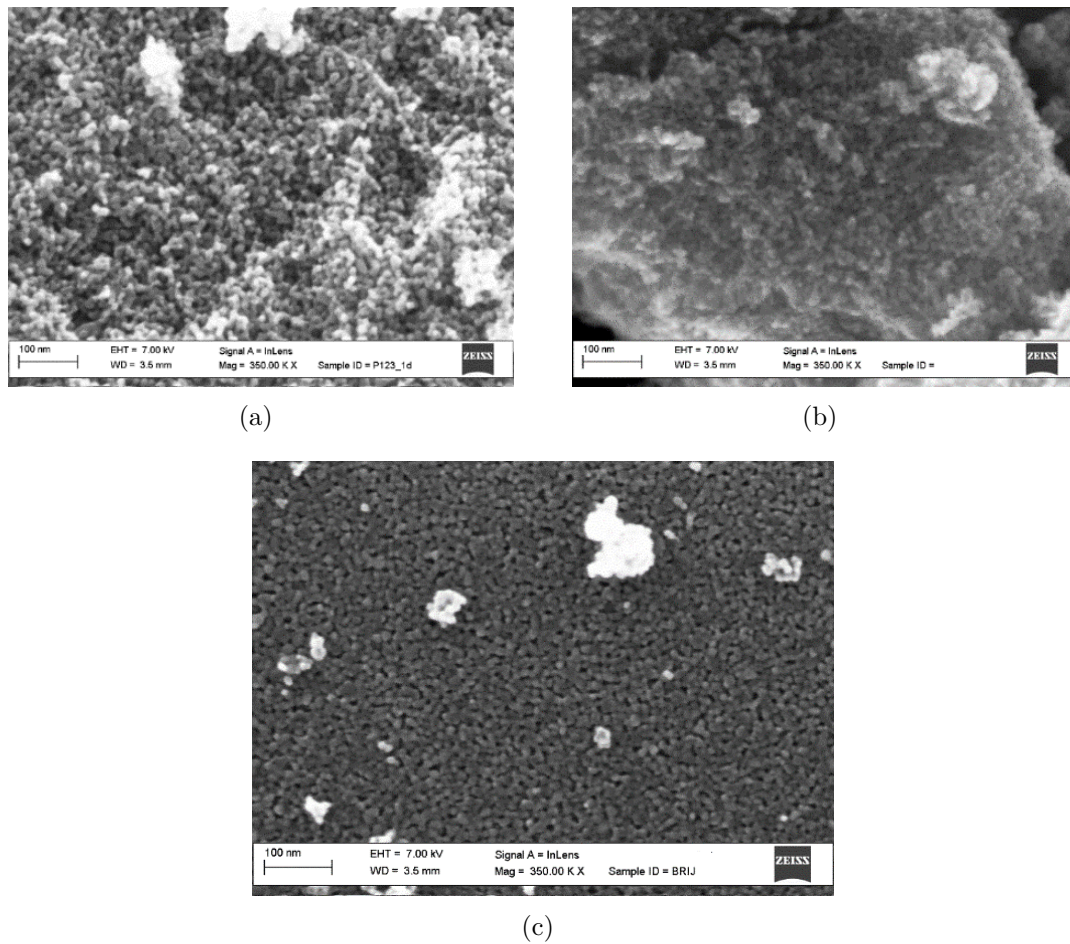


Figure 9.6: FE-SEM micrographs of (a) TiO₂ P-123 (A), (b) TiO₂ P-123 (B), (c) TiO₂-Brij-58.

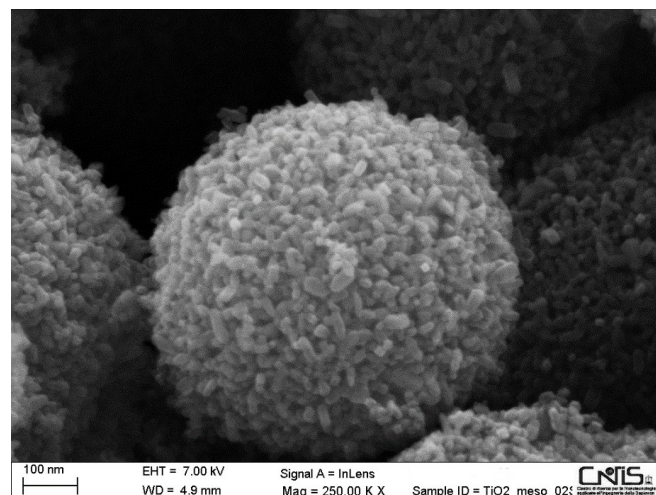
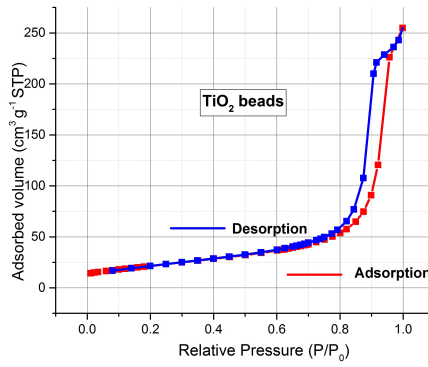


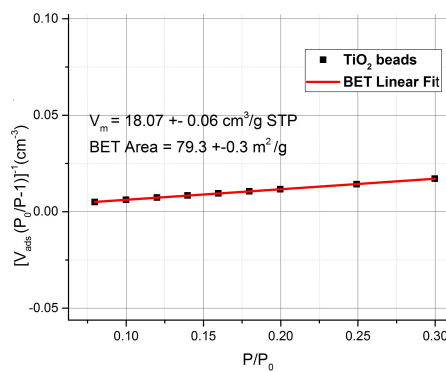
Figure 9.7: TiO₂ mesoporous beads obtained with the aid of HDA template. These beads are comprised of a large number of nanoparticles randomly oriented but organized into a spherical shape to minimize the surface energy.

justifies the high SSA ($120 \text{ m}^2/\text{g}$). On the other hand, the large d values of the of the silica templated samples are compatible with the small surface area. By looking to table 9.1 TiO_2 -Brij-58 should possess a high SSA value. However, its closed-packed structure brings about crystallites aggregation reducing the sample exposed area and leading to an SSA close to the one of the TiO_2 beads. As mentioned in section 8.3.7 this last sample was also characterized by complete N_2 adsorption/desorption isotherm and by porosimetry. Figure 9.8 illustrates the results of the beads' surface characterization. The hysteresis loop in the adsorption isotherm denotes the presence of mesopores [394] (see figure 9.8 **a**)) with a pore size distribution peaking at 18 nm. These properties make the material ideal for the chemisorption of large amounts of N-719 dye. Polymeric-templated samples before calcination were subjected to thermal analysis investigations (see figure 9.9). All samples show three distinct weight losses as well as three thermal events: an endothermic at lower temperature and two exothermic at higher temperature. The first weight loss (Room temperature to 150-200 °C) can be ascribed to moisture and/or solvent loss. The other two losses (a more pronounced one up to about 300 °C and another up to 400-450 °C) can be attributed to two combustion events. After solvent evaporation, the polymeric templating agents remain the only combustible materials. Hence, the two distinct combustion peaks (figure 9.9 **b**)) belong to the templating agents burning off in two different regions of the samples: the outer surface (the most reactive, easily accessible to oxygen) and the inner pores (the least reactive and accessible to oxygen). This provides an indirect proof of the porosity of the samples analyzed.

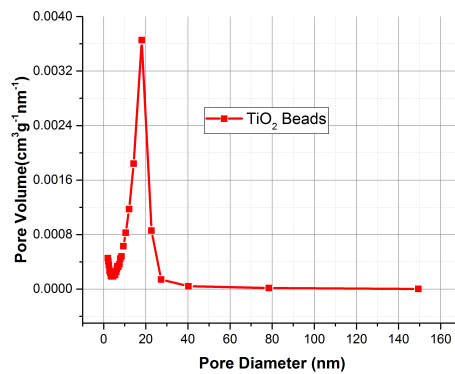
Band gap measurements were performed (through diffuse reflectance Uv-vis spectroscopy) on all titania samples. Since charge injection from the dye and DSSCs' V_{OC} depends on the TiO_2 Fermi level and conduction band position, E_g values for titanias possessing different morphologies and crystallites size could be used as a parameter to compare the J_{SC} and V_{OC} among different photoanodes. E_g values are reported in table 9.3. Quantum size effect is supposed to affect the band gap values of the samples. Thus the lower the crystallite/particles size, the higher the band gap. However, table 9.3 show the opposite trend with the MSC-1, MSC-2 and titania beads samples having the wider band gaps (3.154, 3.190, 3.179 eV, respectively). A similar band gap vs particles size dependence reported for nanostructured TiO_2 have been already reported [406], [407].



(a)

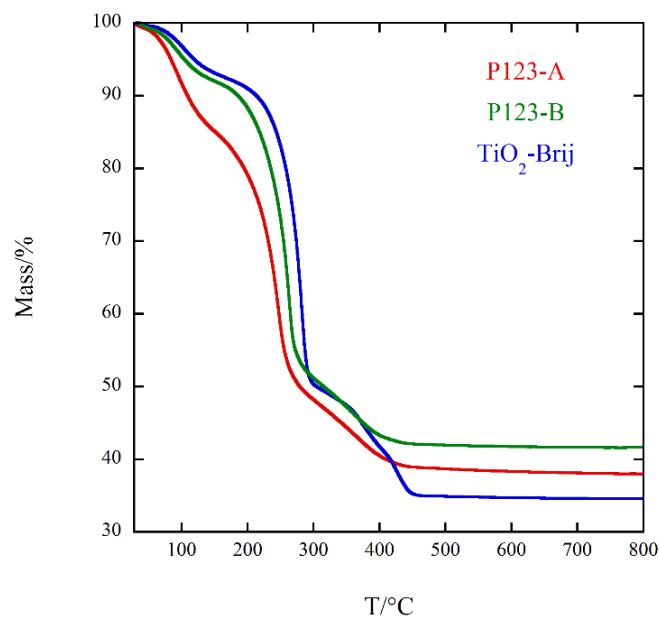


(b)

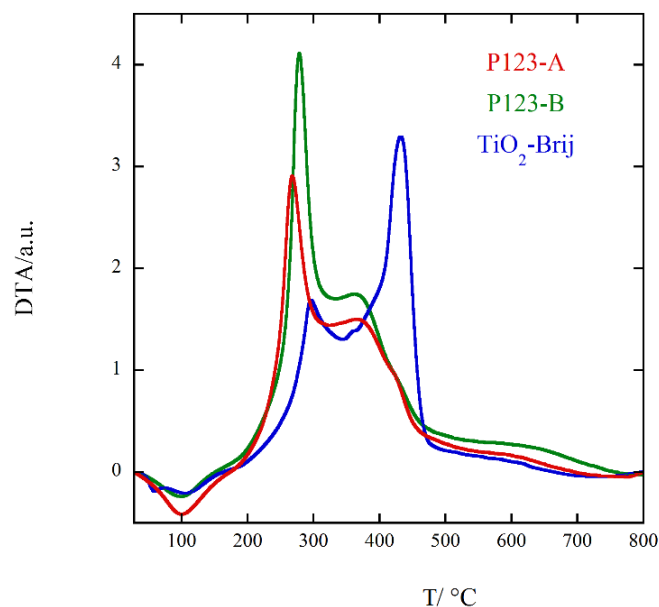


(c)

Figure 9.8: TiO₂ mesoporous beads' complete surface characterization: a) N₂ adsorption isotherm, b) BET fit and c) pore size distribution for TiO₂ mesoporous beads.



(a)



(b)

Figure 9.9: Weight-loss (a) and differential thermal analysis for polymeric templated samples (b).

9.1.2 DSSCs characterization

I-V curves for DSSCs assembled with different morphology materials are illustrated in figures 9.10. Graphs are presented in the form of current density vs voltage (J-V) both in dark and under AM *one sun* 1.5 G irradiance. Table 9.4 reports cells' salient photovoltaic parameters under illumination conditions. R_s was estimated

Sample	E_g (eV)
TiO ₂ -MSC-1	3.154 ± 0.002
TiO ₂ -MSC-2	3.190 ± 0.002
TiO ₂ -P123-A	3.123 ± 0.003
TiO ₂ -P123-B	2.997 ± 0.002
TiO ₂ -Brij-58	3.065 ± 0.002
TiO ₂ -beads	3.179 ± 0.003

Table 9.3: Band gap values of different morphology TiO₂ samples extrapolated from the Tauc plots of the Kubelka-Munk function calculated for the indirect inter-band transition.

from the slope of the polarization curve at the V_{OC} . TiO₂-MSC-1 and MSC-2

Sample	J_{SC} (mA/cm ²)	V_{OC} (V)	η (%)	FF	R_s (Ω)
TiO ₂ -MSC-1	12.5 ± 0.01	0.7311 ± 10^{-4}	6.0 ± 0.1	0.65 ± 0.01	104 ± 3
TiO ₂ -MSC-2	10.9 ± 0.01	0.7422 ± 10^{-4}	5.7 ± 0.1	0.70 ± 0.01	94 ± 3
TiO ₂ -P123-A	13.4 ± 0.01	0.7121 ± 10^{-4}	6.7 ± 0.1	0.70 ± 0.01	84 ± 2
TiO ₂ -P123-B	14.5 ± 0.01	0.7088 ± 10^{-4}	6.8 ± 0.1	0.66 ± 0.01	86 ± 2
TiO ₂ -Brij-58	13.5 ± 0.01	0.7122 ± 10^{-4}	6.4 ± 0.1	0.66 ± 0.01	76 ± 2
TiO ₂ -beads	13.9 ± 0.01	0.7155 ± 0.00301	7.0 ± 0.1	0.70	88 ± 1

Table 9.4: Fundamental photovoltaic parameters (at *one sun* A.M. 1.5G)

Sample	J_0 (nA/cm ²)	m
TiO ₂ -MSC-1	108 ± 3	2.41 ± 0.01
TiO ₂ -MSC-2	90 ± 4	2.78 ± 0.01
TiO ₂ -P123-A	1.7 ± 0.1	1.76 ± 0.01
TiO ₂ -P123-B	0.61 ± 0.004	1.59 ± 0.01
TiO ₂ -Brij-58	1.3 ± 0.1	1.66 ± 0.01
TiO ₂ -beads	0.7 ± 0.3	1.31 ± 0.01

Table 9.5: Saturation dark current and diode's ideality factors of DSSCs containing morphology specific photoanodes

show the lowest short circuit current (and the lowest efficiency) because of their reduced SSA. Low specific surface area are associated with small amounts of dye adsorbed on the TiO₂ resulting in limited short circuit current. Furthermore, silica templated samples show the highest R_s values. The presence of SiO₂ residues in the MSC-1 MSC-2 was ruled out as a cause of high series resistance by EDX spectra that shows no Si signals. Besides, the large R_s is a characteristic common to all photoanodes. Since all samples present good crystallinity and satisfactory levels of particles interconnection, a possible reason accounting for the high series resistance values is the FTO/TiO₂ contact resistance. Indeed, the porous nature of

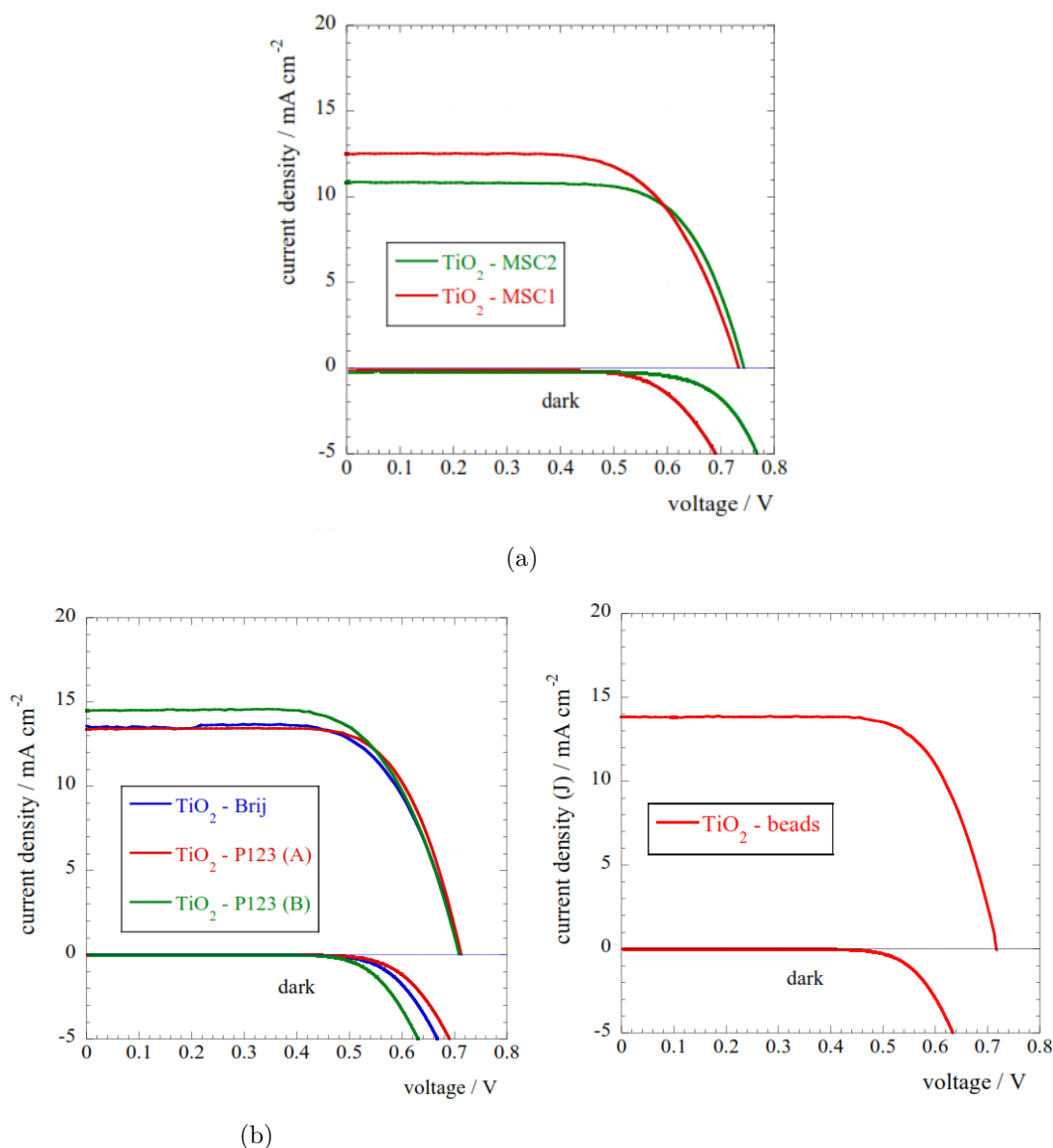


Figure 9.10: J-V curves under illumination and dark for cells assembled by using hard (a), soft-polymeric templated (b), and TiO₂ beads materials

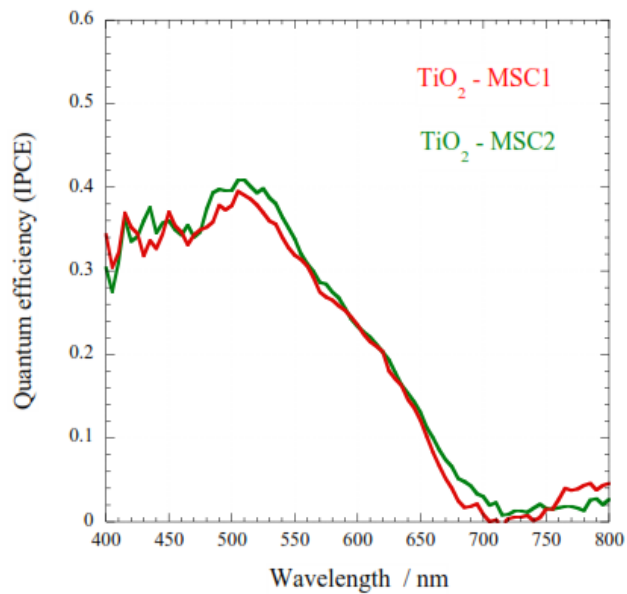
the photoelectrode does not provide an optimal contact between TiO₂ particles and the FTO substrate. Another parameter that depresses the efficiency of TiO₂-MSC-1 and MSC-2 cells is the abnormally high (≈ 2 order of magnitude higher compared to the other morphologies) saturation dark current (combined with an ideality factor > 2 , see table 9.5). These parameters indicate a high level of charge transfer from the TiO₂ to the triiodide ion. In fact, the insufficient electrical contact caused by the TiO₂-MSCs photoanodes reduced surface area limits the electron transfer between the titanium dioxide and the FTO-coated glass. Thus, the electrons remain trapped into the TiO₂ nanostructure increasing the rate of the e⁻ interception

reaction by the I_3^- .

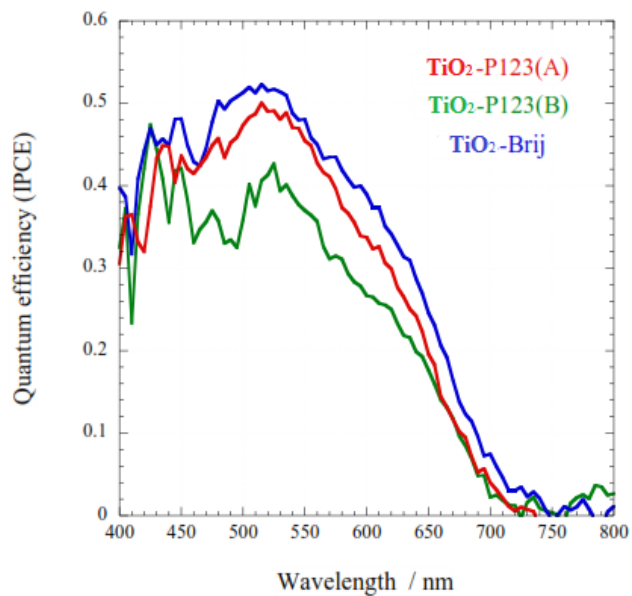
A correlation between DSSCs' V_{OC} and E_g values measured on the powders can be established. Indeed, wider band gaps corresponds to a Fermi level shifted closer to the dye's LUMO and to a larger energy difference with respect to the I_3^-/I^- redox couple. Thus, the TiO_2 -MSC-1 and TiO_2 -MSC-2 cells have the highest open circuit voltage. Besides these two photoanodes benefit from the presence of a small amount of P90 (see Section 8.4.1) added to promote particles' sintering (P90 E_g is about 3.2 eV). On the other hand, the higher band gap brings about detrimental effects on the charge injection from the dye to the TiO_2 . Thereby lower J_{SC} of the MSC titanias can also be partially justified by the higher position of the conduction band edge. The devices employing TiO_2 -P123 (A) and (B) and TiO_2 -Brij-58 present similar efficiency and comparable photovoltaic parameters. This achievement is consistent with the similar structural and optical properties emerging from previous characterization. TiO_2 -P123 (B) cell owns an energy conversion efficiency slightly higher than the of the other the polymeric-templated materials ($\eta = 6.8\%$). Probably, TiO_2 -P123 (B) takes advantages of the larger J_{SC} stemming from both large surface area and narrower band gap (favored charge injection).

Notwithstanding the lower SSA compared to P-123 (A) and P-123 (B) samples, titanias beads are still capable of maintaining a high J_{SC} . To understand the performances of the TiO_2 beads (in terms of short circuit current and overall energy conversion efficiency) it is necessary to investigate the quantum efficiency (IPCE) behavior of the six DSSCs assembled for the morphology study (see Figures 9.11 and 9.12). All cells except the one fabricated with the TiO_2 hierarchical spheres present IPCE curves peaking around 530 nm, which corresponds to the MLTC dye's transition. Titania beads quantum efficiency increases towards the lower wavelengths (below 500 nm) indicating superior light harvesting properties. Indeed, its sub-micrometric mesoporous morphology allows for excellent light scattering properties permitting light absorption and charge generation also to the lower layers of the photoanode. Moreover, the enhanced light scattering characteristic allow to compensate for the lower driving force for electron injection due to the relatively high band gap.

TiO_2 beads are used in the second stage of the research: doping the TiO_2 with trivalent lanthanides.



(a)



(b)

Figure 9.11: IPCE curves of DSSCs assembled by using hard (a), soft-polymeric (b) templated and TiO₂ as photoanode materials.

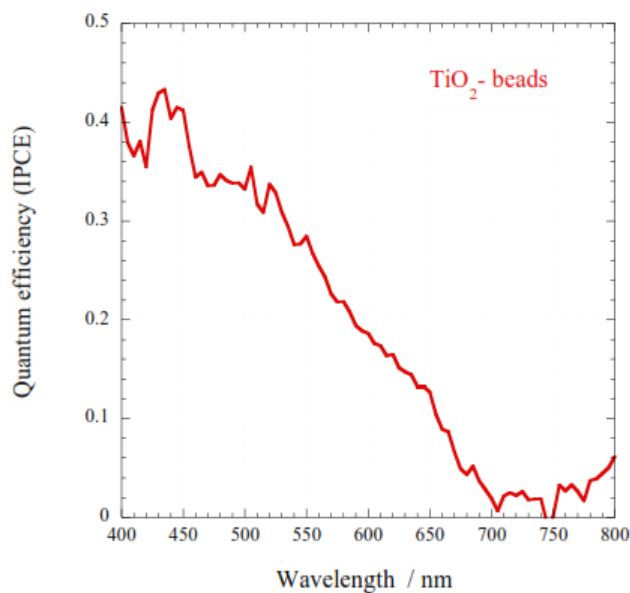
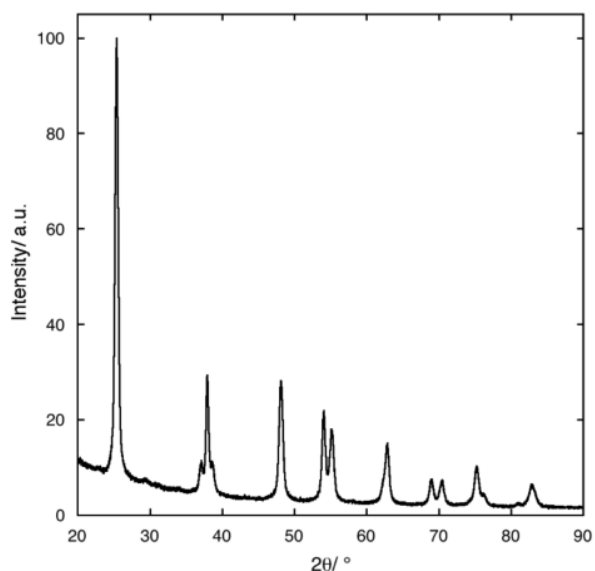


Figure 9.12: IPCE curves of DSSCs assembled by using TiO_2 mesoporous beads as photoanode materials.

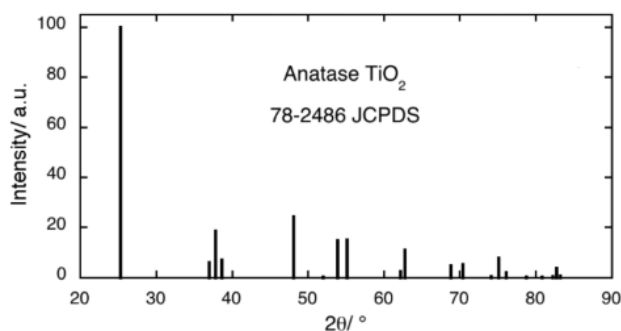
9.2 Lanthanides doped TiO_2 beads

9.2.1 Structural, morphological and optical characterization

Powder X-ray diffraction was used to determine the crystalline phases and estimate the crystal size of the resulting doped titania beads. As an example, figure 9.13 illustrates the XRD pattern of the 2% at Er^{2+} doped sample ($\text{TiO}_2:\text{Er}^{2+}$). Because of the small amount of dopants inserted into the TiO_2 lattice no phase other than anatase can be detected. Thus, doped samples are real solid solution with no phase separation (i.e. absence of the Er_2O_3 phase). However, XRD does not allow to discriminate between substitutional and interstitial solutions. Nonetheless, an indication of the lattice position of the RE dopants can be inferred by the unit cell parameters calculated by the Rietveld refinement procedure (see table 9.6) The dopant nature and concentration have no substantial effect on the unit cell parameters because of the low amount used. In fact a and c are close to the corresponding values for pure anatase beads (3.782 Å and 9.492 Å, respectively, see 9.1.1). Thereby, the lack of lattice strain suggests that the rare earth ions occupy a substitutional position. Moreover, similar findings have been reported for scandium doped TiO_2 [188] where the substitutional position of the dopant have been proved by EXAFS. Thus, we expect to find the same situation for the case of RE dopants



(a)



(b)

Figure 9.13: (a) XRD spectrum of $\text{TiO}_2:\text{Er}^{2+}$ beads sample. Reference JCPDS diffraction pattern of pure tetragonal anatase.

because of the strong similarity they have with the Sc^{3+} cation. The substitutional hypothesis is also supported by other works for trivalent cations in general [194]. It is noteworthy that plotting the crystallite mean size vs. the $\text{RE}^{3+}/\text{Ti}^{4+}$ radius ratio for the best photovoltaic performing compositions, i.e. 0.2% metal atoms, result into a satisfactory linear fit with negative slope (see figure 9.14). A possible explanation of this trend lies in the Fajans's rules [408]. Indeed, cations of equal charge form compounds with less ionic character as the ionic radius decreases (charge density increases). Consequently, their compounds with basic anions (i.e. hydroxides, alkoxides, etc. [409]) become less basic as the ionic radius decreases¹. Thus, lighter (and consequently larger because of the lanthanide contraction)

¹Before the introduction of ion exchange chromatography, the different basicity of lanthanides hydroxides, caused by their different ionic radius used to be employed as a separation technique to

Sample	a/Å	c/Å	d/nm
Pr 0.1 %	3.7832 ± 0.0003	9.4937 ± 0.0008	26.5 ± 0.2
Pr 0.2 %	3.7834 ± 0.0002	9.4945 ± 0.0005	26.0 ± 0.1
Pr 0.3 %	3.7833 ± 0.0002	9.4943 ± 0.0005	26.9 ± 0.1
Nd 0.1 %	3.7834 ± 0.0002	9.4942 ± 0.0005	25.8 ± 0.2
Nd 0.2 %	3.7843 ± 0.0002	9.4977 ± 0.0005	25.4 ± 0.2
Nd 0.3 %	3.7848 ± 0.0002	9.4994 ± 0.0005	25.5 ± 0.1
Sm 0.1 %	3.7835 ± 0.0002	9.4963 ± 0.0005	27.1 ± 0.2
Sm 0.2 %	3.7835 ± 0.0003	9.4953 ± 0.0008	25.5 ± 0.2
Sm 0.3 %	3.7835 ± 0.0005	9.496 ± 0.001	26.3 ± 0.2
Gd 0.1 %	3.7832 ± 0.0002	9.4954 ± 0.0006	26.5 ± 0.2
Gd 0.2 %	3.7829 ± 0.0002	9.5002 ± 0.0006	26.2 ± 0.1
Gd 0.3 %	3.7838 ± 0.0002	9.4964 ± 0.0005	26.8 ± 0.1
Er 0.1 %	3.7842 ± 0.0001	9.4972 ± 0.0004	27.0 ± 0.1
Er 0.2 %	3.7842 ± 0.0001	9.4990 ± 0.0006	27.1 ± 0.2
Er 0.3 %	3.7843 ± 0.0002	9.4975 ± 0.0006	25.9 ± 0.1
Yb 0.1 %	3.7844 ± 0.0002	9.4984 ± 0.0005	27.1 ± 0.2
Yb 0.2 %	3.7848 ± 0.0003	9.4997 ± 0.0008	27.6 ± 0.2
Yb 0.3 %	3.7849 ± 0.0002	9.4986 ± 0.0005	25.9 ± 0.1

Table 9.6: Rietveld refinement unit cell constants for TiO_2 beads doped with different amounts of lanthanide ions.

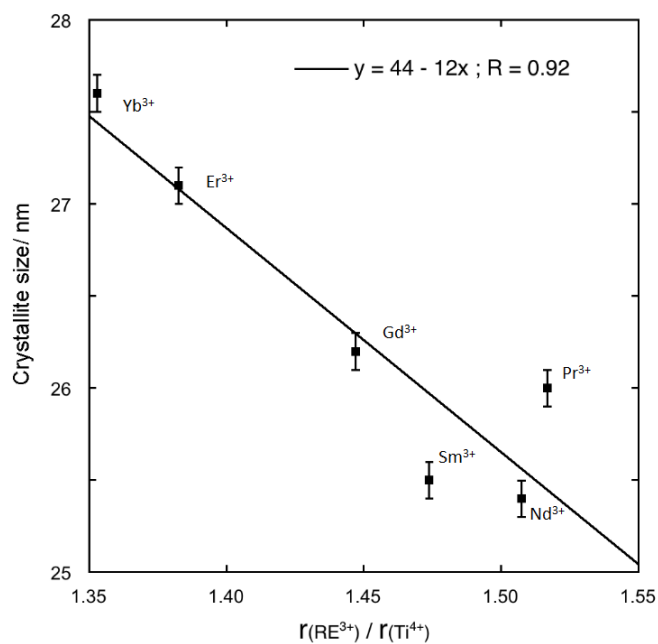


Figure 9.14: Mean crystallites size of RE doped titania beads as a function of the lanthanide ions size (reported as $r_{\text{RE}^{3+}}/r_{\text{Ti}^{4+}}$).

cations form more basic alkoxides capable of catalyzing the hydrolysis reaction. As

extract the 14 elements of the lanthanides series. In fact, the addition of OH^- ions to a solution of different lanthanide nitrates leads to the selective precipitation of the lanthanide hydroxides. For instance, $\text{Lu}(\text{OH})_3$, which is the weakest base of the series, is the first one to precipitate; $\text{La}(\text{OH})_3$ (the strongest base of the series) precipitates last.

a result, more nuclei are generated in the initial stage of the beads growth leading to smaller particles.

SEM micrographs of the 0.2% at doped titania beads are illustrated in figures 9.15 and 9.16 for Pr, Nd, Sm Gd, Er, Yb in panel **a**, **b**, **c**, **d**, **e**, **f**, respectively.

Doped samples retain the same morphology of the undoped titania beads (see

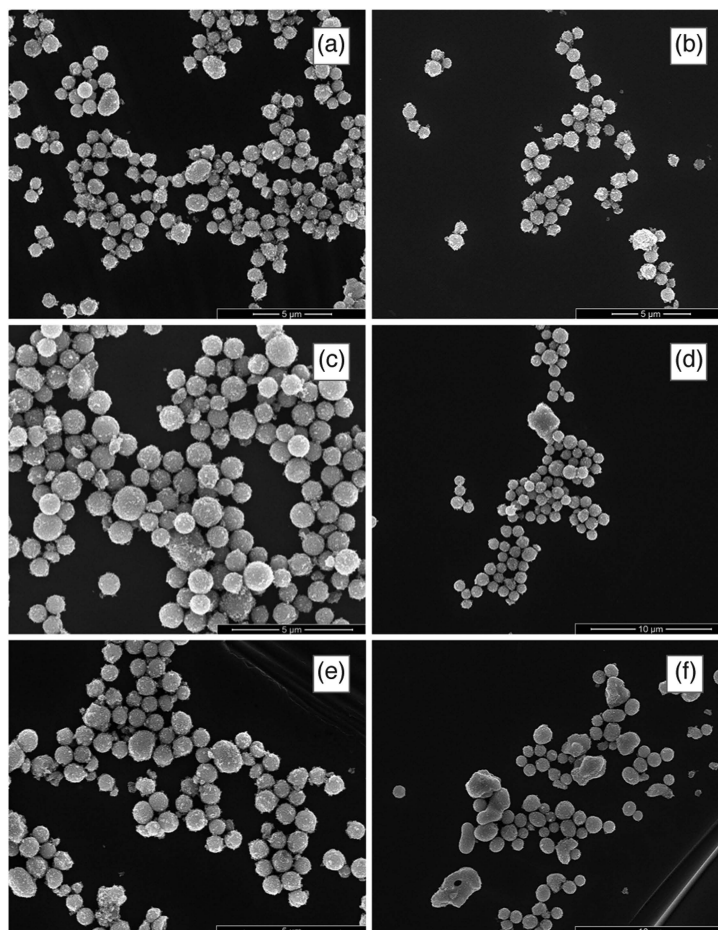


Figure 9.15: SEM micrographs of synthesized bead particles with 0.2% of dopant in anatase. panels **(a)**, **(b)**, **(c)**, **(d)**, **(e)**, and **f** refer to Pr, Nd, Sm, Gd, Er, Yb, respectively.

figure 9.7). Thereby the low RE dopants' percentage keep the good light scattering properties (but improves the photovoltaic parameters, see below) of titania beads. No evident differences are detectable among the various samples with different RE cations. The mesoporous structures with different RE concentrations are practically identical. The beads appear as nearly monodispersed, submicrometric porous spheroidal conglomerates of crystallites with dimensions in agreement with those determined by XRD.

Table 9.7 summarizes SSA values obtained by the BET method and mean pores

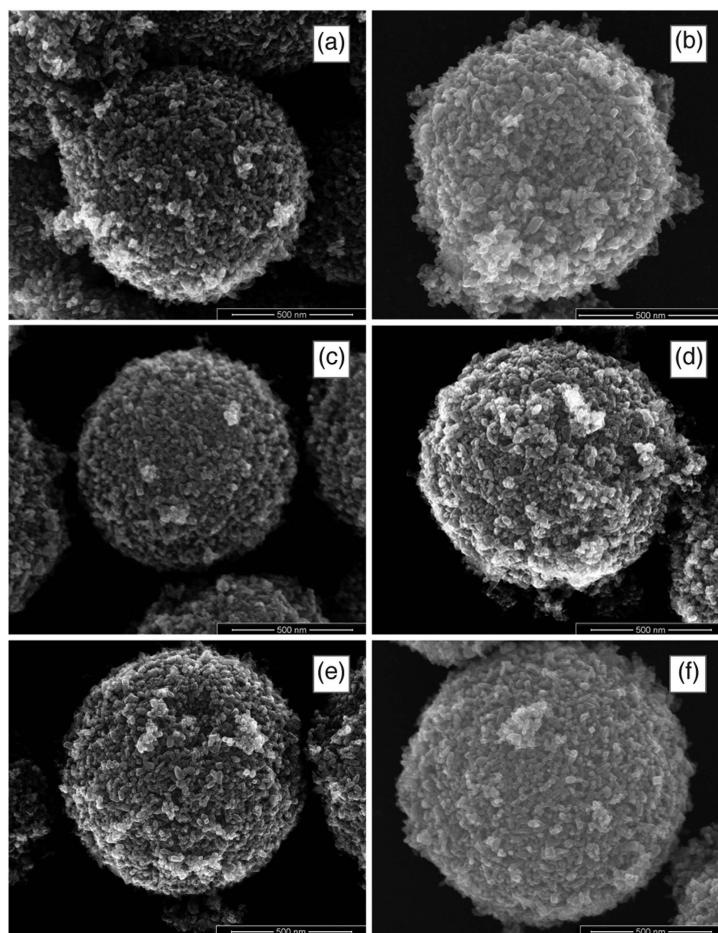


Figure 9.16: High magnification SEM micrographs of synthesized bead particles with 0.2% of dopant in anatase. Panels (a), (b), c, (d), (e), (f) refer to Pr, Nd, Sm, Gd, Er, Yb, respectively.

diameter derived from the BJH algorithm for the 0.2% at samples. The results show

Sample	SSA ($\text{m}^2 \text{g}^{-1}$)	average pore size (nm)
Pr 0.2 %	76.3 ± 0.3	15.6 ± 0.1
Nd 0.2 %	60.1 ± 0.3	16.9 ± 0.1
Sm 0.2 %	73.9 ± 0.3	14.6 ± 0.1
Gd 0.2 %	72.2 ± 0.3	15.6 ± 0.1
Er 0.2 %	105.4 ± 0.3	15.6 ± 0.1
Yb 0.2 %	84.4 ± 0.3	15.6 ± 0.1

Table 9.7: Specific surface area and average pores size for the 0.2 % metal atoms RE doped titania beads.

that, with the notable exception of the erbium doped sample, dopants' nature does not play a significant role in terms of specific surface area and pore size diameter. The results for all compositions are very similar to each other. For this reason, only the 0.2% samples are shown in table 9.7. The larger SSA for erbium and ytterbium

doped TiO₂ have been already reported [7]. However, the higher surface area of the Er³⁺ doped titania do not reflect into larger dye loadings (see table 9.8). Although

Sample	Film thickness μ	Dye loading (mg/cm ²)
Pr 0.1 %	12 \pm 1	0.128 \pm 0.001
Pr 0.2 %	13 \pm 1	0.163 \pm 0.001
Pr 0.3 %	14 \pm 1	0.136 \pm 0.001
Nd 0.1 %	11 \pm 1	0.160 \pm 0.001
Nd 0.2 %	12 \pm 1	0.092 \pm 0.001
Nd 0.3 %	11 \pm 1	0.106 \pm 0.001
Sm 0.1 %	12 \pm 1	0.143 \pm 0.001
Sm 0.2 %	14 \pm 1	0.126 \pm 0.001
Sm 0.3 %	12 \pm 1	0.138 \pm 0.001
Gd 0.1 %	13 \pm 1	0.156 \pm 0.001
Gd 0.2 %	11 \pm 1	0.079 \pm 0.001
Gd 0.3 %	12 \pm 1	0.157 \pm 0.001
Er 0.1 %	12 \pm 1	0.099 \pm 0.001
Er 0.2 %	11 \pm 1	0.093 \pm 0.001
Er 0.3 %	14 \pm 1	0.125 \pm 0.001
Yb 0.1 %	13 \pm 1	0.080 \pm 0.001
Yb 0.2 %	13 \pm 1	0.122 \pm 0.001
Yb 0.3 %	13 \pm 1	0.098 \pm 0.001

Table 9.8: Film thickness and dye loading for all the RE doped TiO₂ samples.

the dye loading data were "normalized" for films' thickness no correlation between the amount of N-719 and either the specific surface area or the dopants radius was found (see figure 9.17). The introduction of RE cations in the anatase lattice seems to modify the surface chemistry of the solid solutions in an unpredictable (or hard to predict) manner. Indeed, as stated in section 4.3, there are countless factors to be taken into account when it comes to the doped TiO₂ surface-dye interaction. In theory, larger SSA and dopants behaving as hard Lewis acids should favor the ruthenium dye adsorption on the oxide's surface by strongly interacting with the carboxylate group of the N-719 (that is a hard-base type group). Hence, the smallest lanthanide cations (the heaviest) should manifest more affinity toward the sensitizer because of their low polarizability (that makes them stronger acids). However, this reasoning does not take into account that the doping is able to modify also the number of Bronsted acid sites on the TiO₂ surface. Furthermore, the number of exposed RE atoms on the anatase surface does not follow any ionic radius trend making hard to quantify the number of Lewis acid sites on the TiO₂ surface. Doping with larger cations brings about a band gap increase as shown in the E_g table and as reported in literature for similar ions [188]. However, relate the band gap values to the DSSCs V_{OC} as done in the previous chapter is not trivial (see below). In fact, once again the surface modification induced by the dopants

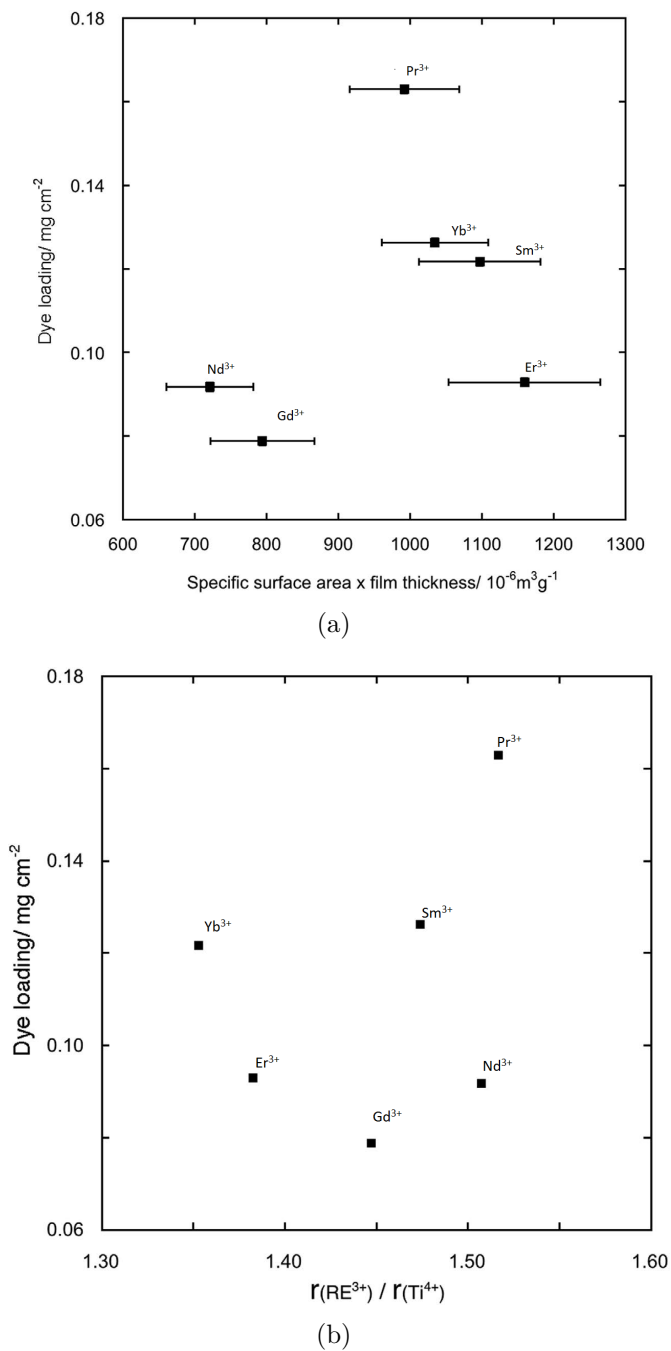


Figure 9.17: (a) Dye loading vs "film's volume" and vs ionic radius ratios, (b), for TiO₂ beads doped with 2 % at RE cations.

affect the chemisorption equilibrium of the additives (TBP, guanidinium cation, Li⁺) that influence the V_{OC} (see chapter 3).

Sample	E_g (eV)
TiO ₂	3.117 ± 0.002
Pr 0.1 %	3.268 ± 0.002
Pr 0.2 %	3.273 ± 0.002
Pr 0.3 %	3.244 ± 0.002
Nd 0.1 %	3.291 ± 0.001
Nd 0.2 %	3.244 ± 0.002
Nd 0.3 %	3.256 ± 0.001
Sm 0.1 %	3.283 ± 0.002
Sm 0.2 %	3.273 ± 0.002
Sm 0.3 %	3.271 ± 0.002
Gd 0.1 %	3.299 ± 0.002
Gd 0.2 %	3.287 ± 0.001
Gd 0.3 %	3.289 ± 0.001
Er 0.1 %	3.217 ± 0.002
Er 0.2 %	3.265 ± 0.002
Er 0.3 %	3.176 ± 0.002
Yb 0.1 %	3.274 ± 0.001
Yb 0.2 %	3.266 ± 0.001
Yb 0.3 %	3.277 ± 0.002

Table 9.9: Band gap values for all doped samples

9.2.2 DSSCs with RE doped photoanodes characterization

Table 9.11 reports the principal photovoltaics parameter for all the RE substituted TiO₂. The data extrapolated from the J-V curves in dark, are reported in table 9.11: J_0 , and ideality factor m were calculated using the single diode model equations (8.13). All the results are compared with pure TiO₂ anatase beads, as a reference. Figure 9.18 presents the polarization curves, under one sun AM 1.5 G irradiance ((a)) and in dark ((b)), of DSSCs with the TiO:RE 2 at % beads, which are the best performing materials. Two considerable results are evident from the photovoltaic parameters analysis:

- All the REs, except Pr and Nd, improve the performance (η) of the devices compared to the pure anatase beads.
- The energy conversion efficiency trend with respect to the amount of dopants introduced into the anatase structure peaks at 0.2 % of metal atoms for all the REs. The highest η value (8.7%) was obtained for the DSSC with Er 0.2% doped anatase.

A possible explanation of these phenomena may be found in the impurities (dopants) mediated electron scattering. The excessive distortion of the anatase lattice caused by the largest cations among the lanthanides series may hinder the electron transport. In fact, the photoanodes made with Pr and Nd doped anatase present the lowest J_{sc}

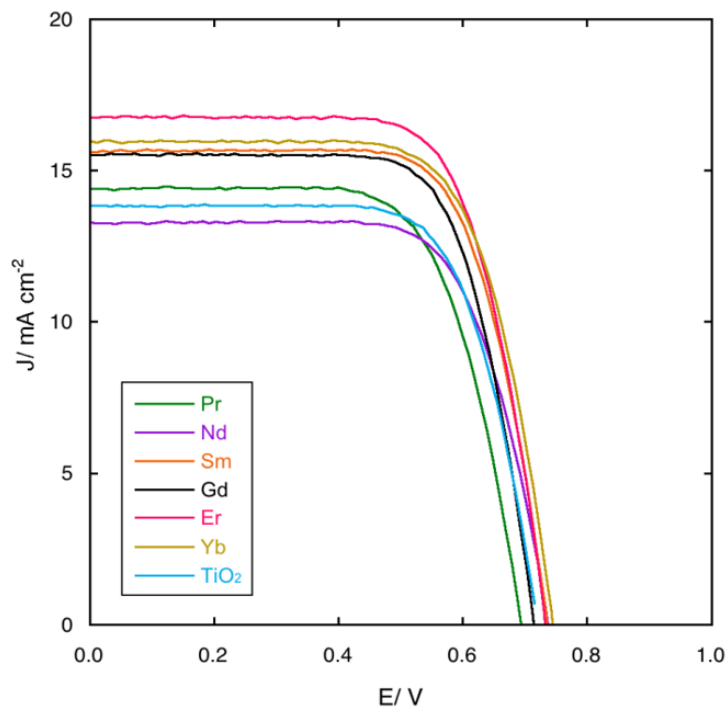
Sample	$J_{SC}(mA)$	$V_{OC}(V)$	η	FF	R_S
TiO ₂ %	13.9 ± 0.1	0.7155 ± 0.0001	7.0 ± 0.1	0.70 ± 0.01	88 ± 1
Pr 0.1 %	12.7 ± 0.1	0.7155 ± 0.0001	6.2 ± 0.1	0.72 ± 0.01	88 ± 1
Pr 0.2 %	14.4 ± 0.1	0.6888 ± 0.0001	6.8 ± 0.1	0.69 ± 0.01	74 ± 1
Pr 0.3 %	10.8 ± 0.1	0.7303 ± 0.0001	5.7 ± 0.1	0.72 ± 0.01	101 ± 1
Nd 0.1 %	12.7 ± 0.1	0.7387 ± 0.0001	6.7 ± 0.1	0.72 ± 0.01	76 ± 1
Nd 0.2 %	13.3 ± 0.1	0.7319 ± 0.0001	6.9 ± 0.1	0.71 ± 0.01	98 ± 1
Nd 0.3 %	12.7 ± 0.1	0.7462 ± 0.0001	6.8 ± 0.1	0.71 ± 0.01	81 ± 1
Sm 0.1 %	15.2 ± 0.1	0.6964 ± 0.0001	7.5 ± 0.1	0.71 ± 0.01	66 ± 1
Sm 0.2 %	15.6 ± 0.1	0.7317 ± 0.0001	8.2 ± 0.1	0.72 ± 0.01	71 ± 1
Sm 0.3 %	14.9 ± 0.1	0.6878 ± 0.0001	7.3 ± 0.1	0.71 ± 0.01	68 ± 1
Gd 0.1 %	14.7 ± 0.1	0.6975 ± 0.0001	7.2 ± 0.1	0.70 ± 0.01	68 ± 1
Gd 0.2 %	15.5 ± 0.1	0.7127 ± 0.0001	7.9 ± 0.1	0.72 ± 0.01	64 ± 1
Gd 0.3 %	13.9 ± 0.1	0.7078 ± 0.0001	6.8 ± 0.1	0.69 ± 0.01	75 ± 1
Er 0.1 %	13.8 ± 0.1	0.7350 ± 0.0001	7.4 ± 0.1	0.73 ± 0.01	78 ± 1
Er 0.2 %	16.7 ± 0.1	0.7313 ± 0.0001	8.7 ± 0.1	0.71 ± 0.01	65 ± 1
Er 0.3 %	14.9 ± 0.1	0.7265 ± 0.0001	7.6 ± 0.1	0.70 ± 0.01	78 ± 1
Yb 0.1 %	13.7 ± 0.1	0.7648 ± 0.0001	7.2 ± 0.1	0.69 ± 0.01	89 ± 1
Yb 0.2 %	16.0 ± 0.1	0.7422 ± 0.0001	8.4 ± 0.1	0.71 ± 0.01	72 ± 1
Yb 0.3 %	12.0 ± 0.1	0.7534 ± 0.0001	6.5 ± 0.1	0.72 ± 0.01	101 ± 1

Table 9.10: Experimental photovoltaic parameters of DSSCs as a function of the RE doping (concentration and cation) of the anatase photoanodes under illumination.

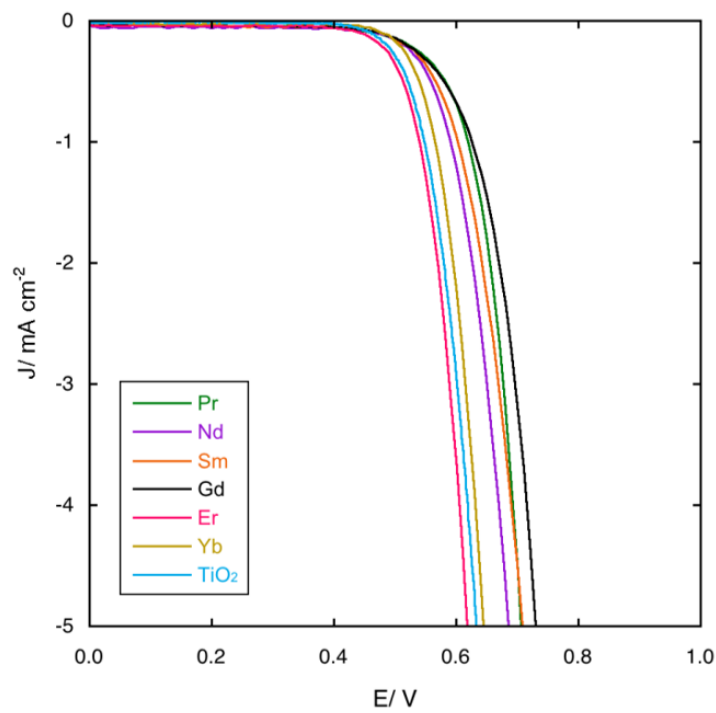
Sample	J_0 (nA/cm ²)	m
TiO ₂ %	0.73 ± 0.03	1.31 ± 0.01
Pr 0.1 %	4.9 ± 0.5	2.03 ± 0.01
Pr 0.2 %	14.4 ± 0.6	2.09 ± 0.01
Pr 0.3 %	5.0 ± 0.5	1.95 ± 0.02
Nd 0.1 %	50 ± 1	2.52 ± 0.01
Nd 0.2 %	5.6 ± 0.7	1.91 ± 0.02
Nd 0.3 %	27 ± 2	2.45 ± 0.01
Sm 0.1 %	5.3 ± 0.3	2.00 ± 0.01
Sm 0.2 %	13 ± 1	2.09 ± 0.02
Sm 0.3 %	5.6 ± 0.4	2.00 ± 0.01
Gd 0.1 %	6.5 ± 0.8	2.07 ± 0.02
Gd 0.2 %	74 ± 2	2.56 ± 0.01
Gd 0.3 %	5.4 ± 0.3	2.06 ± 0.01
Er 0.1 %	0.57 ± 0.06	1.66 ± 0.01
Er 0.2 %	1.5 ± 0.2	1.57 ± 0.01
Er 0.3 %	4.0 ± 0.6	1.90 ± 0.02
Yb 0.1 %	0.63 ± 0.08	1.70 ± 0.02
Yb 0.2 %	0.29 ± 0.06	1.47 ± 0.06
Yb 0.3 %	0.9 ± 0.1	1.73 ± 0.06

Table 9.11: DSSCs' with RE doped photoanodes dark parameters (J_0 and m), calculated from the dark current-voltage curve, and "diode" TiO₂/dye/electrolyte junction.

values. In figure 9.19 J_{SC} is plotted against the radius ratios for the 0.2% samples and its decreasing trend is quite apparent. 0.2 % at may be a doping "threshold" value, above which any beneficial effect introduced by the RE ions is overcome



(a)



(b)

Figure 9.18: J-V polarization curves of DSSCs assembled with titania mesoporous beads doped with the six lanthanides under investigation. The J-V curves under illumination (a) and dark (b) refer to the 2 % at RE doped samples.

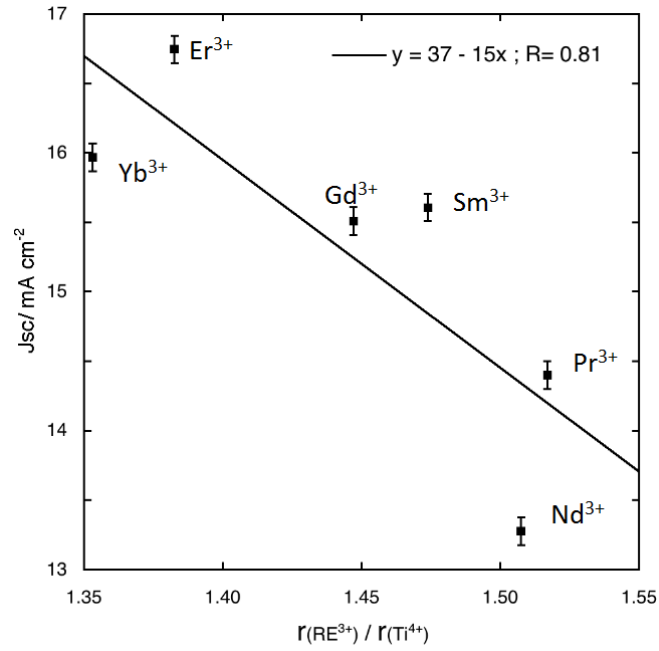


Figure 9.19: J_{sc} trend vs radius ratio of the RE dopants with respect to the Ti^{4+} ion.

by the impurities mediated electron scattering. A similar optimum concentration

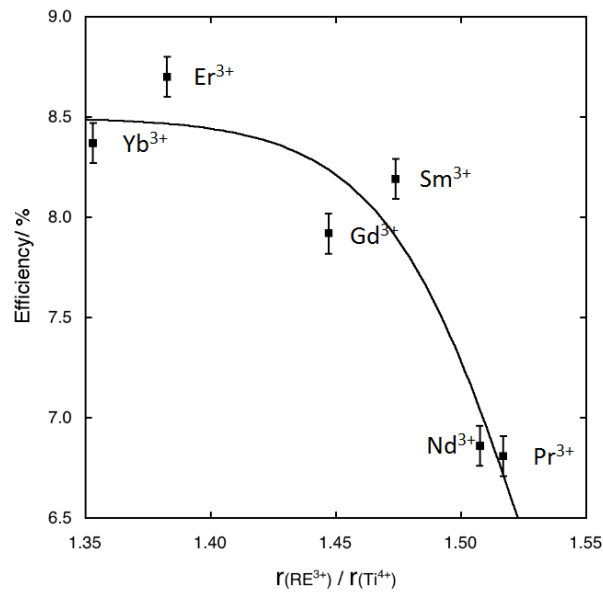


Figure 9.20: Asymptotic fit of the efficiency values of cells assembled with photoanodes with 0.2 RE % cations solid solutions versus the $\text{RE}^{3+}/\text{Ti}^{4+}$ radius ratio

of dopants has been already found for titania photoanodes doped with Sc^3 [188] and Y^{3+} [194] that share most of the chemical properties with the lanthanides. In particular, $\text{TiO}_2:\text{Sc}^{3+}$ solid solutions have shown the best energy conversion

efficiency for sample doped with 0.2 at % [188]. Figure 9.20 shows the plot of η vs the radius ratio for the 0.2 % doped samples. The efficiency asymptotic behavior shown in figure 9.20 can be fitted by the following equation:

$$y = a + \frac{b - a}{1 + \exp\left(\frac{x-c}{d}\right)} \quad (9.1)$$

The energy conversion efficiency reaches a plateau for $r_{RE^{3+}}/r_{Ti^{4+}}$ values greater than 1.40, which corresponds to the Er ($\eta = 8.7\%$) and Yb ($\eta = 8.4\%$). The very close efficiency values for the erbium and ytterbium doped anatase stems from their similar crystal ionic radius (1.03 and 1.01 AA , respectively).

A similar correlation between the DSSC's V_{OC} and the concentration or the ionic radius of the REs is hard to establish because doping introduces plenty of effects all affecting the open circuit voltage. As discussed in the introduction, V_{OC} depends on the TiO_2 Fermi level position with respect to the redox shuttle potential and on J_{SC} and J_0 through equation 2.5. Needless to say, RE doping can shift TiO_2 band edges position and, at the same time, act on the J_0 by modulating the competition between electron transport and recombination with the electrolyte (see below). Furthermore, as already shown for the dye adsorption case, lanthanide dopants may alter the chemisorption equilibrium of electrolyte's additives. Ions adsorbed at the TiO_2 /dye/electrolyte modify both the titania's band edges positions and the kinetics of the interception reaction (see equations 3.6, 2.5 and section 3.3). The overlapping of all these effects did not allow to find a straightforward correlation between dopants' position among the lanthanides series and DSSCs open circuit voltage.

Table 9.12 reports doped photoanodes electron diffusion length and charge collection efficiency extrapolated from the EIS measurements ². Figure 9.21 shows the trends of the electron diffusion length vs. the radius ratios and of the η values vs. electron diffusion length, for the 0.2% samples. L_n decreases with an approximately linear trend as the radius ratios increases, while the efficiency increases with an asymptotic law as the electron diffusion length increases. The best fit for the η vs L_n trend is given by an equation type:

$$y = a - bc^x \quad (9.2)$$

Both these results are in agreement with those obtained from the analyses of J-V curves under light and in dark. Er 0.2% and Yb 0.2% samples electron diffusion

² $\eta_{coll} = 1 - \left(\frac{L}{L_n}\right)^2$ [410].

Sample	L_n (μm)	η_{coll}
Pr 0.1 %	51 ± 4	0.948 ± 0.001
Pr 0.2 %	43 ± 4	0.915 ± 0.001
Pr 0.3 %	70 ± 4	0.961 ± 0.001
Nd 0.1 %	52 ± 4	0.958 ± 0.001
Nd 0.2 %	47 ± 4	0.939 ± 0.001
Nd 0.3 %	46 ± 4	0.946 ± 0.001
Sm 0.1 %	61 ± 4	0.963 ± 0.001
Sm 0.2 %	47 ± 4	0.920 ± 0.001
Sm 0.3 %	55 ± 4	0.955 ± 0.001
Gd 0.1 %	44 ± 4	0.920 ± 0.001
Gd 0.2 %	46 ± 4	0.947 ± 0.001
Gd 0.3 %	46 ± 4	0.937 ± 0.001
Er 0.1 %	97 ± 4	0.985 ± 0.001
Er 0.2 %	94 ± 4	0.986 ± 0.001
Er 0.3 %	66 ± 4	0.956 ± 0.001
Yb 0.1 %	110 ± 4	0.986 ± 0.001
Yb 0.2 %	122 ± 4	0.989 ± 0.001
Yb 0.3 %	93 ± 4	0.981 ± 0.001

Table 9.12: Electron diffusion length (L_n) and charge collection efficiency η_{coll} values obtained by the fit of EIS spectra using the transmission line model.

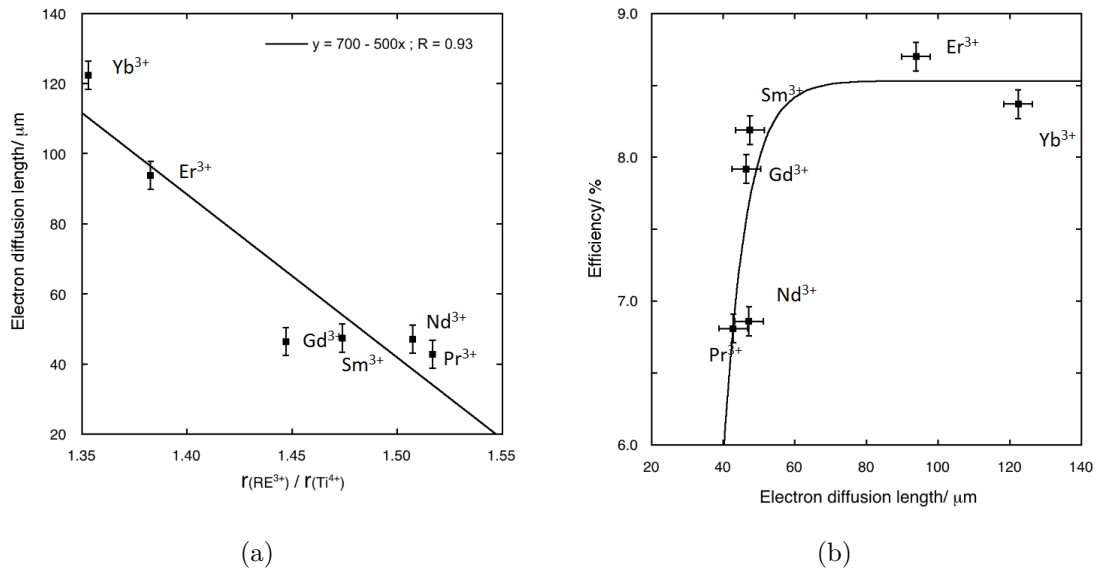


Figure 9.21: (a) L_n vs $r_{RE^{3+}}/r_{Ti^{4+}}$ for the 0.2% samples. A quasi-linear trend appears. (b): η vs L_n for the 0.2% case. An asymptotic law allows to fit the trend of the energy conversion efficiency against the electron diffusion length.

length and charge collection efficiency values apparently contradict the photovoltaic efficiency data. In fact, the Er 0.2% DSSC shows higher η , compared to the Yb

0.2% one despite possessing lower L_n (and η_{coll}). However, Yb^{3+} doped photoanode has a higher series resistance presumably caused by the lower SSA of titania beads containing ytterbium. Similarly to hard templated TiO_2 , low specific surface areas most likely increase the resistance of the TiO_2/FTO contact. Furthermore, the lower SSA brings about less reactivity during the particles sintering step involved in the thermal treatment of the screen printed photoanode consequently producing a lower level of particles interconnection. Besides, a more detailed comparison between the Er 0.2% and Yb 0.2% cells show that:

1. The efficiency values are very similar, being their difference only slightly higher than the uncertainty on the values.
2. The charge collection efficiency depends on the L_n/L ratio. Hence, by taking into account both the electron diffusion length and the thickness of the printed electrodes, the η_{coll} for the Er 0.2% and Yb 0.2% samples are practically identical if the uncertainties are taken into account.

From what observed and discussed until now, a fundamental question does not seem to find an answer: why do RE cations heavier than Nd (i.e. Sm, Gd, Er, Yb) improve energy conversion efficiency of DSSCs' photoanode compared to pure anatase? As mentioned in 4.3 trivalent cations generate holes in the TiO_2 valence band that reduce or suppress the concentration of oxygen vacancies [411]. Oxygen vacancies constitute the main source of electron deep trapping and recombination with the electrolyte. Equivalently trivalent doping can be thought as a passivation the Ti^{3+} traps [7], [412]. A similar effect has been reported by Chandiran et al. [194] for yttrium doped DSSCs. This paper reports the effectiveness of low concentrations (0.1%) of trivalent a dopant (Y^{3+}) in improving the electron recombination life time τ_r . Figure 9.22 illustrates the Bode plots for the 0.2 % doped and pure TiO_2 cells. The suppression of the oxygen defectivity by RE cations is supported by the fact that the maximum frequency peak in the mid-frequency range of the phase Bode plot shifts to lower values for the samples containing rare earths ions compared to pure TiO_2 . Similar features can be observed in the Nyquist plots (see Figure 9.23): the recombination frequency (the maximum in the complex impedance graph) for the doped samples is lower than the one for pure TiO_2 . The peaks at higher frequencies correspond to the charge transfer at the counter electrode, while the peaks at the lower frequencies (mid-frequency range) are related to the charge recombination rate and its reciprocal is regarded as the electron lifetime [413], [414]. Table 9.13 reports

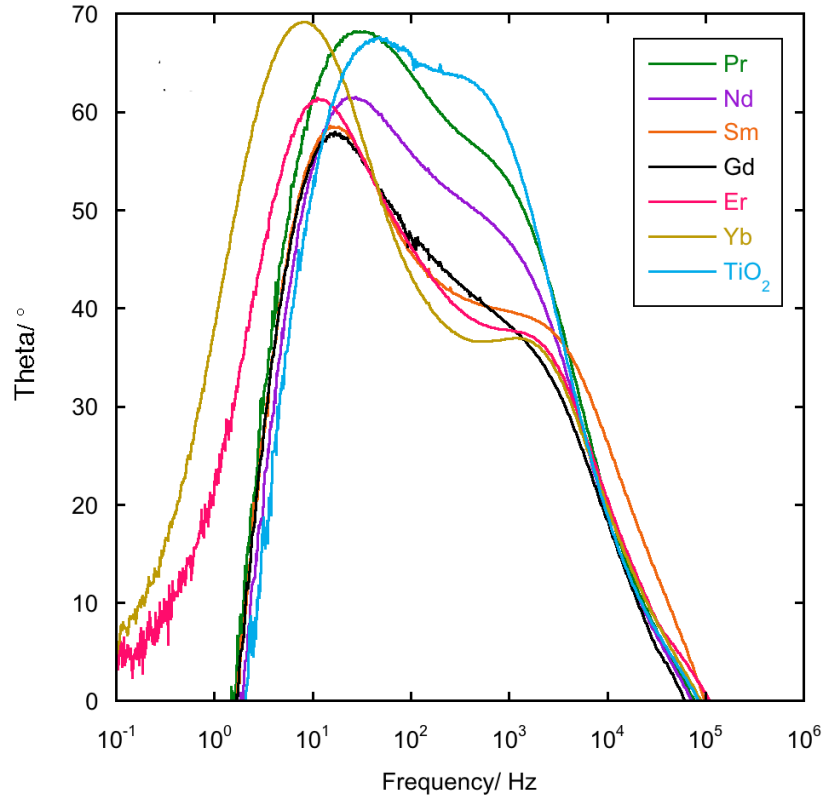


Figure 9.22: Bode plot for DSSCs assembled with pure and RE doped titania beads 0.2 % at.

the electron recombination lifetime derived from the frequencies corresponding to the absolute maximum of each Bode graph ($\tau_r = \frac{1}{2\pi f_{max}}$). Hence, DSSCs containing

Sample	τ_r (ms)
TiO ₂	21 ± 1
Pr 0.2 %	27 ± 1
Nd 0.2 %	29 ± 3
Sm 0.2 %	33 ± 2
Gd 0.2 %	56 ± 7
Er 0.2 %	74 ± 7
Yb 0.2 %	103 ± 8

Table 9.13: Estimated electron recombination lifetimes for RE doped and undoped titania photoanodes (0.2 % at).

RE doped photoanode have longer electron recombination lifetime, indicative of a more effective suppression of the back reaction between the injected electrons and the electrolyte. This is compatible with lower deep trapping and oxygen vacancies catalyzed electron transfer to the triiodide. The shift is maximum for the best performing samples, i.e. Er 0.2% and Yb 0.2 % (that have the highest τ_r : 74 and

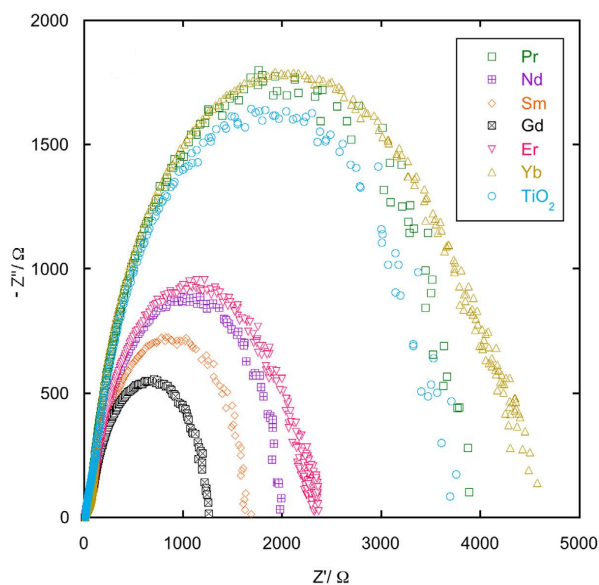


Figure 9.23: Nyquist plots (for 0.2% RE cations solid solutions and pure TiO_2 DSSC photoanodes).

103 ms, respectively). This explanation, coupled with the electron scattering by impurity defects, would justify all the trends shown in figures 9.19-9.21.

Normalized IPCE curves for the 0.2 % at samples are presented in figure 9.24 for sake of comparison. DSSCs containing Pr, Sm, Er and Yb show very similar behaviors. On the other hand, quantum efficiency deviates from the other doped samples for photoanodes containing Nd and Gd. In fact, the 0.2 % Nd sample shows an enhanced response at lower wavelengths (< 500 nm) and a depressed one at higher wavelengths. The 0.2% Gd sample manifest a substantially enhanced response in comparison to the other samples at wavelengths > 500 nm. A possible explanation to these phenomena can be found in the f-f transitions associated with lanthanides ions. Colors of lanthanides ions (both in solution and in the solid state) are determined by the Laporte-forbidden f-f transition. Uv-Vis absorption spectra and colors of lanthanides are almost non-dependent on the particular chemical surroundings because f-orbitals do not take part to chemical bonds. Gd^{3+} does not absorb radiation in the visible range because its $4f^7$ electronic configuration is particularly stable due to a half-filled set of f-orbitals. This is, for example, the reason why Gd^{3+} compounds appear colorless. Hence, doping TiO_2 with Gd^{3+} limits the competition with the dye for light absorption in comparison to the other lanthanides. Thereby, the improved quantum efficiency in the range of N-719 maximum light absorption may justify the fact that the $\text{TiO}_2:\text{Gd}^{3+}$ cell has a high efficiency (7.9%) though it shows the second shortest electron diffusion length

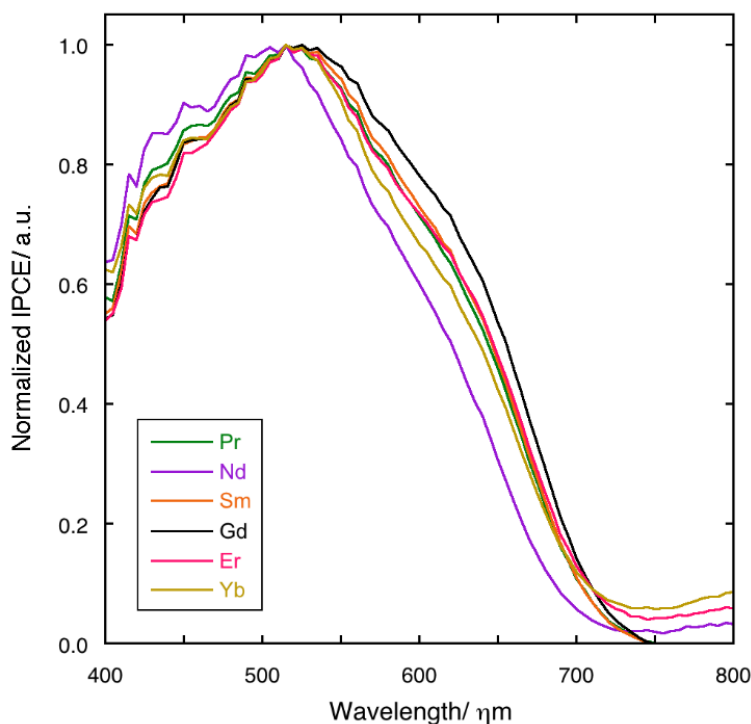


Figure 9.24: Lanthanides doped DSSCs normalized quantum efficiency spectra.

among the 0.2% samples (after Pr). Conversely, Nd^{3+} compounds are reddish-purple colored (like the N-719 dye), thus green light ($\lambda > 510$ nm) is absorbed and used to promote f-f transition. Even if the effect might not be very marked because f-f transitions are characterized by a low molar extinction coefficient, part of the light intended for charge generation is subtracted from the dye. This consideration may justify the lower IPCE response of the Nd doped sample above 500 nm.

9.3 TiO_2 /chirality selected SWCNTs heterojunctions

9.3.1 SWCNTs characterization

Raw SWCNTs

Thermal stability of HiPCO prepared raw carbon nanotubes were investigated by using TGA (see fig. 9.25) The CNTs retained thermal stability until approximately 350 °C, where the amorphous carbon begins to oxidize. At approximately 450 °C, the smaller diameter SWCNTs lose thermal integrity. At this temperature approximately 10% of the bulk weight is lost. The largest burning rate of the CNT

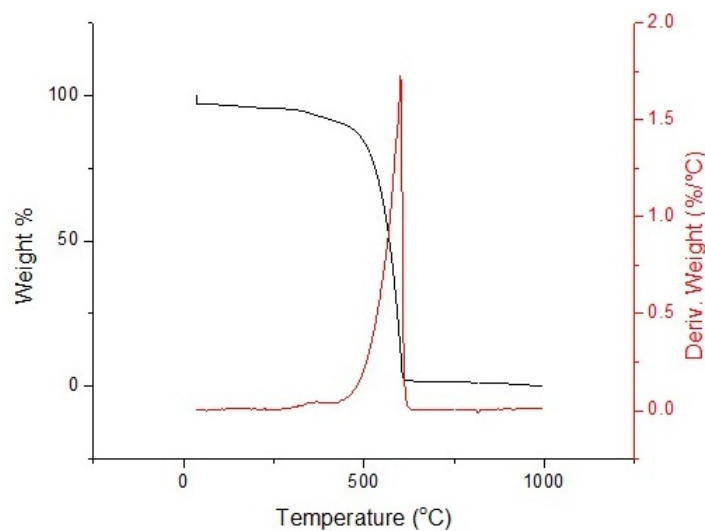


Figure 9.25: Thermogravimetric analysis of HiPCO prepared raw carbon nanotubes

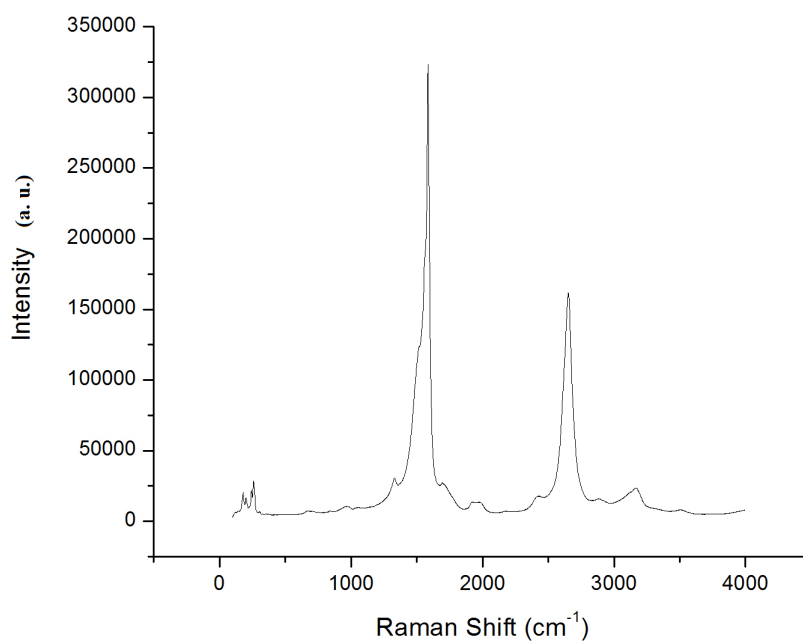


Figure 9.26: Raman spectrum of carbon nanotubes prepared by high-pressure carbon monoxide

mixture (the derivative weight peak), occurs at 550 °C. The residual weight, from the oxidation of the iron catalyst residue, makes up approximately 3.0%.

Figure 9.26 presents the Raman spectra of unsorted HiPCO tubes. The RBM (radial breathing mode) bands are located at 200 cm^{-1} , 242 cm^{-1} , and 263 cm^{-1} . The bands' close proximity is characteristic of the small range in diameters obtained

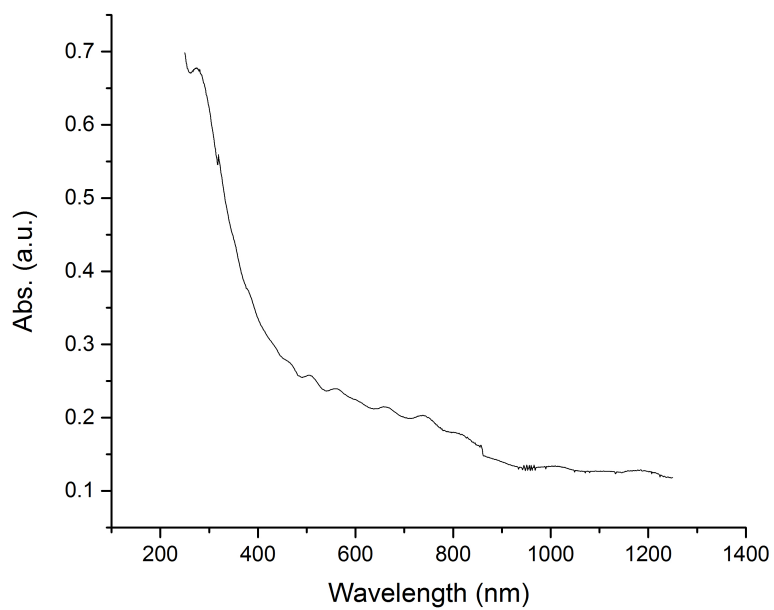
by the HiPCO growth method [415], [416]. The low intensity of the D band (located at 1330 cm^{-1}) suggests the nanotubes grown by the HiPCO procedure contain few defects. The ratio of intensities between the D and G bands is 0.09, indicating a high quality (low defectivity) sample. The G-band is split into G^- (1529 cm^{-1}) and G^+ (1587 cm^{-1}) illustrating a large fraction of small diameter, semiconducting, single-walled carbon nanotubes.

UV-vis-NIR spectrum of raw HiPCO tubes (dispersed in a 2% SDS solution) is shown in figure 9.27 A series of broad peaks in the lower wavelength range is revealed. The existence of a large number of broad peaks in the mid to lower wavelengths confirms Raman spectroscopy data showing a prevalence of small diameter semiconducting carbon nanotubes species.

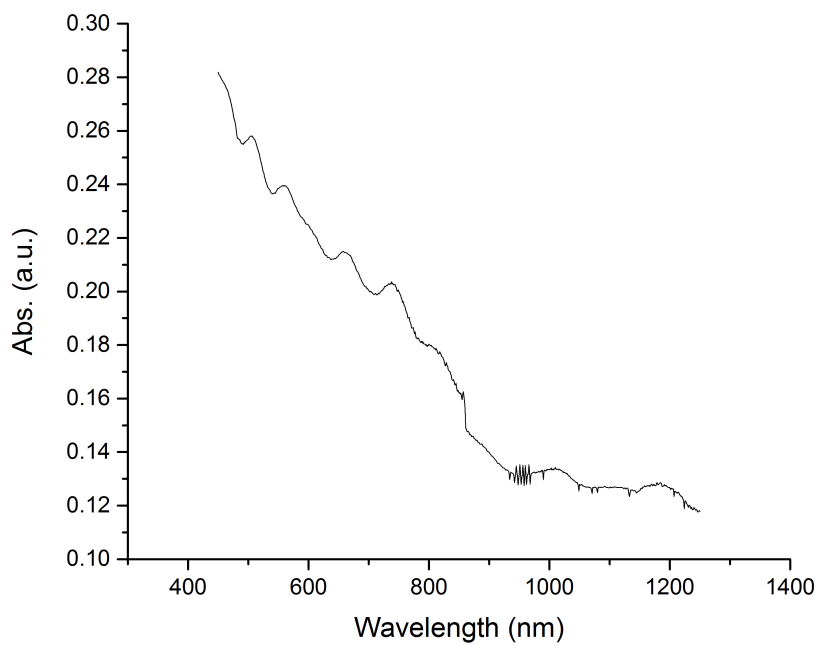
Chirality separated tubes

Single chiralities have been successfully separated through SEGC by Liu et al. [279], Tvrđy et. all [278]. Furthermore, Tvrđy et. all have employed the **(6,5)** as electron donor material for "polymer free" bulk heterojunction solar cells.

On the other hand, for DSSC application, the combination of being a relatively simple chirality to isolate, and the location of its absorption peaks away from the dye absorption features, [417], [418] makes the **(7,3)** species an ideal chirality to target in separation procedures. However, the original SEGC methodology originally developed by the Katura's group ([279]) involves at least two-passes through the chromatographic column. Needless to say, separation procedures based on multiple iterations bring about non-negligible material losses making the collection of a sufficient amount of material for DSSCs photoanodes impracticable. Hence, we targeted and isolated single chiralities from the bulk SWNT solution by adding a sufficient amount of solution to "overload" the column in order to obtain a high enough purity in a single pass. This involves using a different loading procedure for each of the chiralities desired. By taking advantage of this technique an $87\% \pm 0.1$ purity **(7,3)** sample was produced by single pass separation. Figure 9.28 shows the absorption spectra of the **(7,3)** obtained by single the pass procedure. Samples purity was calculated by integrating the E_{11} absorption peaks. The **(7,3)** chirality has a E_{11} absorption band located at 990 nm and an E_{22} absorption band at approximately 510 nm. Depending on the amount of CNTs solution used to overload the column stack, columns containing the **(6,4)**, typically eluted from the 2^{nd} column, are either mixed with **(7,3)** or **(6,5)**. Figure 9.29 shows the absorption spectrum of a **(7,3)/(6,4)** mixture. The calculated purity of the **(7,3)**

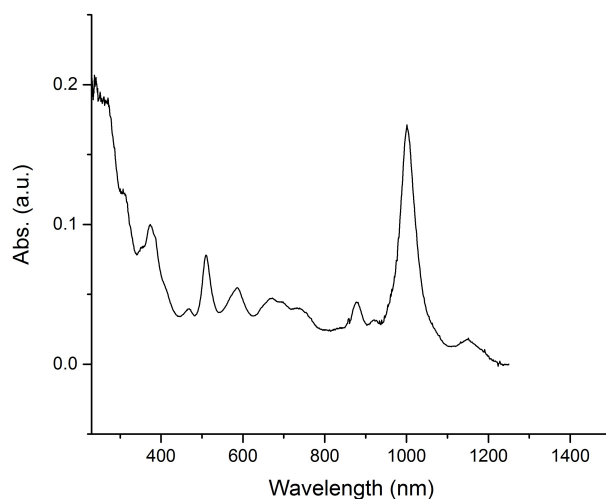


(a)

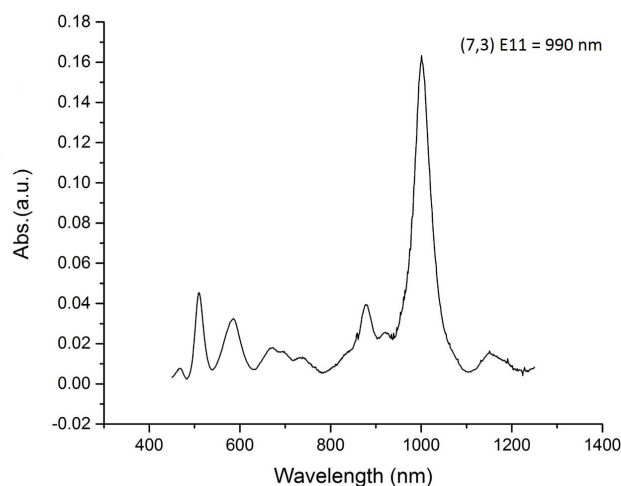


(b)

Figure 9.27: UV-vis-NIR spectroscopy of dispersed HiPCO carbon nanotubes in 2 wt% SDS. Full Spectrum taken from 200 to 1300 nm (a), magnification from 450 to 1300 nm (b).



(a)



(b)

Figure 9.28: **(7,3)** chirality SWCNTs obtained by a single pass separation procedure. **(a)** Absorption spectra in the 1300-200 nm. **(b)** Magnification from 450 to 1300 nm.

and **(6,4)** is $52.8\% \pm 0.1$ and $25.9\% \pm 0.1$, respectively. The remaining fraction is constituted by metallic tubes. Figure 9.30 presents the absorption spectrum of a **(6,5)/(6,4)** mixture and a photoluminescence map showing the presence of **(6,5)** and **(6,4)** chiralities. The calculated purity of the **(6,5)** and **(6,4)** is $45.3\% \pm 0.1$ and $49.7\% \pm 0.1$, respectively. Figure 9.31 shows the absorption spectra of the highly-enriched **(6,5)** solution. A photoluminescence counter map was used to reaffirm the purity of the **(6,5)** chirality, as in figure 9.31 **(b)**. Using the UV-vis-

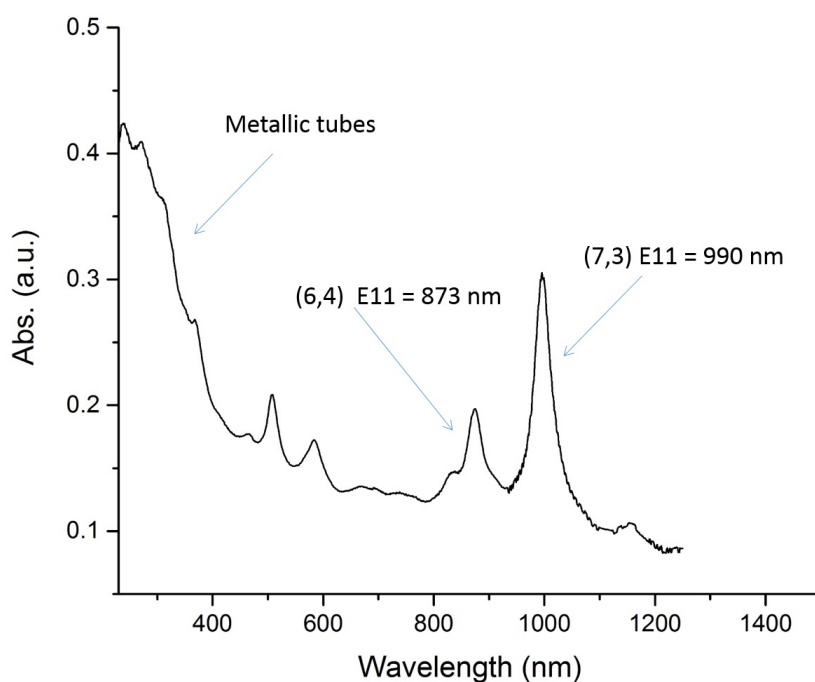
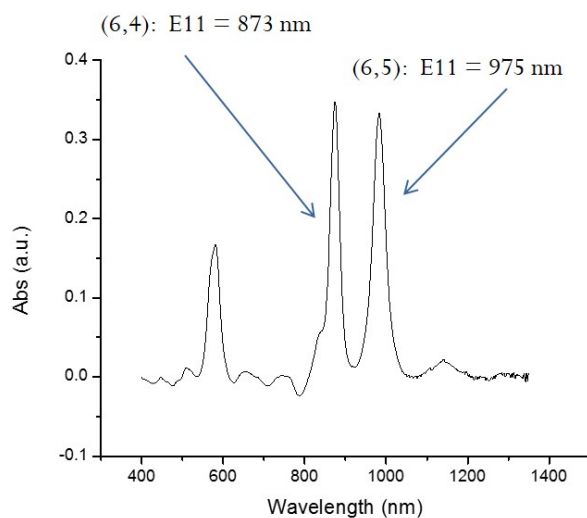


Figure 9.29: UV-vis-NIR spectrum of single-pass separation of $(7,3)/(6,4)$ chiralities.

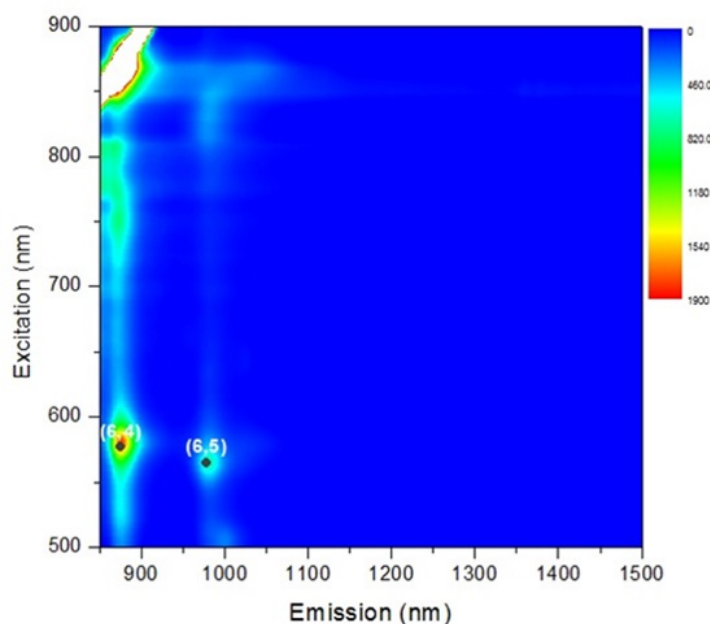
NIR spectrum from figure 9.31 (a), the purity of $(6,5)$ has been calculated to be 93%. Based on the intensity of the metallic range of the UV spectra (200-400 nm), both the $(6,5)/(6,4)$ and $(6,5)$ fractions have very little metallic species. Based on the absorption spectrum of $(7,3)$ in figure 9.28, the intensity of the metallic range is quite small in comparison to the semiconducting peaks. In the case of the mixed $(7,3)/(6,4)$ solution, however, there is a comparatively higher absorption intensity in the M_{11} range, indicating a larger presence of metallic species in the sample (see figure 9.29). Photovoltaic behavior of DSSCs fabricated using single chirality samples ($(6,5)$ and $(7,3)$) and mixtures of two chiralities ($(6,5)/(6,4)$ and $(7,3)/(6,4)$) will reflect both the intrinsic optoelectronic properties of the chiralities and the purity of the samples (see below).

SWCNTs Thin films characterization

The UV-vis-NIR transmittance spectra, in figure 9.32, show the amount of light that can travel through the film. Although none of the films shows absorption peaks in the range of the N-719 dye maximum absorption (see fig. 4.7 in the visible region, MLTC transition), the $(6,5)$ chirality E_{44} transition [419] (at 308 nm, see



(a)

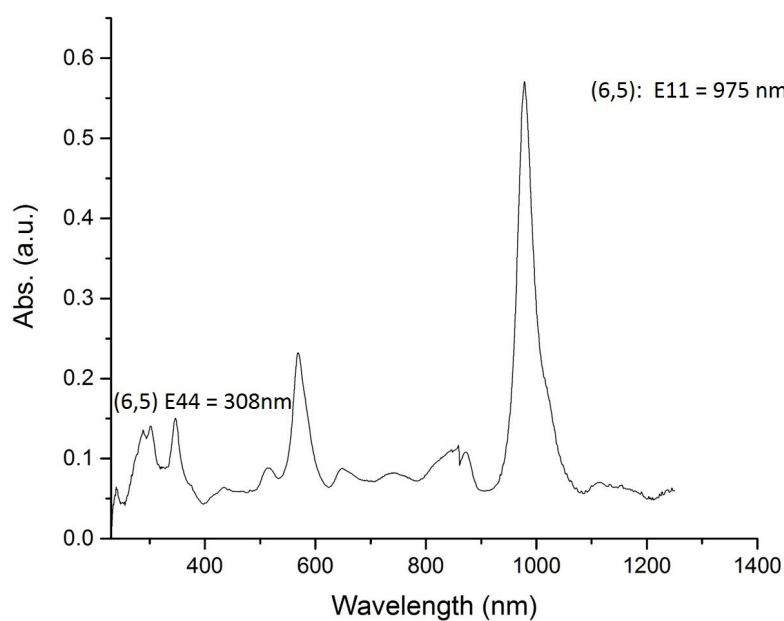


(b)

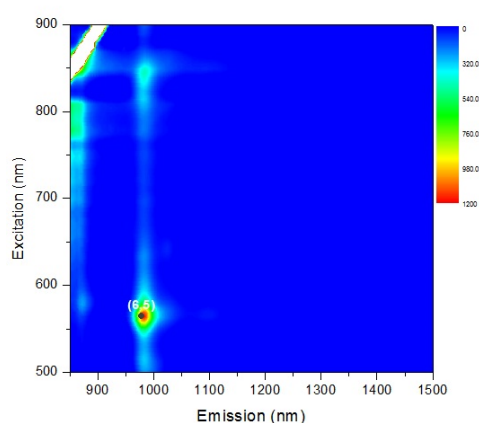
Figure 9.30: Uv-vis. spectrum for a single pass separation of **(6,5)/(6,4)** tubes, **(a)**. Photoluminescence map of the separated chirality, **(b)**.

figure 9.31) partially overlaps with the intraligand (π - π^*) transition of the N-719 at 313 nm. Even if this is not a marked effect because appears in the proximity of the FTO-soda lime glass absorption edge, it still subtracts light for photovoltaic charge generation.

Table 9.14 summarizes the sheet resistance values of chirality separated thin films. The resistance is the lowest for the mixed chirality film due to the presence of



(a)



(b)

Figure 9.31: Uv-vis spectrum for a single pass separation of **(6,5)** tubes, **(a)**. Photoluminescence map of the separated chirality, **(b)**.

metallic tubes. The dual mixed semiconducting chirality films **(6,5)/(6,4)** and **(7,3)/(6,4)** possess the highest resistance due to the films being comprised of two semiconducting chiralities with different band gaps (work function mismatch, intertubes energy barrier) and the absence of metallic species. The single-chirality films demonstrated a low resistance as the high purity films are composed of a single band gap.

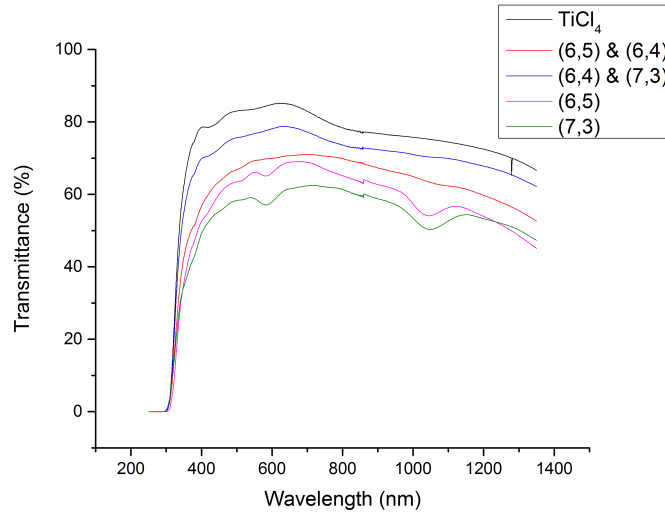


Figure 9.32: Transmittance measurements of chirality-specific films. TiCl_4 treated FTO-glass has been used as reference

Chirality	Sheet Resistance ($\text{k}\Omega/\square$)
Mixed Chirality	3.695
(7,3)	5.822
(6,5)	5.992
(7,3)/(6,4)	46.493
(6,5)/(6,4)	51.464

Table 9.14: Sheet Resistance measurements of chirality-specific films.

9.3.2 Performances of DSSCs with single chiralities CNTs (photoanode)

Figure 9.33 and Table 9.15 report the I-V curve and the salient photovoltaics parameters for DSSCs containing chirality specific SWCNTs in the photoanode structure. DSSCs' performances were related to purity of the deposited SWCNTs films and their optoelectronic (chirality dependent) properties. The mixed film has

Sample	η (%)	FF (%)	I_{sc} (mA)	V_{OC} (V)	R_s (Ω)	R_{sh} (Ω)	I_o (μA)	m
(7,3)	0.98	48	5.03	0.374	19.8	122.4	24	2.12
(6,5)	0.74	47	4.62	0.340	20.1	110.4	45	2.47
Mixed Chirality	0.54	32	5.51	0.307	22.4	31.4	220	3.93
(7,3)/(6,4)	0.28	30	3.99	0.235	28.6	53.4	73	2.80
(6,5)/(6,4)	0.24	33	2.79	0.263	48.5	352.1	20	2.92

Table 9.15: Significant Photovoltaics parameters for chirality specific photoanodes under $1 \text{ kW}/\text{m}^2$ irradiance AM 1.5 G and in dark (I_o and m).

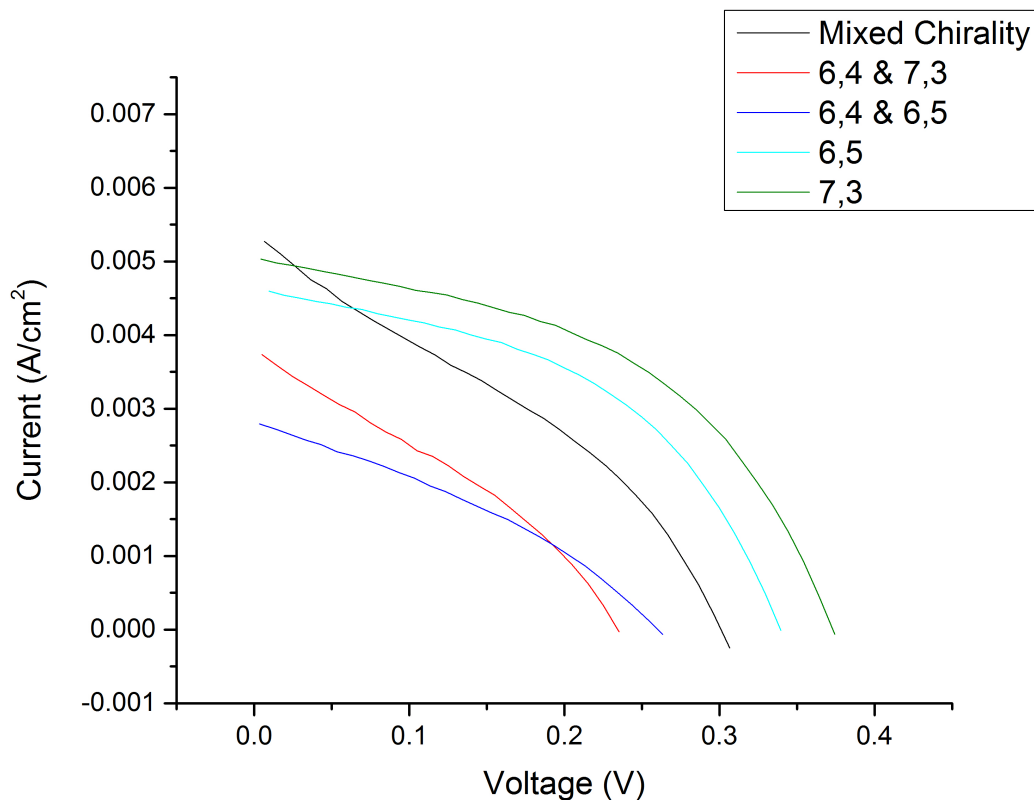


Figure 9.33: I-V Curves of DSSCs taken under an irradiance of 1 sun for chirality specific solar cells.

the largest variation in band gaps, as well as metallic species. The two chirality dual mixed films vary in their purity: the **(7,3)/(6,4)** film has a greater amount of metallic tubes than the **(6,5)/(6,4)** film. The single-chirality films: **(6,5)** and **(7,3)** have the highest purity in semiconducting tubes, as well as a high single-chirality purity.

Two opposite effects act on cells open circuit voltage (V_{OC}): the TiO_2 Fermi level down shift (more positive potentials with respect to the vacuum level) caused by the Fermi level energy equilibration with the SWCNTs [223] and the energy barrier height of the TiO_2 /SWCNTs/FTO interface that keeps electrons from returning into the nanostructured TiO_2 and recombining (through TiO_2 grain boundaries and point defects) with the electrolyte [153], [222]. As stated in 4.4 a simple abrupt type I heterojunction model based on charge transfer by thermionic emission can be used, as a first approximation, to describe the TiO_2 -semiconducting SWCNTs interface. Hence, a "Schottky-like" barrier height can be extrapolated from DSSCs dark I-V curves [153], [223], [420] [222]. Figure 9.34 presents dark polarization

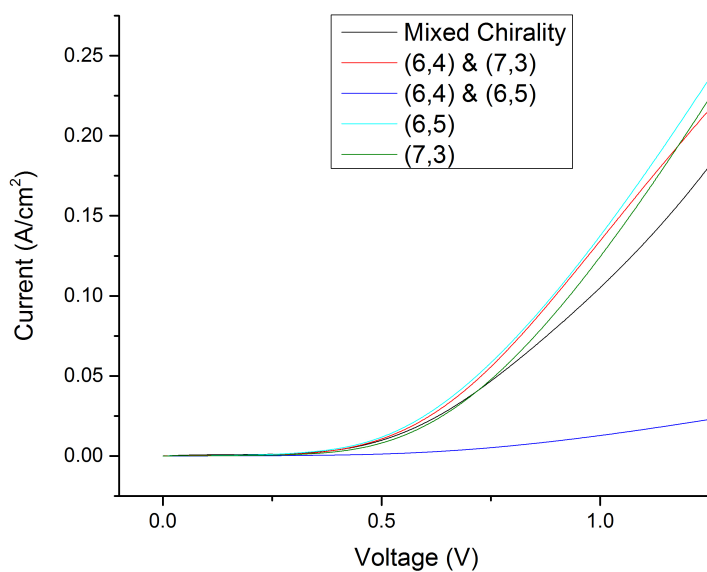
Chirality	Schottky barrier height (eV)
(7,3)	0.68 ± 0.2
(6,5)	0.65 ± 0.1
(6,5)/(6,4)	0.45 ± 0.2
(7,3)/(6,4)	0.39 ± 0.3
Mixed Chirality	0.36 ± 0.1

Table 9.16: “Schottky-like” barrier height at the TiO₂/SWCNTs interface for chirality-specific films into DSSCs

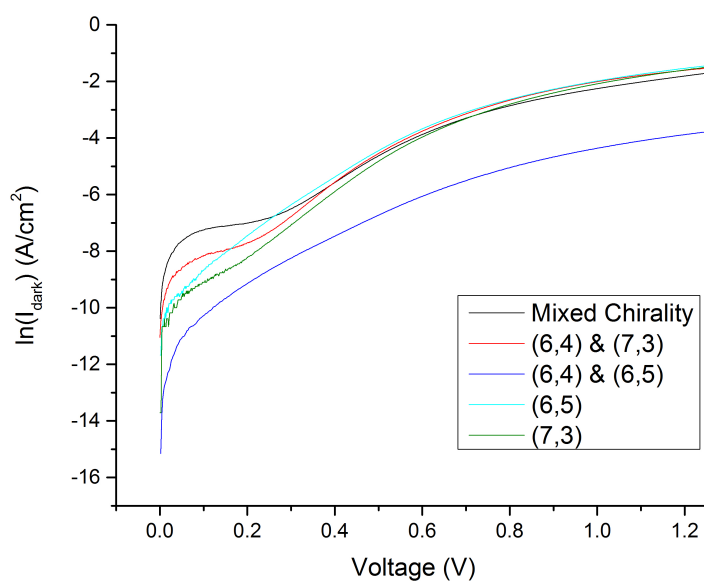
curves for the DSSCs assembled with different chiralities photoanodes. Dark I-V curves are illustrated according to the standard formalism used for homo, hetero and Schottky junction diodes: positive current reported in a linear (Figure 9.34 (a)) and the semi-logarithmic plot against the voltage (see Section 8.5) Figure 9.34 (b)). Two junctions are evident in the semi-logarithmic curve with the one ranging from 0 to 0.2 V belonging to the SWCNTs/TiO₂ interface [153], [222] (and the one visible between 0.3 and 0.6 V belongs to the TiO₂/dye/electrolyte interface). “Schottky-like” barrier heights were calculated as follow: $\ln[1/(1 - \exp(\frac{-eV}{mkT}))]$ was plotted against V allowing for the the determination of the saturation dark current I_o and the ideality factor of the *TiO₂/SWCNTs junction* (in the 0-0.2 V linear range). The Schottky barrier height Φ_B is then obtained through the thermionic emission current equation:

$$\Phi_B = \frac{kT}{e} \ln \frac{aAT^2}{I_{0B}} \quad (9.3)$$

where k is the Boltzmann constant, T the temperature, e the elementary charge, A the Richardson constant for TiO₂ ($6.71 \times 10^6 \text{ AK}^{-1}\text{m}^{-2}$) and a the area of the junction. The values of such as estimated Schottky barrier height at the TiO₂/SWCNTs interface for the different photoanodes are reported in table 9.16. Decreasing the barrier height increases the saturation dark current since more thermally generated electrons can be trapped into the TiO₂ nanostructured network and transferred to the electrolyte. The mixed film has the shortest height and the purer single-chiralities have the largest (**(7,3)** = 0.68 eV, **(6,5)** = 0.65 eV). Thus, the highest $V_{OC}R$ of the two cells containing only single chirality tubes can be then justified in terms of lower recombination (see equation 2.5) caused by an higher energy barrier preventing the electron from recombining with the electrolyte by TiO₂ mediated trapping. Being the electron affinity and work function of the specific chirality not known, we can only speculate the reason of the detrimental effect on the V_{OC} and



(a)



(b)

Figure 9.34: Dark polarization curves on linear (a) and semi-logarithmic (b) scales.

short circuit current (I_{SC}) brought about by the **(6,4)** chirality (dual chirality films). **(6,4)** possesses a comparatively larger band gap than either the **(7,3)** or **(6,5)** chiralities. The effect of the larger band gap shifts the Fermi level up with respect to the electrolyte redox potential, which should increase in theory the open-circuit

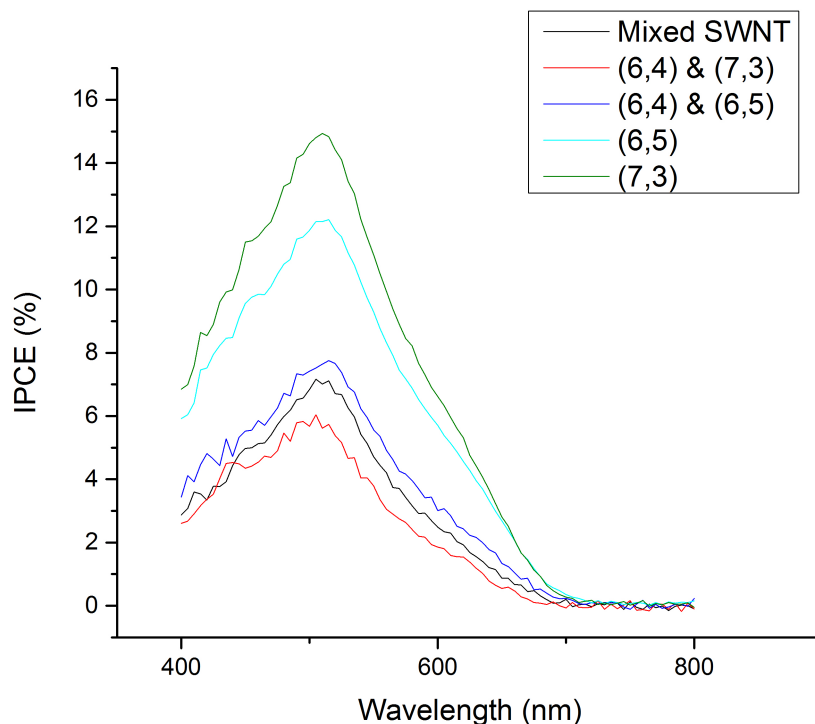


Figure 9.35: Quantum Efficiency performance of the DSSCs with mixed and single chirality films in the photoanode. Maximum incident photon to charge carrier efficiency for each of the DSSCs occurs at 530 nm (maximum N-719 light absorption in the visible range)

voltage. However, the barrier height remains low because the **(6,4)** chirality has its Fermi level close to the conduction band of the TiO_2 . The result is a weaker driving force for the electron injection from the TiO_2 to the SWCNTs, less charge collection and more recombination, and therefore a decreased short-circuit current and a lower open-circuit voltage. This hypothesis is in agreement with the charge injection model reported by Brown et al.[223] which is predicated on the thermionic electron transfer between TiO_2 and SWCNTs and is verified by the quantum efficiency data displayed in figure 9.35. Numeric IPCE values corresponding to the maximum dye's absorption wavelength are reported in table 9.17. In fact, the equilibration of TiO_2 and **(6,4)** chirality Fermi level places the TiO_2 conduction band in the proximity of the N-719 LUMO limiting the charge injection from the dye to the nanostructured semiconductor. Therefore, it can be concluded that the **(6,4)** chirality is not a useful material to be incorporated in the photoanode. On the other hand, the smaller band gap of the **(6,5)** and **(7,3)** chiralities produces a higher energetic distance of the TiO_2 from the dye's LUMO. The better performances of the **(7,3)**

Chirality	IPCE at 530 nm (%)
(7,3)	15
(6,5)	12
(6,5)/(6,4)	7
(7,3)/(6,4)	6
Mixed Chirality	8

Table 9.17: IPCE values at 530 nm measured from curves reported in figure 9.35

over the **(6,5)** film can be explained by the small difference in band gap between the two structures. This difference in band gap translates to less competition for photons between the **(7,3)** carbon nanotubes and the dye since the absorption spectrum of the dye is removed from the absorption of the **(7,3)** chirality (see film transmittance measurements). This results in a higher short-circuit current in the DSSC with the **(7,3)** anode.

The overall cells efficiency is limited by the low values of the shunt resistance (R_{sh}) and saturation dark current caused by the contact between CNTs films underneath the mesoporous double layered TiO_2 photoanode and the electrolyte. The shunt resistance is the lowest (and the saturation dark current is the highest) for the mixed chirality film due to the presence of metallic tubes causing electron transfer between the FTO substrate and the electrolyte and catalyzing the reduction of I_3^- to I^- at the photoanode. Furthermore, the presence of a large number of different band gaps in the mixed chirality film increases the chances that electrons are thermally generated into the CNTs and recombine with the electrolyte. As discussed in the experimental section the purity of semiconducting tubes in the **(7,3)/(6,4)** film is the lowest and the amount of metallic tubes is higher than in the rest of the chirality-specific films (i.e. relatively low value of the series resistance). The presence of metallic tubes increases FTO's catalytic activity for triiodide reduction and allows for shunt pathways for the electrons to travel and increased opportunities for recombination. The film made up mainly of **(6,4)/(6,5)** chiralities has the highest purity of semiconducting tubes and therefore the highest shunt resistance. As identified previously, the conductivity of the **(6,4)/(6,5)** film is also the lowest. This is not only due to the absence of metallic tubes, but also to the mix of the two chiralities in the same film creating electron traps [421], [276]. The highest R_s value for the **(6,4)/(6,5)** is in agreement with this observation. Both **(6,5)** and **(7,3)** films have a high semiconducting nanotube purity; however they are also the most conductive out of the chiral-specific films and their series resistance is comparable to the mixed chirality cell. Moreover, the extremely high

series resistance of the cells where the **(6,4)** chirality is incorporated together with other chiralities affects the V_{OC} (besides the fill factor and the I_{SC}). Finally, it is worth noticing that all the DSSCs assembled with the three layered structure (SWCNTs/P90/TiO₂ beads) show R_s values lower than (at least 50 % smaller) the cells presented in the previous two chapters. This seems to confirm that cells fabricated with mesoporous titanias active layer suffer from contact resistance at the TiO₂/FTO interface causing relatively high series resistances. On the other hand, when a mesoporous material is used only as light retrieving layer and the electron transfer to the transparent conductor occurs via a compact network of well interconnected particles, the series resistance drastically drops.

The ideality factor is about 2 in all of the photoanode materials. The anode resulting in a DSSC performance closest to an ideal diode is the **(7,3)**. None of the DSSCs tested has produced an ideality factor between 1 and 2, due to the exposure of CNTs to the electrolyte and the increased amount of shunt pathways.

9.3.3 Performances of DSSCs with single chiralities CNTs (cathode)

Since carbon nanotubes catalyze the electrolyte reduction reaction [422], [423] experiments were carried out to test how CNT films of mixed and single chirality performed as counter electrodes. The purest film (**96,5** chirality) was chosen as chirality specific counter electrode and a DSSC containing a platinum film cathode was used as a reference. As illustrated in figure 9.36 and table 9.18 the short circuit current is highest in the cell with the platinum (Pt) counter-electrode due to the increased Pt conductivity and charge transfer properties. The conductivity of the

Sample	η (%)	FF (%)	I_{sc} (mA)	V_{OC} (V)	R_s (Ω)	R_{sh} (Ω)	I_o (μ A)	m
Pt	5.2	71	10.37	0.699	8.7	33792.1	0.013	1.67
Mixed	3.7	60	8.8	0.697	20.0	55958.1	0.11	2.16
(6,5)	0.73	24	7.25	0.417	111.1	115	57	2.35

Table 9.18: Significant photovoltaics parameters for chirality specific cathodes derived from I-V curves under illumination (see Figures 9.36 and 9.38)

mixed film is undermined by the presence of tubes with mixed band gaps and while the **(6,5)** has a fairly high purity of a single chirality, it has a lower conductivity in comparison to the Pt and mixed film. In fact, the high value of the series resistance for the **(6,5)** (affecting the fill factor and ultimately the short circuit current) device stems from the presence of semiconducting tubes in the cathodic structure. Indeed,

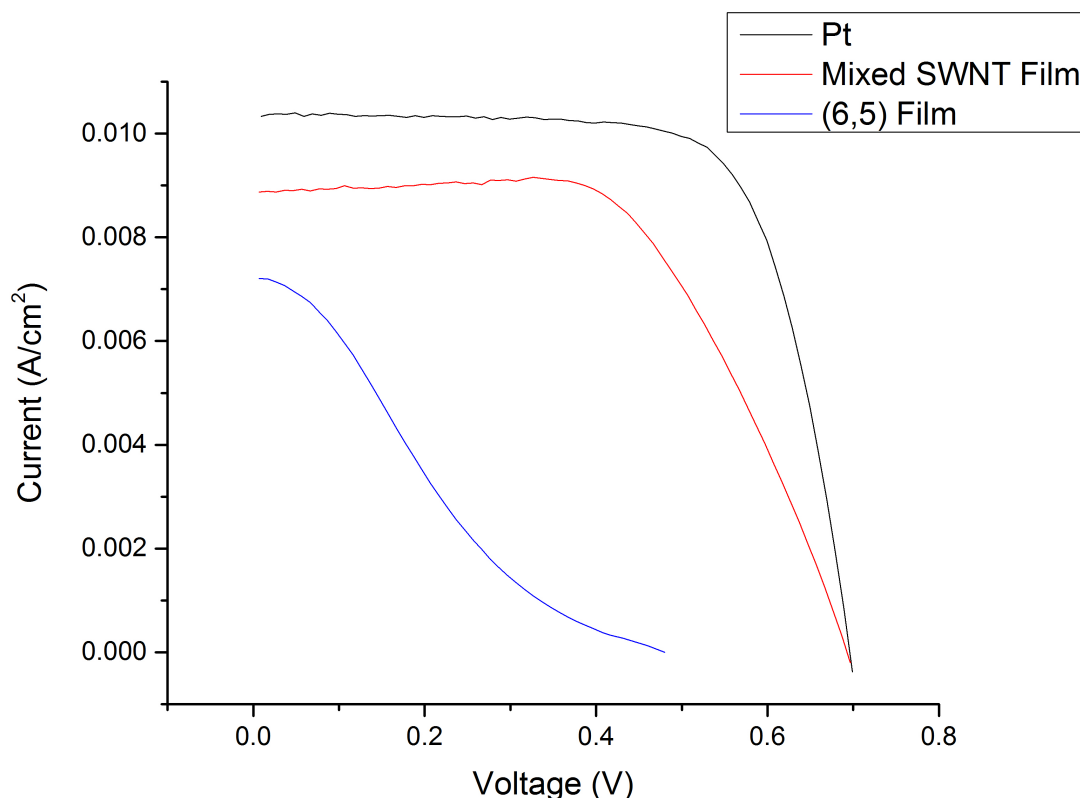


Figure 9.36: I-V Curves of DSSCs taken under an irradiance of 1 sun for DSSCs employing mixed chirality SWCNTs, **(6,5)** chirality and Pt as a counter electrode.

R_S accounts for the series resistance that is related to the sum of all the resistances that produce a loss in the electrochemical potential of the cell outside the active layer [401]. Hence, electrolyte diffusion resistance, FTO sheet resistance (together with contacts and wires) and counter electrode charge transfer and ohmic resistance all contribute to R_S . Based on this, if the mixed film and the Pt are compared, it can be seen that the mixed chirality counter-electrode has a higher series resistance but not as high as the **(6,5)** only film. The reason lies in the fact that the absence of metallic tubes in the **(6,5)** counter electrode leads to low charge transfer rate to the triiodide ion. The lack of catalytic action due to the absence of metallic tubes resulting in a decreased rate of reduction of the tri-iodide to iodide, causes a slow regeneration of the dye. If the rate of injection of electrons from the dye to the TiO_2 is faster than the regeneration of the dye from the electrolyte, it will become more favourable for the oxidized dye to recapture its electrons from the TiO_2 instead [424]. This hinders the generation of current in the photoanode of the cell and thus lowers the short circuit current.

Chirality	IPCE at 530 nm (%)
Pt	27
Mixed Chirality	30
(6,5)	15

Table 9.19: IPCE values at 530 nm measured from curves reported in Figure 9.37

The counter-electrodes composed of Pt and mixed chirality films have comparable quantum efficiency (see figure 9.37 and table 9.19). The discrepancy between the quantum efficiency and the short-circuit current is due to the fact that the change in efficiency does not scale linearly with power. Comparable quantum efficiency values are expected between the DSSCs with Pt and mixed films because the parameter primarily depends on the performance of the photoanode, which is composed of only TiO_2 . The DSSC with the **(6,5)** cathode is also made up of TiO_2 in the photoanode; however the quantum efficiency is quite low in comparison to the other two cells due to the aforementioned slow dye's regeneration. This affects also the open circuit voltage of DSSCs. The V_{OC} is similar between the mixed

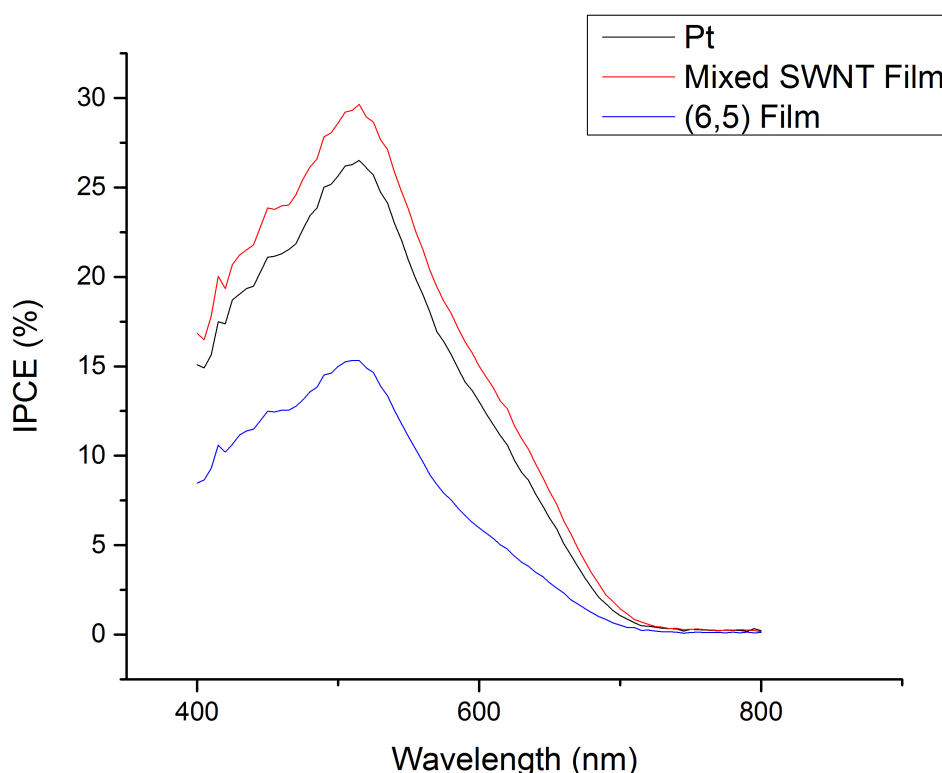


Figure 9.37: Quantum efficiency performance of the DSSCs with platinum, mixed chirality films, and **(6,5)** CNT films

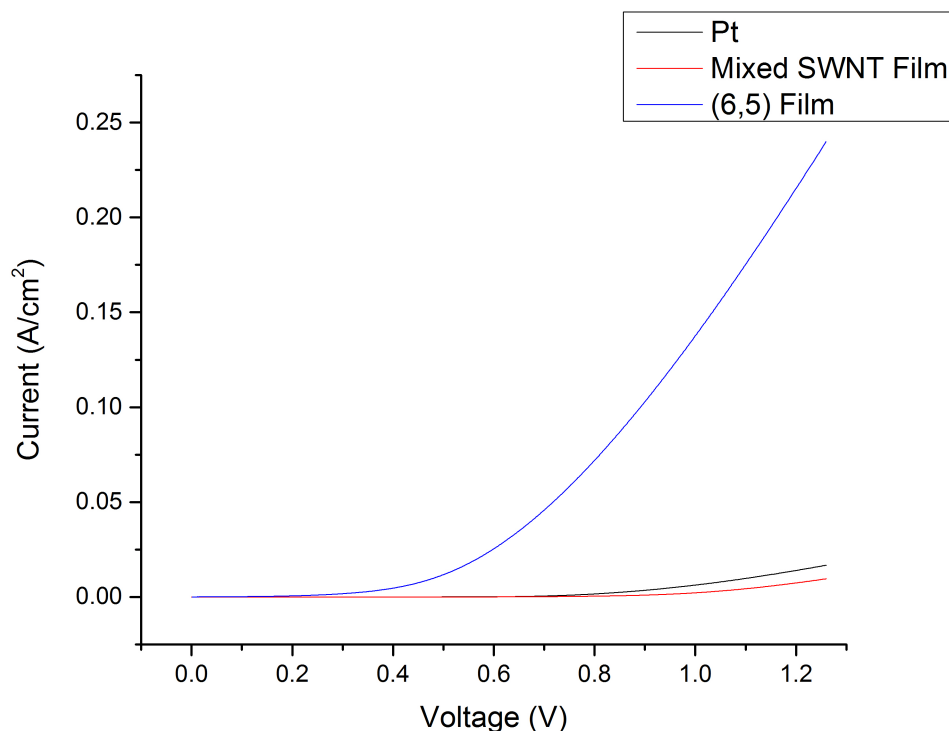


Figure 9.38: I-V Curves of DSSCs in a dark environment for cells employing Pt, mixed and **(6,5)** films as cathodes.

film and platinum counter-electrodes indicating good electron injection from the mixed tubes to the electrolyte. The value of the open-circuit voltage is close to the thermodynamic value of approximately 0.7 V, given by the difference between the Fermi level of the TiO_2 and the redox level of the electrolyte. The **(6,5)** however has a much lower open-circuit voltage than the other two cells which is likely due to the high amount of saturation dark current (two orders of magnitude higher than mixed film, see figure 9.38 and table 9.18) caused by the leakage current due to dye's electron recapture [425] Hence, the saturation dark current for the **(6,5)** cell is dominated by the recapture by the oxidized dye of the thermal excited (no light) electrons across the HOMO-LUMO energy gap. All of the carbon nanotube films used for the counter-electrode produced DSSCs performing with an ideality factor higher than 2. As mentioned above, while this is not ideal for a diode or solar cell, it is not unusual in a DSSC. The cathode composed of the **(6,5)** film had the highest ideality factor due to the high level of recombination. Finally, the DSSC with the Pt counter-electrode has the better ideality factor of between 1 and 2. This could be attributed to the higher rate of reduction of the electrolyte.

9.4 Conclusions

Research on nanostructured materials to be employed as photoanodes in DSSCs has been conducted in three stages summarized below:

Investigation on different TiO₂ morphologies . The goal of this stage was to identify the best performing morphology in terms of energy conversion efficiency to be used in the successive phases of the research. Titania mesoporous beads were found to be the most suitable candidate for the electronics properties optimization work.

Exploring doping of titania mesoporous beads with six RE cation . Doping turned out to influence mostly the electron transport and recombination properties, which means, in terms of DSSCs photovoltaic parameters improvements in the J_{SC} (and its related properties like the electron diffusion length) of the cells.

Research on chirality selected SWCNTs heterojunctions . Since doping had not been found to be effective in changing charge injection properties of the dye/TiO₂ interface, SWCNTs were used to modify the driving force for the electron transfer from the dye to the TiO₂. Different single (and mixed) chiralities were proved to influence all the charge injection, electron transport and recombination parameters. This reflected in chirality selected tubes to affect the V_{OC} , the J_{SC} , the R_S and the R_{SH} of DSSCs.

More specifically, each research stage led to the following conclusions and future perspectives:

- Mesoporous titania samples, prepared from both hard and soft-polymeric template approaches, show lower performances compared to titania mesoporous beads obtained by the HDA route. While being structurally more perfect and apparently more suitable for an easy electron transport through the photoanode, mesoporous titanias prepared from hard templating agents showed the worst photovoltaic behavior as DSSCs photoanodes because of their low specific surface area. Low SSA led to limited values of short circuit current and increased R_S due to the high resistance of the FTO/TiO₂ contact. A substantial performance improvement is expected by optimizing the particles dimension that can be achieved by tailoring the synthesis conditions. On the other hand, titanias prepared from soft-polymeric template approaches give a

better operation and the similarity of their performances allows to choose the synthesis on the basis of lower costs and shorter preparation times. Further improvements can be achieved also for this class of materials, for example, by finding a way to retain the order of mesopores through thermal treatments and improving interparticle connections, which are expected to enhance the dye loading and electron transport, respectively.

Titania mesoporous beads show the best energy conversion efficiency by compensating for their not excessively high SSA ($79 \text{ m}^2/\text{g}$) with good light scattering properties stemming from their hierarchical, sub-micrometric morphology.

- The nature and concentration of the six (Pr, Nd, Sm, Gd, Er, Yb) rare earth cation does not substantially affect the morphology of the beads, which presents similar average dimensions, surface area and porosity. Structurally, the rare earth concentration in the lattice seems too low to affect unit cell parameters, while an evident correlation in 0.2% samples between the rare earth cation size and crystallite average size, probably as a result of the Fajans's rules, was found. The band gap values of the solid solutions do not show significant deviations from that of pure anatase (3.2 eV). The type of cation and its concentration have a profound influence on the behavior of DSSCs. While Pr and Nd suppress the performances of the DSSCs, all the others improve them, and the best efficiency devices are obtained for a RE concentration of 0.2% metal atoms. The maximum efficiency has been obtained for the sample containing 0.2 % Er metal atoms (8.7%). The analysis of the experimental data and a survey of the available literature suggest that RE cations in the anatase lattice produce two conflicting effects that affect DSSC performances: (i) defect-mediated electron scattering due to the lattice distortion induced by the impurities (and scattering with the impurities themselves); (ii) the suppression of natural oxygen defectivity, which reduces intra-gap trap states in anatase improving the electron diffusion length. While for Pr^{3+} and Nd^{3+} , being largest ions of the series, the first effect prevails, decreasing the performances of the DSSC devices in comparison with pure TiO_2 , the opposite is true for heavier cations heavier than Sm. In fact, Gd, Er, Yb and Sm itself produced a substantial increase of DSSCs energy conversion efficiency.
- HiPCO SWNTs of enriched chirality can be prepared in a sufficient amount to

be used in DSSCs photoanodes by modifying the chromatographic procedure originally proposed by Liu et al.. The concept of "gel overloading" can be effectively exploited to produce chirality selected SWCNTs with a single SEGC column pass. Enriched tubes of **(6,5)** and **(7,3)** at purities 93 and 87% have been obtained in a single pass. The procedure was adjusted for each CNTs batch composition but is potentially applicable even to "homemade" small diameter semiconducting tubes. For the first time chirality selected CNTs have been used as photoanodic (and cathodic) materials for DSSCs. Two single chirality (**(7,3)** and **(6,5)**), two dual mixed chirality (**(6,5/6,4)** and **(7,3/6,4)**), and a thirty chirality mixed film were employed as charge collection layer underneath nanostructured the TiO₂ semiconductor (a commercial P90/hierarchical mesoporous spheres double layer). Using single chiralities in the photoanode improved the overall (81% for the **(7,3)** and 37% for the **(6,5)**) compared to the cell employing mixed chirality tubes. The efficiency improvement is mainly due to the "Schottky-like" barrier height tuning at the TiO₂/SWCNTs/FTO interface that prevents trap mediated electron/electrolyte recombination and promotes the charge injection from the dye LUMO to the TiO₂ conduction band. Furthermore, exclusion of metallic tubes from the photoanodes limited the catalytic effect of CNTs toward the triiodide reduction reaction, that constitute the main recombination process in DSSCs. Also the competition between the N-719 dye and the SWCNTs for light absorption was reduced by using the **(7,3)** chirality only because single chirality films absorb light at a single wavelength and do not overlap the maximum absorption of the dye. Besides, **(6,4)** chirality was ruled out as a useful chirality for DSSCs applications. Unfortunately, the cells energy conversion efficiency has been strongly limited by the shunts caused by the contact between the cnts and the electrolyte. Further investigations concerning shunt resistance improvement (i.e. by spray pyrolysis deposition of a compact layer of TiO₂ to protect the SWCNTs film from the electrolyte) are being conducted.

Finally, the catalytic effect of CNTs for triiodide reduction was exploited to produce DSSCs counter-electrodes with thirty chirality mixed and pure **(6,5)** films. The mixed film cell, with presence of metallic species, performs well as the Pt based DSSC in terms of quantum efficiency; however, the higher series resistance (comprised of a ohmic and a charge transfer component) caused by the semiconducting tubes depresses the fill factor and translates

into decreased DSSCs' performances. On the other hand, the slow kinetics of dye regeneration makes the electron recapture by the oxidized dye the main efficiency limiting process of the cell containing the **(6,5)** tubes.

Chapter 10

Iron Colorimetric sensors and electrochromic devices

10.1 Iron Colorimetric sensors

Figure 10.1 illustrates the characterization of the $\text{Fe}(\mathbf{L})_2$ (deposited as SAM) on FTO coated glasses and hydrophilic quartz surfaces. STM analysis shows that the roughness of the $\text{Fe}(\mathbf{L})_2$ functionalized FTO coated glass surface (see figure 10.1 (E)-(H)) is very similar to that of unfunctionalized FTO coated glass (see figure 10.1 (A)-(D)), which suggest the formation of a monolayer. The embedding of the terpy-metal complex on the quartz or FTO coated glass surfaces can be easily observed by the naked eye. On the other hand, when *only* (\mathbf{L}) is adsorbed on the FTO surface no visible color can be detected. However, UV-vis spectroscopy can be used to effectively monitor the adsorption of (\mathbf{L}) and $\text{Fe}(\mathbf{L})_2$ on hydrophilic quartz (see figure 10.1 (J)). (\mathbf{L}) self assembled monolayers on quartz (black curve) and Fe^{2+} treated (\mathbf{L}) self assembled monolayers (exposed to Fe^{2+} *after* the ligand deposition, red curve), show peaks in the Uv region but no absorption bands in the visible. Hence, (\mathbf{L}) pre-deposition on flat surfaces and its successive treatment with a 0.1 mM Fe^{2+} ions solution *does not result* into the formation of the on flat surfaces. On the contrary, if $\text{Fe}(\mathbf{L})_2$ is formed in solution from (\mathbf{L}) and iron(II) perchlorate hydrate (or FeCl_2) and then is deposited on the quartz slides, a significant increase of the intensities at 287 and 332 nm as well as the appearance of the MLCT peak at 569 nm occur (green curve in figure 10.1 (J)). The red shift of the on-surface $\text{Fe}(\mathbf{L})_2$ monolayer with respect to $\text{Fe}(\mathbf{L})_2$ in aqueous solution (278, 321 and 560 nm, respectively) stems from the change in the microenvironment of $\text{Fe}(\mathbf{L})_2$ in the two different media [426].

Hence, functionalization of flat, non-nanostructured, oxides surface *is not* a suitable approach for developing solid state Fe^{2+} colorimetric sensors and detection kits. Further characterization of the $\text{Fe}(\mathbf{L})_2$ complex deposited on FTO coated glass surfaces by XPS (10.1 (I)) verifies the presence of iron, nitrogen, carbon and phosphorous on the surface within ratios close to the molecular stoichiometry. The binding energy of any XPS peak depends on the oxidation state of an element and on its binding sites on the surface (chemical surroundings). Thus, the binding energy of the Fe $2p_{3/2}$ peak is located at 709.6 eV; and that of Fe $2p_{1/2}$ can be seen at 722.1 eV. Both peaks constitute "fingerprint"-like features for the ferrous ion. The N 1s peak at 400.9 eV is evidently associated with aromatic nitrogen, which provides the electron lone pairs to form the complex. The C 1s peak is centered at 286.0 eV, which is in good agreement with aromatic carbon. An asymmetric broad peak observed at 133.6 eV is due to the overlapping between P $2p_{3/2}$ and P $2p_{1/2}$ components, which is characteristic for phosphonates [395]. A possible explanation to the lack of formation of $\text{Fe}(\mathbf{L})_2$ starting from the ligand anchored on the oxide *flat* surface (FTO and hydrophilic quartz) and Fe^{2+} in solution lies in the (\mathbf{L}) close packing on the substrate surface. In fact, as stated before, the surface area occupied by one $\text{Fe}(\mathbf{L})_2$ molecule is 1.43 nm^2 , whereas a single (\mathbf{L}) occupies 0.81 nm^2 (that corresponds to a ligand surface concentration of 1.23 molecules per nm^2). This indicates that (\mathbf{L}) forms well-ordered and densely packed monolayers on relatively smooth surfaces and thus, due to the intermolecular π - π interactions, the rotation of the terpy moieties anchored to the surface is limited. Reduced flexibility of the terpy moieties on the surface, in turn, restricts the participation of two neighboring surface anchored ligands in the complex formation. Hence, experimental evidence suggests that when a nanostructured high specific surface area support is functionalized with (\mathbf{L}) a certain fraction of these molecules might be available for $\text{Fe}(\mathbf{L})_2$ complex formation. Furthermore, support's mesoporosity is supposed to provide the ligand with multiple harboring sites within the pores structure. Modification of commercially available titanium (IV) oxide anatase nanopowder by (\mathbf{L}) followed by treatment of the functionalized (\mathbf{L})- TiO_2 anatase nanopowders with $\text{Fe}(\text{ClO}_4)_2$ solutions results in significant color change (figure 10.2 (A) and (B) insets). Morphology and particles size, around 25 nm, of anatase nanopowders is not affected by (\mathbf{L}) functionalization and Fe^{2+} adsorption as shown in figure 10.2.

To turn these observations into an operative iron (II) sensitive colorimetric device, commercial "benchmark" P90 powders (see Figure 10.3) were used to prepare

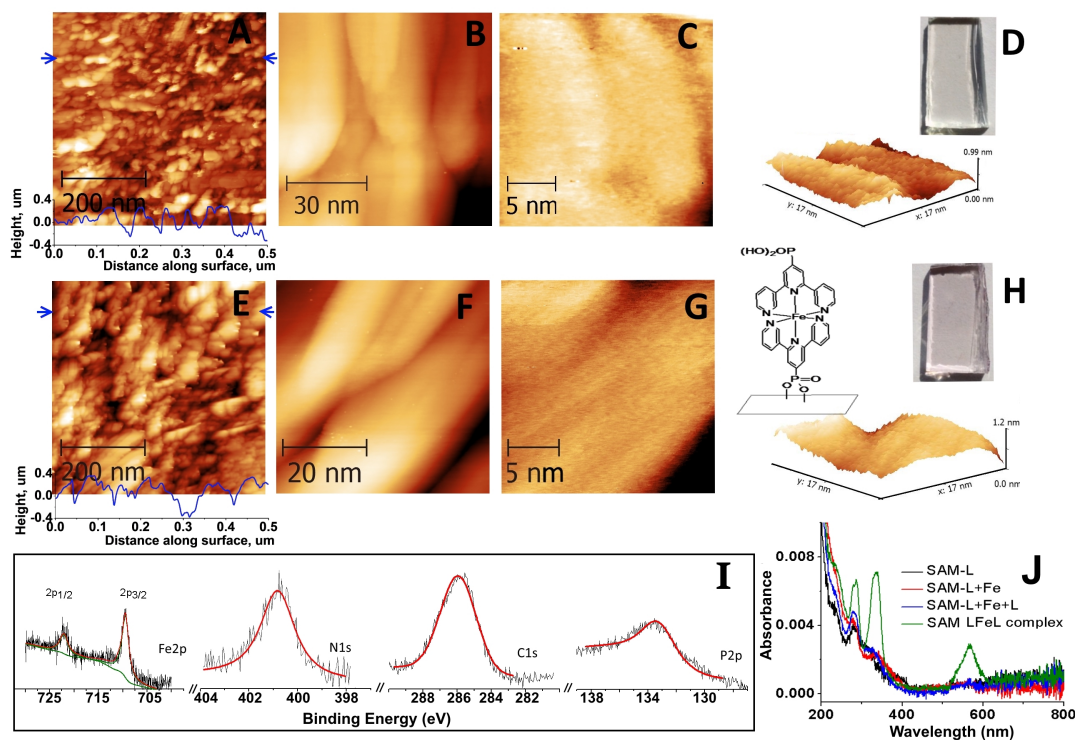


Figure 10.1: Representative STM images for flat substrates : (A-D) bare FTO coated glass and (E-H) SAM-Fe(L)₂ on FTO coated glass slides. (I), representative XPS data for SAM-Fe(L)₂ on FTO coated glass slides: Fe (2p), N(1s), C (1s), and P (2p). The black line shows the experimental data, while the red lines are the overall fitted spectra. (J) UV-vis spectra (on hydrophilic quartz) of as-deposited SAM-L (black), followed by its step by step treatment with Fe²⁺ aqueous solution (red) and solution of L (blue) show no significant change of the spectra suggesting no Fe(L)₂ complex formation. In comparison, UV-vis spectrum of Fe(L)₂ complex *pre-formed* in solution and then deposited as a SAM on quartz surface (green) shows a distinguishable characteristic peak at 569 nm.

α -terpineol/ethyl cellulose pastes to screen print on a 1x1 cm squares on RCA treated soda-lime glasses. Films were thermally treated in air to remove the organic binder and promote particles sintering. One, three, and six layers (2 μ each) were screen printed one by one to increase the volume of the detecting "cell" thus tuning the detection range. When prepared, layered screen printed P90 TiO₂ films were functionalized via immersion into a 0.065 mM aqueous solution of (L) for 1 h followed by washing with isopropyl alcohol (with 3 mL for three times) and dried by a stream of air as described in the experimental part. The resulting sensing strips were treated with 150 μ L of 45 ppm aqueous Fe²⁺ solution. All sensing strips turned deep magenta with comparable intensity as shown in figure 10.4. These results confirm that a terpy derivative chemisorbed on a *nanostructured oxide* can detect Fe²⁺ in aqueous solutions. However, we believe that small particles size

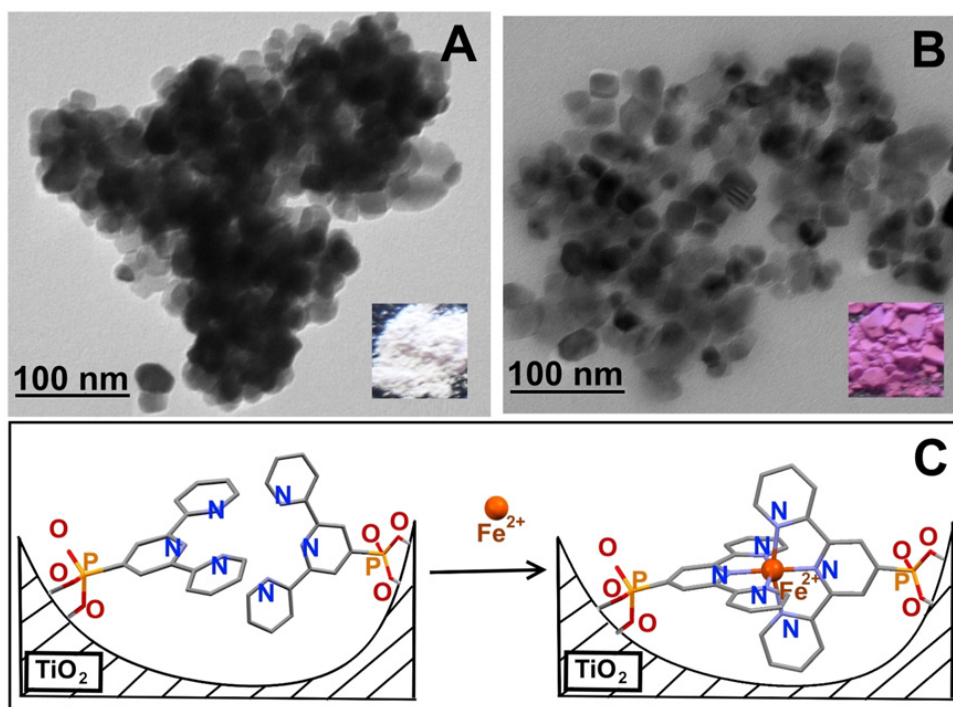


Figure 10.2: Representative TEM images of commercial TiO₂ anatase nanopowder functionalized with (L) before (A) and after (B) treatment with Fe²⁺ aqueous solutions. (C), proposed interaction mechanism of Fe²⁺ with (L) molecules bound to the TiO₂ nanopowder surface.

(typically 15 nm, see figure 10.3) of P-90 "excessively" favors particles sintering. For example, a 6 layers screen printed P-90 film ¹ possesses, after thermal treatment, an SSA equal to $58 \pm 2 \text{ m}^2/\text{g}$ which is 38% shy of the specific surface area of the bare (untreated) P-90 powders ($94 \pm 2 \text{ m}^2/\text{g}$). Hence, particles sintering in the films shallow layers can result in the formation of surfaces where diffusion through the layers is impeded. As such only a reduced amount of surface remains accessible for the functionalization by the molecular receptor (L), which is active in metal ion recognition. As a result, P-90 TiO₂ based screen-printed materials do not allow for reasonable control of sensitivity since no significant difference in color intensity was observed between one and multiple (up to 6 layers) screen printed films.

To validate our hypothesis concerning the role of high SSA and porosity in creating a suitable scaffold for (L) chemisorption and sensitive Fe²⁺ colorimetric detection, we screen printed pastes comprised of the mesoporous titania beads as active filler. A well tunable thickness was achieved by layer by layer printing employing the "high resolution" T 90 screen mesh (see figure 10.5). Needless to say,

¹The film was thermally treated and then mechanically removed (scratched) to allow specific surface area measurements on the resulting powders. The high temperature treatment (up to 500 °C, see chapter ??) ensure the complete removal of the ethyl cellulose binder.

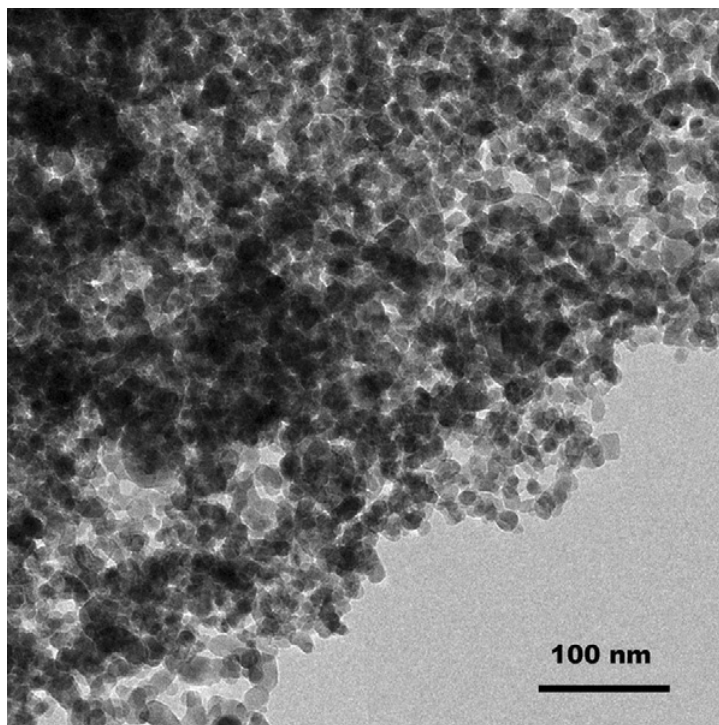


Figure 10.3: TEM micrograph of the P-90 TiO_2 powder (by Evonik, Germany) used to screen print the iron (II) detecting "cells" shown in figure 10.4).

titania beads benefit from extended porosity and an almost monodisperse pore size distribution that allows to accommodate plenty of (**L**) molecules on a curved and indented surface favoring the proper geometrical arrangement for the octahedral coordination of $\text{Fe}(\text{II})$ by two (**L**) molecules. Furthermore, beads' sub-micrometric spherical shape enhance thermal stability and prevents immoderate particles sintering leading to surface plugging and inaccessibility to the film's inner layers by the ligand. Thus, better water (carrying (**L**) or the ferrous ions) diffusion on the film could be exploited for quantitative Fe^{2+} detection. Hence, dropwise addition of $150 \mu\text{L}$ of a 45 ppm aqueous solution of Fe^{2+} on 1, 2, and 3 layered screen printed films of mesoporous titania beads resulted in rapid color change from white to three different shades of purple (see figure 10.5). These observations seem to verify that SSA (and particles size) and porosity are important factors allowing for modulation of sensitivity and better quantitative analysis.

Three layered ($6 \mu\text{m}$ height) screen printed films of mesoporous TiO_2 beads functionalized with (**L**) were further investigated to determine the detectable Fe^{2+} concentration range. Applying $150 \mu\text{L}$ of 0.2 ppm, 2 ppm, and 45 ppm Fe^{2+} solutions to the detecting films resulted in the appearance of a peak at 560 nm on the diffuse reflectance UV-vis spectra (10.6). A slight colour change occurs in the case

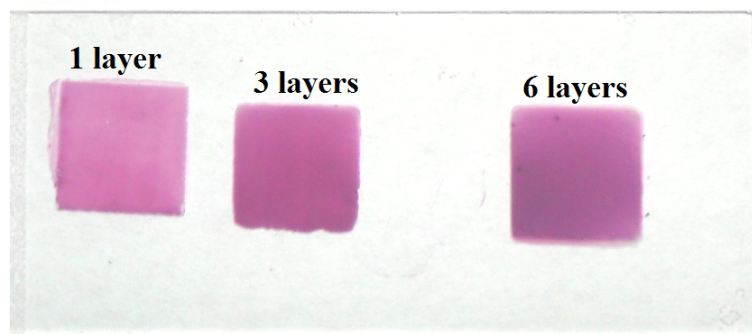


Figure 10.4: P-90 "cells" for iron (II) colorimetric detection. From left to right: 1, 2, and 3 layers. Cells' color doesn't show any significant intensity change as the number of layers (thickness) is increased.

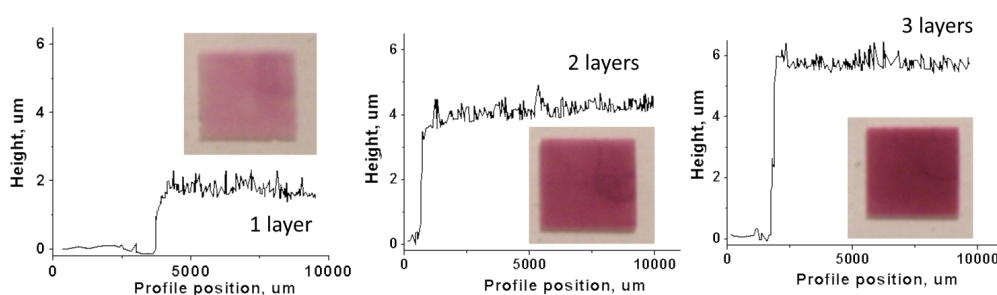


Figure 10.5: Profilometry curves of the mesoporous titania beads films deposited and sintered on RCA treated (basic piranha) substrates showing a thickness of 2 μm per printed layer. Inserts: images of corresponding films after application of 150 μL of 45 ppm aqueous Fe^{2+} .

of 0.2 ppm ferrous perchlorate solution; but the colour change observed when 2 ppm and 45 ppm solutions were used could be easily distinguished by the naked eye. The fact that 0.2 ppm and 2 ppm of $\text{Fe}(\text{II})$ are detectable spectrophotometrically and colorimetrically, respectively, is important in terms of applications. According to the U.S. Environmental Protection Agency secondary drinking water standard and Guidelines for Canadian drinking water quality, maximum contaminant level of iron is 0.3 ppm. The United Nations Food and Agriculture Organization recommends a level of 5 ppm for irrigation waters. On the other hand, iron in groundwater (in ferrous form) varies from 0.1 to 10 ppm [427]. Needless to say, the development of inexpensive, reusable and reliable materials which are able to rapidly detect iron in field conditions is in high demand. Also, portable litmus paper-like colorimetric sensors for semi-quantitative analysis by means of a smartphone accessory and a app [428] are attractive for large scale diffusion of aqueous ions detection. To ensure our detecting films can be used as a material for Fe^{2+} determination, certain

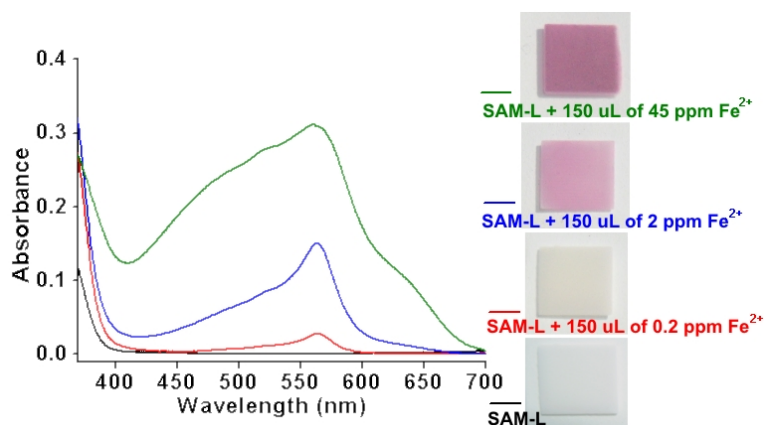


Figure 10.6: Diffuse reflectance UV-vis. spectra and optical photographs of mesoporous titania beads screen printed films (3 screen printed layers) functionalized by (L) before and after treatment with 150 μL of aqueous Fe^{2+} solutions. The characteristic peak at 560 nm verifies the formation of the $\text{Fe}(\text{L})_2$ complex.

amounts of aqueous Fe^{2+} solutions were added to each film creating an appropriate colour wheel (see 10.7) The resulting color wheel is consistent with our expectations: the color intensity depends on the amount of Fe^{2+} added. This permits the visual quantification of iron cations in aqueous solutions ranging from 0.3 ppm to 5 ppm. To investigate the detecting films' selectivity towards Fe^{2+} in the presence of potentially interfering ions, an aqueous solution containing Na^+ , Fe^{2+} , Cr^{3+} , Sn^{2+} , Ca^{2+} , Li^+ , Co^{2+} , Mg^{2+} , Cu^{2+} , Cs^+ , Ni^{2+} , Ba^{2+} , K^+ , (5 ppm each from chloride sources) was prepared and portionwise applied to the detecting films. Figure 10.7(A) clearly shows that the detecting films treated with the multiple ions solution have a similar color intensity to those treated with solution containing solely Fe. This shows that the material is highly selective for Fe^{2+} determination probably because of the higher stability of $\text{Fe}(\text{II})(\text{L})_2$ complex compared to terpy coordination compounds with other metal ions and because of the high molar extinction coefficient of the 560 nm MLCT transition. In addition, we studied the ability of our screen printed material to detect Fe^{3+} ions in the aqueous solutions. Aqueous solutions of Fe do not result in a change of colour of the detecting film. However, aqueous Fe^{3+} can be detected if reduced by hydroxylamine to Fe^{2+} [429] (see figure 10.7 (B)). Notably, the detecting films can be reused after immersion into a 0.5 mM solution of ethylenediaminetetraacetic acid disodium salt (EDTA) for 48 h. Iron release from the films into the EDTA solution can be monitored by the visual colour change of the films. Figure 10.7 (C) shows the behavior of the color on the films for 10 successive cycles of resetting. No evidence of degradation of sensitivity can be detected. Increasing the temperature of the EDTA solution to 80 $^\circ\text{C}$ reduces the

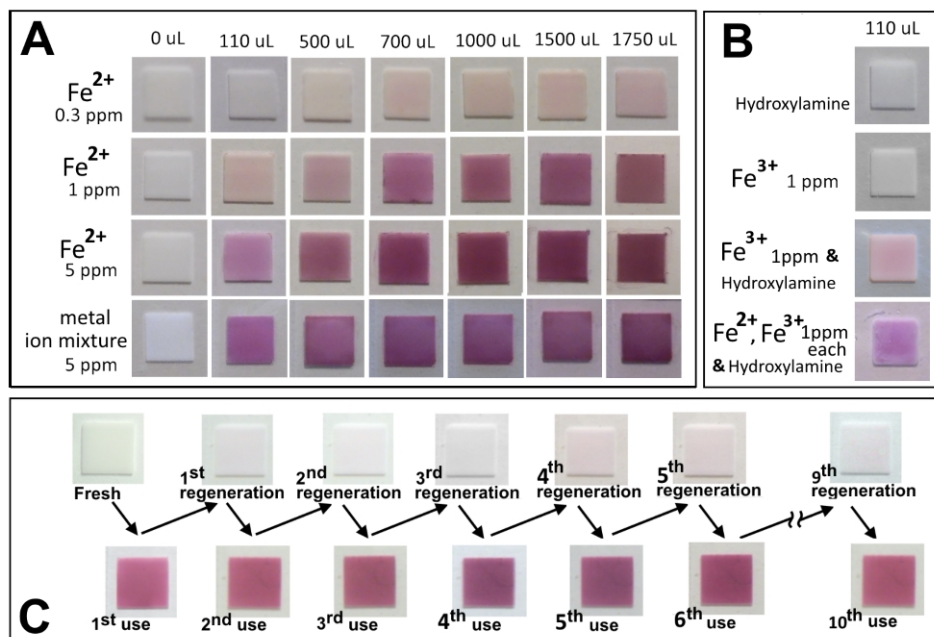


Figure 10.7: (A): Color wheel showing the color change of detecting films after applying varying volumes of aqueous Fe^{2+} solutions: 0.3 ppm (upper row), 1 ppm (2nd line from the top), 5 ppm (3rd line), and a mixture of metal ions (including Fe^{2+}), 5 ppm each (bottom row) see main text for details. (B): Aqueous solutions of hydroxylamine do not change the colour of the detecting film. Using this reagent to reduce Fe^{3+} to Fe^{2+} allows for the detection of the total amount of iron in solution. (C): Detecting films can be recovered by EDTA and reused, see main text for details.

film recovery time to 24 h. However, since to completely reactivate the films is necessary to readsorb (L) on the mesoporous TiO_2 beads film (see ??), EDTA may coordinate also the Ti^{4+} in the TiO_2 crystal lattice.

XPS analysis of detecting films before interaction with Fe confirms the presence of N, C, and P of L on the surface (see figure 10.8 (A)). The sharp (with full width at half-maximum(FWHM) of 1.9 eV) N 1s peak is centered at 400.0 eV. The C 1s peak is centered at 285.8 eV, as expected for aromatic carbon. An asymmetric broad peak observed at 133.8 eV is characteristic for P 2p. The N:C:P ratio of 2.5:17.4:1.0 is close to 3:15:1 of (L) molecular stoichiometry. When 110 μL of 5 ppm aqueous Fe^{2+} solution was applied to the detecting film (see figure 10.8(B)) the appearance of two new peaks was observed. The peaks with the binding energies of 709.9 eV and 722.4 eV are characteristic for Fe 2p_{3/2} and Fe 2p_{1/2} of Fe_{2+} , respectively. Interestingly, the P 2p peak position remains unchanged within the experimental error (133.8 eV) after Fe^{2+} solution application. On the other hand The C 1s peak is insignificantly shifted to 286.1 eV. The N 1s peak undergoes a significant

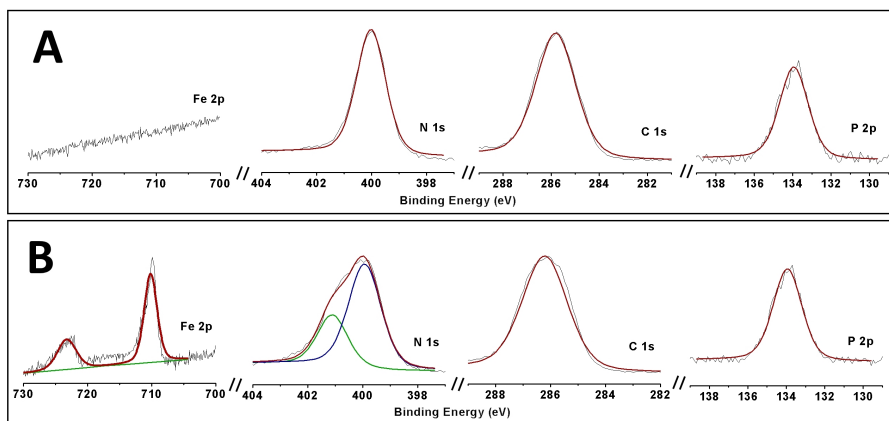


Figure 10.8: Comparative X-ray photoelectron spectra of (**L**) anchored to mesoporous TiO_2 screen-printed films A: before and B: after application of $110 \mu\text{L}$ of 5 ppm aqueous Fe^{2+} solution.

change and now can be deconvoluted using a Powell peak fitting algorithm with FWHM of 1.3 eV yielding a peak centered at 400.0 eV and a new peak centered at 401.1 eV. This value is close to 400.9 eV, which was observed for the $\text{Fe}(\mathbf{L})_2$ complex deposited on the FTO surface (see figure 10.1(I)). The P:Fe ratio is 1:0.01 suggesting that as expected, only a fraction of **L** molecules are able to form the $\text{Fe}(\mathbf{L})_2$ complex. However, assuming that the complex formation takes place not on the flat surface, but inside the pores, the iron content can be underestimated due to the signal attenuation.

10.2 Electrochromic devices

Figure 10.9 illustrates the kinetic chemisorption study intended to determine the amount of (**L**) molecules grafted onto the ITO NPs surface. Indirect determination from the UV-Vis spectroscopy analyses proved that a monolayer of the phosphonic acid-modified terpyridine ligand (**L**) forms on ITO NPs surface in less than 5 hours. In fact, the absorbance of (**L**) remaining in the aqueous solution reaches a stationary value within 4 hours. Furthermore, the amount of ligand deposited on the ITO nanoparticles effectively correspond to a monolayer grafting density of 1.5 molecules per 1 nm^2 , which is close to a single crystal packing density [22]. Indeed, the amount of **L** in the solution that remains after 2 h of deposition was calculated for the solution absorbance at $\lambda = 233 \text{ nm}$, $\lambda = 281 \text{ nm}$, and $\lambda = 322 \text{ nm}$ to give $1.50 \pm 0.03 \times 10^{-6} \text{ mol}$. Then the amount of (**L**) deposited on 400 mg of ITO NPs is $9.904 \times 10^{-6} \text{ mol}$. Thus 1g of ITO NPs will adsorb $2.47 \times 10^{-5} \text{ mol}$ of (**L**). Keeping in

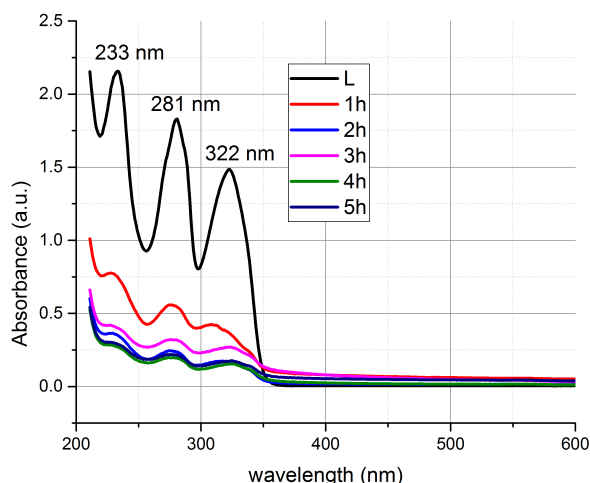
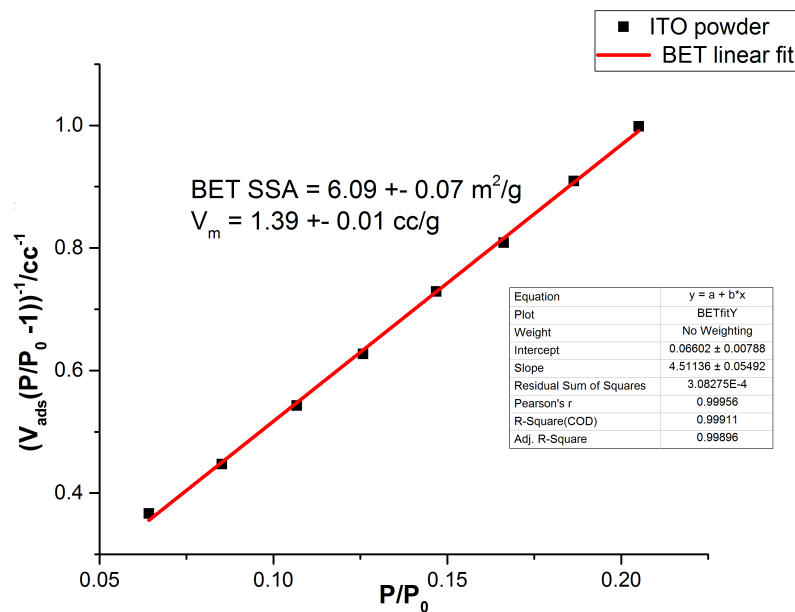


Figure 10.9: Uv-vis spectroscopy analysis reflecting the decrease of (**L**) concentration in the solution when treated with ITO NPs. The peaks at 322, 281 and 233 nm correspond to different intra-ligand transitions.

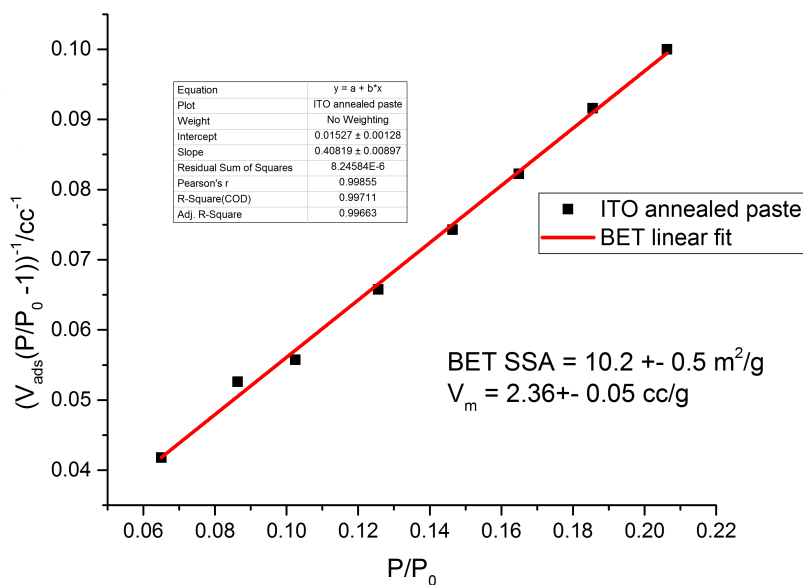
mind that the specific surface area of ITO NPs *after the high temperature treatment necessary for the screen printed film's particles sintering* is $10.2 \text{ m}^2/\text{g}$ (see Figure 10.10), $2.47 \times 10^{-5} \text{ mol}$ of (**L**) will be deposited into the surface of 10.2 m^2 . This corresponds to 1.49×10^{19} molecules deposited on 10.2 m^2 . Thus the surface area occupied by one molecule of (**L**) is equal to 0.68 nm^2 , which is which is close to a single crystal packing density (0.7 nm^2). In addition, TGA of (**L**)-functionalized ITO NPs shows a weight loss of 0.78% (see Figure 10.11) that is in a good agreement with Uv-vis data and confirms the formation of a monolayer of L on the ITO NPs with a relatively small surface area. The spectrophoelectrochemical test results reported in figure 10.2 the feasibility of using nanostructured oxides functionalized with a monolayer of terpyridone ligand.

10.3 Conclusions

A TiO_2 -based screen printed material suitable for selective Fe^{2+} detection in aqueous solutions was implemented by exploiting the knowledge acquired during the research stage concerning nanostructured materials for DSSCs photoanodes. The colorimetric sensor relies on the large affinity of phosphonic acid modified terpyridine, namely 2,2':6',2''-terpyridin-4'-ylphosphonic acid or (**L**), for oxide surfaces and on the specific MLCT transition occurring upon the formation of the Fe(II)L_2 complex. Although (**L**) adsorbs also on flat surfaces like FTO coated glass and



(a)



(b)

Figure 10.10: BET linear fit of ITO nanoparticles before (a) and after annealing. Specific surface area slightly increases (from 6.09 to 10.2 m²/g) upon thermal treatment. The effect is the result between the fine comminution brought about by the prolonged ball milling needed for the screen printing paste preparation and the particles necking provoked by the film's annealing.

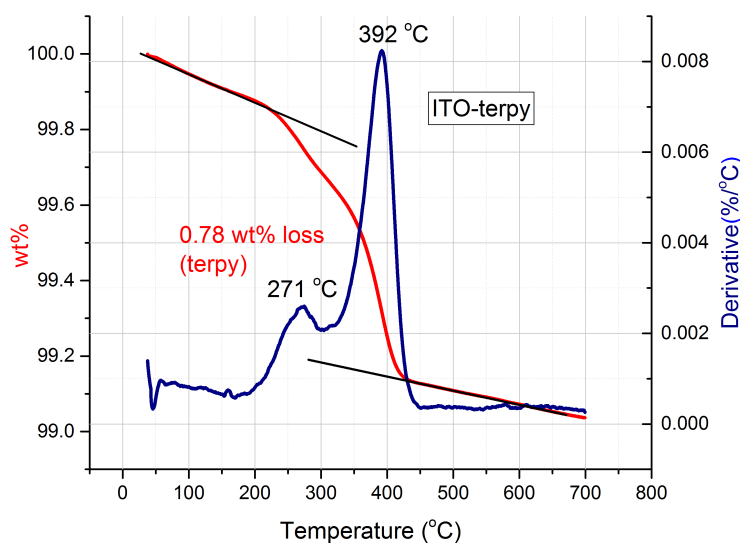
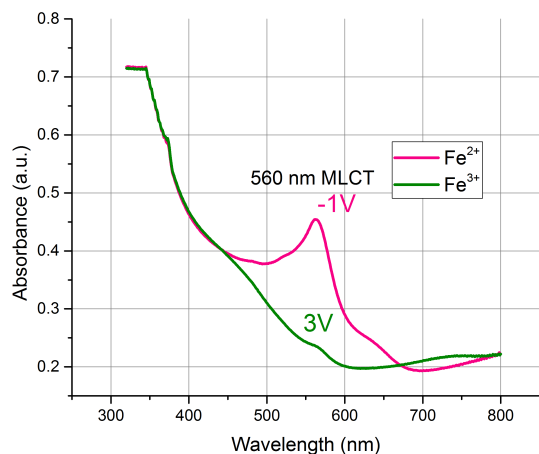
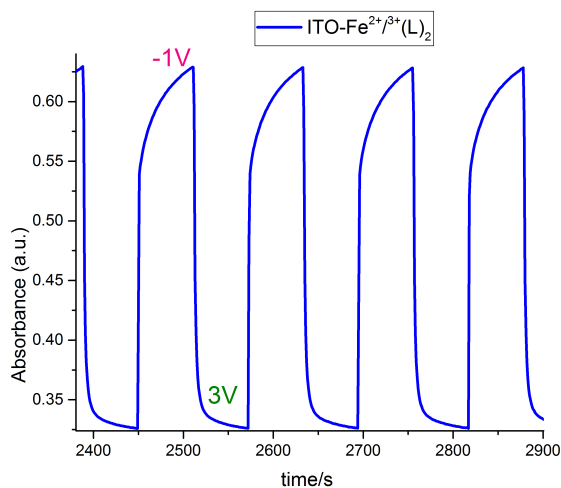


Figure 10.11: Thermal gravimetric analysis in air of L grafted ITO NPs.

hydrophilic quartz, the close molecular packing stemming from the formation of dense (**L**) self assembled monolayers impede the FeL_2 generation in presence of Fe^{2+} precluding iron (II) determination from solutions. On the other hand, nanostructured TiO_2 (or other oxides) surfaces guarantee proper terpyridine molecules orientation for $\text{Fe}(\text{II})$ coordination. Indeed, the formation of the Fe^{2+} complex on nanostructured P-90 TiO_2 thick films led to significant colouring of the material. However, because of excessive particles sinterization due to the small crystallites size, P-90 did not turned out to be a suitable material for ultra-sensitive Fe^{2+} colorimetric determination. Conversely, the surface energy minimization brought about by the titania mesoporous submicrometric beads successfully employed as scaffold material for N-719 sensitization of DSSCs photoanodes, allowed for Fe^{2+} colorimetric detection down to 0.3 ppm. Furthermore, the stability of FeL_2 compared to other transition metals terpyridine complexes, in conjunction with the high molar extinction coefficient of the 560 nm MLCT transition, permitted Fe^{2+} selective determination also in presence of 13 other metal cations. Finally, sensor's reversibility was proved by regenerating the TiO_2 films through the addition of EDTA. Hence, titania-terpyridine materials are expected to be useful for iron fast detection in different fields (irrigation water, drinking water, printed circuits industry, etc.). Moreover, the current research aiming at the integration of the colorimetric sensor on microwaves RFID tags and the eventual use of microfluidic devices should open up the possibility of remote iron detection.



(a)



(b)

Figure 10.12: **(a)** Example of "time driven" absorbance spectrum (at 560 nm) for an electrochromic device relying on the ITO-Fe^{2+/3+}(L)₂ system. Electrical potential allows the device to switch from the iron (III) colorless state (3V) to the iron(II) purple state (-1V) as verified by the absorbance spectrum collected at 560 nm and figure **(a)** inset. Film's yellow color when iron is in the 3+ oxidation state stem from the ITO film rather than the Fe(III)(L)₂ complex. **(b)** Complete Uv-Vis. spectra (800-320 nm) for the electrochromic cell in the two different oxidation states (colored Fe(II) and colorless Fe(III)).

A "spin-off" of the original research on colorimetric sensors is constituted by (L)-functionalized ITO thick films for electrochromic device. The electrochromic effect was verified also for scaffold possessing a low specific surface area (i.e. 10 m²) Investigations on reversibility of the color change triggered by the conversion the electrochemical conversion of Fe(II)(L)₂ to Fe(III)L₂ are in progress.

Chapter 11

Microstrip devices (Microwaves resonators)

11.1 Iron sensitive antenna

The antenna modified with the ITO film was characterized in the microwave frequencies by measuring the reflection coefficient (return loss) at the feed port using (S_{11} is the scattering parameter measured) a Vector Network Analyzer (Agilent E8361A). Return loss plots for the antenna sensitized only with the ligand (**L**) and with the Fe(III)(**L**)₂ complex are reported in figure 11.1. Fe³⁺ adsorption causes a resonant frequency of 710 MHz with respect to the antenna possessing only the ligand chemisorbed on the ITO film surface. Such a shift is presumably due to the paramagnetic properties of the Fe(III)L₂ complex. Further investigation are currently being conducted to verify the dependence of resonant frequency on the magnetism of the metal-terpy complex. For instance, Fe(II)(**L**)₂ is a diamagnetic compound because of the absence of unpaired electrons in a d⁶ low spin configuration. Thus, magnetic permeability and resulting film's inductance are supposed to differ from the Fe(III)L₂ case. However, Fe²⁺ absorption on the ITO polymer thick film is complicated by the presence of the binder and most importantly by the acid groups chemisorbed on the ITO (see Figure 11.2). In fact, carboxylic groups from the dispersing agents can oxidize Fe(II) to Fe(III).

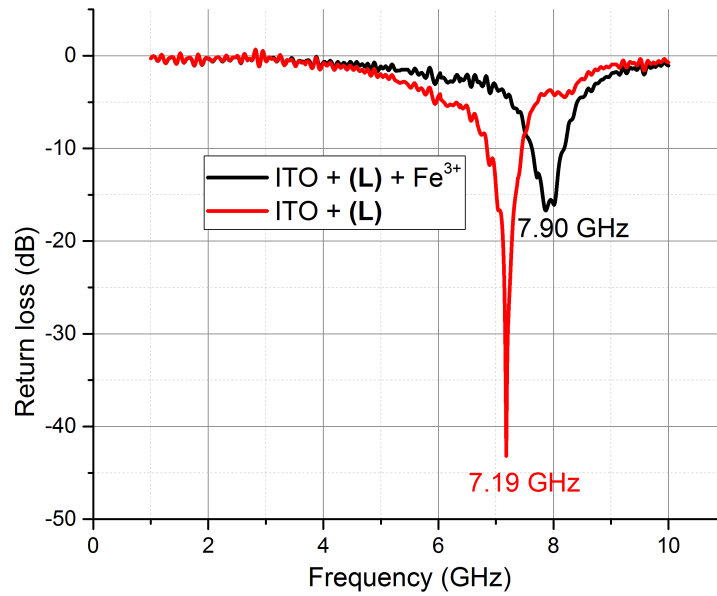


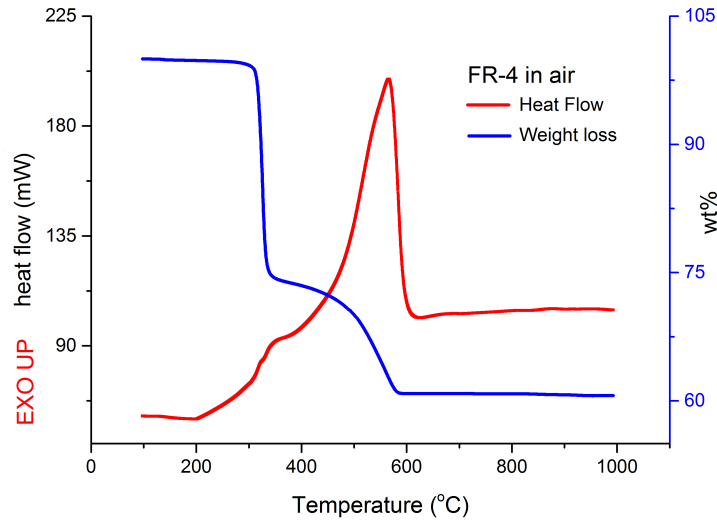
Figure 11.1: Return loss (S_{11} scattering parameter) for a microstrip patch antenna comprised of etched copper traces and ITO screen printed film loaded either with (L) or with Fe(III)(L)_2 . The latter obtained by adsorption of Fe^{3+} on the ITO film sensitized with (L).

11.2 Graphene and MWCNTs loaded antennas

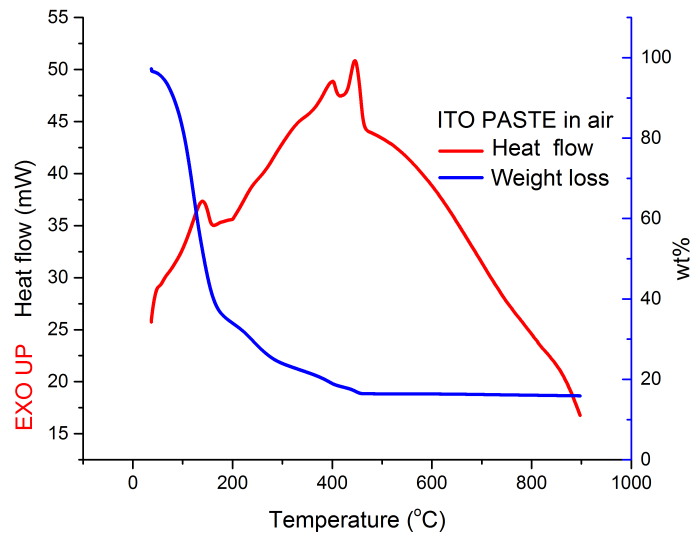
11.2.1 Materials characterization

FE-SEM analysis

Graphene morphology (NIT Graphene Nanoplatelets GNPC97, Nanoinnova, Spain) was investigated by field emission scanning electron microscope (FESEM, Zeiss Merlin). Due to its consistence as fine black powder, precautions were taken in order to avoid its dispersion in air during the characterization. FESEM analysis allows for morphological characterization of graphene aggregates and layers. Selected representative images are depicted in figure 11.3. Low magnification (fig. 11.3(a)) micrographs show three-dimensional agglomerates made of graphene sheets. Figure 11.3 (a), provides further details of such a multilayered structure comprised of graphene flakes stacked together. Other examples concerning the presence of multi-layered nanostructures were collected at increasing magnification and are presented in figures 11.3 (c) and (d). From these micrographs is possible to estimate a thickness of staked graphene planes of about 50 nm. Hence, a high-



(a)



(b)

Figure 11.2: Thermal analysis of FR-4 substrate **(a)** and ITO paste performed in air. Copper foils were removed from a conventional FR-4/copper double-sided laminate by CuCl_2 etching. Composite material decomposition begins at around 280 °C and is accomplished at around 560 °C where only glass fibers are left. On the other hand, ITO paste thermogram shows a continuous evaporation of solvents (α -terpineol, 2-(2-butoxyethoxy)ethyl acetate, and 2-butoxyethanol) from 60 to about 220 °C that at the higher temperatures overlaps with the binder combustion. PVB is completely burned off at 480 °C.

power disgregation procedure was chosen for the preparation of the screen printing

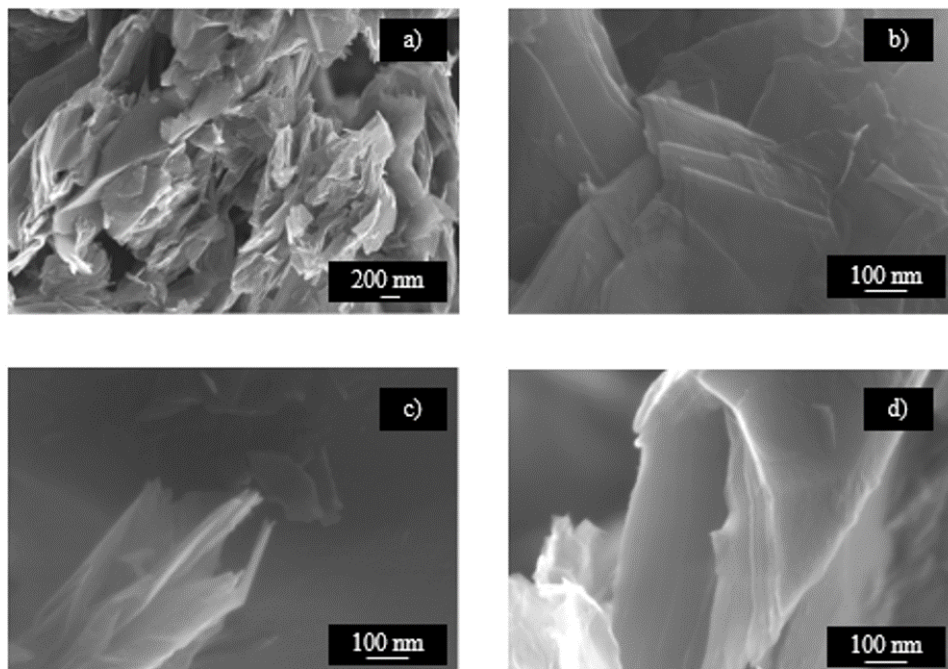


Figure 11.3: Graphene powder FESEM micrographs collected at different magnifications.

graphene ink .

As an example of thick film morphological characterization, figure 11.4 shows the FESEM images of MWCNTs screen printed films on FR-4 substrate. The MWCNTs possess nominal external diameter and length equal to 35 nm and 10 μm , respectively. The CNTs are uniformly entrapped into the binder (ethyl cellulose) matrix in a bird nest-like morphology.

11.2.2 Raman analysis

The Raman spectrum of graphene powder is reported in figure 11.5. The Raman spectrum of carbon materials is usually comprised of two relevant frequency (wavenumber) ranges with different features; the first features' set is located in the range of 1000-1700 cm^{-1} , is related to the G and D bands of carbon [430], [431]. These features are used to estimate material's defectivity (D) and graphitization grade (G), respectively. The G band is associated with the E_{2g} vibration mode of graphite and is characteristic also of polyaromatic hydrocarbons. In fact, it is due to the bond stretching of all pairs of sp^2 atoms in both rings and chains. In perfect graphite, the G band is the only one that can be found in the first-order region. For less ordered carbon materials, additional bands appear in the first-order region

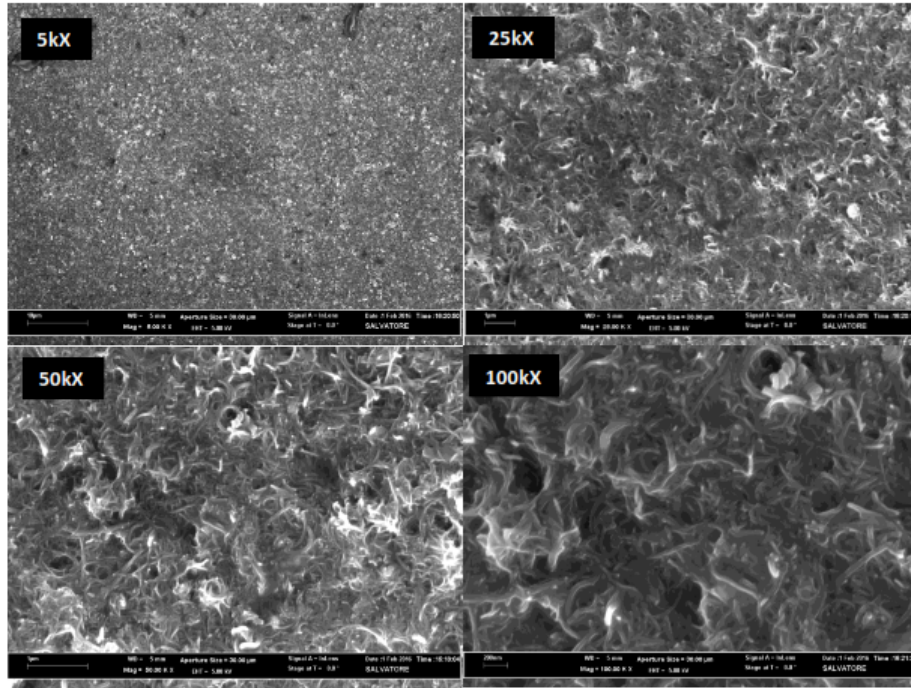


Figure 11.4: FESEM images (at different magnifications) of a MWCNTs thick film deposited on FR4 substrate from a paste containing ethyl cellulose and castor oil dispersed in 80/20 wt% α -terpineol/NMP mixture.

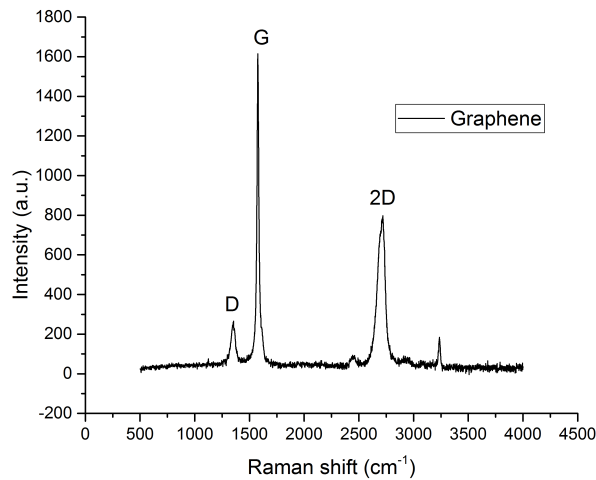


Figure 11.5: Raman spectrum of the NanoInnova graphene used for microstrip patch antenna resonator

at around 1350, 1500, and 1620 cm⁻¹. The 1350 cm⁻¹ band, commonly called the defect band or D band, is frequently attributed to an A_{1g} mode or to the breakdown of translational and local lattice symmetries. The 2200-3500 cm⁻¹ spectral range contains the second-order Raman spectrum. In this frequency region it is possible

Peaks ratios	Value
I_D/I_G	0.21
I_D/I_{2D}	0.15
I_{2D}/I_G	1.43

Table 11.1: Raman peaks' ratio for the graphene employed in the microstrip patch antenna fabrication.

to identify the D vibration mode overtones, namely 2D, the second-harmonic, and the second order product of the D and G peaks. Graphene's quality estimation can be carried out by analyzing the shape and intensity ratio of fundamental and intermodulation peaks. Table 11.1 reports the peaks' intensity ratio obtained from peaks' area. The low intensity of the D peaks compared to the G ones testifies the good quality (low defect content) of the graphene used for the screen printing paste preparation. A shoulder on the left of 2D peak indicates a multilayer structure [432], [433] as confirmed by the FESEM investigation.

Figure 11.6 illustrates the Raman spectrum of the MWCNTs used for the antenna fabrication. It is worth noting that in this case the second-order region is characterized by a quite broad and weak G' peak typical of disordered materials. As expected,

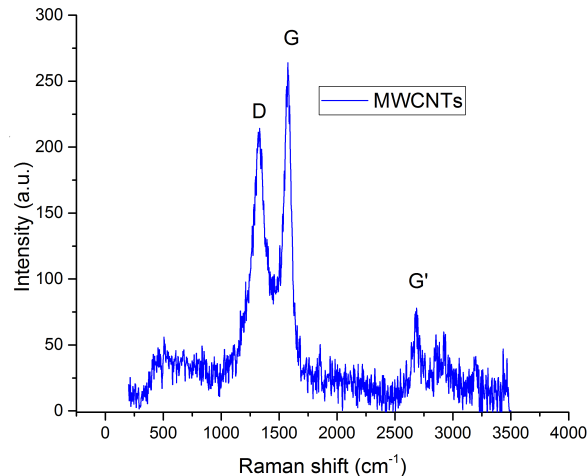


Figure 11.6: Raman spectrum of the MWCNTs under investigation for microwaves devices applications.

Table 11.2 reports the sheet resistance values for the ethyl cellulose binder, the 12.5 wt% and the 25 wt% graphene films.

the ethyl cellulose binder behaves like a lossy insulator with sheet resistance on the order of magnitude of few hundred $M\Omega$. Low amounts of graphene (12.5 wt%) do not reach the percolation threshold and the film resistance is dominated by the EC

Sample	Onelayer	Two Layers
Ethyl cellulose (binder)	$> 10^8$	$> 10^8$
12.5 wt%	2×10^7	2×10^6
25.0 wt%	652	340

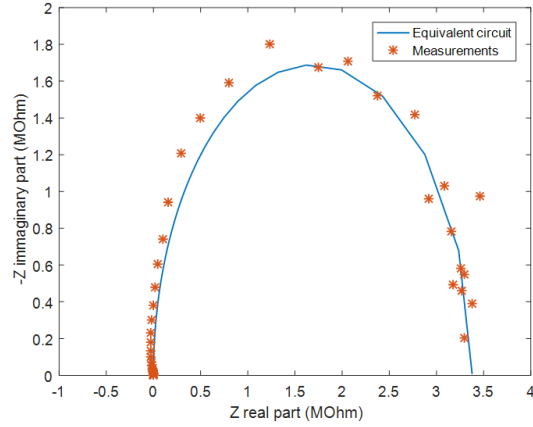
Table 11.2: Sheet resistance (Ω/\square) of different thickness graphene films. The thickness of each layer is approximately $5 \mu\text{m}$. The higher sheet resistance compared to the data reported in figure ?? for the MWCNTs is due to the CNTs' higher aspect ratio and to different inks viscosity leading to thicker films for the carbon nanotubes paste.

contribute. Thus, 12.5 wt% graphene films behaves similarly to the binder. On the other hand, by doubling the graphene loading (25 wt%) the sheet resistance drops by six orders of magnitude. Needless to say, it can be further decreased by increasing the number of printings and curing the films for longer time.

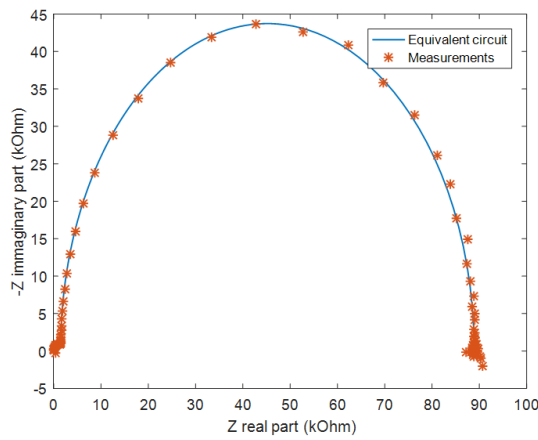
Impedance spectroscopy Nyquist plots of the graphene films (12.5 wt% and 25 wt %, two layers) are shown in figure 11.7. Measured data were fitted with the frequency response of two series-connected parallel RC circuits, predicated on the dielectric response of lossy insulators (ethyl cellulose) and the resistive-capacitive behavior of graphene flakes (due to graphene's chemical capacitance and electron diffusion resistance [?], [434], [435]). The 12.5 wt% graphene film essentially reflects the binder's insulating behavior (only a negligible contribution from graphene is detectable in the Bode plots, not shown). Hence, Nyquist plot for 12.5 wt% graphene loading (figure 11.7 (a)) can be fitted by a *single* parallel RC circuit representing the binder's dielectric losses. Low frequency data dispersion (scattering) has been already reported for "graphene like" exfoliated insulators and justified in terms of flicker ($1/f$) noise [436]. It is worth noting that binder's capacitance component stays the same regardless of graphene loading ($C_{binder\ 12.5\text{wt}\%} = 5.79 \times 10^{-10}$ F; $C_{binder\ 25\text{wt}\%} = 5.95 \times 10^{-10}$ F). On the other hand, the 25 wt% graphene film clearly shows an additional high-frequency parallel RC feature in the Nyquist plot (figure 11.7 (b)), ascribable to randomly distributed graphene sheets distributed within an insulating binder matrix. These nanoplatelets possess a chemical capacitance C_μ related to their density of states. Graphene's C_μ extrapolated from the nonlinear fit of the impedance data is one order of magnitude lower than the binder value ($C_{graphene\ 25\ \text{wt}\%} = 7.06 \times 10^{-11}$ F).

The measured S-parameters (only the transmission coefficient S_{21} is shown for brevity ¹ of the graphene loaded microstrip line of figure 8.9 are displayed in

¹As briefly mentioned in chapter 6 in a two ports *microwave* system the transmission coefficient coincides with the S_{21} scattering parameter and it is related to the insertion loss (IL) like the return



(a)

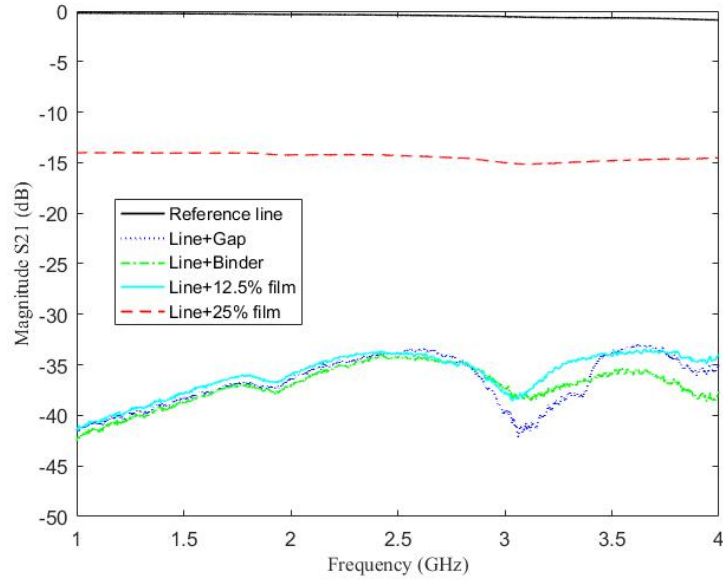


(b)

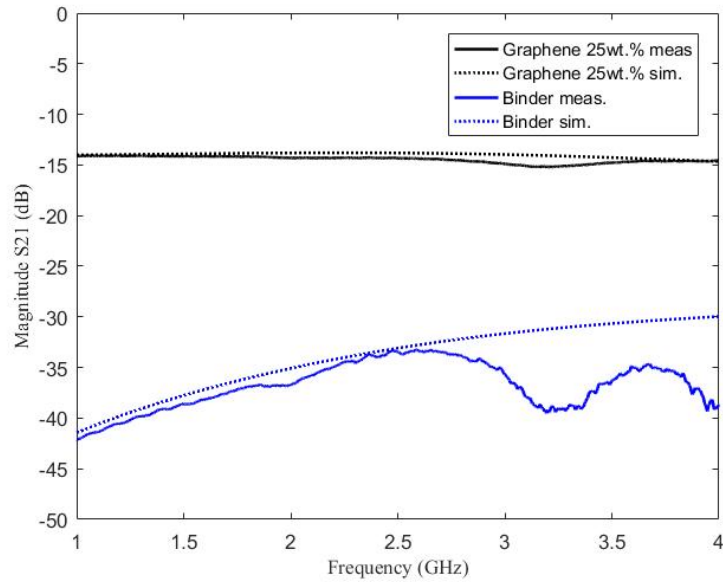
Figure 11.7: Nyquist plot for the 12.5 wt % (a) and 25 wt % (b)

figure 11.8 (a) and (b). the 12.5 wt% graphene film acts like the EC binder . It is not surprising that an unfilled gap has similar low transmission as the binder, thus confirming its insulating behavior emerged from the low frequency impedance spectroscopy measurements. On the other hand, the 25 wt% graphene film shows a marked increase in transmission across the gap due to reduced sheet resistance. A high frequency circuit model can be derived from ADS simulations on the basis of the measured S_{21} (see figure 11.9). Good corroboration is observed between the circuit model and the measurements over a 3 GHz bandwidth. The symmetrical circuit topology of the ADS model for the 25 wt% graphene film is shown in figure 11.9. The resistance (\mathbf{R}) in the series path accounts for printed film losses due to graphene sheet resistance and ethyl cellulose binder dielectric losses. (\mathbf{R}) turned out to be 400Ω which is compatible with graphene high conductivity

loss is related to the reflection coefficient Γ (S_{11}). In fact, $IL = -20\log |S_{21}|$; $RL = 20\log |S_{11}|$



(a)



(b)

Figure 11.8: **(a)**, S_{21} (transmission coefficient) for various loadings configurations. **(b)**, measurements (solid line) and simulations (dotted line) of binder and 25 wt% graphene films **(b)**.

and relatively low ethyl cellulose dielectric losses. Indeed, the substitution of H on some oxydrilic groups of the glucose building units with the $\text{CH}_3\text{-CH}_2\text{-}$ group reduces dipolar relaxation compared to other cellulosic binders (i.e. cellulose, cellulose nitrate, cellulose acetate, carboxymethyl cellulose, etc.). Furthermore, a capacitance (\mathbf{C}), in parallel to the resistance (\mathbf{R}) is necessary to describe film's

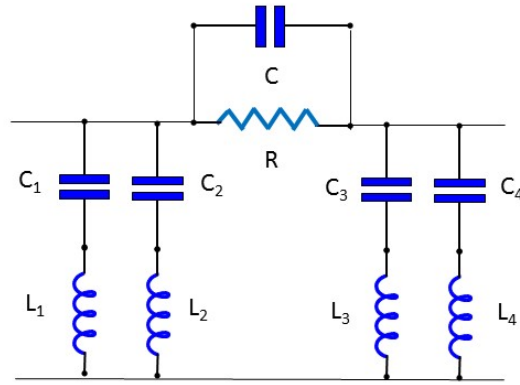


Figure 11.9: Equivalent circuit model of the 25 wt% graphene printed film. C_1 , C_2 , C_3 , C_4 ($C_1 = C_4 = 90$ fF; $C_2 = C_3 = 10$ fF) and L_1 , L_2 , L_3 , L_4 ($L_1 = L_4 = 67$ nH $L_2 = L_3 = 54$ nH) concern the microstrip line rather than the graphene film.

microwave properties. A 0.5 pF value was found for (**C**) from the fit. Since the graphene chemical capacitance, does not contribute to the total capacitance at the microwave frequencies [437], (**C**) accounts for the 3 mm gap capacitance filled with EC and FR-4. In fact, graphene nanoplatelets act as the electrodes of a "classical" electrostatic nanocapacitor employing EC and FR-4 as dielectrics. This picture agrees with data reported in literature. Indeed, different groups (i.e. [368], [438]) reported of the voltage insensitive behavior of pure graphene films deposited on microwaves microstrips line. If any contribution from graphene C_μ was present films capacitance should change as a DC bias is applied. On the contrary, Pierantoni et. al [368], for instance, reported no films capacitance's change upon the application of a DC voltage indicating that the graphene chemical capacitance is inactive at the microwaves frequencies. The shunt capacitors (C_1 - C_4) account for the capacitance between the microstrip electrodes and the bottom ground plane at the junction with the film. These series components are due to contact only and not representative of the graphene film losses. Provided that graphene kinetic inductance due to plasmons' motion becomes a relevant contribution to film's impedance in the THz frequency range (and at the optical frequencies for metals [439], [34]), L_1 - L_4 don't belong to the nanostructured carbon material but rather to the copper microstrip, RF cables, and connectors conventional "magnetic" inductance.

Experimental and simulated RL data for the microstrip patch resonator with and without the graphene films is illustrated in figure 11.10. First, the bare resonator *without* even the copper stub resonates at 4.91 GHz. The simulated data are in good agreement with the experimental data. Next, only the stub loaded with

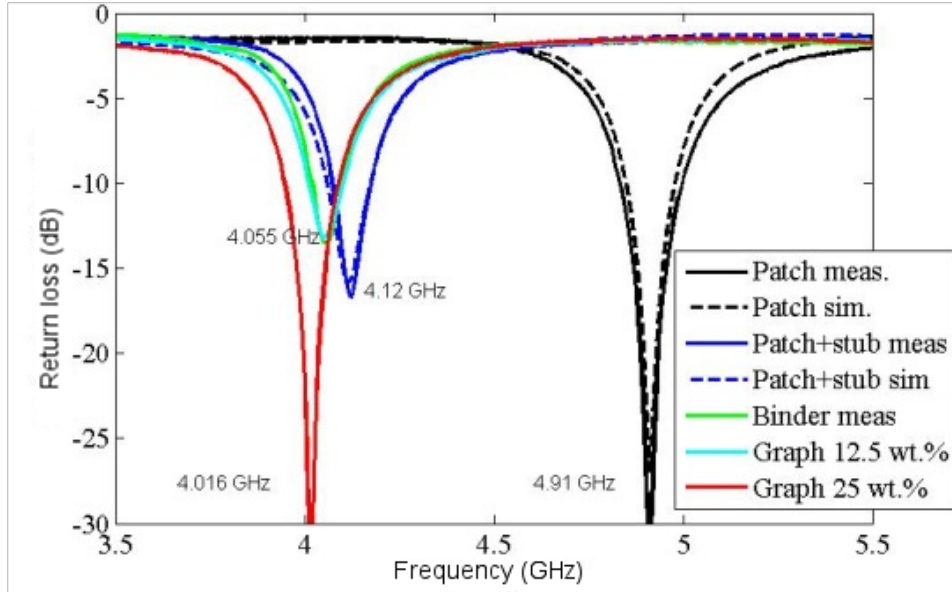


Figure 11.10: Return loss for microstrip patch resonator loaded with different amounts of graphene. Both experimental data and simulations are reported. "Patch" refers to the resonator without the 15 mm stub attached to the patch.

an open (or unfilled) gap is introduced and the return loss of the resonator is measured. Again, good corroboration between measured and simulated data is observed, with the resonance at 4.12 GHz. This is the baseline geometry used to study the effect of graphene films inserted across the electrode gap. It is observed that the resonant frequencies of the device loaded with the 12.5 wt% graphene and with the binder only are in close proximity due to dominance by the binder contribution to film capacitance, as explained in before. The resonance shift of both loadings (binder and 12.5 wt%) with respect to baseline configuration is 65 MHz. On the other hand, the 25 wt% graphene film produces a resonant frequency shift of 104 MHz, suggesting that a sufficient concentration (above the percolation threshold) of graphene nanoplateles entrapped into a polymer matrix can act as nanoscale capacitors modulating the gap dielectric constant.

The quality factor (**Q**) of a resonator is inversely proportional to the resonance bandwidth (**B**)², defined as the frequency spread between two points at which the $|RL| > 10$ dB (see chapter 6). It is observed that the bare, unloaded patch and the resonator loaded with 25 wt% graphene have reasonably close Q values (34.60 for the unloaded resonator and 27.03 for the 25 wt% graphene loaded one), attesting that the resistive and dielectric losses introduced by the printed film generate

²Resonator quality factor and bandwidth are related through the formula: $Q = \frac{\omega_0}{B}$. ω_0 is the center of the resonant frequency.

negligible perturbations to the resonant mode. Therefore, placing the printed film away from the patch is an effective technique to minimize electromagnetic losses due to mutual coupling between the two resonator's elements. This is very important when graphene films need to be used as detecting material for chipless RFID sensing. In fact, as described in chapter 6, detection of environmental changes in the RFID tag surroundings is performed by monitoring the attenuation of the reader's signal through the resonator. Hence, high (Q) structures allow to extend the range of appreciable reader's signal intensity attenuations leading to higher detector's sensitivity.

11.2.3 MWCNTs samples

The previous investigation concerning microstrip patch (antenna) resonators loaded with printed graphene films focused only on materials electrical properties leaving out the device transmitting (and receiving properties) characteristics. On the other hand, MWCNTs films (12.5 wt %) were employed and tested as structures capable of shifting the resonant frequency of an antenna *without compromising its radiation properties*. Hence, an antenna fabricated as described in section ?? was used as a reference and a three layers thick (thickness $\approx 30 \mu\text{m}$ corresponding to a sheet resistance of $105 \Omega/\square$), MWCNTs film was printed in the 3 mm gap on the stub side. Figure 11.11 presents the RL plots for the reference antenna and the MWCNTs loaded one. Furthermore, simulated data are also displayed. The MWCNT printed film was modeled assuming a surface impedance with a resistance $R_s = 105 \Omega$, and reactance X_s varying between 0 and 2 k Ω [440]. The patch and the ground plane are treated as perfect electrically conducting (PEC) media. Considering the experimental return loss, the resonant frequency of the CNTs containing antenna is shifted of 230 MHz compared to the reference device. In the simulation, this frequency shift is obtained with a reactance of 1 k Ω for the film. Simulated and measured resonant frequencies for the MWCNTs device are in good agreement. The discrepancy in magnitude is probably caused by the fact that the DC sheet resistance value was used for R_s . Indeed, skin effect is negligible in direct current and low frequency measurements.

Figure 11.12 The measured gain was 3dBi for the reference antenna and 2.9 dBi for the MWCNTs loaded one. Hence, the impedance mismatch and radiation losses do not affect excessively the device's gain.

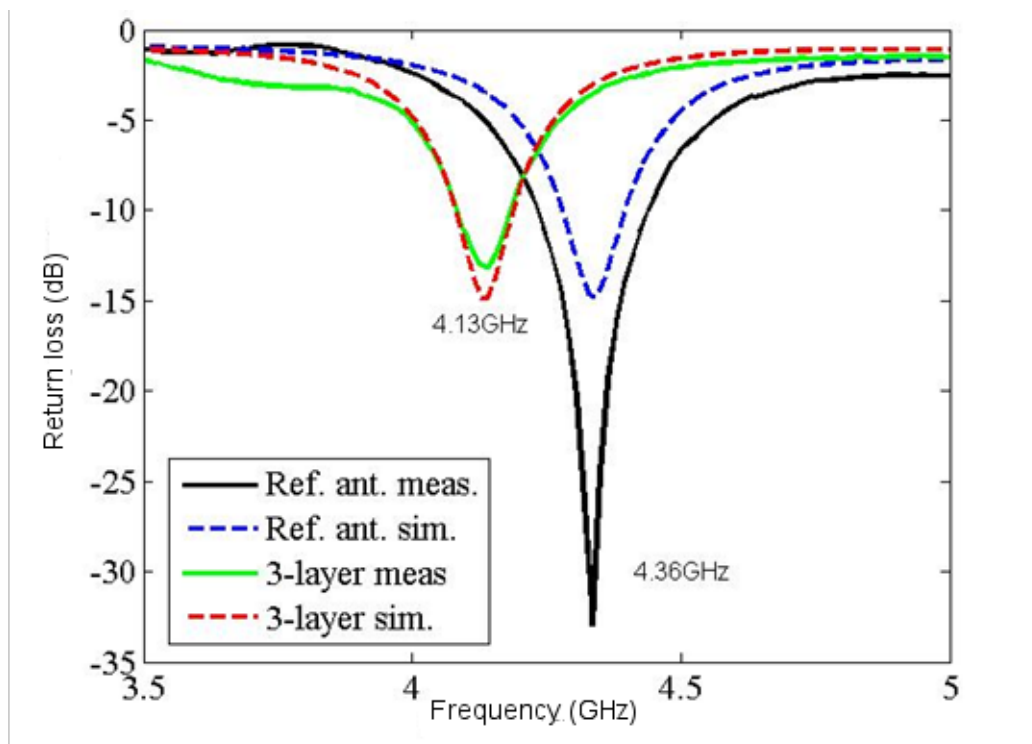


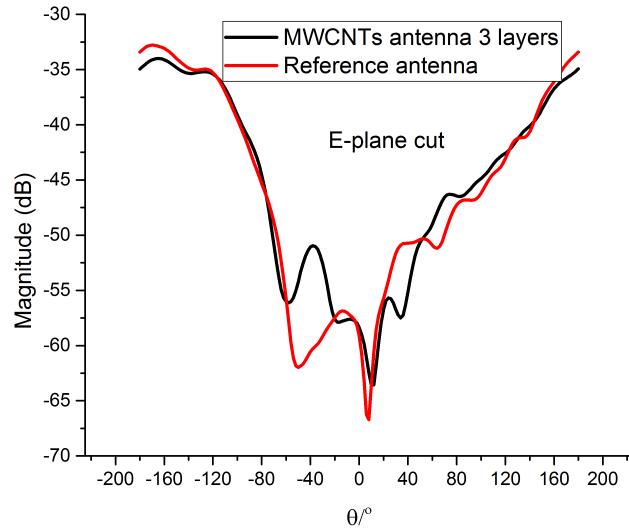
Figure 11.11: Return loss of the reference antenna and of the same devices loaded with a three layers thick MWCNTs film.

11.3 Conclusions

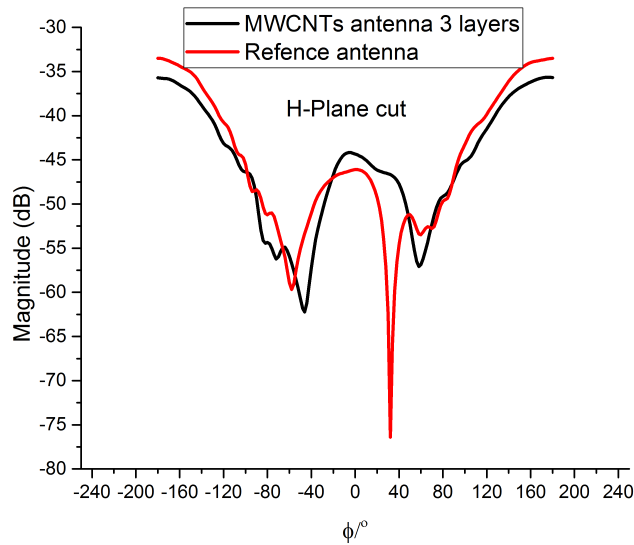
esided the possible application as LED replacement to indicate the battery (for active tags) or the IC status for RFID chipped tags, (**L**)-trivalent iron complex could be exploited for Fe^{3+} non-colorimetric detection. Trials of iron (III) detection predicated on the resonant frequency shift of microwaves resonators (i.e. microstrip patch antennas) are being conducted. Preliminary results seems to suggest that the inductance variation caused by the formation of the Fe(III)L_2 paramagnetic complex can produce an impedance change of ITO films inserted into resonators gaps and a subsequent shift in the resonant frequency.

The second, and last, section of final research stage focused on graphene films microwave properties characterization and on MWCNTs films as resonant frequency tuning element for antennas operating in the microwaves C-band. Both topics are still under investigation.

The characteristics of thick films loaded with graphene were explored. Low- frequency dielectric spectroscopy reveals that low (12.5 wt% upon the screen printing paste total mass) graphene loadings have about the same capacitance of the ethyl cellulose binder used for the polymer thick film deposition. Consequently, graphene



(a)



(b)

Figure 11.12: E-plane (a) and H-cut (b) radiation patterns of reference antenna and 3-layers loaded MWCNTs antenna.

concentration below the percolation threshold produces negligible film's impedance changes. Films comprised of binder alone, as well as binder plus graphene (12.5 wt% and 25 wt%), were printed across the gap of microstrip lines, and experimentally studied as well as using a circuit model. Similarly to the low-frequency case, the binder behaves as a lossy insulator hindering power transmission along the microstrip line. A simple lumped elements equivalent circuit predicated on the

experimental transmission coefficient measurement was introduced to model the graphene-binder film. Finally, a graphene loaded microstrip patch resonator to be employed as active element of sensor-enabled chipless RFID tags was fabricated and characterized for return loss. It is shown that 25 wt% graphene loading produces a resonance frequency shift of 104 MHz, indicating decreased capacitance with respect to the unloaded resonator. It was also demonstrated that resonance quality factors comparable to the unloaded resonator can be achieved if the mutual coupling between patch and the film is reduced. A similar approach, still based on confining printed films of carbon materials (MWCNTs) to a small area of the microwave resonator was used to produce a 230 MHz resonant frequency modulation in a microstrip patch antenna without excessively penalizing the device's gain.

Besides the microwave properties investigation of carbon materials (i.e. carbon black, biochar) thick films employing to temperature removable binders (i.e cellulose nitrate) possible future developments of these research branch includes:

- Graphene and CNTS films functionalization with polymers capable of tumoral markers detection .
- Modification of terpyridine molecules with carboxylic moieties to favor their chemisorption on graphene and CNTs for ion sensing through microwaves resonators.

The former research approach has been being currently carried out at the EPFL.

Part IV

Final conclusions and future work

Chapter 12

Final conclusions and future work

The purpose of the present thesis was to develop low cost nanostructured materials possessing special opto-electronic properties suitable for a wide range of applications spanning from inexpensive photovoltaic devices (DSSCs) to reusable iron colorimetric sensors, to electrochromic devices, to microwave sensors for sensor-enabled RFID. During the investigation a few remarkable points concerning material properties came up:

- Light scattering properties and mesoporosity of sub-micrometric titania hierarchical beads (i.e HDA route) make them a suitable material for both DSSCs and colorimetric sensors. In fact, among the different experimented in DSSCs (stemming from both hard and soft polymeric templating synthetic routes), the titania hierarchical sphere have proved to increase DSSCs energy conversion efficiency mainly because of their light scattering characteristics. Indeed, a beads diameter comparable to light wavelengths enhance the dye's light harvesting efficiency η_{hv} (i.e. quantum efficiency improvement in the lower wavelengths region) that compensate for the relatively high series resistance (88 Ω) due to the contact between FTO and the mesoporous titanium dioxide. On the other hand, the intrinsic thermodynamic stability of the beads, brought about by their spherical shape, was exploited for Fe^{2+} sensors possessing high color contrast, low detection limit and high sensitivity with respect to the amount of Fe(II) to be detected. Indeed, when the beads are deposited as thick films (3-6 μm) no significant surface area shrinking occurs during the annealing procedure. Consequently, a wide portion of the mesoporous TiO_2 surface remains accessible for (**L**) functionalization and Fe^{2+} coordination, increasing the sensitivity with respect to the number of printed layers. Conversely, the high reactivity and sintering ability of commercial P90 TiO_2

renders the printed layers underneath the top one inaccessible to the ligand and the ion producing practically no thickness sensitivity.

- TiO_2 doping with Heavy trivalent Ln^{3+} ions is a satisfactory approach for DSSCs efficiency improvement. Rare earth dopants enhance DSSCs efficiency by impacting on the electron transport properties. In fact, electron life time is improved compared to the cell comprised by pure anatase photoanodes. However, the electron diffusion length follows a decreasing trend with the ionic radius of the dopants. Thereby, the overall energy conversion efficiency increase for dopants heavier than Sm^{3+} (Sm^{3+} , Gd^{3+} , Er^{3+} , Yb^{3+}) stems from the delicate balance between compensation for TiO_2 oxygen vacancies deep traps and electron-dopant scattering.
- SWCNTs' chirality separation could be advantageous for device specific optoelectronic properties tailoring. In the specific case of DSSCs, chirality enrichment was proved to be effective in adjusting the energy barrier height at the $\text{TiO}_2/\text{SWCNTs}$ interface, favoring charge injection, preventing recombination and improving photoanode's transport properties (i.e reduced DSSC series resistance). Detrimental effects caused by the direct contact of SWCNTs, and in particular metallic tubes and the electrolyte manifested as a drastic shunt resistance decrease compared to the cell without CNTs, due to the catalytic effect of carbon species toward the triiodide reduction. Nevertheless, an 85% efficiency improvement was found for the **(7,3)** cell compared to the DSSC containing 30 chiralities. In addition the shunt resistance can be increased by protecting the SWCNTs from the electrolyte by depositing, i.e. by spray pyrolysis a blocking layer of "compact" TiO_2 . Although from the theoretical point of view it would be possible to replace the Pt counter electrode with a thin layer of chirality pure CNTs, limitations concerning the implementation of a large scale chirality separation procedure together with the slow electron from the SWCNTs to the electrolyte make this solution unpractical.
- Phosphonic group modified terpyridine-oxides systems optical properties are applicable to different electronic devices (sensors, electrochromic devices). Indeed, the large electronic delocalization stemming from the coupling between the phosphonic group and the N-aromatic ring give rise to intense MLCT transitions with high charge density ions (i.e. $\text{Ir}^{3+/4+}$, $\text{Ru}^{2+/3+}$, $\text{Fe}^{2+/3+}$). Furthermore, the extended electronic delocalization allows for good electrical

communication with the substrate constituted by thick films of ITO generating a stable electrochromic effect.

- Thick films of carbon materials can be used for resonant frequency “tuning” of resonators and/or antennas. However no resonators and antennas inductive (usually responsible for large resonant frequency shift) was identified). In fact, graphene and MWCNTs entrapped into a polymer binder were modeled as RC circuit comprised of nanocapacitors. Moreover, graphene films require high carbon materials loadings (25 wt% to produce appreciable resonators return loss and insertion loss variations. On the other hand, the higher MWCNTs aspect ratio permits to achieve a decent film’s conductivity also at 12.5 wt%, generating microstrip patch antennas resonant frequency shifts on the order of 200 MHz.

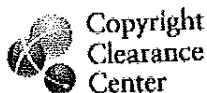
Plenty of new application can be implemented on the grounds of the optoelectronic properties shown by the materials employed for the present research. For example, the light scattering properties and monodispersed porosity shown by the TiO₂ mesoporous beads can be easily extended to other kind of oxides. Indeed, instead of producing semiconducting oxides like titanium dioxide, conductive oxides could be produced by exploiting the hexadecylamine route. For instance, ITO or AZO (aluminum doped zinc oxide) or ATO (antimony doped tin oxide) can be synthesized in the forms of beads using the same procedure of TiO₂. Hence, a conductive material capable of light scattering and potentially applicable to electrochromic devices can be produced. Furthermore, chemical modification of the terpyridine ligands conjugated to the phosphonic moiety, allow for the production of new “terpy” based molecules with intriguing light absorption and emission properties that will find in the TiO₂ beads an ideal candidate support for their integration in solid state devices (e.g OLED). This research field, together with professor Olena Zenkina is currently being carried out at the UOIT in parallel to the investigation of new oxides (e.g. AZO) for the production of low-cost electrochromic devices based also on silanized terpyridine derivative. In addition, TiO₂ beads and other mesoporous oxides thick film can be used in the printed circuit boards industry for iron detection. Metal clads etching produces large amounts of iron(II) rich effluents ¹ to be treated before disposal. On the other hand, Iron contamination in the orders of tens of ppm in solder (Sn-Pb), Sn, Ni, Rh and Au electroplating

¹FeCl₃ is the most employed copper etchant in pcb industry along with CuCl₂ and Alkaline Ammonia

baths used for PCBs surface finishing and metal resist depositions brings about dull deposits, poor adherence, surface roughness, etc. Hence, Iron levels control is crucial in PCB industry. Therefore our mesoporous $\text{TiO}_2\text{-(L)}$ iron detection system can easily find an application in the electronic industry. Besides, SnCl_2 , one of the most used reducing agents in the PCB industry, possesses a redox potential capable of converting Fe^{3+} in solution into Fe^{2+} allowing the total iron content determination.

Each material originally developed for a specific application found or can found application in other fields outside the reason for which it was meant for. Also chirality separated SWCNTs, since have been proved effective in modulating DSSCs photoanodes conductivity, work function and light absorption properties are valuable candidate as charge extraction layers for high efficiency solar cells like perovskite solar cells. Another possible application of chirality selected SWCNTs is the tuning of microwave devices like the graphene and MWCNTs loaded antennas

Finally, once the principle of ions detection through resonant frequency shift of a microwave resonator has been proved, further investigation concerning its applicability to different paramagnetic or diamagnetic ions is required.



RightsLink[®]

[Home](#)[Create Account](#)[Help](#)

ACS Publications
Most Trusted. Most Cited. Most Read.

Title: Electron Transfer Dynamics in Dye-Sensitized Solar Cells
Author: Andrea Listorti, Brian O'Regan, James R Durrant
Publication: Chemistry of Materials
Publisher: American Chemical Society
Date: Aug 1, 2011

Copyright © 2011, American Chemical Society

LOGIN
If you're a [copyright.com](#) user, you can login to RightsLink using your [copyright.com](#) credentials. Already a [RightsLink](#) user or want to [learn more?](#)

PERMISSION/LICENSE IS GRANTED FOR YOUR ORDER AT NO CHARGE

This type of permission/license, instead of the standard Terms & Conditions, is sent to you because no fee is being charged for your order. Please note the following:

- Permission is granted for your request in both print and electronic formats, and translations.
- If figures and/or tables were requested, they may be adapted or used in part.
- Please print this page for your records and send a copy of it to your publisher/graduate school.
- Appropriate credit for the requested material should be given as follows: "Reprinted (adapted) with permission from (COMPLETE REFERENCE CITATION). Copyright (YEAR) American Chemical Society." Insert appropriate information in place of the capitalized words.
- One-time permission is granted only for the use specified in your request. No additional uses are granted (such as derivative works or other editions). For any other uses, please submit a new request.

If credit is given to another source for the material you requested, permission must be obtained from that source.

[BACK](#)[CLOSE WINDOW](#)

Copyright © 2017 Copyright Clearance Center, Inc. All Rights Reserved. [Privacy statement](#). [Terms and Conditions](#).
Comments? We would like to hear from you. E-mail us at customercare@copyright.com

ACS Publications
Most Trusted. Most Cited. Most Read.

Title: Design of Organic Dyes and Cobalt Polypyridine Redox Mediators for High-Efficiency Dye-Sensitized Solar Cells

Author: Sandra M. Feldt, Elizabeth A. Gibson, Erik Gabrielsson, et al

Publication: Journal of the American Chemical Society

Publisher: American Chemical Society

Date: Nov 1, 2010

Copyright © 2010, American Chemical Society

LOGIN

If you're a [copyright.com](#) user, you can login to RightsLink using your [copyright.com](#) credentials. Already a [RightsLink](#) user or want to [learn more?](#)

PERMISSION/LICENSE IS GRANTED FOR YOUR ORDER AT NO CHARGE

This type of permission/license, instead of the standard Terms & Conditions, is sent to you because no fee is being charged for your order. Please note the following:

- Permission is granted for your request in both print and electronic formats, and translations.
- If figures and/or tables were requested, they may be adapted or used in part.
- Please print this page for your records and send a copy of it to your publisher/graduate school.
- Appropriate credit for the requested material should be given as follows: "Reprinted (adapted) with permission from (COMPLETE REFERENCE CITATION). Copyright (YEAR) American Chemical Society." Insert appropriate information in place of the capitalized words.
- One-time permission is granted only for the use specified in your request. No additional uses are granted (such as derivative works or other editions). For any other uses, please submit a new request.

If credit is given to another source for the material you requested, permission must be obtained from that source.

BACK

CLOSE WINDOW

**JOHN WILEY AND SONS LICENSE
TERMS AND CONDITIONS**

Apr 19, 2017

This Agreement between simone Quaranta ("You") and John Wiley and Sons ("John Wiley and Sons") consists of your license details and the terms and conditions provided by John Wiley and Sons and Copyright Clearance Center.

License Number	4092570384402
License date	Apr 19, 2017
Licensed Content Publisher	John Wiley and Sons
Licensed Content Publication	Photochemistry and Photobiology
Licensed Content Title	Near-IR Absorbing Solar Cell Sensitized With Bacterial Photosynthetic Membranes
Licensed Content Author	Kamil Woronowicz, Saquib Ahmed, Archana A. Biradar, Ankush V. Biradar, Dunbar P. Birnie, Tewodros Asefa, Robert A. Niederman
Licensed Content Date	Jul 20, 2012
Licensed Content Pages	6
Type of use	Dissertation/Thesis
Requestor type	University/Academic
Format	Electronic
Portion	Figure/table
Number of figures/tables	1
Original Wiley figure/table number(s)	Figure 1
Will you be translating?	No
Title of your thesis / dissertation	Nanostructured Materials for Photovoltaics and Microwave Electronics: methods and applications
Expected completion date	Apr 2017
Expected size (number of pages)	300
Requestor Location	simone Quaranta 85 taylorwood crt OSHAWA, ON L1G7V7 Canada Attn: simone Quaranta
Publisher Tax ID	EU826007151
Billing Type	Invoice
Billing Address	simone Quaranta 85 taylorwood crt OSHAWA, ON L1G7V7

Canada
Attn: simone Quaranta

Total

0.00 CAD

Terms and Conditions

TERMS AND CONDITIONS

This copyrighted material is owned by or exclusively licensed to John Wiley & Sons, Inc. or one of its group companies (each a "Wiley Company") or handled on behalf of a society with which a Wiley Company has exclusive publishing rights in relation to a particular work (collectively "WILEY"). By clicking "accept" in connection with completing this licensing transaction, you agree that the following terms and conditions apply to this transaction (along with the billing and payment terms and conditions established by the Copyright Clearance Center Inc., ("CCC's Billing and Payment terms and conditions"), at the time that you opened your RightsLink account (these are available at any time at <http://myaccount.copyright.com>).

Terms and Conditions

- The materials you have requested permission to reproduce or reuse (the "Wiley Materials") are protected by copyright.
- You are hereby granted a personal, non-exclusive, non-sub licensable (on a stand-alone basis), non-transferable, worldwide, limited license to reproduce the Wiley Materials for the purpose specified in the licensing process. This license, **and any CONTENT (PDF or image file) purchased as part of your order**, is for a one-time use only and limited to any maximum distribution number specified in the license. The first instance of republication or reuse granted by this license must be completed within two years of the date of the grant of this license (although copies prepared before the end date may be distributed thereafter). The Wiley Materials shall not be used in any other manner or for any other purpose, beyond what is granted in the license. Permission is granted subject to an appropriate acknowledgement given to the author, title of the material/book/journal and the publisher. You shall also duplicate the copyright notice that appears in the Wiley publication in your use of the Wiley Material. Permission is also granted on the understanding that nowhere in the text is a previously published source acknowledged for all or part of this Wiley Material. Any third party content is expressly excluded from this permission.
- With respect to the Wiley Materials, all rights are reserved. Except as expressly granted by the terms of the license, no part of the Wiley Materials may be copied, modified, adapted (except for minor reformatting required by the new Publication), translated, reproduced, transferred or distributed, in any form or by any means, and no derivative works may be made based on the Wiley Materials without the prior permission of the respective copyright owner. **For STM Signatory Publishers clearing permission under the terms of the STM Permissions Guidelines only, the terms of the license are extended to include subsequent editions and for editions in other languages, provided such editions are for the work as a whole in situ and does not involve the separate exploitation of the permitted figures or extracts**, You may not alter, remove or suppress in any manner any copyright, trademark or other notices displayed by the Wiley Materials. You may not license, rent, sell, loan, lease, pledge, offer as security, transfer or assign the Wiley Materials on a stand-alone

basis, or any of the rights granted to you hereunder to any other person.

- The Wiley Materials and all of the intellectual property rights therein shall at all times remain the exclusive property of John Wiley & Sons Inc, the Wiley Companies, or their respective licensors, and your interest therein is only that of having possession of and the right to reproduce the Wiley Materials pursuant to Section 2 herein during the continuance of this Agreement. You agree that you own no right, title or interest in or to the Wiley Materials or any of the intellectual property rights therein. You shall have no rights hereunder other than the license as provided for above in Section 2. No right, license or interest to any trademark, trade name, service mark or other branding ("Marks") of WILEY or its licensors is granted hereunder, and you agree that you shall not assert any such right, license or interest with respect thereto
- NEITHER WILEY NOR ITS LICENSORS MAKES ANY WARRANTY OR REPRESENTATION OF ANY KIND TO YOU OR ANY THIRD PARTY, EXPRESS, IMPLIED OR STATUTORY, WITH RESPECT TO THE MATERIALS OR THE ACCURACY OF ANY INFORMATION CONTAINED IN THE MATERIALS, INCLUDING, WITHOUT LIMITATION, ANY IMPLIED WARRANTY OF MERCHANTABILITY, ACCURACY, SATISFACTORY QUALITY, FITNESS FOR A PARTICULAR PURPOSE, USABILITY, INTEGRATION OR NON-INFRINGEMENT AND ALL SUCH WARRANTIES ARE HEREBY EXCLUDED BY WILEY AND ITS LICENSORS AND WAIVED BY YOU.
- WILEY shall have the right to terminate this Agreement immediately upon breach of this Agreement by you.
- You shall indemnify, defend and hold harmless WILEY, its Licensors and their respective directors, officers, agents and employees, from and against any actual or threatened claims, demands, causes of action or proceedings arising from any breach of this Agreement by you.
- IN NO EVENT SHALL WILEY OR ITS LICENSORS BE LIABLE TO YOU OR ANY OTHER PARTY OR ANY OTHER PERSON OR ENTITY FOR ANY SPECIAL, CONSEQUENTIAL, INCIDENTAL, INDIRECT, EXEMPLARY OR PUNITIVE DAMAGES, HOWEVER CAUSED, ARISING OUT OF OR IN CONNECTION WITH THE DOWNLOADING, PROVISIONING, VIEWING OR USE OF THE MATERIALS REGARDLESS OF THE FORM OF ACTION, WHETHER FOR BREACH OF CONTRACT, BREACH OF WARRANTY, TORT, NEGLIGENCE, INFRINGEMENT OR OTHERWISE (INCLUDING, WITHOUT LIMITATION, DAMAGES BASED ON LOSS OF PROFITS, DATA, FILES, USE, BUSINESS OPPORTUNITY OR CLAIMS OF THIRD PARTIES), AND WHETHER OR NOT THE PARTY HAS BEEN ADVISED OF THE POSSIBILITY OF SUCH DAMAGES. THIS LIMITATION SHALL APPLY NOTWITHSTANDING ANY FAILURE OF ESSENTIAL PURPOSE OF ANY LIMITED REMEDY PROVIDED HEREIN.
- Should any provision of this Agreement be held by a court of competent jurisdiction to be illegal, invalid, or unenforceable, that provision shall be deemed amended to

achieve as nearly as possible the same economic effect as the original provision, and the legality, validity and enforceability of the remaining provisions of this Agreement shall not be affected or impaired thereby.

- The failure of either party to enforce any term or condition of this Agreement shall not constitute a waiver of either party's right to enforce each and every term and condition of this Agreement. No breach under this agreement shall be deemed waived or excused by either party unless such waiver or consent is in writing signed by the party granting such waiver or consent. The waiver by or consent of a party to a breach of any provision of this Agreement shall not operate or be construed as a waiver of or consent to any other or subsequent breach by such other party.
- This Agreement may not be assigned (including by operation of law or otherwise) by you without WILEY's prior written consent.
- Any fee required for this permission shall be non-refundable after thirty (30) days from receipt by the CCC.
- These terms and conditions together with CCC's Billing and Payment terms and conditions (which are incorporated herein) form the entire agreement between you and WILEY concerning this licensing transaction and (in the absence of fraud) supersedes all prior agreements and representations of the parties, oral or written. This Agreement may not be amended except in writing signed by both parties. This Agreement shall be binding upon and inure to the benefit of the parties' successors, legal representatives, and authorized assigns.
- In the event of any conflict between your obligations established by these terms and conditions and those established by CCC's Billing and Payment terms and conditions, these terms and conditions shall prevail.
- WILEY expressly reserves all rights not specifically granted in the combination of (i) the license details provided by you and accepted in the course of this licensing transaction, (ii) these terms and conditions and (iii) CCC's Billing and Payment terms and conditions.
- This Agreement will be void if the Type of Use, Format, Circulation, or Requestor Type was misrepresented during the licensing process.
- This Agreement shall be governed by and construed in accordance with the laws of the State of New York, USA, without regards to such state's conflict of law rules. Any legal action, suit or proceeding arising out of or relating to these Terms and Conditions or the breach thereof shall be instituted in a court of competent jurisdiction in New York County in the State of New York in the United States of America and each party hereby consents and submits to the personal jurisdiction of such court, waives any objection to venue in such court and consents to service of process by registered or certified mail, return receipt requested, at the last known address of such party.

WILEY OPEN ACCESS TERMS AND CONDITIONS

Wiley Publishes Open Access Articles in fully Open Access Journals and in Subscription journals offering Online Open. Although most of the fully Open Access journals publish open access articles under the terms of the Creative Commons Attribution (CC BY) License only, the subscription journals and a few of the Open Access Journals offer a choice of Creative Commons Licenses. The license type is clearly identified on the article.

The Creative Commons Attribution License

The Creative Commons Attribution License (CC-BY) allows users to copy, distribute and transmit an article, adapt the article and make commercial use of the article. The CC-BY license permits commercial and non-

Creative Commons Attribution Non-Commercial License

The Creative Commons Attribution Non-Commercial (CC-BY-NC) License permits use, distribution and reproduction in any medium, provided the original work is properly cited and is not used for commercial purposes.(see below)

Creative Commons Attribution-Non-Commercial-NoDerivs License

The Creative Commons Attribution Non-Commercial-NoDerivs License (CC-BY-NC-ND) permits use, distribution and reproduction in any medium, provided the original work is properly cited, is not used for commercial purposes and no modifications or adaptations are made. (see below)

Use by commercial "for-profit" organizations

Use of Wiley Open Access articles for commercial, promotional, or marketing purposes requires further explicit permission from Wiley and will be subject to a fee.

Further details can be found on Wiley Online Library

<http://olabout.wiley.com/WileyCDA/Section/id-410895.html>

Other Terms and Conditions:

v1.10 Last updated September 2015

Questions? customer@copyright.com or +1-855-239-3415 (toll free in the US) or +1-978-646-2777.

**JOHN WILEY AND SONS LICENSE
TERMS AND CONDITIONS**

Apr 19, 2017

This Agreement between simone Quaranta ("You") and John Wiley and Sons ("John Wiley and Sons") consists of your license details and the terms and conditions provided by John Wiley and Sons and Copyright Clearance Center.

License Number	4092560159958
License date	
Licensed Content Publisher	John Wiley and Sons
Licensed Content Publication	Wiley eBooks
Licensed Content Title	Colloids, Phases, Interfaces
Licensed Content Author	Hans Mollet,Arnold Grubenmann
Licensed Content Date	Dec 14, 2007
Licensed Content Pages	58
Type of use	Dissertation/Thesis
Requestor type	University/Academic
Format	Electronic
Portion	Figure/table
Number of figures/tables	1
Original Wiley figure/table number(s)	FIGURE 1.1
Will you be translating?	No
Title of your thesis / dissertation	Nanostructured Materials for Photovoltaics and Microwave Electronics: methods and applications
Expected completion date	Apr 2017
Expected size (number of pages)	300
Requestor Location	simone Quaranta 85 taylorwood crt OSHAWA, ON L1G7V7 Canada Attn: simone Quaranta
Publisher Tax ID	EU826007151
Billing Type	Invoice
Billing Address	simone Quaranta 85 taylorwood crt OSHAWA, ON L1G7V7 Canada Attn: simone Quaranta

Total 0.00 CAD

Terms and Conditions

TERMS AND CONDITIONS

This copyrighted material is owned by or exclusively licensed to John Wiley & Sons, Inc. or one of its group companies (each a "Wiley Company") or handled on behalf of a society with which a Wiley Company has exclusive publishing rights in relation to a particular work (collectively "WILEY"). By clicking "accept" in connection with completing this licensing transaction, you agree that the following terms and conditions apply to this transaction (along with the billing and payment terms and conditions established by the Copyright Clearance Center Inc., ("CCC's Billing and Payment terms and conditions"), at the time that you opened your RightsLink account (these are available at any time at <http://myaccount.copyright.com>).

Terms and Conditions

- The materials you have requested permission to reproduce or reuse (the "Wiley Materials") are protected by copyright.
- You are hereby granted a personal, non-exclusive, non-sub licensable (on a stand-alone basis), non-transferable, worldwide, limited license to reproduce the Wiley Materials for the purpose specified in the licensing process. This license, **and any CONTENT (PDF or image file) purchased as part of your order**, is for a one-time use only and limited to any maximum distribution number specified in the license. The first instance of republication or reuse granted by this license must be completed within two years of the date of the grant of this license (although copies prepared before the end date may be distributed thereafter). The Wiley Materials shall not be used in any other manner or for any other purpose, beyond what is granted in the license. Permission is granted subject to an appropriate acknowledgement given to the author, title of the material/book/journal and the publisher. You shall also duplicate the copyright notice that appears in the Wiley publication in your use of the Wiley Material. Permission is also granted on the understanding that nowhere in the text is a previously published source acknowledged for all or part of this Wiley Material. Any third party content is expressly excluded from this permission.
- With respect to the Wiley Materials, all rights are reserved. Except as expressly granted by the terms of the license, no part of the Wiley Materials may be copied, modified, adapted (except for minor reformatting required by the new Publication), translated, reproduced, transferred or distributed, in any form or by any means, and no derivative works may be made based on the Wiley Materials without the prior permission of the respective copyright owner. **For STM Signatory Publishers clearing permission under the terms of the STM Permissions Guidelines only, the terms of the license are extended to include subsequent editions and for editions in other languages, provided such editions are for the work as a whole in situ and does not involve the separate exploitation of the permitted figures or extracts**, You may not alter, remove or suppress in any manner any copyright, trademark or other notices displayed by the Wiley Materials. You may not license, rent, sell, loan, lease, pledge, offer as security, transfer or assign the Wiley Materials on a stand-alone basis, or any of the rights granted to you hereunder to any other person.

- The Wiley Materials and all of the intellectual property rights therein shall at all times remain the exclusive property of John Wiley & Sons Inc, the Wiley Companies, or their respective licensors, and your interest therein is only that of having possession of and the right to reproduce the Wiley Materials pursuant to Section 2 herein during the continuance of this Agreement. You agree that you own no right, title or interest in or to the Wiley Materials or any of the intellectual property rights therein. You shall have no rights hereunder other than the license as provided for above in Section 2. No right, license or interest to any trademark, trade name, service mark or other branding ("Marks") of WILEY or its licensors is granted hereunder, and you agree that you shall not assert any such right, license or interest with respect thereto
- NEITHER WILEY NOR ITS LICENSORS MAKES ANY WARRANTY OR REPRESENTATION OF ANY KIND TO YOU OR ANY THIRD PARTY, EXPRESS, IMPLIED OR STATUTORY, WITH RESPECT TO THE MATERIALS OR THE ACCURACY OF ANY INFORMATION CONTAINED IN THE MATERIALS, INCLUDING, WITHOUT LIMITATION, ANY IMPLIED WARRANTY OF MERCHANTABILITY, ACCURACY, SATISFACTORY QUALITY, FITNESS FOR A PARTICULAR PURPOSE, USABILITY, INTEGRATION OR NON-INFRINGEMENT AND ALL SUCH WARRANTIES ARE HEREBY EXCLUDED BY WILEY AND ITS LICENSORS AND WAIVED BY YOU.
- WILEY shall have the right to terminate this Agreement immediately upon breach of this Agreement by you.
- You shall indemnify, defend and hold harmless WILEY, its Licensors and their respective directors, officers, agents and employees, from and against any actual or threatened claims, demands, causes of action or proceedings arising from any breach of this Agreement by you.
- IN NO EVENT SHALL WILEY OR ITS LICENSORS BE LIABLE TO YOU OR ANY OTHER PARTY OR ANY OTHER PERSON OR ENTITY FOR ANY SPECIAL, CONSEQUENTIAL, INCIDENTAL, INDIRECT, EXEMPLARY OR PUNITIVE DAMAGES, HOWEVER CAUSED, ARISING OUT OF OR IN CONNECTION WITH THE DOWNLOADING, PROVISIONING, VIEWING OR USE OF THE MATERIALS REGARDLESS OF THE FORM OF ACTION, WHETHER FOR BREACH OF CONTRACT, BREACH OF WARRANTY, TORT, NEGLIGENCE, INFRINGEMENT OR OTHERWISE (INCLUDING, WITHOUT LIMITATION, DAMAGES BASED ON LOSS OF PROFITS, DATA, FILES, USE, BUSINESS OPPORTUNITY OR CLAIMS OF THIRD PARTIES), AND WHETHER OR NOT THE PARTY HAS BEEN ADVISED OF THE POSSIBILITY OF SUCH DAMAGES. THIS LIMITATION SHALL APPLY NOTWITHSTANDING ANY FAILURE OF ESSENTIAL PURPOSE OF ANY LIMITED REMEDY PROVIDED HEREIN.
- Should any provision of this Agreement be held by a court of competent jurisdiction to be illegal, invalid, or unenforceable, that provision shall be deemed amended to achieve as nearly as possible the same economic effect as the original provision, and the legality, validity and enforceability of the remaining provisions of this Agreement

shall not be affected or impaired thereby.

- The failure of either party to enforce any term or condition of this Agreement shall not constitute a waiver of either party's right to enforce each and every term and condition of this Agreement. No breach under this agreement shall be deemed waived or excused by either party unless such waiver or consent is in writing signed by the party granting such waiver or consent. The waiver by or consent of a party to a breach of any provision of this Agreement shall not operate or be construed as a waiver of or consent to any other or subsequent breach by such other party.
- This Agreement may not be assigned (including by operation of law or otherwise) by you without WILEY's prior written consent.
- Any fee required for this permission shall be non-refundable after thirty (30) days from receipt by the CCC.
- These terms and conditions together with CCC's Billing and Payment terms and conditions (which are incorporated herein) form the entire agreement between you and WILEY concerning this licensing transaction and (in the absence of fraud) supersedes all prior agreements and representations of the parties, oral or written. This Agreement may not be amended except in writing signed by both parties. This Agreement shall be binding upon and inure to the benefit of the parties' successors, legal representatives, and authorized assigns.
- In the event of any conflict between your obligations established by these terms and conditions and those established by CCC's Billing and Payment terms and conditions, these terms and conditions shall prevail.
- WILEY expressly reserves all rights not specifically granted in the combination of (i) the license details provided by you and accepted in the course of this licensing transaction, (ii) these terms and conditions and (iii) CCC's Billing and Payment terms and conditions.
- This Agreement will be void if the Type of Use, Format, Circulation, or Requestor Type was misrepresented during the licensing process.
- This Agreement shall be governed by and construed in accordance with the laws of the State of New York, USA, without regards to such state's conflict of law rules. Any legal action, suit or proceeding arising out of or relating to these Terms and Conditions or the breach thereof shall be instituted in a court of competent jurisdiction in New York County in the State of New York in the United States of America and each party hereby consents and submits to the personal jurisdiction of such court, waives any objection to venue in such court and consents to service of process by registered or certified mail, return receipt requested, at the last known address of such party.

WILEY OPEN ACCESS TERMS AND CONDITIONS

Wiley Publishes Open Access Articles in fully Open Access Journals and in Subscription journals offering Online Open. Although most of the fully Open Access journals publish open access articles under the terms of the Creative Commons Attribution (CC BY) License only, the subscription journals and a few of the Open Access Journals offer a choice of Creative Commons Licenses. The license type is clearly identified on the article.

The Creative Commons Attribution License

The Creative Commons Attribution License (CC-BY) allows users to copy, distribute and transmit an article, adapt the article and make commercial use of the article. The CC-BY license permits commercial and non-

Creative Commons Attribution Non-Commercial License

The Creative Commons Attribution Non-Commercial (CC-BY-NC) License permits use, distribution and reproduction in any medium, provided the original work is properly cited and is not used for commercial purposes.(see below)

Creative Commons Attribution-Non-Commercial-NoDerivs License

The Creative Commons Attribution Non-Commercial-NoDerivs License (CC-BY-NC-ND) permits use, distribution and reproduction in any medium, provided the original work is properly cited, is not used for commercial purposes and no modifications or adaptations are made. (see below)

Use by commercial "for-profit" organizations

Use of Wiley Open Access articles for commercial, promotional, or marketing purposes requires further explicit permission from Wiley and will be subject to a fee.

Further details can be found on Wiley Online Library

<http://olabout.wiley.com/WileyCDA/Section/id-410895.html>

Other Terms and Conditions:

v1.10 Last updated September 2015

Questions? customer care@copyright.com or +1-855-239-3415 (toll free in the US) or +1-978-646-2777.

**ROYAL SOCIETY OF CHEMISTRY LICENSE
TERMS AND CONDITIONS**

Apr 19, 2017

This Agreement between simone Quaranta ("You") and Royal Society of Chemistry ("Royal Society of Chemistry") consists of your license details and the terms and conditions provided by Royal Society of Chemistry and Copyright Clearance Center.

License Number	4092580507833
License date	Apr 19, 2017
Licensed Content Publisher	Royal Society of Chemistry
Licensed Content Publication	Chemical Society Reviews
Licensed Content Title	Ordered mesoporous non-oxide materials
Licensed Content Author	Yifeng Shi,Ying Wan,Dongyuan Zhao
Licensed Content Date	Mar 21, 2011
Licensed Content Volume	40
Licensed Content Issue	7
Type of Use	Thesis/Dissertation
Requestor type	non-commercial (non-profit)
Portion	figures/tables/images
Number of figures/tables /images	1
Format	electronic
Distribution quantity	100
Will you be translating?	no
Order reference number	
Title of the thesis/dissertation	Nanostructured Materials for Photovoltaics and Microwave Electronics: methods and applications
Expected completion date	Apr 2017
Estimated size	300
Requestor Location	simone Quaranta 85 taylorwood crt OSHAWA, ON L1G7V7 Canada Attn: simone Quaranta
Billing Type	Invoice
Billing Address	simone Quaranta 85 taylorwood crt OSHAWA, ON L1G7V7 Canada Attn: simone Quaranta
Total	0.00 CAD

Terms and Conditions

This License Agreement is between {Requestor Name} ("You") and The Royal Society of Chemistry ("RSC") provided by the Copyright Clearance Center ("CCC"). The license consists of your order details, the terms and conditions provided by the Royal Society of Chemistry, and the payment terms and conditions.

RSC / TERMS AND CONDITIONS

INTRODUCTION

The publisher for this copyrighted material is The Royal Society of Chemistry. By clicking "accept" in connection with completing this licensing transaction, you agree that the following terms and conditions apply to this transaction (along with the Billing and Payment terms and conditions established by CCC, at the time that you opened your RightsLink account and that are available at any time at .

LICENSE GRANTED

The RSC hereby grants you a non-exclusive license to use the aforementioned material anywhere in the world subject to the terms and conditions indicated herein. Reproduction of the material is confined to the purpose and/or media for which permission is hereby given.

RESERVATION OF RIGHTS

The RSC reserves all rights not specifically granted in the combination of (i) the license details provided by your and accepted in the course of this licensing transaction; (ii) these terms and conditions; and (iii) CCC's Billing and Payment terms and conditions.

REVOCATION

The RSC reserves the right to revoke this license for any reason, including, but not limited to, advertising and promotional uses of RSC content, third party usage, and incorrect source figure attribution.

THIRD-PARTY MATERIAL DISCLAIMER

If part of the material to be used (for example, a figure) has appeared in the RSC publication with credit to another source, permission must also be sought from that source. If the other source is another RSC publication these details should be included in your RightsLink request. If the other source is a third party, permission must be obtained from the third party. The RSC disclaims any responsibility for the reproduction you make of items owned by a third party.

PAYMENT OF FEE

If the permission fee for the requested material is waived in this instance, please be advised that any future requests for the reproduction of RSC materials may attract a fee.

ACKNOWLEDGEMENT

The reproduction of the licensed material must be accompanied by the following acknowledgement:

Reproduced ("Adapted" or "in part") from {Reference Citation} (or Ref XX) with permission of The Royal Society of Chemistry.

If the licensed material is being reproduced from New Journal of Chemistry (NJC), Photochemical & Photobiological Sciences (PPS) or Physical Chemistry Chemical Physics (PCCP) you must include one of the following acknowledgements:

For figures originally published in NJC:

Reproduced ("Adapted" or "in part") from {Reference Citation} (or Ref XX) with permission of The Royal Society of Chemistry (RSC) on behalf of the European Society for Photobiology, the European Photochemistry Association and the RSC.

For figures originally published in PPS:

Reproduced ("Adapted" or "in part") from {Reference Citation} (or Ref XX) with permission of The Royal Society of Chemistry (RSC) on behalf of the Centre National de la

Recherche Scientifique (CNRS) and the RSC.

For figures originally published in PCCP:

Reproduced ("Adapted" or "in part") from {Reference Citation} (or Ref XX) with permission of the PCCP Owner Societies.

HYPERTEXT LINKS

With any material which is being reproduced in electronic form, you must include a hypertext link to the original RSC article on the RSC's website. The recommended form for the hyperlink is <http://dx.doi.org/10.1039/DOI> suffix, for example in the link <http://dx.doi.org/10.1039/b110420a> the DOI suffix is 'b110420a'. To find the relevant DOI suffix for the RSC article in question, go to the Journals section of the website and locate the article in the list of papers for the volume and issue of your specific journal. You will find the DOI suffix quoted there.

LICENSE CONTINGENT ON PAYMENT

While you may exercise the rights licensed immediately upon issuance of the license at the end of the licensing process for the transaction, provided that you have disclosed complete and accurate details of your proposed use, no license is finally effective unless and until full payment is received from you (by CCC) as provided in CCC's Billing and Payment terms and conditions. If full payment is not received on a timely basis, then any license preliminarily granted shall be deemed automatically revoked and shall be void as if never granted. Further, in the event that you breach any of these terms and conditions or any of CCC's Billing and Payment terms and conditions, the license is automatically revoked and shall be void as if never granted. Use of materials as described in a revoked license, as well as any use of the materials beyond the scope of an unrevoked license, may constitute copyright infringement and the RSC reserves the right to take any and all action to protect its copyright in the materials.

WARRANTIES

The RSC makes no representations or warranties with respect to the licensed material.

INDEMNITY

You hereby indemnify and agree to hold harmless the RSC and the CCC, and their respective officers, directors, trustees, employees and agents, from and against any and all claims arising out of your use of the licensed material other than as specifically authorized pursuant to this licence.

NO TRANSFER OF LICENSE

This license is personal to you or your publisher and may not be sublicensed, assigned, or transferred by you to any other person without the RSC's written permission.

NO AMENDMENT EXCEPT IN WRITING

This license may not be amended except in a writing signed by both parties (or, in the case of "Other Conditions, v1.2", by CCC on the RSC's behalf).

OBJECTION TO CONTRARY TERMS

You hereby acknowledge and agree that these terms and conditions, together with CCC's Billing and Payment terms and conditions (which are incorporated herein), comprise the entire agreement between you and the RSC (and CCC) concerning this licensing transaction, to the exclusion of all other terms and conditions, written or verbal, express or implied (including any terms contained in any purchase order, acknowledgment, check endorsement or other writing prepared by you). In the event of any conflict between your obligations established by these terms and conditions and those established by CCC's Billing and Payment terms and conditions, these terms and conditions shall control.

JURISDICTION

This license transaction shall be governed by and construed in accordance with the laws of

the District of Columbia. You hereby agree to submit to the jurisdiction of the courts located in the District of Columbia for purposes of resolving any disputes that may arise in connection with this licensing transaction.

LIMITED LICENSE

The following terms and conditions apply to specific license types:

Translation

This permission is granted for non-exclusive world English rights only unless your license was granted for translation rights. If you licensed translation rights you may only translate this content into the languages you requested. A professional translator must perform all translations and reproduce the content word for word preserving the integrity of the article.

Intranet

If the licensed material is being posted on an Intranet, the Intranet is to be password-protected and made available only to bona fide students or employees only. All content posted to the Intranet must maintain the copyright information line on the bottom of each image. You must also fully reference the material and include a hypertext link as specified above.

Copies of Whole Articles

All copies of whole articles must maintain, if available, the copyright information line on the bottom of each page.

Other Conditions

v1.2

Gratis licenses (referencing \$0 in the Total field) are free. Please retain this printable license for your reference. No payment is required.

If you would like to pay for this license now, please remit this license along with your payment made payable to "COPYRIGHT CLEARANCE CENTER" otherwise you will be invoiced within 48 hours of the license date. Payment should be in the form of a check or money order referencing your account number and this invoice number {Invoice Number}.

Once you receive your invoice for this order, you may pay your invoice by credit card.

Please follow instructions provided at that time.

Make Payment To:

Copyright Clearance Center

29118 Network Place

Chicago, IL 60673-1291

For suggestions or comments regarding this order, contact Rightslink Customer Support: customercare@copyright.com or +1-855-239-3415 (toll free in the US) or +1-978-646-2777.

Questions? customercare@copyright.com or +1-855-239-3415 (toll free in the US) or +1-978-646-2777.



ACS Publications
Most Trusted. Most Cited. Most Read.

Title: Controlled Formation of Highly Organized Mesoporous Titania Thin Films: From Mesostuctured Hybrids to Mesoporous Nanoanatase TiO₂

Author: Eduardo L. Crepaldi, Galo J. de A. A. Soler-Illia, David Grosso, et al

Publication: Journal of the American Chemical Society

Publisher: American Chemical Society

Date: Aug 1, 2003

Copyright © 2003, American Chemical Society

Logged in as:
simone Quaranta
Account #:
3001141175

[LOGOUT](#)

PERMISSION/LICENSE IS GRANTED FOR YOUR ORDER AT NO CHARGE

This type of permission/license, instead of the standard Terms & Conditions, is sent to you because no fee is being charged for your order. Please note the following:

- Permission is granted for your request in both print and electronic formats, and translations.
- If figures and/or tables were requested, they may be adapted or used in part.
- Please print this page for your records and send a copy of it to your publisher/graduate school.
- Appropriate credit for the requested material should be given as follows: "Reprinted (adapted) with permission from (COMPLETE REFERENCE CITATION). Copyright (YEAR) American Chemical Society." Insert appropriate information in place of the capitalized words.
- One-time permission is granted only for the use specified in your request. No additional uses are granted (such as derivative works or other editions). For any other uses, please submit a new request.

If credit is given to another source for the material you requested, permission must be obtained from that source.

[BACK](#)

[CLOSE WINDOW](#)



Issue 22, 2015

[Previous](#)

[Next](#)



From the journal:

Chemical Society Reviews

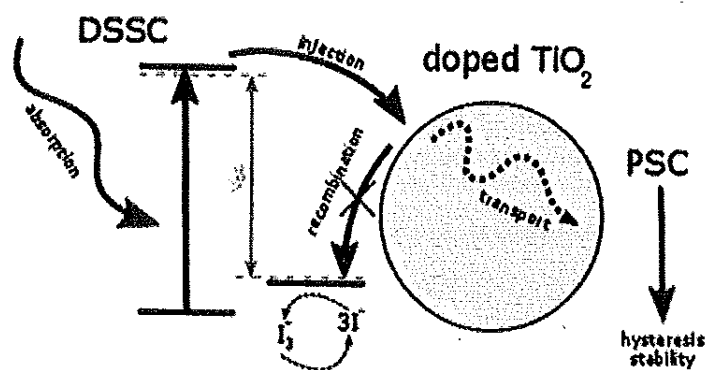
Doping of TiO₂ for sensitized solar cells

[Bart Roose](#),^a [Sandeep Pathak](#)^{*b} and [Ulrich Steiner](#)^{*a}

Author affiliations

Abstract

This review gives a detailed summary and evaluation of the use of TiO₂ doping to improve the performance of dye sensitized solar cells. Doping has a major effect on the band structure and trap states of TiO₂, which in turn affect important properties such as the conduction band energy, charge transport, recombination and collection. The defect states of TiO₂ are highly dependent on the synthesis method and thus the effect of doping may vary for different synthesis techniques, making it difficult to compare the suitability of different dopants. High-throughput methods may be employed to achieve a rough prediction on the suitability of dopants for a specific synthesis method. It was however found that nearly every employed dopant can be used to increase device performance, indicating that the improvement is not so much caused by the dopant itself, as by the defects it eliminates from TiO₂. Furthermore, with the field shifting from dye sensitized solar cells to perovskite solar cells, the role doping can play to further advance this emerging field is also discussed.



About

Cited by

Related

×

Doping of TiO_2 for sensitized solar cells

B. Roose, S. Pathak and U. Steiner, *Chem. Soc. Rev.*, 2015, 44, 8326

DOI: 10.1039/C5CS00352K

This article is licensed under a [Creative Commons Attribution 3.0 Unported Licence](#). Material from this article can be used in other publications provided that the correct acknowledgement is given with the reproduced material.

Reproduced material should be attributed as follows:

- For reproduction of material from NJC:
[Original citation] - Published by The Royal Society of Chemistry (RSC) on behalf of the Centre National de la Recherche Scientifique (CNRS) and the RSC.
- For reproduction of material from PCCP:
[Original citation] - Published by the PCCP Owner Societies.
- For reproduction of material from PPS:
[Original citation] - Published by The Royal Society of Chemistry (RSC) on behalf of the European Society for Photobiology, the European Photochemistry Association, and RSC.
- For reproduction of material from all other RSC journals:
[Original citation] - Published by The Royal Society of Chemistry.

Search articles by author

Bibliography

- [1] H. Tsubomura, M. Matsumura, Y. Nomura, and T. Amamiya. Dye sensitised zinc oxide: aqueous electrolyte: platinum photocell. *Nature*, 261:402–403, 1976.
- [2] M Graetzel and B. O'Regan. A low-cost, high-efficiency solar cell based on dye-sensitized colloidal TiO₂ films. *Nature*, 753:737–740, 1991.
- [3] M. E. Ragoussi and T. Torres. New generation solar cells: concepts, trends and perspectives. *Chem. Commun.*, 51(19):3957–3972, 2015.
- [4] De Silvestro, H. What physical factors affect current-voltage characteristics of dye solar cells?, 2008.
- [5] Sorbello, L. 3rd generation solar technology, 2008.
- [6] Dyesol Corporation. 2012 investor update, 20012.
- [7] B. Roose, S. Pathak, and U. Steiner. Doping of tio2 for sensitized solar cells. *Chem. Soc. Rev.*, 44:8326–8349, 2006.
- [8] C. Cavallo, V. Mantella, A. Dulong, and S. Quaranta. Investigation on zr-, hf-, and ta-doped submicrometric beads for dssc photoanodes. *Appl. Phys. A*, 123(3):1–8, 2017.
- [9] H. S. Kim, C. R. Lee, J. H Im, K. B. Lee, A. Moehl, T. Marchioro, S. J. Moon, R. Humphry-Baker, J. Yum, J.E. H. Moser, M. Graetzel, and N. G. Park. Lead iodide perovskite sensitized all-solid-state submicron thin film mesoscopic solar cell with efficiency exceeding 9. *Sci. Rep.*, (3):4088–4093, 2012.
- [10] N. G. Park. Perovskite solar cells: an emerging photovoltaic technology. *Materials Today*, 18(2):65–71, 2015.

- [11] F. Boccarosso. Debundling and selective enrichment of swnts for applications in dye-sensitized solar cells. *Int. Journal of Photoenergy*, 2010(727134):1–14, 2010.
- [12] M. Faisal, M. Ismail, F. A. Harraz, H. Bouzid, A. Al-Sayari, and A. Al-Hajry. Highly selective colorimetric detection and preconcentration of bi(iii) ions by dithizone complexes anchored onto mesoporous tio₂. *Nanoscale Res. Lett.*, 9(62):1–7, 2014.
- [13] W. E. Duckworth. Sensor materials. *Materials and Design*, 9(2):72–77, 1988.
- [14] D. D. Liana, B. Raguse, J. J. Gooding, and E. Chow. Recent advances in paper-based sensors. *Sensors*, 12(19):11505–11526, 2012.
- [15] M. L. Moss and M. G. Mellon. Colorimetric determination of iron with 2,2' bipyridyl an 2,2',2 terpyridyl. *Indust.l and Chem. Engin.*, 14(11):612–613, 1942.
- [16] Y. Hong, S. Chen, J. W. Y Liu J. Leung, C. W. T. Lam, N. W. Tseng, R. T. K. Kwok, Y. Yu, . Wang, and Z. Tang. Fluorogenic zn(ii) and chromogenic fe(ii) sensors based on terpyridine-substituted tetraphenylethenes with aggregation-induced emission characteristics. *ACS Appl. Mater. Interfaces*, 3(9):3411–3418, 2013.
- [17] B. Eftekhari-Sis and S. Mirdoraghi. Graphene oxide-terpyridine conjugate: A highly selective colorimetric and sensitive fluorescence nano-chemosensor for fe 2+ in aqueous media. *Nanochem. Res.*, 1(2):214–221, 2016.
- [18] B. Eftekhari-Sis and S. Mirdoraghi. Detection of cobalt(ii) and copper(ii) selectively using versatile fluorochemosensors in parts per trillion level in aqueous solution. *The Pharmaceutical and Chemical Journal*, 3(1):149–153, 2016.
- [19] M. Trigo-López, A. Munoz, S. Ibeas, F. Serna, F. C. Garcia, and J. M. Garcia. Colorimetric detection and determination of fe(iii), co(ii), cu(ii) and sn(ii) in aqueous media by acrylic polymers with pendant terpyridine motifs. *Sensors and Actuators B*, 226:118–126, 2016.
- [20] A. Wild, A. Winter, F. Schlutter, and U.S. U.S. Schubert. Advances in the field of π -conjugated 2,2':6',2'-terpyridines. *Chem. Soc. Rev.*, 40(3):1459–1511, 2011.

- [21] N. O. Laschuk, D. Ebralidze, I. I. Spasyuk, , and V. O. Zenkina. Multi-readout logic gate for the selective detection of metal ions at the parts per billion level. *Eur. J. Inorg. Chem.*, pages 3531–3535, 2016.
- [22] C. D. Wagner. Sensitivity factors for xps analysis of surface atoms. *Journal of Electron Spectroscopy and Related Phenomena*, 32(2):99–102, 1983.
- [23] C. G. Granqvist. Electrochromics for smart windows: Oxide-based thin films and devices. *Chem. Mater.*, 27(4):1420–1425, 2015.
- [24] H. C. Moon, T. P. Lodge, and C. D. Frisbie. Polymer- $\dot{\cup}$ nanoparticle electrochromic materials that selectively modulate visible and near-infrared light. *Chem. Mater.*, 28(5):1420–1425, 2016.
- [25] C. J. Barile, D. J. Slotcavage, and M. D McGehee. Polymer- $\dot{\cup}$ nanoparticle electrochromic materials that selectively modulate visible and near-infrared light. *Chem. Mater.*, 28(5):1420–1425, 2016.
- [26] A. M. W. Cargill Thompson. The synthesis of 2,2':6',2'-terpyridine ligands $\dot{\cup}$ versatile building blocks for supramolecular chemistry. *Chem. Mater.*, 164:1–54, 1997.
- [27] S. Shankar, M. Lahav, and M. E. van der Boom. Coordination-based molecular assemblies as electrochromic materials: Ultra-high switching stability and coloration efficiencies. *J. Am. Chem. Soc.*, 131(10):3468–3469, 2009.
- [28] J. Lombard, D. A. Jose, C. E. Castillo, R. Pansu, J. Chauvin, A. Deronzier, and M. N Collomb. Alternated bimetallic [ru-m] (m = fe²⁺, zn²⁺) coordination polymers based on [ru(bpy)(3)](2+) units connected to bis-terpyridine ligands: synthesis, electrochemistry and photophysics in solution or in thin film on electrodes. *J. Mater. Chem. C*, 2(46):4825–4835, 2014.
- [29] Y. Alesanco, J. Palenzuela, R. Tena-Zaera, G. Cabanero, H. Grande, B. Herbig, A. Schmitt, U. Schott, M. and Posset, A. Guerfi, M. Dontigny, K. Zaghbi, and A. Vinales. Plastic electrochromic devices based on viologen-modified tio₂ films prepared at low temperature. *Sol. Energ. Mat. Sol. Cells*, 157:624–635, 2016.
- [30] A. Vena, E. Perret, S. Tedjini, D. Kaddour, A. Alexis, and T. Barro. A compact chipless rfid tag with environment sensing capability. *IEEE MTT-S Int. Microwave Symposium Digest*, 287(5453):1–3, 2000.

- [31] A. Vena, L. Sydanheimo, M. M. Tentzeris, and L. Ukkonen. A novel inkjet printed carbon nanotube-based chipless rfid sensor for gas detection. *2013 European Microwave Conference*, pages 9–12, 2013.
- [32] E. Amin, S. Bhuiyan, C. Karmakar, and B. Winther-Jensen. Development of a low cost printable chipless rfid humidity sensor. *IEEE SENS. J.*, 14(1):140–149, 2014.
- [33] RFID Chipless sensors. *Karmakar, N. C. and Amin, E. A. and Saha, J. K.* Wiley, 1st edition, 2016.
- [34] H. S. P. Wong and D. Akinwande. *Carbon Nanotube and Graphene Device Physics*. Cambridge, 1st edition, 2009.
- [35] A. D. McNaught and A. Wilkinson. *Compendium of Chemical Terminology*. IUPAC, 2nd edition, 1997.
- [36] R. Vajtai. *Springer Handbook of Nanomaterials*. Springer, 1st edition, 2013.
- [37] Luo D. Schricker S.R. Sigmund W. Zauscher S. Bhushan, B. *Handbook of Nanomaterials Properties*. Springer, 1st edition, 2014.
- [38] B. Bhushan. *Springer Handbook of Nanotechnology*. Springer, 4th edition, 2014.
- [39] Feynman. Lecture notes on physics, December 1959.
- [40] X. Fang and L. Wu. *Handbook of Innovative Nanomaterials: From Syntheses to Applications*. CRC Press, 1st edition, 2012.
- [41] G. E. Moore. Cramming components onto integrated circuits. *Proceedings of IEEE*, 86(1):82–85, 1998.
- [42] B. Streetman and B. Sbanerjee. *Solid State Electronic Devices*. Prentice Hall, 6th edition, 2005.
- [43] Alberto Salleo. *Flexible Electronics*. Materials and Applications. Springer, 2009.
- [44] K. S. Birdi. *Handbook of Surface and Colloid Chemistry*. CRC Press, 4th edition, 2012.
- [45] K. Seshan. *Handbook of Thin film deposition*. Elsevier, 3rd edition, 2012.

- [46] J. Lyklema. *Fundamentals of Interface and Colloid Science: Particulate Colloids. Volume IV*. Elseviers, 1st edition, 2005.
- [47] H. Mollet, A. Grubenmann, and V. Payne. *Formulation Technology: Emulsions, Suspensions, Solid Forms*. Wiley, 2008.
- [48] J. Lyklema. *Fundamentals of Interface and Colloid Science: Liquid-Fluid Interfaces*. Elseviers, 1st edition, 2000.
- [49] J. Chen, B. Li, J. Zheng, J. Zhao, and Z. Zhu. The history of colloid science: In memory of wolfgang ostwald. *J. Chem. Educ.*, 32(1):2–9, 1955.
- [50] T. Crossgrove. *Colloid Science: Principles, Methods and Applications*. Wiley, 2nd edition, 2010.
- [51] T. Ngai and S. A. F. Bon. *Particle-Stabilized Emulsions and Colloids*. RCS Soft Matter. RSC Publishing, 1st edition, 2010.
- [52] B. Viswanathan. *Structure and Properties of Solid State Materials*. Alpha Science, 1st edition, 2006.
- [53] D. Hull and D. J. Bacon. *Introduction to Dislocations*. Elsevier, 5th edition, 2011.
- [54] U. Schubert and N. Husing. *Synthesis of Inorganic Materials*. Wiley, 3rd edition, 2012.
- [55] D. Levy and M. Zayat. *The Sol-Gel Handbook: Synthesis, Characterization and Applications*. Wiley-VCH, 3rd edition, 2015.
- [56] K. Byrappa and M. Yoshimura. *Handbook of Hydrothermal Technology A Technology for Crystal Growth and Materials Processing*. Elsevier, 2nd edition, 2011.
- [57] A. E. Hargreaves. *Chemical Formulation: An Overview of Surfactant Based Chemical Preparations Used in Everyday Life*. RSC Papaerbacks, 1st edition, 2003.
- [58] H. Mollet and Grubenmann. *Formulation techology: emulsions, suspensions, solid forms*. Wiley-VCH, 1st edition, 2004.

- [59] T. Kirchartz, J. Bisquert, I. Mora-Sero, and G. Garcia-Belmonte. Classification of solar cells according to mechanisms of charge separation and charge collection. *Phys. Chem. Chem. Phys.*, (17):4007–4014, 2015.
- [60] A. Hagfeldt, J. U. Bjorksten, and S.E. Lindquist. Photoelectrochemical studies of colloidal tio2 films: the charge separation studied by means of action spectra in the uv region. *Sol. Energy Mater. Sol. Cells*, (52):293–304, 1992.
- [61] A. Hagfeldt, J. U. Bjorksten, and S.E. Lindquist. Nature of photovoltaic action in dye sensitized solar cells. *J. Phys. Chem. B*, 9(104):2053–2059, 2000.
- [62] M. A. Sanchez-Garcia, X. Bokhimi, A. Maldonado-Alvarez, and A. E. Jimenez-Gonzalez. Efficient screen-printed n-type solar cells using a spin-on source and thermal oxide/silicon nitride passivation. *IEEE Journal of Photovoltaics*, 1(2):146–152, 2011.
- [63] H. Tang, K. Prasad, R. Sanjinbs, P.E. Schmid, and F. Ley. Electrical and optical properties of tio2 anatase thin films. *J. Appl. Phys.*, 75(4):2042–2047, 1993.
- [64] M. A. Sanchez-Garcia, X. Bokhimi, A. Maldonado-Alvarez, and A. E. Jimenez-Gonzalez. Effect of anatase synthesis on the performance of dye-sensitized solar cells. *Nanoscale Research Letters*, 306(10):1–13, 2015.
- [65] D. Liu, M. Mahesh, K. Gangishetty, and L T. Kelly. Effect of ch3nh3pb3 thickness on device efficiency in planar heterojunction perovskite solar cells. *J. Mater. Chem. A*, (2):19873–19885, 2014.
- [66] J. H. Im, C. R. Lee, J. W. Lee, S. W. Park, and N. G. Park. 6.5 efficient perovskite quantum-dot-sensitized solar cell. *Nanoscale*, (3):4088–4093, 2011.
- [67] M. M. Lee, J. Teuscher, T. Miyasaka, and T. N. Murakami. Efficient hybrid solar cells based on meso-superstructured organometal halide perovskites. *Science*, 338:647–651, 2012.
- [68] Y. Chen, J. Peng, D. Su, X. Chen, and Z. Liang. Efficient and balanced charge transport revealed in planar perovskite solar cells. *Appl. Mater. Interfaces*, (7):4471–4475, 2015.

- [69] M. M. Lee, J. Teuscher, T. Miyasaka, and T. N. Murakami. Efficient planar heterojunction perovskite solar cells by vapour deposition. *Nature*, 338:395–399, 2013.
- [70] B Brunetti, C. Cavallo, A Ciccio, G. Gigli, and A. Latini. On the thermal and thermodynamic (in)stability of methylammonium lead halide perovskite. *Scien, Rep.*, (6):31896:1–10, 2016.
- [71] B. Chen, M. Yang, M. Priya, and K. Zhu. Origin of $J-V$ hysteresis in perovskite solar cells. *J. Phys. Chem. Lett.*, 5(7):905–917, 2016.
- [72] P. Peumans and S. R. Forrest. Separation of geminate charge-pairs at donor-acceptor interfaces in disordered solids. *Chem. Phys. Lett.*, 398(27):27–31, 2004.
- [73] A.C. Morteani, P. Sreearunothai, L. M. Herz, R. H Friend, and C. Silva. Exciton regeneration at polymeric semiconductor heterojunctions. *Phys. Rev. Lett.*, 92(24):247402–24706, 2004.
- [74] M. Theander, A. Yartsev, D. Zigmantas, W. Sundstrom, . Mammo, R. M. Andersson, and O. Inganas. Photoluminescence quenching at a polythiophene/c60 heterojunction. *Phys. Rev. B.*, 61:247402–247, 2000.
- [75] L. A. A. Patterson, L. S. Roman, and O. Inganas. Photoluminescence quenching at a polythiophene/c60 heterojunction. *J. Appl. Phys.*, 86:487–496, 1999.
- [76] K. M. Coakley and M. D. McGehee. Conjugated polymer photovoltaic cells. *Chem. Mater*, 16:4533–496, 2004.
- [77] W. Wu, J. Wang, Z. Zheng, Y. Hue, J. Jin, Q. Zhang, and J. Hua. A strategy to design novel structure photochromic sensitizers for dye-sensitized solar cells. *Scien, Rep.*, (5):8592:1–4, 2015.
- [78] J. Albero, P. Atienzar, and H. Corma A., garcia. Efficiency records in mesoscopic dye-sensitized solar cells. *The Chemical Record*, 15(4):2–9, 2015.
- [79] S. Mathew, A. Yella, P. Gao, B. F. A. Baker, R. P. and. Curchod, N. Ashari-Astani, I. Tavernelli, U. Rothlisberger, K. Nazeeruddin, and M. Gratzel. Dye-sensitized solar cells with 13 efficiency achieved through the molecular engineering of porphyrin sensitizers. *Nature Chemistry*, 6:242–247, 2014.

- [80] T. Higashino and H. Imahori. Porphyrins as excellent dyes for dye-sensitized solar cells: recent developments and insights. *Dalton Transaction*, 44:448–463, 2015.
- [81] M. Nisha, S. Anusha, A. Antony, R. Manoj, and M. K. Jayaraj. Effect of substrate temperature on the growth of its thin films. *Appl. Sur. Sci.*, 19(5):1430–1435, 2005.
- [82] S. Ruhle and D. Thomas. Investigation of the electric field in tio₂/fto junctions used in dye-sensitized solar cells by photocurrent transients. *J. Phys. Chem. B*, 19:9522–9556, 2005.
- [83] Y. Y Chiba, A. Islam, Y. Yuki Watanabe, R. Komiya, N. Koide, and L. Han. Dye-sensitized solar cells with conversion efficiency of 11.1. *J. J. of App. Phys.*, 45:24–28, 2006.
- [84]
- [85] Md. K. Nazeeruddin, R. Splivallo, P. Liska, P. Comte, and M. Gratzel. A swift dye uptake procedure for dye sensitized solar cells. *Chem. Comm.*, pages 1456–1457, 2003.
- [86] A. Latini, F. K. Aldibaja, C. Cavallo, and D. Gozzi. Benzonitrile based electrolytes for best operation of dye sensitized solar cells. *J. Power Sources*, 19:308–316, 2014.
- [87] K. Woronowicz, S. Ahamed, and A. Biridar. Thermal activation of mass transport and charge transfer at pt in the i₃⁻/i⁻ electrolyte of a dye-sensitized solar cell. *Phys. Chem. Chem. Phys.*, 12:10796–10782, 2010.
- [88] D. Wei. Dye sensitized solar cells. *Int. J. Mol. Sci.*, 11(3):1103–1113, 2010.
- [89] K. Woronowicz, S. Ahamed, and A. Biridar. Near-ir absorbing solar cell sensitized with bacterial photosynthetic membranes. *Photochem. and Photobio.*, 88(6):1467–1472, 2012.
- [90] S. Ferrere. New photosensitizers based upon [fe(l)] and [fe(l)₃]₂(cn) (l = substituted 2,2'-bipyridine): Yields for the photosensitization of tio and effects on the band selectivity. *Chem. Mater.*, 12:1083–1089, 2000.
- [91] S. Ferrere. Osmium polypyridyl complexes and their applications to dye-sensitized solar cells. *Chem. Rec.*, 7(2):457–476, 2015.

- [92] S. Ferrere. Iron sensitizer converts light to electrons with 92 yield. *Nat. Chem.*, 7:883–889, 2015.
- [93] T. Renouard, A. Md. Fallahpour, Nazeeruddin, R Humphry-Baker, K. I. Gorelsky, A. B. P. Lever, and M. Graetzel. Novel ruthenium sensitizers containing functionalized hybrid tetradentate ligands: Synthesis, characterization, and indo/s analysis. *Inorg. Chem.*, 41(2):367–378, 2002.
- [94] S. A. Haque, E. Palomares, B. M. Cho, N. . Green, A. L. M. Hirata, N. D. Klug, and J. R. Durrant. Charge separation versus recombination in dye-sensitized nanocrystalline solar cells: the minimization of kinetic redundancy. *J. Am. Chem. Soc.*, 127(10):3456–3462, 2005.
- [95] S. Cazzanti, S. Caramori, R. Argazzi, M. C. Elliott, and C. A. Bignozzi. Efficient non-corrosive electron-transfer mediator mixtures for dye-sensitized solar cells. *J. Am. Chem. Soc.*, 128(31):9996–9997, 2006.
- [96] J. N. Clifford, E. Palomares, Md. K. . Nazeeruddin, M. Grätzel, and J. R. R. Durrant. Dye dependent regeneration dynamics in dye sensitized nanocrystalline solar cells: Evidence for the formation of a ruthenium bipyridyl cation/iodide intermediate. *J. Phys. Chem. C*, 111(17):6561–6567, 2016.
- [97] N. Robertson. Optimizing dyes for dye-sensitized solar cells. *Angew. Chem. Int. Ed.*, 45(15):2338–2445, 2006.
- [98] T. Kaewpuang, N. Prachumrak, S. Namuangruk, S. Jungsuttiwong, T. Sudyoasuk, P. Pattanasattayavong, and V. Promarak. Effects of acetyl acetone-typed co-adsorbents on the interface charge recombination in dye-sensitized solar cell photoanodes. *Electrochimica Acta*, 154:190–196.
- [99] M. Wang, H. Rensmo, S. Plogmaker, S. M. Zakeeruddin, R. Humphry-Baker, M. Graetzel, and P. Pechy. Molecular-scale interface engineering of nanocrystalline titania by co-adsorbents for solar energy conversion. *ChemSusChem*, (154):190–196, 2016.
- [100] A. Mishra, K. R. Fischer, and P. Bauerle. Metal-free organic dyes for dye-sensitized solar cells: From structure: Property relationships to design rules. *Angew. Chem. Int. Ed.*, 48:2474–2499, 2009.
- [101] T. Kaewpuang, N. Prachumrak, S. Namuangruk, S. Jungsuttiwong, T. Sudyoasuk, P. Pattanasattayavong, and V. Promarak. Metal-free organic

- dyes for tio₂ and zno dye-sensitized solar cells. *Sci. Rep.*, (6):18756–18768, 2016.
- [102] W. E. Hung, W. S. Kao, Y. Y. Liao, J. T. Lin, T. H. Lee, T. H. Wei, Y. C. Ting, J. S. Ni, and Y. S. Yen. Eugenic metal-free sensitizers with double anchors for high performance dye-sensitized solar cells. *Chem. Comm.*, 51:2152–2155, 2015.
- [103] J. Yang, P. Comte, P. Ganesan, P. Ganesan, K. Pei, Ms. K. Zakeeruddin, J. Teuscher, T. W. Holcombe, H. Tian, T. Moehl, Y. J. Kim, M. K. Nazeeruddin, and Michael Gratzel. Influence of the donor size in d-p-a organic dyes for dyesensitized solar cells. *J. Am. Chem. Soc.*, 136:5722.
- [104] T. Kaewpuang, N. Prachumrak, S. Namuangruk, S. Jungsuttiwong, T. Sudyoasuk, P. Pattanasattayavong, and V. Promarak. (d π)₂d π a-type organic dyes for efficient dye-sensitized solar cells. *Eur. J. Org. Chem.*, (14):2528–2538, 2016.
- [105] J. H. Yum, E. Baranoff, F. Kessler, T. Moehl, S. Ahmad, M. Marchioro, H. Ghadiri, J. E. Moser, C. Yi, M. D. Nazeeruddin, T. Bessho, and M. Graetzel. A cobalt complex redox shuttle for dye-sensitized solar cells with high open-circuit potentials. *Nat. Comm.*, 3(361):1–8, 2012.
- [106] J. Cong, X. Yang, L. Kloob, and L. Sun. Iodine/iodide-free redox shuttles for liquid electrolyte-based dye-sensitized solar cells. *Energy Environ. Sci.*, 5:1–8, 2012.
- [107] J. Cong, X. Yang, L. Kloob, and L. Sun. Cobalt-based electrolytes for dye-sensitized solar cells: Recent advances towards stable devices. *Energies*, 9(384):1–22, 2014.
- [108] J. Cong, X. Yang, L. Kloob, and L. Sun. Synthesis and photovoltaic properties of powerful electron-donating indeno[1, 2-b]thiophene-based green d-a-p-a sensitizers for dyesensitized solar cells. *ACS Sustainable Chem. Eng*, 4:318–325, 2016.
- [109] S. R. R. Bobe, A. K. Gupta, A. Rananaware, A. Bilic, W. Xiang, J. Li, and S. V. Bhosale. Insertion of a naphthalenediimide unit in a metal-free donor-acceptor organic sensitizer for efficiency enhancement of a dye-sensitized solar cell. *ACS Sustainable Chem. Eng*, 4:318–325, 2016.

- [110] S. Kuwahara, S. Taya, N. Osada, Q. Shen, T. Toyoda, and K. Katayama. Effect of electrolyte constituents on the motion of ionic species and recombination kinetics in dye-sensitized solar cells. *Phys. Chem. Chem. Phys.*, 15:542–549, 2014.
- [111] B. C. Oregan and J. R. Durrant. Kinetic and energetic paradigms for dyesensitized solar cells: Moving from the ideal to the real. *Acc. Chem. Res.*, 42(11):1799–1808, 2009.
- [112] G. Boschloo and A. Hagfeldt. Characteristics of the iodide/triiodide redox mediator in dye-sensitized solar cells. *J. Phys. Chem. B*, 104:1791–1795, 2009.
- [113] R. Bertoluzzi and S. Ma. On the methods of calculation of the charge collection efficiency of dye sensitized solar cells. *Phys. Chem. Chem. Phys.*, 15(11):4283–4285, 2013.
- [114] A. Lisorti, B. C. Oregan, and J. R. Durrant. Electron transfer dynamics in dye-sensitized solar cells. *Chem. Mat.*, 23:3381–3399, 2011.
- [115] A. Kay and M. Graetzel. Dye-sensitized core-shell nanocrystals: Improved efficiency of mesoporous tin oxide electrodes coated with a thin layer of an insulating oxide. *Chem. Mat.*, 14(7):2930–2935, 2002.
- [116] Q. Zhang, C. S. Dandeneau, X. Y. Zhou, and G. Z. Cao. ZnO nanostructures for dye-sensitized solar cells. *Adv. Chem. Mat*, 21(41):4087–4108, 2009.
- [117] Y. Diamant, S. Chappel, S. G. Chen, O. Melamed, and A. Zaban. Core-shell nanoporous electrode for dye sensitized solar cells: the effect of shell characteristics on the electronic properties of the electrode. *Coord. Chem.*, 248(13-14):1271–1276, 2009.
- [118] R. Katoh, A. Furube, H. Barzykin, A. V. Arakawa, and M. Tachiya. Kinetics and mechanism of electron injection and charge recombination in dye-sensitized nanocrystalline semiconductors. *Coord. Chem. Rev.*, 248(13-14):1195–1212, 2004.
- [119] J. E. Moser and M. Graetzel. Observation of temperature independent heterogeneous electron transfer reactions in the inverted marcus region. *J. Phys. Chem. B*, 173(2-3):493–500, 1993.

- [120] S. Pelet, J.-E. Moser, and M. Graetzel. Effect of adsorbed cations and iodide on the interception of back electron transfer in the dye sensitization of nanocrystalline TiO_2 . *J. Phys. Chem. B*, 104:1791–1795, 2000.
- [121] B. C. Oregan and J. R. Durrant. Role of electrolytes on charge recombination in dye-sensitized TiO_2 solar cell (1): The case of solar cells using the I^-/I_3^- redox couple. *J. Phys. Chem. B*, 109(11):3480–3489, 2005.
- [122] Md. K. Nazeeruddin, R. Humphry-Baker, P. Liska, and M. Graetzel. Investigation of sensitizer adsorption and the influence of protons on current and voltage of a dye-sensitized nanocrystalline TiO_2 solar cell. *J. Phys. Chem. B*, 107(34):8981–8987, 2002.
- [123] A. N. M. Green, E. Palomares, J. M. Haque, S. A. and Kroon, and J. Durrant. Charge transport versus recombination in dye-sensitized solar cells employing nanocrystalline TiO_2 and SnO_2 films. *J. Phys. Chem. B*, 109(25):12525–12533, 2005.
- [124] I. Montanari, J. Nelson, and J. R. Durrant. Iodide electron transfer kinetics in dye-sensitized nanocrystalline TiO_2 films. *J. Phys. Chem. B*, 106(47):12203–122103, 2002.
- [125] S. M. Feldt, E. A. Gibson, E. Gabrielsson, L. Sun, G. Boschloo, and A. Hagfeldt. Design of organic dyes and cobalt polypyridine redox mediators for high-efficiency dye-sensitized solar cells. *J. Am. Chem. Soc.*, 132(46):16714–16724, 2010.
- [126] X. Li, Y. Hu, W. Wu, I. Sanchez-Molina, J. Hua, H. Tian, Y. Zhou, N. Robertson, F. Yu, and S. A. Haque. Insight into quinoxaline containing dyes for dye-sensitized solar cells with cobalt and iodine based electrolytes: the effect of p-bridge on the homo energy level and photovoltaic performance. *J. of Mater. Chem. A*, 3:21733–21743, 2015.
- [127] S. Y. Huang, G. Schlichtho, A. J. Nozik, M. Graetzel, A. J. Frank, and J. J. Chang. Charge recombination in dye-sensitized nanocrystalline TiO_2 solar cells. *J. Phys. Chem. B*, 106(47):2576–2582, 1997.
- [128] T. L. Thompson and J. T. Yates. Surface science studies of the photoactivation of TiO_2 -new photochemical processes. *Chem. Rev.*, 106(10):4428–4453, 2006.

- [129] S. Tirosh, T. Dittrich, A. Ofir, L. Grinis, and A. Zaban. Influence of ordering in porous TiO_2 layers on electron diffusion. *J. Phys. Chem. B*, 110(33):16165–16168, 2006.
- [130] Y. Ma, L. Hu, L. Mo, X. Xi, and S. Dai. Trap states comparison of mesoporous TiO_2 photoanodes with different particle sizes. *J. Nanosci. Nanotechnol.*, 110(11):6595–6663, 2016.
- [131] A. Hagfeldt, G. Boschloo, L. Sun, L. Kloo, , and H. Pettersson. Dye-sensitized solar cells. *Chem. Rev.*, 110(11):6595–6663, 2010.
- [132] B. C. O'SRegan and J. R. Durrant. Kinetic and energetic paradigms for dye sensitized solar cells: Moving from the ideal to the real. *Acc. Chem. Res.*, 42(11):1799–1808, 2009.
- [133] S. Munnix and M. Schmeits. Origin of defect states on the surface of TiO_2 . *Phys. Rev. B*, 31:3369–3371, 1985.
- [134] S. Munnix and M. Schmeits. The surface science of titanium dioxide. *Surf. Sci. Rep.*, 48:53–229, 2003.
- [135] Henry J., H. J. Snaith, and L. Schmidt-Mende. Advances in liquid-electrolyte and solid-state dye-sensitized solar cells. *Adv. Mat.*, 19:3187–31200, 2007.
- [136] T. L. Thompson and J. T. Yates. Electrochemical investigation of traps in a nanostructured TiO_2 film. *J. Phys. Chem. B*, 105(13):2529–2533, 2006.
- [137] L. Zhang, S. Wang, and C. Lu. Detection of oxygen vacancies in oxides: defect dependent cataluminescence. *Anal. Chem.*, 87:2529–2533, 2015.
- [138] X. Pan, M. Yang, N. Fu, X. and Zhang, and Y. Xu. Defective TiO_2 with oxygen vacancies: Synthesis, properties and photocatalytic applications. *Nanoscale*, 5:3601–3614, 2013.
- [139] Y. Li, Z. Tang, J. Zhang, and Z. Zhang. Defect engineering of air-treated WO_3 and its enhanced visiblelight-driven photocatalytic and electrochemical performance. *J. Phys. Chem. C*, 120:9750–9763, 2016.
- [140] J. Bisquert. Chemical diffusion coefficient of electrons in nanostructured semiconductor electrodes and dye-sensitized solar cells. *J. Phys. Chem. B*, 108(7):2323–2332, 2004.

- [141] A. B. F. Martinson, M. S. Gomes, J. Fabregat-Santiago, F. Bisquert, M. J. Pellin, and J. T. Hupp. Electron transport in dye-sensitized solar cells based on zno nanotubes: Evidence for highly efficient charge collection and exceptionally rapid dynamics. *J. Phys. Chem. A*, 108(7):2323–2332, 2009.
- [142] M. Adachi, M. Sakamoto, J. Jiu, Y. Ogata, and S. Isoda. Determination of parameters of electron transport in dye-sensitized solar cells using electrochemical impedance spectroscopy. *J. Phys. Chem. B*, 1110(28):13872–13880, 2006.
- [143] J. Bisquert. Hopping transport of electrons in dye-sensitized solar cells. *J. Phys. Chem. C*, 111:17163–17168, 2007.
- [144] M. Adachi, M. Sakamoto, J. Jiu, and S. Ogata, Y. Isoda. Solar energy conversion by dye-sensitized photovoltaic cells. *Inorg. Chem.*, 44(20):13872–13880, 2006.
- [145] J. Bisquert. Interpretation of electron diffusion coefficient in organic and inorganic semiconductors with broad distributions of states. *Phys. Chem. Chem. Phys.*, 10:3175–3194, 2008.
- [146] Y. Wang, D. Wu, L. M. Fu, X. C. Ai, D. Xu, and J. P. Zhang. Correlation between energy and spatial distribution of intragap trap states in the tio2 photoanode of dye-sensitized solar cells. *Chem. Phys. Chem.*, 16:2253–2259, 2015.
- [147] H. G. Yang, C. H. Sun, S. Z. Qiao, J. Zou, G. Liu, S. C. Smith, H. M. Cheng, and G. Q. Lu. Anatase tio2 single crystals with a large percentage of reactive facets. *Nature*, 453:638–641, 2008.
- [148] H. G. Yang, C. H. Sun, S. Z. Qiao, J. Zou, G. Liu, S. C. Smith, H. M. Cheng, and G. Q. Lu. Preparation of carbon nanotube/tio2 mesoporous hybrid photoanode with iron pyrite (fes2) thin films counter electrodes for dye-sensitized solar cell. *Sci. Report*, 6(27052):1–9, 2016.
- [149] B. Liu, K. Nakata, T. Murakami, M. Sakai, H. Takagi, K. Saito, A. Fujishima, and T. Ochiai. Core shell composed of of nanocrystals with exposed high-energy facets: facile synthesis and formation mechanism. *Langmuir*, 27:1–9, 2016.

- [150] H. Yang, J. Li, S. G. Zhou, G. Chiang, H. Du, C. Gan, L. Xu, F. Kanga, and W. Duane. First principles study of ruthenium(ii) sensitizer adsorption on anatase tio₂ (001) surface. *RCS Adv.*, 5:60230–60236, 2015.
- [151] Y. Lu, D. Choi, J. Nelson, O. B. Yang, , and B. A. Parkinson. Adsorption, desorption, and sensitization of low-index anatase and rutile surfaces by the ruthenium complex dye n3. *J. Elec. Soc.*, 153(8):60230–60236, 2015.
- [152] Y. Lu, D. Choi, J. Nelson, O. B. Yang, , and B. A. Parkinson. Material properties controlling photocurrent on tio₂ aggregates with plane orientation for dye-sensitized solar cells. *J. Nanopart. Research*, 12(7):2621–2628, 2010.
- [153] S. Quaranta, D. Gozzi, M. Tucci, L. Lazzarini, and A. Latini. Efficiency improvement and full characterization of dye-sensitized solar cells with mwcnt/anatase schottky junctions. *J. of Power sources*, 204:249–256, 2012.
- [154] S. Ito, P. Liska, P Comte, and M. Graetzel. Fabrication of screen-printing pastes from tio₂ powders for dye-sensitised solar cells. *Prog. Photovolt: Res. Appl.*, 15:602–603, 2007.
- [155] K. Doudrick, O. Monzon, K. Mangonon, A. and Hristovski, and P. Westerhoff. Nitrate reduction in water using commercial titanium dioxide photocatalysts (p25, p90, and hombikat uv100). *J. Environ. Eng.*, 138(8):852–861, 2012.
- [156] M. Kete, E. Pavlica, F. Fresno, G. Bratina, and U. Stangar. Highly active photocatalytic coatings prepared by a low-temperature method. *Environ Sci. Pollut. Res. Int.*, 21(19):11238–49, 2014.
- [157] S. I. In. Comparison of photocatalytic performance of degussa tio₂ p25 and p90 in gas phase photocatalytic reactor. *Asian J. of Chem.*, 23(6):11238–11249, 2011.
- [158] N. N. Papageorgiou, M Graetzel, and P. P. Infelta. On the relevance of mass transport in thin layer nanocrystalline photoelectrochemical solar cells. *Sol. Energy Mater. Sol. Cells*, 44(4):405–438, 1996.
- [159] N. N. Papageorgiou, M Graetzel, and P. P. Infelta. Mediator transport in multilayer nanocrystalline photoelectrochemical cell configurations. *J. Electrochem. Soc.*, 146(3):898–907, 1999.

- [160] N. Papageorgiou, C. Barbe, and M. Graetzel. Morphology and adsorbate dependence of ionic transport in dye sensitized mesoporous tio₂ films. *J. Electrochem. Soc.*, 102(21):4156–4164, 1999.
- [161] T. Berger, T. Lana-Villarreal, D. Monllor-Satoca, and R. Gomez. An electrochemical study on the nature of trap states in nanocrystalline rutile thin films. *J. Phys. Chem C.*, 111(27):9936–9942, 2007.
- [162] M. J. Biermana and J. Song. Potential applications of hierarchical branching nanowires in solar energy conversion. *Energy Environ. Sci.*, 2(27):1050–1059, 2009.
- [163] L. Hu, S. Dai, S. Weng, S. Xiao, Y. Sui, Y. Huang, S. Chen, F. Kong, X. Pan, L. Liang, and K. Wang. Microstructure design of nanoporous tio₂ photoelectrodes for dye-sensitized solar cell modules. *J. Phys. Chem B*, 111(2):358–362, 2006.
- [164] M. Greene Law, J.C. L. E. Johnson, and P. Saykally, R. and Yan. Nanowire dye-sensitized solar cells. *Nat. Mater.*, 4(6):455–459, 2005.
- [165] K. Zhu, N. R. Neale, A. Miedaner, and A. J. Frank. Enhanced charge-collection efficiencies and light scattering in dye sensitized solar cells using oriented tio₂ nanotubes arrays. *Nanoletters*, 7(1):69–74, 2007.
- [166] G. K. Mor, K. Shankar, M. Paulose, O. K. Varghese, and C. A. Grimes. Use of highly-ordered tio₂ nanotube arrays in dyesensitized solar cells. *Nanoletters*, 6(2):215–218, 2006.
- [167] M. Y. Song, D. K. Kim, K. J. Ihn, S. M. . Jo, and D. Y. Kim. Electrospun tio₂ electrodes for dye-sensitized solar cells. *Nanotechnology*, 15(12):1861–1865, 2004.
- [168] K. Pan. Tio₂-b narrow nanobelt/tio₂ nanoparticle composite photoelectrode for dye-sensitized solar cells. *Electr. Acta*, 54:7350–7356, 2009.
- [169] W. Zhang, R. Zhu, L. Ke, X. Liu, B. Liu, and S. Ramakrishna.
- [170] Y. Shi, Y. Wan, and D. Zhao. Ordered mesoporous non-oxide materials. *Chem. Soc. Rev.*, 40(10):4428–4453, 2011.
- [171] J. Livage, M. Henry, and C. Sanchez. Sol-gel chemistry of transition metal oxides. *Prog. Solid State Chem.*, 18(4):259–349, 1988.

- [172] D. M. Antonelli, M. Henry, and J. P. Yinmg. Synthesis of a stable hexagonally packed mesoporous niobium oxide molecular sieve through a novel ligand-assisted templating mechanism. *Angew. Chem., Int. Ed.*, 35(4):426–430, 1996.
- [173] P. Yang, D. I. Zhao, D. Margolese, B. F. Chmelka, and G. Stucky. Generalized syntheses of large-pore mesoporous metal oxides with semicrystalline frameworks. *Nature*, 396:152–155, 1998.
- [174] H. S. Yun, K. Miyazawa, H. S. Zhou, I. Honma, and M. Kuwabara. Synthesis of mesoporous thin TiO_2 films with hexagonal pore structures using triblock copolymer templates. *Adv. Mat.*, 13(18):1377–1380, 2001.
- [175] P. C. A. Alberius, K. L. Frindell, R. C. Hayward, E. J. Kramer, G. D. Stucky, and B. F. Chmelka. General predictive syntheses of cubic, hexagonal, and lamellar silica and titania mesostructured thin films. *Chem. Mat.*, 14(8):3284–3294, 2002.
- [176] E. L. Crepaldi, G. Soler-Illia, D. Grosso, F. Cagnol, F. Ribot, and C. Sanchez. Controlled formation of highly organized mesoporous titania thin films: From mesostructured hybrids to mesoporous nanoanatase TiO_2 . *J. Am. Chem. Soc.*, 125(32):9770–9786, 2003.
- [177] D. Grosso, G. J. A. A. Soler-Illia, F. Babonneau, C. Sanchez, P. A. Albouy, A. Brunet-Bruneau, and A. R. Balkenende. Highly organized mesoporous titania thin films showing mono-oriented 2d hexagonal channels. *Adv. Mat.*, 13(14):1085–1090, 2001.
- [178] P. S. Parmar, E. Ramasamy, J. Leeb, and S. G. Lee. Rapid (10 min.) synthesis of single-crystalline, nanorice TiO_2 mesoparticles with a high photovoltaic efficiency >8 . *Chem. Comm.*, 47:8572–8574, 2011.
- [179] H. C. Van de Hulst. *Light scattering by small particles*. John Wiley and Sons, Inc, 2009.
- [180] J. Sun, X. Cui, C. Zhang, C. Zhang, and Y. Ding, R. Xu. Broadband antireflective coating based on a double-layer system containing mesoporous silica and nanoporous silica. *J. Mat. Chem C.*, 3:7187–7194, 2015.
- [181] F. Sauvage, D. Chen, P. Comte, F. Huang, R. A. Heiniger, L. P. Caruso, and M. Graetzel. Dye-sensitized solar cells employing a single film of mesoporous

- tio₂ beads achieve power conversion efficiencies over 10. *ACS Nano*, 4(8):4420–4425, 2007.
- [182] E. J. W. Crossland, N. Noel, V. Sivaram, T.J. Leijtens, A. Alexander-Webber, and H. J. Snaith. Mesoporous tio₂ single crystals delivering enhanced mobility and optoelectronic device performance. *Nature*, 495(7440):215–219, 2013.
- [183] I. Tamiolakis, I. N. Lykakis, A. P. Katsoulidis, and G. S. S. Armatas. One-pot synthesis of highly crystalline mesoporous tio₂ nanoparticle assemblies with enhanced photocatalytic activity. *Chem. Comm.*, (48):6687–6689, 2012.
- [184] B. Tian, H. Yang, X. Liu, S. Xie, C. Yu, J. Fan, B. Tu, and B. Zhao. Fast preparation of highly ordered nonsiliceous mesoporous materials via mixed inorganic precursors. *Chem. Comm.*, (17):1824–1825, 2002.
- [185] B. Tian, X. Liu, B. Tu, C. Yu, J. Fan, L. Wang, G. D. Xie, S. Stucky, and D. Zhao. Self-adjusted synthesis of ordered stable mesoporous minerals by acid–base pairs. *Nat. Mat.*, 125(2):159–163, 2003.
- [186] D. Chen, L. Cao, F. Huang, P. Imperia, Y. B. Cheng, and R. A. Caruso. Synthesis of monodisperse mesoporous titania beads with controllable diameter, high surface areas, and variable pore diameters (14–23 nm). *J. Am. Chem. Soc.*, 132(12):4438–4446, 2010.
- [187] Y. Duan, N. Fu, Q. Liu, Y. Fang, X. Zhou, J. Zhang, and Y. Lin. Sn-doped tio₂ photoanode for dye-sensitized solar cells. *J. Phys. Chem. C*, 116(16):8888–8893, 2012.
- [188] A. Latini, C. Cavallo, F. A. Aldibaja, and Daniele Gozzi. Efficiency improvement of dssc photoanode by scandium doping of mesoporous titania beads. *J. Phys. Chem. C*, (117):25276–25289, 2013.
- [189] S. Meng and E. Kaxiras. Electron and hole dynamics in dye-sensitized solar cells: Influencing factors and systematic trends. *Nano Lett.*, 10(4):1238–1247, 2010.
- [190] J. Park, S. S. Park, and Y. S. Won. Influence of sn source on the performance of dye-sensitized solar cells based on sn-doped tio₂ photoanodes: A strategy for choosing an appropriate doping source. *Electrochem. Acta*, 107:473–480, 2013.

- [191] F. De Angelis, S. Fantacci, A. Selloni, M. K. Nazeeruddin, and M. Graetzel. First-principles modeling of the adsorption geometry and electronic structure of ru(ii) dyes on extended tio₂ substrates for dye-sensitized solar cell applications. *J. Phys. Chem. C*, 114:6054–6071, 2010.
- [192] S. Meng and E. Kaxiras. Electron and hole dynamics in dye-sensitized solar cells: Influencing factors and systematic trends. *Nano Lett.*, 10(4):1238–1247, 2010.
- [193] J. Park, S. S. Park, and Y. S. Won. Effect of nb and sc doping on the phase transformation of sol-gel processed tio₂ nanoparticles. *J. Nanosci. Nanotech.*, 8(5):2410–2418, 2008.
- [194] A. K. Chandiran, F. Sauvage, L. Etgar, and M. Graetzel. Ga³⁺ and y³⁺ cationic substitution in mesoporous tio₂ photoanodes for photovoltaic applications. *J. Phys. Chem. C*, 115:9232–9240, 2011.
- [195] A. K. Chandiran, F. Sauvage, M. Casas-Cabanas, P. Comte, S. M. Zakeeruddin, and M. Graetzel. Doping a tio₂ photoanode with nb⁵⁺ to enhance transparency and charge collection efficiency in dye-sensitized solar cells. *J. Phys. Chem. C*, 114(37):15849–15856, 2010.
- [196] V. Sivaram, E. J. W. Crossland, T. Leijtens, N. K. Noel, J. Alexander-Webber, P. Docampo, and H. J. Snaith. Observation of annealing-induced doping in tio₂ mesoporous single crystals for use in solid state dye sensitized solar cells. *J. Chem. Phys. C*, 118(4):1821–1827, 2014.
- [197] T. Leijtens, G. E. Eperon, S. Pathak, A. Abata, M. M. Lee, and H. J. Snaith. Overcoming ultraviolet light instability of sensitized tio₂ with meso-structured organometal tri-halide perovskite solar cells. *Nat. Comm.*, 4:28851–8, 2013.
- [198] S. K. Pathak, A. Abate, P. Ruckdeschel, B. Roose, K. C. Godel, Y. Vaynzof, A. Santhala, S. I. Watanabe, D. J. Hollman, N. Noel, A. Sepe, U. Wiesner, R. Friend, H. J. Snaith, and U. Steiner. Performance and stability enhancement of dye-sensitized and perovskite solar cells by al doping of tio₂. *Adv. Func. Mat.*, 4(48):6046–6055, 2013.
- [199] L.C. K. Liao and C. C. Lin. Fabrication and characterization of fe³⁺-doped titania semiconductor electrodes with p-n homojunction devices. *Appl. Surf. Sci.*, 253(21):8798–8801, 2013.

- [200] Y. Xie, N. Huang, S. You, Y. Liu, B. Sebo, L. Liang, X. Fang, W. Liu, S. Guo, and X. Z. Zhao. Improved performance of dye-sensitized solar cells by trace amount cr-doped tio2 photoelectrodes. *J. Power Sources*, 224:168–173, 2013.
- [201] Q. Liu, Y. Zhou, Y. Duan, M. Wang, and Y. Lin. Improved photovoltaic performance of dye-sensitized solar cells (dsscs) by zn + mg co-doped tio2 electrodes. *Electrochem. Acta*, 95:45–48, 2013.
- [202] J. Zhang, Z. Fu, Q. Lv, X. Yang, and W. Cao. Technology of preparing anode films and the effect of co-sensitization in dye-sensitized solar cells. *J. Sol^UGel Sci. Technol.*, 63(4):554–562, 2013.
- [203] A. Malik, M. J. Hameed, J. S. Siddiqui, M. Haque, K. Umar, A. Khan, and M. Muneer. Electrical and optical properties of nickel- and molybdenum-doped titanium dioxide nanoparticle: Improved performance in dye-sensitized solar cells. *J. Mat. Eng. and Perform.*, 23(9):3184–3192, 2014.
- [204] P. S. Archana, A. Kumar, C. Vijila, S. Ramakrishna, M. Yuso, and R. Jose. Random nanowires of nickel doped tio2 with high surface area and electron mobility for high efficiency dye-sensitized solar cells. *Dalton Trans.*, 42:1024–1032, 2013.
- [205] J. Zhang, Z. Fu, Q. Lv, X. Yang, and W. Cao. Technology of preparing anode films and the effect of co-sensitization in dye-sensitized solar cells. *J. Sol^UGel Sci. Technol.*, 63(4):554–562, 2013.
- [206] J. Zhang, Z. Fu, Q. Lv, X. Yang, and W. Cao. Improving photovoltaic performance of dye-sensitized solar cell by downshift luminescence and p-doping effect of gd2o3:sm3+. *J. of Luminescence*, 134:59–62, 2013.
- [207] J. H. Noh, S. Lee, J. Y. Kim, J.-K. Lee, H. S. Han, I. S. Cho, C. M. and Cho, Jung H. S., and K. S Hong. Functional multilayered transparent conducting oxide thin films for photovoltaic devices. *J. Phys. Chem. C*, 113(3):1083–1087, 2009.
- [208] S. Lee, J. H. Noh, H. S. Han, D. K. Yim, D. H. Kim, J. Y. Lee, J.-K. and Kim, H. S. Jung, and K. S. Hong. Nb-doped tio2: A new compact layer material for tio2 dye-sensitized solar cells. *J. Phys. Chem. C*, 113(6):6878–6888, 2009.

- [209] M Hirano and K. Matsushima. Effect of niobium on the structure and photoactivity of anatase (tio₂) nanoparticles. *J. Nanosci. Nanotechnol.*, 6(3):762–770, 2006.
- [210] S. Chen, J. Lin, and J. Wu. Improving photoelectrical performance of dye sensitized solar cells by doping y₂o₃:tb³⁺ nanorods. *J. Mater. Sci.*, 25(5):2060–2065, 2014.
- [211] E. Wada, S. Hayashi, M. Kitano, K. Yamamoto, and M. Hara. Synthesis of niobium-doped titanate nanotubes as solid acid catalysts. *Catal. Sci. and Tech.*, 6:4832–4839, 2016.
- [212] N. Tsvetkov, L. Larina, O. Shevaleevskiy, and B. T. Ahn. Electronic structure study of lightly nb-doped tio₂ electrode for dye-sensitized solar cells. *Energy Environ. Sci.*, 4(4):1480–1486, 2011.
- [213] S. G. Kim, M. J. Ju, W. S. Choi, I. T. Choi, H. J. Choi, J. B. Baek, and H. K. Kim. Nb-doped tio₂ nanoparticles for organic dye-sensitized solar cells. *RSC Adv.*, 3(37):16380–16386, 2013.
- [214] K. H. Ko, Y. C. Lee, and J. Jung. Enhanced efficiency of dye-sensitized tio₂ solar cells (dssc) by doping of metal ions. *J. Colloid Interface Sci.*, 283(2):482–487, 2005.
- [215] X. Zhang, Wang S. T., and Z.-S. Wang. Effect of metal-doping in tio₂ on fill factor of dye-sensitized solar cells. *Appl. Phys. Lett.*, 99(113503):1–4, 2011.
- [216] K. H. Ko, Y. C. Lee, and J. Jung. Tailoring the conduction band of titanium oxide by doping tungsten for efficient electron injection in a sensitized photoanode. *Nanoscale*, 6(7):3875–3880, 2014.
- [217] Z. Tong, T. Peng, W. Sun, W. Liu, S. Guo, and X. Z. Zhao. Introducing an intermediate band into dye-sensitized solar cells by w⁶⁺ doping into tio₂ nanocrystalline photoanodes. *J. Phys. Chem. C*, 118(30):16892–16895, 2014.
- [218] H. Melhem, P. Simon, J. Wang, C. Di Bin, B. Ratier, Y. Leconte, D. Herlin-Boime, M. Malgorzata-Janusik, and A. Kassiba.
- [219] S. Iwamoto, Y. Sazanami, I. Masashi, T. Inoue, T. Hoshi, T. Shigaki, M. Kaneko, , and A. Maenosono. Fabrication of dye-sensitized solar cells with an open-circuit photovoltage of 1 v. *Chem. Sus. Chem.*, 1:401–403, 2008.

- [220] C. Cavallo, A. Salleo, D. Gozzi, F. Di Pascasio, S. Quaranta, R. Panetta, and A. Latini. Solid solutions of rare earth cations in mesoporous anatase beads and their performances in dye-sensitized solar cells. *Scientific Reports*, 16785(5):1–15, 2015.
- [221] R. D. Shannon and C. T. Prewitt. Effective ionic radii in oxides and fluorides. *Acta Cryst.*, 25:925–946, 1969.
- [222] J. Chen, B. Li, J. Zheng, J. Zhao, and Z. Zhu. Role of carbon nanotubes in dye-sensitized tio₂-based solar cells. *J. Phys. Chem. C*, 28(116):14848–14856, 2012.
- [223] P. Brown, K. Takechi, and P. V. Kamat. Single-walled carbon nanotube scaffolds for dye-sensitized solar cells. *J. Phys. Chem C*, 12(112):4776–4782, 2008.
- [224] P. V. Kamat. Manipulation of charge transfer across semiconductor interface. a criterion that cannot be ignored in photocatalyst design. *J. Phy. Chem. Lett.*, 3(5):663–672, 2012.
- [225] H. Li, Z. Bian, J. Zhu, Y. Y Huo, Hu. Li, and H. Lu. Mesoporous au/tio₂ nanocomposites with enhanced photocatalytic activity. *J. Am. Chem. Soc.*, 129(15):4538–4549, 2007.
- [226] M. Abd-Ellah, N. Moghimi, L. Zhang, J. P. Thomas, D. McGillivray, S. Srivastava, and K. T. Leung. Plasmonic gold nanoparticles for zno-nanotube photoanodes in dye-sensitized solar cell application. *Nanoscale*, 8:1658–1664, 2016.
- [227] Y. H. Su, , L. G. Lai, W. H. and Teoh, M. H. Hon, and J. L. Huang. Layer-by-layer au nanoparticles as a schottky barrier in a water-based dye-sensitized solar cell. *Appl. Phys. A*, 88(1):173–178, 2007.
- [228] H. Chang, K. C. Cho, C. G. Kuo, M. J. Kao, K. H. Huang, D. Chu, and X. P. Lin. Application of a schottky barrier to dye-sensitized solar cells (dsscs) with multilayer thin films of photoelectrodes. *J. of All. Comp.*, 509(1):486–489, 2007.
- [229] C. Boerigter, U. Umar Aslam, and S. Linic. Mechanism of charge transfer from plasmonic nanostructures to chemically attached materials. *ACS Nano*, 10:6108–6115, 2016.

- [230] R. H. Baughman, A. A. Zakhidov, and W. A. de Heer. Carbon nanotubes—the route toward applications. *Nature*, 5582(297):787–792, 2002.
- [231] M. F. L. De Volder, R. H. Tawfick, S. H. Baughman, and J. A. Hart. Carbon nanotubes: Present and future commercial applications. *Science*, 339:535–539, 2013.
- [232] B. Arash, Q. Wang, and V. K. Varadan. Mechanical properties of carbon nanotube/polymer composites. *Sci. Report*, 4(6479):1–8, 2014.
- [233] M. Paradise and T. Goswami. Carbon nanotubes \ddot{U} production and industrial applications. *Mat. Design*, 28:1477–1489, 2007.
- [234] C. Li, E.T. Thostenson, and T. W. Chou. Sensors and actuators based on carbon nanotubes and their composites: A review. *Compos. Sci. Technol.*, 68(6):1227–1249, 2014.
- [235] T. Chen, L. Qiu, Z. Cai, F. Gong, Z. Yang, Z. Wang, and H. Peng. Intertwined aligned carbon nanotube fiber based dye-sensitized solar cells. *Nano Letters*, 12(5):2568–2572, 2012.
- [236] A. Kay and M. Gratzel. Low cost photovoltaic modules based on dye sensitized nanocrystalline titanium dioxide and carbon powder. *Sol. Energy Mater. Sol. Cells*, 44(1):99–117, 2012.
- [237] L. Kavan, J.-H. Yum, and M. Gratzel. Graphene nanoplatelets outperforming platinum as the electrocatalyst in co-bipyridine-mediated dye-sensitized solar cells. *Nano Letters*, 11(12):5501–5506, 2011.
- [238] L. Kavan, J.H. Yum, and M. Gratzel. Preparation and properties of a carbon nanotube-based nanocomposite photoanode for dye-sensitized solar cells. *Nanotech.*, 19(375305):1–9, 2008.
- [239] K. T. Dembele, J. R. Rimada, A. Vomiero, G. S. Selopal, I. Concina, C. Sberveglieri, G. Soldano, F. Rosei, and R. Nechache. Hybrid carbon nanotubes-tio₂ photoanodes for high efficiency dye-sensitized solar cells. *J. Phys. Chem C.*, 117:14510–14517, 2013.
- [240] G. Cheng, M. Shaheer Akhtar, G. O-Bong Yang, and J. Stadler. Novel preparation of anatase tio₂ at reduced graphene oxide hybrids for high-performance dye-sensitized solar cells. *ACS Appl. Mater. Interf.*, 5(14):6635–6642, 2013.

- [241] F. Xu, J. Chen, X. Wu, Y. Zhang, Y. Wang, J. Sun, H. Bi, W. Lei, Y. Ni, and L. Sun. Graphene scaffolds enhanced photogenerated electron transport in zno photoanodes for high-efficiency dye-sensitized solar cells. *J. Phys. Chem. C*, 17(117):8619–8627, 2013.
- [242] S. R. Jang, R. Vittal, and K. J. Kim. Incorporation of functionalized single-wall carbon nanotubes in dye-sensitized tio2 solar cells. *Langmuir*, 17(2004):9807–9804, 2004.
- [243] S. L. Kim, S. R. Jang, R. Vittal, J. Lee, and J. K. Kim. Rutile tio2-modified multi-wall carbon nanotubes in tio2 film electrodes for dye-sensitized solar cells. *J. Appl. Electroche.*, 36(12):1433–1439, 2006.
- [244] Y. H. Ng, I. V. Lightcap, K. Goodwin, M. Matsumura, and P. V. J. Kamat. To what extent do graphene scaffolds improve the photovoltaic and photocatalytic response of tio2 nanostructured films? *J. Phys. Chem. Lett.*, 1(15):2222–2227, 2010.
- [245] A. B. Kaiser, G. Dusberg, and S. Roth. Heterogeneous model for conduction in carbon nanotubes. *Phys. Rev. B.*, 57(3):1418–1421, 2001.
- [246] T. Belin and F. Epron. Characterization methods of carbon nanotubes: a review. *Mat. Sci. and Eng. B*, 119(2):105–118, 2005.
- [247] S. C. Chou, R. Y. Yang, M. H. Weng, and C. I. Huang. The applicability of swcnt on the counter electrode for the dye-sensitized solar cell. *Adv. Powd. Tech.*, 20:310–317, 2009.
- [248] B. He, Q. Tang, T. Lianga, and Q. Li. Efficient dye-sensitized solar cells from polyaniline–single wall carbon nanotube complex counter electrodes. *J. Mater. Chem. A*, 2:3119–3126, 2014.
- [249] B. He, Q. Tang, T. Lianga, and Q. Li. Efficient dye-sensitized solar cells from polyaniline–single wall carbon nanotube complex counter electrodes. *J. Mater. Chem. A*, 2:3119–3126, 2014.
- [250] J. E. Trancik, S. C. Barton, and J. Hone. Transparent and catalytic carbon nanotube films. *Nano Letters*, 8(4):982–987, 2008.
- [251] G. Calogero, F. Bonaccorso, O. M. Marag, P. G. Gucciardi, and P. G. Di Marco. Single wall carbon nanotubes deposited on stainless steel sheet substrates

- as novel counter electrodes for ruthenium polypyridine based dye sensitized solar cells. *Dal. Trans.*, 39(4):2903–2909, 2010.
- [252] W. G. Reis, R. T. Weitz, M. Kettner, K. Kraus, M. G. Schwab, Z. Tomovic, K. Krupke, and J. Mikhael. Highly efficient and scalable separation of semiconducting carbon nanotubes via weak field centrifugation. *Sci. Rep.*, 6(26259):1–8, 2016.
- [253] P. N. Nirmalraj, P. E. Lyons, S. De, J. N. Coleman, and J. Boland. Electrical connectivity in single-walled carbon nanotube networks. *Nanoletters*, 9(11):3890–3895, 2009.
- [254] R. M. A. Kongkanand, D. Dominguez, and P. V. Kamat. Single wall carbon nanotube scaffolds for photoelectrochemical solar cells. capture and transport of photogenerated electrons. *Nano Letters*, 7(3):676–680, 2007.
- [255] N. Yang, J. Zhai, D. Wang, Y. Chen, and L. Jiang. Two dimensional graphene bridges enhanced photoinduced charge transport in dye-sensitized solar cells. *ACS Nano*, 4(2):887–894, 2010.
- [256] S. M. Tze and K. G. Kwok. *Physics of Semiconductor Devices*. Wiley, 3 edition, 2007.
- [257] A. Hagfeldt and M. Graetzel. Low bandgap polymers for photon harvesting in bulk heterojunction solar cells. *J. Mat. Chem.*, 14:1077–1086, 2007.
- [258] V. Barone, J. E. Peralta, J. Uddin, and G. E. Scuseria. Screened exchange hybrid density-functional study of the work function of pristine and doped single-walled carbon nanotubes. *J. Chem. Phys.*, 124(024709):1–6, 2007.
- [259] B. Shan and K. Cho. First principles study of work functions of single wall carbon nanotubes. *Phys. Rev. Lett.*, 94(236602):1–4, 2002.
- [260] J. Zhao, J. Han, and J. P. Lu. Work functions of pristine and alkali-metal intercalated carbon nanotubes and bundles. *Phys. Rev. B*, 65(193401):1–4, 2002.
- [261] Y. Battie, D. Jamon, A. En Naciri, J.S. Lauret, and A. Loiseau. Chirality distribution in single walled carbon nanotube films by spectroscopic ellipsometry. *Appl. Phys. Lett.*, 8(091909):1–6, 2013.

- [262] P. Liu, Q. Sun, F. Zhu, K. Liu, L. Jiang, K. Liu, Q. Li, and S. Fan. Measuring the work function of carbon nanotubes with thermionic method. *Nano Letters*, 8(2):647–651, 2008.
- [263] A. Hagfeldt and M. Graetzel. Light-induced redox reactions in nanocrystalline systems. *Chem. Rev*, 95(1):49–68, 1996.
- [264] N. Komatsu and F. Wang. A comprehensive review on separation methods and techniques for single-walled carbon nanotubes. *Materials*, 3:3818–3844, 2010.
- [265] Y. Feng, Y. Miyata, K. Matsuishi, and H. Kataura. High-efficiency separation of single-wall carbon nanotubes by self-generated density gradient ultracentrifugation. *J. Phys. Chem. C*, 115(5):1752–1756, 2011.
- [266] T. Tanaka, H. Jin, Y. Miyata, and H. Kataura. High-yield separation of metallic and semiconducting single-wall carbon nanotubes by agarose gel electrophoresis. *App. phys. Expr.*, 1(114001):1–3, 2008.
- [267] Y. Feng, Y. Miyata, K. Matsuishi, and H. Kataura. Facile isolation of adsorbent-free long and highly-pure chirality-selected semiconducting single-walled carbon nanotubes using a hydrogen-bonding supramolecular polymer. *Sci. Rep.*, 5(18066):1–8, 2016.
- [268] M. S. Arnold, A. A. Green, J. F. Hulvat, S. I. Stupp, and M. C. Hersam. Sorting carbon nanotubes by electronic structure using density differentiation. *Nat. Rep.*, 1:60–65, 2006.
- [269] S. K. Doorn, R. E. Fields, R. C. Haddon, J. P. Selegue, H. Hu, M. A. Hamon, and V. Majidi. High resolution capillary electrophoresis of carbon nanotubes. *J. Amer. Chem. Soc.*, 124(12):2559–2566, 2002.
- [270] M. S. Arnold, S. I. Stupp, and M. C. Hersam. Enrichment of single-walled carbon nanotubes by diameter in density gradients. *NanoLetters*, 5(4):713–718, 2005.
- [271] S. R. Lustig, A. Jagota, C. Khripin, and G. Zheng. Theory of structure-based carbon nanotube separations by ion-exchange chromatography of dna/cnt hybrids. *J. Phys. Chem. B*, 109(7):2559–2566, 2005.

- [272] M. Zheng, A. Jagota, E. D. Semke, B. A. Diner, R. S. Mclean, S. R. Lustig, R. E. Richardson, and N. G. Tassi. Dna-assisted dispersion and separation of carbon nanotubes. *Nat. Mater.*, 2:338–342, 2003.
- [273] D. H. Shin, J. H. Yoon, S. Baik, J. E. Kim, J. Kim, H. C. Shim, S. Jeong, C. S. Han, J. W. Song, and J. Kang. Continuous extraction of highly pure metallic single-walled carbon nanotubes in a microfluidic channel. *NanoLetters*, 8(12):4380–4385, 2008.
- [274] S. Nanot, H. E. Haroz, J. H. Kim, and J. Kono. Optoelectronic properties of single-wall carbon nanotubes. *Adv. Mat.*, 24(36):4977–4994, 2012.
- [275] T. Tanaka, Y. Urabe, and H. Hirakawa, T. Kataura. Simultaneous chirality and enantiomer separation of metallic single-wall carbon nanotubes by gel column chromatography. *Anal. Chem.*, 15(87):9467–9472, 2013.
- [276] R. M Jain, J. Howden, K. Tvrdy, S. Shimizu, A. J. Hilmer, T. P. McNicholas, K. K. Gleason, and M. S. Strano. Polymer-free near-infrared photovoltaics with single chirality (6,5) semiconducting carbon nanotube active layers. *Adv. Mat.*, 32(24):4436–4439, 2012.
- [277] K. Tvrdy, R. M. Jain, R. Han, T. P. Hilmer, A. J. McNicholas, and M. S. Strano. A kinetic model for the deterministic prediction of gel-based single-chirality single-walled carbon nanotube separation. *ACS Nano*, 2(7):1779–1789, 2013.
- [278] R. M. Jain, M. Ben-Naim, M. P. Landry, and M. S. Strano. Competitive binding in mixed surfactant systems for single-walled carbon nanotube separation. *J. Phys. Chem. C*, 39(139):22737–22745, 2015.
- [279] H. Liu, D. Nishide, T. Tanaka, and H. Kataura. Large-scale single-chirality separation of single-wall carbon nanotubes by simple gel chromatography. *Nature Comm.*, 204(309):1–8, 2011.
- [280] N. O. Laschuk, I. I. Ebralidze, S. Quaranta, S. T. W. Kerr, J.G. Egan, S. Gillis, F. Gaspari, A. Latini, and O.V. Zenkina. Rational design of a material for rapid colorimetric fe²⁺ detection. *Materials and Design*, (107):18–25, 2016.
- [281] A. Tatchoi, C. S. Poon, H. W. Liu, H. C. Chenga, and K. K. M. Lo. Rhenium(i) polypyridine complexes functionalized with a diaminoaromatic moiety as phosphorescent sensors for nitric oxide. *New J. Chem.*, 37:1711–1719, 2013.

- [282] S. G. Shepard, S. M. Fatur, A. K. Rappe, and N. H. Damrauer. Highly strained iron(ii) polypyridines: Exploiting the quintet manifold to extend the lifetime of mlct excited states. *J. Am. Chem. Soc.*, 37(9):2949–2952, 2016.
- [283] J. Chen, Z. Luo, Z. Zhao, L. Xie, W. Zheng, and C. Chen. Cellular localization of iron(ii) polypyridyl complexes determines their anticancer action mechanisms. *Biomaterials*, 71:168–177, 2015.
- [284] J. Chen, Z. Luo, Z. Zhao, L. Xie, W. Zheng, and C. Chen. Synthesis, characterization, and in vitro antitumor activity of ruthenium(ii) polypyridyl complexes tethering egfr-inhibiting 4-anilinoquinazolines. *Inor. Chem*, 55(9):4595–4605, 2016.
- [285] J. Chen, Z. Luo, Z. Zhao, L. Xie, W. Zheng, and C. Chen. Adelaye, a. o and and ajibade, p. a. *Molecules*, 55:1241–1260, 2014.
- [286] A. Byrne, C. Dolan, R. D. Moriarty, U. Martin, A. Neugebauer, R. J. Forster, A. Davies, Y. Volkov, and E. Keyes T. Osmium(ii) polypyridyl polyarginine conjugate as a probe for live cell imaging; a comparison of uptake, localization and cytotoxicity with its ruthenium(ii) analogue). *Dalton Trans.*, 44(32):1241–1260, 2015.
- [287] E. M. Kober, J. V. Caspar, B. P. Sullivan, and T. J. Meyer. Synthetic routes to new polypyridyl complexes of osmium(ii). *Inorg. Chem.*, 27(25):4587–4598, 1988.
- [288] K. K. W. Lo. Luminescent rhenium(i) and iridium(iii) polypyridine complexes as biological probes, imaging reagents, and photocytotoxic agents. *Acc. Chem. Res.*, 48(12):2985–2995, 2015.
- [289] M. Sandroni, L. Favereau, A. Planchat, H. Akdas-Kilig, N. Szuwarski, Y. Pellegrin, E. Blart, H. Le Bozec, M. Boujtita, and F. Odobel. Heteroleptic copper(i) polypyridine complexes as efficient sensitizers for dye sensitized solar cells. *J. Mater. Chem. A*, 2:9944–9947, 2014.
- [290] X. Lu, S. Wei, C. M. L. Wu, S. Li, and W. Guo. Can polypyridyl cu(i)-based complexes provide promising sensitizers for dye-sensitized solar cells? a theoretical insight into cu(i) versus ru(ii) sensitizers. *J. Phys. Chem. C*, 115(25):9944–9947, 2014.

- [291] P. Shi, B. J. Coe, S. Sanchez, D. Wang, Y. Tian, M. Nyk, and M. Samoc. Uniting ruthenium(ii) and platinum(ii) polypyridine centers in heteropolymetallic complexes giving strong two-photon absorption. *Inor. Chem.*, 54(23).
- [292] F. Darabi, H. Hadadzadeh, J. Simpsonb, and A. Shahpiric. A water-soluble pd(ii) complex with a terpyridine ligand: experimental and molecular modeling studies of the interaction with dna and bsa; and in vitro cytotoxicity investigations against five human cancer cell lines. *New Journal of Chem.*, 40:9081–9097, 2015.
- [293] B. Pitteri, M. Bortoluzzi, and V. Bertolasi. Chelate polypyridine ligand rearrangement in au(iii) complexes. *Trans. Met. Chem.*, 33(5):11450–11456, 2008.
- [294] M. Graetzel and K. Kalyanasundaram. *Photosensitization and Photocatalysis Using Inorganic and Organometallic compounds*. Catalysis by metal complexes. Springer, 1st edition, 1993.
- [295] K. K. W. Lo. *Luminescent and Photoactive Transition Metal Complexes as Biomolecular Probes and Cellular Reagents*. Structure and Bonding. Springer, 1st edition, 2015.
- [296] K. K. W. Lo. *Inorganic and Organometallic Transition Metal Complexes with Biological Molecules and Living Cells*. Academic Press, 1st edition, 2017.
- [297] M. Zheng, H. Tan, Z. Xie, L. Zhang, X. Jing, and Z. Sun. Fast response and high sensitivity europium metal organic framework fluorescent probe with chelating terpyridine sites for fe 3+. *ACS Appl. Mater. Interfaces*, 5:1078–1083, 2013.
- [298] Z. Yang, W. Yang, C. Yan, Z. Guo, Y. Lu, Y. Chen, W. He, W. Zhu, C. Zhang, and X. Dong. A novel terpyridine/benzofurazan hybrid fluorophore: metal sensing behavior and application. *Dalton Trans.*, 40:2173–2176, 2010.
- [299] Z. Q. Liang, Y. P. Tian, C. X. Wang, X. T. Tao, J. X. Yang, M. H. Jiang, and H. W. Gao. A highly selective colorimetric chemosensor for detecting the respective amounts of iron(ii) and iron(iii) ions in water. *New J. Chem*, 31:906–910, 2007.

- [300] Z. Q. Liang, Y. P. Tian, C. X. Wang, X. T. Tao, J. X. Yang, M. H. Jiang, and H. W. Gao. Charge transfer spectra of transition metal complexes. *J. Chem. Educ.*, 51(9):612–613, 1974.
- [301] R. Shunmugam, G. J. Gabriel, C. E. Smith, A. A. Khaled, and G. N. Tew. A highly selective colorimetric aqueous sensor for mercury. *Chem. Eur. J.*, 14:3904–3907, 2008.
- [302] J. J. Moore, J. J. Nash, P. E. Fanwick, and D. R. McMillin. A superior polypyridine ligand for platinum(ii) lumaphors. methyl substituents with a large stereoelectronic influence. *Inorg. Chem.*, 41(24):6387–6396, 2002.
- [303] S. K. Chung, Y. R. Tseng, C. Y. Chen, and S. S. Sun. A selective colorimetric Hg^{2+} probe featuring a styryl dithiaazacrown containing platinum(ii) terpyridine complex through modulation of the relative strength of ict and mlct transitions. *Inorg. Chem.*, 50:2711–2713, 2011.
- [304] A. Meyer, G. Schnakenburg, R. Glaum, and O. Schiemann. (bis(terpyridine))copper(ii) tetraphenylborate: A complex example for the jahn-teller effect. *Inorg. Chem.*, 54:8456–8464, 2015.
- [305] G. T. Morgan and F. H. Burstall. Dehydrogenation of pyridine by anhydrous ferric chloride. *J. Chem. Soc.*, pages 20–30, 1932.
- [306] K. Takada, R. Sakamoto, S. Yi, S. R. Katagiri, T. Kambe, and H. Nishihara. Modern terpyridine chemistry. *J. Amer. Chem. Soc.*, 137(14):4681–4689, 2015.
- [307] S. Ulrich, H. Schubert, and G. R. Newkome. Modern terpyridine chemistry. *Angew. Chem. Int. Ed.*, 46:118–126, 2007.
- [308] A. D'Aleo, E. Cecchetto, L. De Cola, and R. M. Williams. Metal ion enhanced charge transfer in a terpyridine-bispyrene system. *Sensors*, 9:3604–3626, 2009.
- [309] X. S. Li, X. Chen, B. F. Yuan, and Q. Y. Feng. Phosphonate-modified metal oxides for the highly selective enrichment of phosphopeptides. *RSC Adv.*, 5:7832–7841, 2015.
- [310] H. Ma, O. Acton, D. O. Hutchins, N. Cernetica, and J. K. Jen. Multi-functional phosphonic acid self-assembled monolayers on metal oxides as dielectrics, interface modification layers and semiconductors for low-voltage

- high-performance organic field-effect transistors. *Phys. Chem. Chem. Phys.*, 14:14110–14126, 2012.
- [311] C. Tudisco, V. Oliveri, M. Cantarella, V. Vecchio, and G. G. Condorelli. Cyclodextrin anchoring on magnetic Fe_3O_4 nanoparticles modified with phosphonic linkers. *E. J. Inorg. Chem.*, 32:25603–25605, 2012.
- [312] S. M. Kang, S. C. Jang, G. Y. Kim, C. S. Lee, C. Roh, and S. K. Huh. A rapid in situ colorimetric assay for cobalt detection by the naked eye. *Sensors*, 16(626):1–10, 2016.
- [313] H. Zhu, J. Fan, B. Wang, and X. Peng. Fluorescent, mri, and colorimetric chemical sensors for the first-row d-block metal ions. *Chem. Soc. Rev.*, 44:4337–4366, 2015.
- [314] D. M. Dobkin. *The RF in RFID: passive UHF RFID in practice*. Technology and Engineering. Newnes, 2nd edition, 2012.
- [315] RFID Handbook: Fundamentals, Radio Frequency Identification Applications in Contactless Smart Cards, and Near-Field Communication. *Finken-zeller, K. and Muller, D.* Wiley, 3rd edition, 2010.
- [316] V. Chawla and H. D. Sam. Frequency tunable fluidic annular slot antenna. *Communications Magazine IEEE*, 45(9):11–17, 2007.
- [317] Printed circuits handbook. *Coombs, C. F.* Handbooks. McGraw-Hill, 6th edition, 2006.
- [318] N. Bessis and C. Dobre. *Big Data and Internet of Things: A Roadmap for Smart Environments*. Computers. Springer, 1st edition, 2014.
- [319] I. Singh and V.S. Tripathi. Micro strip patch antenna and its applications: a survey. *AMA Conferences 2015-Sensors*, 2(5):718–722, 2011.
- [320] N. Popovic. Uhf rfid antenna: Printed dipole antenna with a cps matching circuit and inductively coupled feed. *Intern. J. of Engin. Bus. Manag.*, 4(20):718–722, 2012.
- [321] N. Popovic. Uhf rfid antenna: Printed dipole antenna with a cps matching circuit and inductively coupled feed. *Intern. J. of Engin. Bus. Manag.*, 4(20):718–722, 2012.

- [322] J. James and P.S. Hall. *Handbook of Microstrip Antennas*. Electromagnetic waves. IEE, 1st edition, 1989.
- [323] R. Garg. *Microstrip Antenna Design Handbooks*. Artech House, 2nd edition, 2001.
- [324] G. M. Yang, K. Naishadam, and N. X. Sun. Loading effects of self-biased magnetic films on patch antennas with substrate/superstrate sandwich structure. *IET Microwaves, Antennas Propagat.*, 4(8):1172–1181, 2010.
- [325] M. Murray and R. R. Franklin. Frequency tunable fluidic annular slot antenna. *Antennas and Propagation Society International Symposium (APSURSI)*, pages 286–287, 2013.
- [326] M. Van Lieshout, L. Grossi, G. Spinelli, S. Helmus, L. Kool, L. Pennings, R. Stap, T. Veugen, B. Van der Waaij, and C. Borean. A practical test for univariate and multivariate normality. Technical report, Luxembourg, European Commission, Directorate-General Joint Research Centre, Institute for Prospective Technological Studies, 2007.
- [327] N. C. Wu, M. A. Nystrom, T. R Lin, and H. C Yu. Challenges to global rfid adoption. *Technovation*, 26(12):1317–1323, 2012.
- [328] N. C. Wu, M. A. Nystrom, T. R Lin, and H. C Yu. Chipless rfid: Bar code of the future. *Microwave Magazine, IEEE*, 11(7):87–97, 2010.
- [329] V. Subramanian, P. C. Chang, D. Huang, J. B. Lee, J. Molesa, D. R. Redinger, and S. K. Volkman. All-printed rfid tags: Materials, devices, and circuit implications. *19th International Conference on Vlsi Design, Proceedings*, pages 709–714, 2009.
- [330] S. Botao, C. Qiang, Y. Amin, D. S. Mendoza, L. Ran, and Z. Li-Rong. An ultra-low-cost rfid tag with 1.67 gbps data rate by ink-jet printing on paper substrate. *Solid State Circuits Conference (A-SSCC), 2010 IEEE Asian*, pages 1–4, 2010.
- [331] N.C. Karmakar. *Chipless RFID Sensors*. Wiley, 1st edition, 2016.
- [332] C. C. Karmakar. *Handbook of Smart Antennas for RFID Systems*. Wiley, 1st edition, 2010.

- [333] J. Kroupa, J. Fousek, N. R. Ivanov, M. B. Brezina, Pavel, A. Fouskova, V. Lhotska, V. Petricek, and I. Císarova. New data on the phase transition in phenanthrene. *Solid State Comm.*, 66(10):1003–1006, 2011.
- [334] E. Amin, S. Bhuiyan, C. Karmakar, and B. Winther-Jensen. The humidity dependence of the electrical conductivity of a soluble polyaniline/poly(vinyl alcohol) composite. *J. Mat. Chem.*, 7(12):2363–2366, 1997.
- [335] B. Gilleo. *Polymer Thick Film Today's emerging technology for a clean environment tomorrow*. Electrical Engineering. Springer, 1st edition, 1995.
- [336] V. Chawla and H. D. Sam. Colorimetric gas sensor for rfid applications. *AMA Conferences 2015-Sensors*, 1:718–722, 2015.
- [337] J. Coubart, D Briand, J. Damon-Lacoste, J. Wolleinstein, and F. De Rooji. Evaluation of ph-based colorimetric films for ammonia detection using optical waveguides. *Sensors and Actuators B*, 143:62–70, 2009.
- [338] J. Coubart, D Briand, J. Damon-Lacoste, J. Wolleinstein, and F. De Rooji. Colorimetric gas sensors based on waveguides made on plastic foils. *Procedia Chemistry*, 1:576–579, 2009.
- [339] Jr. Erlinger and Philip Charles. Colorimetric gas sensor for rfid applications, 06 2006.
- [340] M. Caironi and Y. Y. Noh. *Large Area and Flexible Electronics*. Wiley, 1st edition, 2015.
- [341] B. H. Nguyen, , and Nguyen V. H. Promising applications of graphene and graphene-based nanostructures. *Adv. Nat. Sci.: Nanosci. Nanotechnol.*, 7(023002):1–16, 2016.
- [342] F. Withers, H. Yang, L. Britnell, E. Rooney, A. P. Lewis, A. Felten, C. R. Woods, V. Sanchez Romaguera, T. Georgiou, A. Eckmann, Y. J. Kim, S. G. Yeates, J. Haigh, A. K. Geim, K. S. Novoselov, and C. Casiraghi. Heterostructures produced from nanosheet-based inks. *Nano Lett.*, 7(023002):3987–33992, 2016.
- [343] H. Kipphan. *Handbook of Print Media*. Technologies and Production Methods. Kipphan, Helmut Ed., 2001.

- [344] T. H. Costa, E. Songa, R. P. Tortoricha, and J. W. Choi. A paper-based electrochemical sensor using inkjet-printed carbon nanotube electrodes. *ECS J. Solid State Sci. Technol.*, 4(10):S3044–S3047, 2015.
- [345] J. A. Lee, J. W. Lee, B. K. Ju, D. S. Yoon, K. P. Paek, and H. Y. Lee. Improvement of field-emission properties of screen printed carbon nanotube films via argon plasma treatment. *J. of Electrochem. Soc.*, 153(6):H111–H114, 2006.
- [346] M. Lisunova, Y. Lisunova, S. Lee, J. Kim, K. Joo, Y. Kim, D. Zang, and H. Moon. Field emission properties of screen-printed activated carbons. *Carbon*, 47(10):1119–1125, 2009.
- [347] A. Kamyshny and S. Magdassi. Conductive nanomaterials for printed electronics. *Small*, 10(17):3515–3525, 2014.
- [348] R. Sangoi, C. G. Smith, M. D. Seymour, N. J. Venkataraman, D. M. Clark, M L. Kleper, and B. E. Kahn. Printing radio frequency identification (rfid) tag antennas using inks containing silver dispersions. *J. of Disp. Sci. and Tech.*, 25(4):513–522, 2004.
- [349] M. L. Kepler. *Printed Electronics and the Automatic Identification of Objects: An Investigation of the Emerging and Developing Technologies Related to the Generation Beyond Print-on-paper*. Graphic Arts Technical Fndt, 1st edition, 2005.
- [350] J. Perruisseau-Carrier. Graphene for antenna applications: Opportunities and challenges from microwaves to thz. *Loughborough Antennas Propagation Conference, 2012, UK*, pages 1–5, 2012.
- [351] E. Jewell, B. Philip, and Peter Greenwood. Improved manufacturing performance of screen printed carbon electrodes through material formulation. *Biosensors*, 6(30):1–10, 2016.
- [352] D. H. Shin, S. Jeong, S. Woo, Y. Kim, H. Yem, H. Kang, M. Cha, S. Cho, Y. Piao, and M. Kang. A self-reducible and alcohol-soluble copper-based metal-organic decomposition ink for printed electronics. *Appl. Mater. Interfaces*, 6:3312–3319, 2014.

- [353] Y. Kim, B. Lee, S. Yang, I. Byun, I. Jeong, and S. M. Cho. Use of copper ink for fabricating conductive electrodes and rfid antenna tags by screen printing. *Curr. Appl. Phys.*, 12:473–478, 2012.
- [354] K. Black, J. Singh, D. Mehta, S. Sung, J. Christopher, S. Sutcliffe, and P. R. Chalker. Silver ink formulations for sinter-free printing of conductive films. *Sci. Rep.*, 6(20814):1–7, 2016.
- [355] I. Puchades, J. E. Rossi, E. Cress, C. D. Naglich, and B. E. Land. Carbon nanotube thin-film antennas. *ACS Appl. Mater. Interfaces*, 8:20986–20982, 2016.
- [356] D. G. Fang. *Antenna Theory and Microstrip Antennas*. Technology and Engineering. Taylor and Francis, 2009.
- [357] R. Garg, B. Prakash, I. Bahal, and A. Ittipiboon. *Microstrip Antenna Design Handbook*. Antennas and propagation. Artech House, 2001.
- [358] I. G. Torgvonikov. *Dielectric Properties of Wood and Wood-Based Materials*. Wood Science. Springer, 1993.
- [359] W. F. Alamusi, H. Yuan, Y. Surina, N. Li, H. M. Hu, Y. L. Ning, L. K. Liu, S. Wu, Atobe, and H. Fukunaga. Ultrasensitive strain sensors of multiwalled carbon nanotube/epoxy nanocomposite using dielectric loss tangent. *Applied Physics Letters*, 103(22):221903(1)–221903(6), 2013.
- [360] Z. Wang and G. H. Zhao. Microwave absorption properties of carbon nanotubes-epoxy composites in a frequency range of 2-20 ghz. *OJCM*, 103(22):17–23, 2013.
- [361] Z. Wang, J. Luo, and G. H. Zhao. Dielectric and microwave attenuation properties of graphene nanoplatelet/epoxy composites. *AIP Advances*, 4(1):017139(1)–221903(9), 2014.
- [362] K. S. Moon, H. D. Choi, H. Lee, L. H. Cho, G. H. Yoon, and H. Su. Dielectric properties of epoxy-dielectrics-carbon black composite for phantom materials at radio frequencies. *Appl. Pol. Scie.*, 4(1):1294–1301, 2000.
- [363] G. W. Hanson. Fundamental transmitting properties of carbon nanotube antennas. *IEEE Transactions on antenna e propagation*, 56(3):3426–3436, 2005.

- [364] M. Aidi and T. Aguilu. Electromagnetic modeling of coupled carbon nanotube dipole antennas based on integral equations system. *Progress In Electromagnetics Research*, 40:179–193, 2014.
- [365] S. M. Abbas, S. Paul, J. Sen, P. R. Gupta, P. Malakar, and S. Chattopadhyay, S. Banerjee. Aspect ratio: A major controlling factor of radiation characteristics of microstrip antenna. *Appl. Pol. Scie.*, 3(11):8337(1)–8337(6), 2011.
- [366] X. Huang, A. K. Geim, T. Leng, X. Zhang, K. S. Novoselov, J. C. Chen, and H. K. Zhirun, H. Chang. Binder-free highly conductive graphene laminate for low cost printed radio frequency applications. *App. Phys. Lett.*, 106(203105):1–4, 2015.
- [367] J.S. Gomez-Diaz, M. Tamagnone, and J. Perruiseau-Carrier. Graphene antennas: Can integration and reconfigurability compensate for the loss? *2013 European Microwave Conference*, pages 369–372, 2013.
- [368] L. Pierantoni, D. Mencarelli, M. Bozzi, R. Moro, and S. Bellucci. Graphene-based electronically tuneable microstrip attenuator. *Nanomaterials and Nanotechnology*, 4(18):1–6, 2014.
- [369] J.S. Gomez-Diaz, C. Moldovan, S. Capdevila, J. Romeu, L. S. Bernard, L. Magrez, A. M. Ionescu, and J. Perruiseau-Carrier. Self-biased reconfigurable graphene stacks for terahertz plasmonics. *Nature Comm.*, 6(6334):925–932, 2013.
- [370] N. Haider, D. Caratelli, and A. G. . Yarovoy. Circular beam-reconfigurable antenna base on graphene-metal hybrid. *Nanomaterials and Nanotechnology*, (869170):1–14, 2013.
- [371] H. Lee, G. Shaker, K. Naishadham, M. Xiaojuan Song, McKinley, B. Wagner, and M. Tentzeris. Carbon-nanotube loaded antenna-based ammonia gas sensor. *IEEE transaction on microwaves theory and techniques*, 59(10):2665–2673, 2011.
- [372] S. Manzari, C. Occhiuzzi, S. Nawale, A. Catini, C. Di Natale, and G. Marrocco. Polymer-doped uhf rfid tag for wireless-sensing of humidity. *IEEE Int. Conf. on RFID*, pages 124–129, 2012.

- [373] A. Flujiwara, K. Ishii, H. Suematsu, K. Kataura, V. Maniwa, S. Suzuki, and Y. Achiba. Gas adsorption in the inside and outside of single walled carbon nanotube. *Chem. Phys. Lett.*, 336(3):622–625, 2001.
- [374] P. G. Collins, K. Bradley, M. Ishigami, and A. Zettl. Extreme oxygen sensitivity of electronic properties of carbon nanotubes. *Science*, 287(5459):1801–1804, 2000.
- [375] C. Marliere, P. Poncharal, L. Vaccarini, and A. Zahab. Effect of gas adsorption on the electrical properties of single-walled carbon nanotube mats. *Proc. Mater. Res. Soc. Symp.*, 593(5453):622–628, 2000.
- [376] M. Zhaozong and L. Zhen. Rfid tag as a sensor - a review on the innovative designs and applications. *Measurement Science Review*, 6(6):305–315, 2016.
- [377] A. S. Finnmore, M. R. J. Scherer, R. Langford, S. Mahajan, S. Ludwigs, F. C. Meldrum, and U. Steiner. Nanostructured calcite single crystals with gyroid morphologies. *Adv. Mat.*, 21(38):3928–3932, 2009.
- [378] D. Zhang, G. Li, X. Yang, and J. C. Yu. A micrometer-size tio₂ single-crystal photocatalyst with remarkable 80 level of reactive facets. *Chem. Comm.*, (29):4381–4383, 2009.
- [379] G. Liu, C. Jimmy, Z. Yu, L Gao Qing, and M. H. Cheng. Crystal facet engineering of semiconductor photocatalysts: motivations, advances and unique properties. *Chem. Comm.*, (47):6763–6783, 2011.
- [380] W. Yue, X. Xu, J. S. Irvine, P. S. Pierrot S. Attidekou, C. Liu, H. He, D. Zhao, and W. Zhou. Mesoporous monocrystalline tio₂ and its solid-state electrochemical properties. *Chem. of Mat.*, 21(12):2540–2546, 2009.
- [381] Z. Bian, J. Zhu, J. Wen, F. Cao, Y. Huo, X. Qian, Y. Cao, M. Shen, H. Li, and Y. Lu. Single-crystal-like titania mesocages. *Angew. Chem. Int. Edn.*, 21(12):1105–1108, 2011.
- [382] G.H. Bogush, M.A. Tracy, and C.F. Zukoski. Preparation of monodisperse silica particles: Control of size and mass fraction. *Journal of Non-Crystalline Solids*, 104(1):95–106, 1988.
- [383] G.H. Bogush, M.A. Tracy, and C.F. Zukoski IV. Correction to ŠŠpreparation of monodisperse silica particles: Control of size and mass fractionŠŠ by g.h.

- bogush, m.a. tracy and c.f. zukoski iv, journal of non-crystalline solids 104 (1988) 95–106. *Journal of Non-Crystalline Solids*, 353(30):2932–2933, 2007.
- [384] G. Liu, C. H. Sun, H. G. Yang, S. C. Smith, L. Z. Wang, G. Q. Lu, and H. M. Cheng. Nanosized anatase tio₂ single crystals for enhanced photocatalytic activity. *Chem. Comm.*, 46:755–757, 2002.
- [385] D. Zhang, G. Li, H. Wang, K. M. Chan, and J. C. Yu. Biocompatible anatase single-crystal photocatalysts with tunable percentage of reactive facets. *Crystal Growth Design*, 10(3):1130–1137, 2010.
- [386] H. G. Yang, G. Liu, S. Z. Qiao, C. H. Sun, Y. G. Jin, S. C. Smith, J. Zou, H. M. Cheng, and G. Q. Lu. Solvothermal synthesis and photoreactivity of anatase tio(2) nanosheets with dominant 001 facets. *J. Am. Chem. Soc.*, 131(11):4078–4083, 2009.
- [387] B. Tian, H. Yang, X. Liu, S. Xie, C. Yu, J. Fan, B. Tu, and D. Zhao. Fast preparation of highly ordered nonsiliceous mesoporous materials via mixed inorganic precursors. *Chem. Comm.*, 17:1824–1825, 2002.
- [388] X. Zeng, J. Hu, X. Zhang, W. Zhou, N. Zhou, H. Liu, and S. Xie. Ethanol-assisted gel chromatography for single-chirality separation of carbon nanotubes. *Nanoscale*, (7):16273–16282, 2015.
- [389] H. Liu, T. Tanaka, Y. Urabe, and H. Kataura. High-efficiency single-chirality separation of carbon nanotubes using temperature-controlled gel chromatography. *Nanoletters*, (13):1996–2003, 2013.
- [390] L. Lutterotti and P. Scardi. Simultaneous structure and size-strain refinement by the rietveld method. *J. of Applied Crystallography*, 4(23):246–252, 1990.
- [391] L. Lutterotti, S. Matthies, H. R. Wenk, and A. S. Schultz. Combined texture and structure analysis of deformed limestone from time-of-flight neutron diffraction spectra. *J. of Applied Crystallography*, 2(81):594–600, 1997.
- [392] H. Rietveld. A profile refinement method for nuclear and magnetic structures. *J. Appl. Cryst.*, 2:4428–4453, 1969.
- [393] R. Lopez and R. Gomez. Band-gap energy estimation from diffuse reflectance measurements on sol-gel and commercial tio₂: a comparative study. *J. Sol-Gel Sci. and Tech.*, 61(1):1–17, 2012.

- [394] E. P. Barrett, L. G. Joyner, and P. P. Halenda. The determination of pore volume and area distributions in porous substances. i. computations from nitrogen isotherms. *J. Am. Chem. Soc.*, 73(1):373–380, 1951.
- [395] I. Gouzman, M. Dubey, M. D. Carolus, J. Schwartz, and S. L. Bernasek. Monolayer vs. multilayer self-assembled alkylphosphonate films: X-ray photoelectron spectroscopy studies. *Surf. Sci.*, 600:773–781, 2005.
- [396] D. Wagner, A.V. Naumkin, A. Kraut-Vass, J.W. Allison, C.J. Powell, and J.R.Jr. Rumble. Nist standard reference database 20, version 3.4 (web version). (<http://srdata.nist.gov/xps/>), 2016.
- [397] Md. K. Nazeeruddin, R. Splivallo, P. Liska, P. Comte, and M. Graetzel. A swift dye uptake procedure for dye sensitized solar cells. *Chem. Comm.*, pages 1456–1457, 2003.
- [398] Z. Wu, Z. Chen, X. Du, J. M. Logan, Nikolou M. Sippel, J., K. Kamaras, J. R. Reynolds, A. F. Tanner, D. B. and Hebard, and A. G Rinzler. Transparent, conductive carbon nanotube films. *Science*, 115:7747–7754, 2011.
- [399] X. Guo, M. Myers, S. Xiao, M. Lefenfeld, R. Steiner, J. Tulevski, G. S. Tang, J. Baumert, F. Leibfarth, J. T. Yardley, L. Michael Steigerwald, P. Kim, and C. T. Nuckolls. Chemoresponsive monolayer transistors. *PNAS*, 103(31):11452–11456, 1991.
- [400] S. Shankar, M. Lahav, and M. E. van der Boom. Coordination-based molecular assemblies as electrochromic materials: Ultra-high switching stability and coloration efficiencies. *J. Am. Chem. Soc.*, 137(12):4050–4053, 2015.
- [401] F. Fabregat-Santiago, G. Garcia-Belmonte, I. Ivan Mora-Sero, and J. Bisquert. Characterization of nanostructured hybrid and organic solar cells by impedance spectroscopy. *Phys. Chem. Chem. Phys.*, 13(20):9083–9118, 2011.
- [402] S. Shankar, M. Lahav, and M. E. van der Boom. Coordination-based molecular assemblies as electrochromic materials: Ultra-high switching stability and coloration efficiencies. *J. Am. Chem. Soc.*, 137(12):4050–4053, 2015.
- [403] J. E. Moser, M. Graetzel, and Q. Wang. Electrochemical impedance spectroscopy analysis of dye sensitized solar cells. *J. Phys. Chem. B*, 109(31):14945–14951, 2005.

- [404] H. G. Yang, G. Liu, S. Z. Qiao, C. H. Sun, Y. G. Jin, S. C. Smith, J. Zou, H. M. Cheng, and G. Q. Lu. Effect of ethanol on the micellization and gelation of pluronic p123. *Langmuir*, 24:12260–12266, 2008.
- [405] J. Schefer, R. McDaniel, , and Benno P. Schoenbom. Small-angle neutron scattering studies on brij-58 micelles. *J. Phys. Chem.*, 92:729–732, 1988.
- [406] K. Nagaveni, M.S. Hegde, N. Ravishankar, and G. Subbanna, G.N. and Madras. Synthesis and structure of nanocrystalline tio₂ with lower band gap showing high photocatalytic activity. *Langmuir*, 20(7):2900–2907, 2004.
- [407] M. Durr, S. Rosselli, A. Yasuda, and G. Nelles. Band-gap engineering of metal oxides for dye-sensitized solar cells. *J. Phys. Chem. B*, 110(43):21899–21902, 2006.
- [408] K. Fajans. Struktur und deformation der elektronenhüllen in ihrer bedeutung für die chemischen und optischen eigenschaften anorganischer verbindungen. *Naturwiss.*, 11:165–172, 1922.
- [409] T. Moeller and H. E. Kremers. Observations on the rare earths. li. an electrometric study of the precipitation of trivalent hydrous rare earth oxides or hydroxides. *J. Am. Chem. Soc.*, 48(6):395–406, 1944.
- [410] L. Bertoluzzi and S. Ma. On the methods of calculation of the charge collection efficiency of dye sensitized solar cells. *Phys. Chem. Chem. Phys.*, 15:4283–4285, 2013.
- [411] S. K. Pathak, A. Abate, P. Ruckdeschel, B. Roose, K. C. Godel, Y. Vaynzof, A. Santhala, S.I. Watanabe, D. J. Hollman, N. Noel, A. Sepe, U. Wiesner, R. Friend, H. J. Snaith, and U. Steiner. Effect of scandium on the structural and photocatalytic properties of titanium dioxide thin films. *Adv. Funct. Mater.*, 24(38):6046–6055, 2014.
- [412] S. K. Pathak, A. Abate, P. Ruckdeschel, B. Roose, K. C. Godel, Y. Vaynzof, A. Santhala, S.I. Watanabe, D. J. Hollman, N. Noel, A. Sepe, U. Wiesner, R. Friend, H. J. Snaith, and U. Steiner. Performance and stability enhancement of dye-sensitized and perovskite solar cells by al doping of tio₂. *Adv. Funct. Mater.*, 24(38).
- [413] G. D. Sharma, M. S. Roy, and S. P. and Singh. Improvement in the power conversion efficiency of thiocyanate-free ru(ii) based dye sensitized solar cells

- by cosensitization with a metal-free dye. *J. Mat. Chem.*, 22:18788–18792, 2012.
- [414] G. D. Sharma, M. S. Roy, and S. P. and Singh. Improved efficiency of over 10 in dye-sensitized solar cells with a ruthenium complex and an organic dye heterogeneously positioning on a single tio2 electrode. *J. Mat. Chem.*, 115(15):7747–7754, 2011.
- [415] F. Hennrich, R. Krupke, S. Lebedkin, K. Arnold, R. Fischer, D. E. Resasco, and M. M. Kappes. Radial breathing mode of single-walled carbon nanotubes: Optical transition energies and chiral-index assignment. *Phys. Rev. B*, 205438(72):1–16, 2005.
- [416] F. Hennrich, R. Krupke, S. Lebedkin, K. Arnold, R. Fischer, D. E. Resasco, and M. M. Kappes. Raman spectroscopy of individual single-walled carbon nanotubes from various sources. *J. Phys. Chem. B*, 21(109):10567–10573, 2005.
- [417] F. De Angelis, E. Fantacci, S. Mosconi, M. K. Nazeeruddin, and M. Graetzel. Absorption spectra and excited state energy levels of the n719 dye on tio2 in dye-sensitized solar cell models. *J. Phys. Chem. C*, 21(109):10567–10573, 2005.
- [418] H. G. Han, H. C. Weerasinghe, K. M. Kim, J. S. Kim, C. YiBing, D. J. Jones, A. B. Holmes, and T. H. Kwon. Ultra fast fabrication of flexible dye-sensitized solar cells by ultrasonic spray-coating technology. *Scientific Reports*, (14645):1–9, 2015.
- [419] J. A Fagan, M Zheng, C. A. Silvera Batista, V. Rastogi, A.R. Walker, J. R. Simpson, and C. Y. Khripin. Analyzing surfactant structures on length and chirality resolved (6,5) single-wall carbon nanotubes by analytical ultracentrifugation. *ACS Nano*, 7(4):3373–3387, 2013.
- [420] H. S. Hafez, I.S. Yahia, G.B. Sakr, M. S. A. Abdel-Mottaleb, and F. Yakuphanoglu.
- [421] W. Gomulya, J. Gao, and M. A. Loi. Conjugated polymer-wrapped carbon nanotubes: physical properties and device applications. *Eur. Phys. J. B*, pages 1–13, 2013.

- [422] P. Dong, Y. Zhu, R. P. Hauge, J. M. Zhang, J. and Tour, H. Feng, J. Wu, and L. Jun. Vertically aligned carbon nanotubes/graphene hybrid electrode as a tco- and pt-free flexible cathode for application in solar cells. *Journal of Materials Chemistry A*, 2:20902–20907, 2014.
- [423] W. J. Lee, E. Ramasamy, D. E. D Lee, and J. S. Song. Efficient dye-sensitized solar cells with catalytic multiwall carbon nanotube counter electrodes. *ACS Appl. Mater. Interfaces*, 6(1):20902–20907, 2009.
- [424] S. A. Haque, D. R. Tachibana, Y. and. Klug, and D. R. Durrant. Charge recombination kinetics in dye-sensitized nanocrystalline titanium dioxide films under externally applied bias. *J. Phys. Chem. B*, (102):1745–1749, 1998.
- [425] S. Ito, P. Liska, P. Comte, R. Charvet, P. Pechy, U. Bach, L. Schmidt-Mende, S. M. Zakeeruddin, A. Kay, N. K. Nazeeruddin, and Michael Graetzel. Control of dark current in photoelectrochemical (tio₂/i²Úi₃-) and dye-sensitized solar cells. *Chem. Commun.*, pages 4351–4353, 2005.
- [426] F. Guerin, Y. Tian, and J. H. Fendler. Dihexadecyl phosphate monolayer supported [ru(bpy)₃]²⁺ crystallites investigated by near-field scanning optical microscopy. *J. Phys. Chem. B*, 103(37):773–781, 1999.
- [427] Multiple Authors. Standard methods for the examination of water and wastewater. Technical report, The American Public Health Association, The American Water Works Association and The Water Environment Federation, 2007.
- [428] V. Oncescu, D. O'Dellb, and D Erickson. Smartphone based health accessory for colorimetric detection of biomarkers in sweat and saliva. *Lab on a chip*, 13(16):3232–3238, 2013.
- [429] R. L. Morris. Determination of iron in water in presence of heavy metals. *Anal. Chem.*, 24(8):1376–1378, 1952.
- [430] A. C. Ferrari, , and D. M. Basko. Raman spectroscopy as a versatile tool for studying the properties of graphene. *Nature Nanotech.*, 8:235–246, 2013.
- [431] J. B. Wu, X. Zhang, M. Ija, W. P. Han, X. F. Qiao, D. S. Jiang, A. C. Ferrari, P. H. Tan, and X. L. Li. Resonant raman spectroscopy of twisted multilayer graphene. *Nature Comm.*, 5(5309):1–11, 2014.

- [432] A.C. Ferrari, V. Meyer, J.C. Scardaci, C. Casiraghi, M. Lazzeri, F. Mauri, S. Piscanec, D. Jiang, K.S. Novoselov, S. Roth, and A.K. Geim. Raman spectrum of graphene and graphene layers. *Phys. Rev. Lett.*, 97(187401):1–4, 2006.
- [433] A. Eckmann, A. Felten, I. Verzhbitskiy, R. Davey, and C. Casiraghi. Raman study on defective graphene: Effect of the excitation energy, typology, and amount of defects. *Phys. Rev. B*, 88(035426):1–11, 2006.
- [434] Y. Y. Wang, T. D. Pham, K. Zand, J. Li, and P. J. Burke. Charging the quantum capacitance of graphene with a single biological ion channel. *ACS Nano*, 8(5):428–438, 2014.
- [435] C. Zhan, C. Neal, J. Wu, and D. Jiang. Quantum effects on the capacitance of graphene-based electrodes. *J. Chem. Phys. C*, 119(39):22297–22303, 2015.
- [436] M.Z. Hossain, S.L. Rumyantsev, D. Teweldebrhan, K. M. F. Shahi, M. Shur, and A. A. Baladin. Low frequency noise in conducting channels of topological insulator materials. *Phys. Status Solidi A*, 208(1):144–146, 2011.
- [437] J. Xia, F. Chen, J. Li, and N. Tao. Measurement of the quantum capacitance of graphene. *Nature Nanotechnology*, (4):505–509, 2009.
- [438] N. Haider, D. Caratelli, and A. G. Yarovoy. Recent developments in reconfigurable and multiband antenna technology. *Nanomaterials and Nanotechnology*, (869170):1–9, 2016.
- [439] J. Xia, F. Chen, J. Li, and N. Tao. Graphene terahertz plasmon oscillators. *IEEE Trans. Nanotechnol.*, 7(1):91–99, 2008.
- [440] J. Xia, F. Chen, J. Li, and N. Tao. Graphene terahertz plasmon oscillators. *IEEE Trans. Nanotechnol.*, 7(1):91–99, 2008.